Elena Ciappi · Sergio De Rosa
Francesco Franco · Jean-Louis Guyader
Stephen A. Hambric · Randolph Chi Kin Leung
Amanda D. Hanford *Editors*

Flinovia—Flow Induced Noise and Vibration Issues and Aspects-II

A Focus on Measurement, Modeling, Simulation and Reproduction of the Flow Excitation and Flow Induced Response

Springer

Flinovia—Flow Induced Noise and Vibration Issues and Aspects-II

Elena Ciappi · Sergio De Rosa
Francesco Franco · Jean-Louis Guyader
Stephen A. Hambric · Randolph Chi Kin Leung
Amanda D. Hanford
Editors

Flinovia—Flow Induced Noise and Vibration Issues and Aspects-II

A Focus on Measurement, Modeling, Simulation and Reproduction of the Flow Excitation and Flow Induced Response

Springer

Editors
Elena Ciappi
Department of Energy
and Transportation—I, INSEAN-C
National Research Council
Rome
Italy

Sergio De Rosa
Dipartimento di Ingegneria Industriale
Università degli Studi di Napoli
"Federico II"
Naples
Italy

Francesco Franco
Dipartimento di Ingegneria Industriale
Università degli Studi di Napoli
"Federico II"
Naples
Italy

Jean-Louis Guyader
Laboratoire Vibrations Acoustique
National Institute of Applied
Sciences of Lyon
Villeurbanne
France

Stephen A. Hambric
Center for Acoustics and Vibrations
ARL/Penn State
State College, PA
USA

Randolph Chi Kin Leung
Department of Mechanical Engineering
The Hong Kong Polytechnic University
Hung Hom, Kowloon
Hong Kong

Amanda D. Hanford
Center for Acoustics and Vibrations
ARL/Penn State
State College, PA
USA

ISBN 978-3-319-76779-6 ISBN 978-3-319-76780-2 (eBook)
https://doi.org/10.1007/978-3-319-76780-2

Library of Congress Control Number: 2018933509

Printed on acid-free paper

This Springer imprint is published by the registered company Springer International Publishing AG part of Springer Nature
The registered company address is: Gewerbestrasse 11, 6330 Cham, Switzerland

Preface

The first International Symposium on Flow Induced Noise and Vibration Issues and Aspects (Flinovia) was held in Rome, Italy, in November 2013 at the Italian Consiglio Nazionale delle Ricerche (CNR), and co-sponsored by CNR-INSEAN, the University of Naples, and the Lyon Acoustics Centre (CELYA). Seventeen presentations were given by authors from Europe, the Americas, and Asia spanning experimental and numerical methods for quantifying flow-induced forcing functions, vibration response, and radiated sound. Most of the presentations were later expanded into chapters in the first book of Flinovia proceedings, also published by Springer.

The second Flinovia was hosted at Penn State University in the USA on April 27–28, 2017. The Flinovia symposia are sponsored events, with no registration fees for participants. Flinovia II was co-sponsored by the Penn State Center for Acoustics and Vibration (CAV), the Penn State Institute for CyberScience (ICS), the International Institute for Noise Control Engineering (I-INCE), and the United States Office of Naval Research (ONR).

The topics at the second Flinovia were broader, with 30 presentations spanning two days. Half of the presentations were from authors outside the USA, with papers from Australia, Belgium, Canada, France, Germany, Hong Kong, Italy, and Spain. USA papers included five from Penn State, and ten from other universities and companies, including Aerohydroplus, ESI, Florida Atlantic University, Illingworth and Rodkin, Kansas University, Lehigh University, University of Michigan, Notre Dame, and Virginia Tech.

Over 100 people attended the conference, representing academia, industry, and government. Twenty-five percent of attendees were from outside the USA, 35% were from industry and government, and 10% were from universities other than Penn State.

The papers in this volume (23 of the 30 presented at the symposium) are subdivided into two main groups: (1) flow and (2) vibroacoustic response. In the flow group, papers are further subdivided into:

- Forcing functions
- Sound sources
- Experiments
- Numerical methods

The vibroacoustic response group is subdivided into:

- Numerical methods
- Experiments
- Innovative applications

However, several papers span both flow and vibroacoustics, as well as numerical and experimental methods so the grouping is not exact. Several papers investigate flow-induced forces, particularly those caused by turbulent boundary layer (TBL) flow. Slow-moving flow over marine vehicles and automobiles along with high-speed flow over aircraft is addressed. The flow-induced forces radiate sound directly (see the 'Sound Sources' papers) as well as excite structures into vibration (see the 'Vibroacoustic' paper group). Numerical methods, like finite element analysis, and experiments are used to assess structural vibration response to flow excitation. Analytic and numerical methods, like boundary element analysis, are used to simulate sound radiated by flow turbulence. In one case, fully coupled fluid–structure interaction modeling is used to emulate human speech.

The second Flinovia was highly successful, growing the number of authors and participants from the first meeting in 2013. Future meetings are being planned and will maintain the features of the first two—two days of presentations with a small number of invited papers (no parallel sessions). Participation by industry and government will be strongly pursued to ensure transition of research. To monitor future developments, please visit www.flinovia.org.

State College, USA — Stephen A. Hambric
State College, USA — Amanda D. Hanford
Rome, Italy — Elena Ciappi
Naples, Italy — Sergio De Rosa
Naples, Italy — Francesco Franco
Villeurbanne, France — Jean-Louis Guyader
Hung Hom, Kowloon, Hong Kong — Randolph Chi Kin Leung
October 2017

Committees

Conference Days

April 27–28, 2017, Penn State Nittany Lion Inn, University Park, PA 16804, USA

Supporting Institutions Committee

Penn State Center for Acoustics and Vibration (CAV)
Penn State Institute for CyberScience (ICS)
International Institute for Noise Control Engineering (I-INCE)
United States Office of Naval Research (ONR)

International Organizing and Editors Committee

Stephen A. Hambric and Amanda D. Hanford, CAV, Center for Acoustics and Vibration, The Pennsylvania State University, University Park, PA, USA
Elena Ciappi, CNR-INSEAN, Marine Technology Research Institute, National Research Council of Italy, Rome, Italy
Sergio De Rosa and Francesco Franco, Department of Industrial Engineering, Aerospace Section, University of Naples Federico II, Italy
Jean-Louis Guyader Laboratoire Vibrations Acoustique, INSA-Lyon, Villeurbanne, France
Randolph Chi Kin Leung, The Hong Kong Polytechnic University, Hong Kong, P. R. China

Local Organizing Committee

Stephen A. Hambric, Amanda D. Hanford, Karen J. Thal

Contents

Part I
Flow–Forcing Functions

Low Wavenumber Models for Turbulent Boundary Layer Excitation of Structures

Peter D. Lysak, William K. Bonness and John B. Fahnline

Abstract When the spatial correlation length of the turbulent boundary layer (TBL) pressure fluctuations is small compared to the structural wavelengths, the vibration response can be determined by forming an equivalent point drive from the effective correlation area. This approach is equivalent to using the zero wavenumber component of the TBL pressure spectrum, so it only works for TBL models that are wavenumber white at low wavenumbers. In this work, a similar simplification is developed for TBL models with a wavenumber-squared dependence, that works for structural modes with a low-pass cutoff wavenumber. This introduces a boundary layer thickness dependence that results in significantly different predictions for structures excited by a developing boundary layer. Based on the analysis, an experimental setup is proposed that may help resolve some of the controversy surrounding the low wavenumber TBL spectrum.

1 Introduction

Turbulent boundary layer (TBL) pressure fluctuations are a source of vibration and noise in applications involving flow over surfaces. The excitation of a structure by TBL flow depends not only on the magnitude of the pressure fluctuations, but also on the spatial correlation. The relative scales of the spatial correlation and structural wavelengths play an important role in the analysis of these problems.

When the characteristic length of the spatial correlation is small compared to the structural wavelength of a mode, the modal response can be determined by integrating the effective correlation area of the pressure, and then driving the structure with an equivalent point load [1, 2]. In terms of the TBL pressure wavenumber-frequency spectrum, this is equivalent to using the value at zero wavenumber. Thus, this simplified analysis works well for TBL models that are wavenumber white at low wavenumbers, such as the Corcos model [3], but cannot be used for TBL models

P. D. Lysak (✉) · W. K. Bonness · J. B. Fahnline
Applied Research Laboratory, The Pennsylvania State University,
P.O. Box 30, State College 16804, USA
e-mail: pdl103@arl.psu.edu

E. Ciappi et al. (eds.), *Flinovia—Flow Induced Noise and Vibration Issues and Aspects-II*,
https://doi.org/10.1007/978-3-319-76780-2_1

with a wavenumber-squared dependence, like the Chase model [4, 5], because the approximation leads to zero net force being applied to the structure.

In this paper, an approximation that is similar to the effective correlation area is developed for the Chase model. The method only works when the mode wavenumber sensitivity function can be approximated as a low-pass filter with a characteristic cutoff wavenumber. However, an interesting outcome of this development is that it introduces a boundary layer thickness dependence to the forcing function, which is not present in the Corcos model or other wavenumber-white models. This can lead to significantly different predictions of the vibration for structures excited by a developing boundary layer.

The nature of the low wavenumber TBL spectrum has not yet been conclusively determined experimentally. While the amplitude of the low wavenumber spectrum has been identified by backing out the forcing function from vibration measurements [6, 7], there is still controversy as to whether it is wavenumber white. Based on the analysis developed in this paper, an experimental setup is proposed that could possibly help to resolve some of the controversy surrounding the low wavenumber spectrum.

2 TBL Excitation of a Structure

Before examining the differences in the low wavenumber TBL models, it is helpful to briefly review the general framework for analyzing the vibration of a structure due to a stochastic forcing function. To start, the analysis will be formulated in physical coordinates rather than wavenumber space, as this is usually more intuitive. Some of the features of the TBL pressure cross-spectrum will be illustrated using the Corcos model.

2.1 General Formulation of the Vibration Response

The vibration of a structure excited by TBL flow can be analyzed using a modal analysis approach [1]. The main idea is to relate the cross-spectrum of the vibration to the cross-spectrum of the TBL pressure fluctuations. First, the cross-spectrum of the acceleration between two points $\mathbf{x}$ and $\mathbf{y}$ is written as a modal expansion:

$$\Gamma_{aa}(\mathbf{x}, \mathbf{y}, \omega) = \sum_m \sum_n \psi_m(\mathbf{x})\, \psi_n(\mathbf{y})\, H_m(\omega)\, H_n^*(\omega)\, \phi_{mn}(\omega)\ , \tag{1}$$

where m and n represent the mode numbers, $\psi_m(\mathbf{x})$ and $\psi_n(\mathbf{y})$ are the corresponding mass-normalized mode shapes, $H_m(\omega)$ and $H_n^*(\omega)$ are the modal frequency response functions (with * representing the complex conjugate), and $\phi_{mn}(\omega)$ is the modal force matrix. The modal frequency response function for mode n depends on the natural frequency ω_n and loss factor η_n and is given by

$$H_n(\omega) = \frac{(\omega/\omega_n)^2}{1-(\omega/\omega_n)^2 + i\eta_n} \ . \tag{2}$$

The modal force matrix is determined from the cross-spectrum of the TBL pressure fluctuations by

$$\phi_{mn}(\omega) = \iint \psi_m(\mathbf{x})\, \psi_n(\mathbf{y})\, \Gamma_{pp}(\mathbf{x}, \mathbf{y}, \omega)\ \mathrm{d}^2\mathbf{x}\ \mathrm{d}^2\mathbf{y} \ . \tag{3}$$

The integrations over $\mathbf{x}$ and $\mathbf{y}$ are performed over the entire surface of the structure that is excited by the TBL.

2.2 Corcos Model for the TBL Pressure Cross-Spectrum

The Corcos model [3] is perhaps the most widely used and straightforward model for the TBL pressure cross-spectrum. In this model, the cross-spectrum is expressed as the product of the point pressure spectrum times streamwise and cross-stream spatial correlation functions. The point pressure spectrum $\Phi_{pp}(\omega)$ is assumed to be the same at both points $\mathbf{x}$ and $\mathbf{y}$ because the TBL is considered to be homogeneous over the region where the spatial correlation is significant. Then, if the streamwise and cross-stream spatial correlation functions are assumed to depend only on the separation distance $\mathbf{r} = \mathbf{y} - \mathbf{x}$, the cross-spectrum can be expressed as

$$\Gamma_{pp}(\mathbf{r}, \omega) = \Phi_{pp}(\omega)\ \exp\left(-\alpha_1 \left|\frac{\omega r_1}{U_c}\right|\right) \exp\left(-\alpha_3 \left|\frac{\omega r_3}{U_c}\right|\right) e^{i(\omega r_1/U_c)} \ , \tag{4}$$

where r_1 and r_3 are the components of $\mathbf{r}$ in the streamwise and cross-stream directions, respectively, U_c is the convection velocity of the TBL pressure fluctuations, and $\alpha_1 \approx 0.1$ and $\alpha_3 \approx 0.7$ are empirical constants. The exponential decay functions model the decreasing correlation between points $\mathbf{x}$ and $\mathbf{y}$ as the separation distance increases. Figure 1 shows the cross-spectrum, normalized by the point spectrum $\Phi_{pp}(\omega)$, in the streamwise and cross-stream directions. For a given frequency ω, the x-axis can be interpreted as the separation distance normalized the quantity U_c/ω. In the streamwise direction, the decay is slower and the phase oscillates due to the convection of the turbulence in this direction.

For an arbitrary spatial correlation function $f(r)$, it is customary to define a correlation length as

$$\Lambda = \frac{1}{f(0)} \int_0^\infty f(r)\, \mathrm{d}r \ . \tag{5}$$

If the correlation function is modeled by an exponential decay, $f(r) = e^{-r/\Lambda}$, then the correlation length is simply equal to Λ. In the Corcos model, the streamwise

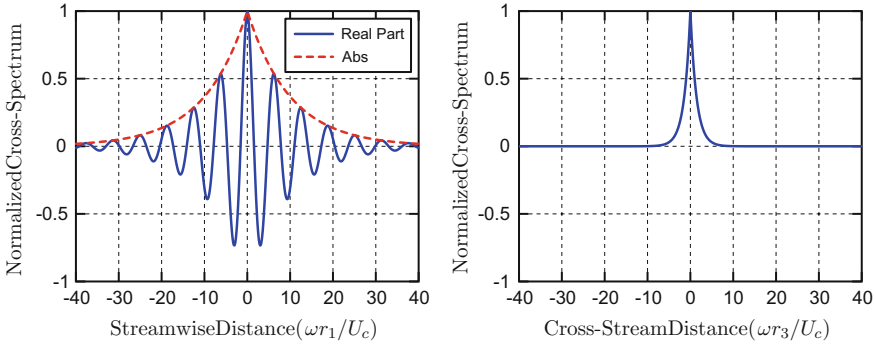

Fig. 1 TBL pressure cross-spectrum normalized by the point pressure spectrum using the Corcos model

and cross-stream (frequency-dependent) correlation lengths of the cross-spectrum are found to be

$$\Lambda_1(\omega) = \int_0^\infty \exp\left(-\alpha_1 \left|\frac{\omega r_1}{U_c}\right|\right) dr_1 = \frac{U_c}{\alpha_1|\omega|} \tag{6}$$

and

$$\Lambda_3(\omega) = \int_0^\infty \exp\left(-\alpha_3 \left|\frac{\omega r_3}{U_c}\right|\right) dr_3 = \frac{U_c}{\alpha_3|\omega|} \,. \tag{7}$$

However, if the phase oscillation is included in the streamwise correlation, the effective streamwise correlation length is about two orders of magnitude smaller:

$$\Lambda_{1,\text{eff}}(\omega) = \frac{1}{2}\int_{-\infty}^\infty \exp\left(-\alpha_1 \left|\frac{\omega r_1}{U_c}\right|\right) e^{i(\omega r_1/U_c)}\, dr_1 = \left(\frac{\alpha_1^2}{1+\alpha_1^2}\right)\frac{U_c}{\alpha_1|\omega|} \,. \tag{8}$$

(Note the integral has been extended from $-\infty$ to ∞ and divided by two because the integrand is no longer symmetric with the complex exponential included). The smaller effective correlation length is due to the cancellation of the positive and negative regions of the real and imaginary parts of the streamwise correlation. It is also useful to define an effective correlation area:

$$A_{\text{eff}}(\omega) = \left[2\Lambda_{1,\text{eff}}(\omega)\right]\left[2\Lambda_3(\omega)\right] = 4\left(\frac{\alpha_1/\alpha_3}{1+\alpha_1^2}\right)\left(\frac{U_c}{\omega}\right)^2 \,. \tag{9}$$

This represents the total area surrounding a reference point over which the pressure fluctuations can be considered to be acting coherently in order to produce a net force.

2.3 Simplifed Modal Force

As illustrated by the Corcos model, the TBL pressure cross-spectrum decays to zero as the separation between $\mathbf{x}$ and $\mathbf{y}$ increases. Also, the rate of decay increases with increasing frequency. This implies that in the high frequency range, the cross-spectrum will decay so rapidly that the variation in the mode shape becomes negligible over the scale of the correlation length [1]. Then, the modal force integrals defined in Eq. (3) can be separated:

$$\begin{aligned}\phi_{mn}(\omega) &= \iint \psi_m(\mathbf{x})\, \psi_n(\mathbf{x}+\mathbf{r})\, \Gamma_{pp}(\mathbf{r},\omega)\ \mathrm{d}^2\mathbf{r}\ \mathrm{d}^2\mathbf{x} \\ &\approx \left(\int \psi_m(\mathbf{x})\, \psi_n(\mathbf{x})\, \mathrm{d}^2\mathbf{x}\right)\left(\int \Gamma_{pp}(\mathbf{r},\omega)\, \mathrm{d}^2\mathbf{r}\right) . \end{aligned} \tag{10}$$

This greatly simplifies the calculation of the modal force compared to the full double integration, because the first factor is just a constant (independent of frequency) for each mode pair (m, n). The second factor represents the point pressure spectrum times the effective correlation area:

$$\int \Gamma_{pp}(\mathbf{r},\omega)\, \mathrm{d}^2\mathbf{r} = \Phi_{pp}(\omega) A_{\mathrm{eff}}(\omega) . \tag{11}$$

This simplified formulation of the modal force is equivalent to driving the structure with uncorrelated point drives distributed over the surface, which is sometimes called "rain-on-the-roof" loading [2]. It is important to understand that each point drive is not just the local pressure fluctuation, but the lumped sum force (squared per unit area) representing all the pressure fluctuations in the effective correlation area surrounding each point.

3 Wavenumber Formulation

In the previous section, the TBL excitation has been expressed in terms of the pressure cross-spectrum. Additional insight can be gained by transforming from the spatial domain to the wavenumber domain [8, 9]. In particular, the Chase model lends itself more naturally to analysis in the wavenumber domain. For simplicity, the structure will be assumed to be a rectangular flat plate in this section.

3.1 Wavenumber Transformations

If the TBL is assumed to be homogeneous, the pressure cross-spectrum depends only on the separation vector $\mathbf{r} = \mathbf{y} - \mathbf{x}$. In this case, the space-time characteristics

of the TBL pressure can be described by either the cross-spectrum $\Gamma_{pp}(\mathbf{r}, \omega)$ or the wavenumber-frequency spectrum $P(\mathbf{k}, \omega)$. These functions are related by the spatial Fourier transform:

$$\Gamma_{pp}(\mathbf{r}, \omega) = \int P(\mathbf{k}, \omega)\, e^{i\mathbf{k}\cdot\mathbf{r}}\, \mathrm{d}^2\mathbf{k}\ , \tag{12}$$

$$P(\mathbf{k}, \omega) = \frac{1}{(2\pi)^2} \int \Gamma_{pp}(\mathbf{r}, \omega)\, e^{-i\mathbf{k}\cdot\mathbf{r}}\, \mathrm{d}^2\mathbf{r}\ . \tag{13}$$

(The limits of integration extend from $-\infty$ to ∞ and are omitted for simplicity.) Likewise, the mode shape can be specified in physical space, $\psi_n(\mathbf{x})$, or in modal space, $F_n(\mathbf{k})$. Again, the two forms are related through the Fourier transform:

$$\psi_n(\mathbf{x}) = \int F_n(\mathbf{k})\, e^{i\mathbf{k}\cdot\mathbf{x}}\, \mathrm{d}^2\mathbf{k}\ , \tag{14}$$

$$F_n(\mathbf{k}) = \frac{1}{(2\pi)^2} \int \psi_n(\mathbf{x})\, e^{-i\mathbf{k}\cdot\mathbf{x}}\, \mathrm{d}^2\mathbf{x}\ . \tag{15}$$

The function $F_n(\mathbf{k})$ is often called the wavenumber sensitivity function. Using these relations, the modal force from Eq. (3) can also be calculated in wavenumber space:

$$\begin{aligned}
|\phi_{mn}(\omega) &= \iint \psi_m(\mathbf{x})\, \psi_n(\mathbf{x}+\mathbf{r})\, \Gamma_{pp}(\mathbf{r}, \omega)\ \mathrm{d}^2\mathbf{r}\ \mathrm{d}^2\mathbf{x} \\
&= \iint \psi_m(\mathbf{x})\, \psi_n(\mathbf{x}+\mathbf{r}) \left(\int P(\mathbf{k}, \omega)\, e^{i\mathbf{k}\cdot\mathbf{r}}\, \mathrm{d}^2\mathbf{k} \right) \mathrm{d}^2\mathbf{r}\ \mathrm{d}^2\mathbf{x} \\
&= \int \left\{ \int \psi_m(\mathbf{x}) \left(\int \psi_n(\mathbf{x}+\mathbf{r})\, e^{i\mathbf{k}\cdot\mathbf{r}}\, \mathrm{d}^2\mathbf{r} \right) \mathrm{d}^2\mathbf{x} \right\} P(\mathbf{k}, \omega)\, \mathrm{d}^2\mathbf{k} \\
&= \int \left\{ \int \psi_m(\mathbf{x}) \left[(2\pi)^2 F_n^*(\mathbf{k})\, e^{-i\mathbf{k}\cdot\mathbf{x}} \right] \mathrm{d}^2\mathbf{x} \right\} P(\mathbf{k}, \omega)\, \mathrm{d}^2\mathbf{k} \\
&= (2\pi)^4 \int F_m(\mathbf{k})\, F_n^*(\mathbf{k})\, P(\mathbf{k}, \omega)\, \mathrm{d}^2\mathbf{k}\ .
\end{aligned} \tag{16}$$

The interpretation of this result is that the mode shape acts as a wavenumber filter weighting the wavenumber distribution of the TBL pressure.

3.2 Low Wavenumber Modal Force Simplification

A simplification equivalent to the approximate modal force given by Eq. (10) can be formulated in the wavenumber domain:

$$\phi_{mn}(\omega) \approx \left[(2\pi)^2 \int F_m(\mathbf{k})\, F_n^*(\mathbf{k})\, \mathrm{d}^2\mathbf{k}\right]\left[(2\pi)^2 P(0,\omega)\right] . \tag{17}$$

The first factor follows from Parseval's theorem:

$$\int \psi_m(\mathbf{x})\, \psi_n(\mathbf{x})\, \mathrm{d}^2\mathbf{x} = (2\pi)^2 \int F_m(\mathbf{k})\, F_n^*(\mathbf{k})\, \mathrm{d}^2\mathbf{k} . \tag{18}$$

The second factor can be obtained from Eq. (13) with $\mathbf{k}$ set to zero:

$$\int \Gamma_{pp}(\mathbf{r},\omega)\, \mathrm{d}^2\mathbf{r} = (2\pi)^2 P(0,\omega) . \tag{19}$$

Since this factor was previously shown to equal the point pressure spectrum times the effective correlation area, it follows that the correlation area is related to the zero-wavenumber level of the TBL pressure spectrum. This is an important result, because it shows that if the spectrum is not wavenumber white and instead goes to zero, then no modal force is produced using this approximation. In other words, the modal force simplification only works for wavenumber-white TBL models.

3.3 TBL Pressure Wavenumber-Frequency Spectrum Models

The differences between the TBL pressure models are best understood in terms of the wavenumber-frequency spectrum. The Corcos and Chase models are representative of two classes of models with different low wavenumber behaviour.

Corcos Model. Taking the spatial Fourier transform of Eq. (4), the wavenumber-frequency spectrum representation of the Corcos model [3] is found to be

$$P(\mathbf{k},\omega) = \frac{\Phi_{pp}(\omega)}{\pi^2}\left[\frac{\Lambda_1}{1+\Lambda_1^2(k_1-\omega/U_c)^2}\right]\left[\frac{\Lambda_3}{1+\Lambda_3^2 k_3^2}\right] , \tag{20}$$

where as above $\Lambda_1 = \alpha_1^{-1}|U_c/\omega|$ and $\Lambda_3 = \alpha_3^{-1}|U_c/\omega|$. Figure 2 shows the Corcos wavenumber-frequency spectrum as a function of the streamwise wavenumber k_1 for a fixed frequency and with $k_3 = 0$. Most of the energy is located near the peak at the convective wavenumber $k_c = \omega/U_c$. At low wavenumbers, the spectrum is wavenumber white. The level of the low wavenumber spectrum in the Corcos model is known to be too high [10], and several alternative models keep the wavenumber-white behaviour but adjust the amplitude [11].

Chase Model. The Chase model [4, 5] is formulated directly in the wavenumber domain:

$$P(\mathbf{k},\omega) = \frac{\rho^2 U_\tau^3}{\left[K_+^2 + (b\delta)^{-2}\right]^{5/2}}\left\{C_T(k_1^2+k_3^2)\left[\frac{K_+^2+(b\delta)^{-2}}{k_1^2+k_3^2+(b\delta)^{-2}}\right] + C_M k_1^2\right\} , \tag{21}$$

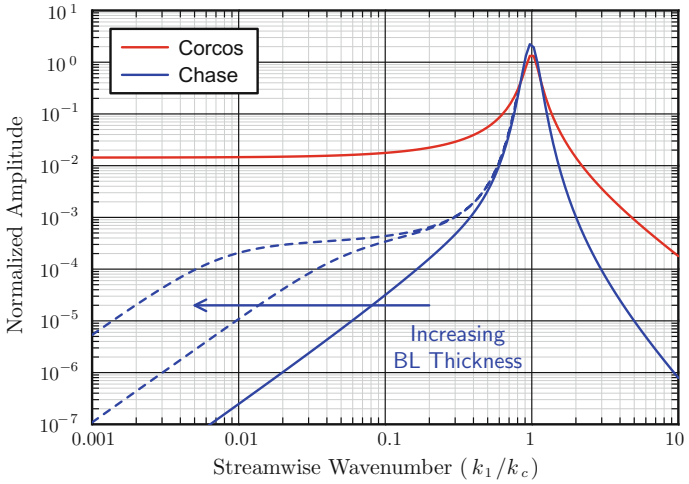

Fig. 2 TBL pressure wavenumber-frequency spectrum models, normalized by $\Phi_{pp}(\omega)/k_c^2$, for a fixed frequency with $k_3 = 0$

where

$$K_+^2 = \left(\frac{\omega - U_c k_1}{hU_\tau}\right)^2 + k_1^2 + k_3^2 \tag{22}$$

and the empirical constants are $b = 0.75$, $h = 3$, $C_T = 0.0047$, and $C_M = 0.155$. The Chase model also depends on two properties of the boundary layer: the friction velocity U_τ and the boundary layer thickness δ. At high frequencies, where $\omega \gg U_c/(b\delta)$, and assuming $U_c \gg U_\tau$, integrating over all wavenumbers gives a simple approximate result for the point pressure spectrum:

$$\Phi_{pp}(\omega) \approx \rho^2 U_\tau^4 \omega^{-1} \ . \tag{23}$$

The decision to model the wavenumber-frequency spectrum directly rather than beginning with the spatial correlation arises from a desire to explicitly model the low wavenumber behaviour based on theoretical considerations. Specifically, as the wavenumber approaches zero, the model takes on the asymptotic form

$$P(\mathbf{k}, \omega) = C_T h^3 b^2 \left(\frac{U_\tau}{\omega}\right)^2 \left(|\mathbf{k}|\delta\right)^2 \Phi_{pp}(\omega) \ . \tag{24}$$

Thus, the model has a k^2 dependence and vanishes at zero wavenumber, as follows from the Kraichnan-Phillips theorem [12]. (Note Chase also formulated a model that includes compressibility effects for very low wavenumbers, but only the

incompressible domain is considered here.) As seen in Fig. 2, the main difference between the Corcos and Chase models is in the low wavenumber region.

Although the Chase model is not wavenumber white at low frequencies, it does have a wavenumber-white plateau over intermediate wavenumbers ranging from about $1/(b\delta) < k_1 < 0.1(\omega/U_c)$, provided there is a wide enough separation between these two scales. The intermediate wavenumber range is captured by modifying Eq. (24) to include the wavenumber-white plateau:

$$P(\mathbf{k}, \omega) = C_T h^3 \left(\frac{U_\tau}{\omega}\right)^2 \left[\frac{|\mathbf{k}|^2}{|\mathbf{k}|^2 + (b\delta)^{-2}}\right] \Phi_{pp}(\omega) \ . \tag{25}$$

The level of the plateau (found by taking the limit for large $|k|$ in the above equation) does not depend on the boundary layer thickness, whereas the low wavenumber region below the plateau is proportional to $(k\delta)^2$. Figure 2 shows how the plateau becomes more apparent as the boundary layer thickness increases. The plateau level can be used as an alternative wavenumber-white model, since the Corcos level is known to be too high.

3.4 Approximate Modal Force for a k^2 Low Wavenumber Spectrum

As discussed above, if the low wavenumber spectrum is not wavenumber white, the effective correlation area approximation cannot be applied, since this would give a modal force of zero. In general, the Chase model requires full integration of the modal force using Eq. (16). Figure 3 illustrates this process for the (1,1) mode of a simply supported plate. To get the modal force, the TBL pressure spectrum is multiplied by the wavenumber sensitivity function, which acts as a wavenumber filter, and then integrated over all wavenumbers (including over k_3, which is not shown in the plot). For the (1,1) mode, the wavenumber sensitivity function acts as a low-pass filter, so the modal force is primarily produced by the low wavenumber region. However, the situation is more complicated than with a wavenumber-white model, because the low wavenumber region of the Chase model depends on the boundary layer thickness and the k^2 region starts below the wavenumber-white plateau.

Noting from Fig. 3 that certain modes resemble a low-pass wavenumber filter, it is possible to develop an approximation that retains the simplicity of the effective correlation area for these modes. Considering an idealized low-pass filter, which would correspond to a sinc function mode shape, and assuming radial symmetry for simplicity, Eq. (16) can be approximated by

$$\phi_{mn}(\omega) \approx \left[(2\pi)^2 \int F_m(\mathbf{k})\, F_n^*(\mathbf{k})\, \mathrm{d}^2\mathbf{k}\right] \left[\frac{(2\pi)^2}{\pi k_o^2} \int\limits_{|\mathbf{k}| \le k_o} P(\mathbf{k}, \omega)\, \mathrm{d}^2\mathbf{k}\right] , \tag{26}$$

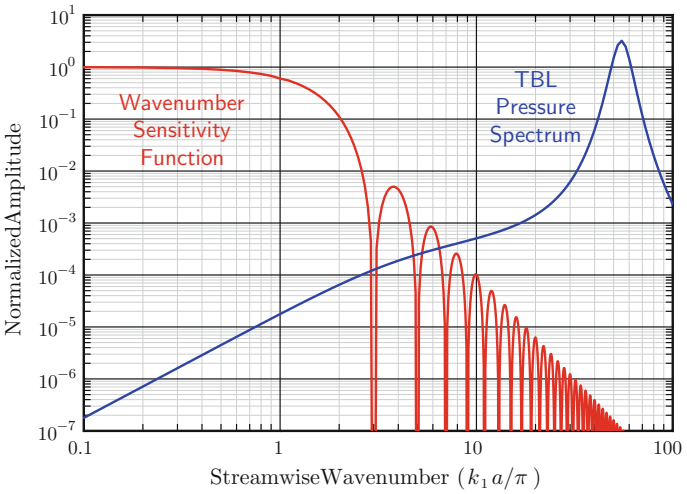

Fig. 3 Wavenumber sensitivity function of the fundamental mode of a simply supported square plate with side length a, along with the Chase model of the TBL pressure wavenumber-frequency spectrum at the resonance frequency of the mode

where k_o is an assumed cutoff wavenumber. The second factor represents the effective low wavenumber spectrum averaged over a circle in wavenumber space, with the radius equal to the cutoff wavenumber. Written in this form, the approximation is similar to Eq. (17), except an average low wavenumber value is used instead of the value at zero. Assuming the boundary layer is thin compared to the plate size, the cutoff wavenumber will fall in the k^2 region. Then, substituting the Chase k^2 low wavenumber model from Eq. (24), the second integral can be evaluated as

$$\int_{|\mathbf{k}|\le k_o} P(\mathbf{k},\omega)\,\mathrm{d}^2\mathbf{k} = \int_0^{k_o} (2\pi k)\left[C_T h^3 b^2 \left(\frac{U_\tau}{\omega}\right)^2 (k\delta)^2 \Phi_{pp}(\omega)\right]\mathrm{d}k$$
$$= \frac{\pi}{2} C_T h^3 b^2 \left(\frac{U_\tau}{\omega}\right)^2 k_o^4 \delta^2 \Phi_{pp}(\omega)\,. \tag{27}$$

Finally, the modal force approximation for the Chase model reduces to

$$\phi_{mn}(\omega) \approx \left[(2\pi)^2 \int F_m(\mathbf{k})\, F_n^*(\mathbf{k})\,\mathrm{d}^2\mathbf{k}\right]\left[2\pi^2 C_T h^3 b^2 \left(\frac{U_\tau}{\omega}\right)^2 (k_o\delta)^2 \Phi_{pp}(\omega)\right]. \tag{28}$$

This result is very similar to using a wavenumber-white model with Eq. (17), except that it depends on the cutoff wavenumber. In fact, the only difference between this result and using the Chase wavenumber-white plateau level from Eq. (25) is the factor

$\frac{1}{2}(bk_o\delta)^2$. This introduces a dependence on the boundary layer growth that will be examined in the next section.

4 Comparison of Model Results and Proposed Experiment

The approximate modal force equation developed in the previous section suggests there is a fundamental difference between using a wavenumber-white model and a k^2 model that could possibly be detected experimentally. In general, it is very difficult to directly measure the low wavenumber TBL pressure spectrum, because the measured pressures are usually dominated by the convective part of the fluctuations. The low wavenumber level can be inferred from the vibration response, but these measurements have not conclusively shown if the spectrum is wavenumber white. The idea proposed here only depends on the trend of the vibration measurements, which might be easier to determine.

Figure 4 shows an example structure where the two low wavenumber models lead to significantly different results. The structure consists of an array of plates (or panels) attached to a rigid frame, such that the vibration of the panels is not coupled. Considering only the first mode of each panel, the wavenumber sensitivity function acts as a low-pass filter, as previously shown in Fig. 3. When this structure is analyzed, an interesting dependence on the growth of the boundary layer emerges, as shown in Fig. 5. If the panels are rigid enough (see the figure caption for the parameters used in the example calculation), the resonance will occur in the frequency range where the point pressure spectrum is independent of the boundary layer thickness and only depends on the friction velocity, as in Eq. (23). The friction velocity slowly decreases as the boundary layer grows, leading to the prediction using a wavenumber-white model that the vibration of the panels at the first resonance decreases downstream. In contrast, the wavenumber-squared model depends on the square of the boundary layer thickness. This is a much stronger effect than the decreasing friction velocity, giving the opposite prediction that the vibration increases downstream. Because the two models predict opposite trends, an experiment based on this concept may be able to show which model is more accurate.

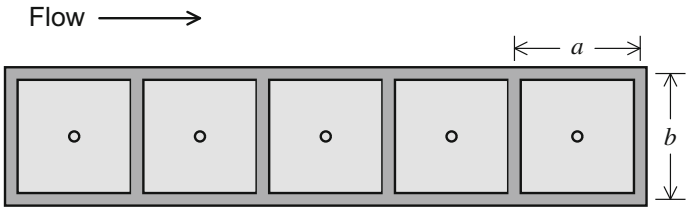

Fig. 4 Example structure that responds differently to wavenumber-white and wavenumber-squared excitation. The panels shown in light gray are attached to a rigid frame shown in dark gray, and accelerometers are located at the center of each panel

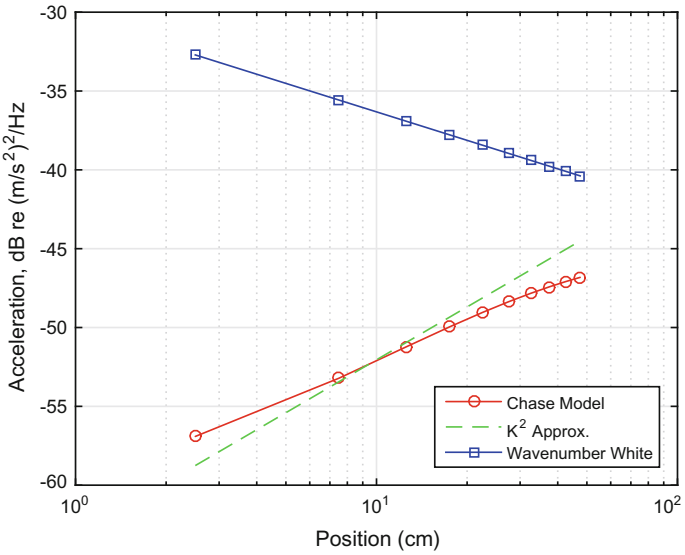

Fig. 5 Example calculations of the vibration at the first resonance peak (1943 Hz) for an array of 5 cm square aluminum panels of thickness 1 mm, excited by a developing TBL with free-stream velocity 5 m/s in water

Figure 5 also shows a comparison between using the full Chase model and numerically integrating over all wavenumbers to get the modal force with Eq. (16), and using the simple low-pass filter approximation from Eq. (28). For this calculation, the cutoff wavenumber was assumed to be $2\pi/a$. It can be seen that the approximate model gives a reasonable (but not highly accurate) result and explains the upward trend in the vibration as the boundary layer thickens downstream. The wavenumber-white results shown in Fig. 5 are based on the Chase low wavenumber plateau level.

5 Conclusion

A simplified modal force formulation similar to the effective correlation area approximation has been developed for the Chase TBL pressure model. The method works for modes that have a wavenumber sensitivity function approximating a low-pass filter, such as the fundamental mode of a simply supported plate. Comparing the results to using a wavenumber-white TBL model reveals a fundamental difference in the role of the boundary layer thickness on the forcing function. With a wavenumber-white model, such as the Corcos model or other models that adjust the wavenumber-white level, the local forcing function is predicted to be independent of the boundary layer thickness. In contrast, the wavenumber-squared dependence in the low wavenumber region of the Chase model predicts the forcing function to increase with the boundary

layer thickness. This leads to significantly different vibration predictions for structures excited by a developing boundary layer, such as an array of plates attached to a rigid frame aligned in the flow direction. It is proposed that an experiment based on this concept may help to resolve some of the controversy surrounding the nature of the low wavenumber TBL pressure spectrum.

References

1. Bonness, W.K., Fahnline, J.B., Lysak, P.D., Shepherd, M.R.: Modal forcing functions for structural vibration from turbulent boundary layer flow. J. Sound Vib. **395**, 224–239 (2017)
2. Ichchou, M.N., Hiverniau, B., Troclet, B.: Equivalent 'rain on the roof' loads for random spatially correlated excitations in the mid-high frequency range. J. Sound Vib. **322**, 926–940 (2009)
3. Corcos, G.M.: Resolution of pressure in turbulence. J. Acoust. Soc. Am. **35**(2), 192–199 (1963)
4. Chase, D.M.: Modeling the wavevector-frequency spectrum of turbulent boundary layer wall pressure. J. Sound Vib. **70**(1), 29–67 (1980)
5. Chase, D.M.: The character of the turbulent wall pressure spectrum at subconvective wavenumbers and a suggested comprehensive model. J. Sound Vib. **112**(1), 125–147 (1987)
6. Martin, N.C., Leehey, P.: Low wave number wall pressure measurements using a rectangular membrane as a spatial filter. J. Sound Vib. **52**(1), 95–120 (1977)
7. Bonness, W.K., Capone, D.E., Hambric, S.A.: Low-wavenumber turbulent boundary layer wall-pressure measurements from vibration data on a cylinder in pipe flow. J. Sound Vib. **329**, 4166–4180 (2010)
8. Hwang, Y.F., Maidanik, G.: A wavenumber analysis of the coupling of a structural mode and flow turbulence. J. Sound Vib. **142**(1), 135–152 (1990)
9. Hambric, S.A., Hwang, Y.F., Bonness, W.K.: Vibrations of plates with clamped and free edges excited by low-speed turbulent boundary layer flow. J. Fluids Struct. **19**, 93–110 (2004)
10. Borisyuk, A.O., Grinchenko, V.T.: Vibration and noise generation by elastic elements excited by a turbulent flow. J. Sound Vib. **204**(2), 213–237 (1997)
11. Graham, W.R.: A comparison of models for the wavenumber-frequency spectrum of turbulent boundary layer pressures. J. Sound Vib. **206**(4), 542–565 (1997)
12. Bull, M.K.: Wall-pressure fluctuations beneath turbulent boundary layers: some reflections on forty years of research. J. Sound Vib. **190**(3), 299–315 (1996)

Development of a Generalized Corcos Model for the Prediction of Turbulent Boundary Layer-Induced Noise

Anna Caiazzo, Roberto D'Amico and Wim Desmet

Abstract The characterization of the wall pressure field generated by a turbulent boundary layer (TBL) is a challenging problem in different fields. Its description is strictly dependent on the prediction of the noise and vibration induced by the flow-excited structure. TBL characterization often requires specific experimental setups and huge facilities, like wind tunnels, which are quite expensive. Usually, for simple configurations, semi-empirical or empirical models fit to experimental data are used to model the wall pressure characteristics. Many TBL models have been developed since the 1950s. Among others, the Corcos model has been widely used, especially because of its advantageous mathematical features that allow significantly reduced computational effort. However, an obvious problem with the Corcos model is its behaviour for wavenumbers below the convective peak. Within this paper, a Generalized Corcos model is considered for the prediction of TBL-induced noise. Being built on a two-dimensional Butterworth filter, such a model is characterized by two more parameters than Corcos, which are the order of the filters along the streamwise and spanwise direction. The applicability of such a model is here investigated considering two representative flow conditions: (1) low-speed flow; (2) high-speed flow. Particular attention is drawn to the effect of the order of the filters. In this way, it will be shown how an accurate description of the wavenumber-frequency spectrum at and below the convective peak can be given by using the Generalized Corcos model.

Keywords Turbulent boundary layer · Vibro-acoustic · Corcos · Generalized corcos

A. Caiazzo (✉) · R. D'Amico · W. Desmet
Department of Mechanical Engineering, Division PMA, KU Leuven,
Celestijnenlaan 300 B Box 2420, 3001 Heverlee, Belgium
e-mail: caiazzo89anna@gmail.com

W. Desmet
e-mail: wim.desmet@kuleuven.be

A. Caiazzo · W. Desmet
Flanders Make, Lommel, Belgium

E. Ciappi et al. (eds.), *Flinovia—Flow Induced Noise and Vibration Issues and Aspects-II*,
https://doi.org/10.1007/978-3-319-76780-2_2

1 Introduction

The wall pressure fluctuations induced by turbulent boundary layers (TBL) constitute a fundamental source of aerodynamic noise. Over the past years, their study is receiving a significant amount of attention, particularly when considering the need for improved vehicle comfort.

The flow-induced pressure associated with turbulence excites the vehicle structure, causing vibration and, therefore, noise. In the transportation industry, a large contribution to the interior noise of vehicles is due to such excitation. This has motivated engineers to properly model the wall pressure fluctuations induced by TBL. Different approaches can be used for this purpose. The most accurate and straightforward approach consists in Computational Fluid Dynamics (CFD) calculations, but this method is quite computationally intensive. On the other side, a stochastic source reconstruction is considered as an alternative to methods based on CFD simulations, particularly in the early design stage. Such stochastic models are an ideal choice to account for turbulent excitation, because they lead to a quick understanding and an efficient computation. These TBL models, being semi-empirical in nature, are based on fits to experimental data and are accurate only for simple configurations of the structure.

Among the existing mathematical models of TBL wall pressure fluctuations [1, 16, 17], the Corcos model [7, 8] is favored for its advantageous mathematical features and its accurate description of the wavenumber-frequency spectrum of the wall pressure in the convective domain. However, for wavenumbers below the coincidence frequency, experimental evidence suggests that it tends to overpredict the spectrum even up to 20 dB. On the contrary, other models such as Chase [4] or Smol'yakov-Tkachenko [22] are more accurate in that range, but they lack simplicity in the mathematical descriptions, with a significant impact on the computation time. This explains the versatility of the known Corcos model [5].

In this paper, a new model for turbulent boundary layer excitation in vibro-acoustic problems is analyzed [2]. As it generalizes the widely used Corcos model, it is called Generalized Corcos. Such a model is based on a two-dimensional Butterworth function rather than on a Lorentzian one as in the classic Corcos. From the latter, it preserves the main advantages, namely simple mathematics and a closed form solution. Indeed, as shown by D'Amico in [10, 11], integrating the Butterworth filter over an infinite frequency range leads to a procedure that is analogous to the one used for the Lorentzian function. Additionally, by changing the order of the Butterworth filters, it is possible to modify the rate of decay of the pressure distribution and, therefore, improve the classic Corcos model in the low-wavenumber domain.

The paper is organized as follows. In Sect. 2, the features of the wall pressure fluctuations of a TBL and of the most used semi-empirical models are summarized. Then, the spatial and wavenumber distributions of the Generalized Corcos model are given in Sect. 3. In Sect. 4, the position of the proposed model with respect to

the others is underlined by comparing it to the most used TBL models. Section 5 presents two application cases to benchmark the proposed findings against the most used models. Furthermore, a more detailed analysis on the effect of different order of the square magnitude of the Butterworth filter is addressed in Sect. 5.3. Finally, the conclusions of the work are summarized in Sect. 6.

2 Modelling of TBL Wall Pressure Fluctuations

The wall pressure disturbances generated by a TBL can be modelled as stochastic fluctuations riding on a steady current with vortexes conveyed in the direction of the flow at the convective velocity $U_c = h_c U_\infty$, with free-stream velocity U_∞ and convective constant h_c [21]. In general, the pressure field generated by a fully developed TBL on a flat and rigid surface, in a low Mach number with zero mean pressure gradient, can be considered as homogeneous in space and stationary in time. It can be represented by a space-time correlation function and its corresponding Fourier transform or wavevector-frequency spectrum. In particular, considering a flow in the x direction over the (x, z) plane, the following function can be defined

$$R_{pp}\left(\xi_x, \xi_z, \tau\right) = < p\left(x, z, t\right) p\left(x + \xi_x, z + \xi_z, t + \tau\right) > , \tag{1}$$

which represents the space-time cross correlation function of the pressure at two arbitrary space-time points (x, z) at time t, and $(x + \xi_x, z + \xi_z)$ at $t + \tau$. In Eq. (1), $\boldsymbol{\xi} \equiv (\xi_x, 0, \xi_z)$ is the spatial separation vector and the brackets $<>$ denote an ensemble average. By doing a time Fourier transformation, the spatial cross spectral density function (CSD) of the wall pressure fluctuations is then found as follows

$$\Psi_{pp}\left(\boldsymbol{\xi}; \omega\right) = \frac{1}{2\pi} \int_{-\infty}^{+\infty} R_{pp}(\boldsymbol{\xi}; \tau) \mathrm{e}^{-\mathrm{i}\omega\tau} \, \mathrm{d}\tau \ , \tag{2}$$

in which ω is the radian frequency.[1] Then, the spatial 2D Fourier transform of $\Psi_{pp}\left(\boldsymbol{\xi}; \omega\right)$ upon spatial separation gives the CSD function in the wavenumber-frequency domain as follows

$$\Psi_{pp}\left(\mathbf{k}; \omega\right) = \frac{1}{(2\pi)^2} \int_{-\infty}^{+\infty} \int_{-\infty}^{+\infty} \Psi_{pp}\left(\boldsymbol{\xi}; \omega\right) \mathrm{e}^{-\mathrm{i}(\boldsymbol{\xi} \cdot \mathbf{k})} \, \mathrm{d}\boldsymbol{\xi} \ , \tag{3}$$

where $\mathbf{k} \equiv (k_x, 0, k_z)$ is the two-dimensional wavevector containing the wavenumber components in the streamwise and spanwise directions of the fluid flow.

[1] The convention used here for the Fourier transform $\tilde{f}(\omega)$ of a function $f(t)$ is such that $\tilde{f}(\omega) = \frac{1}{2\pi} \int_{-\infty}^{+\infty} f(t) \mathrm{e}^{-\mathrm{i}\omega t} \, \mathrm{d}t$.

Throughout the years, many semi-empirical models of TBL have been developed in order to represent statistically the turbulent fluctuations. One of the earliest models that represents the wall pressure fluctuations of a TBL is proposed by Corcos [7, 8]. This model is nowadays used for its multiple advantages (such as, separable and convertible model, simple mathematical form that allows analytical integration and accurate description of the wavevector-frequency spectrum in the convective domain). Despite these advantages, it overpredicts the sub-convetive spectrum, varying slowly, as indicated by experimental data of low-wavenumber spectra [6, 12, 18].

It is important to notice that, for low Mach number flow, the low-wavenumber region is important for the possible coincidence with structural modes. Therefore, later researchers, notably Chase [4] and Smol'yakov-Tkachenko [22], proposed empirical models in order to describe the low-wavenumber range more accurately but keeping similar behaviour to Corcos in the convective domain. Given that, those models lack simplicity in the mathematical descriptions, requiring computationally costly numerical integrations. They are both non-separable in frequency and wavevector and characterized by many semi-empirical parameters strongly depending on the test conditions.

Therefore, even today, the complex nature of the TBL makes its modelling an active subject of research. In particular, the need of an accurate and, at the same time, efficient description of the wall pressure fluctuations in the low-wavenumber and convective range is still a challenge for researchers.

3 The Generalized Corcos Model

This section presents a generalization of the known Corcos model. The proposed model, called the Generalized Corcos model, is characterized by a Butterworth filter formulation and addresses some of the limitations found in modelling the wall pressure fluctuations generated by a TBL.

In the following subsections, some basic concepts of the Butterworth filter formulation are recalled in order to present the development of the generalized model. The spatial and frequency distribution of the Generalized Corcos model is also presented.

3.1 The Butterworth Filter Formulation

It is known [10, 11] that the square magnitude of a Butterworth filter represents a generalization of the Lorentzian function and is characterized by its order. For orders of unity, the Butterworth filter matches the Lorentzian. In the same way, the proposed model, characterized by a Butterworth filter formulation, can be defined as a generalization of the classic Corcos, which is instead based on a Lorentzian distribution. The analytical development of the model is presented in [2]; here only the basic steps are given. Essentially, in the Corcos wavenumber-frequency spectrum,

it is possible to identify the Lorentzian curve used in two dimensions:

$$\Psi_{pp}(k_x, k_z, \omega) = \phi(\omega) \frac{\frac{1}{\pi\alpha_\omega}}{1 + \left(\frac{k_x - k_\omega}{\alpha_\omega}\right)^2} \frac{\frac{1}{\pi\beta_\omega}}{1 + \left(\frac{k_z}{\beta_\omega}\right)^2} , \tag{4}$$

in which $\phi(\omega)$ the auto-spectrum and k_ω the centre wavenumber. The parameters α_ω and β_ω are here defined as follows [19],

$$\alpha_\omega = k_\omega \alpha_x = \frac{\omega}{U_c}\alpha_x \quad \text{and} \quad \beta_\omega = k_\omega \alpha_z = \frac{\omega}{U_c}\alpha_z . \tag{5}$$

Those parameters specify the width in the two directions. In Eq. (5), α_x and α_z are the longitudinal and lateral decay rates of the coherences, respectively. In general, for smooth rigid walls, the decay rates are in the range of $\alpha_x = 0.11$–0.12 and $\alpha_z = 0.7$–1.2, [21].

Equivalently, Eq. (4) can be written in the following form:

$$\Psi_{pp}(k_x, k_z, \omega) = \phi(\omega) B_1(k_x) B_1(k_z) , \tag{6}$$

where B_1 is the square magnitude of a Butterworth filter of order equal to one (i.e. the Lorentzian function). In general, for a filter of order n, it is given by the real-valued function of mathematical form:

$$B_n(k_x) = \frac{A_{k_x}}{1 + \left(\frac{k_x - k_\omega}{\alpha_\omega}\right)^{2n}} \quad \text{with} \quad A_{k_x} = \frac{n \sin\left(\frac{\pi}{2n}\right)}{\pi\alpha_\omega} , \tag{7}$$

where the constant A_{k_x} is the amplification factor of the filter with centre k_ω and cut-off value α_ω [9]. The $2n$ filter poles are then defined as

$$s_k = k_\omega + \alpha_\omega e^{-i\theta_k} \quad \text{with} \quad \theta_k = \frac{\pi}{2n}(1 + 2k) , \tag{8}$$

where the value k is an integer defining the position of a pole over a circle of radius α_ω and centre k_ω.

Figure 1 shows the square magnitude of the Butterworth filter for different orders n. The $k-$pole is in the lower half of the complex s plane (LHP) when $0 \leq k \leq n - 1$ and in the upper half of the complex s plane (UHP) when $n \leq k \leq 2n - 1$ [9]. If the order of the filter is increased, the shape of $B_n(k_x)$ becomes closer to the shape of a perfectly rectangular window. Whereas, if $n = 1$, the square magnitude of the Butterworth filter is equivalent to a Lorentzian funcion. A similar procedure is used on the k_z axis, such that $B_m(k_z)$ of order m can be defined with amplification factor A_{k_z} and cut-off value β_ω.

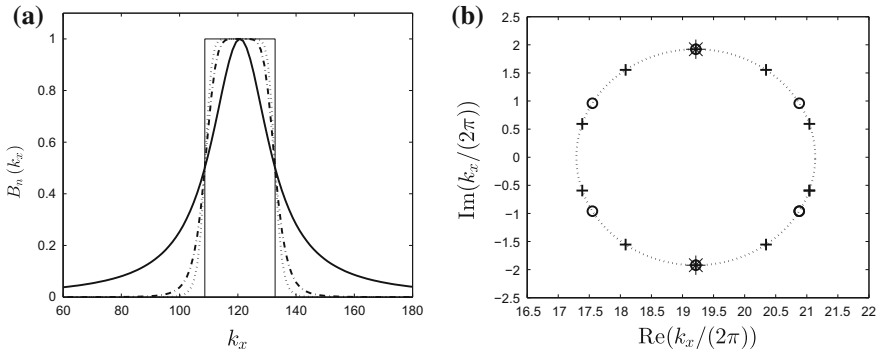

Fig. 1 **a** Comparison between rectangular window (*thin solid line*) and Butterworth filter of order n, centred at $k_\omega = \omega/U_c = 120$ with cut-off value $\alpha_\omega = 0.1k_\omega$; Butterworth filter of order $n = 5$ (*dotted line*), $n = 3$ (*dashed-dotted line*); Lorentzian function $n = 1$ (*bold solid line*). **b** Position of the $2n$ filter poles over the complex plane, $n = 5$ (+), $n = 3$ (∘), $n = 1$ (∗) [2, 9]

3.2 TBL *Spatial Correlation Function*

By generalizing Eq. (6) for a filter of order n along the streamwise direction and m along the spanwise direction, the spatial distribution of the Generalized Corcos model is obtained by the inverse transformation of the wavenumber spectral density function as follows:

$$\Psi_{pp}(\xi_x, \xi_z, \omega) = -\phi(\omega)\frac{A_{k_x} A_{k_z} \pi^2 \alpha_\omega \beta_\omega \exp(\mathrm{i}k_\omega \xi_x)}{nm} \sum_{k=0}^{n-1} \exp(-\mathrm{i}\theta_k - \mathrm{i}|\xi_x|\alpha_\omega \exp(-\mathrm{i}\theta_k)) \times \sum_{k=0}^{m-1} \exp(-\mathrm{i}\theta_k - \mathrm{i}|\xi_z|\beta_\omega \exp(-\mathrm{i}\theta_k)) \ , \tag{9}$$

for any real value of ξ_x and ξ_z.

The spatial CSD function found for the Generalized Corcos model, Eq. (9), is a weighted sum of exponential functions rather than a single exponential as found in Corcos. Even so, such a model is equivalent to the classic Corcos model when the order of the filter along the two directions equal to one [2].

The normalized spatial components of the Generalized Corcos model in the streamwise and spanwise directions are shown in Fig. 2 for $(n, m) = (2, 1)$ and decay rates of the coherences equal to $\alpha_x = 0.115$ and $\alpha_z = 0.7$. As found in Corcos, the CSD function decays exponentially in the streamwise and spanwise directions and the convective effect in the streamwise direction produces a waved profile of the CSD function with wavelength $\lambda_\omega = 2\pi/k_\omega$.

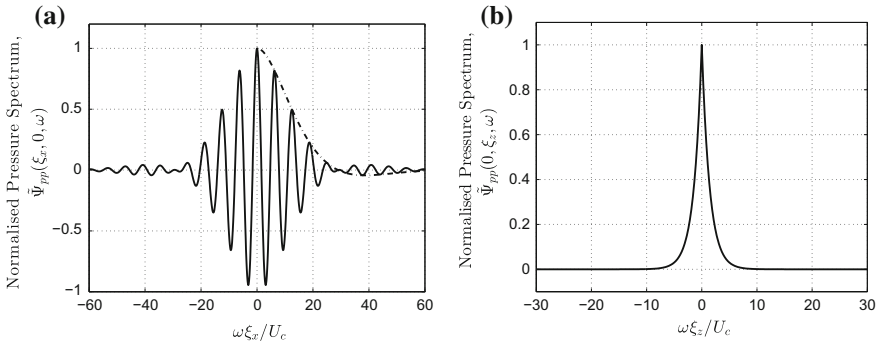

Fig. 2 Normalized spatial components of the CSD function of the Generalized Corcos model for $U_c = 0.65\ U_\infty$ with $U_\infty = 35.8$ m s^{-1} at 500 Hz. **a** Streamwise component for $n = 2$ with $\alpha_x = 0.115$. **b** Spanwise component for $m = 1$ with $\alpha_z = 0.7$

3.3 TBL *Wavenumber-frequency Spectrum*

The Generalized Corcos wavenumber-frequency spectrum normalized to one, dividing by the area, can be written as:

$$\hat{\Psi}_{pp}(k_x, k_z, \omega) = \frac{\phi(\omega) B_n(k_x) B_m(k_z)}{\left(\frac{-A_{k_x} A_{k_z} \pi^2 \alpha_\omega \beta_\omega}{nm}\right) \sum_{k=0}^{n-1} \exp(-\mathrm{i}\theta_k) \sum_{k=0}^{m-1} \exp(-\mathrm{i}\theta_k)}, \tag{10}$$

where

$$B_n(k_x) = \frac{\frac{n \sin(\pi/2n)}{\pi \alpha_\omega}}{1 + \left(\frac{k_x - k_\omega}{\alpha_\omega}\right)^{2n}} = \frac{A_{k_x}}{1 + \left(\frac{k_x - k_\omega}{\alpha_\omega}\right)^{2n}}, \tag{11}$$

$$B_m(k_z) = \frac{\frac{m \sin(\pi/2m)}{\pi \beta_\omega}}{1 + \left(\frac{k_z}{\beta_\omega}\right)^{2m}} = \frac{A_{k_z}}{1 + \left(\frac{k_z}{\beta_\omega}\right)^{2m}}. \tag{12}$$

Then, normalizing to conform to Graham's development [2, 16], Eq. (10) gives:

$$\tilde{\Phi}_{pp}(k_x, k_z, \omega) = \frac{\omega^2}{U_c^2} \frac{4 B_n(k_x) B_m(k_z)}{\left(\frac{-A_{k_x} A_{k_z}\ \alpha_\omega \beta_\omega}{nm}\right) \sum_{k=0}^{n-1} \exp(-\mathrm{i}\theta_k) \sum_{k=0}^{m-1} \exp(-\mathrm{i}\theta_k)}. \tag{13}$$

The contour plot and normalized wavevector spectrum of the Generalized Corcos model are shown in Fig. 3. This model is still convertible and separable in space. Its advantages are mainly twofold: (1) the mathematical form of the model allows to preserve the main advantages of the known Corcos model (notably analytical integrations), and (2) the two parameters introduced, n along the streamwise direction

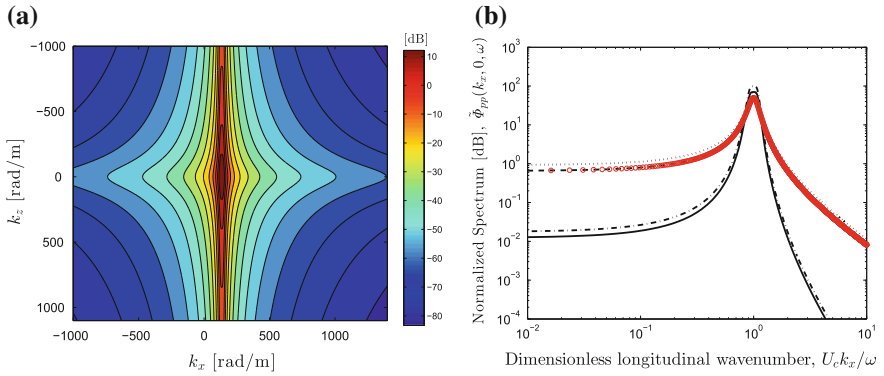

Fig. 3 Generalized Corcos's normalized wavevector spectrum for $U_c = 0.65\, U_\infty$ with $U_\infty = 35.8$ m s^{-1} at 500 Hz, and with $\alpha_x = 0.115$ and $\alpha_z = 0.7$. **a** Contour plot for $(n, m) = (2, 1)$. **b** Normalized wavevector spectrum in k_x with $k_z = 0$ with $(n, m) = (1, 1)$ (*red circle*), $(n, m) = (2, 1)$ (*solid line*), $(n, m) = (1, 2)$ (*dotted line*) and $(n, m) = (2, 2)$ (*dashed-dotted line*); Corcos's normalized wavevector spectrum (*dashed line*)

and m along the spanwise one, allow controlling the decay of the TBL model, making it steeper if necessary in the low-wavenumber range. Given that Corcos decays too slowly in the low-wavenumber range, such results are an improvement with respect to the classic Corcos. In Fig. 3b, the normalized spectrum is shown versus the dimensionless longitudinal wavenumber $U_c k_x/\omega$, for $k_z = 0$ and different order of the filters. By increasing the order of the filter along the streamwise direction, n, and keeping m fixed, the curve decays more quickly in the low-wavenumber range and the convective peak becomes slightly more concentrated. On the other side, decreasing the order of the filter along the spanwise direction, m, for a fixed n, the slope of the curve increases more slowly [2]. This behaviour is a direct consequence of having a Butterworth filter formulation, whose amplitude decays quickly when increasing the order of the filter [10].

Furthermore, in Fig. 4, the Generalized Corcos normalized wavevector spectrum $\tilde{\Phi}_{pp}(k_x, 0, \omega)$ is plotted for 35.8 m s^{-1} as function of frequency and k_x for different order of the filters. It is shown how the wavenumber-frequency distribution is affected by a change in the order of the filters. Therefore, an increment of the filter order along the streamwise direction n produces a slight increase of the convective bridge with frequency, while the spectra levels outside the convective domain decrease more quickly. On the other side, an increase in m does not really affect the wavenumber-frequency distribution. To conclude, those behaviours must be considered when tuning the order of the filters such to adapt the Generalized model distribution to different flow configurations.

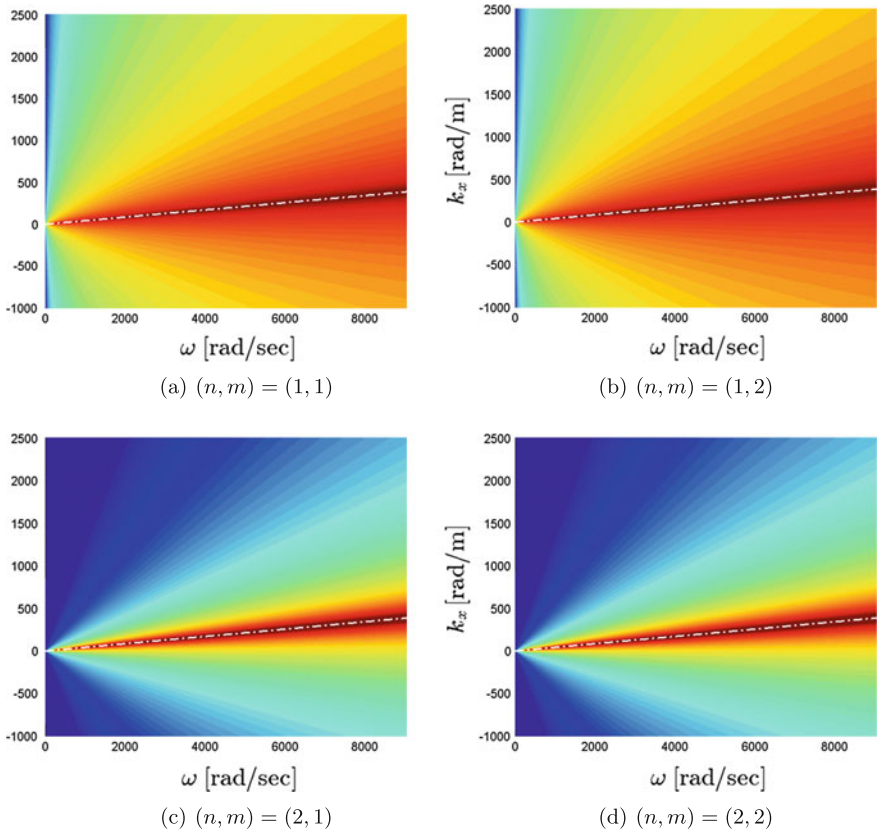

(a) $(n, m) = (1, 1)$ (b) $(n, m) = (1, 2)$

(c) $(n, m) = (2, 1)$ (d) $(n, m) = (2, 2)$

Fig. 4 Generalized Corcos's normalized wavevector spectrum $\tilde{\Phi}_{pp}(k_x, 0, \omega)$ with different orders of the filter for $U_c = 0.65\, U_\infty$ with $U_\infty = 35.8$ m s^{-1} (**a**–**d**)

4 Model Comparison

In order to position the Generalized Corcos model with respect to the existing TBL models, within this section a comparison with the most used TBL models is presented.

On one side, for high flow speed applications (i.e. aircraft boundary layers), the Corcos model [7, 8], with its accurate description of the convective ridge, is considered as a suitable model for the characterization of the wall pressure fluctuations. On the other side, for low flow speed applications (i.e. underwater acoustics) and, therefore, when interested in the sub-convective (or low-wavenumber) region of $\tilde{\Phi}_{pp}(\mathbf{k}; \omega)$, the models described by Chase [4] and Smol'yakov-Tkachenko [22] are found to be more accurate [1, 12, 18].

In Fig. 5, the normalized wavevector spectrum of the model of Corcos, Smol'yakov-Tkachenko [22] and Chase [4] is considered for the comparison with the Generalized Corcos model (given by Eq. 13). These models are normalized

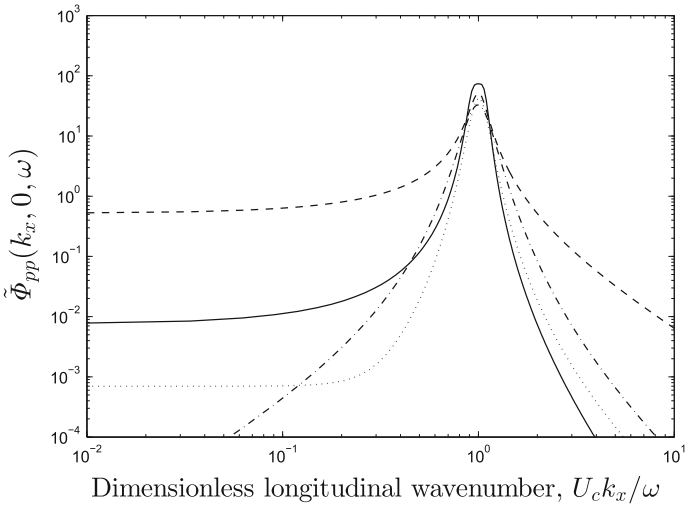

Fig. 5 Normalized wavevector spectrum in k_x for $St = 25.4$ at 500 Hz. Chase (*dashed-dotted line*), Corcos (*dashed line*), Smol'yakov-Tkachenko (*dotted line*), Generalized Corcos with $(n, m) = (2, 1)$ (*solid line*)

to conform to Graham's development [16]. Therefore, their integrated functions $\tilde{\Phi}_{pp}(\mathbf{k}; \omega)$ with respect to wavevector is unity, and consequently, the sums of energies of the various spectral models are identical. Such comparison is analyzed in detail in [2] and recalled here to better state the position of the proposed model.

In Fig. 5, the normalized wavenumber-frequency spectra are plotted versus the dimensionless longitudinal wavenumber $U_c k_x/\omega$, for $k_z = 0$ with a Strouhal number of $St = 25.4$. The spectral levels of the different TBL models shown are characterized by similar fluctuating energies around the convective ridge, but different low-wavenumber tails. In particular, the Corcos model shows high low-wavenumber levels compared to the other models, which is an indication of significant sound radiation from a low speed flow. According to experimental data, this level should be reduced by about 20 dB [17]. Models like Chase or Smol'yakov-Tkachenko instead show a lower low-wavenumber distribution than Corcos. In particular, the Smol'yakov-Tkachenko model [22] is characterized by a low-wavenumber white distribution, representing the flat spectrum at low-wavenumber better than Chase. However, it is important to state that the models of Chase and Smol'yakov-Tkachenko do not possess the convenient property of convertibility [20].

On the other side, lower levels at low-wavenumbers are seen when the Generalized model is used, about 20 dB less than Corcos. In Fig. 5, a steeper curve along the streamwise direction is found using $n = 2$ and $m = 1$. In general, by properly tuning the order of the filter, n in the streamwise direction and m in the spanwise direction, it is possible to control the decay in the low-wavenumber domain. By doing so, the spectra levels in the low-wavenumber range get closer to that of Smolyakov-Tkachenko and Chase, which are found to be more accurate in such a range [1, 18].

Nevertheless, the convective ridge of the Generalized model with orders $(n, m) = (2, 1)$ is still close to the classic Corcos, accurate instead in this range.

Overall, an improvement with respect to the classic Corcos is seen in the low-wavenumber range when the Generalized Corcos model is used. However, the order of the filters must be defined opportunely such to preserve a behaviour similar to Corcos in the vicinity of the convective peak.

5 Application to a Baffled Flat Plate

The applicability of the proposed model is here investigated by considering as test case a baffled flat plate. The analyzed model is a simply supported rectangular plate of length $a = 0.5$ m in the direction of the mean flow and width $b = 0.2$ m, as shown in Fig. 6. The simply supported rectangular panel, placed in a flat infinite rigid baffle, is characterized by: bending stiffness $B_p = 6$ N m, membrane tensions N_{xp} =58,600 N m^{-1}, N_{zp} =124,200 N m^{-1}, mass per unit area $M = 2.77$ kg m^{-2} and structural damping factor $\xi_s = 0.02$. A stationary TBL with zero mean pressure gradient is applied over one side of the panel. As shown in Fig. 6, x is defined as the flow direction, z is the cross-flow direction, and y is normal to the plate. The external and internal fluid properties (density and sound speed) are defined as c_0, ρ_0 and c_1, ρ_1, respectively. The driving pressure is given by $p_t(x, y, z, t)$, blocked turbulence pressure, and $p_i(x, y, z, t)$, acoustic pressures with $i = 0, 1$. A weak-coupling approximation is assumed, which means that the flow structure is not influenced by the panel motions [2, 14]. Additionally, the acoustic pressure is unaffected by the external flow speed.

The modal expansion method is chosen for the following analysis, for which an analytical solution exists [2, 13, 16]. The sound power radiated inwards by the plate is investigated when the models summarized in Sect. 4 are used to define the excitation term.

By following Graham's analysis [13, 16], the panel velocity is given by a sum of characteristic functions, the in-vacuo modes of the simply supported plate:

$$v(x, z, \omega) = \sum_{s,r} v_{rs}(\omega)\, \psi_{rs}(x, z) \ , \tag{14}$$

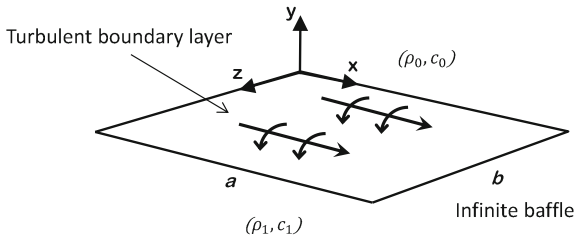

Fig. 6 A simply supported rectangular panel inserted in an infinite rigid baffle and driven by a TBL on one side [2]

where

$$\psi_{rs}(x,z) = \frac{2}{\sqrt{ab}} \sin(k_s x) \sin(k_r z) \ , \tag{15}$$

in which $k_s = s\pi/a$ and $k_r = r\pi/b$. The modal velocities, v_{rs}, can be found by solving the plate governing equation (see [2, 13] for an extensive analysis). Then, the dimensionless form of the spectrum of the sound power radiated inwards by the plate can be written as follows

$$\tilde{S}_1(\omega) = \frac{M\omega^3}{U_c^2 \phi(\omega)} S_1(\omega) = 2\xi_{f1} \sum_{r,s} Re\left(Z_{rs}^1\right) \frac{\tilde{\Phi}_{rs}}{|d_{rs}|^2} \ , \tag{16}$$

in which, the dimensionless modal impedance, d_{rs}, is defined as

$$d_{rs} = \mathrm{i}\left(\frac{B_p \left(k_s^2 + k_r^2\right)^2 + N_{xp} k_s^2 + N_{zp} k_r^2}{M\omega^2} (1 - \mathrm{i}\xi_s) - 1 \right) + \xi_{f0} Z_{rs}^0 + \xi_{f1} Z_{rs}^1 \ , \tag{17}$$

where

$$Z_{rs}^i = \frac{k_i}{(2\pi)^2} \int_{-\infty}^{+\infty} \int_{-\infty}^{+\infty} \frac{|S_{rs}(k_x, k_z)|^2}{\left(k_i^2 - k_z^2 - k_x^2\right)^{1/2}} \mathrm{dk_x\, dk_z} \ \text{ with } \ \mathrm{i} = 0, 1 \ . \tag{18}$$

In Eqs. (17)–(18), $\xi_{f1} = c_1 \rho_1 / M\omega$ and Z_{rs}^1 are the fluid-loading parameter and the acoustic modal impedance for the internal fluid, respectively, and, ξ_{f0} and Z_{rs}^0 for the external one; $S_{rs}(\mathbf{k})$ is the shape function given by the spatial Fourier transform of Eq. (15) as follows

$$S_{rs}(k_x, k_z) = \int_0^a \int_0^b \psi_{rs}(x,z) \exp(-\mathrm{i}k_x x) \exp(-\mathrm{i}k_z z) \ \mathrm{dx\, dz} \ , \tag{19}$$

$$S_{rs}(k_x, k_z) = \frac{2k_r k_s}{\sqrt{ab}} \frac{\left[\exp(-\mathrm{i}k_z b)(-1)^r - 1\right]\left[\exp(-\mathrm{i}k_x a)(-1)^s - 1\right]}{\left(k_z^2 - k_r^2\right)\left(k_x^2 - k_s^2\right)} \ . \tag{20}$$

Note that for the conditions considered in our analysis, the coupling $((s,r) \neq (p,q))$ terms can be neglected [15]. The radiated sound power, Eq. (16), is normalized as done by Graham such that the effect of a different $\phi(\omega)$ is not taken into account. In this way, the spectra levels given by $\tilde{S}_1(\omega)$ will differ in relation to the different behaviour of the TBL models used to excite the structure.

In Eq. (16), the real part of the acoustic modal impedance gives the radiation efficiency, whereas $\tilde{\Phi}_{rs}$ is the dimensionless modal excitation, which represents the influence of the boundary layer wavenumber-frequency spectrum on the radiated sound. Such modal excitation term can be expressed by the following wavenumber integral:

$$\tilde{\Phi}_{rs} = \frac{1}{(2\pi)^2} \int_{-\infty}^{+\infty} \int_{-\infty}^{+\infty} \tilde{\Phi}_{pp}(k_x, k_z, \omega) \, |S_{rs}(k_x, k_z)|^2 \, \mathrm{dk_x} \, \mathrm{dk_z} \,, \tag{21}$$

where $|S_{rs}(\mathbf{k})|^2$ is the wavenumber sensitivity function and $\tilde{\Phi}_{pp}(\mathbf{k}; \omega)$ the normalized wavevector-frequency spectrum of the wall pressure fluctuations.

On one side, if non-separable models are considered to represent the wall pressure fluctuations, $\tilde{\Phi}_{pp}(\mathbf{k}; \omega)$, this is the case of Chase or Smol'yakov-Tkachenko, a numerical integration is necessary to solve Eq. (21). In this work, a uniform Gaussian quadrature is used, entailing a high computation time to evaluate the integral. On the other side, for separable models (i.e. Corcos), a closed form solution for the integral shown in Eq. (21) is possible.

As demonstrated in [2], an analytical expression for $\tilde{\Phi}_{pp}(\mathbf{k}; \omega)$ can be also found for the Generalized Corcos model, which is defined as follows

$$\tilde{\Phi}_{rs} = \left(\frac{\omega^2}{U_c^2}\right) \frac{\tilde{\Phi}_r \tilde{\Phi}_s}{\sum_{k=0}^{m-1} \exp(-\mathrm{i}\theta_k) \sum_{k=0}^{n-1} \exp(-\mathrm{i}\theta_k)} \,. \tag{22}$$

The analytical development of the modal excitation term for the Generalized Corcos model as well as the functions $\tilde{\Phi}_r$ and $\tilde{\Phi}_s$ is found in [2]. As a result, by using the Generalized Corcos model, the computational effort is definitively reduced [3].

As Graham discussed in his works [13, 16], modes can be highly excited, or not, depending on the match between the modal wavenumbers and the convective ones. On one side, for modes strongly driven by the boundary layer, the convective peak of $\tilde{\Phi}_{pp}(\mathbf{k}; \omega)$ determines the excitation levels, and therefore, an accurate description of the convective ridge is necessary. On the other side, for modes weakly driven by the boundary layer, the radiated sound predictions are influenced by the low-wavenumber levels of the TBL model, and therefore, this region must be described accurately.

In the following sections, the applicability of the Generalized Corcos model is analyzed by considering two application cases representative of those two limit conditions. In this way, the benefits achieved by properly tuning the order of the filters of the Generalized model are discussed in terms of sound power radiated by the structure. The flow and plate properties considered in this work are taken from [2, 16] with the convection velocity given by the empirical fit obtained by Efimtsov.

5.1 Application Case 1: Low-Wavenumber Domain

In the first application case, a low Mach number flow is considered with $U_\infty = 140$ m s^{-1} in order to analyze the effect of the different low-wavenumber portions of the spectrum $\tilde{\Phi}_{pp}(\mathbf{k}; \omega)$ on the radiated sound power (Fig. 5). In Fig. 7, the resonance frequencies of the simply supported plate for different lateral mode indices are compared

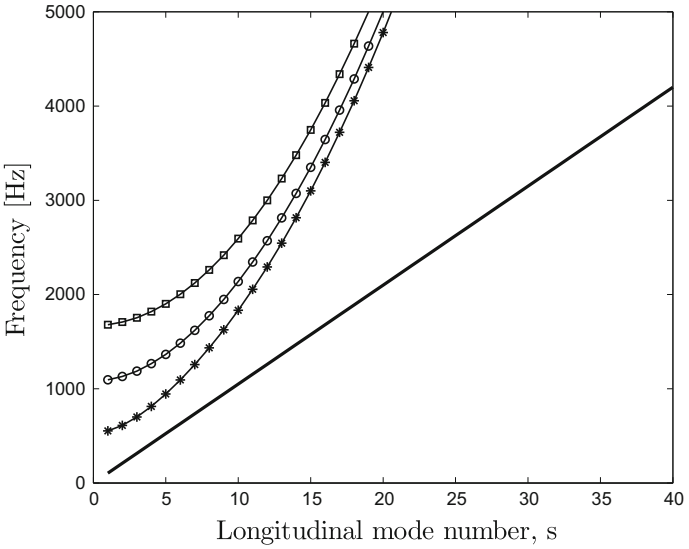

Fig. 7 Resonance frequencies of the simply supported plate for $r = 1$ ($*$), $r = 2$ ($\circ$), $r = 3$ ($\square$) and convective peak frequency (*solid line*)

to the convective peak frequencies, defined by $\omega/U_c = s\pi/a$. The modal wavenumbers are away from the convective peak, and, for this first application case, there is no hydrodynamic coincidence. As a consequence, the structure should receive most of the energy from the sub-convective components of the wavenumber-frequency spectrum. Thus, the slope of the low-wavenumber region of $\tilde{\Phi}_{pp}(\mathbf{k};\omega)$ is important. In this situation, as found in [1, 6], models such as Smol'yakov-Tkachenko or Chase are more accurate in that range, and therefore, they may be suitable TBL models.

Figure 8 shows the power radiated by the plate when different $\tilde{\Phi}_{pp}(\mathbf{k};\omega)$ are considered. The solution for different wavenumber-frequency spectrum models reflects their low-wavenumber behaviour and it is dominated by the resonant modes. $\tilde{S}_1(\omega)$ is higher for the Corcos model than the other three models, due to its high low-wavenumber spectra levels. On the contrary, the low-wavenumber spectra seen for the Generalized Corcos model lie at a lower radiated sound power than Corcos. Actually, the order of the filter is chosen in order to see an improvement with respect to the classic Corcos that decays too slowly and to address its low-wavenumber limitations, $(n, m) = (2, 1)$. As expected, the solution found for the Generalized Corcos model is between Chase and Smol'yakov-Tkachenko, which means an improved accuracy at low-wavenumbers over the original Corcos model.

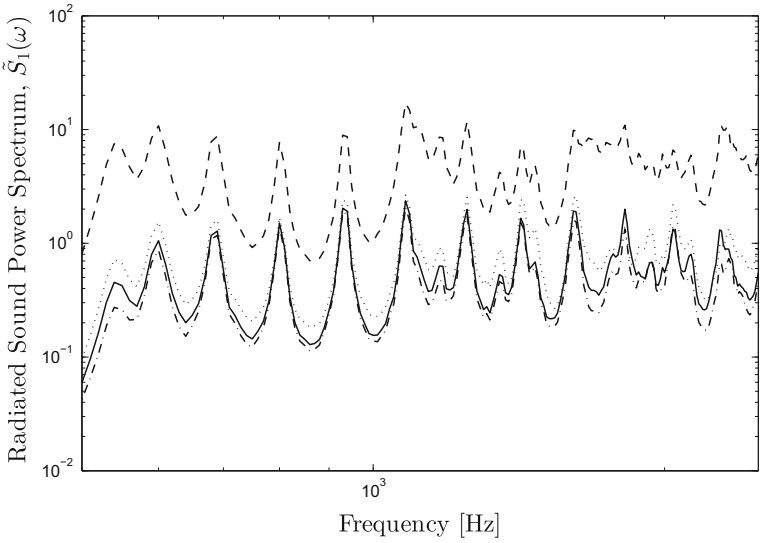

Fig. 8 Radiated sound power spectra for $U_\infty = 140$ m s^{-1} [2]. Chase (*dashed-dotted line*), Corcos (*dashed line*), Smol'yakov-Tkachenko (*dotted line*), Generalized Corcos with $(n, m) = (2, 1)$ (*solid line*)

5.2 Application Case 2: Convective Domain

For the second application case, a free-stream velocity of $U_\infty = 240$ m s^{-1} is considered, and, in addition, the stiffness of the structure is reduced by halving the in-plane tensions (see [16]). In this condition, the hydrodynamic coincidence is evident over the majority of the frequency range, as seen in Fig. 9, and therefore, the structural modes are strongly driven by the boundary layer. Now, the structure should receive most of the energy from the convective component of $\tilde{\Phi}_{pp}(\mathbf{k}; \omega)$, and a suitable TBL model must describe accurately the convective region of the spectrum. This can be the model of Corcos (Sect. 2).

As shown in Fig. 10, the sound power radiated by the plate is found to be sensitive to details of the shape and location of the peak, which start to become important when the shape function lobes are narrow in comparison to the convective peak. In Fig. 10, this is observed at frequencies higher than 1 kHz, where the different models show a slight difference in $\tilde{S}_1(\omega)$ due to the different levels of the spectrum in the convective region. In particular, the highest levels at the convective peak are found in the Smol'yakov-Tkachenko model, and this is directly reflected in the high level seen in the sound power radiated by the plate.

By using the Generalized Corcos model with $(n, m) = (2, 1)$, the excitation levels are still close to the one given by Corcos, Fig. 10. In fact, as seen in Fig. 3, by increasing m for a fixed n, $\tilde{\Phi}_{pp}(k_x, 0, \omega)$ shift up uniformly and this gives a generally higher radiated sound power than Corcos, whereas a small increase in the streamwise

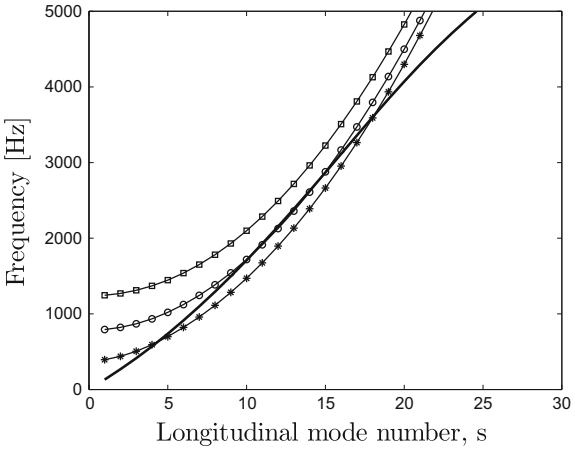

Fig. 9 Resonant frequencies for the simply supported plate for $r = 1$ ($*$), $r = 2$ ($\circ$), $r = 3$ ($\square$) and convective peak frequency (*solid line*)

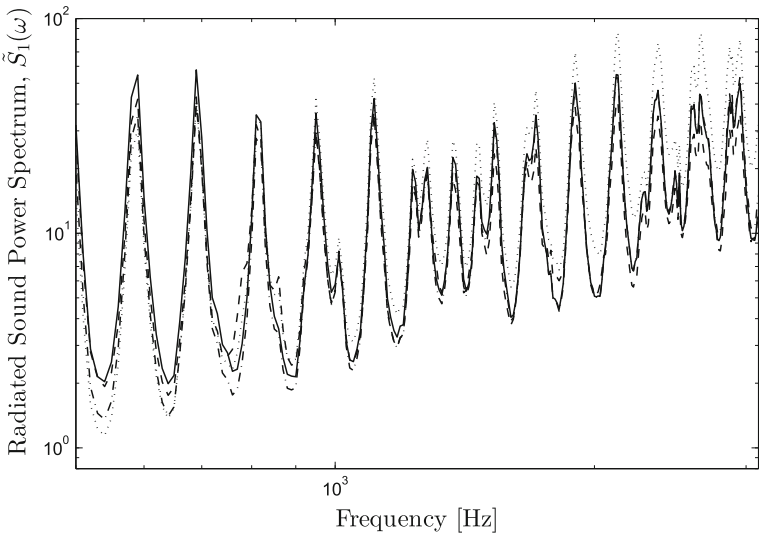

Fig. 10 Radiated sound power spectra for $U_\infty = 240\,\mathrm{m\,s^{-1}}$. Chase (*dashed-dotted line*), Corcos (*dashed line*), Smol'yakov-Tkachenko (*dotted line*), Generalized Corcos with $(n, m) = (2, 1)$ (*solid line*)

direction, $n = 2$, with m fixed equal to one, leads to a narrower convective peak with a steeper spectrum in the low-wavenumber range. As a consequence, the energy concentrated in the convective range is nearly the same of Corcos if the order of the filters is chosen to be $(n, m) = (2, 1)$.

5.3 *Effect of the Different Order of the Filters on the Radiated Sound Power*

In the following section, the effect of the different order of the filters on the radiated sound power is analyzed considering the application case 1, Sect. 5.1.

One of the advantages of a Butterworth filter formulation is to have two additional parameters, n along k_x and m along k_z, that can be properly tuned in order to control the decay of the TBL model and possibly to adapt it to different flow configurations. Figure 11 shows the normalized wavevector spectra of the model of Corcos, Chase and Generalized Corcos for different orders of the filter versus the dimensionless longitudinal wavenumber $U_c k_x/\omega$, for $k_z = 0$ at 140 m s^{-1} and 1 kHz. The generated $\tilde{S}_1(\omega)$ is shown in Fig. 12. By changing the value of m and n, the excitation levels are found to lie between the one of Corcos and Chase. As a consequence of the

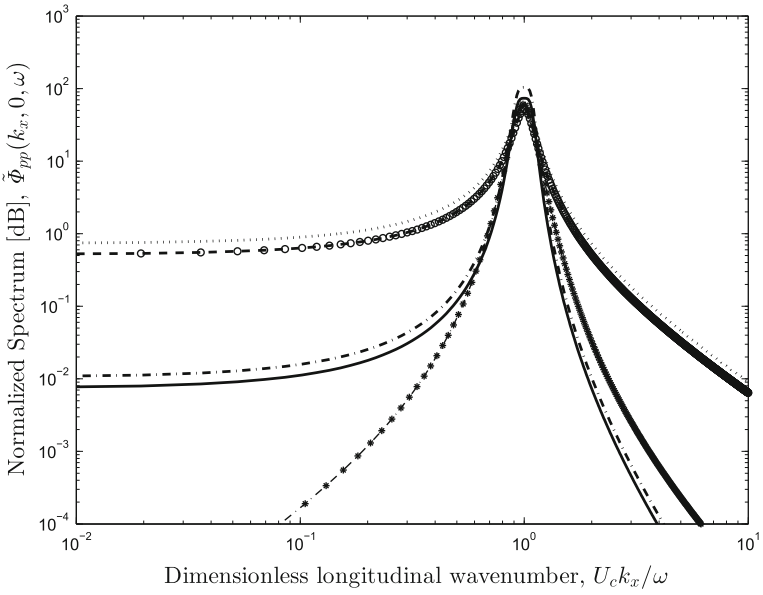

Fig. 11 Normalized wavevector spectrum for $U_\infty = 140$ m s^{-1} at 1 kHz. Generalized Corcos with $(n, m) = (1, 1)$ (*circle*), $(n, m) = (2, 1)$ (*solid line*), $(n, m) = (1, 2)$ (*dotted line*) and $(n, m) = (2, 2)$ (*dashed-dotted line*); Corcos (*dashed line*); Chase (*dashed-dotted line with asterisk*)

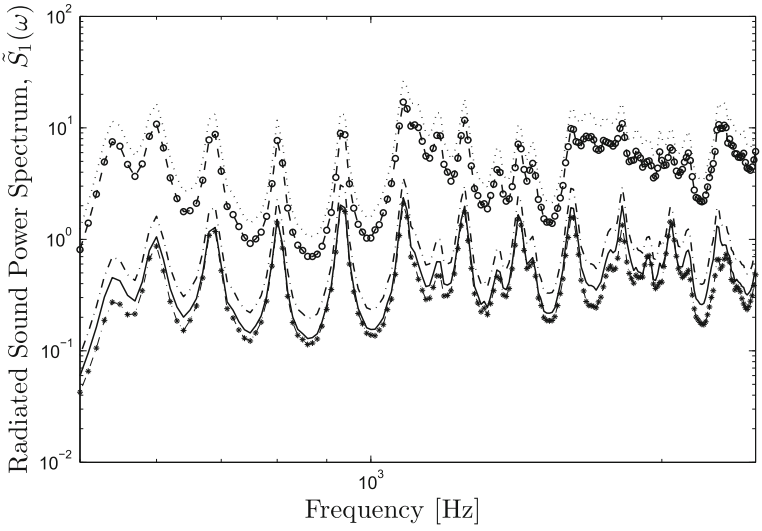

Fig. 12 Radiated sound power spectra at $U_\infty = 140$ m s^{-1}. Generalized Corcos with $(n, m) = (1, 1)$ (*circle*), $(n, m) = (2, 1)$ (*solid line*), $(n, m) = (1, 2)$ (*dotted line*) and $(n, m) = (2, 2)$ (*dashed-dotted line*); Corcos (*dashed line*); Chase (*dashed-dotted line with asterisk*)

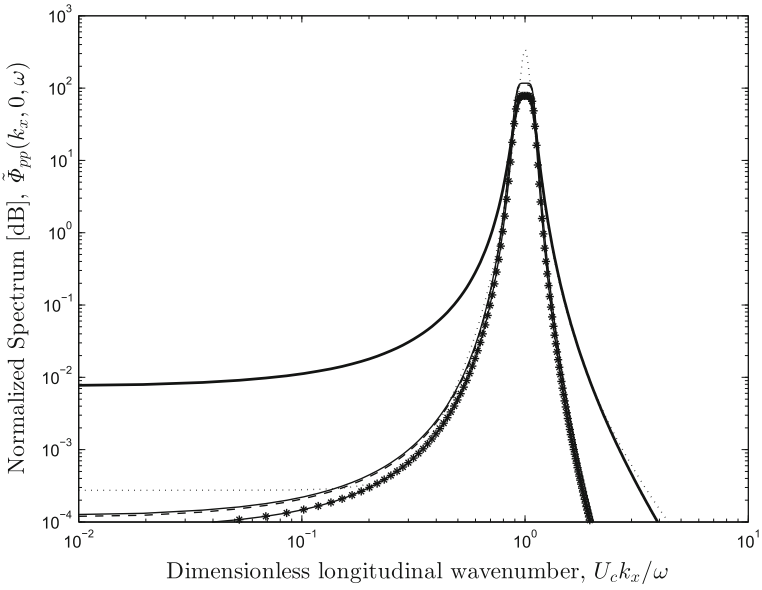

Fig. 13 Normalized Wavevector Spectrum for $U_\infty = 140$ m s^{-1} at 1 kHz. Smol'yakov-Tkachenko (*dotted line*); Generalized Corcos with $(n, m) = (2, 1)$ (*bold solid line*), $(n, m) = (3, 1)$ (*solid line with asterisk*), $(n, m) = (3, 2)$ (*dashed line*) and $(n, m) = (3, 3)$ (*solid line*) [2]

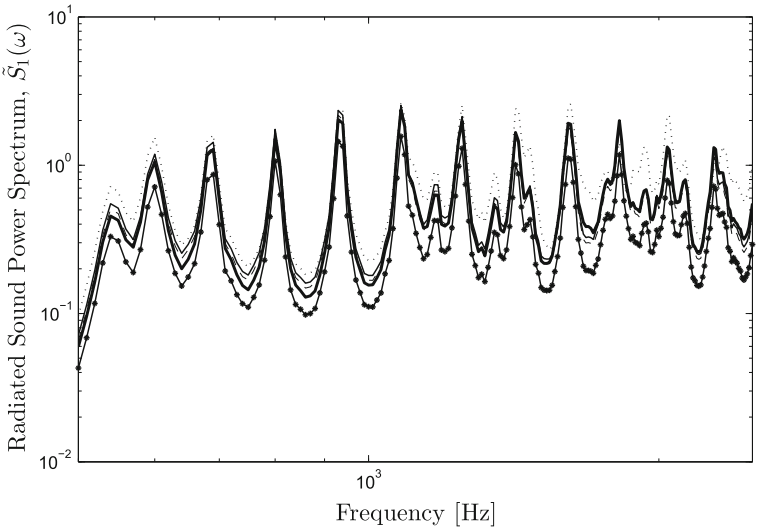

Fig. 14 Radiated sound power spectra at $U_\infty = 140$ m s^{-1}. Smol'yakov-Tkachenko (*dotted line*); Generalized Corcos with $(n, m) = (2, 1)$ (*bold solid line*), $(n, m) = (3, 1)$ (*solid line with asterisk*), $(n, m) = (3, 2)$ (*dashed line*) and $(n, m) = (3, 3)$ (*solid line*)

characteristics of the Butterworth filter, it is possible to see how for higher order along k_x, n, the excitation level is very low compared to the $\tilde{S}_1(\omega)$ seen for Corcos and it is close to Chase. On the contrary, high values of m give high level in $\tilde{S}_1(\omega)$, reflecting the behaviour of $\tilde{\Phi}_{pp}(\mathbf{k}; \omega)$ in the low-wavenumber range (Fig. 11).

Furthermore, in Figs. 13 and 14, the value of n and m that gives the best fit for the Smol'yakov-Tkachenko model in the low-wavenumber range is found by changing the order of the filters along k_x and k_z [2]. As shown in Figs. 13 and 14, the Generalized Corcos model is close to that of Smol'yakov-Tkachenko in the low-wavenumber range for order of the filter $(n, m) = (3, 1–3)$.

To conclude, with the use of the Generalized Corcos model, it is possible either to reach the excitation level given by Corcos when $(n, m) = (1, 1)$, or lower getting close to Chase or Smol'yakov-Tkachenko by properly tuning the order of the filter.

6 Conclusions

A Generalized Corcos model is here described for modelling turbulent boundary layer wall pressure fluctuations. To position the new model with respect to the existing TBL models, two different application cases are considered. Firstly, the effect of the different low-wavenumber portion of the wavenumber-frequency spectrum is analyzed considering a case representing a low-speed vehicle. Secondly, the effect of the convective component of the different wavenumber-frequency spectra on the

sound power radiated by the plate is considered with a case representing a high-speed subsonic aircraft. The comparison with some of the existing models shows how the Butterworth filter formulation provides an accurate description of the wavenumber-frequency spectrum at and below the convective peak. In particular, the main benefits obtained using the Generalized Corcos model are: (1) a closed form solution for the excitation term is possible since the model is still convertible, and therefore, the computational effort is effectively reduced; (2) by tuning two parameters, n and m, it is possible to address the low-wavenumber limitation found in Corcos and make the spectrum steeper when necessary.

However, a comparison with experimental data is fundamental to define, given a free-stream velocity, the order of the filters for which the model physically matches measured normalized wavevector spectra. This is topic of currently ongoing research. Furthermore, future research will focus on further investigating the potential of the proposed model and extending its application to more complex cases.

Acknowledgements The research work of A. Caiazzo has been funded by the European Commission within the ITN Marie Curie Action project BATWOMAN under the 7th Framework Programme (EC grant agreement no. 605867). This research was partially supported by Flanders Make, the strategic research centre for the manufacturing industry. The Research Fund KU Leuven is also gratefully acknowledged for its support.

References

1. Borisyuk, A.O., Grinchenko, V.T.: Vibration and noise generation by elastic elements excited by a turbulent flow. J. Sound Vib. **204**(2), 213–237 (1997)
2. Caiazzo, A., D'Amico, R., Desmet, W.: A generalized corcos model for modelling turbulent boundary layer wall pressure fluctuations. J. Sound Vib. **372**, 192–210 (2016). https://doi.org/10.1016/j.jsv.2016.02.036
3. Caiazzo, A., D'Amico, R., Desmet, W.: Use of a generalized corcos model to predict flow-induced noise in a cavity-plate system. In: ISMA2016 & USD2016. Leuven, Belgium (2016)
4. Chase, D.: Modeling the wavevector-frequency spectrum of turbulent boundary layer wall pressure. J. Sound Vib. **70**(1), 29–67 (1980)
5. Ciappi, E., De Rosa, S., Franco, F., Guyader, J.L., Hambric, S.A.: Flinovia—Flow Induced Noise and Vibration Issues and Aspects. Springer (2015)
6. Ciappi, E., Magionesi, F., De Rosa, S., Franco, F.: Hydrodynamic and hydroelastic analyses of a plate excited by the turbulent boundary layer. J. Fluids Struct. **25**, 321–342 (2009)
7. Corcos, G.M.: Pressure fluctuations in shear flows. Technical Report, Institute of Engineering Research, University of California (1962)
8. Corcos, G.M.: The structure of the turbulent pressure field in boundary-layer flows. J. Fluid Mech. **18**(03), 353–375 (1964)
9. D'Amico, R.: Efficient frequency averaging techniques for noise and vibration simulations. Ph.D. thesis, KU Leuven (2014)
10. D'Amico, R., Huybrechs, D., Desmet, W.: A refined use of the residue theorem for the evaluation of band-averaged input power into linear second-order dynamic systems. J. Sound Vib. **333**(6), 1796–1817 (2014)
11. D'Amico, R., Koo, K., Huybrechs, D., Desmet, W.: On the use of the residue theorem for the effcient evaluation of band-averaged input power into linear second-order dynamic systems. J. Sound Vib. **332**(26), 7205–7225 (2013)

12. Farabee, T.M., Geib, F.E.: Measurements of boundary layer pressure fields with an array of pressure transducers in a subsonic flow. Technical Report, Naval Ship Research and Development Center (1976)
13. Graham, W.: Boundary layer induced noise in aircraft. part I: the flat plate model. J. Sound Vib. **192**(1), 101–120 (1996)
14. Graham, W.R.: Boundary layer induced noise in aircraft. Technical Report, Cambridge University Engineering Department, CUED/A-AERO/TR18 (1992)
15. Graham, W.R.: High frequency vibration and acoustic radiation of fluid loaded plates (1995)
16. Graham, W.R.: A comparison of models for the wavenumber—frequency spectrum of turbulent boundary layer pressures. J. Sound Vib. **206**(4), 541–565 (1997) (June 1995)
17. Hwang, Y.F., Bonness, W.K., Hambric, S.A.: On modeling structural excitations by low speed turbulent boundary layer flows. Techort Report, The Pennsylvania State University (2003)
18. Martin, N.C., Leehey, P.: Low wavenumber wall pressure measurements using a rectangular membrane as a spatial filter. J. Sound Vib. **52**(1), 95–120 (1977)
19. Mellen, R.H.: On modeling convective turbulence. J. Acoust. Soc. Am. **88**(6), 2891–2893 (1990)
20. Miller, T., Gallman, J., Moeller, M.: Review of turbulent boundary layer models for acoustic analysis. In: 49th AIAA Aerospace Sciences Meeting Including the New Horizons Forum and Aerospace Exposition, vol. 49, no. 6, pp. 1739–1754 (2012)
21. Munich, F.P., Wien, F.G.R., Palaiseau, J.S.: Noise Sources in Turbulent Shear Flows: Fundamentals and Applications. Springer Science & Business Media, CISM, Udine (2013). https://doi.org/10.1007/978-3-7091-1458-2
22. Smol'yakov, A.V., Tkachenko, V.M.: Model of a field of pseudosonic turbulent wall pressures and experimental data. Sov. Phys. Acoust. **37**(6), 627–631 (1991)

Wall Pressure Identification by Using the Force Analysis Technique in Automotive, Naval and Aeronautic Applications

Charles Pezerat, Océane Grosset, Justine Carpentier, Jean-Hugh Thomas and Frédéric Ablitzer

Abstract The aim of this research activity is to identify wall pressures which excite the structure, for automotive, aeronautic and naval domains, by using an inverse vibration method, such as FAT (Force Analysis Technique) and/or CFAT (Corrected Force Analysis Technique). The method is based on the local dynamic equilibrium equation of the structure, in which the partial derivatives are approximated by a finite difference scheme. Two schemes are proposed: the first (FAT method) consists in filtering the calculated force distribution by using an adequate spacing, but the associated wavenumber filtering presents a singularity at the flexural wavenumber of the structure, introducing an error around its value. The second uses a corrected finite difference scheme which acts as a complete low-pass wavenumber filter (CFAT method). In order to highlight the relevance of using both methods, results from simulations in the three industrial domains, automotive, aeronautic and naval are then presented where the comparison of FAT and CFAT results gives an interesting indicator to analyze the nature of the excitation. Moreover, for the naval application, a strategy for the identification of the strong fluid-structure coupling due to the pressure radiated by the structure is proposed. It is based on the identification of an effective wavenumber by using CFAT on a preliminary experiment where the structure immersed in the fluid is excited by a shaker. Finally, an experimental validation of the FAT/CFAT identification is shown for the car application. First, it is shown how both techniques identify very well the wall pressure on glass windows when the excitation is acoustic only (reverberant room). Second, the FAT/CFAT methods are applied to a car placed in a wind tunnel, where the analysis of results allows one to extract the whole acoustic component in a frequency range below the critical frequency of glass windows.

C. Pezerat (✉) · O. Grosset · J. Carpentier · J.-H. Thomas · F. Ablitzer
LAUM UMR CNRS 6613, Le Mans University, avenue O. Messiaen, 72085
Le Mans Cedex 09, France
e-mail: charles.pezerat@univ-lemans.fr

O. Grosset
IRT Jules Verne – Chemin du Chaffault, 44340 Bouguenais, France

E. Ciappi et al. (eds.), *Flinovia—Flow Induced Noise and Vibration Issues and Aspects-II*,
https://doi.org/10.1007/978-3-319-76780-2_3

1 Introduction

The Force Analysis Technique (FAT) and the Corrected Force Analysis Technique (CFAT) are experimental approaches that were developed for the identification of vibration sources exciting a structure. The first developments were made for the location and the quantification of point forces or point moments at the attachment points of a source and/or a coupled system. The FAT was written and applied to analytically known structures like beams [1], plates [2] or shells [3, 4], but it was also adapted to more complex structures by using a numerical FEM operator instead of an analytical equation of motion [5, 6]. For some years now, the development of FAT and CFAT are under progress for the identification of the wall pressure due to turbulent flows exciting structures. The first investigation was made by Chevillotte et al. [7], followed by the Ph.D. work of Lecoq [8–10]. This research topic is today the subject of the actual Carpentier's and Grosset's PhD works. The paper in the first FLINOVIA book [11] gives a good synthesis of FAT and CFAT applied for turbulent flow excitations. This new paper is a logical follow up of [11]. It gives a little overview of wall pressure identifications for different kinds of flow. Typical automotive, naval and aeronautic characteristics are studied here in order to point out what is possible with FAT and CFAT in each industrial application. In this paper, the interest to use both FAT and CFAT techniques is also underlined. CFAT was developed to improve FAT at the origin, but combining the results given by both techniques, it can be shown that relevant information on the distribution of the excitation in the wavenumber domain can be carried out.

To give an independent reading of this paper, the first section explains briefly FAT and CFAT methods. The possibility to extract some interesting information from both techniques is also highlighted. The second section presents the three industrial cases, where the most important characteristics are recalled in order to understand why FAT and CFAT objectives cannot be the same in each application. The third section constitutes the core of the paper, it presents results obtained from numerical simulations. The particular conditions and the kinds of result obtained from FAT and CFAT are discussed. The fourth section presents a final experimentation that was made on a real car, where the identification and the analysis of the wall pressure, exciting the driver window, is given.

2 Overview of FAT and CFAT Methods

The basic principle of the FAT is extremely simple. It consists in measuring the displacement field on an area of interest of the structure and in injecting it in the equation of motion in order to calculate the external force distribution at each studied frequency. In the simple example of a thin plate, the used harmonic equation of motion can be the well-known fourth order differential equation obtained under the Love-Kirchhoff's assumption:

$$D\left(\frac{\partial^4 w}{\partial x^4} + 2\frac{\partial^4 w}{\partial x^2 \partial y^2} + \frac{\partial^4 w}{\partial y^4}\right) - \rho h \omega^2 w = f(x, y, \omega), \tag{1}$$

where D is the flexural rigidity, is the mass density and h is the thickness of the plate, w is the out-of-plane displacement field and f is the external force distribution exciting the plate at the angular frequency ω.

The principle of the inverse problem consists in calculating the hand right side term of Eq. (1). Note that the knowledge of this local equation is sufficient. Hence, boundary conditions and/or excitations and/or dynamic laws outside the area where the force distribution is identified can be completely ignored.

Of course, the spatial derivatives in Eq. (1) cannot be obtained directly by measurements and the displacement field cannot be measured continuously. The use of a discretized equation of motion is then proposed, where the force distribution is identified on a measurement regular cartesian meshgrid and where the fourth derivatives of the displacement are approximated by a finite difference scheme. In order to limit the number of measurement points, a finite difference scheme developed at the first order is proposed. In the case of plates, the calculation of one force distribution point requires the measurement of thirteen transverse displacements:

$$D\left(\delta_\Delta^{4x} + 2\delta_\Delta^{2x2y} + \delta_\Delta^{4y}\right) - \rho h \omega^2 w = f(x, y, \omega), \tag{2}$$

where δ_Δ^{4x}, δ_Δ^{2x2y}, δ_Δ^{4y} are the finite differences:

$$\delta_\Delta^{4x} = \frac{1}{\Delta^4}(w(x-2\Delta, y) - 4w(x-\Delta, y) + 6w(x, y) - 4w(x+\Delta, y) + w(x+2\Delta, y)),$$

$$\delta_\Delta^{4y} = \frac{1}{\Delta^4}(w(x, y-2\Delta) - 4w(x, y-\Delta) + 6w(x, y) - 4w(x, y+\Delta) + w(x, y+2\Delta)),$$

$$\begin{aligned}\delta_\Delta^{2x2y} = &\frac{1}{\Delta^4}(w(x-\Delta, y-\Delta) - 2w(x-\Delta, y) + w(x-\Delta, y+\Delta) - 2w(x, y-\Delta) \\ &+ 4w(x, y) - 2w(x, y+\Delta) + w(x+\Delta, y-\Delta) - 2w(x+\Delta, y) + w(x+\Delta, y+\Delta)\end{aligned}$$

where Δ is the spacing between points in both directions x and y.

The use of Eq. (2) corresponds to the origin of FAT. Of course, the approximation of derivatives of a measured quantity is very difficult, since this operation amplifies drastically the measurement noise. To limit this noise amplification, a regularization based on a low-pass wavenumber filtering can be proposed [2]. Since the finite difference scheme introduces itself a low-pass wavenumber filter, a good regularization can also be obtained by the choice of an adequate spacing Δ between points. Figure 1 shows the shapes of the filter in the wavenumber domain corresponding to the finite difference scheme use in Eq. (2). Note that the obtained shape depends on the frequency, n indicating here the number of points per wavelength. It is clear that the finite difference scheme eliminates high wavenumbers and keeps the information for wavenumbers lower than the flexural wavenumber, the expression of which is:

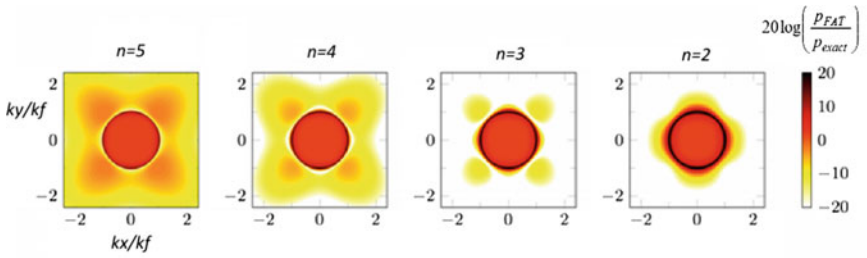

Fig. 1 Wavenumber filtering effect of FAT due to the classic finite difference scheme used in Eq. (2) for various numbers n of points per wavelength. p_{FAT} indicates the pressure identified by FAT, p_{exact} indicates the exact wall pressure

$$k_f = \sqrt[4]{\frac{\rho h}{D}}\sqrt{\omega}. \tag{3}$$

Of course, the higher the spacing, the more efficient the filter is. In the same figure, one can also observe that the finite difference scheme amplifies around the flexural wavenumber (circle of radius 1). Since the obtained value is upper than one (or upper than zero in dB), this amplification implies an overestimation of the reconstructed force distribution around the flexural wavenumber.

The Corrected Force Analysis Technique (CFAT) has the same principle, except that the coefficients of the finite difference scheme are chosen to obtain a better low-pass wavenumber filtering, without amplification around the flexural wavenumber. The calculation of the coefficients at each frequency is completely described in [12], where the proposed corrected finite difference scheme is:

$$D\left(\mu^4\delta_\Delta^{4x} + 2\upsilon^4\delta_\Delta^{2x2y} + \mu^4\delta_\Delta^{4y}\right) - \rho h\omega^2 w = f(x, y, \omega), \tag{4}$$

where $\mu^4 = \frac{\Delta^4 k_f^4}{4\left(1-\cos\left(k_f\Delta\right)\right)^2}$ and $\upsilon^4 = \frac{\Delta^4 k_f^4}{8\left(1-\cos\left(k_f\Delta/\sqrt{2}\right)\right)^2} - \mu^4$.

In fact, the new coefficients are here calculated to eliminate the singularity at $k_x = k_f, k_y = k_f$ and $\sqrt{k_x^2 + k_y^2} = k_f$. As shown in Fig. 2, the singularity at k_f is considerably reduced on the entire circle of radius 1.

In [12], it was then proposed to use CFAT instead of FAT, because the amplification around k_f is eliminated. In this paper, we propose to use both finite difference schemes and to compare both results. Indeed, since the difference between both methods is essentially located around the flexural wavenumber k_f, the comparison of both techniques can give information about the distribution of the energy around k_f.

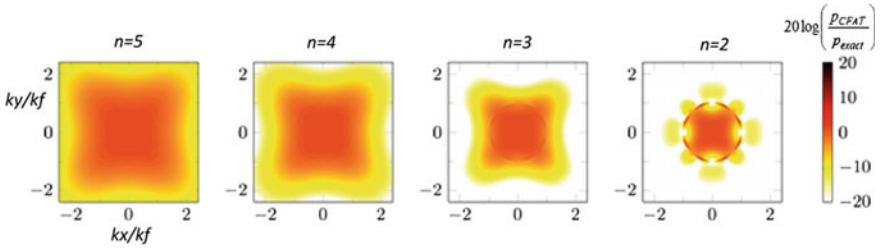

Fig. 2 Wavenumber filtering effect of CFAT due to the corrected finite difference scheme used in Eq. (4) for various numbers n of points per wavelength. p_{CFAT} indicates the pressure identified by CFAT, p_{exact} indicates the exact wall pressure

3 Characteristics of Turbulent Excitations in the Different Transportation Contexts

One of the goal of this paper is to study what can provide FAT and CFAT in different environmental contexts. In the following, ground, naval and air transportations are considered. Figure 3 gives a summary of the characteristics of these three contexts.

3.1 Naval Applications

It is clear that the naval sector concerns the case for which the velocity of flows are the smallest, especially since the velocity of a boat is small and the speed of sound in water is high. In this case, the acoustic wavenumber and the convective wavenumber have very different values such that their linear laws are extremely distant. The convection frequency, corresponding to the coincidence between the convection wavenumber and the flexural wavenumber, is very small whereas the critical frequency, corresponding to the coincidence between the acoustic

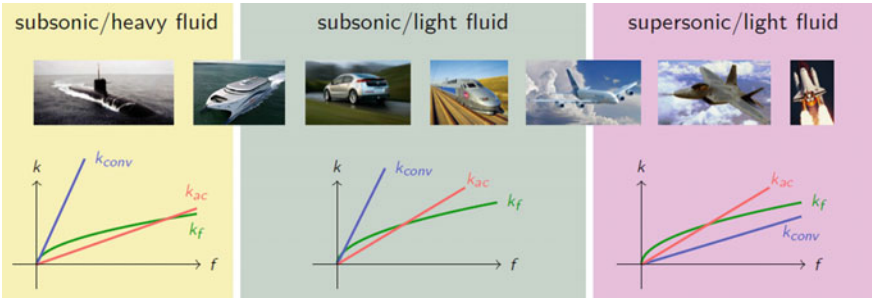

Fig. 3 Different transportation contexts and their characteristics in terms of wavenumber tendencies

Table 1 Characteristics of the simulation made for naval applications

Structure	Steel plate 25 mm thick
Flow velocity	12.9 (m/s)
Convection frequency	0.5 (Hz)
Critical frequency	9594 (Hz)
Spacing	10 (cm)

wavenumber and the flexural wavenumber, is very high. Hence, the frequency range where the acoustic wavenumber is smaller than the flexural wavenumber and where the convective wavenumber is higher than the flexural wavenumber is very large. As an example, considering the flow and structure characteristics given in Table 1, the convection frequency corresponds to 0.5 Hz, whereas the critical frequency is equal to 9594 Hz.

The convective component (associated to the pressure fluctuation due to eddies) and the acoustic component (associated to the acoustic waves radiated by eddies) of the excitation are then very separated, such that their effects should influence the plate in separate frequency ranges.

It is also important to note that in naval applications, a strong fluid-structure coupling must be considered, because of the high mass density of the fluid. In this case, the equation of motion of a plate immersed in water becomes:

$$D\left(\frac{\partial^4 w}{\partial x^4} + 2\frac{\partial^4 w}{\partial x^2 \partial y^2} + \frac{\partial^4 w}{\partial y^4}\right) - \rho h \omega^2 w = f(x, y, \omega) + p_{radiated}(x, y, \omega), \quad (5)$$

where $p_{radiated}$ is the wall pressure induced by the vibration of the plate on the water side.

Hence, in the inverse problem, if the strong coupling is not considered in the equation of motion, the result of FAT or CFAT will contain the wall pressure due to the fluid-structure coupling. To avoid that, it is proposed to modify the equation of motion by using an effective wavenumber γ as follows:

$$\left(\frac{\partial^4 w}{\partial x^4} + 2\frac{\partial^4 w}{\partial x^2 \partial y^2} + \frac{\partial^4 w}{\partial y^4}\right) - \gamma^4 w = f(x, y, \omega)/D, \quad (6)$$

where $\gamma^4 = k_f^4 + \frac{p_{radiated}(x,y,\omega)}{D.w(x,y,\omega)}$.

Of course, the value of γ is not known a priori, but it depends on the radiation impedance of the plate. Hence, for infinite plates, γ does not depend on space, but for finite plates, it depends on space: its calculation could be obtained in the modal basis of the plate, provided that the boundary conditions and the environmental conditions are well known.

Since the influence of the strong fluid-structure coupling on the effective wavenumber is due to a wall pressure, its quantification should be measurable by CFAT. This is the goal of Sect. 4.4, where a two-step procedure is proposed in order to extract the wall pressure responsible for the excitation only.

Table 2 Characteristics of the simulation made for car applications

Structure	Glass plate 3.85 mm thick
Flow velocity	50 m/s
Convection frequency	34 Hz
Critical frequency	3200 Hz
Spacing	6.8 cm

3.2 Ground Transportation Applications

Ground transportation applications correspond to automotive and/or train industrial sectors. In these cases, the fluid is air and has the property to be a lightweight fluid. Since its mass density is small enough, the dynamic coupling can be neglected. Compared to naval applications, another difference is also in the velocity values since cars and trains travel faster than boats. Hence, acoustic and convective wavenumbers are closer, a narrower medium frequency range appears here (see Fig. 3). Taking into account the typical characteristics given in Table 2, the convection frequency is equal to 34 Hz and the critical frequency is equal to 3200 Hz. As a consequence, a higher overlap of both components is possible, such that the identification of the most responsible component for the vibration of the structure can be difficult in the audible frequency range.

3.3 Aeronautic Transportation Applications

In aeronautic and aerospace applications, the fluid is air, but the velocities become very high and can be close to the speed of sound and greater for supersonic transportations. The acoustic and convective components follow closer linear laws, such that the medium frequency range is very narrow or not available when the critical frequency becomes smaller than the convection frequency in supersonic flows. In the wavenumber domain, both components present an important overlap at all frequencies. The major influence on the vibration should then be due to the aerodynamic component, since its amplitude is always very high compared to that of the acoustic component. In this paper, the studied aeronautic case corresponds to a subsonic flow, where the characteristics are given in Table 3. The corresponding convection and critical frequencies are respectively 448 and 1272 Hz.

Table 3 Characteristics of the simulation made for aeronautic applications

Structure	Aluminium plate 2 mm thick
Flow velocity	252 m/s
Convection frequency	1590 Hz
Critical frequency	4448 Hz
Spacing	5 cm

4 Numerical Simulations

4.1 Principle of the Simulations

In order to understand the potential of FAT and CFAT in the different industrial cases, numerical simulations are proposed. All of them are made from the same approach summarized in Fig. 4. The principle is here to obtain numerically and easily the wall pressures and the displacement fields in the case of a finite plate excited by a turbulent boundary layer (TBL). Note that the idea is here to be able to understand what kind of results FAT and CFAT can provide in conditions close to the characteristics of the vibration due to the TBL. It is not to calculate precisely or to reproduce with fidelity the direct problem.

First, the blocked pressure field, corresponding to the wall pressure field when considering a rigid structure, is calculated on a meshgrid from a signal processing synthesis. The principle consists in computing time signals from auto and cross-spectra samples which contain an acoustic component and a convective component. The auto-spectra of both components are chosen to be proportional to the Goody's model [13], the cross-spectrum of the acoustic component is chosen to be a sinc function supposed to model the diffuse field, the cross-spectrum of the convective component is chosen to be close to that of the well-known Corcos' model [14]. The global sample is given in [9].

The difference between the acoustic and the convection component levels is chosen to be around 20 dB which is the value experimentally determined by Arguillat et al. [15] in the case of an example close to the characteristics of a car application. For other domains, this difference is not known, but it should be probably big also. The generation of time signals is obtained from a Cholesky decomposition approach that is already described in [9].

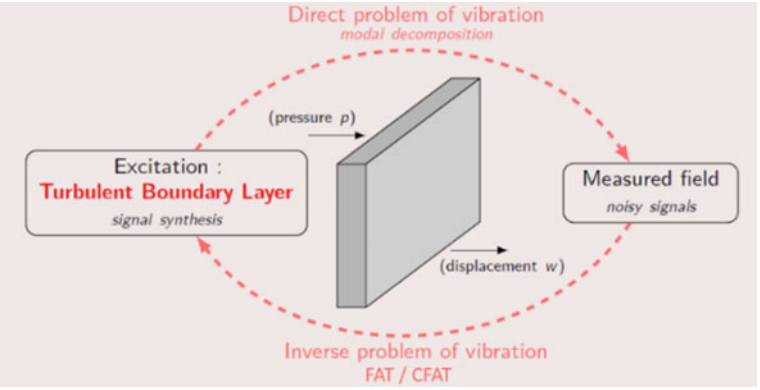

Fig. 4 Principle of the numerical simulations

Second, the displacement field of a simply supported plate excited by the blocked wall pressure field is computed by using a modal decomposition in the time domain. This step is also completely described in the previous Flinovia publication [11]. For naval application, the direct problem is calculated by taking into account the radiation impedances coupling the eigen modes of the plate and the acoustic radiation.

Third, a noise is added to the displacement field in order to get close to measurements. In the following, the Signal to Noise Ratio (SNR) is chosen to be equal to 40 dB.

Fourth, the FAT and the CFAT approaches are applied for one position of a given observation mesh where the 13 input data are noisy displacements. The results are then compared to the blocked wall pressure obtained at the same position (center of the observation mesh).

4.2 Identification of Wall Pressures in the Automotive Domain

The characteristics of the simulation in the case of car application are given in Table 2. The considered structure is a glass plate 3.85 mm thick for which the critical frequency is 3200 Hz. The velocity of the flow is 50 m/s corresponding to a convection velocity equals to 35 m/s if we consider that the ratio between them is 0.7 (close to most of the experimental observations made in the literature [16]). The corresponding convection frequency is 34 Hz.

The autospectra of both components of the blocked pressures and the results obtained by FAT and CFAT on the plate excited by the total blocked pressure are given in Fig. 5. Below 500 Hz, that corresponds to the frequency for which the wavelength λ is equal to the observation mesh dimension $\lambda_f = 4\Delta$, FAT and CFAT give similar results and the obtained value appears to be between both components. In fact, in this frequency range, it is well known that FAT does not eliminate the noise, the observation mesh dimension is too small, filtering is not sufficient [12]. Between 500 and 1200 Hz, both techniques give also similar levels. Hence, we can deduce that the wall pressure does not contain information around the flexural wavenumber since the difference between both filters is located in this wavenumber region. Moreover, the frequency range 500–1200 Hz is significantly below the critical frequency, where the acoustic wavenumber is known to be smaller than the flexural wavenumber and the convection wavenumber, upper than the flexural wavenumber. The fact that there is no difference in the processing of FAT and CFAT allows us to deduce that there is no energy around the flexural wavenumber, both components are then well separated and that FAT and CFAT extract the acoustic component only. This is the reason why the obtained values correspond well to the level of the acoustic component here.

Above 1200 Hz, the acoustic wavenumber becomes closer to the flexural wavenumber, the excitation starts to have a non null level around the flexural wavenumber of the plate. Consequently, both filtering procedures FAT and CFAT

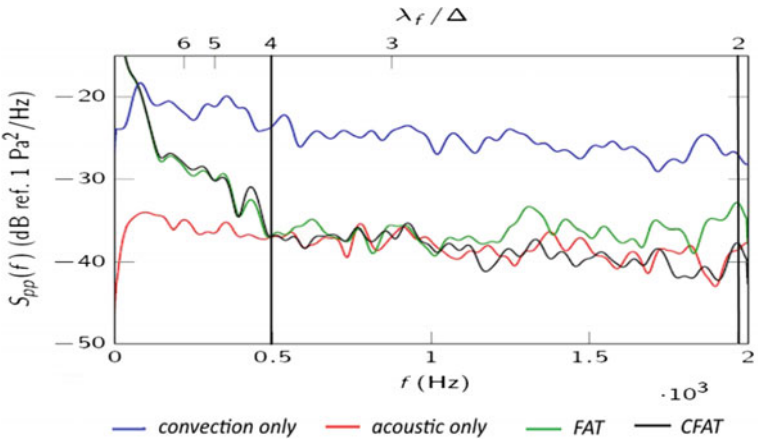

Fig. 5 Wall pressure autospectra on a glass window excited by a Turbulent Boundary Layer in the case of a car application, for which the characteristics are given in Table 2. Vertical lines correspond to frequencies where $\lambda_f = 4\Delta$ and $\lambda_f = 2\Delta$

are getting different results, FAT overestimates the real value because of the singularity at k_f, CFAT gives values close to the acoustic level.

For this kind of application, FAT and CFAT allow one to identify the level of the acoustic component in a frequency range below the critical frequency of the plate and above the lowest frequency limit of the method that is fixed to the size of the observation mesh. The interest of applying both post-processing FAT and CFAT is that this frequency range can be easily determined by finding the frequency range where both techniques give the same result above the frequency for which $\lambda_f = 4\Delta$.

4.3 Identification of Wall Pressures in the Aeronautic Domain

The characteristics of the simulation in the case of the airplane application are given in Table 3. The considered structure is a steel plate 2 mm thick for which the critical frequency is 4448 Hz. The velocity of the flow is 252 m/s corresponding to a convection velocity equal to 176 m/s if the ratio between them is set to 0.7 (close to most of the experimental observations made in the literature). The corresponding convection frequency is 1590 Hz.

The autospectra of both components of the blocked pressures and the results obtained by FAT and CFAT on the plate excited by the total blocked pressure are given in Fig. 6. In the low frequency range, below 500 Hz, it appears that both post-processing FAT and CFAT give similar values and are close to the aerodynamic component, but quickly, they differ from 500 Hz. This difference indicates that the

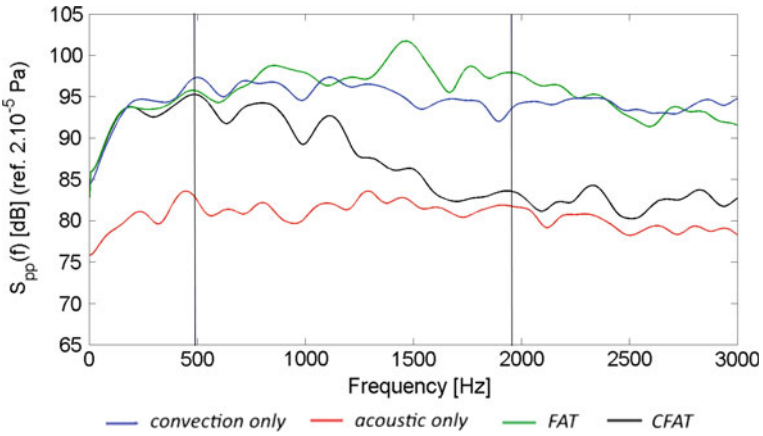

Fig. 6 Wall pressure autospectra on a steel plate excited by a Turbulent Boundary Layer in the case of an aeronautic application, according to the characteristics given in Table 3. Vertical lines correspond to frequencies where $\lambda_f = 4\Delta$ and $\lambda_f = 2\Delta$

excitation contains some energy at the flexural wavenumber, but it is difficult to know here if this energy is due to the acoustic and/or to the aerodynamic component of the excitation.

4.4 Identification of Wall Pressures in the Naval Domain

For the first simulation made in the case of the naval application, the strong fluid-structure is neglected. The characteristics of the test case are given in Table 1. The considered structure is a steel beam 25 mm thick for which the critical frequency is 9594 Hz. The choice to study a beam was necessary because of the high computational cost required to cover both scales associated with the acoustic and the convective wavelengths. The velocity of the flow is 12.9 m/s corresponding to a convection velocity equal to 9.03 m/s if the ratio between them is supposed to be 0.7 (close to most of the experimental observations made in the literature). The corresponding convection frequency is 0.5 Hz.

The autospectra of both components of the blocked pressures and the results obtained by FAT and CFAT on the beam excited by the total blocked pressure are given in Fig. 7. For this kind of flow, it is clear that both components of the excitation are extremely separated, such that both techniques identify only the acoustic component, the aerodynamic component being completely filtered by the finite difference scheme. As in the previous results, the amplification of the noise is important in the low frequency range, below 900 Hz here. One can also observe a small overestimation of FAT in the high frequency range, certainly due to a small participation of the acoustic component around the flexural wavenumber of the structure.

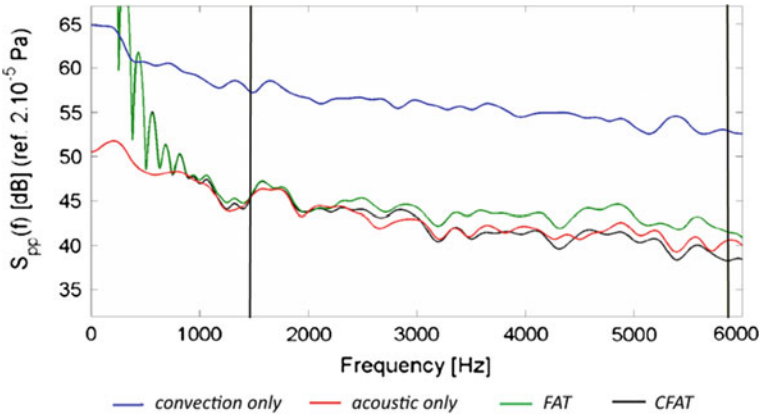

Fig. 7 Wall pressure autospectra on a steel plate excited by a Turbulent Boundary Layer in the case of a naval application, according to the characteristics given in Table 1, ignoring the strong fluid-structure coupling. Vertical lines correspond to frequencies where $\lambda_f = 4\Delta$ and $\lambda_f = 2\Delta$

Of course, the strong coupling is not negligible when considering a heavy fluid like water. Ignoring the strong coupling in the inverse problem consists then in identifying the excitation plus the wall pressure radiated by the structure. The extraction of the acoustic component of the excitation cannot be obtained without knowing $p_{radiated}$ (see Eq. 5) To do that, it is proposed to use the following two-step procedure:

Step 1: identification of the effective wavenumber of the plate, by using CFAT. Here, the flow is off and the plate is excited by a point force. CFAT is then applied in an area where there is no external force. γ^4 can then be identified from CFAT by extracting the ratio $\frac{\left(\mu^4\delta_\Delta^{4x}+2\upsilon^4\delta_\Delta^{2x2y}+\mu^4\delta_\Delta^{4y}\right)}{w}$. For finite (or small) plates, γ depends on the space, it must then be identified in several zones of the plate.

Step 2: application of FAT and CFAT by using the local "wet" equation of motion containing γ instead of k_f. Since both techniques have a local aspect, the spatial dependence of γ for finite plates can be used in specific zones.

To illustrate the identification of the strong coupling for the use of FAT/CFAT techniques, the result of a simulation is given here. Figure 8 shows the effective wavenumber found by the CFAT technique that is compared to the flexural wavenumber which is proportional to the square root of the frequency. It is clear that γ follows a similar law, but its values are greater, because of the added mass effect of the fluid.

Let us consider now that the same plate (immersed in water) is excited by two point harmonic forces at 3800 Hz. It is proposed to see what the result is when applying CFAT by considering the strong coupling (with γ in the equation of motion) or not (with k_f in the equation of motion). Figure 9 shows the result obtained by using k_f (given by the blue curve of Fig. 8) on the plot to the left. The point forces are well located, but, some residual forces appear on the whole surface of the plate. They correspond to the wall pressure radiated by the plate, that interacts with the vibration.

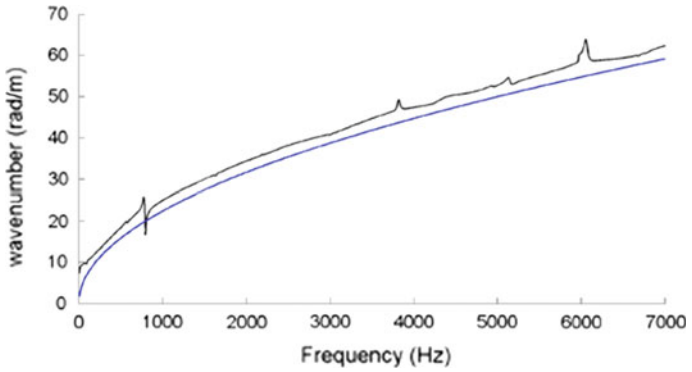

Fig. 8 Local natural wavenumber of a steel plate 25 mm thick. In blue: flexural wavenumber in vacuo, in black: effective wavenumber identified by CFAT, when the plate is in the water

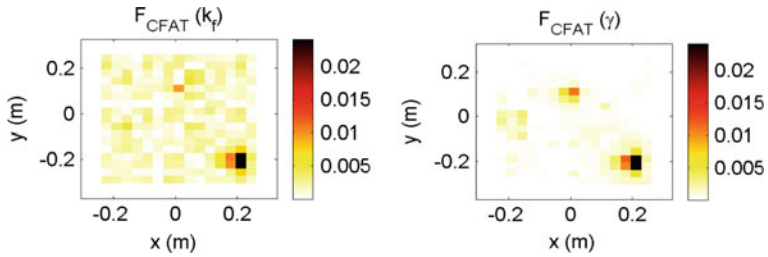

Fig. 9 Force distribution reconstructed by CFAT on a plate in water, excited by two point forces. On the left: by using k_f (the fluid-structure is ignored), On the right: by using γ (identified previously by CFAT)

On the plot to the right, Fig. 9 shows the same calculation where k_f is replaced with γ (given by the black curve of Fig. 8). It is clear that the effect of the coupling is well reduced here.

5 Example of a Real Experimental Test

In this section, a first experimental validation is exposed. It corresponds to the automotive application studied for both French car manufacturers Renault and PSA. The goal is to analyze the aeroacoustic excitation on the driver and passenger windows of a car, that are excited by a detached flow behind the exterior side mirror and/or a turbulent boundary layer.

5.1 Experimentation in a Reverberant Room

In a first phase, a Renault Megane car was placed in a reverberant room, in order to see the results given by FAT and CFAT when the window is excited by an acoustic excitation only. Figure 10 shows the car where two observation meshes are visible on two windows. The first observation mesh (Point 1) is larger than the second (Point 3), the respective spacings are 7 cm and 3.5 cm.

Figure 11 shows the wall pressure identified by FAT/CFAT and directly measured by a microphone at the central point of the first observation mesh (Point 1). The results are particularly remarkable since both inverse techniques give results similar to what a microphone receives. The difference is obtained in the high frequency range, where we can observe clearly that FAT begins to overestimate the pressure from 2000 Hz, just before the critical frequency (3200 Hz here). As shown previously, this difference can be explained by the fact that the studied frequency becomes close to the critical frequency. In a higher frequency range, CFAT gives erroneous values. This phenomenon is due to the fact that the spacing is too large, the spatial sampling (Nyquist criteria) is not available here.

Figure 12 shows the wall pressure identified by FAT/CFAT and directly measured by a microphone at the central point of the second observation mesh (Point 3). Here also, both inverse techniques provide results very similar to what a microphone receives. The difference is obtained in the low frequency range, where the size of the observation mesh is too small, such that both techniques cannot filter the noise. Above 2000 Hz, one can also observe that FAT overestimates the wall pressure, because the frequency range becomes closer to the critical frequency of the glass window, but CFAT gives good values until 10 kHz, the spacing being small enough to cover all this high frequency range.

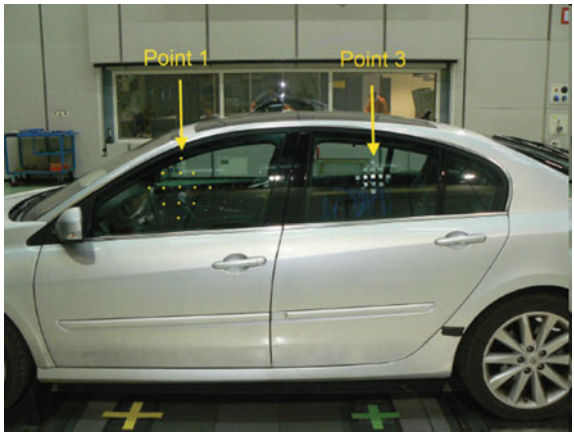

Fig. 10 Photography of the Renault Megane car used for the identification of acoustic wall pressures when the car is placed in a reverberant room

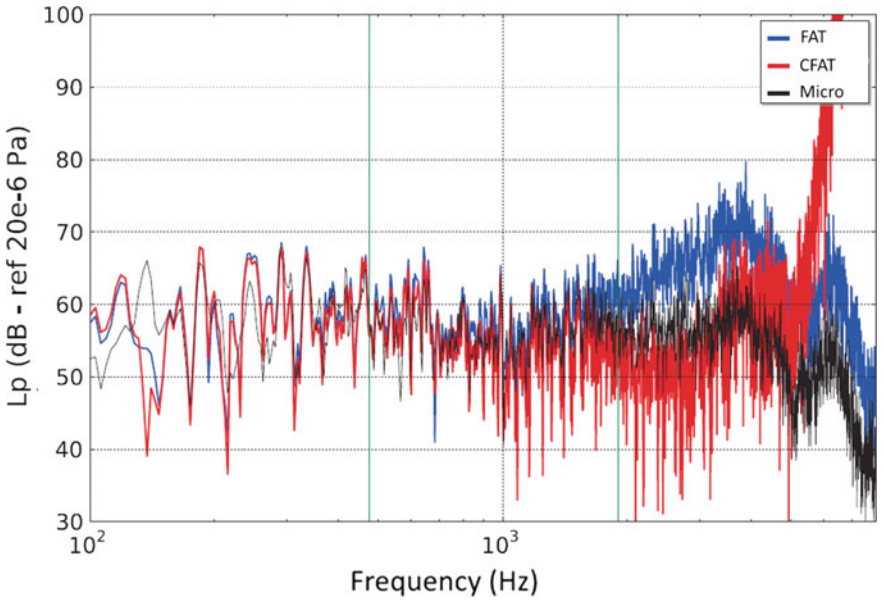

Fig. 11 Identification of the wall pressure exciting the driver window at Point 1 (see Fig. 10)

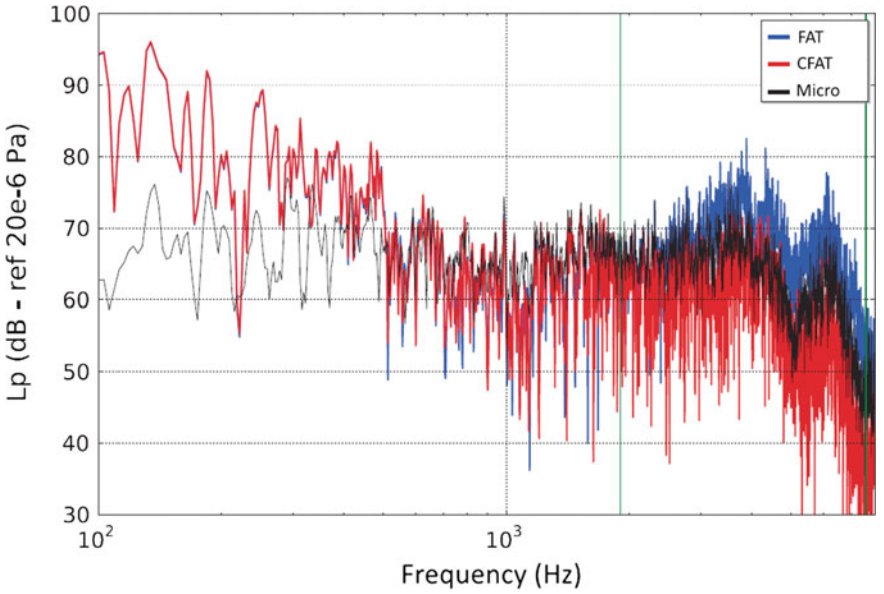

Fig. 12 Identification of the wall pressure exciting the passenger window at Point 3 (see Fig. 10)

Fig. 13 Photography of the PSA 308 car placed in the S2A wind tunnel

5.2 Experimentation in a Wind Tunnel

The second experiment corresponds to a car placed in a wind tunnel. This experimentation was made in the French "S2A" wind tunnel (PSA/Renault/Nissan common platform), where the studied vehicle is a Peugeot 308 car. The photography of the experiment is given in Fig. 13. In the following the flow velocity is 140 km/h.

As shown by the photography in Fig. 14, a FAT/CFAT observation mesh was made of thirteen accelerometers glued in the interior side of the driver window. A 1/4" flush microphone was also fixed at the center of the observation mesh in order to give a direct measurement of the wall pressure (not shown in Fig. 14).

Figure 15 shows FAT and CFAT identifications and direct measurement of the wall pressure at the center of the observation mesh. It is clear that levels given by both inverse methods are very small in comparison with the level of the pressure measured by the microphone. This difference is clearly due to low-pass wavenumber filtering. The most interesting thing is that FAT and CFAT give exactly the same result until 2000 Hz. This frequency range is under the critical frequency range,

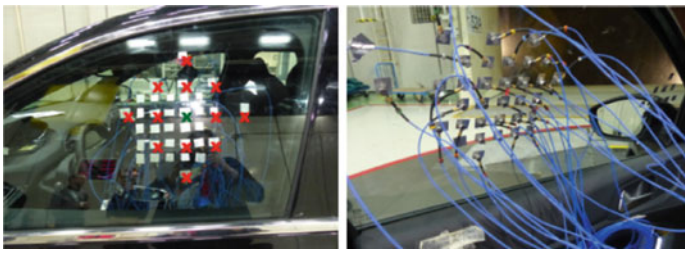

Fig. 14 Photography of the observation mesh fixed on the driver window. On the left: view from outside the car. On the right: view from inside the car

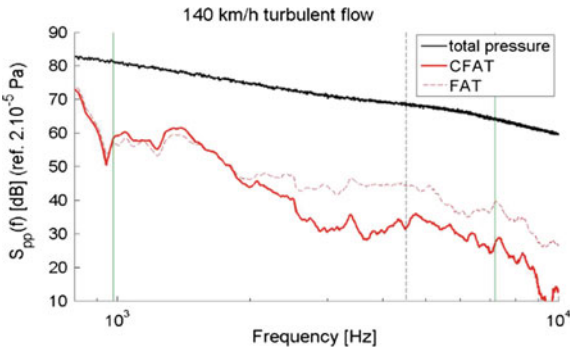

Fig. 15 Identification of the wall pressure exciting the driver window when the car is in a wind tunnel with a flow velocity of 140 km/h

where the acoustic component is known to be entirely below the flexural wavenumber. In addition, the convection frequency is here very small here (12 Hz) and the convection wavenumber is also known to be upper than the flexural wavenumber in the frequency range 12–2000 Hz. The fact that both techniques give the same result is a very important information because it tells us that there is no energy around the flexural wavenumber. Both components are then deduced to be very separated and the FAT/CFAT results contain the whole acoustic component. After 2000 Hz, the difference between FAT and CFAT appears clearly, the acoustic component begins to excite the window at its flexural wavenumber k_f. In this high frequency range, the acoustic component level is expected between both curves since FAT overestimates the result (because it amplifies the level at k_f) and CFAT underestimates the result (because it begins to filter the acoustic component).

6 Conclusion and Perspectives

The identification of the wall pressure due to turbulent flows is possible by using an inverse problem of vibration. FAT and CFAT methods bring a functional simplicity since they consist in applying locally a finite difference scheme, discretizing the local equation of motion of the structure. In the case of thin plates, the standard observation mesh, made of thirteen accelerometers, gives very good results. Of course, the choice of the spacing between points is very important, since it is directly linked to the required low-pass wavenumber filter, eliminating the amplification of noise. In this paper, the interest to use both FAT and CFAT methods is highlighted, since the comparison provides an indicator about the nature of the result (acoustic only or not) between the convection frequency and the critical frequency. The other goal of this paper is to show what can be obtained in the three different transportation applications. In automotive applications, FAT and CFAT can be clearly used to identify the acoustic component in a large audible frequency range. Simulations and experiments made on a car have given very good results, showing the importance of the acoustic component on the glass window vibrations, that transmits the

noise inside the car. In naval applications, the extreme separation of the acoustic and the convection components implies that the influence of the acoustic component is very important, such that FAT and CFAT identify it very well. The most difficult problem here is the strong fluid-structure coupling such that the acoustic component contains that of the turbulence and that of the structure radiation. In order to separate them, a novel strategy is proposed, it consists in taking into account the fluid-structure coupling in the used equation of motion, that can be embedded in an effective wavenumber. The latter can then be experimentally identified by CFAT in a preliminary step. This approach is shown numerically here, but an experimental validation is in progress. In aeronautic applications, the problem is more complex, because an overlap exists between both acoustic and convective components. FAT and CFAT give then different results because the excitation contains always (some) energy at the flexural wavenumber. The most interesting result is certainly that of CFAT which does not introduce any amplification around k_f. However it must be interpreted as a "low wavenumber result" that does not contain all the excitation responsible for the vibration to which both acoustic and aerodynamic components contribute.

Acknowledgements This paper gives a synthesis of several projects. For automotive applications, the work is funded by the consortium "Le Mans Acoustics" and the CNRT R2A association linked to the common wind tunnel of PSA, Renault, Nissan and CNAM. The authors would also like to give a special thank to Renault who accepts to show the results obtained in the reverberant room. For naval and aeronautic applications, the work is funded by the French technological research institute IRT Jules Verne in the frame of the Chair program VIBROLEG (Vibroacoustics of lightweight structures) financially supported by Airbus, Daher, Naval Group, STX, General Electric, Cetim and Bureau Veritas and scientifically supported by the acoustic laboratory of Le Mans LAUM UMR CNRS 6613.

References

1. Pezerat, C., Guyader, J.L.: Two inverse methods for localization of external sources exciting a beam. Acta Acustica **3**, 1–10 (1995)
2. Pezerat, C., Guyader, J.L.: Force analysis technique: reconstruction of force distribution on plates. Acust. U. Acta Acust. **86**, 322–332 (2000)
3. Djamaa, M.S., Ouelaa, N., Pezerat, C., Guyader, J.L.: Mechanical radial force identification of a finite cylindrical shell by an inverse method. Acta Acust. **92**(3), 398–405 (2006)
4. Djamaa, M.S., Ouelaa, N., Pezerat, C., Guyader, J.L.: Reconstruction of a distributed force applied on a thin cylindrical shell by an inverse method and spatial filtering. J. Sound Vib. **301**(3–5), 560–575 (2007)
5. Renzi, C., Pezerat, C., Guyader, J.-L.: Vibratory source identification by using the finite element model of a subdomain of a flexural beam. J. Sound Vib. **332**(3), 545–562 (2013)
6. Renzi, C., Pezerat, C., Guyader, J.-L.: Local force identification on flexural plates using reduced finite element models. Comput. Struct. **144**, 75–91 (2014)
7. Chevillotte, F., Leclere, Q., Totaro, N., Pezerat, C., Souchotte, P., Robert, G.: Identification d'un champ de pression pariétale induit par un écoulement turbulent à partir de mesures vibratoires (Identification of a wall pressure field induced by a turbulent flow from vibration measurements), 10ème Congrès Français d'Acoustique, 12–16 avril. Lyon, France (2010)

8. Lecoq, D.: Identification par problème inverse vibratoire des bas nombres d'onde de pressions pariétales turbulentes (Identification of the low wavenumber components of turbulent wall pressures by an inverse problem), Ph.D. thesis, Université du Maine, Le Mans, France (2013)
9. Lecoq, D., Pezerat, C., Thomas, J.-H., Bi, W.: Extraction of the acoustic component of a turbulent flow exciting a plate by inverting the vibration problem. J. Sound Vib. **333**(12), 2505–2519 (2014)
10. Lecoq, D., Pezerat, C., Chevillotte, F., Bessis, R.: Measurement of the low-wavenumber component within a turbulent wall pressure by an inverse problem of vibration. J. Acoust. Soc. Am. **140**(3), 1974–1980 (2016)
11. Totaro, N., Pezerat, C., Leclere, Q., Lecoq, D., Chevillotte, F.: Identification of boundary pressure field exciting a plate under turbulent flow. In: Ciappi, E. et al. (eds.) Flinovia—Flow Induced Noise and Vibration Issues and Aspects. Springer International Publishing Switzerland (2015). ISBN: 978-3-319-09712-1. https://doi.org/10.1007/978-3-319-09713-8_9
12. Leclere, Q., Pezerat, C.: Vibration source identification using corrected finite difference schemes. J. Sound Vib. **331**, 1366–1377 (2012)
13. Goody, M.: Empirical spectral model of surface pressure fluctuations. AIAA J. **42**, 1788–1794 (2004)
14. Corcos, G.M.: Resolution of pressure in turbulence. J. Acoust. Soc. Am. **35**, 192–199 (1963)
15. Arguillat, B., Ricot, D., Bailly, C., Robert, G.: Measured wavenumber: frequency spectrum associated with acoustic and aerodynamic wall pressure fluctuations. J. Acoust. Soc. Am. **128**, 1647–1655 (2010)
16. Farabee, T.M.: T.M., Casarella M. J., Spectral features of wall pressure fluctuations beneath turbulent boundary layers. Phys. Fluids A: Fluid Dyn. **3**, 2410 (1991)

Part II
Flow–Sound Sources

Flow-Induced Noise of Shedding Partial Cavitation on a Hydrofoil

Harish Ganesh, Juliana Wu and Steven Ceccio

Abstract The cavitation dynamics on a NACA0015 hydrofoil can have different cavitation shedding behaviors depending upon the attack angle and flow conditions, as discussed in Arndt et al. (Instability of partial cavitation: a numerical/experimental approach, 2000) [1] and Kjeldsen et al. (J Fluids Eng 122(3):481–487, 2000) [8]. Shedding can exhibit varying shedding frequencies (Strouhal numbers) measured based on measurements of the resulting surface pressure and body forces. Moreover, the transition from one regime of shedding to another can be abrupt with changes in cavitation number. In this work, we present an analysis of the acoustic signatures measured by a hydrophone for different shedding conditions using a Morse wavelet analysis. Using measurements of the cavity dynamics based on X-ray densitometry and high-speed video observations (Ganesh et al., 31st symposium on naval hydrodynamics, ONR 2016) [6], we present an explanation for the observed acoustic behavior.

1 Background

Hydrodynamic cavitation occurs when the local pressure of a flowing liquid reaches close to vapor pressure. Such conditions can occur on low-pressure regions of lifting surfaces, blade passages of marine propulsors, and the separated flow behind bluff objects, among other scenarios. Cavitation occurring in low-pressure regions can remain attached to the geometry, forming stable partial cavities. The stable vapor filled regions under certain conditions can exhibit periodic change in volume characterized by shedding of vapor clouds. This phenomenon of periodic shedding of vapor clouds, termed as cloud cavitation, is detrimental to performance of hydrodynamic devices and a significant source of noise. A basic review of the observations and associated processes can be found in [5].

Cavitation on spanwise uniform (2D) hydrofoil sections, by the virtue of its similarities to cavitation on a propulsor blade, has also been studied extensively. [1, 8]

H. Ganesh (✉) · J. Wu · S. Ceccio
University of Michigan, 48109 Ann Arbor, MI, USA
e-mail: gharish@umich.edu

E. Ciappi et al. (eds.), *Flinovia—Flow Induced Noise and Vibration Issues and Aspects-II*,
https://doi.org/10.1007/978-3-319-76780-2_4

studied cavitation dynamics of a NACA0015 hydrofoil at different attack angles and cavitation number. Based on the spectral analysis of the lift measurements and surface pressure measurements, it was found that the spectral characteristics changed significantly with a reduction in cavitation number. They found that the Strouhal number associated with surface pressure and lift fluctuations dropped by 50%, signifying appreciable change in dynamics when $\sigma_0/2\alpha$ approached a value of 4. Since this transition also occurred when the cavity length was close to 75% of the chord, an explanation for the observed change that relied on the quarter chord length instability derived from potential theory was posited. Another hypothesis that was suggested was the presence of bubbly shocks that could alter the dynamics abruptly. [9] performed PIV measurements of the velocity fields in the vicinity of a cavitating plates and NACA0015 hydrofoils and noted how the topology of the cavitation varied with changing attack angle and cavitation number.

In the present study, we revisit the issue of the underlying mechanism for the transition to large-scale cavity shedding on a hydrofoil from an acoustic perspective. This paper focusses on the acoustic behavior of shedding cavities studied by the authors in [6]. Particularly, we present the different types of acoustic noise emitted by different types of cavitation. Upon performing a Morse wavelet analysis on the hydrophone signal, flow features responsible for observed acoustic behavior are identified. Based on the observations reported in [6] by the same authors, an explanation for the observed acoustic signature is proposed.

2 Cavitation on a NACA0015 Hydrofoil

In the present study, experiments were carried out at the Michigan 9-inch water tunnel with a reduced test section area of 3×3 in. Figure 1 shows a schematic of the experimental setup with the hydrofoil. Two important parameters that dictate observed cavitation dynamics on a hydrofoil are the inlet cavitation number σ_0 and the attack angle α. Here the cavitation number σ_0, in terms of the inlet pressure p_0, velocity v_0, vapor pressure p_v, and density of liquid ρ_L, is defined as

$$\sigma_0 = \frac{(p_0 - p_V)}{\frac{1}{2}\rho U_0^2} \tag{1}$$

Figure 2 shows different types of cavitation events that were observed at an attack angle of 10° at an instance of maximum cavity length. Figure 2a shows a typical incipient cavity of constant length. These types of cavities were observed at higher cavitation number, $\sigma_0 = 2.7$. A snapshot of cavities of Type 2 at $\sigma_0 = 2.0$, with the classification based on the observed dynamics, is shown in Fig. 2b. The observed cavity is longer in length and the length of the cavity oscillates. Figure 2c shows a snapshot of type 1 cavity at $\sigma_0 = 1.4$. An important observation from the above figure is that as the cavitation number decreases, the cavity grows in length. The dynamics

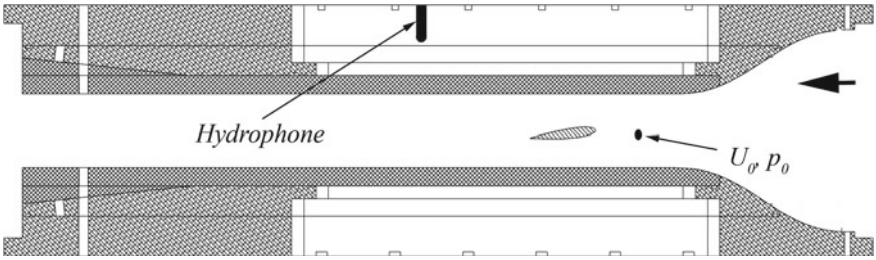

Fig. 1 Schematic of experimental setup

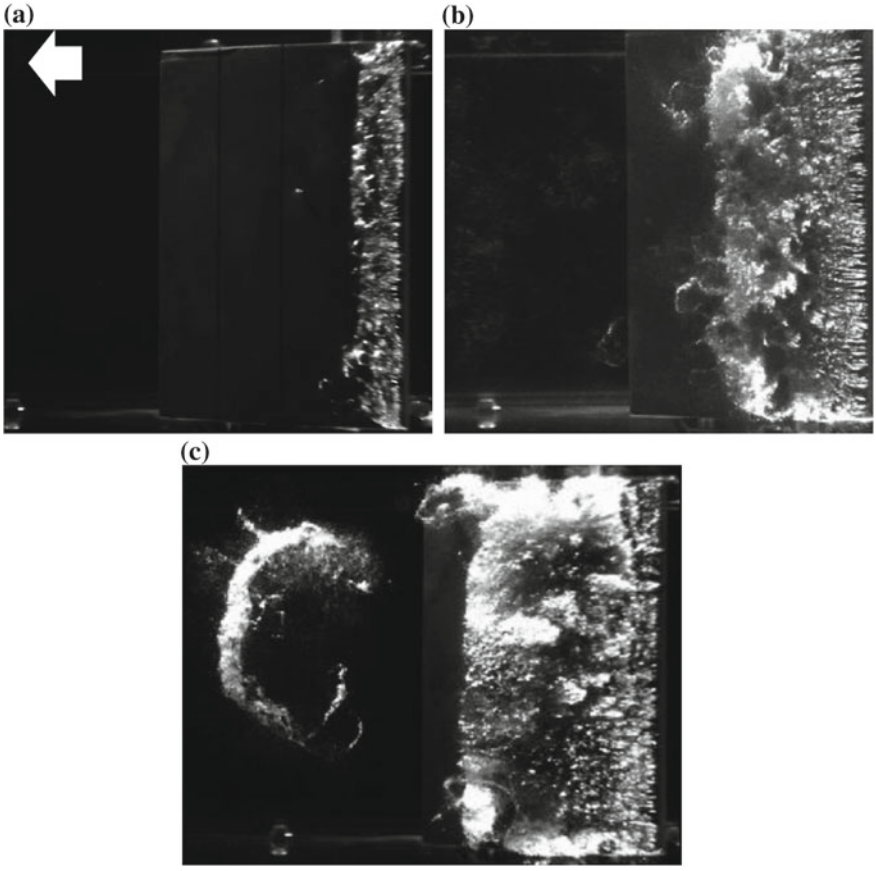

Fig. 2 Three types of cavities forming on the leading edge of a NACA0015 hydrofoil at different σ_0. **a** is an incipient cavity at $\sigma_0 = 2.7$, **b** snapshot of a Type 2 cavity at $\sigma_0 = 2.0$, and **c** Type 1 cavity at $\sigma_0 = 1.4$

of cavitation also change with a change in cavitation number. In the current work, the attack angle of the hydrofoil is set to be 10°. Next section discusses the observed dynamics in detail.

3 Cavitation Dynamics

Cavitation dynamics on the surface of the foil changed significantly with changes in the cavitation number. Stable incipient cavities were typically a bubbly shear layer with a relatively stable length. With a reduction in the inlet cavitation number, larger scale cavity shedding with complex dynamics was observed. Figure 3 shows a schematic diagram of four different types of cavity shedding cycles observed on the foil. Based on the observations, four different regimes are defined.

(1) Incipient: A stable cavity is primarily a bubbly shear flow with nearly constant cavity length.

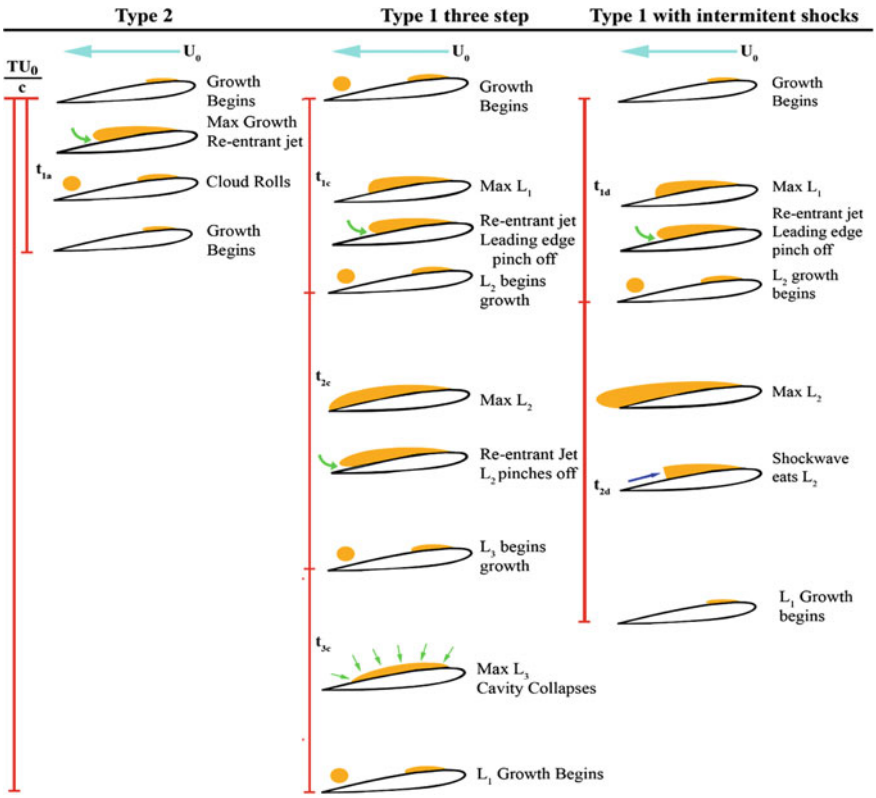

Fig. 3 Different cavity shedding mechanisms illustrating Type 1 and Type 2 cavity shedding

(2) Type 2 Shedding: Shedding is from the rear of the cavity and is primarily caused by a liquid reentrant flow. Smaller cavity clouds form primarily at the cavity closure region.

(3) Type 1 Shedding—Three-Step Cycle: At lower values of σ_0, shedding occurs as a multi-step process. A cavity begins to grow to attain a length (L_1), and it is partially pinched off during this growth process. The collapse of the pinched off cloud interferes with, but does not arrest, the cavity growth, which subsequently reaches its maximum length (L_2). Upon attaining maximum length, the cavity is pinched off from the leading edge, and the resulting vapor cloud rolls up to collapse. This collapse arrests the growth of the cavity at a length (L_3), causing it to implode and shed from the leading edge. The resultant shed cloud collapse is not strong enough to arrest the growth of the subsequent cavity, and the cycle continues.

(4) Type 1 Shedding—Intermittent Shocks: At still lower values of σ_0, strong bubbly shock waves begin to form at the cavity closure, propagating upstream along within the bubbly flow of the cavity, and then impinging on the leading edge. The roll-up of the cloud induced by the strong bubbly shock wave often caused the subsequent growing cavity to collapse.

At sufficiently low values of σ_0, the shedding dynamics may be a combination of the different type 1 shedding cycles. Shock wave-induced shedding was more prominent for three-step type 1 shedding. The next section discusses the measurement of acoustic emissions by such cavities and analysis.

4 Acoustic Measurements and Analysis

Acoustic pressure associated with cavitation dynamics was measured using Bruel and Kjaer hydrophone as shown in Fig. 1. The hydrophone was mounted in a water pocket on the top window and was located approximate two chords downstream of the hydrofoil trailing edge. The acoustic signal from the hydrophone was charged amplified and band passed between 10 Hz to 200 kHz using a filter. The filtered analog signal was then passed to A/D converter sampling at 500 kHz. Obtained hydrophone signals were analyzed using a continuous Morse wavelet transform routine in MATLAB to obtain a time–frequency analysis.

Time variation of frequency is important while studying multimodal dynamics. A standard fast Fourier transform (FFT) gives the presence of different frequencies in the whole signal, but does not provide any information about the time variation. Spectrograms, which are windowed FFT, can provide time variation of frequency as the window moves. However, the frequencies within the windows are still averaged over the window length. This prevents the possibility of resolving sharp variations without compensating on either the frequency or time resolution. Wavelets are being used extensively for the ability to perform better in resolving sharp changes in frequency while preserving resolution. A good overview of wavelets in time–frequency analysis can be found in [4].

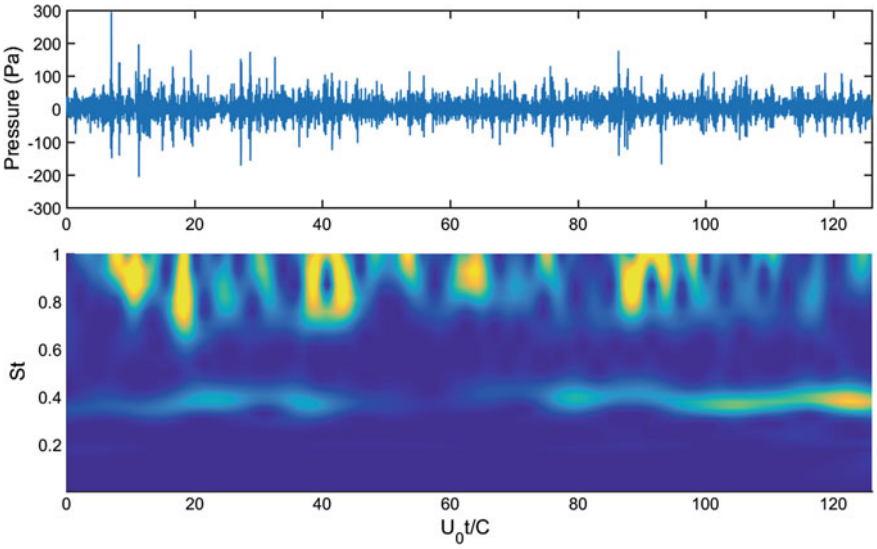

Fig. 4 Top: Acoustic pressure recorded for a Type 2 shedding cavity at $\sigma_0 = 1.63$. Bottom: Morse wavelet analysis of the acquired signal

Hydrophone signals and their corresponding wavelet transforms are discussed below. The length of the time signal in real time corresponds to about 0.787 s. This duration was chosen to match time-resolved densitometry measurements of the same duration. Since the contribution from the higher frequencies was more prominent, the range of frequencies only those corresponding to a Strouhal number (S_t) of $S_t < 1$ was chosen to be presented. Strouhal number in terms of the frequency, f, chord, C is given by

$$S_t = \frac{fC}{U_0} \tag{2}$$

Figure 4 shows the acoustic measurement (top) and its corresponding continuous wavelet transform (CWT) for a Type 2 shedding cavity at $\sigma_0 = 1.6$ (bottom). The X-axis in CWT is non-dimensional timescale defined in terms of the inlet speed (U_0) and chord length, C. This type of cavity has a reentrant flow-induced shedding at the rear of the cavity. Observations are reported in [6]. The dominant Strouhal number for this type of shedding was close $S_t \sim 0.45$, with lower Strouhal numbers also featuring in the time–frequency analysis. With a reduction in cavitation number, the dynamics change significantly as shown in Fig. 5. The dominant frequency is centered around $S_t \sim 0.35$. Time–frequency analysis reveals that dominant Strouhal number changes with time. This is due to the multi-step nature of the shedding as discussed before. The influence of cloud collapse on cavity growth results in different dynamics that Type 2 shedding effectively reducing the Strouhal number.

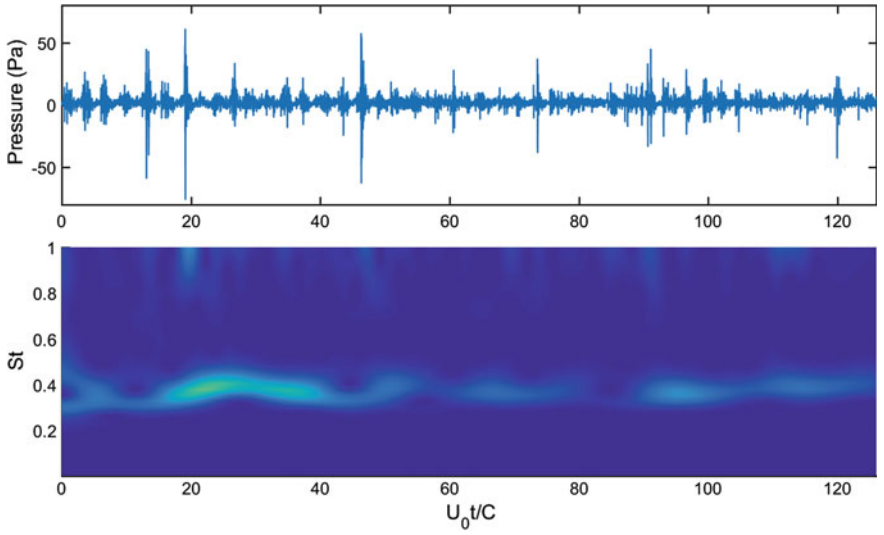

Fig. 5 Top: Acoustic pressure recorded for a Type 2 shedding cavity at $\sigma_0 = 1.25$. Bottom: Morse wavelet analysis of the acquired signal

Figure 6 shows the time–frequency analysis of a Type 1 shedding with the presence of shocks. Propagating bubbly shocks were observed using time-resolved X-ray densitometry, and the results are presented in [6]. Void fraction values close to 0.6 result in low speed of sounds that make the flow susceptible to shocking as discussed in [2, 3, 7]. This results in an additional timescale which can influence the observed dynamics. Time–frequency analysis based on wavelets shows that there are several modes existing at a given time. In addition, strong cloud collapse produces broadband noise that can be seen across frequencies. In some instances, the shock propagation resulted in shedding and re-growth cycle which was different from multi-step Type 1 shedding. On several occasions, collapse of the shed cloud near the trailing edge caused trailing edge closer to pressure side of the foil to cavitate. This resulted in another cloud being shed. The observations are discussed in [6]. Occurrence of one or more of these processes at a given instance results in rich multimodal acoustic behavior. Figure 7 shows the FFT of acoustic signals at different cavitation numbers acquired over a period of 30 s. The signal is multimodal, and the multimodal behavior increases with decreasing cavitation number. This observation is similar to that obtained by time–frequency analysis using wavelets. However, the dominant frequency at lower cavitation numbers based on FFT has a value close 0.15.

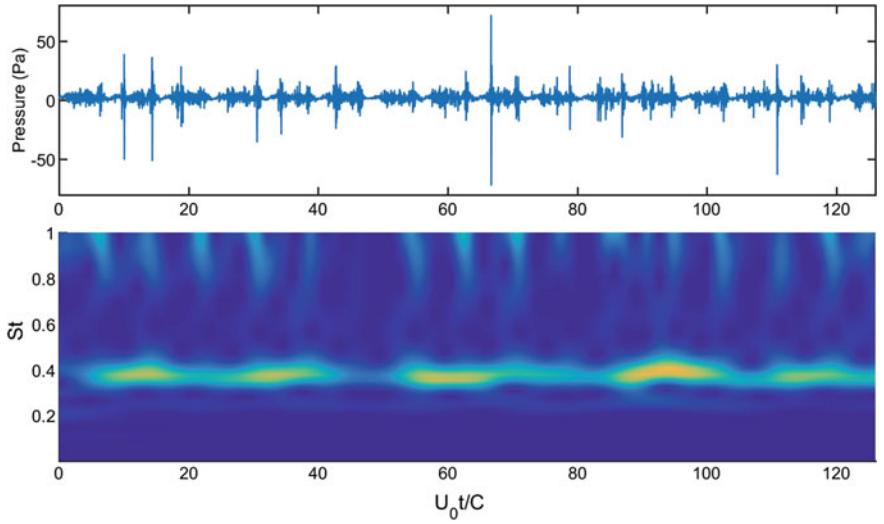

Fig. 6 Top: Acoustic pressure recorded for a Type 2 shedding cavity at $\sigma_0 = 1.06$. Bottom: Morse wavelet analysis of the acquired signal

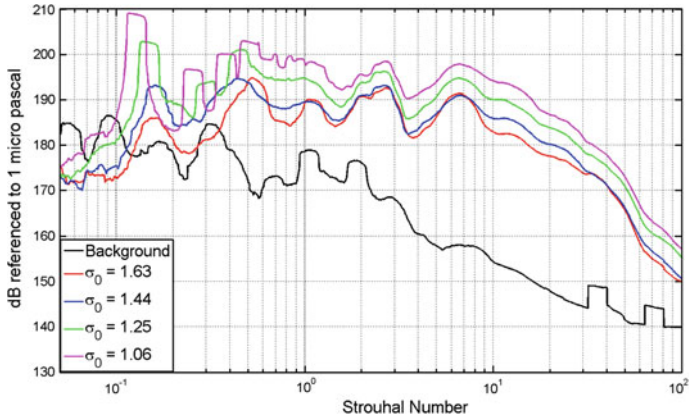

Fig. 7 FFT of acoustic pressure for varying cavitation numbers for a duration of 30 s

5 Conclusions

The physical mechanism responsible for multimodal cavitation shedding dynamics on a NACA0015 hydrofoil was studied in [6]. The acoustic characteristics of these shedding cavities were studied using wavelet analysis. Wavelets capture the multimodal nature of this cavitating flow to a reasonable extent. Using time-resolved X-ray densitometry measurements of void fraction flow fields, the observed multimodal acoustic behavior is associated with flow specific flow features and processes

associated with shock-induced cavity collapse. At lower cavitation numbers, the presence of multiple flow processes that can occur simultaneously or in succession results in a strong multimodal behavior. This coincides with the observation of bubbly shocks as a mechanism of cavity pinch off and shedding.

Acknowledgements This work was supported by the Office of Naval Research under grant N00014-14-1-0292, Dr. Ki-Han Kim Program Manager.

References

1. Arndt, R.E., Song, C., Kjeldsen, M., He, J., Keller, A.: Instability of partial cavitation: a numerical/experimental approach (2000)
2. Brennen, C.E.: Fundamentals of Multiphase Flow. Cambridge University Press (2005)
3. Crespo, A.: Sound and shock waves in liquids containing bubbles. Phys. Fluids. **12**(11), 2274–2282 (1969)
4. Debnath, L.: Wavelets and Signal Processing. Springer Science & Business Media (2012)
5. Franc, J.P., Michel, J.M.: Fundamentals of Cavitation, vol. 76. Springer Science & Business Media (2006)
6. Ganesh, H., Wu, J., Ceccio, S.: Investigation of cavity shedding dynamics on a naca0015 hydrofoil using time resolved x-ray densitometry. In: 31st Symposium on Naval Hydrodynamics, ONR (2016)
7. Ganesh, H., Mäkiharju, S.A., Ceccio, S.L.: Bubbly shock propagation as a mechanism for sheet-to-cloud transition of partial cavities. J. Fluid Mech. **802**, 37–78 (2016)
8. Kjeldsen, M., Arndt, R.E., Effertz, M.: Spectral characteristics of sheet/cloud cavitation. J. Fluids Eng. **122**(3), 481–487 (2000)
9. Kravtsova, A.Y., Markovich, D., Pervunin, K., Timoshevskiy, M., Hanjalić, K.: High-speed visualization and piv measurements of cavitating flows around a semi-circular leading-edge flat plate and naca0015 hydrofoil. Int. J. Multiph. Flow **60**, 119–134 (2014)

Sound Sources of Radial Compressors—A Numerical Study on the Outlet Side

Lars Enghardt, Armin Faßbender and Jakob Hurst

Abstract As follow-up work of an experimental investigation performed by Raitor and Neise (J Sound Vib 314:738–756, 2008) [1] from 2001–2006, a numerical study using the unsteady RANS code for turbomachinery applications from the DLR (TRACE, Ashcroft et al., J Turbomach 136:021002, 2013 [2]) was performed by the University of Aachen (RWTH) and thoroughly analysed in collaboration with the Technical University of Berlin (TUB). Raitor and Neise were discriminating dominating noise source mechanisms in different frequency ranges both on the suction and the pressure side of the investigated radial compressor setups. Their elaborated work was focussed on the suction side of the experiment. In contrast to the suction side, where Raitor and Neise installed a multitude of microphones that allowed for a sound field decomposition into circumferential modes as well as—utilising the ISO 5136 methodology—the determination of the sound power, the pressure side was equipped with just a few microphones providing only spectral but no spatial information nor the sound power of the excited compressor sound field. In order to gain more insight into the sound propagation to the pressure side of radial compressors, the dominant tonal components of the conducted numerical study were acoustically analysed in terms of their radial mode constituents and the downstream transmitted sound power. The ongoing research is a first step towards the deeper physical understanding of the dominant constituents of sound fields propagating into the downstream ducts of radial compressors.

L. Enghardt (✉) · J. Hurst
Institute of Fluid Dynamics and Technical Acoustics (ISTA),
Technical University Berlin, 10623 Berlin, Germany
e-mail: lars.enghardt@dlr.de

L. Enghardt
German Aerospace Center, Engine Acoustics, 10623 Berlin, Germany

A. Faßbender
Institute of Jet Propulsion and Turbomachinery (IST), RWTH Aachen University,
52062 Aachen, Germany

E. Ciappi et al. (eds.), *Flinovia—Flow Induced Noise and Vibration Issues and Aspects-II*,
https://doi.org/10.1007/978-3-319-76780-2_5

1 Introduction

Radial compressors are, e.g., used for turbocharging the diesel engines of large ships or power stations, as turbochargers in automotive applications, or in helicopter engines enabling high air compression rates in confined spaces. The growing demand for higher engine power output requires that mass flow rate and pressure ratio of the compressors are constantly increased. While the aerodynamic power of turbomachines is proportional to the third power of the rotor tip speed, the sound power usually grows with the fifth or sixth power of the circumferential Mach number. In particular, the tonal components of the compressor noise, the blade passing frequency and its harmonics are annoying and therefore deserve special attention when it comes to reducing the overall machine noise. Operational safety and health regulations force manufacturers of turbomachinery to comply with regulatory limits of noise emissions.

In order to design low-noise compressor and secondary noise insulation, a detailed knowledge of the emitted sound field in terms of sound power as well as modal structure is crucial. The long-term goal of this study is to understand the blade tone noise of high-speed high-pressure centrifugal compressors. To develop primary noise reduction methods that diminish the strength of the aeroacoustic sources directly, the dominant noise generation mechanisms of centrifugal compressors have to first be known and understood both on the suction and on the pressure side.

Raitor and Neise [1] carried out detailed acoustic measurements on two shroudless radial impellers running on a typical compressor test bed. They identified three major sound source mechanisms, dominating the different operating conditions as well as speed areas of their investigated radial compressors:

Buzz-saw noise

Turbomachinery blade rows operated at supersonic tip speeds are generating a tonal sound spectrum spread over a range of harmonics of the engine shaft rotation frequency, typically starting from very low orders. These harmonics are commonly termed buzz-saw-tones or buzz-saw-noise, as the pressure signature attached has a sawtooth waveform. This type of rotor-alone noise or rotor-locked noise is caused by the shock waves in the rotating blade channels, beginning to exist from certain rotor speeds on.

Blade passing frequencies

For most operating conditions, the blade passing frequency (BPF) component and its harmonics are clearly visible in the spectrum. Here, the blade passing frequency is defined to be equal to the rotor shaft frequency multiplied by the number of main rotor blades of the impeller. This frequency components are caused by the interaction of the rotor wakes with diffusor vanes or by instationary inflow disturbances, both periodically interfering with the rotating pressure field stemming from the rotor blades.

Tip clearance noise (TCN)

Typically at highly throttled operating conditions, narrow-band noise components are observed at about half the blade passing frequency increasing with speed. Certain conditions exist, where the level of the narrow-band components dominates over the BPF-level, consequently even dominating the overall noise of the compressor. The narrow-band components are produced by the secondary flow through the gap between the compressor casing and the impeller blade tips, the physical origin of which being similar to the tip clearance noise (TCN) observed in axial-flow machines. Raitor and Neise [1] kept the notation TCN for radial compressors.

A brief summary of the experimental study to explore the dominant sound generation mechanisms governing the overall noise level of centrifugal compressors from Raitor and Neise [1] are the following findings:

1. At design speed with supersonic flow conditions in the rotor blade channels, they found blade tone noise and buzz-saw noise to be the main contributors.
2. On the inlet, Raitor and Neise detected rotor-alone noise as the main noise source while rotor–stator interaction noise dominated the outlet side in the case of vaned outlet diffusers.
3. Over a large range of rotor speeds with subsonic flow conditions, radial compressor noise was found to be dominated by TCN.

The experimental study in the early 2000 years was concentrated on the acoustic field on the suction side. Only a few measurement positions were situated on the pressure side of the compressor. Therefore, a modal decomposition of the tones on the pressure side was not possible nor a calculation of the downstream propagating acoustic power.

In an experimental study conducted on the pressure side by Habing and Feld [3] in 2013, the modal contents where determined using a rotatable sensor array holding six sensors. The results showed high discrepancies towards the ISO 5136. It was suggested that a future detailed computational analysis is required to design a reliable experimental method to determine the modal sound power.

With the aim of developing a new, robust and low costly acoustic measurement method, fulfilling industrial needs to determine the acoustic power, a research project is jointly conducted by the Institute of Fluid Dynamics and Technical Acoustics of the TU Berlin and the Institute of Jet Propulsion and Turbomachinery of the RWTH Aachen. The goal of this measurement method is to determine the in-duct sound power level emitted by a radial compressor into the discharge pipe.

To obtain a better understanding of the acoustic spectrum and the modal structure of the emitted sound field, extensive transient numerical simulations, consisting of a full annulus model of the whole compressor stage, were conducted and post-processed. The results of the simulations are presented in the following giving a better insight in the sound source mechanisms and the propagation of sound through a radial compressor with a vaneless diffuser and a volute. A similar numerical study was conducted considering a vaned diffuser by Banica et al. [4].

2 Numerical Analysis

So far, measurement attempts in the discharge pipe of radial compressors are either expensive and complex or yield unsatisfactory results. For the present numerical investigations, a test rig located in Aachen is utilised, which consists of the transonic impeller Design 603 [5] with 13 main and 13 splitter blades, a vaneless diffuser and a volute. A cross-sectional view of the compressor stage is shown in Fig. 1. To obtain moderate measuring conditions and lower frequencies, the impeller was simulated at the reduced speed of $n_{70\%} = 22022$ RPM with a toast-to-total pressure ratio of $\Pi_{tt,5} = 2.6$ for the acoustic analysis presented in the following. Basic information about the compressor stage operating at its design point is summarised in Table 1.

In order to get a better understanding of the acoustic spectrum and the modal structure of the emitted sound field, extensive transient numerical simulations consisting of a full annulus model of the whole compressor stage were conducted and post-processed. The results of these simulations are presented in the following.

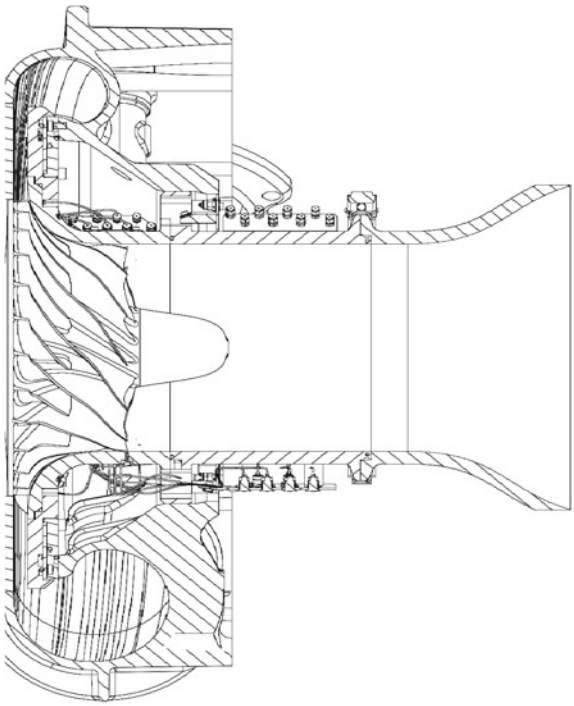

Fig. 1 Cross section of compressor stage

Table 1 Basic information on Design 603

Parameter		Value
No. of blades (main + splitter)	Z	13 + 13
Diameter at impeller outlet	D_2	356 mm
Diameter at diffuser outlet	D_5	580 mm
Nominal speed	n	31461 RPM
TPR in ADP	$\Pi_{tt,5}$	6.5

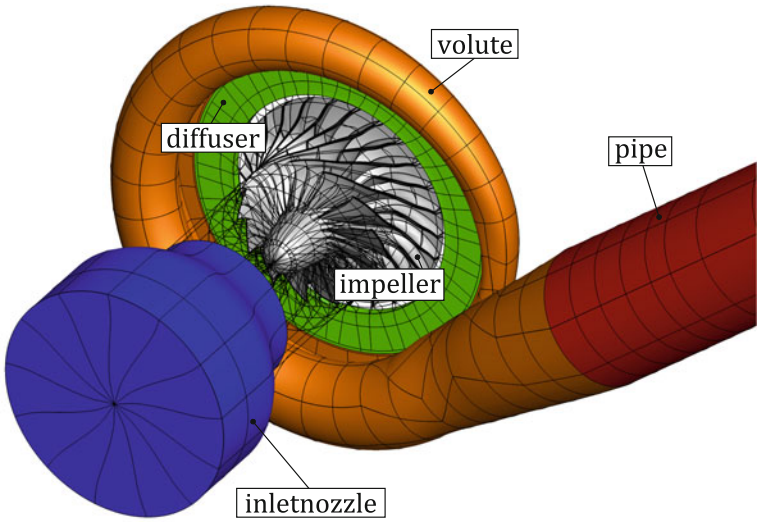

Fig. 2 Computational domain for unsteady simulations

2.1 Numerical Setup

In order to model the aerodynamic and acoustic behaviour of the investigated compressor stage, the unsteady 3D CFD-code TRACE [6] was used, which was developed for turbomachinery flows by the German Aerospace Center (DLR). In this code, the finite-volume discretisation of the compressible, unsteady Reynolds-Averaged Navier–Stokes (URANS) equations is solved in the relative frame of reference. The viscous fluxes are discretised by a second-order accurate central scheme. For time integration, the implicit, multi-stage Runge–Kutta scheme of the second-order kind with pseudo-time stepping is used. Turbulence effects are captured with the two equation k-w turbulence model, developed by Wilcox.

Figure 2 shows the computational domain used for the unsteady simulations consisting of the inlet-nozzle, impeller, vaneless diffuser, volute and parts of the discharge pipe. Due to its geometry, the volute induces asymmetries in the pressure pattern

upstream in the diffuser and impeller. To most accurately capture these flow conditions, a full annulus 360° model was used, whose meshing methodology is described in the following. In common steady CFD-simulations, the local mesh size must be chosen with regard to local flow gradients. Especially in the regions of boundary layers, the mesh must be refined. In order to capture the sound source mechanisms in the compressor stage most accurately, the boundary layers in the impeller and diffuser are fully resolved with adequate levels of the non-dimensional wall distance y+. In the volute, in contrast, the boundary layers were modelled with wall functions to reduce the number of cells. If, in addition, aeroacoustic effects are to be investigated, increased attention is to be paid to numerical dissipation and dispersion effects. To keep these detrimental effects at a tolerable level, acoustic waves must be resolved with an appropriate number of cells. Therefore, the grid resolution must be kept high even in regions with small flow gradients. From this, two conclusions can be drawn for the meshing process: Firstly, it becomes clear that the mesh size is directly dependent on the wavelength of the acoustic fluctuations, and thus, on the frequencies and mode orders being investigated. Secondly, due to the limited cell size, large volumes call for exceptional computer resources and therefore should be avoided if possible. In the mesh used for the simulations presented in the following, the free-field wavelength was used simplistically to estimate the necessary cell size. It was resolved with 60 and 30 grid points for the first and second blade passing frequency, respectively. This fine mesh resolution was kept until the beginning of the discharge pipe, where the sound field was extracted and a modal analysis was conducted. Further downstream, at an axial distance of 1,5 times the pipe diameter, the mesh was coarsened towards the pipe outlet inducing artificial damping. In this way, reflections at the pipe outlet could be avoided even if simple Riemann-boundary conditions were applied. In order to avoid damping of pressure fluctuations, not only the spatial, but also the temporal resolution has to be chosen carefully. For the simulations presented in this paper, a total of 160-time steps per period (TSPP) were used, resulting in 2080-time steps for one compressor revolution. A further increase in the temporal resolution did not show relevant effects on the acoustic field. Due to the high requirements on the grid resolution, a total of 170 million cells were needed to model the whole compressor stage, of which 100 million cells were used for the 360° model of the impeller. The high temporal and spatial resolution used in the numerical simulations made the access to a high-performance cluster (HPC) inevitable. The simulations were therefore conducted on the Cluster Aix-la-Chapelle (CLAIX) in Aachen, which is part of the HPC-partition of the Jülich Aachen Research Alliance (JARA).

2.2 Rotor-Alone Noise

Different possible source mechanisms exist for tonal noise at the outlet of compressors with vaneless diffusers, as described before in Sect. 1. Due to the large distance between the impeller outlet and the volute tongue, unsteady interactions between the

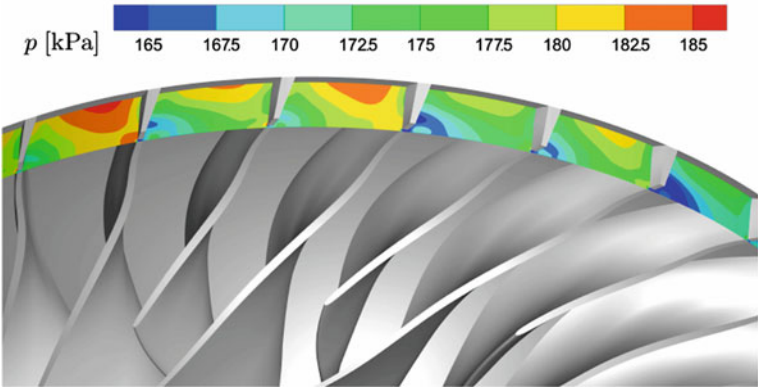

Fig. 3 Static pressure distribution at impeller outlet

rotor wakes and the tongue were found to be negligible. Therefore, the main source mechanism in the investigated compressor stage is given by the rotor-alone noise, which will be described in the following. Figure 3 shows the pressure distribution at a constant radius close to the compressors trailing edge. It can be seen that the pressure distribution is highly non-uniform in circumferential and axial direction. This is caused by the jet-wake structure of the impeller flow resulting in large spatial pressure gradients with low-pressure regions at the tip of the blade suction side, respectively. Together with the inhomogeneities caused by the blunt trailing edges, these gradients are rotor-locked and therefore induce pressure fluctuations in the diffuser. Applying a timewise DFT, the pressure fluctuations show up a frequency spectrum dominated by the blade passing frequency and its harmonics. Another non-uniformity originates from the volute. Due to its asymmetric geometry, the volute generates a pressure distortion upstream resulting in a circumferential variation of pressure and mass flow. The extent of this effect is highly dependent on the component matching between impeller, diffuser and volute and changes with different operating conditions [7]. This pressure gradient, however, is stationary and therefore does not cause fluctuations in the diffuser in a direct manner.

The pressure fluctuations in the diffuser are not purely sinusoidal, and therefore a DFT shows a frequency spectrum dominated by the blade passing frequency and its harmonics. Figure 4 shows the static pressure at the impeller outlet as well as the unsteady pressure fluctuations for the first (left) and second (right) BPF in the diffuser at 50% relative span at a given time step. As the static pressure distribution indicates, the circumferential flow distortions resulting from the volute are comparatively small at the investigated operating point explained by a good matching between compressor and volute. At the first BPF shown on the left, the pressure fluctuations form a clear pattern of thirteen maxima and minima at the diffuser inlet, and therefore the dominating circumferential mode order can easily be determined to m = 13. Further downstream in the diffuser, the pressure pattern forms patches, which are inclined

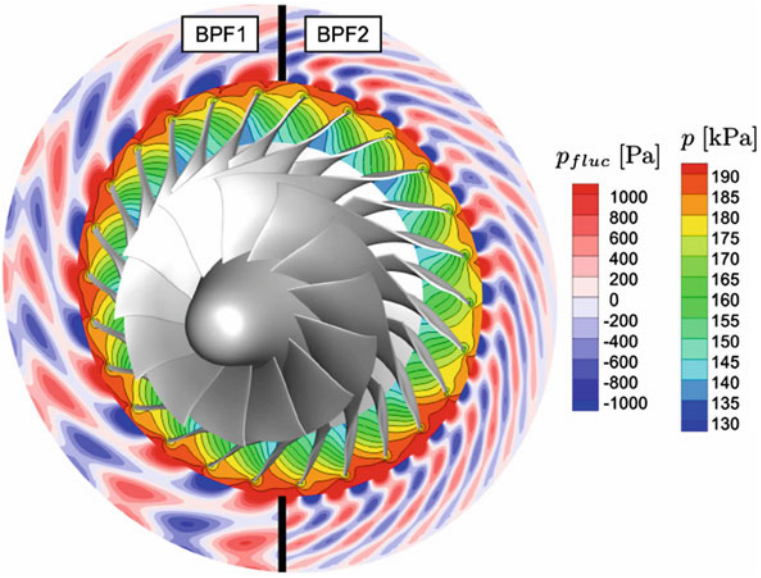

Fig. 4 Static pressure fluctuations in the diffuser at first (left) and second (right) BPF

opposite to the direction of flow and show two nodes in the radial direction. With the impeller having thirteen main and splitter blades, the fluctuations at the first BPF arise from different flow conditions in adjacent main and splitter blade passages. The pressure fluctuations for the second BPF, shown on the right, form a similar pattern. Applying a spatial DFT yields a dominant circumferential mode order of m = 26, which coincides with the number of maxima and minima shown. With the impeller having 26 blades in total, the fluctuations at the second BPF are induced by circumferential inhomogeneities in the impeller outflow of one passage, caused by the before mentioned jet-wake flow as well as by the wakes forming at the blunt trailing edges. In radial direction, 3–4 nodes are noticeable, and it becomes clear that the amplitude of the fluctuations decays in radial direction, which is expected due to the with radius increasing area. In the circumferential direction, however, the distortions show very little variation. In addition to the first and second BPF, even more harmonics are present. However, the first and second BPF are dominant, and therefore the higher harmonics will not be analysed here.

In order to understand the propagation of the rotor-alone noise towards the discharge pipe, the influence of the volute on the sound fields modal structure must be conceived. Figure 5 shows the pressure fluctuations on the volute walls occurring at the first BPF for an arbitrary time step. Similar to the diffuser, the pressure fluctuations form a pattern of minima and maxima. Due to the changing, asymmetric cross section of the volute, however, the structure of the sound field is hard to describe in terms of modes. The sound field structure shows nodes—separating minima and maxima—in the circumferential direction as well as in both directions of the cross

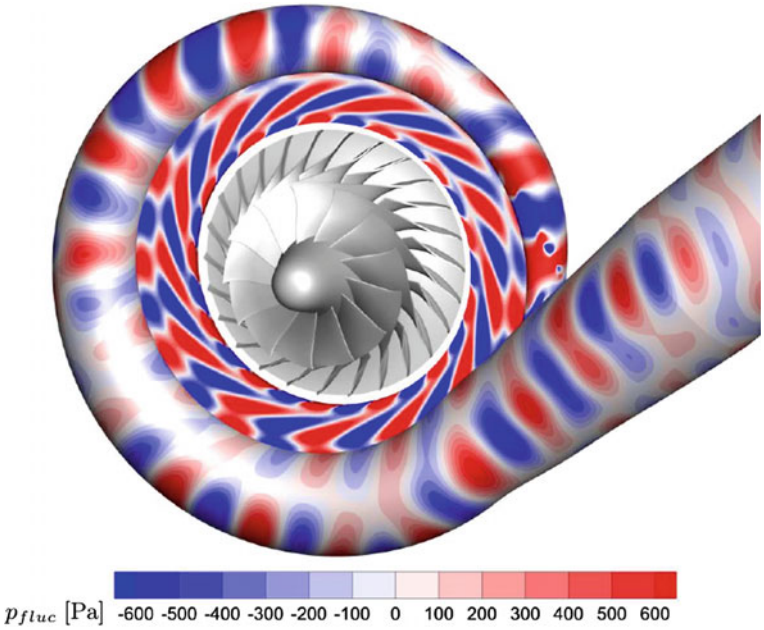

Fig. 5 Static pressure fluctuations in the volute at first BPF

section. The number of nodes in the cross section varies at different circumferential positions resulting in a three-dimensional sound pressure pattern. In Fig. 5, it can be observed that the pressure fluctuations are attenuated towards the volute outlet, which is to some extent due to the change in cross section. In addition, the flow field in the volute is highly vortical and strong interactions between the flow and the sound field may occur.

Figure 6 shows the sound pressure level (SPL) for the first BPF in the vicinity of the volute outlet. As the distribution states, the sound field is highly non-uniform and varies between 122 and 140 dB. The variations with time are neglectable indicating a steady base flow at the chosen operating point. Given the inhomogeneous sound field, it becomes clear that a single probe measurement would lead to inaccurate predictions of the in-duct sound power. Previously, it was shown that a single circumferential mode is dominant in the diffuser at the first BPF. Propagating through the volute, however, due to the complex, vortical flow conditions and geometry variations, this modal structure is not conserved. At the volute outlet, the sound field is given by a superposition of different low-order modes, which will be discussed in detail in the following chapter.

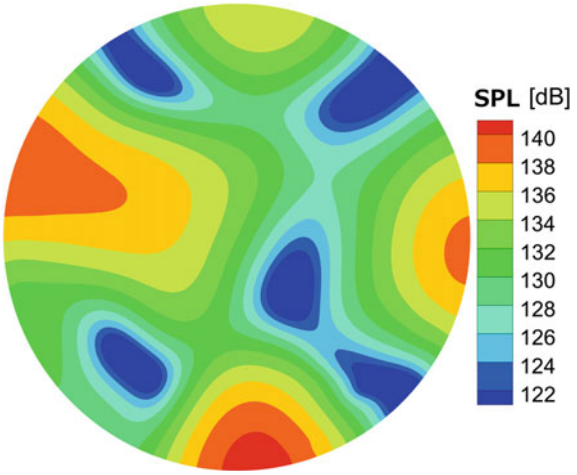

Fig. 6 Sound pressure level (SPL) at volute outlet at first BPF

3 Mode Analysis in Discharge Pipe

The radial mode analysis (RMA) is conducted by applying the extended Triple-Plane-Pressure (XTPP) Method [8] at the evaluation section shortly downstream of the volute of the discharge pipe. The XTTP Method consists of the following three steps: 1. determination of the acoustic eigenmodes based on an analytic derivation of an in-duct sound field solving the convective Helmholtz equation; 2. include convective pressure perturbations into the model using the convective wavenumber as axial wavenumber and the same orthogonal radial shape functions as for the acoustic modes; 3. Fitting the acoustic and convective modes to pressure data extracted at three planes over a finite amount of radial discretisation points to conclude the complex amplitudes of all cut-on radial modes.

Note, the individual radial mode shapes are described in the case of a hollow duct by the well-known Bessel functions of the first-order kind considering a uniform mean flow and constant duct section. The corresponding axial wavenumbers of each mode were derived by the dispersion relation, also considering a uniform mean flow and constant duct section. Although inhomogeneities are present in the axial and circumferential flow at the outflow section (Figs. 7a, b), where the RMA was conducted, a mass flow averaging concluding a uniform mean flow at the evaluation section is considered accurate, due to (i) the mass flow averaged axial Mach number being low and (ii) the variation of the flow field being small. A mode analysis considering swirl was carried out by Hurst et al. [9] considering an analytic solid-body-like swirl flow approach and has shown that swirl, at comparable low Mach numbers as illustrated in Fig. 7b influences mainly the sound power level of modes near the cut-off region. As the following analysis will show, these modes do not carry the majority of the acoustic energy and the effect of swirl is therefore negligible.

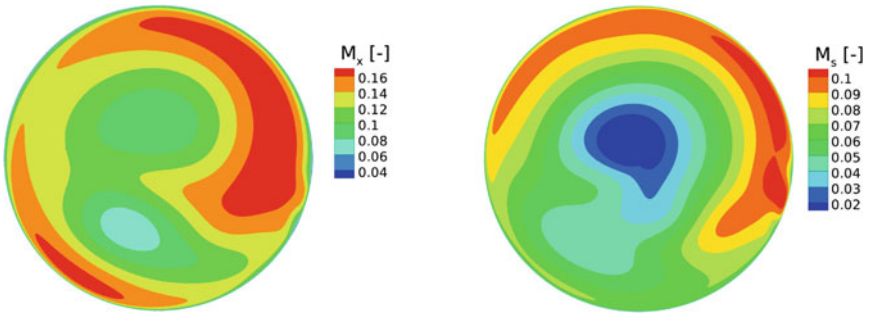

Fig. 7 Flow field at evaluation section, axial machnumber (**a**), swirlflow machnumber (**b**)

The cut-on factor described by

$$\alpha_{mn} = \sqrt{1 - \left(1 - M_x^2\right) \frac{\sigma_{mn}^2}{(kR)^2}} \tag{1}$$

is derived by the dispersion relation [10] considering a uniform mean flow and is plotted for the first BPF in Fig. 8a. The radial eigenvalues, axial Mach number, free-field wave number and the outer radius of the duct are denoted by σ_{mn}, M_x, k and R, respectively. The modes with the cut-on factor being larger than zero conclude all possible cut-on modes. As illustrated, the cut-on modes are ordered symmetrically around azimuthal mode of order m = 0. The modes near the cut-off region (higher order modes) become noticeable due to a decrease in value of the cut-on factor. The axial wavenumbers of the up-and downstream propagating modes ($k_{x,mn}^-$ and $k_{x,mn}^+$, respectively) are computed via

$$k_{x,mn}^{\pm} = \frac{1}{1 - M_x^2}(-M \pm \alpha_{mn}) \tag{2}$$

and combined with the aforementioned radial eigenfunctions form the modal basis. From the modal basis and extracted pressure field at finite discretisation points, a set of linear equations is derived, which is solved via the least-squares fit to determine the complex amplitudes of each radial mode (XTPP) concluding the radial mode analysis (RMA). Note, in the here conducted analysis, only downstream propagating modes are of relevance due to the end of the duct being designed so that no acoustic reflections occur.

The sound power levels (L_+ with $P_{ref} = 10^{-12}$) of each mode of the first BPF is determined in the final step and are illustrated in Fig. 8b. The contour plot range was set between 85 dB and the maximum occurring power level of 103 dB. Hence, only modes carrying the main sound field energy are presented. The highest dominating

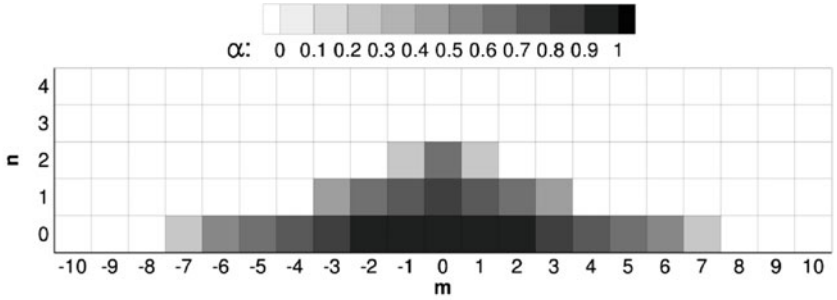

(a) Cut-on factor at evaluation section for the first BPF.

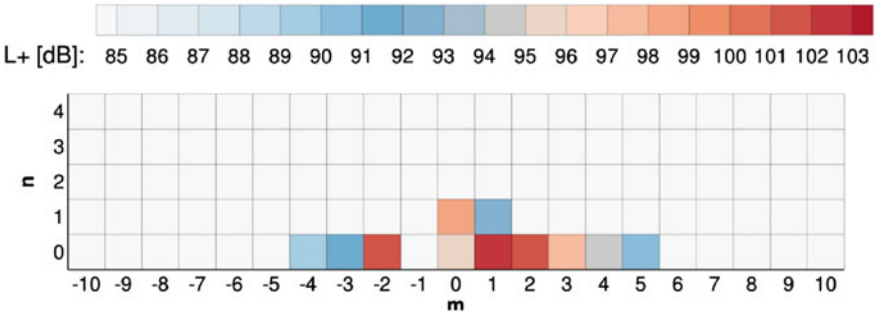

(b) Modal power level at evaluation section for the first BPF.

Fig. 8 Cut-on factor and mode sound power level at evaluation section resulting from the RMA

mode is of order (1, 0) followed by two counter rotating modes of equal mode order (−2, 0) and (2, 0). Also worth mentioning is the asymmetry of the energy distribution concerning the sign of the azimuthal mode orders. Clearly, a higher amount of energy is distributed into positive modes, which represent the azimuthal counter-clockwise spinning modes. In the aforementioned study conducted by Hurst et al. [9], it was also shown that highly complex modal energy distributions result from single incident modes passing through bent duct discontinuities considering Euler flows. Therefore, and as indicated in Fig. 5 due to the strong curvature, complex flow gradients and possible flow separation effects occurring in the volute, the mode energy distribution originating from the rotor is distorted in a highly complex manner when passing through the volute. This concludes that mapping a measured mode structure to sound sources on the pressure side seems not feasible in a simplified equation as on the inlet side, i.e. the Tyler and Sofrin rule [11]. The Tyler and Sofrin rule is defined as

$$m = hR - nS \tag{3}$$

and determines the azimuthal source mode order (m) depending on the amount of rotor blades (Z) or/and stator (V) vanes. Furthermore, h denotes the order of the

bypass frequency (BPF) ($h = 1, 2, \ldots$) and n describes the amount of rotor–stator interactions in each rotor revolution. Note, a vaneless diffusor is present in the current setup reducing the Tyler and Sofrin rule dependency to the rotor-alone noise ($n = 0$). Therefore, the dominating Tyler and Sofrin modes are directly linked to the amount of rotor blades and its harmonics.

4 Conclusion

An extensive numerical calculation was performed using 170 Million cells with the DLR TRACE code to evaluate the sound field on the pressure side of a radial compressor. A vaneless diffusor setup was chosen for the exercise.

The expected rotor–stator interaction modes m = 13 or m = 26 are visible close to the diffusor. Further downstream of the volute exit, the aforementioned modes are no longer cut on and therefore not present in the propagating mode field. Due to the complex geometry and flow variation inside the volute, the energy is scattered into lower order cut-on modes with only a few being dominant. In comparison, complex scattering effects were established for a 90° bend by Hurst [9] and assert these findings.

The results show a relatively low count of acoustic modes propagating downstream near the measurement section. In conclusion, a comparably low microphone count in the exhaust duct might be sufficient to capture all modes of interest. On the other hand, a proper prediction of the sound field seems from the current state of the art of prognosis technique not feasible. Future developments will have to focus on an experimental technique to estimate the sound power on the pressure side of the compressor.

Acknowledgements The authors gratefully acknowledge the computing time granted by the JARA-HPC Vergabegremium and provided on the JARA-HPC partitions part of RWTH Claix Cluster in Aachen. Also the funding by the Research Association for Combustion Engines e.V. and the German Research Foundation is highly appreciated.

References

1. Raitor, T., Neise, W.: Sound generation in centrifugal compressors. J. Sound Vib. **314**, 738–756 (2008)
2. Aschroft, G., Frey, C., Heitkamp, K., Weckmüller, C.: Advanced numerical methods for the prediction of tonal noise in turbomachinery–Part I: Implicit Runge-Kutta Scheme. J. Turbomach. **136**, 021002 (2013)
3. Habing R.A., Feld H.J.: On the modal sound field at the outlet of a turbocharger centrifugal compressor. In: Proceedings of the 10th European Conference on Tubomachinery Fluid dynamics and Thermodynamics ETC10, April, pp. 15–19. Lappenranta, Finnland (2013)

4. Banica, M.C., Limacher, P., Feld, H.-J., Spinder, C.: Numerical prediction of the sources and the modal content of the acoustic field in a radial compressor outflow. J. Eng. Gas Turbines Power, GTP-16-1483 **139**(9), 092605-092605-17 (2017). https://doi.org/10.1115/1.14036284
5. Hehn, A., Mosdzien, M., Grates, D., Jeschke, P.: Aerodynamic optimization of a transonic centrifugal compressor by using arbitrary blade surfaces. In: Proceedings of ASME Turbo Expo 2017: Turbomachinery Technical Conference and Exposition, GT2017-63470, June 11–15, Charlotte (2017)
6. Nürnberger, D., Eulitz, F., Schmitt, S., Zachcial, A.: Recent progress in the numerical simulation of unsteady viscous multistage turbomachinery flow. In: Proceedings of the 15th International Symposium on Air
7. Braembussche, R.A., Van den.: Radial Compressor Design and Optimization. Course Note 192. von Karman Institute for Fluid Dynamics (2015)
8. Weckmueller, C., Fritzsch, A., Guerin, S.: A robust extension to the triple plane pressure mode matching method by filtering convecti perurbations. Int. J. Aeroacoust (2015)
9. Hurst, J.D., Tapken, U., Faßbender, A., Jeschke, P., Enghardt, L.: Scattering of high order modes in diffuser and 90° bend ducts. In: 23rd AIAA/CEAS Aeroacoustics Conference, Denver, Colorado, June 2017, AIAA-2017-4039
10. Rienstra, S.W.: Fundamentals of Duct Acoustics. Technische Universiteit Eindhoven, 16. November (2015)
11. Tyler, J., Sofrin, T.: Axial flow compressor noise studies. Trans. Soc. Automot. Eng. **90**, 309–332

Noise and Noise Reduction in Supersonic Jets

Philip J. Morris and Dennis K. McLaughlin

Abstract This paper describes a novel noise reduction method for supersonic jets. It involves the injection of relatively small amounts of air into the diverging section of a convergent-divergent nozzle. The air is injected through a series of injectors that are aligned axially. The injected air diverts the jet core flow and forms "fluid inserts." These inserts have the same effect as hard-walled corrugated seals, but can be modified by changes to the injector pressure ratios. The inserts change the effective area ratio of the nozzle and can enable the jet to operate closer to an on-design condition. This has the effect of weakening the shock cell structures in the jet and reducing the broadband shock-associated noise. In addition, streamwise vortices are generated that break up the large-scale turbulent structures in the jet and result in a reduction in the supersonic mixing noise in the peak noise radiation direction. Experiments are described that examine the levels of noise reduction achieved by the fluid inserts. The effects of the number and azimuthal distribution of the inserts are examined. The effect of a change of experimental scale from small to moderate model sizes is also given. Noise reductions in the peak noise direction of up to 6 dB are obtained and broadband shock-associated noise is reduced. Ongoing plans and open questions are also discussed.

Keywords Supersonic jets · Noise reduction · Fluid injection · Fluid inserts

1 Introduction

The noise generated by turbulence convecting at high speed, such as encountered in the exhausts of tactical fighter aircraft, has been the subject of research for well over half a century. A great deal is now understood about the noise generation process. Though there remain some doubts, it is generally agreed that when the turbulence convects supersonically with respect to the ambient speed of sound a direct coupling

P. J. Morris · D. K. McLaughlin
Penn State University, University Park, State College, PA 16802, USA
e-mail: pjm@psu.edu
URL: http://www2.aero.psu.edu/morris/

E. Ciappi et al. (eds.), *Flinovia—Flow Induced Noise and Vibration Issues and Aspects-II*,
https://doi.org/10.1007/978-3-319-76780-2_6

occurs between the unsteady pressure field generated by the turbulence and the radiated noise. The relevant turbulent structures have a large scale and remain coherent over relatively large distances and times. Models based on representing the pressure field of the large-scale structures with that of wavepackets have proved successful in describing the noise radiation. Such models also appear to be relevant to subsonic noise generation and radiation, since the noise spectra at low and high speeds are so similar. However, methods based on acoustic analogies, starting with the original analogy of Lighthill, especially in their most recent versions, appear to offer an alternative explanation. The apparent conflict between these two approaches remains unresolved.

Whatever the outcome of the theoretical discussion, the aim of all the different approaches is to provide sufficient insight into the noise generation mechanisms to lead to noise reduction techniques. Though significant progress has been made in the understanding of the noise generation and its radiation, practical methods proposed for noise reduction have been few and far between. In the commercial arena, the introduction of chevrons has shown promise and chevrons have also been proposed and installed on fighter aircraft engines with some limited success. Active control may eventually prove the most effective approach, but the operation of actuators and sensors in the harsh environments encountered in high-performance aircraft engines is problematic. Robustness must be a key ingredient in any noise reduction strategy. In addition, performance should not be compromised. This is important in the military environment to maintain air superiority and for profitability in the commercial arena.

The noise reduction methodology described here is focussed on military applications where the turbofan engines have low bypass ratios. On take off, for example, from an aircraft carrier deck, engines are typically operating in an overexpanded condition. In classical compressible nozzle flow theory, this occurs when the pressure at the jet exit has expanded to below the ambient pressure. In such a situation, shocks appear in the jet plume to eventually equalize the pressure. In reality, such equalization can occur inside the diverging section of the supersonic converging-diverging nozzle. In any event, the pressure mismatch results in a reduction in thrust. One way to overcome this problem is to change the area ratio between the nozzle throat and the nozzle exit. Recognizing this, Seiner et al. [17] proposed to replace the seals in the diverging section of the nozzle with corrugated seals. This changed the effective area ratio of the nozzle and improved thrust. A bonus of this approach was that the corrugations generated streamwise vortices that broke up the coherence of the large-scale structures, much like the actions of chevrons, and reduced the noise generated by these structures in the peak noise direction. Seiner's approach was an excellent lesson into how to combine basic understanding with practical implementation.

Unfortunately, like many things in life, nothing comes without a cost. In the case of corrugated seals, the cost comes with resulting performance losses at cruise. Proposed methods to overcome these problems by redesign of the corrugations have resulted in an improvement in performance but a decrease in the noise reduction benefits. To overcome these issues, a novel noise reduction method was introduced by Morris et al. [11]. They replaced the hardwall corrugations, called "Contoured Inserts (COINs)" by Murray and Lyons [13], with "fluid inserts." The inserts were

generated by a row of injectors in the diverging section of the convergent-divergent nozzle that diverted the nozzle flow in the same way as the hardwall corrugations. The initial experiments produced the same level of noise reductions as achieved with the hardwall corrugations.

In this paper, an overview is provided of the development of the fluid inserts concept including the noise reductions achieved for a range of insert geometries and operating conditions. First, the experimental setup is described including the anechoic jet facility, the use of helium/air mixtures to simulate the effects of jet heating, and the model nozzles. Examples are then given of the noise reductions. An example of the effect of nozzle scale is provided based on experiments conducted by General Electric Aviation. Finally, some plans for future research are given.

2 Experimental Setup

2.1 Anechoic Facility and Instrumentation

The majority of the experiments described below were conducted in the Penn State High Speed Jet Aeroacoustics Laboratory. The facility, a plan view of which is shown in Fig. 1, is an anechoic chamber that measures 5.02 × 6.04 × 2.79 m and is covered in fiberglass wedges. The anechoic chamber has an approximate cutoff frequency of 250 Hz. The facility air is provided by a CS-121 compressor combined with a KAD-370 air dryer. Both are manufactured by Kaeser Compressors. Air is stored in two tanks and then piped to a control cabinet located directly outside of the anechoic chamber that houses a series of valves and pressure regulators to regulate the flow into the nozzle and injectors. The facility has a collector and an exhaust fan to capture the jet exhaust and minimize air and helium recirculation. Acoustic data

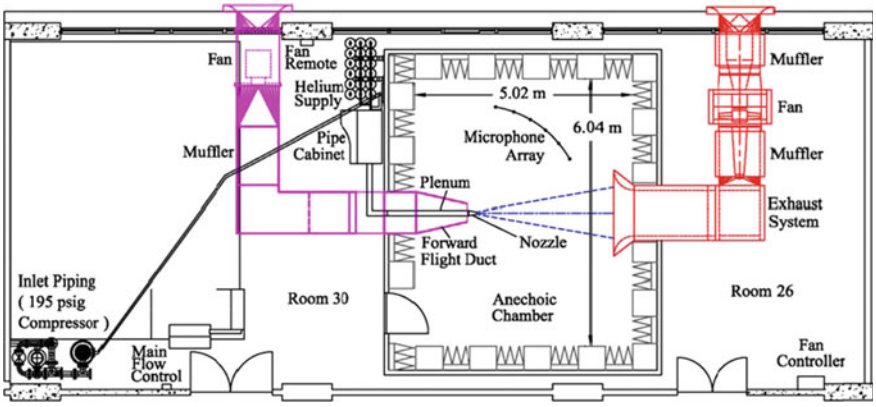

Fig. 1 Plan view of the Penn State Anechoic jet facility

is measured using sixteen 1/8 in. (3.2 mm) pressure field GRAS type 40DP microphones. The microphones are spaced at 5–10° increments along a semicircular arc, centered at the nozzle exit, from 20° to 130° to the jet downstream axis. The arc radius is approximately 1.8 m. The microphones are placed at grazing incidence with respect to the jet centerline. The microphone calibrations are performed using a B&K acoustic calibrator, model 4231, and the microphone calibration constants are recorded to provide the conversion from the measured voltages to the equivalent pressure. For each microphone, the power spectral density is calculated and converted to a non-dimensional, lossless power spectrum that includes corrections for microphone actuator response, free-field response, and the removal of atmospheric absorption. Assuming spherical spreading of the acoustic field, the resulting data are (back) propagated to a radius of 100 nozzle exit diameters. Additional details on the facility configuration, operation, far-field microphones, and acoustic data processing can be found in Powers [14].

To simulate the exhaust temperatures of a full-scale military aircraft engine, without the need to heat the exhaust air, helium is mixed into the air flow. The helium–air mixture increases the jet exit velocity and decreases the jet exit density similar to the effect experienced by heated flows. This method has been shown to simulate the dominant noise characteristics of actual heated jets and is the methodology used in the Penn State facility to simulate heated jet flows. For heat-simulation tests, three helium cylinders pressurized to approximately 14.5 MPa (2100 psi) separately feed into the pressure control cabinet. Accurate mixing of air and helium is achieved via piping and valves and monitoring of air and mixture pressures. For the typical jet conditions measured in the studies described here, the ratio of specific heats changes from 1.4 with a pure air jet to over 1.5 with the helium–air mixture (depending on the helium concentration). The mixture total pressure is typically controlled to within 2% of the target value during data acquisition. Further details of the methodology are given by Kinzie and McLaughlin [4] and Doty and McLaughlin [1]. Comparisons between high-speed jet noise measurements made using the helium/air mixture approach and actual heated jets are given in McLaughlin et al. [7]. The agreement is very good.

2.2 Nozzles with Fluid Inserts

For the experiments in the Penn State facility, a series of model scale exhaust nozzles were used. The nozzles were manufactured using additive manufacturing rapid prototyping techniques by StratSys, Ltd (formerly Solid Concepts Inc). The technique for the fabrication of the nozzles in this study was PolyJet HD with the PolyJet Amber Clear material, with standard layer thickness of 0.015 mm (0.0006 in.). Military style nozzles representative of aircraft engines of the F404 family were used in this study. The inner contours of the military style nozzles were provided by GE Aviation. Such military engines have nozzles that are capable of varying their geometry to produce different exit to throat area ratios to adapt for different flight regimes. The

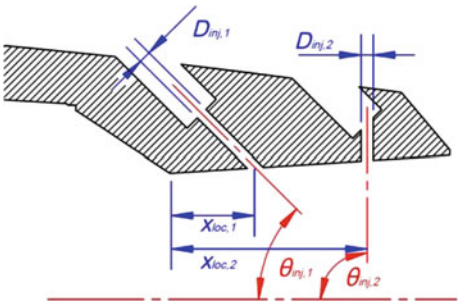

Fig. 2 Schematic showing the parameters defining the fluid inserts' injector ports. This example shows two injectors per insert

expansion portion of these nozzles contains 12 large flat seals that are interleaved with 12 smaller flaps to allow for area ratio adjustment. For the experiments described below, the area ratio selected was 1.295, which results in a design Mach number, $M_d = 1.65$, typical of a take off configuration. The model nozzles were designed with the same multifaceted (12 segment) inside conical contour. Further details about these nozzles can be found in Kuo [5] and Kuo et al. [6]. The fluid inserts are generated by axially aligned injectors in the diverging section of the nozzle. Experiments have been conducted using 2–5 injectors per insert. In addition to the number of injectors and their azimuthal position, there are three geometric parameters that can be varied in the design of the fluid inserts. These parameters are x_{inj}, the distance of the injector exit from the nozzle throat expressed as a percentage of the length of the diverging section of the nozzle, D_{inj}, the injector hole diameter, and θ_{inj}, the angle between the injector centerline and the core jet centerline. These parameters are sketched in Fig. 2 for a case with two injectors per fluid insert. The injector ports in the divergent section of the nozzle are machine drilled while the nozzle is clamped onto a rapid-prototyped mounting block. The nozzles are completed by epoxying polyethylene/nylon tubing into the drilled injection holes. A mass flow rate meter is then installed upstream of the injector to measure and record mass flow rates for each injection condition. The injection delivery system allows for two separate injection pressures and measured mass flow rates. Each air supply feeds a ring of 6.35 mm (1/4 in.) tubing. Separate 3.18 mm (1/8 in.) tubes supply the air from each ring to each individual injector port. A T-connector connected to a Setra pressure transducer, typically just upstream of the nozzle injection port, measures the injection pressure. In general, each injection pressure ratio (IPR) is measured and recorded for every injection port, as they can vary slightly depending upon the delivery ring. The injection pressure ratio (IPR) is defined as the ratio of the upstream stagnation pressure of the injection jet divided by the ambient pressure of the test chamber. Typical injection pressure ratios vary between injection ports in the same ring by less than 1.0%. A photograph of one nozzle assembly with three fluid inserts, two injectors per insert and separate pressure supplies to the upstream and downstream injectors, is shown in Fig. 3.

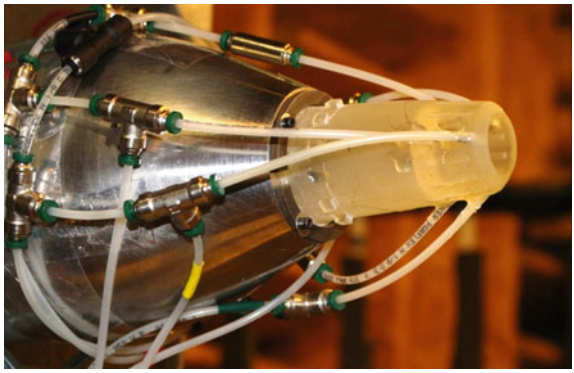

Fig. 3 Photograph of nozzle with three fluid inserts and two injectors per insert

3 Noise Measurements

3.1 Experiments with Three Fluid Inserts

This section provides some examples of the noise reductions achieved with different fluid insert geometries and different injector operating conditions. Both unheated and heat-simulated cases are included. It has been found that, in general, larger noise reductions are obtained for the heated cases.

The early experiments testing this concept used up to 3 fluid inserts with 2 injectors per insert. Figure 4 shows a sample result from those experiments. The left panel shows SPL spectra for a baseline jet (no injector holes) and a fluid insert nozzle at several polar angles relative to the jet downstream axis. It can be seen that in the peak noise directions, $30° < \theta < 50°$ there is a reduction in the mixing noise levels across the entire spectrum. In the polar range where broadband shock-associated noise (BBSAN) is evident, $\theta > 90°$, the BBSAN peak is flattened and reduced. For this case, the nozzle pressure ratio (NPR) equals 3.0 and the total temperature ratio (TTR) is 3.0. This gives a fully-expanded jet Mach number, $M_j = 1.36$. Recall that the design Mach number, $M_d = 1.65$. The injector pressure ratio (IPR) also equals 3.0, and the far-field measurements are taken in an azimuthal plane that bisects a pair of injectors ($\phi = 60°$). In this case, all injectors have the same diameter and the total injector mass flow rate is approximately 3.8% of the core jet mass flow rate. The right-hand panel shows a comparison of the variation in the change of the overall sound pressure level (OASPL) as a function of polar angle (negative values indicate a noise reduction). Two injector configurations are shown. 3FID06B has equal diameters for the upstream and downstream injectors while 3FID06V has a larger downstream injector diameter. The total injector exit area and the total mass flow rate are the same in the two cases. It can be seen that OASPL reductions of greater than 5 dB are achieved in the peak noise directions and reductions of 2 dB are seen in the BBSAN. It should be noted that the baseline spectra show evidence of jet screech—shown as a sharp peak that is approximately independent of polar

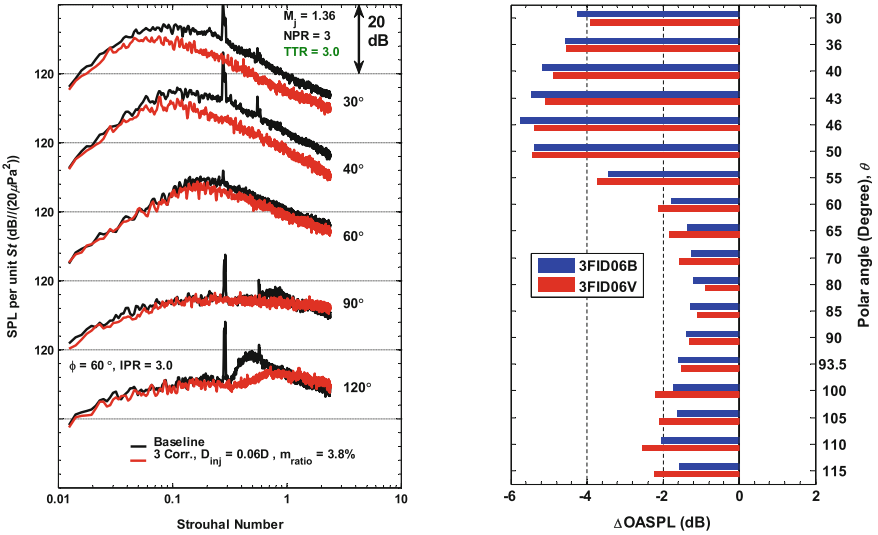

Fig. 4 Far-field spectra and OASPL comparison from the measurements conducted with $M_d = 1.65$ baseline nozzle, $NPR = 3.0$, $TTR = 3.0$, $M_j = 1.36$, and 3 fluid insert nozzles. Shown as well as the baseline nozzle are measurements for the 3FID06B ($D_{inj,1} = D_{inj,2} = 0.059D_j$, $IPR_1 = 2.7$, $IPR_2 = 3.0$) and 3FID06V ($D_{inj,1} = 0.040D_j$, $D_{inj,2} = 0.072D_j$, $IPR_1 = 4.0$, $IPR_2 = 3.0$). From Morris et al. [12] with permission

angle. Screech is rarely present in full-scale jets but it increases the OASPL. The use of the fluid inserts eliminates the screech. However, in the OASPL noise reductions shown here, the peak has been removed electronically by smoothing the spectrum in the vicinity of the peak, so that there is no artificial benefit gained from the screech elimination. In these experiments, it was noticed that the noise reductions had a significant variation with the observer's azimuthal position. The noise reductions were greatest in the azimuthal planes that bisected the inserts and was the least, though still a noise reduction, in the azimuthal planes that contained the inserts. An example is shown in Fig. 5 for similar operating conditions as the case shown in Fig. 4. The core jet operating conditions are the same, but the injector diameters are equal and $IPR_1 = 1.89$ and $IPR_2 = 4.5$. Clearly, the noise reductions are less for $\phi = 0°$, which is the azimuthal plane in line with an injector. However, the azimuthal variation in the noise reductions can be used to advantage so that the greatest noise reductions are in the most effective directions. One example has been considered by Powers et al. [16] where the case of a jet with fluid inserts above a simulated aircraft carrier deck was studied. By steering the "quiet plane," the radiated noise in the direction of carrier deck personnel was reduced. The case where the jet impinged on a blast deflector was also considered and again noise in critical directions was reduced by 4–7 dB.

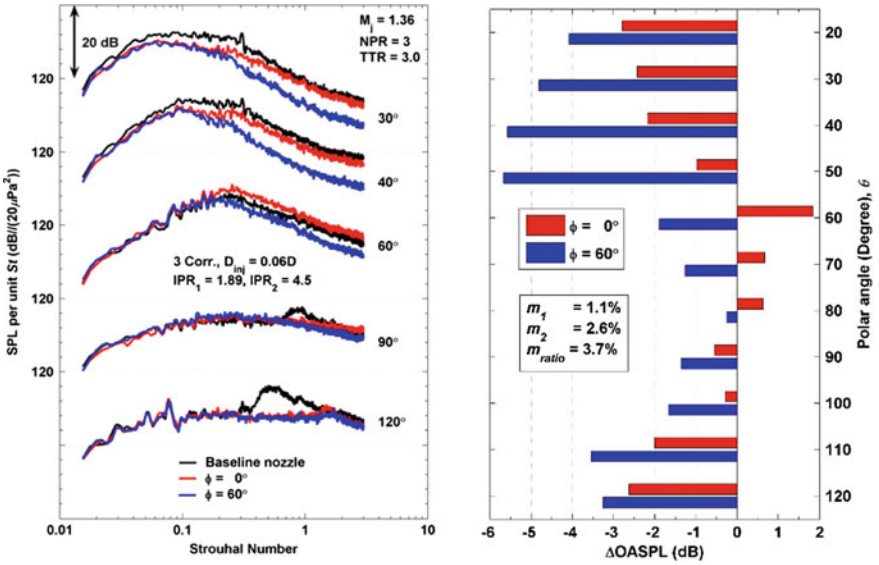

Fig. 5 Far-field spectra and OASPL comparison from the measurements conducted with $M_d = 1.65$ baseline nozzle, $NPR = 3.0$, $TTR = 3.0$, $M_j = 1.36$, and 3 fluid insert nozzles. Shown as well as the baseline nozzle are measurements for the 3FID06B ($D_{inj,1} = D_{inj,2} = 0.059D_j$, $IPR_1 = 1.89$, $IPR_2 = 4.5$) in azimuthal planes $\phi = 0°$, in line with the inserts, and $\phi = 60°$, bisecting the inserts. From Powers et al. [15] with permission

3.2 *Effect of the Number of Fluid Inserts*

To provide additional understanding of the azimuthal variation of the radiated noise reductions, model nozzles have been used with 2, 4, and 6 fluid inserts. Morgan et al. [10] used 2 fluid inserts separated azimuthally by 120°. Radiated noise measurements were made at azimuthal angles of 0° (in plane with an insert), 60° (between the inserts with the smaller azimuthal spacing), 180° (directly opposite an insert), and 240° (between the inserts with the larger azimuthal spacing). The maximum noise reduction of 6 dB occurred in the 240° azimuthal plane. But this measurement location also increased the noise level at some polar angles. Comparison of the change in OASPL for all four azimuthal measurement planes revealed that the 60° measurement plane was the quietest, since it was the only measurement plane that reduced the noise at every polar angle. The other measurement planes overall had very similar noise reduction levels with no clear loud plane.

Morgan et al. [9] considered nozzles with four fluid inserts with different azimuthal separations—some symmetric and some asymmetric. For the case, where the inserts had equal azimuthal spacing, the "quiet planes" were again found to bisect the azimuthal planes of the inserts. However, the noise reductions achieved (3–4 dB) were not as great as for the three insert cases. Though it should be noted that the highest total temperature ratio considered was 2.0, which was lower than in the three

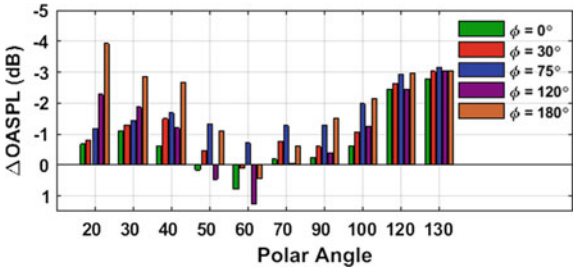

Fig. 6 Variation with polar and azimuthal angle of ΔOASPL for a nozzle with 4 azimuthally asymmetric fluid inserts with 3 injectors per insert operating at $M_j = 1.36$ with $TTR = 2.0$ $IPR = 3.5$, compared to a baseline nozzle. From Morgan et al. [9] with permission

insert cases. It was also observed that there was far less overall azimuthal variation in the noise reductions. A nozzle with four asymmetrically placed inserts was also studied. The inserts were located at $\phi = \pm 30°$ and $\phi = \pm 120°$. In this case, there was clearly a quiet plane located at $\phi = 180°$. The variation in the OASPL noise reductions as a function of polar angle are summarized in Fig. 6. The greatest noise reductions are achieved in the peak noise directions. In addition, the reductions in BBSAN are nearly independent of observer azimuthal position. Hromisin et al. [2] considered noise reductions from nozzles with six evenly spaced fluid inserts. He compared the reductions with those achieved using a hard-walled corrugation nozzle. For this geometry, it was found that the noise reductions for an unheated jet case were greater than those observed for a heated jet. This is opposite to the observations with all the other configurations. However, the range of possible core and fluid insert operating conditions has not been fully explored so a complete picture has still to be obtained.

3.3 Effect of Model Scale

To establish the effects of model scale on the noise reductions, experiments have been conducted by General Electric Aviation in the Cell 41 anechoic jet noise facility. A new model was constructed with an increase in scale of approximately 5. A completely new design of injector air delivery was designed to accommodate the constraints of the larger facility. Some details of the facility used, the modifications to the fluid insert design, and preliminary results are given in McLaughlin et al. [8]. The noise reductions obtained either equaled or exceeded those measured in the smaller Penn State facility. Figure 7 shows a comparison of the OASPL noise reductions obtained at the two scales. Note that the TTR values are similar but not identical. The case shown is for 3 fluid inserts with 3 injectors per insert with $NPR = 3.0$ and $TTR = 2.5$ or 3.0. It is clear that the fluid insert noise reduction concept works to reduce both supersonic mixing noise as well as broadband shock-associated noise at both small and moderate scales, and by inference, at full scale.

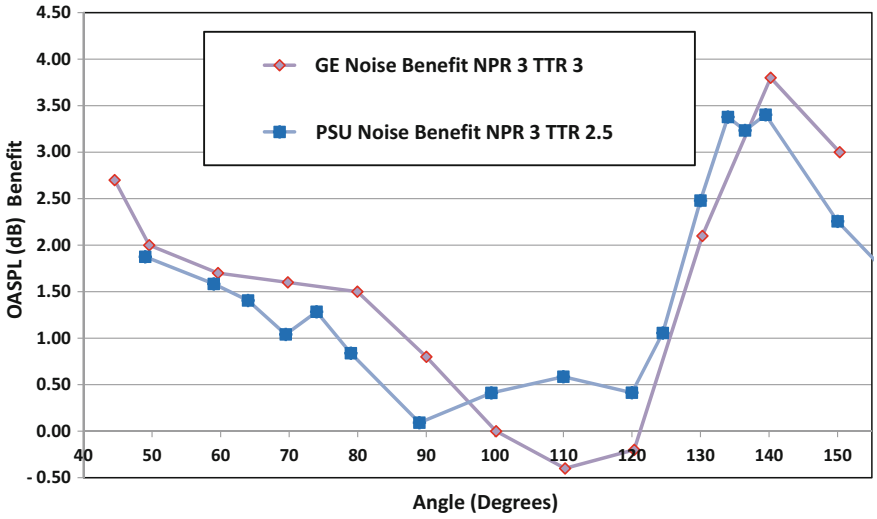

Fig. 7 Comparison of ΔOASPL for PSU and GE nozzles with 3 injectors at $NPR = 3.0$. The angle is measured from the upstream jet axis. From McLaughlin et al. [8] with permission

4 Discussion

A successful method for supersonic jet noise reduction has been described. The technique is based on the generation of "fluid inserts" in the diverging section of a converging-diverging nozzle. These fluid wall corrugations change the effective area ratio of the nozzle and generate streamwise vorticity. This reduces both broadband shock-associated noise and supersonic mixing noise. Noise reductions of up to 6 dB in the peak noise direction are achieved. Experiments with a larger scale nozzle (a factor of approximately five) show that the same noise reductions can be achieved at this larger scale.

Several issues and questions remain to be addressed. As noted above, initial experiments with six fluid inserts did not achieve the same levels of noise reduction as obtained with fewer inserts. However, only a limited range of jet and injector operating conditions were considered. Mention has not been made of the role of numerical simulations in the present study, though steady RANS CFD has been a complementary component of the present research: see Kapusta et al. [3]. It is clear that both steady and unsteady flow simulations can help to understand the flow and noise modifications caused by the fluid inserts and help with their optimization. Further exploitation of azimuthal asymmetry could be considered, especially if twin jet configurations are involved. Studies at this time have only considered circular nozzle geometries and single stream jets, but these may not be the configurations to be used in future tactical aircraft engines. Finally, the issue of the practicality of the technique for implementation on a full-scale engine must be considered since the fluid inserts require the use of bypass air—even though the required mass flow rate

is small. However, if future tactical aircraft engines were to be subject to a noise level requirement, the noise reduction method described here could be included in the overall engine design process. Finally, it is important to emphasize that the fluid insert noise reduction method is active, in the sense that it can be modified or turned off, unlike mechanical devices. So it could be used only when noise reduction is an important operational consideration.

Acknowledgements The authors are very grateful for the invaluable support provided by former and current students and post-doctoral scholars: Ching-Wen Kuo; Russell Powers; Scott Hromisin; Jessica Morgan; Chris Shoemaker. Though not detailed here, computational support was provided by Matt Kapusta, Jake Lampenfield, and Chitrarth Prasad. The SMART scholarship program supported Russell Powers and Scott Hromisin. The General Electric Aviation participants included Steve Martens and Erin Lariviere and several support engineers. The advice given by Dr. John Spyropoulos at NAVAIR is also acknowledged. The majority of the research was funded by the Office of Naval Research with Drs. Joe Doychak and Knox Millsaps as Program Officers.

References

1. Doty, M.J., McLaughlin, D.K.: Acoustic and mean flow measurements of high-speed, helium-air mixture jets. Int. J. Aeroacoust. **2**(2), 293–334 (2003)
2. Hromisin, S.M., Powers, R.W., McLaughlin, D.K., Morris, P.J.: Extending on-demand noise reduction technology to military-style nozzles with 6 fluidic corrugations. AIAA Paper 2017–4042 (2017)
3. Kapusta, M., Powers, R.W., Morris, P.J., McLaughlin, D.K.: Numerical simulations for supersonic jet noise reduction using fluidic inserts. AIAA Paper 2016–0758 (2016)
4. Kinzie, K.W., McLaughlin, D.K.: Measurements of supersonic helium/air mixture jets. AIAA J. **37**(11), 1363–1369 (1999)
5. Kuo, C.W.: Extending acoustic data measured with small-scale supersonic model jets to practical aircraft exhaust jets. Ph.D. thesis, The Pennsylvania State Unversity, Department of Aerospace Engineering (2010)
6. Kuo, C.W., Veltin, J., McLaughlin, D.K.: Advanced acoustic assessment of small-scale military-style nozzles with chevrons. Noise Control Eng. J. **60**(5), 559576 (2012)
7. McLaughlin, D.K., Bridges, J., Kuo, C.W.: On the scaling of small, heat simulated jet noise measurements to moderate size exhaust jets. Int. J. Aeroacoust. **9**(4 & 5), 627–654 (2010)
8. McLaughlin, D.K., Morris, P.J., Martens, S., Lariviere, E.: Extending on-demand noise reduction to industry scale models for tactical aircraft. AIAA Paper 2016-2990 (2016)
9. Morgan, J., McLaughlin, D.K., Morris, P.J.: Experimental results for supersonic jet noise reduction using nozzle fluidic inserts. AIAA Paper 2017-3518 (2017)
10. Morgan, J., McLaughlin, D.K., Morris, P.J., Prasad, C.: Further development of supersonic jet noise reduction using nozzle fluidic inserts. AIAA Paper 2017-0683 (2017)
11. Morris, P.J., McLaughlin, D.K., Kuo, C.W.: Noise reduction in supersonic jets by nozzle fluidic inserts. J. Sound Vibrat. **332**(17), 3992–4003 (2013)
12. Morris, P.J., McLaughlin, D.K., Powers, R.W., Kapusta, M.: Prediction, experiments and optimization of high-speed jet noise reduction using fluidic inserts. AIAA Paper 2014-3737 (2014)
13. Murray, N.E., Lyons, G.W.: On the convection velocity of source events related to supersonic jet crackle. J. Fluid Mech. **793**, 477503 (2016)
14. Powers, R.W.: Experimental investigation of the noise reduction of supersonic exhaust jets with fluidic inserts. Ph.D. thesis, The Pennsylvania State University, Department of Aerospace Engineering (2015)

15. Powers, R.W., Kuo, C.W., McLaughlin, D.K.: Experimental comparison of supersonic jets exhausting from military style nozzles with interior corrugations and fluidic inserts. AIAA Paper 2013–2186 (2013)
16. Powers, R.W., McLaughlin, D.K., Morris, P.J.: Noise reduction with fluidic inserts in supersonic jets exhausting over a simulated aircraft carrier deck. AIAA Paper 2015-2374 (2015), to appear, Journal of Aircraft (2017)
17. Seiner, J.M., Ukeiley, L.S., Jansen, B.J.: Aero-performance efficient noise reduction for the F404-400 engine. AIAA Paper 2005–3048 (2005)

Part III
Flow–Experiments

Numerical and Experimental Investigation of the Flow-Induced Noise of a Wall-Mounted Airfoil

Paul Croaker, Danielle Moreau, Manuj Awasthi, Mahmoud Karimi, Con Doolan and Nicole Kessissoglou

Abstract A numerical and experimental investigation into the flow field around a finite wall-mounted airfoil is presented. Measurements were performed in an open-jet anechoic wind tunnel for a finite wall-mounted NACA 0012 airfoil with an aspect ratio of one. The airfoil was tested at zero degree angle of attack, with a Mach number of 0.06 and Reynolds number based on chord of 274,000. The measurements include single hotwire anemometry in the near-wake of the airfoil at a number of locations in the mid-span and tip regions. A large eddy simulation (LES) of flow past the airfoil was performed, and good agreement with measurements was obtained. Based on Lighthill's acoustic analogy, flow-induced noise sources were then extracted from the LES data. Sound radiation to the far-field and the incident acoustic pressure on the airfoil were both predicted using a near-field formulation for the aeroacoustic pressure. The boundary element method (BEM) was then used to predict the scattering of the incident pressure field by the airfoil as well as the total far-field acoustic pressure.

Keywords Computational fluid dynamics · Aeroacoustics · Wall-mounted foils Experimental measurements

1 Introduction

The sound produced by flow over finite wall-mounted airfoils is of practical interest in the design of quiet aircraft and marine vessels. Many of the lifting and control surfaces on these structures, such as the tailplane of an aircraft or a ship's rudder, can be approximated as wall-mounted airfoils. The flow past a finite wall-mounted airfoil is characterised by complex three-dimensional flow features. Vortex structures form at the airfoil tip which grow as they travel downstream and exert a strong influence on the flow over the airfoil in the near-tip region [4]. In the mid-span of the airfoil, a turbulent boundary layer develops and turbulent eddies are convected downstream

P. Croaker (✉) · D. Moreau · M. Awasthi · M. Karimi · C. Doolan · N. Kessissoglou
The University of New South Wales, UNSW Sydney, Sydney, NSW 2052, Australia
e-mail: p.croaker@unsw.edu.au

E. Ciappi et al. (eds.), *Flinovia—Flow Induced Noise and Vibration Issues and Aspects-II*,
https://doi.org/10.1007/978-3-319-76780-2_7

and past the trailing edge. For a blunt trailing edge, vortex shedding will also occur in the mid-span region. In the boundary layer of the wall, a horseshoe vortex forms around the base of the airfoil starting at the leading edge and extending into the wake [3, 9]. For low Mach number flows, the nature and strengths of these flow structures vary with Reynolds number, airfoil section and aspect ratio as well as the incoming wall boundary layer thickness [10]. Due to the complex flow over a wall-mounted airfoil, a number of different flow-induced noise mechanisms occur. Interaction between the flow structures in the turbulent boundary layer of the wall and the airfoil leading edge produces low-frequency noise. Convection of turbulent eddies past the trailing edge as well as vortex shedding from the blunt trailing edge contributes to broadband noise. Further, the interaction between the tip vortices and the trailing edge of the airfoil tip can produce strong broadband noise peaks at higher frequencies [7].

This paper presents numerical prediction and measurements of the flow field around a finite wall-mounted NACA 0012 airfoil with an aspect ratio of one at a Reynolds number based on chord Re_c = 274,000 and zero degree angle of attack. Mean and root-mean-square (rms) velocity profiles as well as velocity spectra are measured using hotwire anemometry in the near-wake of the airfoil in the mid-span and tip regions. These measurements are used to validate the numerical prediction of the hydrodynamic field obtained using an LES model. The hybrid CFD-BEM technique of Croaker et al. [2] is used to extract flow-induced noise sources from the flow and predict the propagation of the resulting pressure waves and their interaction with the airfoil.

2 Numerical Flow-Induced Noise Prediction

2.1 Hydrodynamic Data and Acoustic Sources

A wall-mounted airfoil with a NACA 0012 profile of reference chord length $c = 0.2$ m is considered. The airfoil has a rounded trailing edge with diameter of 0.003 m with a resulting chord length of 0.19 m. The airfoil has a span $s = 0.2$ m corresponding to an aspect ratio of 1 and was oriented at zero degree angle of attack relative to the incoming free stream velocity $U_\infty = 20$ m/s. This corresponds to a Mach number of 0.06 and a Reynolds number based on chord of 274,000. An LES of the unsteady flow field around the wall-mounted airfoil is performed by applying a filter to the incompressible Navier–Stokes equations and separating the hydrodynamic fluctuations into a component that can be resolved by the computational grid and a sub-grid scale component. The filtered incompressible Navier–Stokes equations are given by

$$\rho_f \frac{\partial \hat{u}_i}{\partial t} + \rho_f \frac{\partial}{\partial y_i}\left(\hat{u}_i \hat{u}_j\right) = -\frac{\partial \hat{p}}{\partial y_j} + 2\left(\mu_f + \mu_{\mathrm{SGS}}\right)\frac{\partial}{\partial y_j}\hat{S}_{ij} \tag{1}$$

$$\frac{\partial \hat{u}_j}{\partial y_j} = 0 \tag{2}$$

where $\hat{p}$ is the filtered pressure and $\hat{u}_i$ represents the components of the resolved velocity vector. μ_f and ρ_f are the viscosity and density of the fluid at rest. $\hat{S}_{ij}$ is the strain rate tensor of the resolved scales. The wall-adapting local eddy viscosity model of Nicoud and Ducros [8] is used to define the eddy viscosity, μ_{SGS}, which accounts for the influence of the sub-grid scales on the filtered motion.

A fully structured CFD model of the wall-mounted airfoil was created using a total of 88×10^6 hexahedral cells. The first cell height was placed within $y^+ \approx 0.5$ normalised wall units, and a fine mesh was used throughout the boundary layer and near-wake regions. The wall-mounted airfoil is located in a square tunnel with side length 0.93 m. The computational model extends 1.7 m upstream of the leading edge and 3.7 m downstream of the trailing edge. Figure 1 shows the computational model and associated mesh, whereby every second grid line is shown. Figure 1a shows an image of the airfoil surface and the surrounding tunnel floor. Figure 1b and c

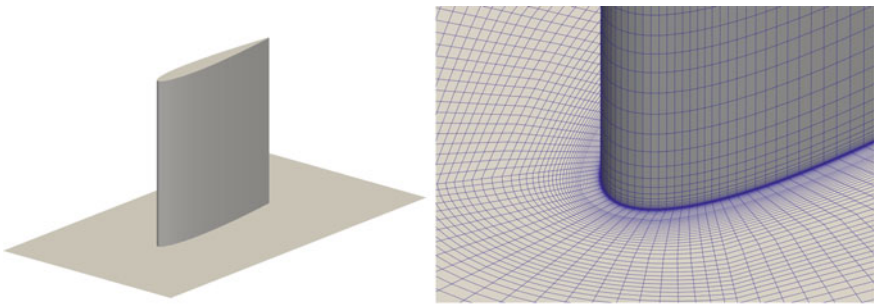

(a) Wall-mounted airfoil

(b) Mesh of junction leading edge

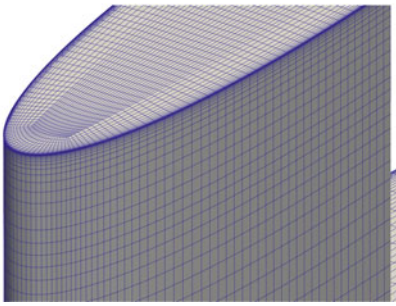

(c) Mesh of tip leading edge

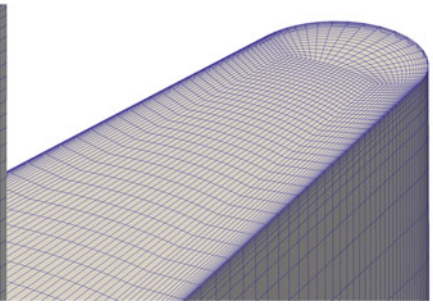

(d) Mesh of tip trailing edge

Fig. 1 CFD mesh for the wall-mounted airfoil, every second grid line shown

shows mesh details of the airfoil leading edge near the wall junction and airfoil tip, respectively. Figure 1d shows the mesh detail of the trailing edge of the airfoil tip.

The LES equations were solved using an iterative, segregated solution method with the pressure–velocity coupling handled using the pressure implicit with splitting of operator algorithm. A blended spatial differencing scheme was used with 95% second-order central differencing and 5% second-order upwind differencing. The blending of the upwind differencing adds numerical diffusion and increases the stability of the convection equation. A second-order backward implicit scheme was used for the temporal discretisation.

The transient simulation was executed with a time step size of 2×10^{-7} s and was allowed to progress until the flow field achieved quasi-periodicity. Recording of the acoustic source data then commenced with the entire flow field stored at intervals of 5×10^{-5} s. Lighthill [5] demonstrated that fluctuations in the stresses acting on a fluid generate pressure waves which travel to the far field as sound. For low Mach number flows, these Lighthill stresses are approximately equal to the Reynolds stress tensor and are given by $T_{ij} = \rho_f u_i u_j$, where u_i represents the components of the velocity vector. Time histories of these Lighthill stresses were extracted from the recorded hydrodynamic data and divided into equal segments with a length of 248 records and 50% overlap. A Hanning window function was applied to each segment of the Lighthill tensor time histories before converting them to frequency spectra.

2.2 Propagation of Flow-Induced Pressure Waves

The pressure waves generated by fluctuations in the Lighthill stress tensor propagate to the far field and are reflected, scattered and diffracted by a body in their path. The reflection, scattering and diffraction of the pressure waves by a body can be resolved using the boundary element method, provided that the pressure field incident on the body is known. Using a near-field formulation, the pressure on the body p_a^{inc} is given by Croaker et al. [1]

$$p_a^{\text{inc}} = \lim_{\epsilon \to 0} \int_{\Omega - V_\epsilon} T_{ij}\left(\mathbf{y}, \omega\right) \frac{\partial^2 G_h}{\partial y_i \partial y_j} dy \tag{3}$$

where y_i is the ith component of the flow-induced noise source position vector $\mathbf{y}$, Ω represents the computational domain, and V_ϵ is an exclusion neighbourhood taken around the point on the body $\mathbf{x}$ where the near-field pressure is computed. Singularities occur when $\mathbf{y} = \mathbf{x}$, and the exclusion neighbourhood is used to solve the resulting singular integrals using a semi-analytical technique [1]. The three-dimensional harmonic free-field Green's function is used to describe the propagation of the acoustic waves

$$G_h = \frac{e^{ik_a r}}{4\pi r} \tag{4}$$

where $i = \sqrt{-1}$, k_a is the acoustic wave number, and $r = |\mathbf{x} - \mathbf{y}|$.

The scattering by the body of the near-field incident pressure is solved using the inhomogeneous Helmholtz equation given by

$$\triangle p_a(x) + k_a^2 p_a = -Q \tag{5}$$

where $\triangle$ is the Laplacian operator and Q is the acoustic source. Equation (5) is combined with the near-field formulation for the pressure given by Eq. (3) and the hard-walled boundary condition on the surface of the airfoil $\frac{\partial p_a}{\partial n} = 0$ to calculate the scattered field on the wall-mounted airfoil as follows [6]:

$$c(\mathbf{y})\, p_a(\mathbf{y}) + \int_\Gamma p_a(\mathbf{x}) \frac{\partial G_h}{\partial n(\mathbf{x})} d\Gamma = p_a^{\text{inc}}(\mathbf{y}) \tag{6}$$

where n is the unit normal to the boundary. $c(\mathbf{y})$ is a free-term coefficient which equals 1 in the interior domain and 0.5 on a smooth boundary. Γ is the boundary of the domain.

In the current work, Eq. (6) is solved using a conventional boundary element method (BEM). Linear, discontinuous boundary elements were used to create the three-dimensional BEM model. The leading and trailing edges are discretised with a finer resolution mesh to ensure that interaction of the incident field with the geometry is accurately captured. A half-space Green's function was used to account for reflection of sound waves by the tunnel floor. The nodal points of the BEM elements also represent the locations used to calculate the incident pressure using Eq. (3). Once the scattered pressures on the airfoil have been determined, the total far-field pressure is then calculated.

3 Experimental Set-up

The measurements were conducted in the UNSW Acoustic Tunnel (UAT) which is an open-jet type facility. The UAT consists of a square open jet with a 0.455 m × 0.455 m cross section exhausting into a 3 m × 3.2 m × 2.15 m anechoic chamber treated on the inside with Melamine foam. All measurements in the present work were performed at a free stream velocity of 20 m/s with a free stream turbulence intensity, measured using a hotwire probe, of approximately 0.6%.

Two 6 mm thick, 300 mm long end plates were attached to the top and bottom edges of the test section inlet, and the airfoil was bolted to the bottom plate. The leading edge of the airfoil was positioned 30 mm downstream of the inlet. A coordinate

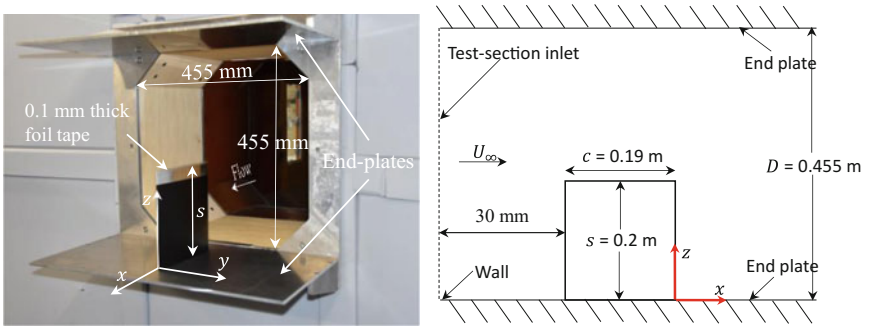

(a) Airfoil mounted in the test section of the UAT

(b) Schematic diagram showing the position of the airfoil in the tunnel

Fig. 2 Wall-mounted airfoil set-up in the UAT

system with origin at the trailing edge is shown in Fig. 2. The coordinate system was defined such that the streamwise coordinate x is positive in downstream direction, spanwise coordinate z is positive in the wall-normal direction, and y is the chord-normal coordinate. Figure 2 shows (a) the airfoil mounted in the UAT during the measurements and (b) a schematic view of the airfoil's location with respect to the wall and test section inlet.

A Dantec Dynamic 55P16 single-sensor constant temperature hotwire probe was used to measure the mean and fluctuating components of the streamwise velocity across the wake of the airfoil at a streamwise distance of $x/c = 0.025$ from the trailing edge and at spanwise locations $z/s = 0.5, 0.9$ and 0.975. The probe was mounted such that the sensor wire was parallel to the spanwise coordinate z and traversed through the wake on a Dantec Dynamic traverse which has a positional accuracy of $6\,\mu$m. The hotwire probe was connected to a Dantec Dynamic multichannel CTA 54N80, and the hotwire voltage was sampled at 51.2 kHz. The mean velocity and rms of hotwire velocity were obtained by averaging 10 records each with 8192 data points. For the spectral measurements, 50 records with 8192 data points were used. The auto-spectral densities were obtained by applying a Hanning window to each record before Fourier transforming and averaging them.

4 Hydrodynamic Results and Measurements

Figure 3 shows the flow structures present around the wall-mounted airfoil. Contour surfaces of constant Q-criterion were used to identify the main structures in the flow. The Q-criterion surfaces are coloured by the magnitude of the vorticity. Strong vortex structures are observed in the tip region. At the mid-span, a laminar boundary layer forms over the leading edge of the airfoil. This laminar boundary layer experiences break-up at approximately 60% of the chord and then transitions to turbulence over

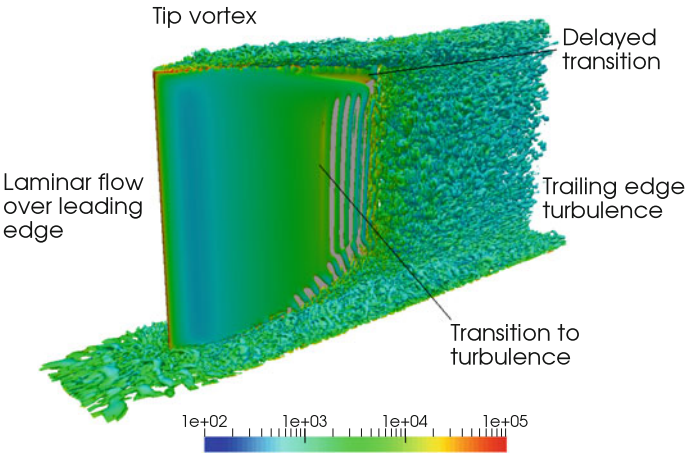

Fig. 3 Flow structures around the wall-mounted airfoil. Q-criterion iso surfaces coloured by the magnitude of the vorticity vector

the remainder of the chord. The generation of vortical structures is also observed at the airfoil–wall junction and within the wall boundary layer. At approximately 90% span close to the trailing edge, the strong pressure gradients induced by the tip vortices suppress the growth of the boundary layer and delay the break-up of the laminar boundary layer.

Figures 4, 5 and 6 compare the normalised mean velocity profile U/U_∞, normalised rms of the velocity fluctuations u'/U_∞ and velocity auto-spectral densities $G_{uu}(f)$ obtained from the numerical simulation with the measurements at 50%, 90% and 97.5% span, respectively. Figures 4f, 5f and 6f show the spanwise vorticity at an instant in time for the region near the trailing edge. The black line indicates the line over which the normalised mean and rms velocity profiles are recorded. The black dots positioned at $y/c = 0, 0.01$ and 0.02 represent the three locations at which the auto-spectral densities were recorded. The normalised mean velocity profiles predicted with the LES compare favourably with the measurements at all spanwise locations. The LES results are approximately symmetric about the mean chord line, with the minimum normalised velocity occurring at $y/c = 0$ at all spanwise locations. The measurements exhibit asymmetry, and the minimum normalised velocity occurs at a slight offset from $y/c = 0$. Uncertainty in hotwire positioning and the finite size of the sensor, which results in area averaging of the velocity fluctuations, is likely responsible for these quantitative discrepancies. Additionally, a single-sensor hotwire can be expected to have larger errors in a three-dimensional flow field due to its inability to resolve all three components of the velocity. Despite the observed discrepancies, there is good agreement between numerical results and measurements for the normalised mean velocity. The numerical normalised rms velocity profiles also show good agreement with the measurements. The magnitude and main features of the rms velocity fluctuations are well captured in the LES results.

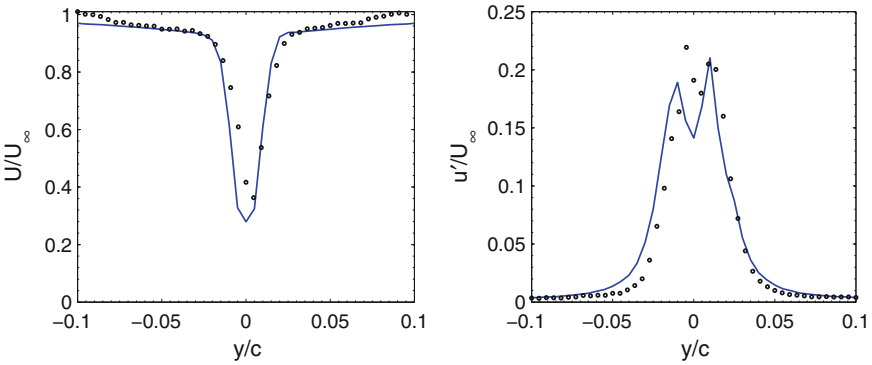

(a) Normalised mean velocity (b) Normalised rms velocity

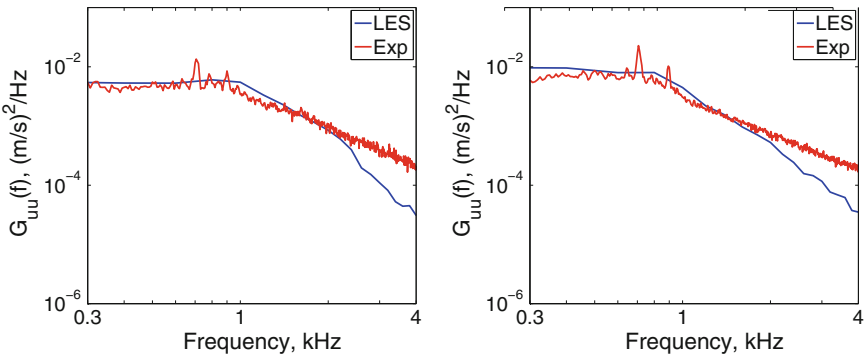

(c) Velocity autospectrum at $y/c = 0$ (d) Velocity autospectrum at $y/c = 0{\cdot}01$

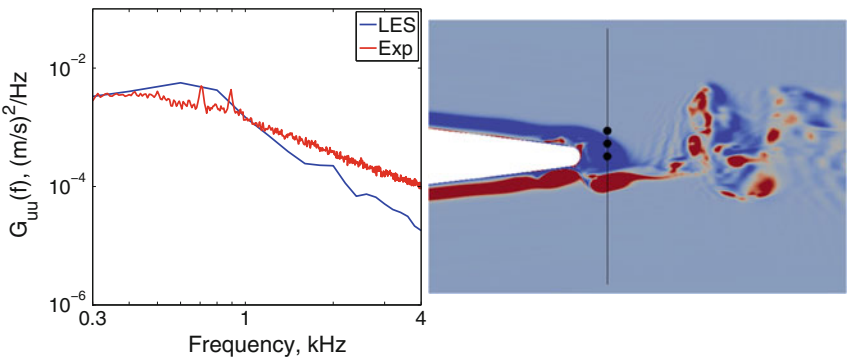

(e) Velocity autospectrum at $y/c = 0.02$ (f) Instantaneous spanwise vorticity

Fig. 4 Normalised mean and rms velocity profiles and auto-spectral densities at 50% of span. Results show comparison between LES (blue) and measurements (black). Spanwise vorticity plot shows measurement locations with the vorticity contours from -5000 to 5000 s^{-1}

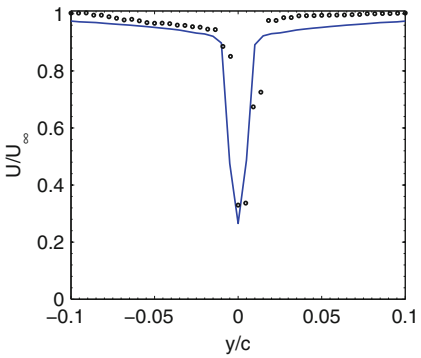

(a) Normalised mean velocity

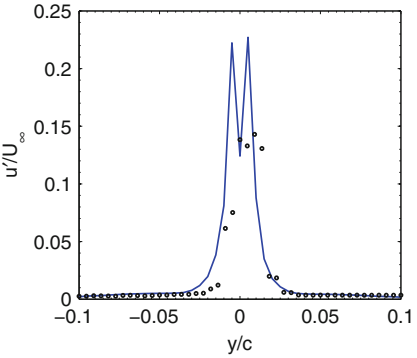

(b) Normalised rms velocity

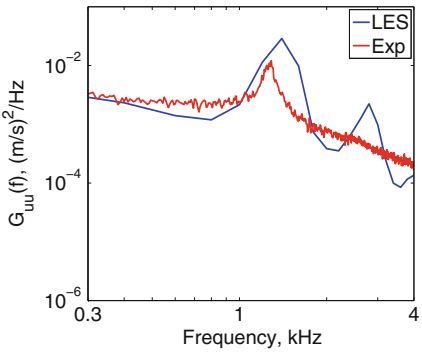

(c) Velocity autospectrum at $y/c = 0$

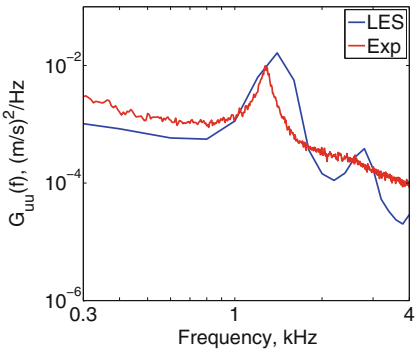

(d) Velocity autospectrum at $y/c = 0.01$

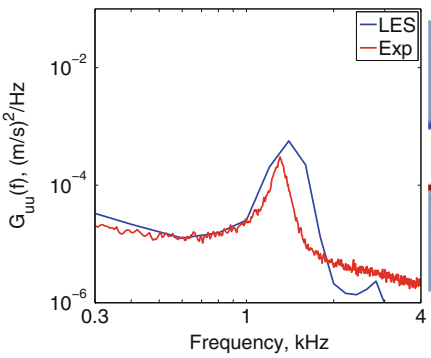

(e) Velocity autospectrum at $y/c = 0.02$

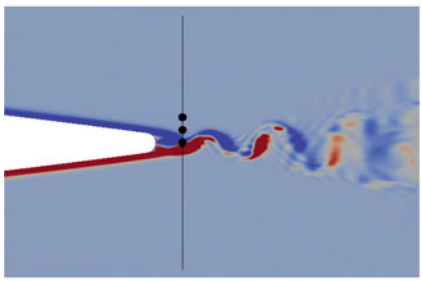

(f) Instantaneous spanwise vorticity

Fig. 5 Normalised mean and rms velocity profiles and auto-spectral densities at 90% of span. Results show comparison between LES (blue) and measurements (black). Spanwise vorticity plot shows measurement locations with the vorticity contours from -5000 to 5000 s^{-1}

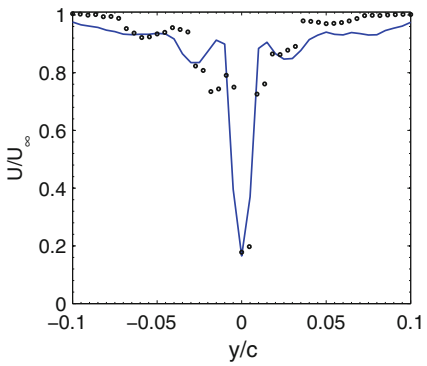

(a) Normalised mean velocity

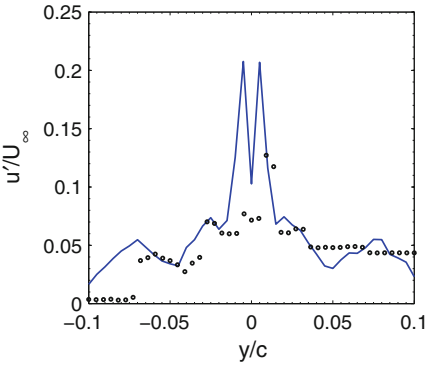

(b) Normalised rms velocity

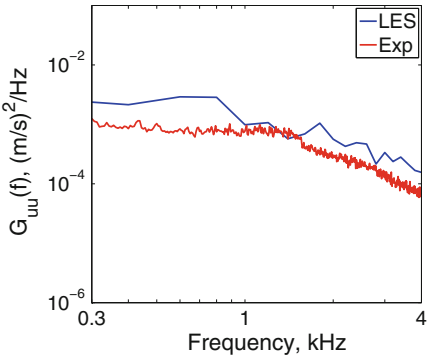

(c) Velocity autospectrum at $y/c = 0$

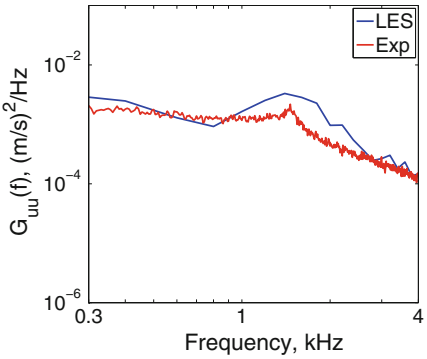

(d) Velocity autospectrum at $y/c = 0.01$

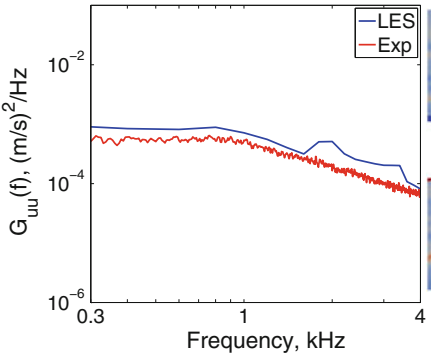

(e) Velocity autospectrum at $y/c = 0.02$

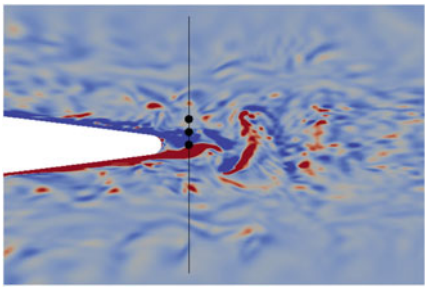

(f) Instantaneous spanwise vorticity

Fig. 6 Normalised mean and rms velocity profiles and auto-spectral densities at 97.5% of span. Results show comparison between LES (blue) and measurements (black). Spanwise vorticity plot shows measurement locations with the vorticity contours from -5000 to 5000 s^{-1}

Due to the asymmetry in the measured mean velocity profiles and the offset of the peak mean velocity from $y/c = 0$, the auto-spectral densities predicted from the LES data were averaged over a ± 1 mm range around the measurement point. Figure 4c and d shows that the auto-spectral densities at 50% span predicted with the LES data are in excellent agreement with the measurements at $y/c = 0$ and 0.01 for frequencies up to approximately 2 kHz. Beyond this frequency, the mesh resolution is no longer able to sufficiently resolve the velocity fluctuations and the energy decreases more rapidly than is observed in the measurements. For $y/c = 0.02$ in Fig. 4e, the auto-spectral density predicted with the LES contains more energy at lower frequencies than is observed in the measured data and the decrease in energy with frequency is slightly higher. However in general, there is good agreement between simulation results and measurements up to approximately 2 kHz.

Figure 5f shows the instantaneous spanwise vorticity of the flow at 90% span. The vorticity contours indicate that the flow is free of small-scale structures near the trailing edge of the airfoil and that laminar vortex shedding occurs downstream of the trailing edge. These vortices begin to break up into smaller scale structures as they travel further downstream. Figure 5c–e shows the velocity auto-spectral densities at 90% span for $y/c = 0$, 0.01 and 0.02, respectively. At all measurement locations, the broadened tone associated with the vortex shedding is well predicted with the LES; however, the peak level and shedding frequency are slightly over-predicted with the LES. The numerical results also capture a broadened tone at the second harmonic of the vortex-shedding frequency that is not present in the measured data. The reason for this discrepancy is under investigation. Both LES results and measured data show two orders of magnitude reduction in the auto-spectral density level at $y/c = 0.02$ compared to $y/c = 0.01$, which indicates that at this spanwise location the wake is very thin.

At 97.5% span, the flow in the vicinity of the trailing edge contains many small-scale flow features as shown in Fig. 6f. This is a combination of flow structures that develop in the boundary layer and flow structures from the tip vortices that travel past the trailing edge. Figure 6c–e shows the velocity auto-spectral densities at 97.5% span for $y/c = 0$, 0.01 and 0.02, respectively. The magnitude and extent of the broadband hump observed in the measured data at approximately 1.5 kHz at $y/c = 0.01$ are over-predicted with the LES; however, the overall levels and shape of the spectra agree favourably with measurements.

5 Far-Field Acoustic Predictions

Figure 7 shows the directivity of the far-field pressure magnitude in the plane of the airfoil tip on a 1 m arc about the centre of the airfoil chord, from 450 Hz to 1.65 kHz in 400 Hz increments. At the lower frequencies corresponding to 450 and 850 Hz, the maximum far-field pressure is oriented towards the positive streamwise axis. This indicates that at these frequencies, the far-field pressure is dominated by turbulence interaction with the leading edge at the junction and tip of the airfoil. This

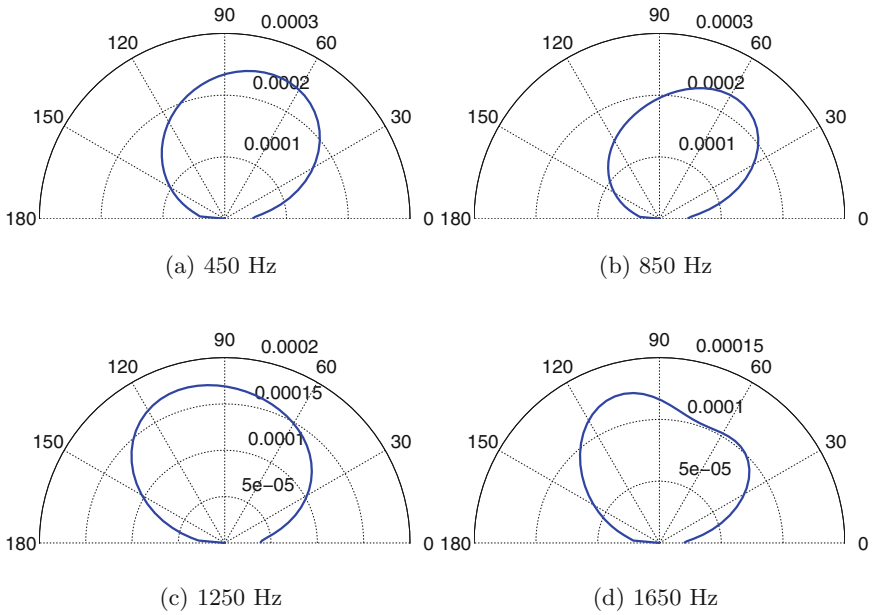

(a) 450 Hz (b) 850 Hz

(c) 1250 Hz (d) 1650 Hz

Fig. 7 Directivity of the far-field sound pressure level in at a distance 1 m from the centre of the airfoil chord calculated in the plane of the airfoil tip

result is consistent with the experimental findings of Moreau et al. [7]. At the higher frequencies corresponding to 1.25 and 1.65 kHz, the maximum far-field pressure is oriented upstream of the leading edge. This suggests that at these frequencies, trailing edge noise and blunt vortex-shedding noise are the dominant flow-induced noise mechanisms. Similar observations were made from the measurements of Moreau et al. [7]. The directivity at 1.65 kHz shows the formation of a secondary lobe due to backscattering of the acoustic pressure by the leading edge of the airfoil. This occurs as the chord length of the airfoil becomes comparable to the acoustic wavelength at this frequency and the airfoil is no longer acoustically compact.

Figure 8 shows the power spectral density of the acoustic pressure predicted at a distance of 1 m from the centre of the airfoil chord at the airfoil tip height and normal to the mean chord line. The low-frequency component of the noise, attributed to turbulence interaction with the leading edge of the airfoil, is of comparable magnitude to the high-frequency component which is attributed to trailing edge noise mechanisms. A similar trend was observed by Moreau et al. [7], although the airfoil in that study had a larger chord length and was subjected to higher Reynolds numbers.

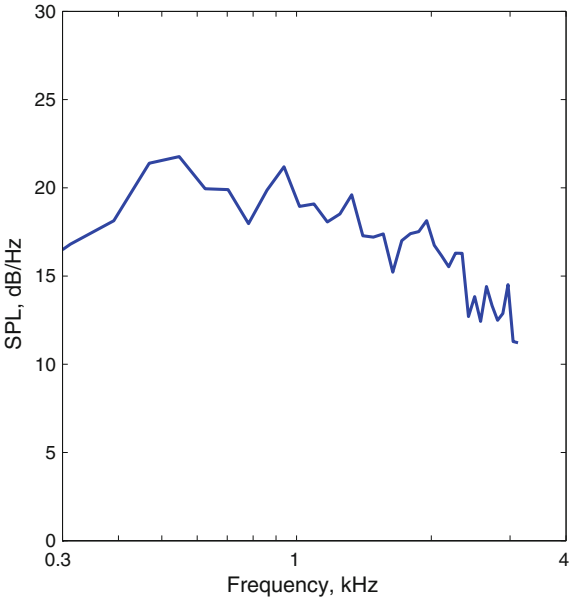

Fig. 8 PSD of the far-field sound 1 m from the centre of the airfoil chord and normal to the mean chord line

6 Summary

The flow field around a wall-mounted airfoil at a Reynolds number Re_c = 274,000 and Mach number $M = 0.06$ has been numerically predicted and experimentally measured. The numerical results obtained from an LES model are in good agreement with the measurements. A hybrid CFD-BEM technique was then used to predict the flow-induced noise produced by the wall-mounted airfoil. The directivity of the far-field sound reveals that the lower frequency noise is dominated by interaction of turbulent pressure fluctuations with the leading edge. At higher frequencies, trailing edge noise mechanisms dominate the far-field sound. Future work will focus on experimental validation of the far-field sound predicted with the hybrid CFD-BEM technique.

References

1. Croaker, P., Kessissoglou, N., Marburg, S.: Strongly singular and hypersingular integrals for aeroacoustic incident fields. Int. J. Num. Methods Fluids **77**, 274–318 (2015)
2. Croaker, P., Kessissoglou, N., Marburg, S.: Aeroacoustic scattering using a particle accelerated computational fluid dynamics/boundary element technique. AIAA J. **54**(7), 2116–2133 (2016)
3. Devenport, W.J., Simpson, R.L.: Time-dependent and time-averaged turbulence structure near the nose of a wing-body junction. J. Fluid Mech. **210**(1), 23–55 (1990)
4. Giuni, M., Green, R.B.: Vortex formation of squared and rounded tip. Aerosp. Sci. Technol. **29**(1), 191–199 (2013)

5. Lighthill, M.J.: On sound generated aerodynamically, I. General theory. Proc. R. Soc. A **211**, 564–587 (1952)
6. Marburg, S., Nolte, B. (eds.): Computational Acoustics of Noise Propagation in Fluids. Springer, Berlin, Germany (2008)
7. Moreau, D.J., Doolan, C.J., Alexander, W.N., Meyers, T.W., Devenport, W.J.: Wall-mounted finite airfoil-noise production and prediction. AIAA J. **54**(5), 1637–1651 (2016)
8. Nicoud, F., Ducros, F.: Subgrid-scale stress modelling based on the square of the velocity gradient tensor. Flow Turbul. Combust. **62**(3), 183–200 (1999)
9. Olcmen, S.M., Simpson, R.L.: Some features of a turbulent wing-body junction vortical flow. Int. J. Heat Fluid Flow **27**(6), 980–993 (2006)
10. Simpson, R.L.: Junction flows. Ann. Rev. Fluid Mech. **33**(1), 415–443 (2001)

Turbulence Ingestion Noise from an Open Rotor with Different Inflows

W. Nathan Alexander, William J. Devenport, Nicholas J. Molinaro, N. Agastya Balantrapu, Christopher Hickling, Stewart A. L. Glegg and Jack Pectol

Abstract Measurements have been performed on a scaled version of a Sevik rotor ingesting both a planar turbulent wake and a turbulent boundary layer flow. In both cases, detailed measurements were made of the inflow turbulence, including three-component turbulence profiles and the full cross-sectional 4-dimensional space-time correlation function. Far-field sound measurements were also made of the turbulence ingestion noise for a comprehensive range of rotor advance ratios varying from zero to high thrust, for rotor yaw angles out of the plane of the wake from −15 to 15°, and for a range of wake strike positions on the rotor disk. Probes mounted on two of the rotor blades were used to measure upwash fluctuations seen in the rotating frame, as well as blade-to-blade coherence spectra. Comparisons have been made with predictions of the far-field sound levels based on the measured inflow turbulence for both configurations and good results were obtained in all cases.

Keywords Aeroacoustics · Rotor noise · Turbulence ingestion

1 Introduction

Sound radiation from rotors operating in turbulent flow has been studied extensively following the pioneering work of Sevik [1] in the water tunnel at Penn State. Sevik measured the unsteady loading on a rotor operating in a homogeneous turbulent flow downstream of a rectangular grid. He also outlined a procedure to predict the unsteady loading and the radiated sound from the rotor based on the wavenumber spectrum of the turbulent inflow. This problem has been reconsidered many times over the years since Sevik's early experiment and, with suitable modifications to Sevik's theory, rotor noise caused by homogeneous or quasi-homogeneous turbulent

W. N. Alexander · W. J. Devenport (✉) · N. J. Molinaro · N. A. Balantrapu · C. Hickling
Center for Renewable Energy and Aerodynamic Technology, Virginia Tech, Blacksburg, VA, USA
e-mail: Devenport@vt.edu

S. A. L. Glegg · J. Pectol
Florida Atlantic University, Boca Raton, FL, USA

E. Ciappi et al. (eds.), *Flinovia—Flow Induced Noise and Vibration Issues and Aspects-II*,
https://doi.org/10.1007/978-3-319-76780-2_8

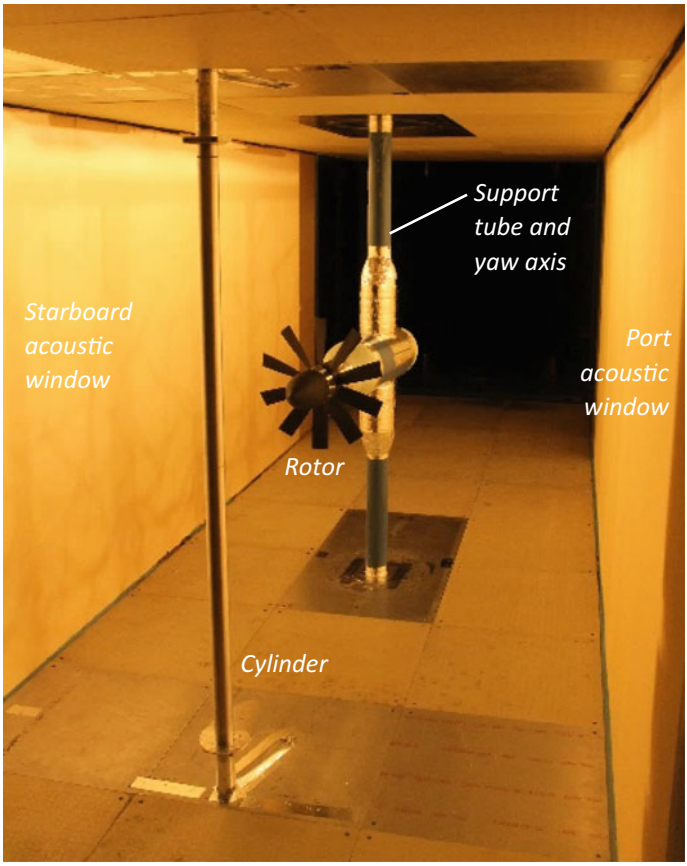

Fig. 1 Cylinder and rotor mounted in the anechoic section of the Virginia Tech Stability Wind Tunnel

inflows is well understood, providing that the wavenumber spectrum of the turbulent inflow can be suitably modeled, and turbulence lengthscales estimated using rapid distortion theory (RDT). Example studies have been completed on helicopter rotors, wind turbines, and fans operating in a duct wall boundary layer as well as in grid turbulence [2–8]. However, the problem of an inhomogeneous turbulent inflow, for which the wavenumber spectrum of the flow is undefined, has received less attention. Over the last few years, a series of theoretical, experimental, and numerical studies have been carried out to advance the understanding of this problem by specifically considering the sound radiation from a rotor that is in the wake of a cylinder (Fig. 1) or placed close to a flat wall so it ingests the wall boundary layer over a limited part of the rotor disk plane (Fig. 2). In this paper, we will review these studies and summarize the similarities and differences between the two sets of inflow conditions.

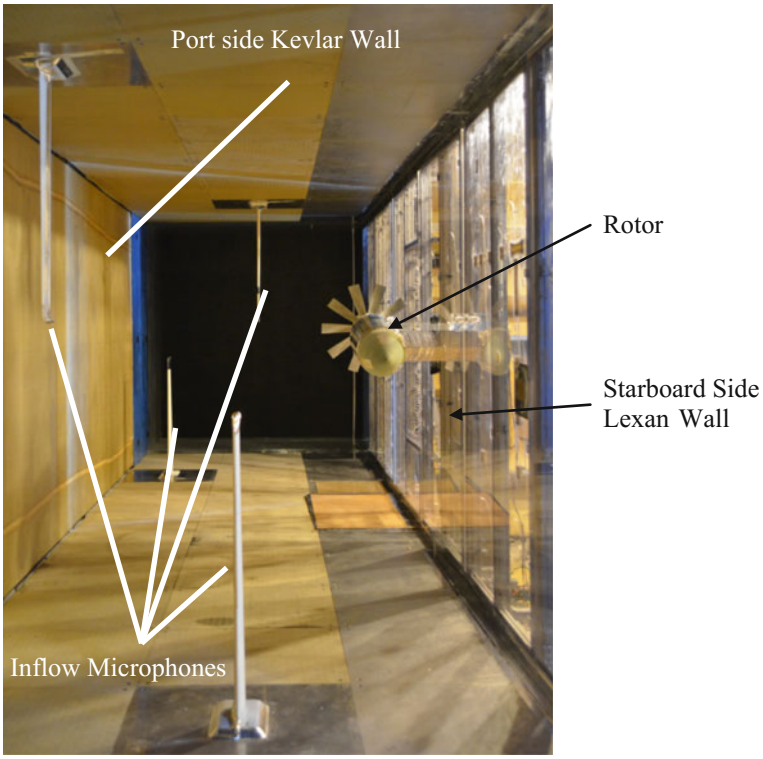

Fig. 2 Rotor mounted near a wall in the Virginia Tech Stability Wind Tunnel

The initial work focused on the ingestion of a thick planar turbulent wall boundary layer by a rotor next to a wall as shown in Fig. 2. Morton et al. [9] documented the complete cross-sectional space-time correlation of this flow to serve as the inflow boundary condition. Alexander et al. [10], Wisda et al. [11, 12], and Murray et al. [13] examined the rotor sound field. Alexander et al. [14] presented direct measurement of two-point blade-to-blade upwash correlations in the rotating frame, and Glegg et al. [15, 16] made predictions of the rotor noise based on the measured inflow correlations. The broadband spectra were found to be predictable for low and moderate thrust cases but at high thrust the experimental measurements of the far-field sound showed the spectral peaks becoming almost tonal and this will be discussed in more detail in Sect. 3.

Following the initial study, a second set of experiments were carried out [17] to investigate the sound produced by the rotor when it ingested a wake shed from a cylinder located upstream of the rotor (Fig. 1). As described below, the results from these two experiments show substantial differences that can be related to the details of the inflow turbulence.

2 The Rotor Systems and the Wind Tunnel

Measurements were performed in the hybrid anechoic test section of the Virginia Tech Stability Wind Tunnel [18]. Sound generated in the test section radiates through Kevlar windows (that are transparent to sound) into anechoic chambers on either side where individual microphones or microphone arrays are placed. The test section floor and ceiling are formed by Kevlar flow surfaces backed by acoustic absorbers and the facility is anechoic down to 180 Hz. Flow in the empty test section is closely uniform and of very low turbulence level (0.021% at 21 m/s). Further facility details are given by Devenport et al. [18].

The rotor used in this study is a left-handed 225% scale model of the rotor first used by Sevik [1], see Figs. 1 and 2. It has a diameter of 457 mm with a 127 mm hub. The rotor has 10 square tipped blades each with a chord of 57.2 mm. The blades are twisted from a pitch angle of 55.6° at the hub to 21.2° at the tips and have a thickness to chord ratio close to 9%. The design advance ratio is 1.17 and the zero-thrust advance ratio is 1.44 estimated using JavaProp [11].

In the study of wake ingestion from a cylinder, a 50.8-mm-diameter cylinder was mounted vertically in the test section 20 diameters upstream of the rotor disk, (see Fig. 1). The cylinder mounting allowed for its lateral position to be adjusted to vary the strike location of the wake center on the rotor. When the rotor yaw angle was changed, the lateral position of the cylinder was adjusted to maintain the same strike location on the rotor disk. Fences were placed on the cylinder 165-mm from the floor and ceiling to improve the two-dimensionality of its wake, verified using cross-sectional measurements with the rotor system removed [17]. All measurements were made for a fixed free stream velocity U_∞ of 20 ± 0.1 m/s corresponding to a Mach number of 0.057 and cylinder Reynolds number of 59,000.

3 Far-Field Sound Spectra

First, we will consider the results for the rotor ingesting the wake of the cylinder (Fig. 1). Figure 3a shows contours of sound pressure level (SPL) referenced at 20 μPa as a function of the advance ratio for a single microphone at receiver angle of 53° to the rotor upstream axis. These results are for the 100% starboard strike case where the cylinder axis is at the same lateral location as the starboard edge of the rotor and about half the rotor face was immersed in the wake. The dashed lines denote the blade passing frequency (BPF) and its harmonics. The far-field sound is characterized by broad haystacks centered around the blade passing frequency and its multiples due to the unsteady coherent loading on successive blades of the rotor. Haystacking is first seen for the blade passing frequency at an advance ratio of about 1.3 and becomes more pronounced as the advance ratio is reduced, appearing at about $J = 0.95$ for two BPF and at $J = 0.8$ for three BPF. Overall sound levels increase as the advance ratio is reduced because of the increase in rotor speed and the haystacking

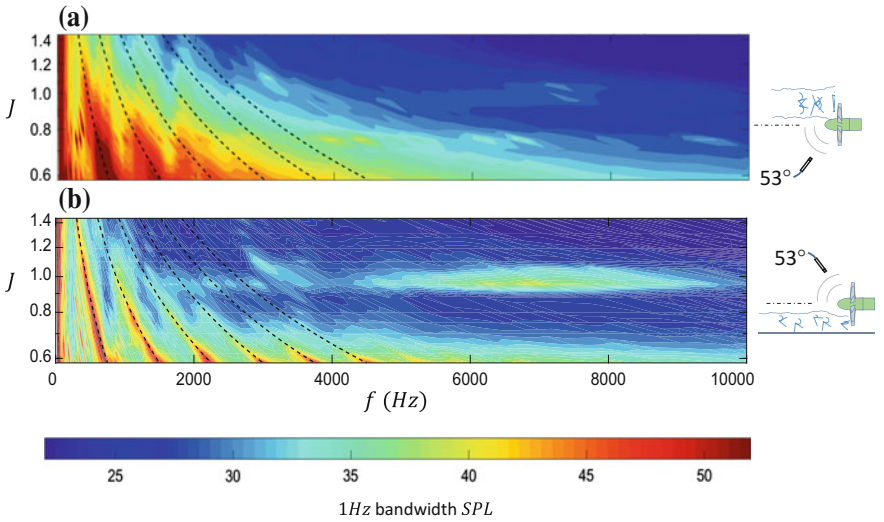

Fig. 3 Far-field noise spectra at an observer angle of 53° plotted as a function of advance ratio for the unyawed rotor. Dashed lines show the blade passing frequency and harmonics. **a** Wake ingestion, 100% starboard strike. **b** Boundary layer ingestion [12], with the rotor immersed in the top 80% of the boundary layer thickness δ, $\delta/R = 44\%$. Spectral levels scaled to an observer distance of 1.903 m

becomes more pronounced for the same reason—higher blade speed means a greater correlation between cuts of successive blades through the same turbulent eddy.

For comparison, Fig. 3b shows sound measurements of turbulent boundary layer ingestion into the same rotor from the study of Wisda et al. [12]. The horizontal ridge that is visible at frequencies of above 5 kHz for advance ratios around one is believed to be the result of trailing edge noise produced by coherent vortex shedding from the rotor blades, similar to that observed by Hersh et al. [19]. Spectral levels have been scaled to reflect the same observer radial distance as the wake measurement. As shown in the thumbnail sketch in Fig. 3b, the outer 1/3rd of the rotor radius is immersed in the boundary layer. Overall, sound levels caused by the boundary layer ingestion are substantially lower than those produced by the wake. There are two reasons for this; the boundary layer covers a significantly smaller portion of the rotor disk, and it is much less turbulent than the wake. Figure 4 compares mean velocity and turbulence profiles measured over the portion of the boundary layer swept by the rotor (in blue), with those measured in the wake. Despite having a higher mean velocity gradient, turbulence stresses in the boundary layer are 1/3rd to 1/6th of those in the wake, and thus upwash fluctuations experienced by the blades will be proportionately smaller. There are also detail differences between the wake and boundary layer ingestion. The sound spectrum for the boundary layer shows a much stronger trailing edge noise signature, the peak between 6 and 8 kHz and $J \approx 0.9$ (likely due to the much larger area of the rotor not exposed to turbulent inflow), and shows narrower more distinct

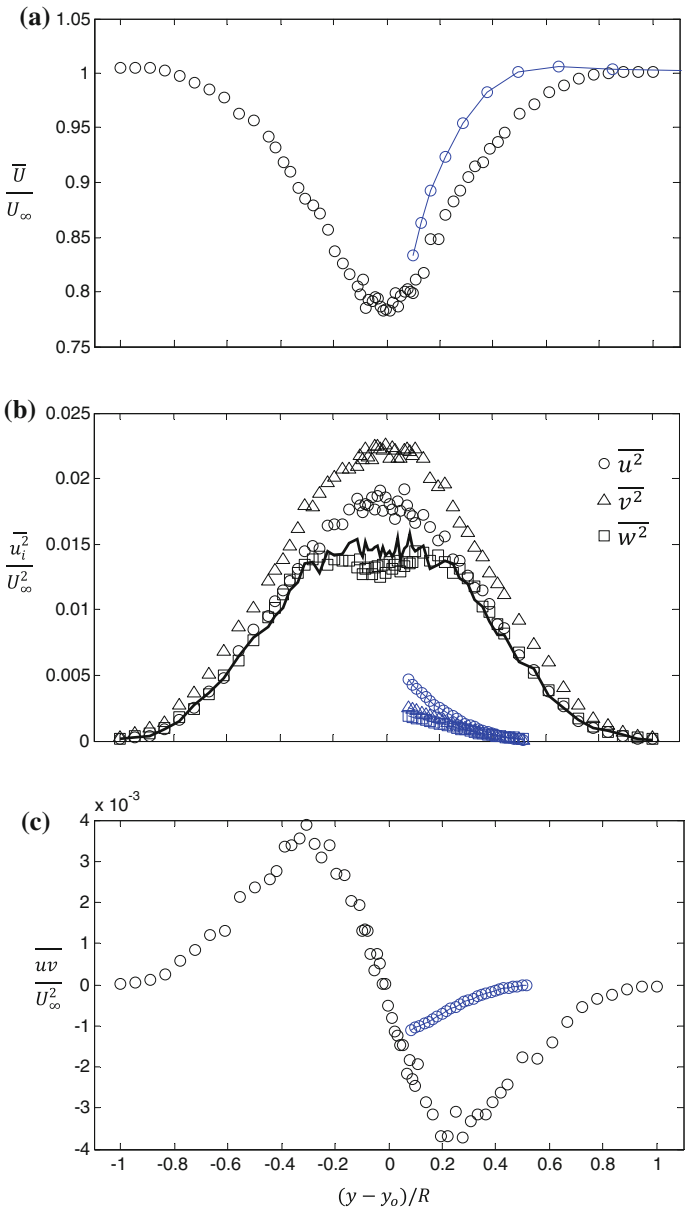

Fig. 4 Velocity profiles through the cylinder wake at $(x - x_{cyl})/D = 20$ (black markers) compared rotor-location boundary layer profiles from Morton et al. [9] (blue markers). **a** Mean velocity profile. **b** Reynolds normal stresses (solid black line shows $\overline{u^2}/U_\infty^2$ after high pass filtering at $fD/U_\infty = 0.015$). **c** Reynolds shear stress profile. Distances normalized on the rotor radius R

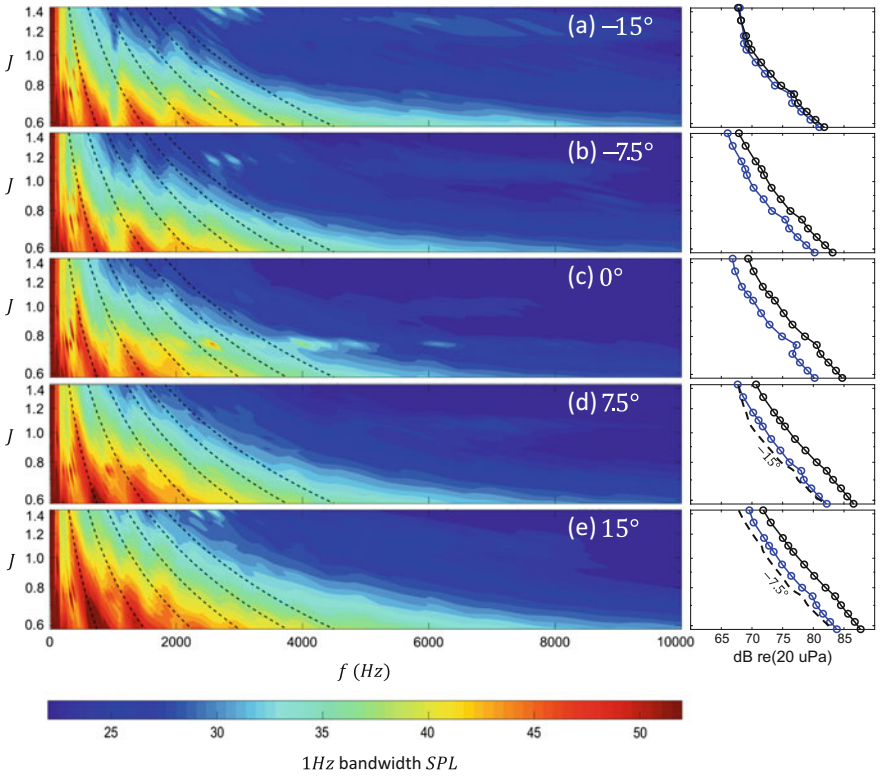

Fig. 5 Far-field noise spectra at an observer angle of 74° plotted as a function of advance ratio for different rotor yaw angles, 100% starboard strike. Dashed lines show the blade passing frequency and harmonics. Plots to the right of each contour set show OASPL as a function of advance ratio for observer angles of 53° (black) and 74° (blue) and use the same vertical axis as the spectral plots. Spectral levels scaled to an observer distance of 1.903 m

haystacks that extend to higher harmonics at a given advance ratio. The high level of the harmonics at high thrust was discussed in detail by Glegg et al. [15, 20] and is a consequence of the flow reversing direction near the wall at low advance ratios and causing clearly defined coherent structures, or an arch vortex system, that results in high sound levels caused by a blade-vortex interaction. These conclusions were substantiated by detailed PIV measurements made by Murray [21].

Figure 5 shows the effects of rotor yaw on the sound generated by wake ingestion for the same strike position as in Fig. 3. The spectral maps are shown for an observer angle of 74° to the rotor axis at −15, −7.5, 7.5, and 15° yaw. This figure includes plots (to the right) showing the variation of OASPL with advance ratio for both 53° (in black) and 74° (in blue), obtained by integrating over the frequency range from half the BPF to 20 times the BPF, capturing the full range of the broadband noise while eliminating background contamination at very low frequencies. As the rotor is

yawed positively (Fig. 5c through e), overall spectral levels increase and the haystacks become less distinct. Negative yaw (Fig. 5a through c) produces the reverse effect. OASPL increases by about 6 dB from −15 to 15° yaw. The change in the degree of haystacking is likely due to the influence of yaw on the path taken by the rotor blades through the space-time correlation of the wake. The results suggest that there is a reduction of the blade-to-blade correlation with positive yaw. The change in overall sound levels can be explained in terms of directivity. If the sound directivity is fixed relative to the rotor axis, then a −15° to 15° change in yaw angle changes the angle of a fixed observer measured from the rotor axis by the same amount. Assuming the rotor sound field to be directed primarily along the rotor axis, this results in an increase in sound levels with yaw. This equivalence between yaw and directivity holds quantitatively also. For example, an observer at $\theta = 53°$ is at an angle of 68° and 60.5° to the rotor axis for yaw angles of −15 and −7.5°, almost the same angles seen at $\theta = 74°$ for yaw angles of 7.5° and 15° and thus sees similar sound levels. This is shown in the OASPL plots of Fig. 5d and e where OASPLs measured at a receiver angle of 74° for yaw angles of 7.5° and 15° (blue curves) are compared with those measured at a receiver angle of 53° for yaw angles of −15 and −7.5° (black dashed lines). Sound levels are the same, to within 1–2 dB.

4 Characteristics of the Undistorted Wakes

Figure 4 shows mean velocity and turbulence stress profiles through the undisturbed wake measured 20 cylinder diameters downstream without the rotor present. Also shown are the turbulence profiles for the boundary layer flow that impinges on the rotor when it is near the wall as shown in Fig. 2. The wake is almost symmetric with a maximum mean velocity deficit, Fig. 4a, of 22% and an overall width of approximately 2 rotor radii, just sufficient to immerse almost the entire rotor face when the projected centerline of the wake is on the rotor axis. The turbulence normal stress profiles (Fig. 4b) show levels to be quite high in the center of the wake with a peak intensity of about 14% in the v component. The anisotropy is evident here with normal-to-wake stress having the largest magnitude followed by the streamwise and spanwise stresses. The streamwise normal-stress profile is somewhat misleading as it includes contributions from some very low-frequency fluctuations. High-pass filtering at frequencies $fD/U_\infty > 0.015$ reduces streamwise turbulence levels to the profile indicated by the solid line, while having little discernable influence on the other stress components. We suspect that this is due to low-frequency flapping of the wake. Upwash measurements made in the rotor frame of reference, to be shown later, suggest that this motion may be stabilized when the rotor is installed. The Reynolds shear stress profile (Fig. 4c) appears closely antisymmetric, with a peak magnitude of about $0.004\ U_\infty^2$.

Also shown in these plots are the corresponding results for the boundary layer flow, with the same outer mean flow (where y_o defines the wall location). While the

mean flow deficit is similar, as shown in Fig. 4c, the turbulence stresses are much smaller in each case, as discussed above.

Figure 6 shows velocity correlation results for the wake and the boundary layer. Figure 6a shows streamwise integral length scales inferred from integral timescales and Taylor's hypothesis. The u component fluctuations have the longest streamwise scale of between 20 and 30% R (where R is the rotor radius) depending on position in the wake, whereas the integral scales of v and w are about half as large. Looking at the time delay correlation coefficient functions on the wake centerline, Fig. 6b, we see that v correlation function is oscillatory with a period close to $1.18\,R/U_\infty$ implying a Strouhal number, normalized on the cylinder diameter, $f\,D/U_\infty$ of 0.19. This is therefore the coherent vortex shedding from the cylinder, and the streamwise integral scale in v is clearly much smaller than the true correlation distance because of the negative excursions in its correlation function. The u and w correlation functions have a much more monotonic form and decay to coefficients of 10% over timescales equivalent to streamwise distances of 90% and 20% R, respectively. The spanwise correlation coefficient functions measured at the wake center, Fig. 5c, show more uniform behavior among the three velocity components, with correlation coefficients falling monotonically to 10% over about one rotor radius in all cases.

Also shown in Fig. 6 are the corresponding results for the boundary layer flow normalized on the same parameters. First, we note that the lengthscale for the u component is similar to the lengthscale in the wake, but the lengthscales in the direction normal to the flow are much smaller for the boundary layer than in the wake when $(y - y_o)/R$ is about 0.5. This is also apparent when considering the spanwise scale shown in Fig. 6c, where the wake is clearly an order of magnitude more coherent in the spanwise direction than the turbulent boundary layer. This highlights the fundamental differences between these flows. In the case of the wake, the flow is clearly dominated by large turbulent structures that are of extended spanwise extent, whereas the boundary layer is more likely dominated by streamwise structures.

5 Turbulence Measurements in the Rotor Frame

The acoustic effect of decreasing advance ratio has been discussed above, but in order to predict the acoustic response of the rotor to the turbulent inflow, the distorted inflow itself must be known. An on-blade hotwire system as shown in Fig. 7 was used to measure this directly, particularly the unsteady upwash which is the dominant component of the unsteady blade loading. The data were phase-averaged to compute mean and unsteady velocity components as a function of blade angle. The phase-averaging was completed by dividing the blade rotation into one-degree bins.

Figure 8 shows the mean square unsteady upwash profile through the wake as measured by the on-blade hotwire at 90% radius with the cylinder at the center strike position (Note these measurements were made at 10 m/s rather than 20 m/s as used in the rotor noise tests). The profiles measured during the top and bottom passes through the wake are plotted separately as contours as a function of advance ratio,

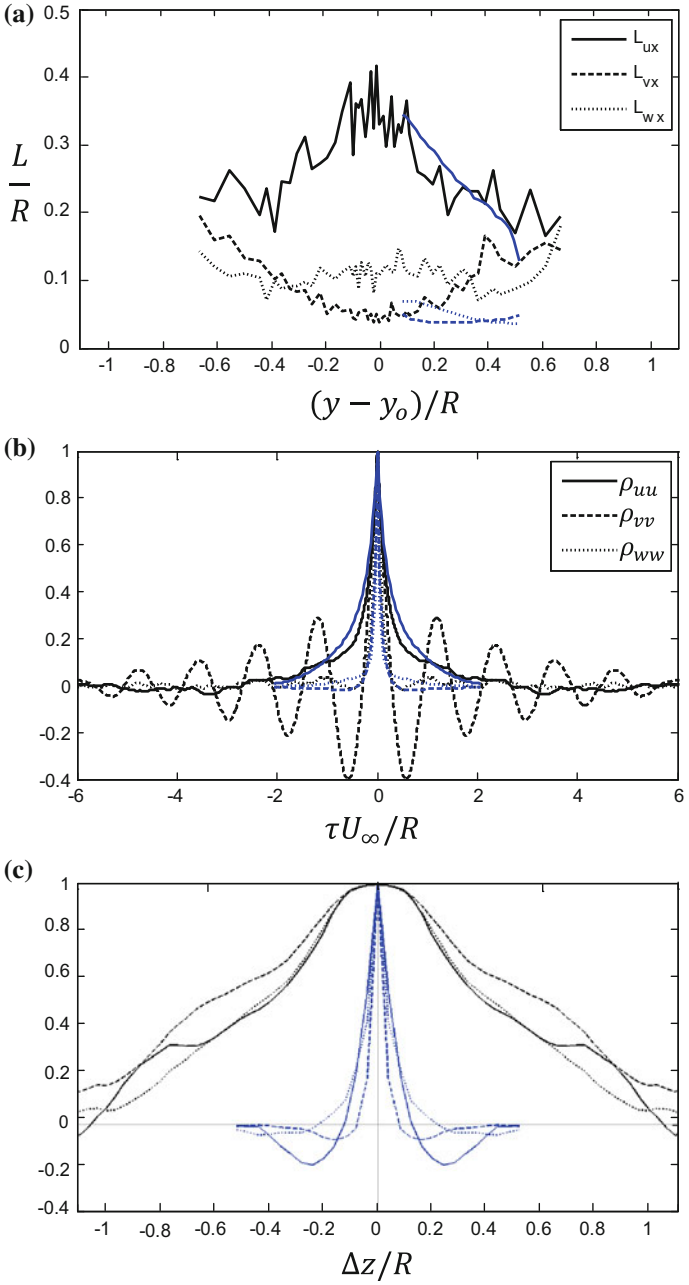

Fig. 6 Correlation statistics for the cylinder wake at $(x - x_{cyl})/D = 20$ (black markers) compared to rotor-location boundary layer profiles from Morton et al. [9] (blue markers). **a** Streamwise integral scale profile. **b** Time delay correlation coefficient functions, and **c** spanwise correlation coefficient functions at the wake center and 20% of the boundary layer thickness. Legend for part (**c**) is same as part (**b**)

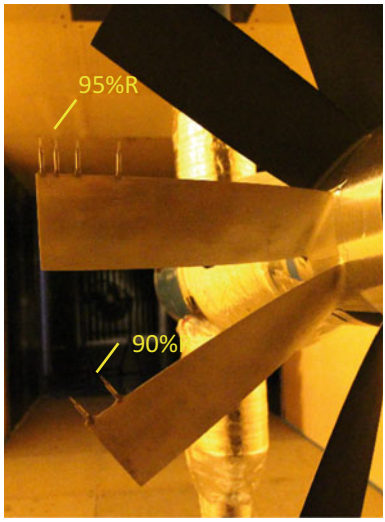

Fig. 7 View from upstream of the instrumented rotor blades showing the two probes for which results are reported

J. Note that profiles measured during the bottom pass appear shifted slightly (about 0.05 R) in the lateral direction compared to those measured during the top pass, but are otherwise very similar. This is not distortion. It is because the blade orientation is reversed during the two passes and thus the orientation of the upwash component is different. Because of the anisotropy of the wake turbulence structure, this results in a differently skewed profile. Distortion is apparent in the streamtube contraction that narrows the wake with increasing thrust and decreasing advance ratio. From $J = 1.44$ to 0.58, the width of the wake contracts by 16% before impact with the rotor face, but retains its roughly symmetric form. Note that peak upwash turbulence levels at low thrust (high J) are most similar to streamwise turbulence levels measured in the undisturbed wake (Fig. 4b) when low-frequency flapping motions are filtered out.

Figure 9 shows the unsteady upwash as seen by the probe at 90% radius, but in this case, the cylinder is at the 75% port strike location. Near zero-thrust, the center of the wake appears at the 75% R location as expected, but as the advance ratio decreases, the center of the wake is drawn across the rotor disk face toward its center, shifting by about 20% of the rotor radius at the lowest advance ratio. Comparing Figs. 8 and 9, it appears that the streamtube contraction is more drastic when the center of the wake is on the edge of the rotor disk, as might be expected from actuator disk theory. This difference impacts both the wake turbulence and the produced noise. For this single probe position, the relative velocity of the probe increases with decreasing advance ratio. One may expect the far-field noise from this particular blade strip to increase roughly as the sixth power of velocity (dipole source efficiency), but the observed changes, both distortion and wake movement, must also be considered when predicting the noise at a particular observer location. The dipole for this particular section of blade has a rotating directivity pattern. Movement in the center of the wake slides the peak radiative efficiency for this particular strip to another observer

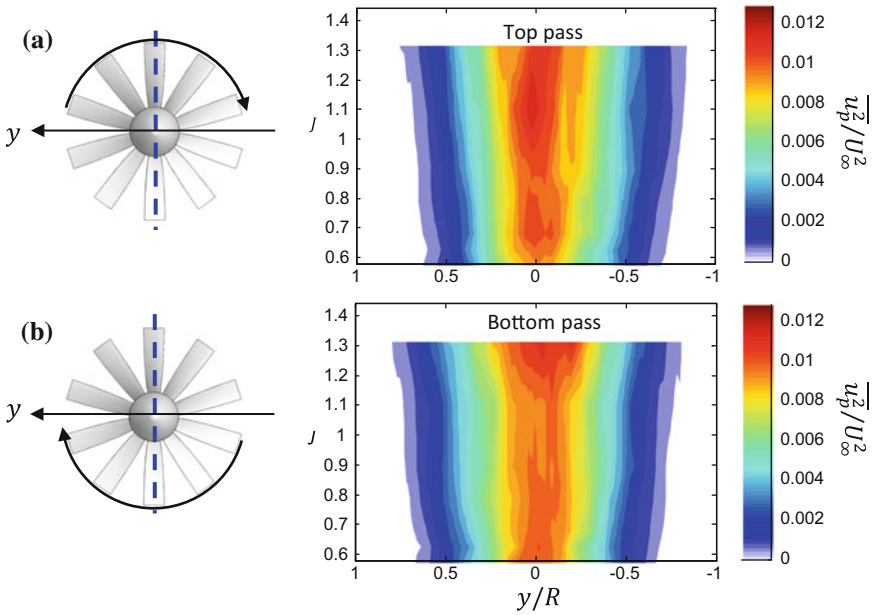

Fig. 8 Profiles of mean square upwash velocity seen at the 90% rotor radius as a function of advance ratio with the wake striking the center of the rotor. Profiles measured **a** during the top (positive z) pass, and **b** during the bottom pass

location. Of course, this effect will get integrated across the entire rotor disk in a full strip theory approach. Accurate prediction of the noise must fully account for this three-dimensional movement of the ingested wake even if the undisturbed wake could otherwise be considered two-dimensional and statistically stationary.

6 Rotor Noise Predictions

The noise levels from these rotor configurations were predicted using the method described by Glegg et al. [22]. In this approach, the far-field sound spectrum is predicted by considering the unsteady loading on each section of the blade. A strip theory approach is used and the spectral density in the far field is directly related to the cross-correlation of the unsteady loadings on each blade section and also between blades. To obtain the unsteady loading correlation, the blade response to an incoming gust is evaluated in the time domain. This allows the unsteady force correlation function to be directly related to the velocity correlation function of the unsteady inflow. The hotwire measurements by Morton [9] of the boundary layer flow and the measurements by Molinaro [23] of the wake provide the two-point correlation function in the detail required as an input to the code. This data set is

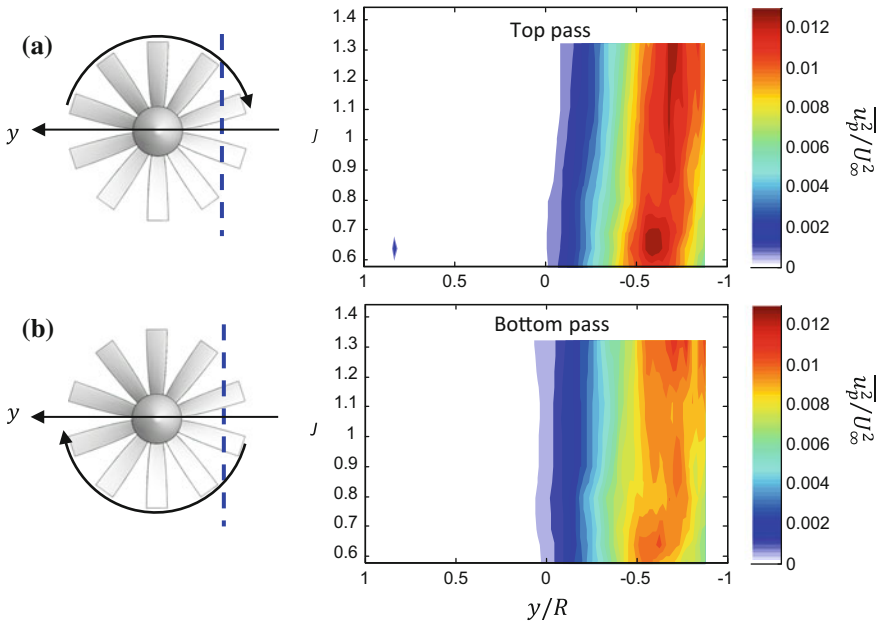

Fig. 9 Profiles of mean square upwash velocity seen at the 90% rotor radius as a function of advance ratio with the wake striking at the 75% port location. Profiles measured **a** during the top (positive) pass, and **b** during the bottom pass

not trivial since the correlation function is four-dimensional if Taylor's hypothesis is assumed. One of the added advantages of assuming Taylor's hypothesis is that the correlation function is defined as a function of time delay, which is exactly equivalent to the drift function of the local turbulent flow so the only correction required for the distortion as the turbulence enters the rotor is a small amplitude correction caused by the contraction of the stream tube. This amplitude correction is illustrated in Figs. 8 and 9 as a function of advance ratio and gives a correction to the far-field sound of only a fraction of a dB.

Using this approach, the predicted far-field sound spectra for various cases is illustrated in Figs. 10 and 11. The conclusion for these studies is that providing sufficient information about the inflow turbulence is available; then, rotor noise prediction can be quite accurate. The only significant error in the predictions shown in Figs. 10 and 11 is for the lowest advance ratio for the case of the rotor operating in the boundary layer (Case D, Fig. 10). However, this poor prediction is the result of the formation of a coherent, non-turbulent structure in the flow and is discussed in detail in [20] and in Sect. 3.

The results in Fig. 11 are for a yawed rotor and the predictions are based on the hypothesis that the inflow is unaffected by the yaw, and the main effect is the change in directivity cause by the relative position of the observer to the rotor axis.

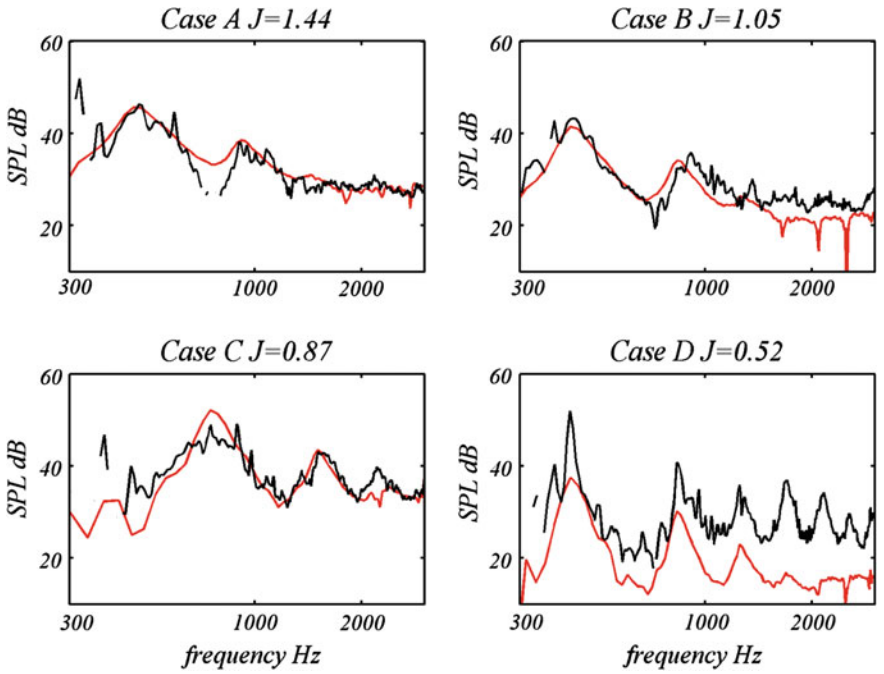

Fig. 10 Predicted (red) and measured (black) far-field sound spectra for the rotor operating in a wall boundary layer for a fixed microphone and at different advance ratios, see [15, 16]

This approach appears to work well for the case shown, and for all the other cases considered, as discussed in Sect. 3.

7 Conclusions

Measurements have been performed on a scaled version of a Sevik rotor ingesting both a planar turbulent wake and a turbulent boundary layer flow. In both cases, detailed measurements were made of the inflow turbulence, including three-component turbulence profiles and the full cross-sectional 4-dimensional space-time correlation function. Far-field sound measurements were also made of the turbulence ingestion noise for a comprehensive range of rotor advance ratios varying from zero to high thrust, for rotor yaw angles out of the plane of the wake from -15 to $15°$, and for a range of wake strike positions on the rotor disk. Probes mounted on two of the rotor blades were used to measure upwash fluctuations seen in the rotating frame, as well as blade-to-blade coherence spectra. Comparisons have been made with predictions based on the measured inflow turbulence for both configurations and good results were obtained in all cases.

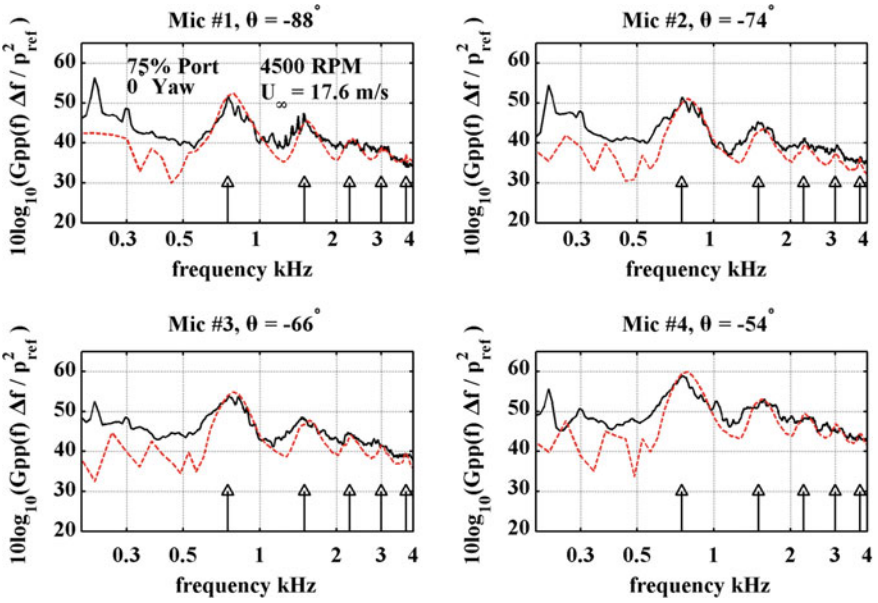

Fig. 11 Predicted (red) and measured (black) far-field sound spectra for the rotor operating in the wake of a cylinder for a fixed speed and different microphone locations

The wake was found to produce an intense and anisotropic turbulent inflow with a width approximately equal to the rotor diameter. Streamwise correlations at the rotor plane were found to be dominated by vortex shedding at a Strouhal number of 0.19, the train of eddies producing correlated velocity fluctuations over time delays equivalent to the passage of about 6 rotor radii. Correlations in the spanwise direction extended over about 1 rotor radius. Sound spectra measured with the rotor showed haystacking at the blade passing frequency and higher harmonics for a range of thrusting conditions produced by multiple cutting of the same turbulent eddies by successive blades. Compared to boundary layer ingestion, wake ingestion produced much louder sound, because of the higher wake turbulence levels and the greater area of the rotor disk immersed. With the boundary layer, however, the haystacks are more distinct and extend to higher harmonics. This is partly because the boundary layer eddies have a much smaller spanwise extent so that successive blade interactions with the large eddies are more impulsive and partly because of the reverse flow effects near the wall that cause the formation of a coherent vortex structure under the rotor.

Yawing the rotor in the wake produces some change in the definition of the haystacks, due to the change in the correlation structure of the turbulence cut by the blades, but the major effect is a change in overall sound levels. This change is a directivity effect, the sound field being determined primarily by the observer angle relative to the rotor axis rather than the flow axis.

On-blade hotwire measurements reveal the distortion of the wake as it is drawn into the rotor. With the center of the wake striking the center of the rotor, the principal effect of the distortion is the narrowing of the wake with increasing thrust due to streamline contraction. With the wake striking closer to the edge of the disk, the principal effect is the drawing of the wake toward the center of the rotor disk increasing the area of turbulence interaction.

Acknowledgements The authors would first like to thank Henry Murray, Ian Clark, and Anthony Millican for their assistance during the wind tunnel entries, and Mr. Michael Marcolini for his insightful observations and help with reviewing the manuscript. The authors would also like to thank the Office of Naval Research, in particular Dr. Ki-Han Kim and Dr. John Muench, for their support of this research through grants N00014-14-1-0141 and N00014-16-1-2395.

References

1. Sevik, M.: Sound radiation from subsonic rotor subjected to turbulence. In: International Symposium on Fluid Mechanics and Design of Turbo Machinery. University Park, Pennsylvania (1973)
2. Scharpf, D.F., Mueller, T.J.: An experimental investigation of the sources of propeller noise due to the ingestion of turbulence at low speeds. Exp. Fluids **18**, 277–287 (1995)
3. Minniti, R.J.I., Blake, W.K., Mueller, T.J.: Inferring propeller inflow and radiation from near-field response, part 1: analytic development. AIAA J. **39**, 1030–1036 (2001)
4. Minniti, R.J.I., Blake, W.K., Mueller, T.J.: Inferring propeller inflow and radiation from near-field response, part 2: empirical application. AIAA J. **39**, 1037–1046 (2001)
5. Wojno, J.P., Mueller, T.J., Blake, W.K.: Turbulence ingestion noise, part 1: experimental characterization of grid-generated turbulence. AIAA J. **40**, 16–25 (2002)
6. Wojno, J.P., Mueller, T.J., Blake, W.K.: Turbulence ingestion noise, part 2: rotor aeracoustic response to grid-generated turbulence. AIAA J. **40**, 26–32 (2002)
7. Ganz, U.W., Joppa, P.D., Patten, T.J., Scharpf, D.F.: Boeing 18-Inch Fan Rig Broadband Noise Test, in, NASA (1998)
8. Stephens, D.B., Morris, S.C.: Sound generation by a rotor interacting with a casing turbulent boundary layer. AIAA J. **47**, 2698–2708 (2009)
9. Morton, M.A., Devenport, W.J., Glegg, S.: Rotor inflow noise caused by a boundary layer: inflow measurements and noise predictions. In: 18th AIAA/CEAS Aeroacoustics Conference. Colorado Springs, Colorado (2012)
10. Alexander, W.N., Devenport, W., Morton, M., Glegg, S.: Noise from a rotor ingesting a planar turbulent boundary layer. In: 19th AIAA/CEAS Aeroacoustics Conference. Berlin (2013)
11. Wisda, D., Alexander, W.N., Devenport, W.J., Glegg, S.A.: Boundary layer ingestion noise and turbulence scale analysis at high and low advance ratios. In: 20th AIAA/CEAS Aeroacoustics Conference. Atlanta GA (2014)
12. Wisda, D., Murray, H., Alexander, N., Nelson, M.A., Devenport, W.J., Glegg, S.: Flow distortion and noise produced by a thrusting rotor ingesting a planar turbulent boundary layer. In: Aviation 2015. Dallas, TX (2015)
13. Murray, H., Wisda, D., Alexander, N., Nelson, M.A., Devenport, W.J., Glegg, S.: Sound and distortion produced by a braking rotor operating in a planar boundary layer with application to wind turbines. In: Aviation 2015. Dallas, TX (2015)
14. Alexander, W.N., Devenport, W.J., Wisda, D., Morton, M.A., Glegg, S.A.: Sound radiated from a rotor and its relation to rotating frame measurements of ingested turbulence. In: 20th AIAA/CEAS Aeroacoustics Conference. Atlanta, GA (2014)

15. Glegg, S., Buono, A., Grant, J., Lachowski, F., Devenport, W., Alexander, N.: Sound radiation from a rotor partially immersed in a turbulent boundary layer. In: Aviation 2015. Dallas, TX (2015)
16. Glegg, S., Grant, J., Wisda, D., Murray, H., Alexander, N., Devenport, W.: Broadband noise from a rotor at an angle to the mean flow. In: AIAA Scitech 2016. San Deigo, CA (2016)
17. Alexander, W.N., Molinaro, N.J., Hickling, C., Murray, H., Devenport, W.J., Glegg, S.A.: Phased array measurements of a rotor ingesting a turbulent shear flow. In: 22nd AIAA/CEAS Aeroacoustics Conference. Lyon, France (2016)
18. Devenport, W.J., Burdisso, R.A., Borgoltz, A., Ravetta, P.A., Barone, M.F., Brown, K.A., Morton, M.A.: The Kevlar-walled anechoic wind tunnel. J. Sound Vib. **332**, 3971–3991 (2013)
19. Hersh, A.A., Soderman, P.T., Hayden, R.E.: Investigation of acoustic effects of leading-edge serrations on airfoils. J. Aircr. **11**, 197–202 (1974)
20. Glegg, S., Grant, J., Murray, H., Devenport, W., Alexander, N.: Sound radiation from a rotor operating at high thrust near a wall. In: AIAA/CEAS 22nd Aeroacoustics Conference. Lyon, France (2016)
21. Murray, H.H.: Turbulence and Sound Generated by a Rotor Operating Near a Wall, MS Thesis. Aerospace and Ocean Engineering, Virginia Tech (2016)
22. Glegg, S.A.L., Devenport, W.J., Alexander, A.: Broadband rotor noise predictions using a time domain approach. J. Sound Vib. **335**, 115–124 (2015)
23. Molinaro, N.J.: The Two Point Correlation Structure of a Cylinder Wake, MS Thesis. Aerospace and Ocean Engineering, Virginia Tech (2017)

Numerical and Experimental Assessment of the Linflap Technology for Regional Aircraft Noise Reduction

Mattia Barbarino, Ignazio Dimino and Antonio Concilio

Abstract Within Green Regional Aircraft (GRA), a JTI Integrated Technology Development (ITD) program, an acoustically treated flap (called lined-flap), has been assessed. The design of such a lined-flap, conceived as a low-noise high-lift device, has been optimized through a suitable evolutionary algorithm that refers to an acoustic finite element (FE) model. An original turbulent empirical model has been implemented to estimate the noise, generated by the trailing edge and scattered by the wing body. A semiempirical model has instead supported the design process, relating the acoustic impedance to structural and materials properties. The capability of the proposed system has been finally checked within devoted wind tunnel test experiments.

Keywords Linflap · Aeroacoustic tests

1 Introduction

Commuters serve several locations with a large variety of airport characteristics. They operate within international hubs and local infrastructures, aimed at serving the peripheral areas. In this case, the airport extension is limited but very close to densely populated zones. Nowadays, the number of flights is constantly growing, and this naturally translates in an equal increment of takeoffs and landings. They are the travel phases with the highest impact on the so-called community noise that is the noise perceived by the population living in the airport vicinity. These issues may strongly limit the growth of regional airliners that are envisaged to face more and more demanding environmental constraints in the next future, following the novel

M. Barbarino (✉)
Aeronautics Environmental Impact Division, The Italian Aerospace Research Center, CIRA SCpA, Capua (CE), Italy
e-mail: m.barbarino@cira.it

I. Dimino · A. Concilio
Adaptive Structures Division, The Italian Aerospace Research Center, CIRA SCpA, Capua (CE), Italy

E. Ciappi et al. (eds.), *Flinovia—Flow Induced Noise and Vibration Issues and Aspects-II*,
https://doi.org/10.1007/978-3-319-76780-2_9

orientation of civil aviation certification and political authorities toward the emissions level, whatever is their origin (chemical, acoustic, and so on). Among the others, the deployment of the well-known high-lift device (HLD) is a main source of exterior noise generation, [1, 2]. This simple consideration justifies the effort that the scientific community is producing to restrain this unwanted phenomenon by interventions on the overall systems while preserving their aerodynamic performance (HLD is necessary flight enablers). Present technologies reduce somehow their capability: At landing, such degradation often demands in turn higher aircraft speeds, making the expected gain almost vanish. The research herein reported has been developed within the Green Regional Aircraft (GRA) program for the technological innovation of current commuter configurations, [3]. HLD noise is a complex phenomenon, requiring sophisticated approaches and tools to be modeled. It involves several separate physical processes, from unsteady vortex recirculation to edge-scattered tonal noise, and many others. In the end, it results in the generation of a broadband acoustic disturbance with tonal components that are more and more relevant as the angle of attack increases (for instance, during landing and takeoff phases). Generally, two main contributions may be identified, associated with slat- and flap-like systems, respectively. The former exhibits a strong power dependency on the aircraft velocity and is responsible for the tonal part; the latter gives rise to a pure broadband contribution, with some exceptions linked to crossed interactions. Deflection of spoilers may in fact modify the overall wing circulation and therefore the slat radiation. Flaps may interact with the main landing gear wake and generate an intense low-frequency noise, [4, 5]. In this context, a non-conventional device has been developed [1–6], consisting of a flap working also as a passive acoustic treatment. This concept has been named linflap and has been explored within numerical and experimental investigations. The novel architecture bypasses the elaborated solutions that have been up to now tried in literature; they usually imply a remarkable increase of the system complexity, with impacts on the reliability and safety levels. The proposed idea has been based on the integration of a passive system within the existing arrangement; therefore, it does not modify the reference geometry while increasing its acoustic performance. For these characteristics, it can retrofit existing devices.

2 The LinFlap Concept

Full-extended flaps, like whatever aircraft hyper-lift device, are significant sources of exterior noise. Radiated sound may have a dramatic impact on the acceptance of the airplane type by the authorities, because it may have dramatic impacts on the life quality of the community, living in the closeness of the airports. The consequences may be severe and can even determine the ban of the specific noisy aircraft. Aiming at reducing the noise impact of HLD, a non-conventional flap has been developed with augmented passive acoustic properties [1–6]. This concept, called lined-flap (or linflap), is conceived as an acoustic liner with one or two degrees of freedom (DOFs). A conventional single DOF liner consists of one-layer sandwich with a

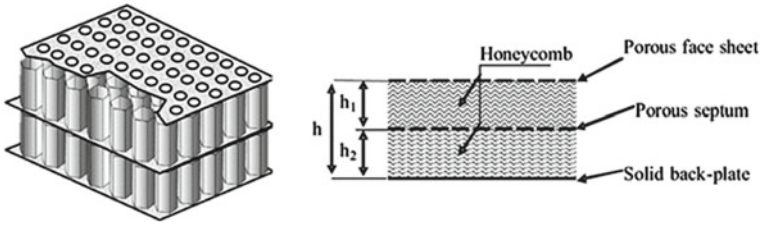

Fig. 1 2-Degree of freedom liner

Fig. 2 Conceptual scheme of the lined-flap

solid back plate, a microperforated facesheet and a honeycomb core. The concept can be extended to a 2-DOF liner by adding a second honeycomb core separated by a porous septum, as depicted in Fig. 1.

The lined-flap can be conceived as a classical liner, by introducing one or more honeycomb layers inside the flap; the external surface is a microperforated skin. The cavities, combination of the microholes and the honeycomb cells, behave like Helmholtz resonators, giving rise to a certain sound absorption. The shape and the structural system remain instead unchanged. A sketch of the lined-flap arrangement is shown in Fig. 2.

The proposed setup consists of a 2-DOF liner with a porous facesheet at the lower surface. It allows using the whole thickness of the flap to host the honeycomb structure, thus expanding low-frequency capability. Moreover, the bottom perforation enables a natural drainage of the water that can be retained during wet aircraft operations. In the proposed layout, the cavity is divided into two blocks, Fig. 2, to explore cavity depth variation effects in the chordwise direction.

3 LinFlap Acoustic Design and Optimization

The linflap design has started from a computational analysis based on computational fluid dynamics (CFD) and computational aeroacoustics (CAA) tools, addressed to optimize its layout. A two-dimensional double-slotted section has been extracted from a turboprop aircraft wing. The investigation has been performed at its maximum extension, corresponding to the landing configuration, as shown in Fig. 3.

In a first step, a 2D simulation has been carried out by using the CFD software FLUENT by ANSYS, assuming a Mach number of 0.149 and a 5.4° incidence.

Fig. 3 2D wing section of the turboprop aircraft configuration

Such configuration has been defined by requiring that the airfoil works at the same lift coefficient than the relative 3D wing section. A pressure-based second-order upwind scheme has been employed to converge fully coupled RANS equations with turbulence, taken into account through a K-ω SST model. An O-grid structured computational mesh has been used, extending all around the geometrical components, forcing a high resolution of the laminar sublayer through a unitary value of y+, Fig. 4. Therein, the computed turbulent kinetic energy contour plots are also shown.

The characteristic boundary-layer parameters, computed at 95% of the main body chord, have been extracted from CFD simulations and synthetically reported in Table 1. These quantities are used to determine the wall-pressure root mean square at the trailing edge through the Schlinker and Amiet [7] model, imposed as a Dirichlet boundary condition to the implemented CAA-FEM propagation model [6].

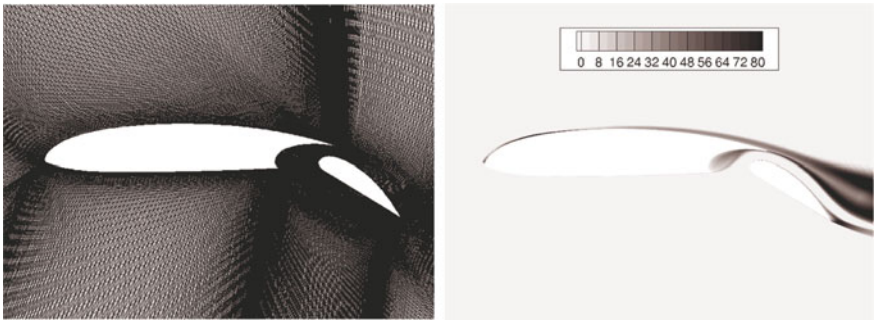

(a) Computational CFD mesh

(b) Contour plot of the turbulent kinetic energy

Fig. 4 A view of the computational mesh and the contour plots of the computed turbulent kinetic energy

Table 1 Boundary-layer RANS results at 99.5% chord (main body). In the order, *Ua* and *Ue* are the freestream and the boundary-layer asymptotic velocity, while δ^* and θ are the boundary-layer displacement and momentum thickness, respectively

Ua (m/s)	*Ue* (m/s)	δ^* (m)	θ (m)
50.7	40.9	5.326×10^{-3}	3.822×10^{-3}

In a second step, a CAA approach has allowed propagating the acoustic field through the CFD mean flow till the far field over a defined frequency range. Such a method solves the Howes acoustic analogy equation [8, 9] in the frequency domain. The Myers impedance boundary condition [10] has been implemented to represent the acoustic treatment influence. The reference impedance value depends on the lin-flap constructive properties. A bibliographic semiempirical model [11] has allowed the simulation of the treatment behavior and permitted also defining the flow properties, e.g., boundary-layer momentum thickness and asymptotic Mach number. For a 2-DOF liner, the non-dimensional impedance takes the following expression [11]:

$$Z = Z_f + \left[\left(Z_s \frac{\cos(kh_f)\sin(kh_s)}{\sin(kh)} + iX_c / \left(1 + iZ_s \frac{\sin(kh_f)\sin(kh_s)}{\sin(kh)}\right)\right)\right] \quad (1)$$

where $Z_f = R_f + iX_{mf}$ and $Z_f = R_s + iX_{ms}$ are the non-dimensional impedance of the facesheet and of the septum, being R_f, R_s and X_{mf}, X_{ms}, respectively, the porous-surface resistance and the porous-surface mass reactance, $X_c = -\cot(kh)$ is the cavity reactance, h_f, h_s, h are the facesheet, septum, and total cavity depth (honeycomb thickness), and k is the acoustic wave number. The general impedance formula for a 1-DOF liner can be achieved assuming $Z_s = 0$. Hence, the facesheet and septum resistance and mass reactance are estimated using the following formulas:

$$R = \frac{64\mu\tau}{2\rho_a c_a \varrho C_d d^2} + \frac{M_e}{\varrho(2 + 1.256\frac{\delta^*}{d})} \quad (2)$$

$$X_m = \frac{k[\tau + 0.85d(1 - 0.7\sqrt{\varrho}/(1 + 305M_e^2))]}{\varrho} \quad (3)$$

where τ is the porous-surface thickness, μ is the fluid viscosity, d is the orifice diameter, C_d is a non-dimensional orifice discharge coefficient due to the contraction of the flow passage section across the orifice, δ^* is the boundary-layer displacement thickness, M_e is the boundary-layer asymptotic Mach number, and $\varrho = N_s \pi d^2/4$ is the surface porosity (defined as the ratio between the orifices area and the total area), N_s being the number of orifices for unit surface. A typical value of C_d is 0.76. The septum resistance and mass reactance are estimated by setting $M_e = 0$ in the formulas above.

FEM simulations have been carried out in the frequency range between 20 and 1,500 Hz with a 20 Hz frequency step. Being λ the acoustic wavelength, the extension of the CAA computational domain, Fig. 5, has been tuned with its largest value: The farfield boundaries have been set 1.35 λ away from the airfoil at the minimum frequency. The size of the CAA mesh has been instead tuned with the smallest value of that parameter: A density of about five grid points per λ is guaranteed at the max frequency.

For each frequency, the Sound Pressure Level (SPL) has been numerically computed along a 121-mic, 17-m-radius (R_m) circular array, centered at the flap trailing

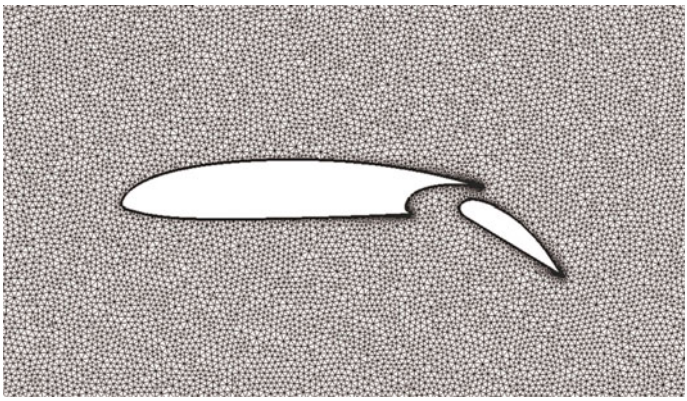

Fig. 5 A view of the computational CAA mesh

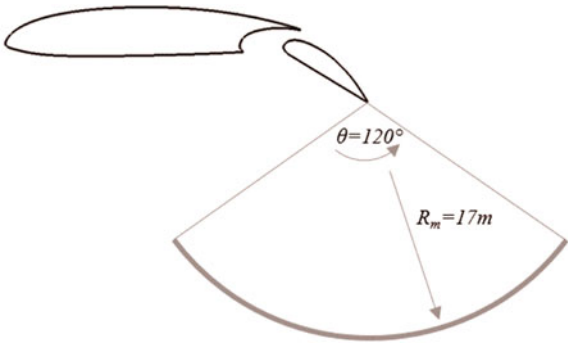

Fig. 6 121-mic circular array ($R_m = 17$ m), centered at the flap trailing edge

edge and covering a 120 deg-arc. Such a virtual rack has been extracted from the FEM output (Fig. 6) and has been used to estimate the source directivity pattern.

To compute the Overall Sound Pressure Level (OASPL), the Noesis Solutions commercial software OPTIMUS [12] has been used. It has embedded the reference FEM code and has allowed carrying out a parametric study for optimizing the liner configuration. Through the implementation of DOE (design of experiment) methods, an RSM (response surface model) cost function has been built. A self-adaptive evolution genetic algorithm applied to RSM has been then applied to optimize the linflap design. A scheme of the complete design process is reported in Fig. 7.

Considering the conceptual scheme of Fig. 7, for construction simplicity it is assumed that the perforated facesheet has a constant surface porosity ϱ_f and thickness τ_f. In principle, the orifices' diameter can instead have different values for the two honeycomb packs, close to the leading (d_f^{LE}) and the trailing edge (d_f^{TE}). Analogously, the two septa have the same surface porosity ϱ_s and thickness τ_s, but may have different orifices' diameter (d_s^{LE} and d_s^{TE}). The septum cavity depth h_s is supposed to be a constant percentage η of the total cavity depth h at the same chordwise location. η can assume different values at the two liner packs (η^{LE}, η^{TE}).

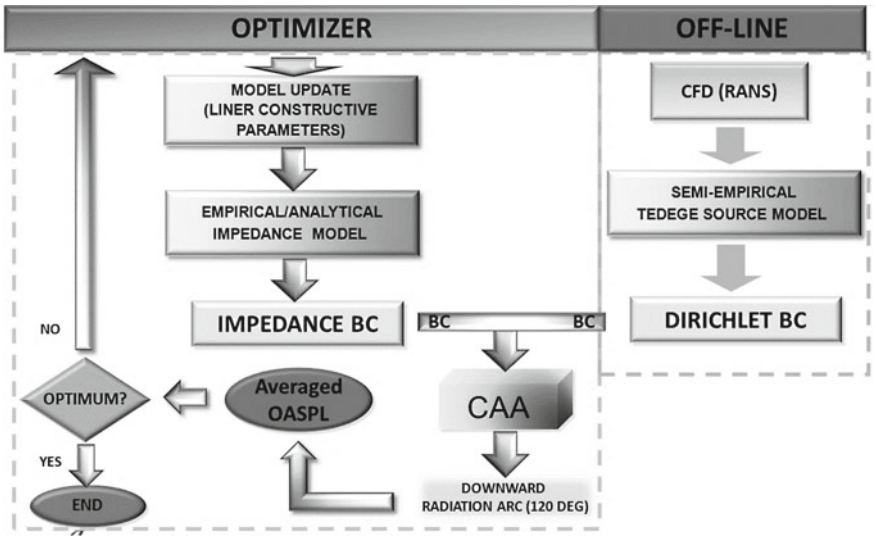

Fig. 7 Flowchart of the lined-flap design

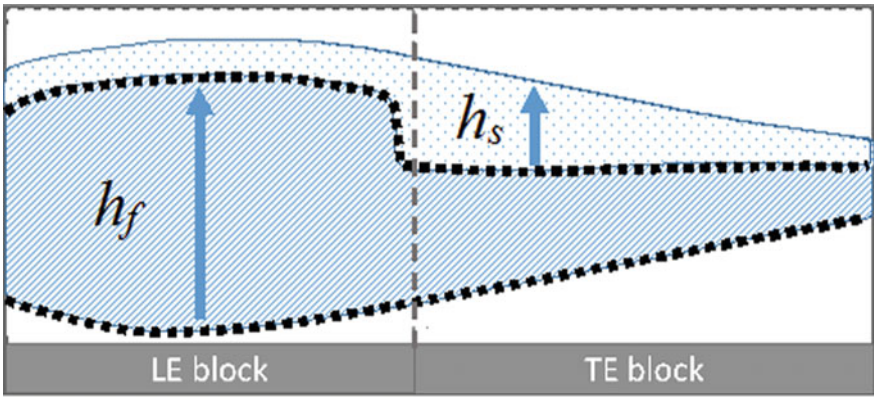

Fig. 8 Schematic representation of the optimal lined-flap configuration

To reduce the optimization design space, the orifices' diameter is assumed the same for the two blocks. Thus, the number of the optimization parameters is four: d_f, d_s, η^{LE}, and η^{TE}. A three-level full-factorial DOE has been generated, corresponding to 81 numerical experiments. Computations have been carried out using 16 CPUs, and the overall optimization has required about 160 CPU hours (10 h elapsed time). The graphical representation of the optimal lined-flap achieved by the implemented optimization process is sketched in Fig. 8 along with the corresponding optimal design parameters in Table 2.

Table 2 Optimal design parameters

Parameter	Value
d_f	1.5 mm
d_s	0.9 mm
η^{LE}	10%
η^{TE}	36.2%

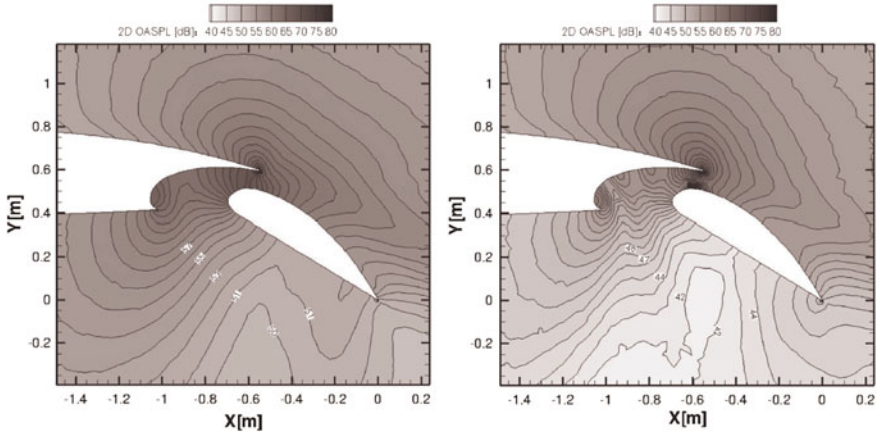

Fig. 9 FE analysis: OASPL baseline (left) versus optimal (right) configuration

It is interesting to notice that the optimization converges toward the minimum value of the septum thickness. It therefore follows that with a small loss in noise absorbing performances, a 1-DOF liner could be used in alternative to a 2-DOF liner, thus resulting in a gain in terms of manufacturing and system complexity.

In Fig. 9, the OASPL contour plots are reported: They show very well the noise reduction that has been achieved by the use of the optimal linflap configuration. Therein, the baseline is compared with the treated flap surface noise levels. In the upward semispace, the situation is practically unchanged, whereas a significant difference can be observed downward, both in the relatively far and in near fields.

Figure 10 shows the SPL in the frequency range of the FEM analysis. The liner is effective up to 1 kHz with peaks of abatement up to 10 dB. The OASPL directivity is plotted in Fig. 11. Reductions ranging from 4 to 8 dB may be observed along the reference arc, for an estimated average reduction of 6.4 dB.

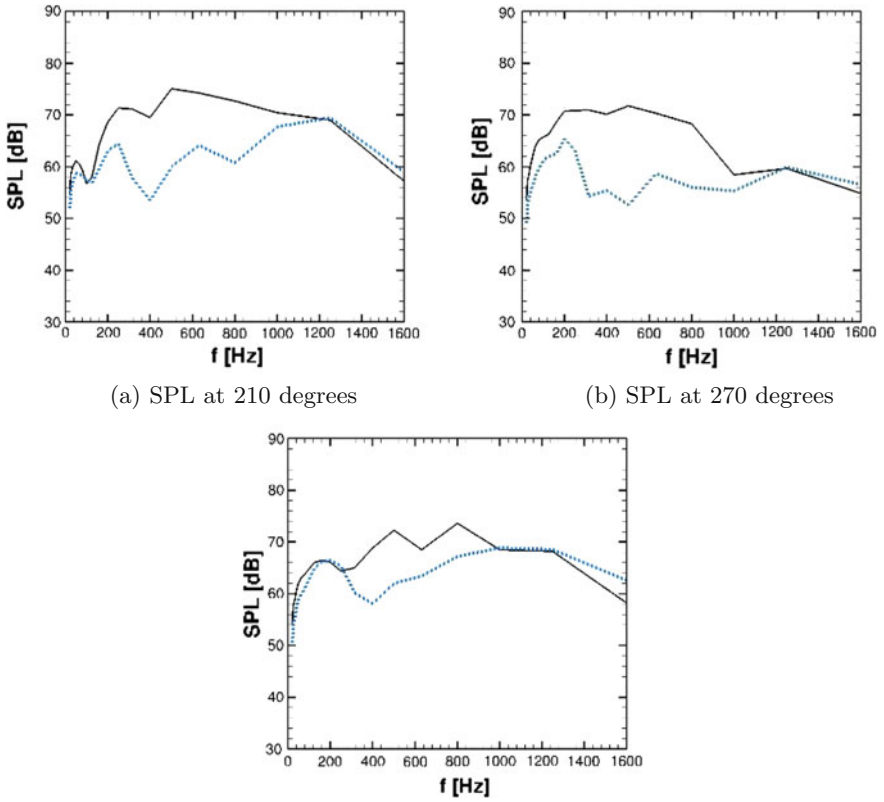

(a) SPL at 210 degrees

(b) SPL at 270 degrees

(c) SPL at 330 degrees

Fig. 10 SPL spectra sample at 210, 270, and 330°. Baseline (solid line) versus optimal linflap configuration (dashed line)

4 Wind Tunnel Experiments

The aeroacoustic performance of the developed device has been evaluated within an experimental test campaign, carried out at the wind tunnel facility (subsonic wind tunnel) of INCAS, the Romanian aerospace research center, and supervised by CIRA and Leonardo Aircraft Division. Both turboprop and open-rotor wing configurations have been considered. A 1-m-diameter, 72-mic circular array allowed performing noise measurements. The sensor system has been deployed over a stiff foam plate and has been installed at the top of the test section. A digital signal processing system (DSP) managed the acquired data, transferred via an ethernet connection. Commercial software implementing an original beamforming algorithm was used to detect the noise sources; the process was supported by an integrated camera. Classical Fourier analyses have been finally carried out, off-line. A number of Kulite XCS-062 devices measured the aerodynamic pressure for correlating the flow conditions

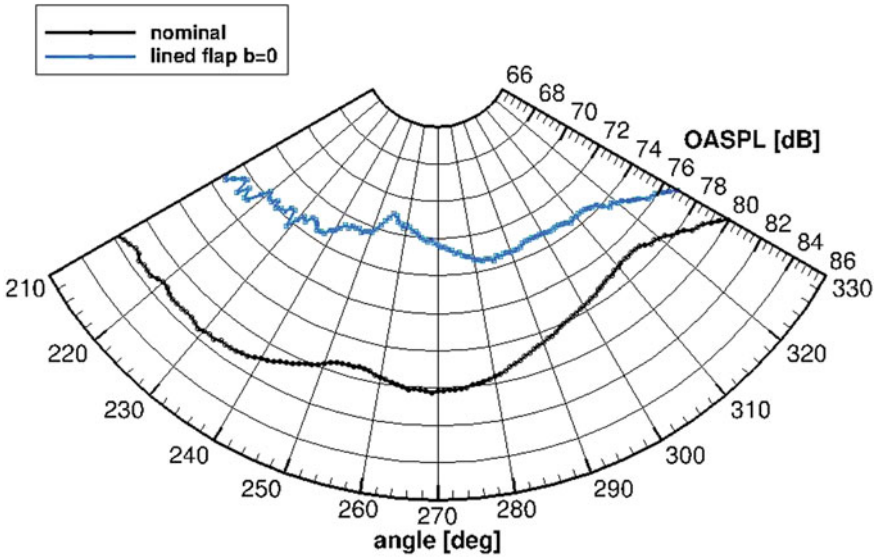

Fig. 11 OASPL directivity. Baseline configuration (black line with circles), optimal configuration (blue lines with squares)

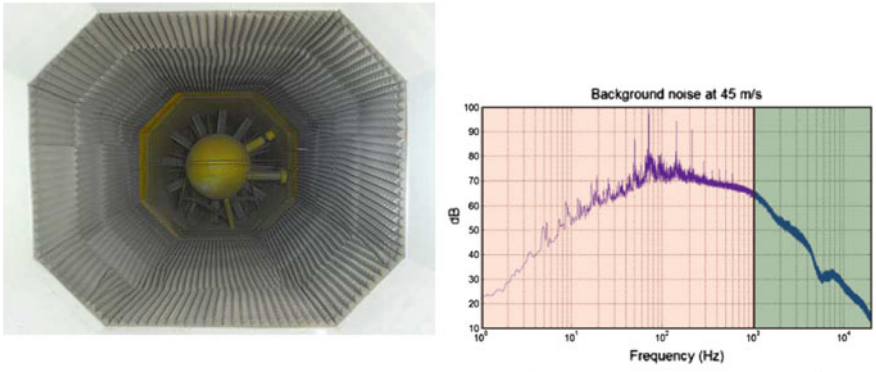

(a) Wind Tunnel Fan (b) Background noise at 45m/s

Fig. 12 Background noise measured inside the acoustic chamber

with the emitted noise. These devices have been installed within the flap tip, close to the fence regions. An independent acquisition system recorded the related signals. As a first step, the background noise level inside the test room has been measured (Fig. 12). The tonal fan-induced noise of about 90 dB around 100 Hz (50 m/s) has been marginally reduced after some targeted interventions. The measurement chain and the beamforming approach have been validated by eolian tones, as shown in Fig. 13.

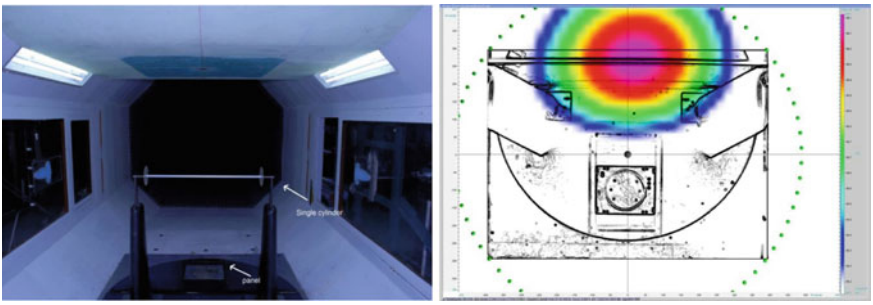

(a) Acoustic benchmark (single rod of 2cm diameter, 1m span) tested at 50m/s

(b) Noise source identification through beamforming technique

Fig. 13 Setup validation through benchmark experiments

A dedicated arrangement has permitted measuring the radiated noise from the bottom of the wind tunnel models, simply turning them upside down and arranging the balances, consequently. The sensor system and the model region of interest have been 0.78 m distant. Noise sensor system data have been acquired at 96 kHz rate, along an 8 s measurement time, while Kulite signals have been recorded at 40 kHz rate along the same period. Different models and different speeds have been used. As a result, an extensive collection of digital acoustic images and noise spectra have been produced and compared. The acoustic performance of the lined-flap model is shown in Fig. 14. It has been manufactured by INTA, according to CIRA and Leonardo specs. Measurements of Fig. 4b show that a wing equipped with a lined-flap technology is able to reduce the airframe noise by about 3 dB with respect to a standard single-slotted one.

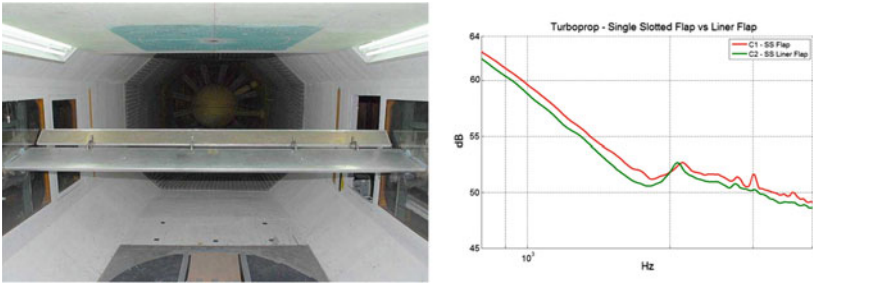

(a) Set-up of the lined flap installed into the wind tunnel test section at INCAS

(b) Experimental airframe noise comparison between the lined and single slotted flap configurations

Fig. 14 Wind tunnel acoustic experiments on the lined-flap

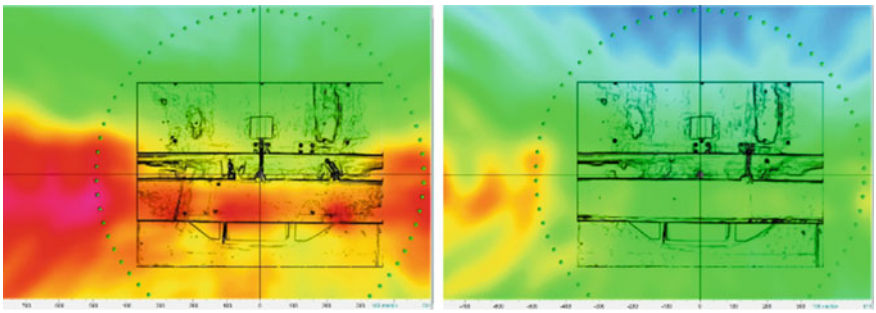

(a) Flap performance without liner (b) Flapper formance with liner

Fig. 15 Lined-Flap performance evaluated by beamforming

Beamforming images, Fig. 15, and measured noise levels Fig. 14 validated the potentiality of the proposed, highly integrated solution, in improving the aeroacoustic performance of a generic flap system. Numerical predictions well matched the experimental results.

5 Discussion

The main achievements of this study are following listed:

- an exterior acoustic liner for a standard flap was designed, according to an established methodology, available at CIRA, predicting around 6 dB OASPL attenuation with respect to the naked flap;
- a prototype of that liner was manufactured and installed on an aeroacoustic wind tunnel model to verify its functionality;
- the wind tunnel facility was adjusted to match minimal aeroacoustic requirements; after an intensive activity, the system was considered to perform the envisaged tests with the limitation of referring to a band over 1 kHz;
- an additional system was included to conduct the necessary beamforming investigations to characterize the acoustic sources, following the aerodynamic excitation;
- tests repeatability was verified by comparing the aerodynamic results in different test campaign; the agreement was far more than acceptable;
- the experimental results indicated an attenuation of something between 1 and 2 dB in the investigated frequency range;
- the significant differences between numerical predictions and experimental achievements may be linked to many factors.

The differences between the numerical and the experimental prediction can be linked to many factors, opening the room to further investigations, such as:

- the actual limitation of the test facility as an aeroacoustic tool, even after the massive activity to increase its performance.

- the necessity to further improve the theoretical characterization of the implemented liners that could affect somehow the design parameters; to this aim, it is forecast to develop a dedicated test campaign, both numerical and experimental, to:
  - evaluate the numerical sensitivity of the different design parameters with respect to the liner performance;
  - define targeted experiments to better characterize the implemented materials from the point of view of the constitutive laws and the general mechanical behavior;
  - define targeted experiments to verify the correspondence of the estimated (numerical) and actual (real) liner parameters;
  - characterize the deviations between numerical and experimental parameters to individuate the physical sources of the differences that could lead to a further adjustment of the referred models or simply establish the recurrent variations.
- the influence of the bonding between the liner and the flap, that is something that was not addressed in this research, neither is commonly cited in bibliography.

In order to allow an industrial implementation on real aircraft in common operation, several other studies should be focused, as but not limited to:

- establish the resistance of the selected material in a typical aeronautical (exterior!) environment concerning the:
  - affordable temperature and humidity range;
  - aging aspects;
  - survivability of the system (detachment and other);
  - maintenance needs and issues like:
  - inspection intervals;
  - replacement times;
  - repairing possibility.
- establish a Functional Hazard Analysis (FHA) to verify the criticality of such system when implemented on real aircraft, such as:
  - safety issues affected by the installation of these devices;
  - to manage the possible detachment of the liner or part of it;
  - the system behavior against a forced strike.
- evaluate the general effect on the aerodynamic performance, including the phases of landing and takeoff.

In the end, it may be stated that:

- the proposed system is promising, standing:
  - the theoretical forecast;
  - its intrinsic passive nature;
  - its low cost.

- some effort should be devoted to improve the experimental numerical correlation by, for instance:
  - better characterizing the mechanical behavior of the material;
  - better characterizing the deviations between numerical and experimental mode;
  - better characterizing some specific aspects of the installation, as the binding quality, the layout uniformity, and so on;
  - formulating an estimation of the effect of this installation on the general aircraft aerodynamic performance that could be critical in assessing its overall benefit.
- some attention should be finally devoted to real implementation aspects, including:
  - maintenance aspects;
  - in-service material behavior;
  - safety.

5.1 Conclusions

The design and testing of an acoustically treated single-slotted flap have been presented. The design process relies on the use of a numerical CFD solution that provides both the time-averaged flow about the flapped airfoil and the boundary-layer quantities at the trailing edge of the main airfoil component. The time-averaged flow is used as background flow for a FEM simulation of the acoustic propagation about the airfoil, whereas the boundary-layer quantities are used to prescribe, through an empirical model, the wall-pressure fluctuations at the trailing edge of the main wing that act, in the present approach, as the unique source of aerodynamic noise. The FEM simulations have been conducted in the frequency domain with an impedance boundary condition applied on the surface of the flap to simulate the presence of an acoustic liner. The frame of the flap has been filled with two 2-DOF liner packs, with perforation only on the lower side of the flap. Among other possible configurations, this liner setup has the advantage of the natural drainage of the water eventually absorbed by the flap. The optimal cavity depth of the liner septum and the orifice diameter have been determined by minimizing the OASPL averaged over a set of microphones located below the airfoil. A preliminary assessment of the acoustic properties of the wind tunnel chamber was firstly carried out. Using conventional liners, lined-flaps ensured noise reduction for a wide range of frequencies. The noise benefits associated with the lined-flap configuration were then evaluated by both FFT measurements and acoustic beamforming data. The experimental results confirmed the potential of this innovative low-noise solution in reducing the aeroacoustic emission of the treated flap region. Although many technological questions still need to be addressed, innovative high-lift systems may be key contributors to enable future aircraft to achieve a significant reduction in community noise and environmental impact.

Acknowledgements This work was carried out in the framework of Green Regional Aircraft funded by Clean Sky Programme.

Author Contributions In this paper, M. Barbarino was involved in the development of the lined concept and its numerical simulation. I. Dimino carried out the wind tunnel tests aimed at verifying the performance of the proposed device. A. Concilio formulated an evaluation of the achievements and proposed further objectives of the research.

References

1. Barbarino, M., Dimino, I., Carozza, A., Nae, C., Stoica, C., Pricop, V., Peng, S.H., Eliasson, P., Grundestam, O., Tysell, L., Davidson, L., Eriksson, L.E., Yao, H.D., Ben Khelil, S., Moens, F., Le Garrec, T., Mincu, D.C., Simon, F., Manoha, E., Godard, J.L., Averardo, M.A.: Airframe noise reduction technologies applied to high-lift devices of future green regional aircraft. In: Proceedings of the 3AF/CEAS Greener Aviation Conference (2014)
2. Dimino, I., Aliabadi, M.H.: Active Control of Aircraft Cabin Noise. Imperial College Press (2015)
3. Dimino, I., Vigliotti, A., Aliabadi, M.H., Concilio, A.: Vibro-acoustic design of an aircraft-type active Window, Part 1: Dynamic modelling and experi-mental validation. J. Theor. Appl. Mech. **50**(1), 169–192 (2012)
4. Gly, D., Delfs, J.: Aeroacoustic installation effects on transport aircraft research at Onera and DLR. In: 16th Workshop of the Aeroacoustics Specialist Committee of CEAS and 2nd Workshop of the European X-Noise EV network, Braunschweig, October 2012
5. Leylekian, L., Lebrun, M., Lempereur, P.: An overview of aircraft noise reduction technologies. Aerosp. Lab J. 7, 15, AL07-01 (2014)
6. Casalino, D., Barbarino, M.: Optimization of a single-slotted lined flap for wing trailing-edge noise reduction. J. Aircr. **49**(4), 1051–1063 (2012). https://doi.org/10.2514/1.C031561
7. Schlinker, R.H., Amiet, R.K.: Helicopter trailing edge noise. NASA CR-3470 (1981)
8. Howe, M.S.: Contributions to the theory of aerodynamic sound with application to excess jet noise and the theory of the flute. J. Fluid Mech. **71**, 625–673 (1975)
9. Casalino, D.: Finite element solutions of a third-order wave equation for sound propagation in sheared flows. AIAA 3762 (2010)
10. Myers, M.K.: On the acoustic boundary condition in the presence of flow. J. Sound Vib. **71**(3), 429–434 (1980). https://doi.org/10.1016/0022-460X(80)90424-1
11. Motsinger, R.E., Kraft, R.E.: Design and performance of duct acoustic treatment. In: Hubbard, H.H. (ed) Aeroacoustics of Flight Vehicles: Theory and Practice, Volume 2: Noise Control, p. 16506. NASA Langley Research Center, Hampton, VA (1991)
12. Optimus: Software Package, Ver. 5.2, Noesis Solutions, Leuven, Belgium (2006)

Measurement, Prediction, and Reduction of High-Frequency Aerodynamic Noise Generated and Radiated from Surfaces of Various Textures

Paul R. Donavan and Wlliam K. Blake

Abstract We examine the acoustic characteristics of wind tunnels with and without acoustic foam liners, illustrate how the aeroacoustics of the liner can control the sound in the facility, and provide analytical evidence on the existence of the acoustic impedance of the liner in altering the dipole strengths of the wall's roughness sources that produce sound in the facility.

1 Introduction

This paper is an account of work done in two phases over a period of time. The first phase was a work on quieting a large industrial wind tunnel and that work resulted in a successful mitigation recommendation that addressed flow over rough acoustic absorbing surfaces. However, several scientific questions went unanswered. The second phase was displaced in time from the first by 10 years and was conducted independently of the first. The motivation of this phase was entirely scientific and resulted in a comprehensive theory of the flow-induced sound from rough-wall boundary layers on surfaces of arbitrary impedance. The test data discussed here were acquired many years ago to support the tunnel quieting efforts, and the specifications of the various materials were not retained. This paper represents a re-examination of the data, using approximate material properties and new theory, to explain some of the reductions observed.

P. R. Donavan (✉)
Illingworth & Rodkin, Inc., 1 Willowbrook Court, Suite 120, Petaluma, CA 94952, USA
e-mail: pdonavan@illingworthrodkin.com

W. K. Blake
Department of Mechanical Engineering, Johns Hopkins University, Baltimore, MD, USA

E. Ciappi et al. (eds.), *Flinovia—Flow Induced Noise and Vibration Issues and Aspects-II*,
https://doi.org/10.1007/978-3-319-76780-2_10

2 Phase 1: Observations of Background Sound in a Wind Tunnel

One of the issues for creating low background noise levels for closed test section wind tunnels is minimizing the noise generated by flow interacting with the wall surface treatment. The nature of the problem is illustrated in Fig. 1 which shows spectra of sound in a wind tunnel facility with both levels and frequencies are all normalized on wind speed at the centerline; this normalization follows the concept of dipole sound sources. The sound levels at normalized frequencies greater than 3 Hz/km/h are increased by the flow over the liner suggested as due roughness dipoles at the surface.

To address this concern, a series of the aeroacoustic measurements were conducted in an existing closed test section wind tunnel using a series of finite panels with controlled surface finish. To set bounds on the potential for noise generation due to surface roughness, testing included a smooth wooden surface, a surface with coarse sandpaper over its entire length and one-half of its length, and two versions of a sound absorbing foam lining material, one uncoated and one coated. The measurements included surface pressure collected along an array of four flush-mounted microphones, sound pressure level data collected near isolated panels of various materials, and sound intensity acquired above floor mounted panels. Of primary concern was noise produced in higher frequencies beginning at about 2,000 Hz. Figure 2 shows the configuration that was used the acoustic intensity probe in place which used two microphones displaced ¼ in. apart. The sound intensity measurement has several benefits over the sound pressure measurement in providing a vector measurement of sound, therefore allowing rejection of flow noise over the probe surface as

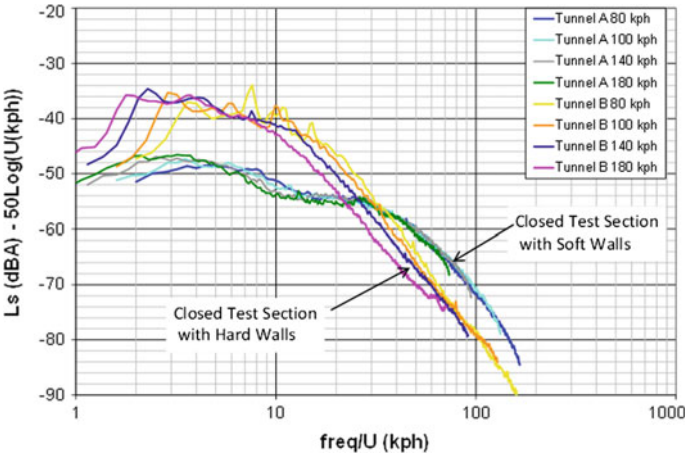

Fig. 1 Sound levels in a closed jet wind tunnel normalized on center-line wind speed with and without acoustic absorber lining

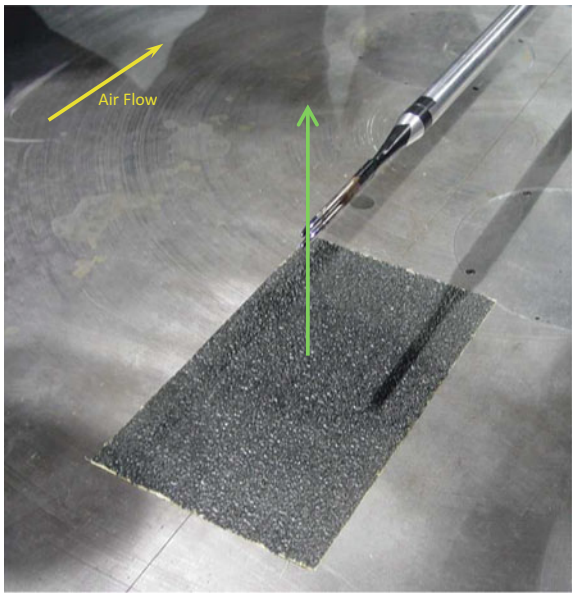

Fig. 2 Photograph of a rough patch panel and sound intensity probe above the patch. Scans were made in the flyover direction along the flow

well as rejection of off-axis background. The post-processing of the intensity probe also allows other indicators of data quality. Accordingly, the intensity probe allowed unequivocal sensing of sound from the patches preferentially over other sounds in the facility.

Based on the inflow sound intensity level results above the floor panel tests, it was found that the uncoated foam produced higher noise levels than the smooth, hard surfaces in the higher frequencies as shown in Fig. 3. Further, adding surface roughness to an existing smooth surface was found to increase the noise as measured in the flow. Also, it was confirmed that applying the coating to the foam lining material reduced the high frequency noise. The results for the full versus ½ roughened (added sand paper) panel indicated that, at least for this case, the increased high frequency noise is due to locally generated sound by the surface roughness and not merely rough versus smooth turbulent boundary layer differences.

From measurements of surface pressure, the addition of roughness to a hard, smooth wall was found to increase both the convected fluctuating pressures and the higher frequency acoustic pressures consistent with classical surface pressure data for rough and smooth walls. For the uncoated foam, the convected fluctuating pressures were also higher than a smooth wall and similar to those of the roughened wall. However, in the higher acoustic frequencies, the surface pressure levels were actually lower than a smooth wall. From the in-flow data, there was evidence that this unexpected result was due to the absorptive effect of the foam surface. This was supported by the coated foam results which demonstrated a reduction in the convected components similar to a smooth wall while still indicating reduced levels at the higher frequencies. The surface pressure measurements obtained with the array

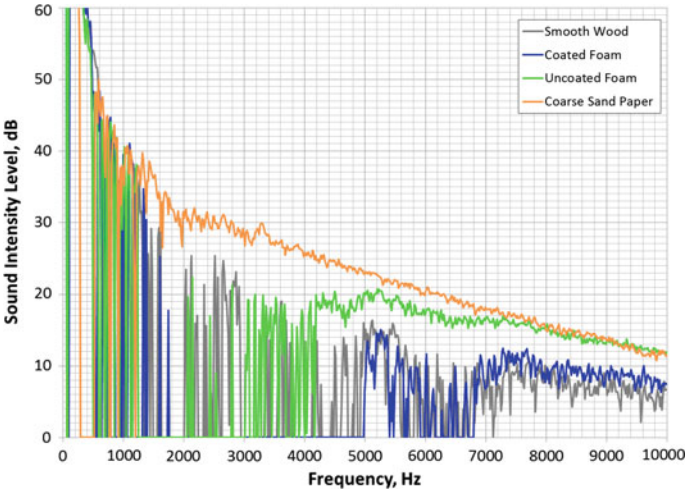

Fig. 3 Sound intensity level measured above panels with four different surface treatments

of four microphones spanning the transition from coarse sandpaper to a smooth also indicated that the size of the source region was on the order of 1 in. for frequencies above 1,800 Hz.

The best definition of the potential reduction provided by coating the foam surface was indicated by the sound intensity measurements made above the floor panel as shown Fig. 3. These data indicated that a reduction of about 5 dB was achieved with the coated foam versus the uncoated foam consistent with the sound pressure results. This reduction occurred over a frequency range from about 4,000–10,000 Hz. Below 4,000 Hz, the overall background noise in the test facility obscured measurement of any reductions provided by the coating. At higher speeds, the range of verified noise reduction moves up even further in frequency reaching 6,000 Hz at 140 km/h. Consistent with the in-flow sound pressure data and the small source region (~1 in.) identified from the surface pressure data, the sound intensity measurements indicated that the levels above 2,000 Hz were 3 dB higher for the panel fully covered with coarse sandpaper than for the one-half covered panel. This implies that the sound levels produced are function of roughness source areas for these frequencies.

3 Phase 2: Re-analysis and Current Interpretation

In addition to the data analysis described above, the results of this study were compared with recently developed theoretical models of rough-wall turbulent boundary layer sound radiation theories. These theories were developed for rough surfaces on both rigid and finite impedance surfaces. Analyses of the cross-spectra from the surface pressure measurement array were also performed. These provided definition of

source functions for comparison with the theory. Furthermore, the theory was developed to characterize both the roughness aerodynamics and the interaction of surface impedance with the various dipole orientations that exist at roughness elements as previously described by Blake [1] and Blake and Anderson [2]. These physical results assisted in interpreting the applicability of the theory to these measurements. It is now known that the sound field of a distribution of roughness elements on a surface depends not only on the distribution, shape and sizes of the roughness elements, but also on the acoustic impedance of the substrate that supports the elements. Specifically, the role of the acoustic impedance of the surface appears in a theoretical model of the radiated sound as a reflection coefficient that determines the in situ strengths of the aerodynamic roughness dipoles; see Blake [1] and Blake and Anderson [2].

The actual impedance characteristics of the liners extant in this study are not known, so we relied on published data for fiber and urethane liner examples in the literature; see Delany and Bazley [3], Dunn and Davern [4], and Quinli [5]. Figure 4 shows calculated reflection coefficients for three urethane liners compared with that of a fiber liner. Foam number 1 was selected for simulation of the roughness sound. Further, the simulations examined separate effects of roughness size and wall impedance on the roughness noise. The sizes of the patches were fixed for all cases as was the spacing of elements in relation to roughness size, flow dipoles on the elements were assumed to be aerodynamically similar, meaning that the dipole force spectra scaled as in Blake [1] and Blake and Anderson [2].

The model of sound from the distributed elements on impedance surfaces was that in Blake [1] to provide relative levels as functions of wind speed, roughness size, and impedance of the wall (rigid and foam) for sound at various elevations above the roughness test patch in the wind tunnel floor.

To show the effect of wall impedance on the near and far field sound of a patch of roughness dipoles as generated by an example roughness, Fig. 5 shows calculated color contour maps of the sound at two elevations and 140 kph above a rough patch of eight grit roughness (0.91 m long by 0.3 m wide) on either rigid wall or Foam #1. Sound levels are shown on the same color scales for a given elevation. In the far field of the rigid wall patch, we see the expected null in directivity due to the cancelation of lift dipoles and the reinforcement of drag dipoles by the rigid wall for which the reflection coefficient, R_w, is unity. The far field of the Foam wall #1 is without that null in the flyover plane and has similar levels, overall. In the near field, $H = 0.15$ m, the null is missing for both cases impedances. The maximum sound is simply at the center of the patch a simple superposition of dipoles and the sound levels for the foam wall are only slightly lower than for the roughness on the rigid wall. Thus aside from a redistribution of the far field sound, the use of the foam wall absorbing surface appears to minimally influence the radiated sound for a given roughness.

Figure 6 shows simulated and measured sound levels at the $H \sim 0.15$ m elevation. The simulated sound levels are the results of the constraints as described above. Accordingly, the levels are approximate relative to the measurements, but they are reasonably accurate portrayals of the relative values of roughness sound.

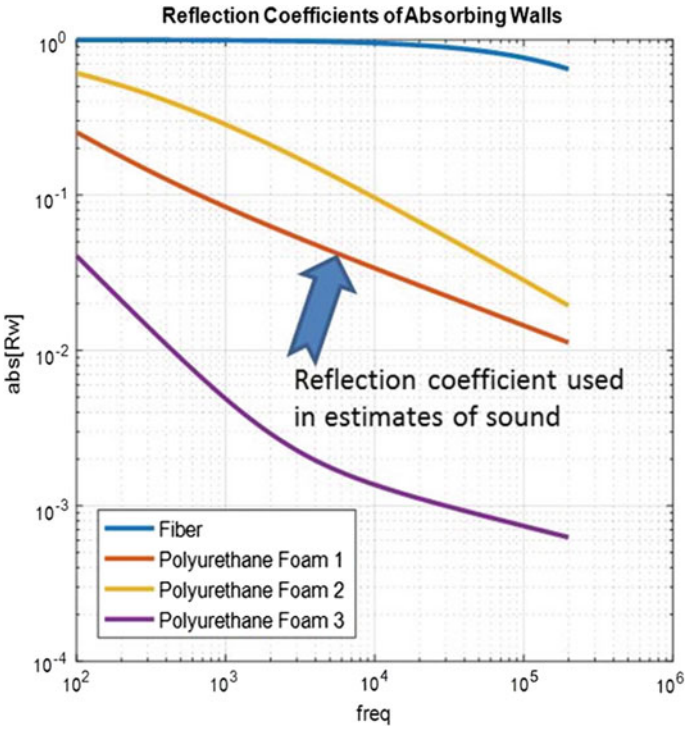

Fig. 4 Acoustic reflection coefficients for 4 examples of surface treatment materials calculated using parametric coefficients found in the references

4 Conclusion

Success of the original work was due to the availability of the simultaneous measurements of sound pressure, sound intensity, and wall pressure. The sound intensity provided the expected localization of sources; the wall pressure allowed independent characterization of the source levels as function of speed. Overall this combination allowed high confidence in spite of absence of comprehensive theory at the time of the first phase.

The results of the later post-analysis further confirm the interpretations of the on-site measurements as due to the presence of roughness dipoles on the foam. In summary, the foam absorber lining appears to provide additional roughness dipoles to the background sound, but does not substantially reduce the radiation efficiency of the roughness dipoles. This is due to the introduction of "lift" dipoles at the roughness elements that would have been otherwise missing if there had been reflective interaction as at a rigid wall. In the case of the rough absorbing wall, then, both normally directed and in-plane directed dipoles exist in nearly equal magnitudes. Thus, the analysis would seem to explain the observation made at the time that the

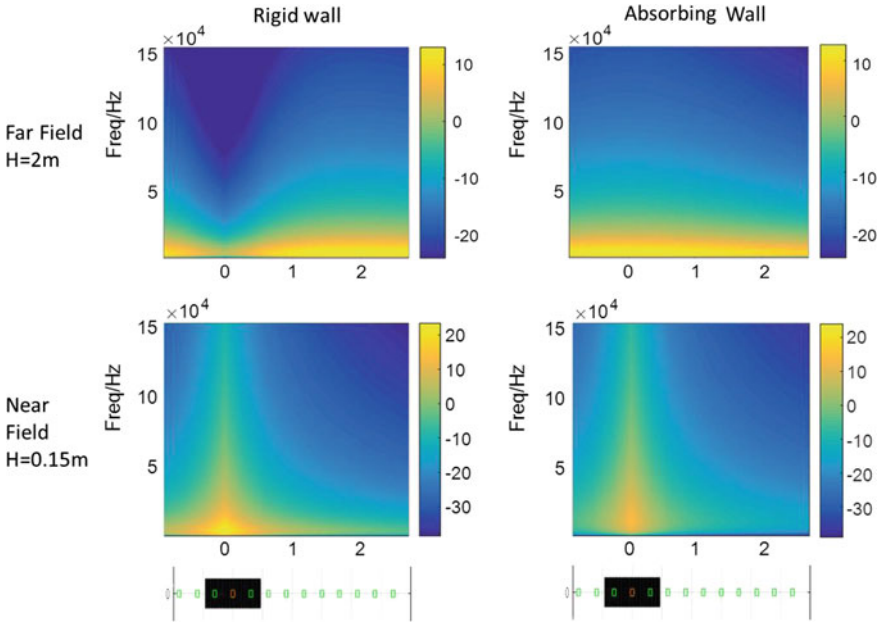

Fig. 5 Sound levels in 1 Hz band are 20 μPa at 2 elevations, ~0.15 and 2 m, above roughness patch at a wind speed of 140 kph. The roughness patch is shown beneath the figures and the flyover line is down the patch center in the flow direction

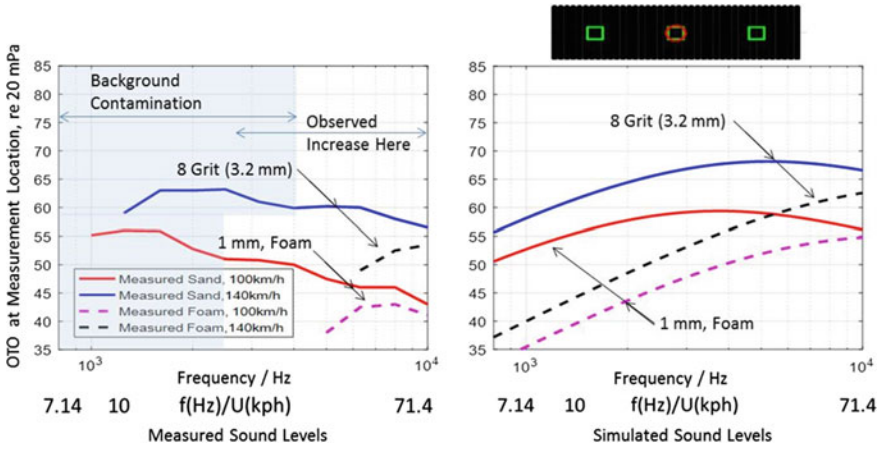

Fig. 6 One-third octave band levels re 20 μPa at H ~ 0.15 m above a roughness patches at wind speeds of 100 and 140 kph. On the left is the measurement; on the right is the simulation as described above

sound appeared effectively omnidirectional. Single compact dipoles, recall, are not omnidirectional. The level of the sound from the roughness is not precisely given by

the theory given the absence of information on roughness density on the foam, but the frequency shift between large grain sand and finer surface roughness of the foam would appear to be reasonably approximated.

References

1. Blake, W.K.: Mechanisms of Flow Induced Sound and Vibration, 2nd edn. Academic Press, New York (2017)
2. Blake, W.K., Anderson, J.A.: The acoustics of flow over rough elastic surfaces. In: Ciappi, E. (ed.) FLINOVI-A-Flow Induced Noise and Vibration Issues and Aspects. Springer, New York (2015)
3. Delany, M.E., Bazley, E.: Acoustical properties of fibrous absorbent materials. Appl. Acoust. **3**, 105–116 (1970)
4. Dunn, I.P., Davern, W.A.: Calculation of acoustic impedance of multi-layer absorbers. Acoustics **19**, 321–334 (1986)
5. Quinli, W.: Empirical relations between acoustical properties and flow resistivity of porous plastic open-cell foam. Appl. Acoust. **25**, 141–148 (1988)

Part IV
Flow–Numerical Methods

Accelerated Acoustic Boundary Element Method and the Noise Generation of an Idealized School of Fish

Nathan Wagenhoffer, Keith W. Moored and Justin W. Jaworski

Abstract A transient, two-dimensional acoustic boundary element solver is developed using double-layer potentials accelerated by the fast multiple method for application to multibody, external field problems. The formulation is validated numerically against canonical radiation and scattering configurations of single and multiple bodies, and special attention is given to assessing model error. The acoustic framework is applied to model the vortex sound generation of schooling fish encountering 2S and 2P classes of vortex streets. Vortex streets of fixed identity are moved rectilinearly in a quiescent fluid past representative schools of two-dimensional fish, which are composed of four stationary NACA0012 airfoils arranged in a diamond pattern. The induced velocity on the fish-like bodies determines the time-dependent input boundary condition for the acoustic method to compute the sound observed in the acoustic far field. The resulting vortex noise is examined as a function of Strouhal number, where a maximum acoustic intensity is found for $St \approx 0.2$, and an acoustic intensity plateau is observed for swimmers in the range of $0.3 < St < 0.4$. In the absence of background mean flow effects, numerical results further suggest that the value of Strouhal number can shift the acoustic directivity of an idealized school in a vortex wake to radiate noise in either upstream or downstream directions, which may have implications for the the study of predator-prey acoustic field interactions and the design of quiet bio-inspired underwater devices.

1 Overview

Animal collectives such as schools of fish can generate flow-induced noise from the wake production of individuals members and by the scattering of these wakes by their neighbors [5, 13]. Hydrodynamic locomotion of fish for engineering applications

N. Wagenhoffer (✉) · K. W. Moored · J. W. Jaworski
Lehigh University, Bethlehem, PA 18015, USA
e-mail: nate@lehigh.edu

E. Ciappi et al. (eds.), *Flinovia—Flow Induced Noise and Vibration Issues and Aspects-II*,
https://doi.org/10.1007/978-3-319-76780-2_11

continues to attract attention [7, 14, 18, 21] while the literature on flow-induced noise generation by fish and fish schools remains relatively unexplored. In contrast, many techniques exist to estimate the scattered acoustic field off of a fish school produced by a prescribed pulse, primarily for determining its population size [1, 6, 13, 20]. The distinct approach here seeks to estimate the hydrodynamic self-noise due to vorticity production of single swimmers and swimming collectives. An improved understanding of the noise generation of fish may enable strategies to mimic the vortex self-noise signature of an animal in an underwater vehicle(s). Alternatively, an improved understanding of fish noise signatures may help detect and distinguish bio-robotic underwater vehicles from their biological counterparts.

The reduction of this complex physical problem, involving acoustic interactions among multiple bodies, to a predictive numerical model requires a rapid framework to assess multiple configurations efficiently. To this end, a transient, two-dimensional acoustic boundary element method (BEM) is developed to solve for the acoustic field resulting from a vortical field or distribution of acoustic sources scattered by the solid bodies in a collective. To accelerate this numerical framework, the boundary element solution and subsequent evaluation of the resulting acoustic field are computed with the fast multipole method [22]. This method reduces the computational cost of the boundary element solution in two spatial dimensions from $O(n^2)$ to $O(n \log n)$ for n elements and is accompanied by a large reduction in memory cost [16], which would otherwise hamper the boundary element approach in the case of many elements and/or bodies, as well as future extensions to three spatial dimensions. To effect a transient solution, the acoustic solver aggregates individual frequency-domain solutions to produce a time-domain solution using the convolution quadrature method [10, 17]. The present study implements distributions of Gaussian cores with fixed identity and prescribed movement to represent the vortical field and its transient interactions with nearby solid bodies [15]. The induced velocity of the vortical field is then fed forward into the boundary element solver to produce the acoustic field. The novelty of the acoustical numerical framework presented lies in the development and implementation of a transient double-layer potential accelerated by the fast multipole method.

The present work outlines the development, validation, and application of a transient, two-dimensional, acoustic boundary element solver to multibody, external field problems, including application to a model school of fish. Section 2 details the acoustic boundary element formulation with a double-layer potential and its acceleration via the fast multipole method. Section 3 validates the numerical method against a canonical scattering configuration with an analytical solution and further demonstrates the capability of the method to handle multiple scatterers and transient forcing. Section 4 applies the acoustic framework to a model fish schooling arrangement encountering $2S$ and $2P$ classes of vortex streets and examines the resulting vortex noise as a function of Strouhal number. Concluding remarks from this study are made in Sect. 5.

2 Boundary Element Method

The propagation of linear waves through domain $\mathcal{V}$ with a boundary S_b is described by the non-dimensional wave equation:

$$\begin{aligned} \partial_t^2 p - \nabla^2 p = 0 \quad \text{in} \quad \mathcal{V}, \\ p(\mathbf{x}, t = 0) = \partial_t p(\mathbf{x}, t = 0) = 0, \\ p = g(t) \quad \text{on} \quad S_b, \end{aligned} \tag{1}$$

where $\mathbf{x}$ is the position in the exterior domain $\mathcal{V}$, t is time, g is some prescribed forcing function on the boundary, and p is the acoustic pressure. The combination of the Green's function solution to the wave equation in an infinite domain with Green's second identity yields a general solution for the pressure field external to a body or a set of bodies expressed as a boundary integral equation [12]:

$$p(\mathbf{x}, t) = \int_0^t \left[\int_{S_b} m(\mathbf{x} - \mathbf{x}', t - \tau) \eta(\mathbf{x}', \tau) dS_b - \int_{S_b} l(\mathbf{x} - \mathbf{x}', t - \tau) \frac{\partial \eta}{\partial n}(\mathbf{x}', \tau) dS_b \right] d\tau, \tag{2}$$

$$t \in [0, T].$$

Here η is the vector potential associated with a single-layer potential, and the normal derivative, $\partial \eta / \partial n$, is associated with the double-layer potential, m and l are, respectively, single- and double-layer retarded-time potential operators, $\mathbf{x}'$ is a source point, $\hat{n}$ is the outward normal of the body surface, and τ is a temporal dummy variable.

The substitution of boundary condition (1) into the fundamental solution (2) produces the time-varying boundary value problem,

$$\begin{aligned} \int_0^t \left[\int_\Gamma m(\mathbf{x} - \mathbf{x}', t - \tau) \eta(\mathbf{y}, \tau) dS_b \right. \\ \left. - \int_{S_b} l(\mathbf{x} - \mathbf{y}, t - \tau) \frac{\partial \eta}{\partial n}(\mathbf{y}, \tau) dS_b \right] d\tau = g(t), \quad \mathbf{x} \in S_b, \end{aligned} \tag{3}$$

which is to be solved by the boundary element method. For the two-dimensional wave equation, the fundamental solutions of the single-layer and double-layer potentials are

$$M(\mathbf{r}, \kappa) = \frac{i H_0^{(1)}(\kappa r)}{4}, \tag{4}$$

$$L(\mathbf{r}, \kappa) = \frac{i \kappa H_1^{(1)}(\kappa r)}{4} \frac{\mathbf{n} \cdot \mathbf{r}}{r}, \tag{5}$$

where $H_n^{(1)}$ are Hankel functions of the first kind of order n. The operators, M and L, are Laplace transforms of the retarded-time potentials, m and l. Here, $\mathbf{r} = \mathbf{x} - \mathbf{x}'$,

is position vector from a source to an observer, $r = |\mathbf{r}|$, and κ is the wavenumber. The frequency-domain potential operators (4) and (5) are used by the convolution quadrature method [10] to generate a time-stepping procedure to solve (3).

Imposing a velocity on the boundary, the frequency-domain double-layer indirect formulation of (3) becomes

$$\left(-\frac{1}{2}I + L'(\mathbf{r}, \kappa)\right)\eta = -\mathbf{V}_{\mathrm{i}}, \tag{6}$$

$$P_{\mathrm{field}} = L_{\mathrm{field}}(\mathbf{r}, \kappa)\eta, \tag{7}$$

where I is the identity matrix, $\mathbf{V}_{\mathrm{I}}$ is the incident velocity, L' is the adjoint of the double-layer operator using the outward normal at the observation point instead of the normal of the source, and P_{field} is the pressure at an observation point in the field.

2.1 Time Discretization

The retarded-time potential operators found in (2) are evaluated as convolution integrals. The Laplace transforms of the single-layer and double-layer potential operators, (4) and (5), respectively, are convolved with an associated potential field. The potential field is evaluated by a convolution quadrature. The quadrature has an associated weight that is defined by a power series. This methodology of time discretization can be achieved via a convolution quadrature method put forth by Lubich [17]:

$$V\frac{\partial \Phi}{\partial t} = \int_0^t v(t-\tau)\phi(\tau)d\tau.$$

Here, V represents a Laplace transform of the v operator, a characteristic differential operator of the transient wave equation, and ϕ is some known potential distribution. The interested reader can look to [10] for a detailed explanation of the convolution quadrature method. For problems with a form similar to (3), the retarded-time operator is a convolution that can be discretized as

$$v(\mathbf{x}, t-\tau)\phi(\tau) = \int_0^t V(\mathbf{x}-\mathbf{x}', t-\tau)\phi(\tau)d\tau. \tag{8}$$

Splitting the time domain into $N+1$ time steps of equal spacing, $\Delta t = T/N$ and $t_n = n\Delta t$ for $n = [0, 1, \ldots, N]$, the discrete convolution can be viewed as a sum of weights of the V operator at discrete times of ϕ:

$$V\frac{\partial \Phi(t_n)}{\partial t}^{\Delta t} = \sum_{j=0}^{n} \omega_{n-j}^{\Delta t}(V)\phi^{\Delta t}(t_j), \tag{9}$$

where the superscript Δt indicates the weight for a specific time-step size. The series expansion can be arranged to solve for the convolution weights, ω:

$$V\left(\frac{\gamma(\zeta)}{\Delta t}\right) = \sum_{n=0}^{\infty} \omega_{n-j}^{\Delta t} \zeta^n, \quad |\zeta| < 1, \tag{10}$$

$$\omega_{n-j}^{\Delta t} = \frac{1}{2\pi i} \oint_C \frac{V(\frac{\gamma(\zeta)}{\Delta t})}{\zeta^{j+1}} d\zeta, \tag{11}$$

where C is a circle of radius $0 < \lambda < 1$ centered at the origin. A second-order backwards difference function, $\gamma(\zeta) = (1-\zeta) + \frac{1}{2}(1-\zeta)^2$, is used to define the spacing of the integration. A review of other integration methods that can be incorporated into the convolution quadrature method is presented in [10]. Employing a scaled inverse transform, the weights become

$$\omega_{n-j}^{\Delta t,\lambda}(V) = \frac{\lambda^{-j}}{N+1} \sum_{l=0}^{N} V(s_l) \zeta_{N+1}^{lj}, \tag{12}$$

with

$$\zeta_{N+1} = \exp\left(\frac{2\pi i}{N+1}\right) \tag{13}$$

being the temporal quadrature spacing, and

$$s_l = \gamma(\lambda \zeta_{N+1}^{-l})/\Delta t \tag{14}$$

is the accompanying time-dependent complex wavenumber that is generated. The value of s_l is different for each time step and provides the link between the frequency-domain solver and a transient boundary integral equation such as (3). For this formulation, $\lambda = \Delta t^{3/N}$ is selected based on the error analysis of Banjai and Sauter [2].

Placing (12) into the boundary value problem (3) yields

$$\frac{\lambda^{-j}}{N+1} \sum_{l=0}^{N} M(s_l, \mathbf{x}) \hat{\eta}_l(\mathbf{x}) \zeta_{N+1}^{lj} = \frac{\lambda^{-j}}{N+1} \sum_{l=0}^{N} \hat{g}_l \zeta_{N=1}^{lj} \tag{15}$$

for a double-layer boundary representation. Here, g_n is a discrete representation of the boundary conditions. This transformation can be applied to other potential distributions, such as the double-layer potential, in the same manner. The inverse of the convolution transform of (12) is

$$\hat{\eta}_l = \sum_{j=0}^{N} \lambda^j \eta_j^{\lambda} \xi_{N+1}^{-lj}. \tag{16}$$

By applying the discrete inverse Fourier transform (16) to (15), a system of $N + 1$ equations is generated:

$$K(s_l, \mathbf{x})\hat{\eta}_l(\mathbf{x}) = \hat{g}_l(\mathbf{x}). \tag{17}$$

The convolution quadrature method [2] is employed to discretize the wave problem into a system of wave equations that are uncoupled in time. This discretization allows one to solve $N + 1$ independent problems in the frequency domain using wavenumbers that are generated via the convolution quadrature method. The time-domain solution is recovered by applying the inverse Fourier transform (16).

The convolution quadrature method is applied to (3) and a velocity-based boundary condition is applied. This approach allows the use of the indirect Neumann condition double-layer formulation seen in (6), which then is used to define the test problems presented in Sect. 3.

2.2 Spatial Discretization

The boundaries of noise-scattering bodies are discretized here using equal-length line elements. The boundary condition for the problem represented by the boundary integral equation (3) is enforced at collocation points located at the midpoint of each element. The boundary elements are constant strength elements in the current study, but Gaussian quadrature elements could also be easily implemented by evaluating the integration points as collocation points and summing the products with the appropriate weights for each element [12].

2.3 Fast Multipole Method

The boundary element system (17) creates a dense influence matrix when a direct calculation is performed at each time step. Therefore, the total number of operations is $O(Nn^2)$, where N is the total number of time steps and n is the number of boundary elements. The fast multipole method (FMM) put forth by Rohklin and Greengard [9, 22] reduces the order of operations needed to solve these types of systems to $O(Nn \log n)$.

The reduction in computational effort is achieved by embedding the FMM into an iterative linear equation solver. Figure 1 compares the computational speed of a direct solution of boundary values against its FMM counterpart. This embedded approach removes the calculation of the dense matrix and associated linear solve with a series of FMM calculations. FMM2DLIB is an open-source version of the FMM

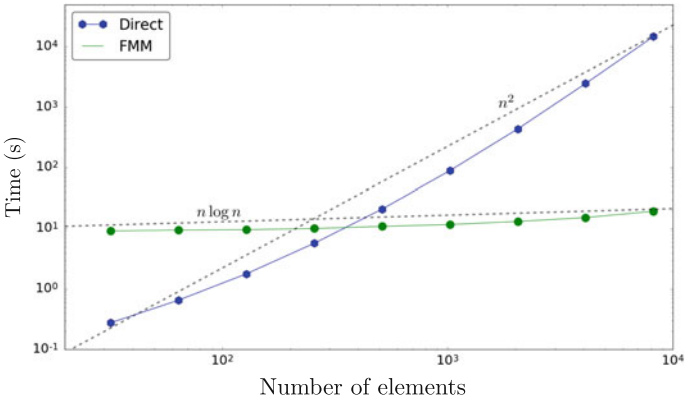

Fig. 1 Comparison of a direct computation with its FMM counterpart for an increasing number of boundary elements. The system used was set to T = 1 with 100 time steps. A field of 256 points was evaluated at each time step

that was implemented due to its easy implementation and multi-core optimization [8]. The FMMLIB2D library evaluates the potential field due to particle sources governed by the Helmholtz equation in free space.

The FMM consists of several steps that make it an efficient algorithm for matrix-vector multiplication to find a potential ϕ of the form

$$\phi(x_j) = \frac{i}{4} \sum_{k=0}^{N} \phi(x_k) H_0^1(s_l|x_j - x_k|) + \frac{\partial \phi(x_k)}{\partial n} H_1^1(s_l|x_j - x_k|) \frac{\kappa n_k (x_k - x_k)}{|x_j - x_k|}.$$

There are three main operations to making the FMM-BEM work. The first is an implementation of a quad-tree structure onto the domain. The second is the definition of translation operators that are used to relate different nodes of the quad-tree to each other. Finally, the FMM is coupled with an iterative linear solver (e.g., bi-conjugate gradient, generalized minimal residual) to determine the strength of each element. The generalized minimal residual (GMRES method) [23] is an iterative scheme to compute the solution of a system of linear equations that approximates the solution by finding the vector that produces a minimal residual error. At each iteration of GMRES, the FMM accelerates a matrix-vector multiplication used to evaluate the convergence criteria of that iteration. The natural fit of FMM into a GMRES solver is the main reason why this particular linear solver was selected. The GMRES, with a tolerance of 10^{-5}, is employed here to solve (17).

The discrete geometry is recursively subdivided by placing it into a quad-tree structure. The quad-tree structure is constructed such that the quad-tree will descend to a set number of branches. Figure 2 shows the descent of a branch of an arbitrarily sized quad-tree with four levels. Once the data structure is developed, the calculation of the method begins with the "upward pass." A weighted summation of the elemental

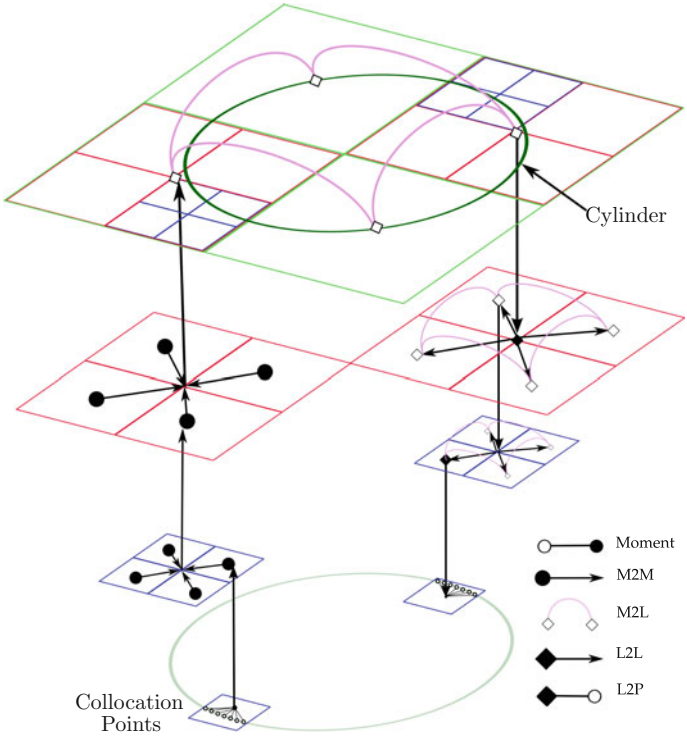

Fig. 2 Schematic of information transfer of the fast multipole method using a partial quad-tree structure. Small green circles represent the collocation points of a discretized cylinder. The entire domain is recursively divided into smaller and smaller squares, shown here as green, red, and then blue in decreasing size. The above quad-tree shows a four-level tree. The depiction shows only a simplified version of the actual FMM, representing the contribution of one far-field terminal leaf on the potential values at another terminal leaf

potential strengths is computed into a moment at each terminal node. The moments of four children nodes are translated up to the parent node. The upward translation process occurs until the level before the tree's root. Now each of the top four nodes contains the translated values of the potentials of their children nodes in a single value. The values at this level are in effect a representation of how the local nodes influence each other at each level in the quad-tree structure. The next step is to then cascade these values back down into the tree structure. The "downward pass" step passes the moments down the tree structure. The "downward pass" is calculated over nodes with adjacent but distinct parents and is performed to the terminal node. The value that is passed into the terminal nodes is then translated to all of the elements in the node. The prior steps define the far-field interaction between elements. The potential of all elements found in a terminal node is deemed to be in the near field. The potentials of near-field elements are directly evaluated. The near field is defined by the tolerance set. For a low error tolerance, the near field contains more elements.

The use of these steps approximates far-field interactions, and thus, a full matrix is not built for a matrix-vector multiplication. Note that here the near-field and far-field designators in this section refer to the relationship between elements placements in the quad-tree structure and not the acoustic near field or far field.

The translation operators necessary to pass information from source points to a far-field observer are defined as multipole-to-multipole, multipole-to-local, and local-to-local, which are respectively shortened to M2M, M2L, and L2L. All of these translation operators make use of an initial moment summation that needs to be calculated only once. The GMRES solver is set to an error that is found to be less than the model error and should therefore not impact the accuracy of the results [23].

The translation and moments for the two-dimensional frequency-domain problem are summarized in Lui [16] and are reproduced here:

$$\text{Moment}: M_n(y^*) = \frac{i}{4}\int_{\mathcal{S}} i^n J_n(s_l(y-y^*))\eta(y)d\Gamma(y)e^{in\alpha}, \tag{18}$$

$$\text{M2M}: M_n(y') = \sum_{m=-\infty}^{\infty} I_{n-m}(y-y')M_m(y), \tag{19}$$

$$\text{M2L}: L_n(x) = \sum_{m=-\infty}^{\infty} (-1)^m O_{n-m}(x-y)M_m(y), \tag{20}$$

$$\text{L2L}: L_n(x^*) = \sum_{m=-\infty}^{\infty} I_m(x^*-y)L_{n-m}(x^*). \tag{21}$$

Here, α is the angle from the source point to the center of the leaf at the terminus of the quad-tree, s_l is the wavenumber associated with each independent time step, $\mathcal{S}$ is the area of the terminal node, and $O_n(\mathbf{x}) = i^n H_n^{(1)}(s_l r)\exp(in\alpha)$ and $I_n = (-i)^n J_n(s_l r)\exp(in\alpha)$ are auxiliary functions that translate the influence of the multipole potentials over a distance r at angle α. In the auxiliary functions, J_n is a Bessel function of the first kind of order n.

The fast multipole frequency-domain operators (18)–(21) are sufficient for the present study, as the convolution quadrature method transforms the time-domain problem into sets of frequency-domain problems. The quad-tree structure will remain constant at each time step, as the domain contains a static rigid body or bodies in the scenarios considered in this work.

3 Validation and Demonstration

This section presents the capability of the transient acoustic BEM to accurately simulate vortex-solid or acoustic-solid interactions in single- and multibody scenarios. A validation case of plane wave scattering on a cylinder establishes the temporal and spatial model errors. The validation case is extended to include multiple bodies

to demonstrate how the model can compute many degrees of freedom rapidly and with the same order of error as the single scatterer study. A qualitative demonstration of a soliton wave impinging onto an irregular arrangement of cylinders shows the capability of the solver to model the interactions between scattering bodies. Each of the validation cases was selected to ensure that the method is suitable for modeling noise generation due to wake-body interactions in an idealized school of fish. The plane wave scattering study Sect. 3.1 demonstrates the capability of the solver to model wake-body interactions and establishes the model error. The multiple-scatterer study Sect. 3.2 demonstrates that there is no loss in model error when multiple body interactions are introduced. Finally, the capability of the method to define transient acoustic interactions between multiple bodies is demonstrated in Sect. 3.3.

The accuracy of the BEM is measured by the absolute error in the acoustic field since exact boundary potential values are not readily available for all of the validation cases considered. The error is determined at 25 points in the acoustic field at locations shown in Fig. 4. The L_2 norm is used to show the relative error between the numerical and the analytic values at each time step. The maximum of these L_2 values for all simulated time is designated as the error.

$$E_{L_2} = \max_{t \in T} \left(\frac{\sqrt{\sum_x |P_{\text{exact}}(\mathbf{x}, t) - P_{\text{BEM}}(\mathbf{x}, t)|^2}}{\sqrt{\sum_x |P_{\text{exact}}(\mathbf{x}, t)|^2}} \right) \tag{22}$$

The numerical problem is rendered dimensionless by using bulk modulus ρc^2, radiator diameter $2a$, and parameter $2a/c$ as the pressure, length, and time scales, respectively, where ρ is the fluid density and c is the speed of sound.

3.1 Plane Wave Scatterers

The capability of the method to model acoustic scattering by a solid body is now demonstrated and validated. Figure 3 illustrates the model of a rigid circle of radius a placed at the origin that is bombarded by a harmonic field of plane waves. The incident field of unit strength has the form

$$P_{\text{i}}(x, t) = \exp[i(\kappa r \cos\theta - \omega t)],$$

where ω is the angular frequency, κ is the wavenumber, and $x = r\cos\theta$. The analytical result for the scattered field is [11]

$$P_{\text{s}}(x, t) = e^{i\omega t} \sum_{n=0}^{\infty} \epsilon_n i^n \left[J_n(\kappa a) - \frac{J_n'(\kappa a) H_n(\kappa r)}{H_n'(\kappa a)} \cos n\theta \right]. \tag{23}$$

The total acoustic field is the sum of the incident and scattered fields, $P_{\text{t}} = P_{\text{s}} + P_{\text{i}}$.

The interaction of the harmonic incident field with the solid cylinder is as follows. The incoming plane waves propagate in the positive x-direction and make initial contact with the cylinder at $(r, \theta) = (a, \pi)$. In the area in front of the cylinder, the plane waves are reflected back onto themselves. The waves reflect at the front of the cylinder to create a shadow region aft of the body. The length of the shadow region is dictated by the wavenumber, with larger values resulting in a smaller shadow region. An annular grid of 25 observation points shown in Fig. 4 is used to sample all of the regions of the scattered field and determine the L_2 error norm.

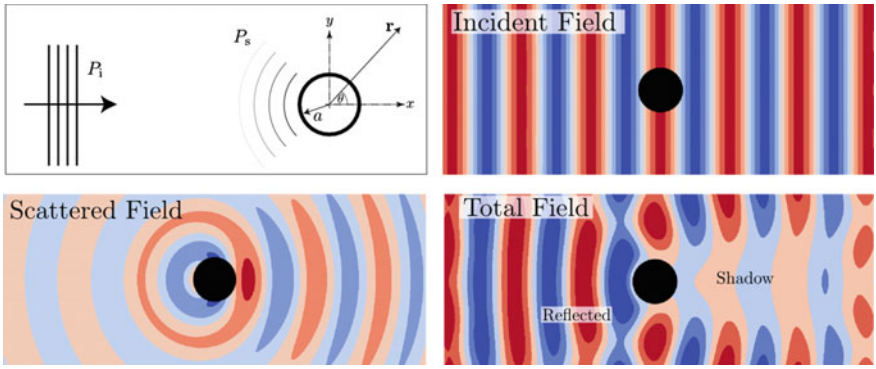

Fig. 3 Schematic of a harmonic plane wave, P_i impinging upon a rigid cylinder of radius a, to produce scattered field P_s. The total field is the linear superposition of the incident field and the scattered wave, which includes a reflected wave region ahead of the cylinder and a shadow region behind the body

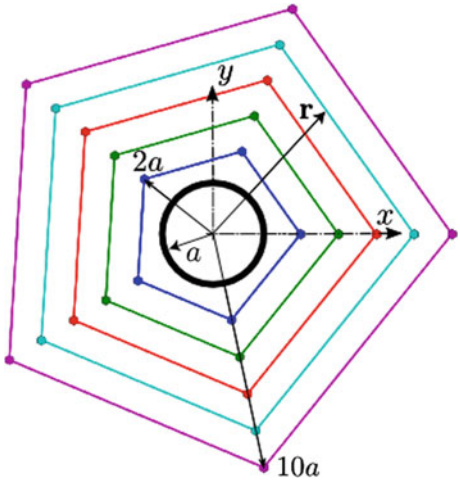

Fig. 4 Schematic of the arrangement of observation points used to evaluate error. Not drawn to scale

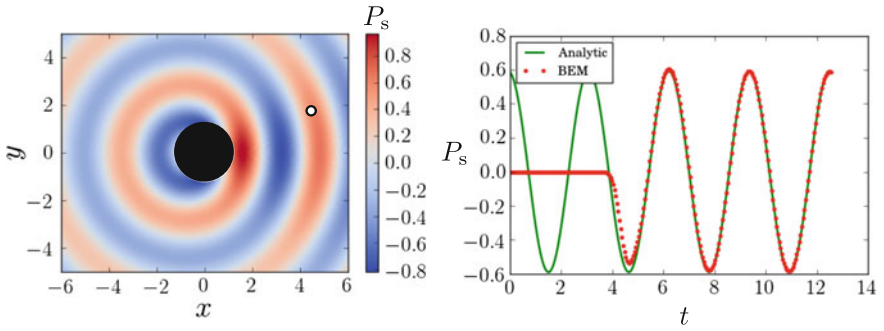

Fig. 5 A comparison of the analytical to BEM results of the plane wave scatterer study. The image on the left shows the fully developed scattered field. The observation point, denoted by a black circle in the left image, is placed at the arbitrary point $(r, \theta) = (5, \frac{\pi}{9})$. The right image compares the time history of the scattered field at the observation point. $\omega = 1$ and $\kappa = 2$

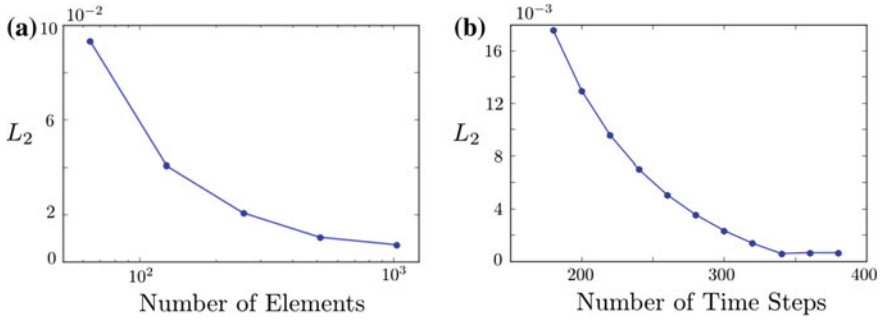

Fig. 6 Spatial and temporal convergence of the indirect double-layer formulation for a single scatterer. The sample of 25 points in the field is compared to the analytic solution of the plane wave case for this spatial convergence study. The L_2 norm is calculated at time steps after the field becomes fully developed at the observation location

Figure 5 compares the transient acoustic response at a point in the acoustic field to the analytical solution to harmonic wave forcing. Here, $\omega = 1$, $\kappa = 2$, and arbitrary point $(r, \theta) = (5, \frac{\pi}{9})$ are selected for this example. Note the absence of a signal in the BEM solution until the initial scattered wave reaches the observation point, after which the numerical solution quickly converges to the analytical result.

Temporal and spatial discretization independence of the numerical solution are shown in Fig. 6 for the indirect double-layer formulation (6). For the spatial convergence study, a period of $\mathrm{T} = 4\pi$ is divided into 256 equidistant time steps. An increasing number of elements on the boundary was used to compare the BEM solution with (23). The temporal convergence study (Fig. 6b) had a boundary of 1024 equal-length elements over a total period of $\mathrm{T} = 4\pi$. The total period is divided into increasing numbers of equidistant time steps. Spatial convergence occurs at approximately 512 elements, showing a relative error of less than 0.1% when using more than 256 time steps.

3.2 *Multiple Scatterers*

To underscore the capabilities of an FMM-accelerated BEM solver, a problem involving many degrees of freedom is now proposed. The model problem consists of a ring of cylinders arranged into a circular pattern that is bombarded by a plane wave from the acoustic far field. If the spacing between cylinders is sufficiently small and the ring is acoustically compact, then the resulting scattered field will be qualitatively similar to the plane wave study of Sect. 3.1. A spatial convergence study is performed across the scattered field in a manner similar to Sect. 3.1.

The ring of cylinders is composed of 36 cylinders each with a radius of $a/20$, as shown in the schematic of Fig. 7. The vertical and horizontal spacing between

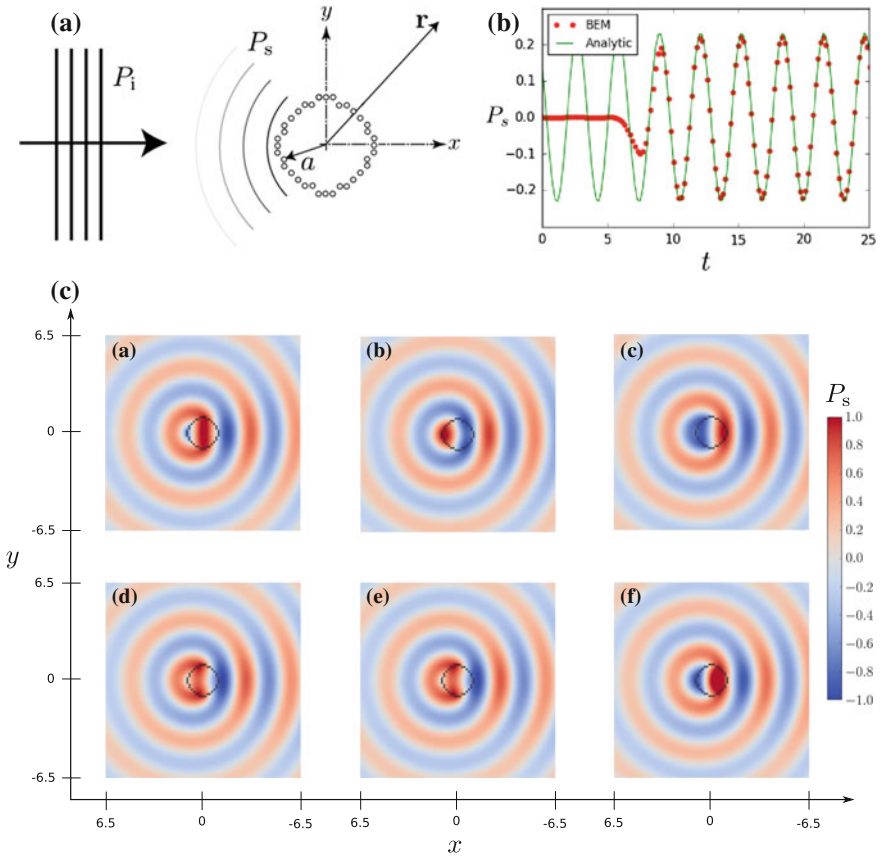

Fig. 7 Image **a** shows a schematic of the multiple-scatterer problem. Image **b** is a comparison of (23) with the BEM scattered field of multiple bodies at arbitrary observation point $(r, \theta) = (9.2, \frac{\pi}{4})$. After two periods, the scattered wave reaches the observation point and good quantitative agreement is seen. Image **c** depicts the progression of the scattered field due to a plane wave over one period is shown below, developing in order (a → f)

Table 1 A ring of 36 cylinders is bombarded by an incoming plane wave. The simulation has to have 128 time steps over a period of 8π, and the number of elements doubles for each successive simulation. The most resolved system is designated the reference solution to compute the relative L_2 error for the less resolved cases. Each simulation was computed with an Intel® Core i7-4930K CPU @ 3.40 GHz with 64 GB of RAM

Elements per cylinder	Total elements	L_2 norm	Time (s)
128	3968	0.909	108
256	7936	0.498	155
512	15,872	0.285	256
1024	31,744	0.149	478
2048	63,488	0.079	802
4096	126,976	0.035	1642
8192	253,952	0.012	3047
16,384	507,904	Reference	5889

cylinders is the same as the radius of the individual cylinders. The radius of the system of cylinders is approximately unity, $a \approx 1$. The indirect double-layer distribution defined by (6) is used to find the boundary strengths. Table 1 shows system convergence of relative error, where a reference case of 16,384 elements per cylinder was used to compute the L_2 norm. The multibody system requires considerably more elements to reach convergence than the simple scatterer of Sect. 3.1. This increase in resolution should be expected, as the boundary must account for the interaction of a cylinder with the incoming wave in addition to the scattered fields of the other cylinders. The total time period of the simulation is $\mathrm{T} = 8\pi$ and is discretized into 128 equally spaced time steps. The acoustic field calculation is performed over the annular grid found in Fig. 4. All of the time calculations include the field evaluation step. The evolution of the acoustic field for the multiple scatters can be seen in Fig. 7. The given wave speed and radial dimension of the multiple scatterers are $\kappa a = 2$, resulting in a scattered field similar to that of Fig. 5. The interior of the ring of cylinders can be observed as the spacing of the system allows the plane wave to penetrate this area. A comparison of the scattered acoustic field with the analytic solution (23) of a single scatterer is shown in Fig. 7.

3.3 Transient Multibody Scattering

Figure 8 depicts a system with four cylinders designed to illustrate the transient interactions among multiple bodies. A single soliton wave is used for transient acoustic forcing instead of a harmonic field. The wave has a form

$$P_{\mathrm{i}} = 2\sin(\omega(t-x))\sin(\omega\lambda)\exp\left(-\left[\frac{t-x}{\lambda^2}\right]^2\right)/\lambda^2,$$

where λ is the wavelength. The radius of the scatterers is equal to λ for the configuration shown in the schematic of Fig. 8. The soliton wave has a single interaction with each rigid body, whose scattered field then interacts with neighboring scatterers. Figure 8 illustrates the interactions between four irregularly-placed rigid bodies. Primary scattering off of the two leftmost bodies can be seen in images (a $\rightarrow$ d). By image (g), secondary scattering can be observed near the leftmost body. The scattered waves continue to reflect off of the other cylinders as the incoming wave completes its movement across the arrangement of cylinders.

4 Noise Production of a Small Idealized Fish School

The validation of the acoustic solver in Sect. 3 enables the investigation of vortex sound generated by prescribed wakes interacting with fish, modeled as two-dimensional rigid foils. The noise generation of swimming schools of fish has historically received little attention due to the challenges associated with recording reliable sound from specific species and the low amplitude noise associated with fish locomotion [5]. Presented here is an approximation of the scattered noise due to interaction with the wake from a leading fish in an idealized school. The wake is treated as an acoustic forcing function for the BEM described in Sect. 2, allowing observation of how the scattered acoustic field interacts in an idealized school.

An idealized model is now put forth to approximate a school of fish configuration and is used to find the scattered noise due to wake interaction in the school. A school of four fish is set into a diamond shape [25] at a distance of one chord between the fish [19]. A diamond arrangement of three static NACA 0012 airfoil cross sections is used to define the solid boundary of the school of fish. The spacing of the fish is set to one fish length [19], at 45° from the tail of a swimmer to the follower's front. The wake generated by a fish swimming rectilinearly would not impinge on its body, allowing the replacement of the leading fish with a characteristic wake.

The characteristic wake of an individual fish is approximated here as a vortex street that would be observed downstream [4]. Two common wakes that can be observed downstream of a fish are the $2S$ wake (two single vortices per stroke cycle, also known as a reverse von Kármán vortex street) and a $2P$ wake (two pairs of vortices per stroke cycle) [24]. The strength and spacing of the vortices in the prescribed wake can be expressed as a function of the Strouhal number, $St = fA/U$, where A is the amplitude of motion, f is the frequency of tail beats, and U is the velocity. For the study, a length of 0.1 m, a velocity of 1 m/s, and an amplitude-to-length ratio of 0.2 are used to model the fish and the kinematics of the lead fish. The strength and distance of the vortices are based on these values and the Strouhal number. The

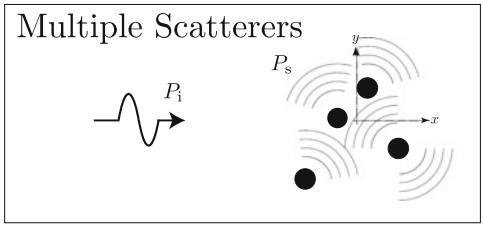

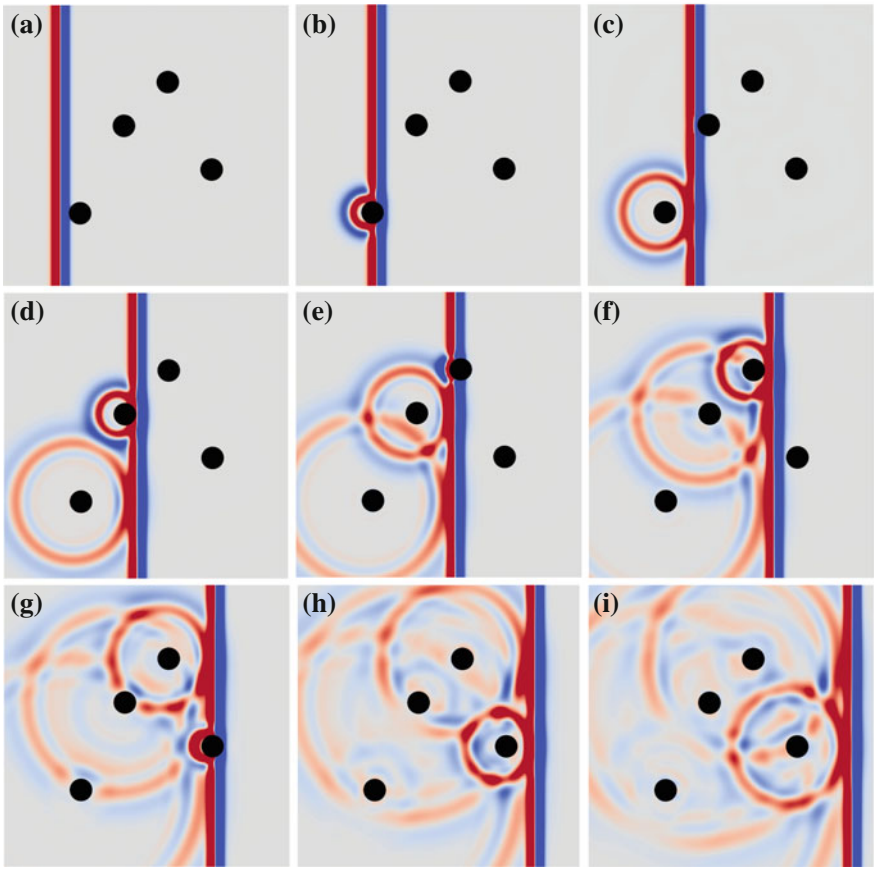

Fig. 8 An incident soliton wave impingement onto a collection of staggered cylinders. Images (**a** → **i**) illustrate the transient total acoustic field arising from primary and secondary scattering of a single wave by multiple bodies

strength of circulation ($\Gamma = 2\pi \tan^{-1}(\pi\ St)$), frequency ($f = U_\infty\ St/b$), and the horizontal ($a = U/f$) and vertical ($b = A$) spacings are the parameters for the study.

Figures 9 and 10 show the setup of the frozen $2S$ and $2P$ vortex streets as they advect linearly with the free stream past the other idealized fish. Vorticity in a vortex core is represented by a radially symmetric Gaussian blob. The Biot-Savart law is applied to determine velocity components for each of the vortices, yielding [3]:

$$u(\mathbf{x}, t) = \sum_{i=1}^{N} \frac{-x'\ \Gamma_i}{2\pi r^2} \left(1 - \exp\left(\frac{-r^2}{2r_{\text{cut}}^2}\right)\right), \tag{24}$$

$$v(\mathbf{x}, t) = \sum_{i=1}^{N} \frac{x\ \Gamma_i}{2\pi r^2} \left(1 - \exp\left(\frac{-r^2}{2r_{\text{cut}}^2}\right)\right), \tag{25}$$

where $r_{\text{cut}} = \Delta t U_\infty$ is the cut-off radius of the blobs, Γ is the circulation of the vortex blob, and $r = x^2 + x'^2$ [15]. The time step is chosen to ensure the core of a vortex does not intersect the solid geometry. At each time step, the velocity induced by the vortices is defined by the Biot-Savart law. The velocities induced by the vortex street are then used as the boundary condition to the BEM formulation in Sect. 2. The motion of the vortices is idealized, as a more realistic model would feature vortex motions that are directly influenced by the flow induced by each of the rigid bodies.

The limitations of the present numerical approach are listed here. The vortex street is defined and then translated at fixed speed over the idealized school of fish. Therefore, the dynamical interaction between the vortices and bodies is neglected. The numerical model also neglects several potential acoustic features that would be found in an actual school of fish. The most notable of these features is the lack of a background flow, which would generate a boundary layer and subsequent trailing-edge noise as well as require a Kutta condition and a wake behind swimmers, which would affect the overall school noise signature.

The system of foils is subject to an semi-infinite vortex street, that starts and ends at $\pm 15 U_\infty \Delta t$ from the front and back of the school of fish. This ensures that the end

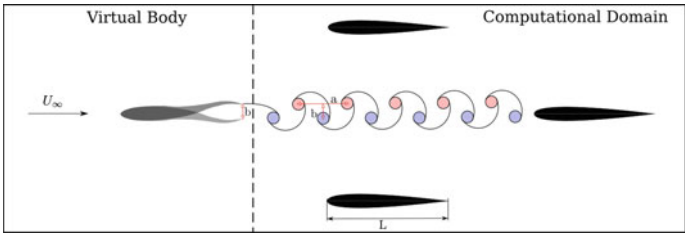

Fig. 9 A schematic of a the $2S$ vortex street interaction is shown. The leading fish is a virtual body that is replaced by the idealized vortex street. In the vortex street, blue indicates negative vorticity and red is positive vorticity. The vortex blobs in the street are spaced horizontally by distance a vertically by distance b. The fish has a length of L, which is used as the spacing between the fish

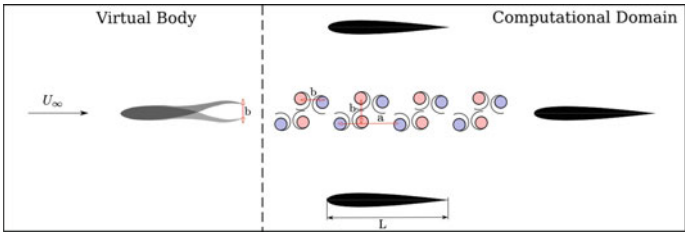

Fig. 10 A schematic of a the $2P$ vortex street interaction is shown. The virtual leading fish creates an idealized two pair, 2P, vortex street. In the vortex street, blue indicates negative vorticity and red is positive vorticity. The vortex blobs in the street are spaced horizontally by distance a vertically by distance b. The pairs of vortices are horizontally spaced by b, with each pair being the same distance from the centerline of the trailing fish. The fish have a length of L, which is also the spacing between the fish

of the vortex street does not have an effect on the velocity induced onto the bodies, allowing the school to reach a time-averaged steady state. Each of the foils, acting as a proxy to a fish, is approximated by 4096 boundary elements. A series of 16 vortex pairs are allowed to pass through the system. Each period, $1/f$, is discretized with 32 equidistant time steps.

When a steady state is achieved, a time average of the acoustic intensity is determined by

$$< I >= \frac{1}{T} \int_0^T \frac{|p(\tau)|^2}{\rho c} d\tau, \tag{26}$$

where T is the period of a passing $2S$ or $2P$ vortex system, corresponding to a cycle of fish tail motion.

The increasing circulation does not necessarily correspond to a greater intensity, as can be seen in Fig. 11. Figure 11 plots an average intensity that is scaled by the square of the circulation, with the $2P$ being scaled by $4\Gamma^2(St)$ as the system has twice as much circulation per pair. The $2S$ system shows a decreasing intensity as the Strouhal number rises, while the $2P$ system shows a maximum intensity for $St \approx 0.2$. The $2P$ street configuration initially has a lower intensity than the $2S$, then it rises to a maximum intensity at $St \approx 0.2$, before decreasing as the Strouhal number increases similar to the $2S$ street. A plateau of acoustic intensity is seen for the $2S$ street for $0.3 < St < 0.4$ in Fig. 11, where the $2P$ street has a slightly greater intensity than the $2S$ counterpart. A similar, but not as prominent, plateau is seen for the $2P$ street configuration in the range of $0.3 < St < 0.4$. The observation of an intensity plateau for that range of Strouhal numbers is interesting as this is the regime of Strouhal numbers where efficient swimming typically occurs. A rapid decrease for both street configurations is observed for $St > 0.4$, which is outside of the Strouhal range of what is generally considered an efficient swimmer [4].

Figure 12 shows an example of a near-field scattered pressure field of a $2S$ wake interacting with the foil arrangement at $St = 0.3$, which is a common wake

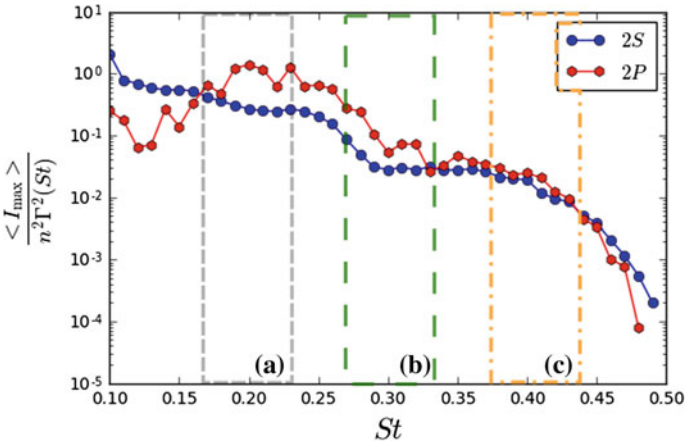

Fig. 11 A scaled maximum intensity for a range of Strouhal numbers is shown for a Strouhal range, $0.1 < St < 0.5$. The scaling is $n^2\Gamma^2(St)$, with $n = 1$ for the $2S$ street and $n = 2$ for the $2P$ street. The average intensity is found after steady state is reached. Three sections of the plot are labeled (a $\rightarrow$ c), which correspond to the directivity plots of Fig. 12

structure and Strouhal number observed in swimming fish. The definition of prescribed circulation results in increasing values with increasing Strouhal number. The bottom row of Fig. 12 shows the directivity of the average acoustic intensity for the $2S$ and $2P$ streets over the range of Strouhal numbers. The directivity is measured at 10 fish lengths from the center of the school. The $2S$ vortex streets are dominated by forward scattering of noise, which decreases as the Strouhal number increases. For intermediate Strouhal numbers, ($0.275 < St < 0.325$), a many-lobed directivity pattern is observed. The pattern is created when the middle two foils scatter the pressure wave as it propagates from the rear foil. Figure 12b $\rightarrow$ d shows directivity plots for different ranges of Strouhal number where it can be observed that there is a switch from a front scattering to a backward scattering pattern as the Strouhal number increases. Although these are only idealized results that neglect some noise sources, further investigations into the noise production of fish could help to deepen our knowledge of predator/prey interactions. If predators swim at higher Strouhal numbers, ($St > 0.35$), they could scatter noise backwards, effectively making them silent to any prey in front of them. In addition, the field in front the predator would be less polluted by noise scattered off of their own body, making the backscattered noise of low Strouhal number swimmers easier to detect. Similarly, these directivity patterns could be used in the design of silent bio-inspired underwater vehicles. Modulating the Strouhal number of swimming a school of bio-robotic devices could dramatically alter their sound directivity from forward to backscattering, providing a silent region behind or in front of the device.

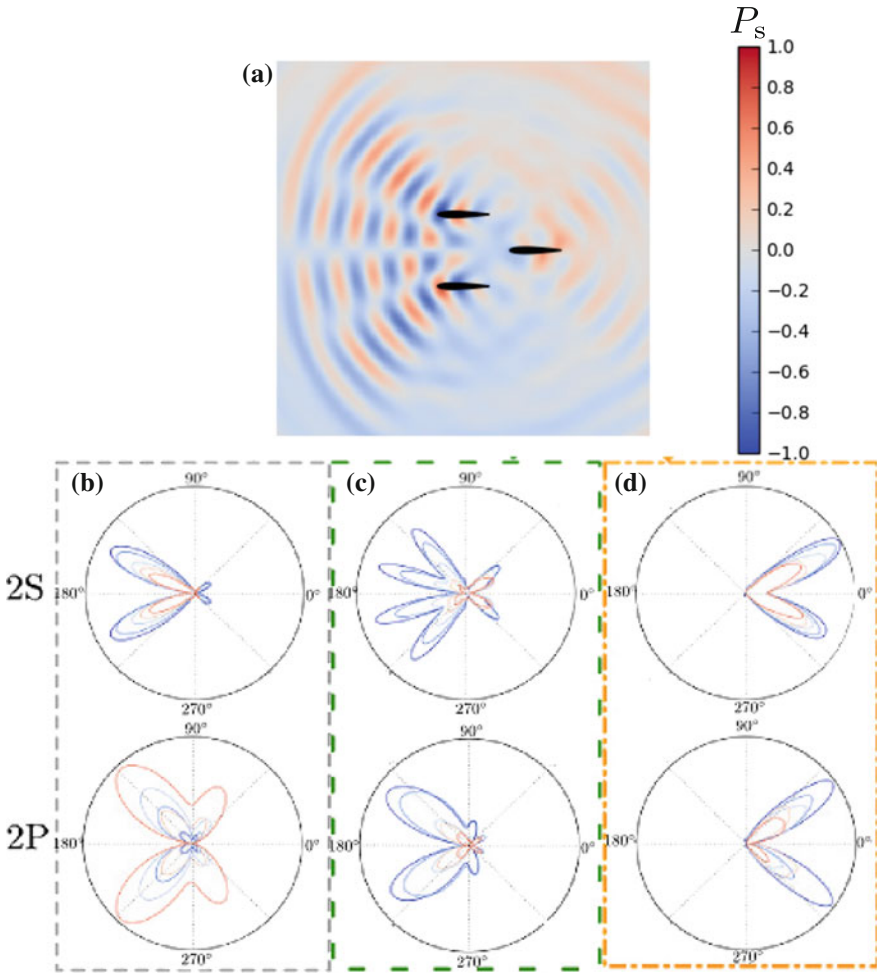

Fig. 12 Near-field scattered pressure of a $2S$ street with $St = 0.3$ is shown in image (**a**). The bottom row of images shows the changing intensity directivity patterns for varying Strouhal number ranges. The top directivity plot is for $2S$ vortex streets and the bottom is for $2P$ vortex streets. Image **b** is for $0.175 < St < 0.225$, **c** is for $0.275 < St < 0.325$, and **d** is for $0.375 < St < 0.425$. Three sections of the plot are labeled (b $\rightarrow$ d), which correspond to the regions of the intensity plot in Fig. 11

5 Conclusions

This chapter presents a rapid transient, two-dimensional acoustic boundary element method based upon a double-layer formulation developed to examine the sound field produced by idealized vortex wakes of schooling fish. The resulting time-domain solver is validated and demonstrated to predict the scattered noise and the acoustic interaction between several rigid bodies. The time-domain boundary element method

was accelerated with a fast multipole method to enable rapid evaluation of the acoustic field interactions generated by many bodies.

The boundary element method is further applied to examine the sound produced by an idealized school of fish. The wake of a virtual leader fish is fixed and moved past a formation of three rigid, static foils (fish) in the absence of a background mean flow. The simplified model presented demonstrates how the leading-edge noise of an idealized school varies over a range of Strouhal numbers that are typical of swimming fish. The directivity of the noise has a large variation within the range of Strouhal numbers examined. At lower Strouhal numbers ($0.1 < St < 0.25$), a forward scattering of the wake dominates the field while the directivity pattern transitions to a backscattering pattern for higher Strouhal numbers ($St > 0.3$). The acoustic intensity decreases as the Strouhal number increases for the $2S$ street configurations, with a similar pattern for $2P$ streets occurring after a maximum intensity is found at $St \approx 0.2$. The Strouhal range of $0.3 < St < 0.4$, commonly considered part of the range of efficient swimming, exhibits a plateau of acoustic intensity. Outside of the range of efficient swimming, a sharp decrease in acoustic intensity is observed. Future work will examine the impact of a background flow, the formation of unsteady wakes from the swimmers, and the three-dimensionality and viscous effects of the flow.

Acknowledgements This work was supported by the Lehigh University CORE grant. The authors would like to thank Dr. Matthew Hassel for discussions on the convolution quadrature method.

References

1. Alvarez, A., Ye, Z.: Effects of fish school structures on acoustic scattering. ICES J. Mar. Sci. **56**(3), 361–369 (1999)
2. Banjai, L., Sauter, S.: Rapid solution of the wave equation in unbounded domains. SIAM J. Numer. Anal. **7**, 227–249 (2011)
3. Cottet, G.H., Koumoutsakos, P.D.: Vortex Methods: Theory and Practice. Cambridge University Press (2000)
4. Eloy, C.: Optimal strouhal number for swimming animals. J. Fluids Struct. **30**, 205–218 (2012)
5. Fay, R.R.: Fish Bioacoustics. Springer (2009)
6. Feuillade, C., Nero, R., Love, R.: A low-frequency acoustic scattering model for small schools of fish. J. Acoust. Soc. Am. **99**(1), 196–208 (1996)
7. Fish, F., Lauder, G.: Passive and active flow control by swimming fishes and mammals. Annu. Rev. Fluid Mech. **38**, 193–224 (2006)
8. Gimbutas, Z., Greengard, L.: FMMLIB2D, FORTRAN libraries for fast multiple method in two dimensions (2012). http://www.cims.nyu.edu/cmcl/fmm3dlib/fmm3dlib.html
9. Greengard, L., Rokhlin, V.: A fast algorithm for particle simulations. J. Comput. Phys. **73**(2), 325–348 (1987)
10. Hassell, M., Sayas, F.J.: Convolution quadrature for wave simulations. In: Numerical Simulation in Physics and Engineering, pp. 71–159. Springer (2016)
11. Junger, M.C., Feit, D.: Sound, Structures, and Their Interaction, vol. 225. MIT press Cambridge, MA (1986)
12. Kirkup, S.M.: The Boundary Element Method in Acoustics. Integrated Sound Software (2007)

13. Ladich, F., Fine, M.L.: Sound-generating mechanisms in fishes: a unique diversity in vertebrates. Commun. Fishes **1**, 3–43 (2006)
14. Lauder, G.V.: Fish locomotion: recent advances and new directions. Ann. Rev. Mar. Sci. **7**, 521–545 (2015)
15. Leonard, A.: Vortex methods for flow simulation. J. Comput. Phys. **37**(3), 289–335 (1980)
16. Liu, Y.: Fast Multipole Boundary Element Method: Theory and Applications in Engineering. Cambridge University Press (2009)
17. Lubich, C.: Convolution quadrature revisited. BIT Numer. Math. **44**, 503–514 (2004)
18. Moored, K.W., Fish, F.E., Kemp, T.H., Bart-Smith, H.: Batoid fishes: inspiration for the next generation of underwater robots. Mar. Technol. Soc. J. **45**(4), 99–109 (2011)
19. Partridge, B.L.: The structure and function of fish schools. Sci. Am. **246**(6), 114–123 (1982)
20. Raveau, M.P., Feuillade, C.: Time domain investigations of acoustical scattering from schools of swim bladder fish. J. Acoust. Soc. Am. **135**(4), 2177–2177 (2014)
21. Read, D.A., Hover, F., Triantafyllou, M.: Forces on oscillating foils for propulsion and maneuvering. J. Fluids Struct. **17**(1), 163–183 (2003)
22. Rokhlin, V.: Rapid solution of integral equations of scattering theory in two dimensions. J. Comput. Phys. **86**, 414–439 (1990)
23. Saad, Y., Schultz, M.H.: GMRES: A generalized minimal residual algorithm for solving nonsymmetric linear systems. SIAM J. Sci. Stat. Comput. **7**(3), 856–869 (1986)
24. Schnipper, T., Andersen, A., Bohr, T.: Vortex wakes of a flapping foil. J. Fluid Mech. **633**, 411–423 (2009)
25. Weihs, D.: Hydromechanics of fish schooling. Nature **241**(5387), 290–291 (1973)

Simultaneous Finite Element Computation of Direct and Diffracted Flow Noise in Domains with Static and Moving Walls

Oriol Guasch, Arnau Pont, Joan Baiges and Ramon Codina

Abstract Curle's acoustic analogy allows one to compute aerodynamic noise due to flow motion in the presence of rigid bodies. However, the strength of the dipolar term in the analogy depends on the values of the total flow pressure on the body's surface. At low Mach numbers, that pressure cannot be obtained from the computational fluid dynamics (CFD) simulation of an incompressible flow, because the acoustic component cannot be captured. To circumvent this problem, and still being able to separate the flow and body noise contributions at a far-field point, an alternative approach was recently proposed which does not rely on an integral formulation. Rather, the acoustic pressure is split into incident and diffracted components giving rise to two differential acoustic problems that are solved together with the flow dynamics, in a single finite element computational run. In this work, we will revisit the acoustics of that approach and show how it can be extended to predict the flow noise generated in domains with moving walls.

Keywords Computational aeroacoustics · Flow noise · Finite elements Arbitrary Lagrangian–Eulerian · Diffraction · Acoustic analogy

1 Introduction

For low Mach number flows, hybrid approaches have become the most widespread formulations in computational aeroacoustics (CAA) (see e.g. [3]). The reason is that, along with the computational cost, the strong disparity between the flow speed and the speed of sound leads to convergence problems when attempting direct noise

O. Guasch (✉)
GTM-Grup de Recerca en Tecnologies Mèdia, La Salle, Universitat Ramon Llull, C/Quatre Camins 30, 08022 Barcelona, Catalonia, Spain
e-mail: oguasch@salle.url.edu
URL: http://users.salleurl.edu/~oguasch/

A. Pont · J. Baiges · R. Codina
Universitat Politècnica de Catalunya, C/Jordi Girona 1-3, Edifici C1, 08034 Barcelona, Catalonia, Spain

E. Ciappi et al. (eds.), *Flinovia—Flow Induced Noise and Vibration Issues and Aspects-II*,
https://doi.org/10.1007/978-3-319-76780-2_12

computations (DNC), which rely on the full compressible Navier–Stokes equations (see e.g. [4]). As opposed to this, hybrid approaches consist of a first computational fluid dynamics (CFD) simulation of the incompressible Navier–Stokes equations. This serves to determine the source terms of an acoustic analogy, Lighthill's being the most celebrated one [29]. The analogy is then solved using an integral formulation, making use of Green functions. If rigid bodies are present within the flow, one usually resorts to Curle's analogy [12] and, if those can move, to its generalization, namely the Ffowcs Williams–Hawkings equation [36].

From a computational point of view, hybrid approaches imply working with two codes; typically a finite element method (FEM) one for the CFD and a boundary element method (BEM) for the acoustics. If one is not interested in the solution at large distances from the aeroacoustic sources, the two codes can be avoided and one can simply use FEM to get the flow and the acoustic fields (see e.g. [19, 20, 28, 31]). This has the advantage of only needing one computational code, but the disadvantage is that one can no longer separate the noise contributions, at a far-field point, from the unsteady flow (quadrupolar term in Curle's analogy), and from the rigid body itself (dipolar term in Curle's analogy). However, Curle's analogy is not free of problems in low Mach number simulations. This is because only incompressible pressure fluctuations can be recovered from incompressible CFD computations, not the acoustic ones. Unfortunately, the latter are also needed on the rigid surface for a proper implementation of Curle's analogy.

To circumvent this difficulty, make use of a single FEM code for both the flow and the acoustic fields, and be able to distinguish between the direct flow and the body noise contributions, a different approach was proposed in [21]. In that work, advantage was taken from the fact that the dipolar term in Curle's analogy corresponds to the turbulent noise diffracted by the rigid body (see e.g. [17]). The acoustic pressure in Lighthill's acoustic analogy was split into a direct plus diffracted components as in classical diffraction problems. At every time step of a single FEM run, the incompressible Navier–Stokes equations were first solved. The resulting velocity field was then inserted as a source term in a wave equation for the direct incident acoustic pressure, and that was finally used in the boundary conditions of another wave equation for the diffracted acoustic pressure. Some benchmark cases to test the methodology were presented in [21], and in [33] the approach has been recently applied to voice production, for better understanding the generation mechanisms of sibilant [s].

In this work, we will revisit the main results in [21] and show how they can be extended to account for the prediction of flow noise in domains with moving walls. Focus will be placed on the acoustics formulation rather than on the CFD. Working with moving domains will require setting the governing equations in an arbitrary Lagrangian–Eulerian (ALE) frame of reference. As we shall see, the irreducible wave equation will be no longer valid in this case, and we will have to work with the wave equation in mixed form (see e.g. [7]). The splitting into incident and diffracted components in [21] will be applied to the ALE mixed wave equation and we will show how to solve it resorting to the stabilized FEM in [18]. Some numerical examples will be presented. First, we will briefly summarize the case with static boundaries

in [33], which consists of a large-scale three-dimensional CAA simulation for the production of the sibilant [s]. Second, we will present a case with moving walls which comprises a flow exiting a two-dimensional duct, with a teeth-shaped obstacle at its end that evolves from an almost closed aperture to an open one.

2 Diffracted Sound and Curle's Analogy

To begin with, let us consider the problem depicted in Fig. 1. A low Mach flow is impinging on a rigid body Ω_b, which we assume stationary for the moment, and a wake develops past the body. As a result, aerodynamic noise is generated due to unsteady flow motion. At a far-field point in Ω_{ac}, the acoustic pressure, $p(\boldsymbol{x}, t)$, will have a contribution directly stemming from the flow motion and a contribution arising from the diffraction of the flow noise by the body. Assuming that one has already performed a CFD computation to get the flow velocity and pressure, Curle's analogy can be used to determine those acoustic contributions with the sole use of the free-space Green function for the wave equation. Curle's final integral formulation [12] for the acoustic pressure reads (neglecting the viscous stress tensor contributions),

$$p\,(\boldsymbol{x}, t) = \rho_0 \partial_{ij}^2 \int_{\Omega_{ac}} \frac{1}{4\pi\,|\boldsymbol{x} - \boldsymbol{y}|} \left[u_i^0 u_j^0\right]_{t'} d^3\boldsymbol{y} - \partial_i \int_{\Gamma_b} \frac{1}{4\pi\,|\boldsymbol{x} - \boldsymbol{y}|} [P]_{t'} n_i d^2\boldsymbol{y}. \quad (1)$$

Following the convention for retarded potentials, the squared brackets in the equation stand for evaluation at the retarded time $t' := t - |\boldsymbol{x} - \boldsymbol{y}|/c_0$. The parameters

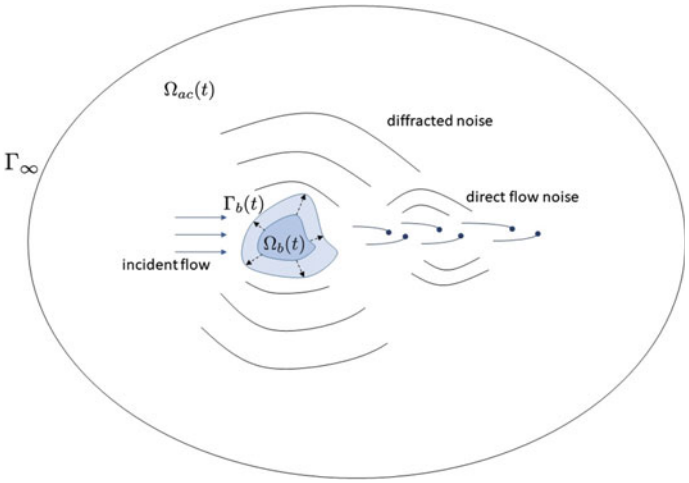

Fig. 1 Computational domain. The body $\Omega_b(t)$ can change its shape with time and consequently so does $\Omega_{ac}(t)$

c_0 and ρ_0 respectively denote the speed of sound and the mean air density, whereas ∂_i designates the first-order spatial derivative with respect to the component x_i, and ∂^2_{ij} represents the second-order cross-derivative with respect to x_i and x_j.

The first integral in (1) provides the direct flow noise contribution to $p(\boldsymbol{x}, t)$ assuming the low Mach number approximation to Lighthill's tensor, namely $\mathcal{S}^0 = \rho_0 \partial^2_{ij}(u^0_i u^0_j)$, with $\boldsymbol{u}^0(\boldsymbol{x}, t)$ denoting the incompressible flow velocity. The second integral contains the contribution from the sound diffracted by the rigid body [10, 13, 17, 21]. While $\boldsymbol{u}^0(\boldsymbol{x}, t)$ in the first integral can be obtained from an incompressible CFD simulation, the problem is that this is not possible for the pressure $P(\boldsymbol{x}, t)$ in the second integral, because $P(\boldsymbol{x}, t)$ accounts for the total compressible pressure at the body's boundary.

3 Splitting the Acoustic Pressure into Incident and Diffracted Components

3.1 General Linear Acoustic Wave Operator

To avoid the difficulties with Curle's analogy described in the preceding section and still being able possible to separate the direct and diffracted flow noise contributions using a single FEM code, an alternative was proposed in [21]. To introduce it, let us consider a more general situation for the aeroacoustic problem presented in Fig. 1, also in the framework of acoustic analogies.

Assume again that we have already computed an aeroacoustic source term $\mathcal{S}$ from a CFD simulation of the incompressible Navier–Stokes equations (for the time being not necessarily the low Mach approximation to Lighthill's tensor). We will first state the problem of computing the aerodynamic noise generated by such a term in an acoustic computational domain Ω_{ac}. Suppose that the acoustic wave propagation is driven by a linear wave operator $\mathcal{L}$ acting on the acoustic pressure p (explicit indication of dependence on space and time will be hereafter omitted), that B_b represents another linear operator defining the boundary conditions on the body immersed in the flow, and that B_∞ stands for a third linear operator accounting for a non-reflecting boundary condition at Γ_∞ (see Fig. 1). The acoustic pressure p in Ω_{ac} can be obtained from the solution of

$$\mathcal{L}p = \mathcal{S} \quad \text{in } \Omega_{ac},\ t > 0, \tag{2a}$$

$$\nabla p \cdot \boldsymbol{n} = B_b p \quad \text{on } \Gamma_b,\ t > 0, \tag{2b}$$

$$\nabla p \cdot \boldsymbol{n} = B_\infty p \quad \text{on } \Gamma_\infty,\ t > 0, \tag{2c}$$

$$p(\boldsymbol{x}, 0) = 0,\ \partial_t p(\boldsymbol{x}, 0) = 0 \quad \text{in } \Omega_{ac},\ t = 0. \tag{2d}$$

To determine, at a given position, the separate acoustic pressure contribution of the direct sound generated by the aeroacoustic source $\mathcal{S}$, say p_i, from that diffracted

by the rigid body, p_d, we can split the total acoustic pressure as $p = p_i + p_d$ and substitute into (2). This results in the following problem for p_i,

$$\mathcal{L}p_i = \mathcal{S} \quad \text{in } \Omega_{ac} \cup \Omega_b,\ t > 0, \tag{3a}$$

$$\nabla p_i \cdot \boldsymbol{n} = B_\infty p_i \quad \text{on } \Gamma_\infty,\ t > 0, \tag{3b}$$

$$p_i(\boldsymbol{x}, 0) = 0,\ \partial_t p_i(\boldsymbol{x}, 0) = 0 \quad \text{in } \Omega_{ac} \cup \Omega_b\ t = 0, \tag{3c}$$

which once solved can be used to obtain p_d,

$$\mathcal{L}p_d = 0 \quad \text{in } \Omega_{ac},\ t > 0, \tag{4a}$$

$$\nabla p_d \cdot \boldsymbol{n} - B_b p_d = -\nabla p_i \cdot \boldsymbol{n} + B_b p_i \quad \text{on } \Gamma_b,\ t > 0, \tag{4b}$$

$$\nabla p_d \cdot \boldsymbol{n} = B_\infty p_d \quad \text{on } \Gamma_\infty,\ t > 0, \tag{4c}$$

$$p_d(\boldsymbol{x}, 0) = 0,\ \partial_t p_d(\boldsymbol{x}, 0) = 0 \quad \text{in } \Omega_{ac},\ t = 0. \tag{4d}$$

Note that we can recover the original problem (2) from the summation of problems (3) and (4). To solve (3), we need to remove Ω_b from the computational domain and make the computations as if the body was absent. Once we get p_i, we include the body back in the computational domain and use p_i at its boundary Γ_b, to compute the diffracted pressure p_d.

The above splitting procedure is nothing but the standard way to deal with diffraction and scattering problems in acoustics (see e.g. [30]). As explained in the Introduction, the novelty in [21] consisted in exploiting that factorization in CAA to avoid the problems encountered when applying Curle's analogy to low-speed subsonic flows.

3.2 Domains with Static Walls

A first application of the splitting approach (3)–(4) is that of finding the incident and diffracted flow noise contributions at a far-field point. Let us take the irreducible wave equation as the linear operator in (2), i.e. $\mathcal{L} \equiv c_0^{-2}\partial_{tt}^2 - \nabla^2$, and suppose the body to be acoustically rigid. Assume once more that we have obtained an incompressible pressure field, p^0, and an incompressible velocity field, $\boldsymbol{u}^0$, from the solution of the incompressible Navier–Stokes equations. We could then build an aeroacoustic source term by taking, for instance, $\mathcal{S}^0 = \rho_0 \partial_{ij}^2 (u_i^0 u_j^0)$, which as said before is nothing but the approximation to Lighthill's tensor at low Mach numbers. In the case of sound propagating in non-quiescent flow areas, however, convective and refraction effects should be removed from the source term and incorporated into the wave operator. Otherwise, non-acoustic pressure fluctuations that do not correspond to proper sound could manifest in the solution (this is usually referred to as *pseudosound*, see e.g. [11]). Several options exist to remedy the situation that range from the linearized Euler equations (LEE) [2], to the acoustic perturbation equations (APE) which filter the LEE to get rid of its entropy and vorticity modes [15]. A simplified version

of the APE for low Mach numbers can be found in [22, 23]. In the case of almost negligible convection velocities, the latter reduces to Roger's acoustic analogy in [34] with source term $\mathcal{S}^0 = c_0^{-2}\partial_{tt}^2 p^0$. The latter allows one to filter some pseudosound and will be considered in this work together with Lighthill's one.

With the above considerations, the splitting into incident and diffracted components yields the following particular cases of problems (3) and (4),

$$\frac{1}{c_0^2}\partial_{tt}^2 p_i - \nabla^2 p_i = \mathcal{S}^0 \quad \text{in } \Omega_{ac} \cup \Omega_b,\ t > 0, \tag{5a}$$

$$\nabla p_i \cdot \boldsymbol{n} = \frac{1}{c_0}\partial_t p_i \quad \text{on } \Gamma_\infty,\ t > 0, \tag{5b}$$

$$p_i(\boldsymbol{x}, 0) = 0,\ \partial_t p_i(\boldsymbol{x}, 0) = 0 \quad \text{in } \Omega_{ac} \cup \Omega_b\ t = 0, \tag{5c}$$

and

$$\frac{1}{c_0^2}\partial_{tt}^2 p_d - \nabla^2 p_d = 0 \quad \text{in } \Omega_{ac},\ t > 0, \tag{6a}$$

$$\nabla p_d \cdot \boldsymbol{n} = -\nabla p_i \cdot \boldsymbol{n} \quad \text{on } \Gamma_b,\ t > 0, \tag{6b}$$

$$\nabla p_d \cdot \boldsymbol{n} = \frac{1}{c_0}\partial_t p_d \quad \text{on } \Gamma_\infty,\ t > 0, \tag{6c}$$

$$p_d(\boldsymbol{x}, 0) = 0,\ \partial_t p_d(\boldsymbol{x}, 0) = 0 \quad \text{in } \Omega_{ac},\ t = 0. \tag{6d}$$

Note that (5b) and (6c) correspond to the Sommerfeld radiation condition that prevents outward propagating waves to be reflected back from the outer boundaries of the computational domain.

The above formulation was used in [21] to compute the turbulent and diffracted components of sound generated past a two-dimensional cylinder (aeolian tones), and also to determine the incident and diffracted flow noise contributions of an obstacle placed at the exit of a three-dimensional duct. More recently, the methodology in [21] has been applied to voice production in [33] to determine the contributions of the sound diffracted by the upper teeth in the generation of sibilant /s/ (see Sect. 5.1).

3.3 Domains with Moving Walls

The main goal of the present work is to show how to extend the above splitting procedure to the case of flow noise generated in domains with moving walls. As mentioned, an example could be that of the aeroacoustics of a flow emanating from a duct with a time-varying exit section. Typical cases also arise once more in voice production, for example, when pronouncing a syllable that involves a sibilant sound.

When dealing with acoustic waves propagating in moving domains, it becomes no longer possible to resort to the acoustic wave equation in irreducible form. The

linearized continuum and momentum conservation equations used to derive the latter need to be expressed in an ALE frame of reference, which precludes obtaining a scalar wave equation for the acoustic pressure [18]. One is then forced to work with the linearized momentum and continuity equations, sometimes referred to as the wave equation in mixed form (see e.g. [7]). This reads,

$$\frac{1}{\rho_0 c_0^2}\partial_t p + \nabla \cdot \boldsymbol{u} = Q, \tag{7a}$$

$$\rho_0 \partial_t \boldsymbol{u} + \nabla p = \boldsymbol{f}, \tag{7b}$$

where p stands anew for the acoustic pressure while $\boldsymbol{u}$ represents the acoustic particle velocity. Q denotes a volume source distribution and $\boldsymbol{f}$ an external body force per unit volume.

To express (7) in an ALE domain, a quasi-Eulerian approximation is often used [24, 27], which basically consists in expressing the time derivative of any fluid property, say g, in a referential frame moving with the domain, i.e. replacing $\partial_t g \leftarrow \partial_t g - \boldsymbol{u}_{\text{dom}} \cdot \nabla g$, while keeping the spatial derivatives Eulerian. $\boldsymbol{u}_{\text{dom}}$ denotes the domain velocity and it will be hereafter termed the mesh velocity, because it corresponds to the mesh node velocities in the computational implementation. The ALE counterpart of (7) becomes

$$\frac{1}{\rho_0 c_0^2}\partial_t p - \frac{1}{\rho_0 c_0^2}\boldsymbol{u}_{\text{dom}} \cdot \nabla p + \nabla \cdot \boldsymbol{u} = Q, \tag{8a}$$

$$\rho_0 \partial_t \boldsymbol{u} - \rho_0 \boldsymbol{u}_{\text{dom}} \cdot \nabla \boldsymbol{u} + \nabla p = \boldsymbol{f}. \tag{8b}$$

The source terms corresponding to Lighthill's analogy and the Roger one in [34] are given by,

$$\text{Roger's analogy:} \quad \boldsymbol{f} = \boldsymbol{0},\ Q = -(1/\rho_0 c_0^2)\left[\partial_t p^0 - \boldsymbol{u}_{\text{dom}} \cdot \nabla p^0\right], \tag{9a}$$

$$\text{Lighthill's analogy:} \quad f_i = -\rho_0 \partial_j (u_i^0 u_j^0),\ Q = 0. \tag{9b}$$

To solve (8) in a computational domain $\Omega_{ac}(t),\ t > 0$, we need to supplement the equation with appropriate boundary conditions and initial conditions. Assuming again a rigid body for simplicity, we get

$$\boldsymbol{u} \cdot \boldsymbol{n} = 0 \quad \text{on } \Gamma_b(t)\ t > 0, \tag{10a}$$

$$\boldsymbol{u} \cdot \boldsymbol{n} = \frac{1}{Z_0} p \quad \text{on } \Gamma_\infty\ t > 0, \tag{10b}$$

$$p(\boldsymbol{x}, 0) = 0\ \boldsymbol{u}(\boldsymbol{x}, 0) = \boldsymbol{0}, \quad \text{in } \Omega_{ac}(t),\ t = 0 \tag{10c}$$

where (10b) is the Sommerfeld radiation condition for the wave equation in mixed form (see e.g. [14]) and $Z_0 = \rho_0 c_0$.

We can next apply the splitting strategy into incident and diffracted fields for the ALE mixed wave Eq. (8). Notice that the general linear operator $\mathcal{L}$ in (2) herein acts both on the acoustic pressure p and on the acoustic particle velocity $\boldsymbol{u}$. Taking $\boldsymbol{u} = \boldsymbol{u}_{in} + \boldsymbol{u}_d$ and $p = p_{in} + p_d$ in (8), we get the incident field problem

$$\frac{1}{\rho_0 c_0^2}\partial_t p_{in} - \frac{1}{\rho_0 c_0^2}\boldsymbol{u}_{\text{dom}} \cdot \nabla p_{in} + \nabla \cdot \boldsymbol{u}_{in} = Q \quad \text{in } \Omega_{ac}(t) \cup \Omega_b(t),\ t > 0, \tag{11a}$$

$$\rho_0 \partial_t \boldsymbol{u}_{in} - \rho_0 \boldsymbol{u}_{\text{dom}} \cdot \nabla \boldsymbol{u}_{in} + \nabla p_{in} = \boldsymbol{f} \quad \text{in } \Omega_{ac}(t) \cup \Omega_b(t),\ t > 0, \tag{11b}$$

$$\boldsymbol{u}_{in} \cdot \boldsymbol{n} = \frac{1}{Z_0} p_{in} \quad \text{on } \Gamma_\infty,\ t > 0, \tag{11c}$$

$$p_{in}(\boldsymbol{x}, 0) = 0,\ \boldsymbol{u}_{in}(\boldsymbol{x}, 0) = \boldsymbol{0}, \quad \text{in } \Omega_{ac}(t) \cup \Omega_b(t),\ t = 0, \tag{11d}$$

and the diffracted field one,

$$\frac{1}{\rho_0 c_0^2}\partial_t p_d - \frac{1}{\rho_0 c_0^2}\boldsymbol{u}_{\text{dom}} \cdot \nabla p_d + \nabla \cdot \boldsymbol{u}_d = 0 \quad \text{in } \Omega_{ac}(t),\ t > 0, \tag{12a}$$

$$\rho_0 \partial_t \boldsymbol{u}_d - \rho_0 \boldsymbol{u}_{\text{dom}} \cdot \nabla \boldsymbol{u}_d + \nabla p_d = \boldsymbol{0} \quad \text{in } \Omega_{ac}(t),\ t > 0, \tag{12b}$$

$$\boldsymbol{u}_d \cdot \boldsymbol{n} = -\boldsymbol{u}_{in} \cdot \boldsymbol{n} \quad \text{on } \Gamma_b(t),\ t > 0, \tag{12c}$$

$$\boldsymbol{u}_d \cdot \boldsymbol{n} = \frac{1}{Z_0} p_d \quad \text{on } \Gamma_\infty,\ t > 0, \tag{12d}$$

$$p_d(\boldsymbol{x}, 0) = 0,\ \boldsymbol{u}_d(\boldsymbol{x}, 0) = \boldsymbol{0}, \quad \text{in } \Omega_{ac}(t),\ t = 0. \tag{12e}$$

The source terms Q and $\boldsymbol{f}$ in (11) need to be obtained from the solution of the incompressible Navier–Stokes in an ALE framework. Our objective is to solve the latter together with (11) and (12) in a single finite element computational run, following the strategy in [21].

4 Numerical Discretization for Waves in Moving Domains

4.1 Continuous Weak Form

The FEM discretization of Eqs. (11) and (12) relies on their weak formulation rather than on the differential one. The continuous weak forms of the equations can be found multiplying Eqs. (11a) and (12a) with a scalar test function q, and Eqs. (11b) and (12b) with a vector test function $\boldsymbol{v}$, and then integrating over the respective computational domains $\Omega_{ac}(t) \cup \Omega_b(t)$ and $\Omega_{ac}(t)$. Let us denote by $(f, g) := \int_\Omega f g d\Omega$ the integral of the product between two arbitrary functions f and g, and assume that we want to solve the problem in a given time interval $[0, T]$. The variational problems for the incident and diffracted acoustic pressure and velocity can be posed as follows.

First, find $p_{in} \in \mathcal{W}_p^{in}([0,T], V_p^{in})$ and $\boldsymbol{u}_{in} \in \boldsymbol{\mathcal{W}}_{\boldsymbol{u}}^{in}([0,T], \boldsymbol{V}_{\boldsymbol{u}}^{in})$ such that

$$\frac{1}{\rho_0 c_0^2}(\partial_t p_{in}, q) - \frac{1}{\rho_0 c_0^2}(\boldsymbol{u}_{\text{dom}} \cdot \nabla p_{in}, q) + (\nabla \cdot \boldsymbol{u}_{in}, q) = (Q, q)\ \forall\, q \in V_p^{in}, \tag{13a}$$

$$\rho_0(\partial_t \boldsymbol{u}_{in}, \boldsymbol{v}) - \rho_0(\boldsymbol{u}_{\text{dom}} \cdot \nabla \boldsymbol{u}_{in}, \boldsymbol{v}) + (\nabla p_{in}, \boldsymbol{v}) = (\boldsymbol{f}, \boldsymbol{v})\ \forall\, \boldsymbol{v} \in \boldsymbol{V}_{\boldsymbol{u}}^{in}, \tag{13b}$$

where $\mathcal{W}_p^{in}$, $\boldsymbol{\mathcal{W}}_{\boldsymbol{u}}^{in}$, V_p^{in} and $\boldsymbol{V}_{\boldsymbol{u}}^{in}$ denote appropriate functional spaces in $\Omega_{ac}(t) \cup \Omega_b(t)$, not to be detailed herein (see e.g. [18] for more details). As for the diffracted fields, we will have to find $p_d \in \mathcal{W}_p^d([0,T], V_p^d)$ and $\boldsymbol{u}_d \in \boldsymbol{\mathcal{W}}_{\boldsymbol{u}}^d([0,T], \boldsymbol{V}_{\boldsymbol{u}}^d)$ such that

$$\frac{1}{\rho_0 c_0^2}(\partial_t p_d, q) - \frac{1}{\rho_0 c_0^2}(\boldsymbol{u}_{\text{dom}} \cdot \nabla p_d, q) + (\nabla \cdot \boldsymbol{u}_d, q) = (Q, q) \quad \forall\, q \in V_p^d, \tag{14a}$$

$$\rho_0(\partial_t \boldsymbol{u}_d, \boldsymbol{v}) - \rho_0(\boldsymbol{u}_{\text{dom}} \cdot \nabla \boldsymbol{u}_d, \boldsymbol{v}) + (\nabla p_d, \boldsymbol{v}) = (\boldsymbol{f}, \boldsymbol{v}) \quad \forall\, \boldsymbol{v} \in \boldsymbol{V}_{\boldsymbol{u}}^d, \tag{14b}$$

with $\mathcal{W}_p^d$, $\boldsymbol{\mathcal{W}}_{\boldsymbol{u}}^d$, V_p^d and $\boldsymbol{V}_{\boldsymbol{u}}^d$ standing now for appropriate functional spaces in $\Omega_{ac}(t)$.

The Dirichlet boundary conditions (11c), (12c) and (12d) are to be imposed strongly on $\Gamma_b(t)$ and Γ_∞. Alternatively, one could integrate the terms $(\nabla \cdot \boldsymbol{u}_{in}, q)$ in (13a) and $(\nabla \cdot \boldsymbol{u}_d, q)$ in (14a) to impose the conditions weakly. The consequences of such an option are detailed in [1].

4.2 Finite Element Spatial Discretization

The Galerkin FEM solution to variational mixed problems like (13) and (14) is known to exhibit strong oscillations if equal order interpolations are used for the pressure and velocities (see e.g. [7, 8, 18]). One could prevent them by resorting to stabilized FEM strategies like the variational multiscale (VMS) method in [25, 26]. In this work, orthogonal subgrid scales (OSS), see [6, 9], will be used to stabilize the Galerkin FEM approach to (13) and (14), following the strategy depicted in [18].

Let us consider the finite element spaces $V_{p_h} \subset V_p$ and $\boldsymbol{V}_{\boldsymbol{u}_h} \subset \boldsymbol{V}_{\boldsymbol{u}}$ constructed from a finite element partition $\Omega^e(t)$ of $\Omega(t)$, where the index e ranges from 1 to the number of elements n_{el}. The discrete stabilized FEM approach to the incident problem (13) consists in finding $p_{in_h} \in \mathcal{W}_{p_h}^{in}([0,T], V_{p_h}^{in})$ and $\boldsymbol{u}_{in_h} \in \boldsymbol{\mathcal{W}}_{\boldsymbol{u}_h}^{in}([0,T], \boldsymbol{V}_{\boldsymbol{u}_h}^{in})$ such that

$$\frac{1}{\rho_0 c_0^2}(\partial_t p_{in_h}, q_h) - \frac{1}{\rho_0 c_0^2}(\boldsymbol{u}_{\text{dom}} \cdot \nabla p_{in_h}, q_h) + (\nabla \cdot \boldsymbol{u}_{in_h}, q_h)$$
$$+ \sum_{e=1}^{n_{el}} (\tau_p \mathcal{P}\big[- \frac{1}{\rho_0 c_0^2} \boldsymbol{u}_{\text{dom}} \cdot \nabla p_{in_h} + \nabla \cdot \boldsymbol{u}_{in_h} - Q\big], - \frac{1}{\rho_0 c_0^2} \boldsymbol{u}_{\text{dom}} \cdot \nabla q_{in_h}$$
$$+ \nabla \cdot \boldsymbol{v}_h)_{\Omega_e(t)} = (Q, q_h), \tag{15a}$$
$$\rho_0(\partial_t \boldsymbol{u}_{in_h}, \boldsymbol{v}_h) - \rho_0(\boldsymbol{u}_{\text{dom}} \cdot \nabla \boldsymbol{u}_{in_h}, \boldsymbol{v}_h) + (\nabla p_{in_h}, \boldsymbol{v}_h)$$
$$+ \sum_{e=1}^{n_{el}} (\tau_{\boldsymbol{u}} \mathcal{P}\big[- \rho_0 \boldsymbol{u}_{\text{dom}} \cdot \nabla \boldsymbol{u}_{in_h} + \nabla p_{in_h} - \boldsymbol{f}\big], - \rho_0 \boldsymbol{u}_{\text{dom}} \cdot \nabla \boldsymbol{v}_h + \nabla q_h)_{\Omega_e(t)}$$
$$= (\boldsymbol{f}, \boldsymbol{v}_h), \tag{15b}$$

for all $q_h \in V^{in}_{p_h}$ and $\boldsymbol{v}_h \in \boldsymbol{V}^{in}_{\boldsymbol{u}_h}$.

The first and fourth rows in the above equations contain the Galerkin FEM terms, whereas the second and fifth rows account for the stabilization terms. $\mathcal{P}$ in (15) stands for a projection to be applied either to scalars or vectors depending on the argument. In the OSS method, $\mathcal{P}$ is computed as $\mathcal{P} = \boldsymbol{I} - \Pi_h$, with $\boldsymbol{I}$ being the identity and Π_h the L^2-projection onto the corresponding finite element space. On the other hand, the following expressions can be obtained for the stabilization parameters τ_p and $\tau_{\boldsymbol{u}}$, (see [18])

$$\tau_p = \frac{\rho_0 c_0^2 h}{C_1 |\boldsymbol{u}_d| + c_0 C_2},$$
$$\tau_{\boldsymbol{u}} = \frac{h}{C_1 \rho_0 |\boldsymbol{u}_d| + \rho_0 c_0 C_2}, \tag{16}$$

with C_1 and C_2 being constants to be determined from numerical experiments (a value of $C_1 = C_2 = 100$ was taken in [18]).

Analogously, the discrete stabilized FEM approach to the diffraction problem (14) is that of finding $p_{d_h} \in \mathcal{W}^d_{p_h}([0, T], V^d_{p_h})$ and $\boldsymbol{u}_{d_h} \in \boldsymbol{\mathcal{W}}^d_{\boldsymbol{u}_h}([0, T], \boldsymbol{V}^d_{\boldsymbol{u}_h})$ such that

$$\frac{1}{\rho_0 c_0^2}(\partial_t p_{d_h}, q_h) - \frac{1}{\rho_0 c_0^2}(\boldsymbol{u}_{\text{dom}} \cdot \nabla p_{d_h}, q_h) + (\nabla \cdot \boldsymbol{u}_{d_h}, q_h)$$
$$+ \sum_{e=1}^{n_{el}} (\tau_p \mathcal{P}\big[- \frac{1}{\rho_0 c_0^2} \boldsymbol{u}_{\text{dom}} \cdot \nabla p_{d_h} + \nabla \cdot \boldsymbol{u}_{d_h} - Q\big], - \frac{1}{\rho_0 c_0^2} \boldsymbol{u}_{\text{dom}} \cdot \nabla q_h$$
$$+ \nabla \cdot \boldsymbol{v}_h)_{\Omega_e(t^n)} = (Q^{n+1}, q_h), \tag{17a}$$
$$\rho_0(\partial_t \boldsymbol{u}_{d_h}, \boldsymbol{v}_h) - \rho_0(\boldsymbol{u}_{\text{dom}} \cdot \nabla \boldsymbol{u}_{d_h}, \boldsymbol{v}_h) + (\nabla p_{d_h}, \boldsymbol{v}_h)$$
$$+ \sum_{e=1}^{n_{el}} (\tau_{\boldsymbol{u}} \mathcal{P}\big[- \rho_0 \boldsymbol{u}_{\text{dom}} \cdot \nabla \boldsymbol{u}_{d_h} + \nabla p_{d_h} - \boldsymbol{f}\big], - \rho_0 \boldsymbol{u}_{\text{dom}} \cdot \nabla \boldsymbol{v}_h + \nabla q_h)_{\Omega_e(t)}$$
$$= (\boldsymbol{f}, \boldsymbol{v}_h), \tag{17b}$$

for all $q_h \in V^d_{p_h}$ and $\boldsymbol{v}_h \in \boldsymbol{V}^d_{\boldsymbol{u}_h}$.

4.3 Fully Discrete Numerical Scheme

To get the final numerical scheme, we need to discretize Eqs. (15) and (17) in time. To that purpose, we split the time interval $[0\ T]$ into N equal steps $0 < t^1 < t^2 < \cdots < t^n < \cdots < t^N \equiv T$ with $\Delta t := t^{n+1} - t^n$ the time step size. For a time-dependent function $g(t)$, g^n will denote its evaluation at $t^n = n\Delta t$. A second-order backward differentiation formula (BDF2) will be used to approximate the first-order time derivative of g, which results in $\delta_t g^{n+1} := (1/2\Delta t)(3g^{n+1} - 4g^n + g^{n-1})$.

The time discrete version of the incident problem (15) then becomes

$$\begin{aligned}
&\frac{1}{\rho_0 c_0^2}(\delta_t p_{in_h}^{n+1}, q_h) - \frac{1}{\rho_0 c_0^2}(\boldsymbol{u}_{\text{dom}} \cdot \nabla p_{in_h}^{n+1}, q_h) + (\nabla \cdot \boldsymbol{u}_{in_h}^{n+1}, q_h) \\
&+ \sum_{e=1}^{n_{el}} (\tau_p \mathcal{P}\big[- \frac{1}{\rho_0 c_0^2}\boldsymbol{u}_{\text{dom}} \cdot \nabla p_{in_h}^{n+1} + \nabla \cdot \boldsymbol{u}_{in_h}^{n+1} - Q^{n+1}\big], -\frac{1}{\rho_0 c_0^2}\boldsymbol{u}_{\text{dom}} \cdot \nabla q_h \\
&+ \nabla \cdot \boldsymbol{v}_h)_{\Omega_e(t^{n+1})} = (Q^{n+1}, q_h), \qquad (18a) \\
&\rho_0(\delta_t \boldsymbol{u}_{in_h}^{n+1}, \boldsymbol{v}_h) - \rho_0(\boldsymbol{u}_{\text{dom}} \cdot \nabla \boldsymbol{u}_{in_h}^{n+1}, \boldsymbol{v}_h) + (\nabla p_{in_h}^{n+1}, \boldsymbol{v}_h) \\
&+ \sum_{e=1}^{n_{el}} (\tau_{\boldsymbol{u}} \mathcal{P}\big[- \rho_0 \boldsymbol{u}_{\text{dom}} \cdot \nabla \boldsymbol{u}_{in_h}^{n+1} + \nabla p_{in_h}^{n+1} - \boldsymbol{f}^{n+1}\big], -\rho_0 \boldsymbol{u}_d \cdot \nabla \boldsymbol{v}_h + \nabla q_h)_{\Omega_e(t^{n+1})} \\
&= (\boldsymbol{f}^{n+1}, \boldsymbol{v}_h). \qquad (18b)
\end{aligned}$$

Note that $\mathcal{P}(\delta_t p_h) = 0$ and $\mathcal{P}(\delta_t \boldsymbol{u}_h) = 0$ in (18) because we are considering orthogonal subscales.

Similarly, the time discrete version of the diffraction problem (17) is given by

$$\begin{aligned}
&\frac{1}{\rho_0 c_0^2}(\delta_t p_{d_h}^{n+1}, q_h) - \frac{1}{\rho_0 c_0^2}(\boldsymbol{u}_{\text{dom}} \cdot \nabla p_{d_h}^{n+1}, q_h) + (\nabla \cdot \boldsymbol{u}_{d_h}^{n+1}, q_h) \\
&+ \sum_{e=1}^{n_{el}} (\tau_p \mathcal{P}\big[- \frac{1}{\rho_0 c_0^2}\boldsymbol{u}_{\text{dom}} \cdot \nabla p_{d_h}^{n+1} + \nabla \cdot \boldsymbol{u}_{d_h}^{n+1} - Q^{n+1}\big], -\frac{1}{\rho_0 c_0^2}\boldsymbol{u}_{\text{dom}} \cdot \nabla q_h \\
&+ \nabla \cdot \boldsymbol{v}_h)_{\Omega_e(t^{n+1})} = (Q^{n+1}, q_h), \qquad (19a) \\
&\rho_0(\delta_t \boldsymbol{u}_{d_h}^{n+1}, \boldsymbol{v}_h) - \rho_0(\boldsymbol{u}_{\text{dom}} \cdot \nabla \boldsymbol{u}_{d_h}^{n+1}, \boldsymbol{v}_h) + (\nabla p_{d_h}^{n+1}, \boldsymbol{v}_h) \\
&+ \sum_{e=1}^{n_{el}} (\tau_{\boldsymbol{u}} \mathcal{P}\big[- \rho_0 \boldsymbol{u}_{\text{dom}} \cdot \nabla \boldsymbol{u}_{d_h}^{n+1} + \nabla p_{d_h}^{n+1} - \boldsymbol{f}^{n+1}\big], -\rho_0 \boldsymbol{u}_d \cdot \nabla \boldsymbol{v}_h + \nabla q_h)_{\Omega_e(t^{n+1})} \\
&= (\boldsymbol{f}^{n+1}, \boldsymbol{v}_h). \qquad (19b)
\end{aligned}$$

Finally, let us mention that the motion of the computational mesh in the numerical examples of the forthcoming sections has been driven through the solution of an elastic problem [5]. Though efficient remeshing strategies are currently available (see e.g. [32]), they can be avoided if the deformations are not very large, which saves a considerable amount of computational cost.

5 Numerical Examples

5.1 Generation of a Sibilant /s/

As an example to show the performance of the proposed splitting strategy in the case of stationary domains (see Sect. 3.2), we will briefly summarize the results reported in [33] concerning the generation of sibilant fricative /s/. This sound is produced when the turbulent jet flow leaving the glottis becomes accelerated in the palatal constriction, passes through the incisors gap and finally impinges in the cavity between the lower incisors and the lower lips. In Fig. 2a, we can observe the portion of the vocal tract needed for the numerical production of /s/. A snapshot of the flow accelerating through the palatal constriction and impinging on the lower lips, which results in a highly developed turbulent flow, is shown in Fig. 2b. Figure 2c depicts the emission of acoustic wavefronts in a semi-hemisphere, which propagate outwards to infinity. Finally, in Fig. 2d we present the acoustic pressure for the total, incident

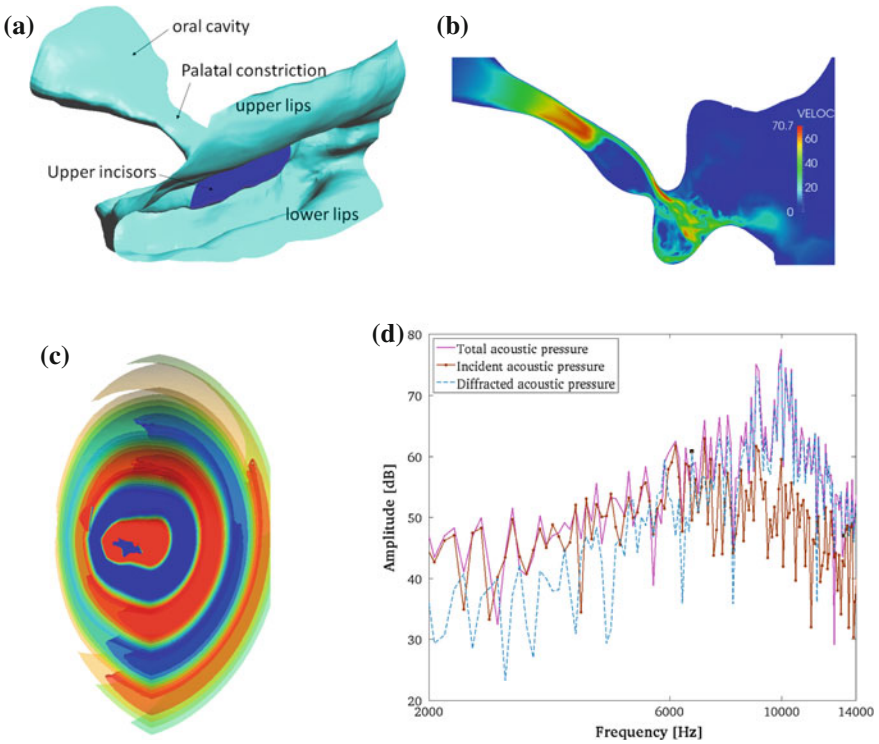

Fig. 2 Generation of sibilant /s/: **a** vocal tract geometry, **b** snapshot of the velocity profile, **c** acoustic front-waves, **d** spectra of the incident, diffracted and total acoustic pressure for a point at the far field

and diffracted acoustic pressure for a point located at the far field. The total pressure exhibits the typical wideband spectral content of an /s/ that usually peaks between 8–10 kHz, as observed on human speakers (see e.g. [16, 35]). The incident field directly originated by the flow motion dominates the spectrum up to 2 kHz; both the incident and diffracted components have similar contributions from 2 to 8 kHz, and the diffracted component dominates the spectrum for frequencies higher than 8 kHz.

The above three-dimensional simulations are computationally costly. To perform them, we have used a computational mesh of 45 million linear tetrahedral elements with equal interpolation for all variables. A total of three problems have been solved in the same finite element computational run (the incompressible Navier–Stokes equations plus the wave equations for the incident and diffracted acoustic pressure). A domain decomposition with an MPI distributed memory scheme has been carried out so as to run the problem at the MareNostrum computer cluster, of the Barcelona Supercomputing Centre (BSC). A period of 10.8 ms with a time step of $\Delta t = 5 \times 10^{-6}$ s has been simulated. The reader is referred to [33] for full details on the numerical simulations and the above-outlined results.

5.2 *Aeroacoustics of an Opening Teeth-Shaped Obstacle*

To demonstrate the extended splitting approach for domains with moving boundaries (see Sect. 3.3), and to test as well the numerical proposal in Sect. 4, we have considered a two-dimensional example. This consists of a duct with a teeth-shaped obstacle near to its exit, which evolves from a minimum opening of 3 mm to a maximum one of 18 mm (see Fig. 3). A velocity of $U_0 = 2.4$ m/s is imposed at the duct entrance and no-slip conditions are considered for the flow at the duct walls. The latter are also

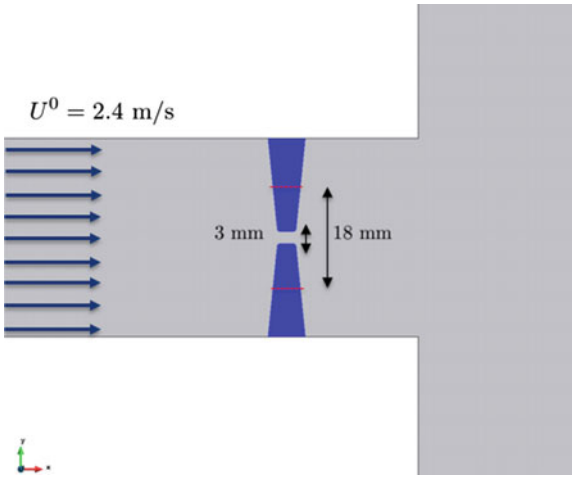

Fig. 3 Scheme of the computational domain close to the duct exit. The obstacle evolves from minimum to maximum opening

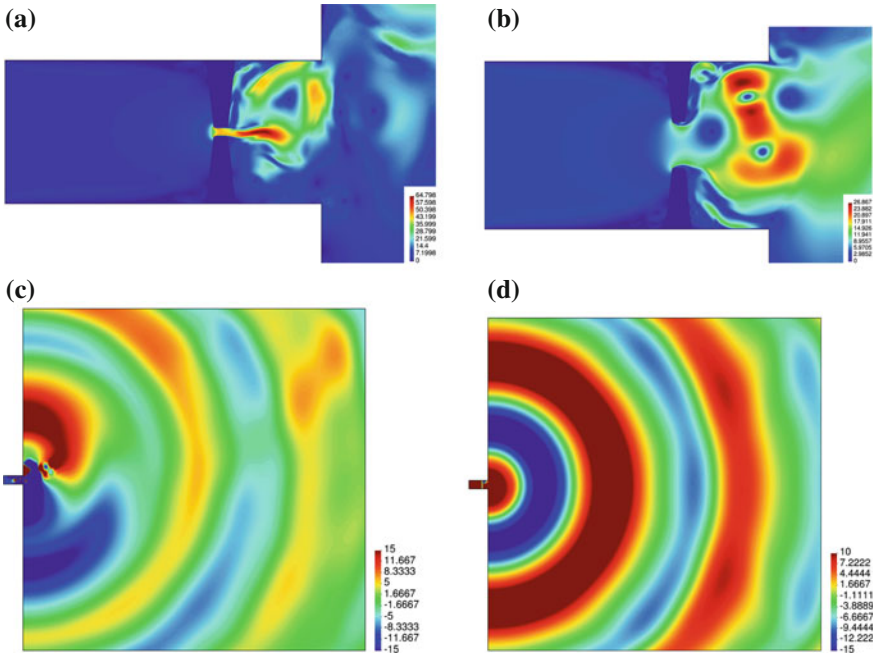

Fig. 4 Opening teeth-shaped obstacle: **a** velocity snapshot at minimum opening, **b** velocity profile at maximum opening, **c** incident acoustic pressure at minimum opening, **d** diffracted acoustic pressure at minimum opening

considered as being acoustically rigid, and a Sommerfeld non-radiating condition is imposed at the outer boundaries of the computational domain.

The results of the simulations are presented in Fig. 4. When the opening is minimum, an oscillating jet is developed after the obstacle, which results in the generation of intense flow noise after the obstacle. A snapshot of the velocity field at minimum opening is shown in Fig. 4a. As the teeth open, the jet stops oscillating and transitions to a fully developed turbulent flow, which radiates in a much weaker fashion (see Fig. 4b for a velocity snapshot at maximum opening). In Fig. 4c, we have plotted the incident pressure field for the minimum opening situation, when radiation is more intense, whereas a snapshot of the diffracted one is given in Fig. 4d. The diffracted component clearly dominates at the far field, as expected.

6 Conclusions

In this book chapter, we have first revisited a strategy for CAA at low Mach numbers, which allows one to compute the separate contributions of the incident flow noise, and of the noise diffracted by a stationary rigid body, on the acoustic pressure at

a point far away from the aeroacoustic sources. The strategy avoids some of the difficulties of Curle's analogy when resorting to incompressible computational fluid dynamics to compute the acoustic source terms, and only requires a single FEM code, as opposed to hybrid approaches to CAA. As an application, we have shown how the method could be used to produce a fricative sound like /s/, providing useful information of its underlying generation mechanisms.

Yet, the core of this work has consisted in extending the above approach to deal with aerodynamic sound generation in domains with moving boundaries. The standard irreducible wave equation has proved inadequate for such purposes, and the splitting strategy into incident and diffracted acoustic components has consequently been applied to the wave equation in mixed form. Hence, not only the pressure but also the acoustic particle velocity has become split into components. However, the Galerkin FEM for mixed problems is known to fail if an equal interpolation is used for both the acoustic pressure and velocity fields, so a stabilization approach has been presented to remedy this problem. Finally, an example consisting of a flow impinging on a teeth-shaped obstacle placed close to the exit of a duct, and transitioning from a minimum gap opening to a bigger one, has illustrated the potential of the formulation.

References

1. Badia, S., Codina, R., Espinoza, H.: Stability, convergence and accuracy of stabilized finite elements methods for the wave equation in mixed form. SIAM J. Numer. Anal. **52**, 1729–1752 (2014)
2. Bailly, C., Bogey, C.: Contributions of computational aeroacoustics to jet noise research and prediction. Int. J. Comput. Fluid Dyn. **18**(6), 481–491 (2004)
3. Bailly, C., Bogey, C., Gloerfelt, X.: Some useful hybrid approaches for predicting aerodynamic noise. Comptes Rendus Mécanique **333**(9), 666–675 (2005)
4. Bogey, C., Bailly, C., Juvé, D.: Numerical simulation of sound generated by vortex pairing in a mixing layer. AIAA J. **38**(12), 2210–2218 (2000)
5. Chiandussi, G., Bugeda, G., Oñate, E.: A simple method for automatic update of finite element meshes. Int. J. Numer. Method. Biomed. Eng. **16**(1), 1–19 (2000)
6. Codina, R.: Stabilized finite element approximation of transient incompressible flows using orthogonal subscales. Comput. Methods Appl. Mech. Eng. **191**, 4295–4321 (2002)
7. Codina, R.: Finite element approximation of the hyperbolic wave equation in mixed form. Comput. Methods Appl. Mech. Eng. **197**(13–16), 1305–1322 (2008)
8. Codina, R., González-Ondina, J., Díaz-Hernández, G., Principe, J.: Finite element approximation of the modified Boussinesq equations using a stabilized formulation. Int. J. Numer. Meth. Fluids **57**(9), 1249–1268 (2008)
9. Codina, R., Principe, J., Guasch, O., Badia, S.: Time dependent subscsales in the stabilized finite element approximation of incompressible flow problems. Comput. Methods Appl. Mech. Eng. **196**(21–24), 2413–2430 (2007)
10. Crighton, D.: Basic principles of aerodynamic noise generation. Prog. Aerospace Sci. **16**(1), 31–96 (1975)
11. Crighton, D., Dowling, A., Ffowcs Williams, J., Heckl, M., Leppington, F.: Modern Methods in Analytical Acoustics-Lecture Notes. Springer-Verlag (1992)
12. Curle, N.: The influence of solid boundaries upon aerodynamic sound. Proc. R. Soc. Lond. A **231**(1187), 505–514 (1955)

13. Doak, P.: Acoustic radiation from a turbulent fluid containing foreign bodies. Proc. R. Soc. Lond. A **254**(1276), 129–146 (1960)
14. Espinoza, H., Codina, R., Badia, S.: A Sommerfeld non-reflecting boundary condition for the wave equation in mixed form. Comput. Methods Appl. Mech. Eng. **276**, 122–148 (2014)
15. Ewert, R., Schröder, W.: Acoustic perturbation equations based on flow decomposition via source filtering. J. Comput. Phys. **188**(2), 365–398 (2003)
16. Fujiso, Y., Nozaki, K., Van Hirtum, A.: Towards sibilant physical speech screening using oral tract volume reconstruction: some preliminary observations. Appl. Acoust. **96**, 101–107 (2015)
17. Gloerfelt, X., Pérot, F., Bailly, C., Juvé, D.: Flow-induced cylinder noise formulated as a diffraction problem for low Mach numbers. J. Sound Vib. **287**(1), 129–151 (2005)
18. Guasch, O., Arnela, M., Codina, R., Espinoza, H.: A stabilized finite element method for the mixed wave equation in an ALE framework with application to diphthong production. Acta Acust. United Acust. **102**(1), 94–106 (2016)
19. Guasch, O., Codina, R.: An algebraic subgrid scale finite element method for the convected Helmholtz equation in two dimensions with applications in aeroacoustics. Comput. Methods Appl. Mech. Eng. **196**(45–48), 4672–4689 (2007)
20. Guasch, O., Codina, R.: Computational aeroacoustics of viscous low speed flows using subgrid scale finite element methods. J. Comput. Acoust. **17**(3), 309–330 (2009)
21. Guasch, O., Pont, A., Baiges, J., Codina, R.: Concurrent finite element simulation of quadrupolar and dipolar flow noise in low Mach number aeroacoustics. Comput. Fluids **133**, 129–139 (2016)
22. Guasch, O., Sánchez-Martín, P., Pont, A., Baiges, J., Codina, R.: Residual-based stabilization of the finite element approximation to the acoustic perturbation equations for low Mach number aeroacoustics. Int. J. Numer. Meth. Fluids **82**(12), 839–857 (2016)
23. Hueppe, A., Kaltenbacher, M.: Spectral finite elements for computational aeroacoustics using acoustic perturbation equations. J. Comput. Acoust. **20** (2), 1240005 (2012)
24. Huerta, A., Liu, W.: Viscous flow with large free surface motion. Comput. Methods Appl. Mech. Eng. **69**, 277–324 (1988)
25. Hughes, T.: Multiscale phenomena: Green's function, the dirichlet-to-neumann formulation, subgrid scale models, bubbles and the origins of stabilized formulations. Comput. Methods Appl. Mech. Eng. **127**, 387–401 (1995)
26. Hughes, T., Feijo, G., Mazzei, L., Quincy, J.: The variational multiscale method, a paradigm for computational mechanics. Comput. Methods Appl. Mech. Eng. **166**, 3–24 (1998)
27. Hughes, T., Liu, W., Zimmermann, T.: Lagrangian-eulerian finite-element formulation for compressible viscous flows. Comput. Methods Appl. Mech. Eng. **29**, 329–349 (1981)
28. Kaltenbacher, M., Escobar, M., Becker, S., Ali, I.: Numerical simulation of flow-induced noise using LES/SAS and lighthill's acoustic analogy. Int. J. Numer. Meth. Fluids **63**(9), 1103–1122 (2010)
29. Lighthill, M.J.: On sound generated aerodynamically I. General theory. Proc. R. Soc. Lond. A **211** (1107), 564–587 (1952)
30. Morse, P.M., Ingard, K.U.: Theoretical Acoustics. McGraw-Hill, New York (1968)
31. Oberai, A.A., Roknaldin, F.R., Hughes, T.J.: Computation of trailing-edge noise due to turbulent flow over an airfoil. AIAA J. **40**(11), 2206–2216 (2002)
32. Pont, A., Codina, R., Baiges, J.: Interpolation with restrictions between finite element meshes for flow problems in an ALE setting. Int. J. Numer. Meth. Eng. **110**(13), 1203–1226 (2017)
33. Pont, A., Guasch, O., Baiges, J., Codina, R., Van Hirtum, A.: Computational aeroacoustics to identify sound sources in the generation of sibilant /s/. Submitted (2017)
34. Roger, M.: Aeroacoustics: some theoretical background–The acoustic analogy, Anthoine, J., Colonius, T. (Eds.), vol. LS 2006-05. Von Karman Institute, Rhode-St-Genese (2006)
35. Van Hirtum, A., Fujiso, Y., Nozaki, K.: The role of initial flow conditions for sibilant fricative production. J. Acoust. Soc. Am. **136**(6), 2922–2925 (2014)
36. Williams, J.F., Hawkings, D.L.: Sound generation by turbulence and surfaces in arbitrary motion. Phil. Trans. Roy. Soc. A **264**(1151), 321–342 (1969)

Part V
Vibroacoustic Response–Numerical Methods

Panel Vibrations Induced by Supersonic Wall-Bounded Jet Flow from an Upstream High Aspect Ratio Rectangular Nozzle

Stephen A. Hambric, Matthew D. Shaw and Robert L. Campbell

Abstract The panel vibrations induced by fluctuating wall pressures within wall-bounded jet flow downstream of a high aspect ratio rectangular nozzle are simulated. The wall pressures are calculated using a Hybrid RANS/LES method, where LES models the large-scale turbulence in the shear layers downstream of the nozzle. The convecting turbulence in the shear layers loads the structure in a manner similar to that of turbulent boundary layer flow. However, at supersonic discharge conditions the shear layer turbulence also scatters from shock cells, generating backward-traveling surface pressure loads that drive the structure at low frequencies. The panel is rectangular with clamped edges along the sides oriented in the flow direction and free edges at the nozzle discharge and downstream edge. The panel modes of vibration are simulated with Finite Element Analysis. The structural vibration time histories are simulated by Fourier transforming the loading to the complex frequency domain, combining with the structural frequency response functions and inverse transforming the response back to the time domain. Simulated wall pressures and structural vibration agree well with measurements at on-design and underexpanded (about 50% higher pressure ratio) nozzle operating conditions. Filtering the negative wavenumber components from the loading and recomputing the structural response shows that the backward-traveling loading is responsible for about 12% of the overall structural vibration at on-design conditions and 25% of the response at underexpanded conditions.

1 Introduction

The wall-bounded jet discharge flow from an embedded aircraft propulsion system 'washes' over the downstream aft deck [2]. At high speeds, the jet discharge flow is supersonic and highly turbulent, inducing strong structural vibration and alternating

S. A. Hambric (✉) · M. D. Shaw · R. L. Campbell
Applied Research Lab, Penn State University, PO Box 30,
State College, PA 16804, USA
e-mail: sah19@arl.psu.edu

E. Ciappi et al. (eds.), *Flinovia—Flow Induced Noise and Vibration Issues and Aspects-II*,
https://doi.org/10.1007/978-3-319-76780-2_13

stresses in the deck structure. Alternating stresses that exceed allowable material limits can cause fatigue cracking and failure.

The vibration response of plates driven by surface pressure fluctuations beneath spatially homogeneous subsonic TBL flow has been studied extensively [3]. In these studies, it is common to use wavenumber analysis to determine the types of pressure fluctuations which best excite structural modes of vibration. For subsonic flows on aircraft and high-speed vehicles, wavenumber analysis shows that the fluctuating pressures induced by the convecting flow (commonly called the 'convective ridge' in a wavenumber spectrum) usually excite flexural waves in structures most efficiently. For slower moving structures, such as marine vehicles, the low-wavenumber subconvective forcing components are usually most important [1].

However, insufficient attention has been given to spatially inhomogeneous supersonic flow excitation of structures, such as those just downstream of embedded jet nozzles on very high-speed aircraft. The jet flow washing over a downstream panel includes the usual convecting turbulent eddies (most prominently in the shear layer originating from the top lip of the nozzle), but the core flow also contains shock cells which interact with the convecting turbulence to form positive and negative propagating pressure pulsations which also excite the underlying structure.

The combination of convecting and scattered wall pressure sources in supersonic jet wash excitation is much more complex than the simpler subsonic TBL wall pressure field, with uncertain interaction of the wall pressures with structural modes. An important and unresolved question is the relative importance of the jet shear layer–shock cell interaction terms compared to the traditional convective excitation components. We explore this subject with a converging–diverging rectangular nozzle (8:1 ratio) discharge flow excitation of a downstream flat rectangular plate.

CFD Hybrid RANS/Large Eddy Simulation (LES) analyses of the wall pressure fluctuations downstream of the nozzle discharge for subsonic and supersonic discharge flow [7] are applied to a finite element model of a structural panel, and time histories and frequency spectra are computed using a modal summation approach. The pressure and vibration calculations are compared to measurements made at the United Technologies Research Center (UTRC) to confirm the reasonableness of the simulation procedures [6, 10]. The calculations are further analyzed using wavenumber analysis to assess the relative importance of convective and turbulence/shock cell interaction contributions to the panel response. The wavenumber analyses are performed for subsonic, on-design, and underexpanded nozzle flow conditions.

2 Approach

2.1 Problem Definition

A converging–diverging round-to-rectangular nozzle with 8:1 aspect ratio and downstream plate structure are shown in Fig. 1. Also shown in Fig. 1 is an image of the

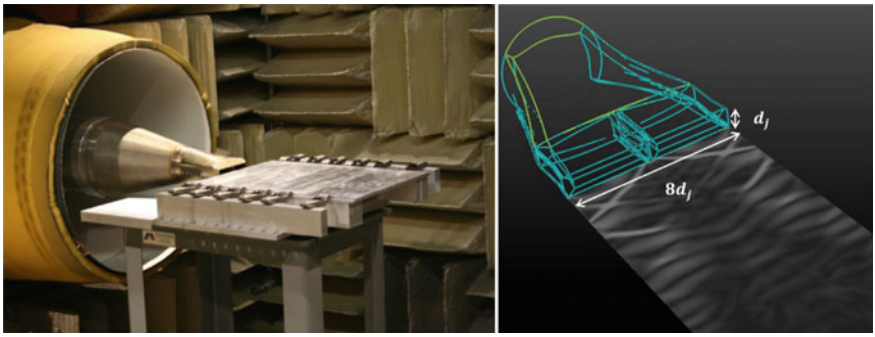

Fig. 1 Photograph of the test nozzle and aft plate (left) and schematic of the nozzle with representative supersonic flow numerical density gradient at the wall (right)

density gradient at the wall computed using CFD analysis at on-design nozzle conditions. Shock cells are clearly visible (the lighter sections) in the CFD wall solution. A vertical septum subdivides the discharge nozzle into two 4:1 aspect ratio sections, leading to shock cell patterns symmetric about the nozzle center. More details on the test hardware and facility at UTRC are in [10]. In this paper, we nondimensionalize the nozzle and plate hardware with the nozzle height d_j.

Converging–diverging nozzle discharge flow varies significantly with nozzle pressure ratio (NPR). Low NPR conditions lead to subsonic jet discharge flow. As operating pressure increases, the supersonic portion of the jet flow moves downstream of the nozzle discharge, leading to shock cell formation. At on-design NPR for the nozzle studied here, there are several downstream shock cells as shown in the image in Fig. 1. As pressure further increases, the discharge flow becomes 'underexpanded,' with stronger shock cells which persist further downstream. For wall-bounded jets, the shocks and expansions reflect off the wall, leading to more complex interactions with the shear layer and TBL flow. For more details on the physics of the wall-bounded jet flow, see the PhD thesis by Lurie [8].

A flat rectangular aluminum plate with aspect ratio of $a/b = 0.845$ (where a is length and b is width, and $h/d_j = 0.22$, where h is thickness) is directly downstream of the nozzle. The test plate is wider than the nozzle discharge (19.55 d) and extends 16.52 d downstream. The edges adjacent to the nozzle and downstream are free, and the edges along the sides in the direction of flow are approximately clamped with a series of screws. A baffle extends around the sides and past the downstream edge (a total surface size of 33 d long and 26 d wide), so that only wall-bounded surface pressures generated by the exhausting jet excite the structure. Simulations and measurements of the flow and structural response were computed for three conditions: subsonic (roughly 50% lower than on-design flow rate), on-design, and underexpanded (roughly 50% higher than on-design flow rate). These conditions may be quantified using the parameter suggested in [10]:

$$\beta = \frac{M_j^2 - M_d^2}{M_d^2}$$

where M_j is the ideally expanded jet Mach number for condition j and M_d is the on-design Mach number. Using this definition, $\beta = -0.55$ for the subsonic case, $\beta = 0$ for the on-design case, and $\beta = 0.53$ for the underexpanded conditions.

2.2 Measurement Procedures

Measurements of the panel vibration and wall pressure fluctuations were made at the United Technologies Research Center (UTRC), under sponsorship provided by Pratt and Whitney. For details, see [6, 10]. For completeness, a short overview is provided here. Static and fluctuating wall pressures were measured using arrays of Kulite pressure sensors (XCS-152) flush-mounted into a very thick downstream plate. The thick plate resonance frequencies are out of the measurement range of interest to minimize vibration contamination of the wall pressure measurements. Vibrations were measured with accelerometers attached to the thinner plate described in the previous section. The plate was replaced by a window to take Schlieren photographs of the velocity fields, which clearly show shock cell patterns (see the images in [10]).

2.3 Analysis Methodology

Detailed analyses of the time-varying flow, resulting wall surface pressures, and structural vibration response were conducted using a combination of CFD Hybrid RANS/LES [7] and ARL/Penn State's CHAMP (Combined HydroAcoustic Modeling Programs) procedure [4, 5]. Previously, CHAMP had been applied only to the analysis of time-averaged vibration and radiated sound frequency spectra, using a multiple-input/multiple-output random analysis approach. However, for alternating stress and fatigue assessments, the peak excitation and response over time are required so that extreme events are properly captured. Therefore, CHAMP was expanded to allow for time-domain analysis.

A flowchart comparing frequency- and time-domain CHAMP procedures is shown in Fig. 2. The standard CHAMP method is summarized at the top of the chart, where a cross-spectral density of the excitation pressure field $|P(f)|^2$ is pre- and post-multiplied by frequency response function (FRF) matrices H, which represent the FRFs between input forces on the surface and vibration at desired response locations. The FRFs may be computed using finite element (FE) or analytic models. In CHAMP, the FRFs are based on modal summations to reduce computational resource requirements, so that the overall response calculation is based on computing modal forcing functions (analogous to joint acceptance functions), then modal response

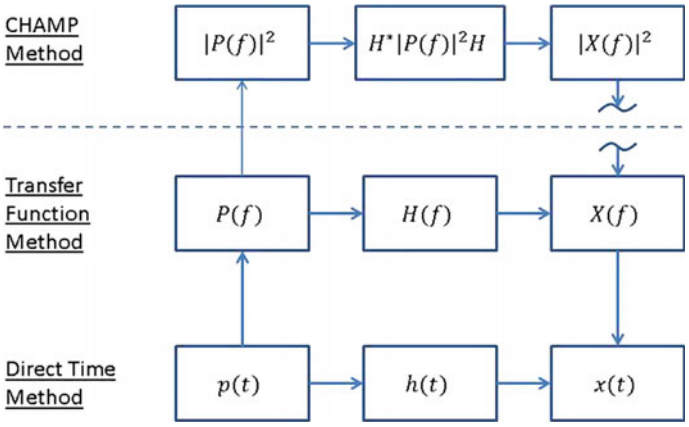

Fig. 2 Flowcharts of forced response calculation procedures

amplitudes, and finally reconstructing response based on the mode shapes. Details are available in [4, 5]. The output $|X(f)|^2$ is a cross-spectral density matrix over all response locations. This procedure, however, provides only averaged spectral densities of the response, since the input power spectral density matrix is also a spectral average.

To capture any extreme transient events in the excitation and subsequent vibration response, a time-integration procedure may be used (the bottom of the diagram). This is possible when a full space-time representation of the wall pressure excitation field is available (which is the case in this study). However, time-integration calculations are computationally expensive and require excessive storage resources. Instead, a transfer function approach is used, where the excitation time history is transformed into complex Fourier coordinates (assuming the time history repeats continuously) and multiplied by the complex FRF matrix to compute complex output response. This response may be inverse-transformed to the time domain. Once again, a modal summation approach is used to reduce computational requirements. The transfer function approach requires orders of magnitude less computational time and storage space, and is not influenced by initial transient response artifacts. Prior to applying the procedure to the problem here, the procedure was confirmed using a simple oscillator demonstration in [9].

2.3.1 Simulated and Measured Surface Pressures

The discharging jet flow causes different types of wall pressure fluctuations acting on the structure. A turbulent boundary layer forms and grows as flow propagates along the surface. Also, shear layers form adjacent to the top lip of the nozzle and along the sides of the nozzle and septum, generating strong coherent structures which grow and decelerate as the shear layers diffuse downstream. For supersonic flow (on-design and

underexpanded conditions), shock cells form as in the example shown in Fig. 1. The shock cells by themselves do not excite the structure dynamically, but the TBL and shear layer turbulence interact with the shock cells, causing the entire shock 'web' to oscillate. Also, pressure, acoustic, and entropic waves scatter from the interaction between the turbulence and the shock cells, propagating forward and backward. Correlation analyses described in [10] indicate backward-propagating wall pressures near the nozzle discharge where the shock cells are strongest. Downstream, the shock cells weaken, and fluctuating pressures are dominated by the usual convecting turbulence (traveling at about 60% of the bulk velocity).

These phenomena are difficult to simulate. Time-accurate CFD methods which resolve both the mean and fluctuating flow fields, including turbulence, are required. For flow-field predictions, a hybrid compressible RANS/LES method, termed the LESB-shield model [7], was developed. The hybrid method relies on the baseline RANS model to simulate the small unresolved scales within the boundary layer and the initial regions of the developing shear layer. LES simulates the shear layers from the upper lip, side walls, and septum. Analysis to date shows that for jet discharge flow the TBL wall pressures are less significant than those caused by the shear layer turbulence. Future simulations may include TBL wall pressure excitation so that its relative importance may be assessed.

The RANS part of the model used a two-equation Menter SST turbulence model which blends near-wall k-ω modeling with k-ε modeling in the shear layer. Fifteen million grid points comprise the multi-zoned structured analysis grid, which is refined in the wall normal direction to resolve high gradients in the outer shear layer. Uniform flow is specified within the nozzle (3.5 d upstream), with constant static pressure specified along all outflow boundaries. No-slip boundary conditions are applied to the walls.

The CFD analyses are computationally intensive and were limited by computer resources to 205,000 time steps, of which 6,213 were used in the structural analysis (a much finer time step size is required for converged CFD solutions than is necessary for FE structural response analysis). The nondimensional time step size used for structural analysis varies with NPR, but is roughly $\mathrm{dt}(U/d) \sim 2$. Only the portion of the time histories free of initial transients was applied to the structural model. The short time histories likely have not captured the most extreme events expected in these types of flow fields. The measured data, however, are sufficiently extensive so that better extreme value statistics may be calculated. For details, see the PhD thesis by Shaw [9].

Figure 3 shows snapshots over time of the wall pressure distribution field computed for on-design nozzle conditions. Animations of the pressure distributions for all three conditions are available in Appendix G of [9]. Static shock cell pressure peaks are evident adjacent and just downstream of the nozzle discharge, and convecting wall pressures are more clear downstream where the shock cells weaken and eventually disappear as the flow decelerates. The shock cell peak pressures are about 15% of the dynamic head, and the convecting wall pressure peaks are about half the shock cell amplitudes.

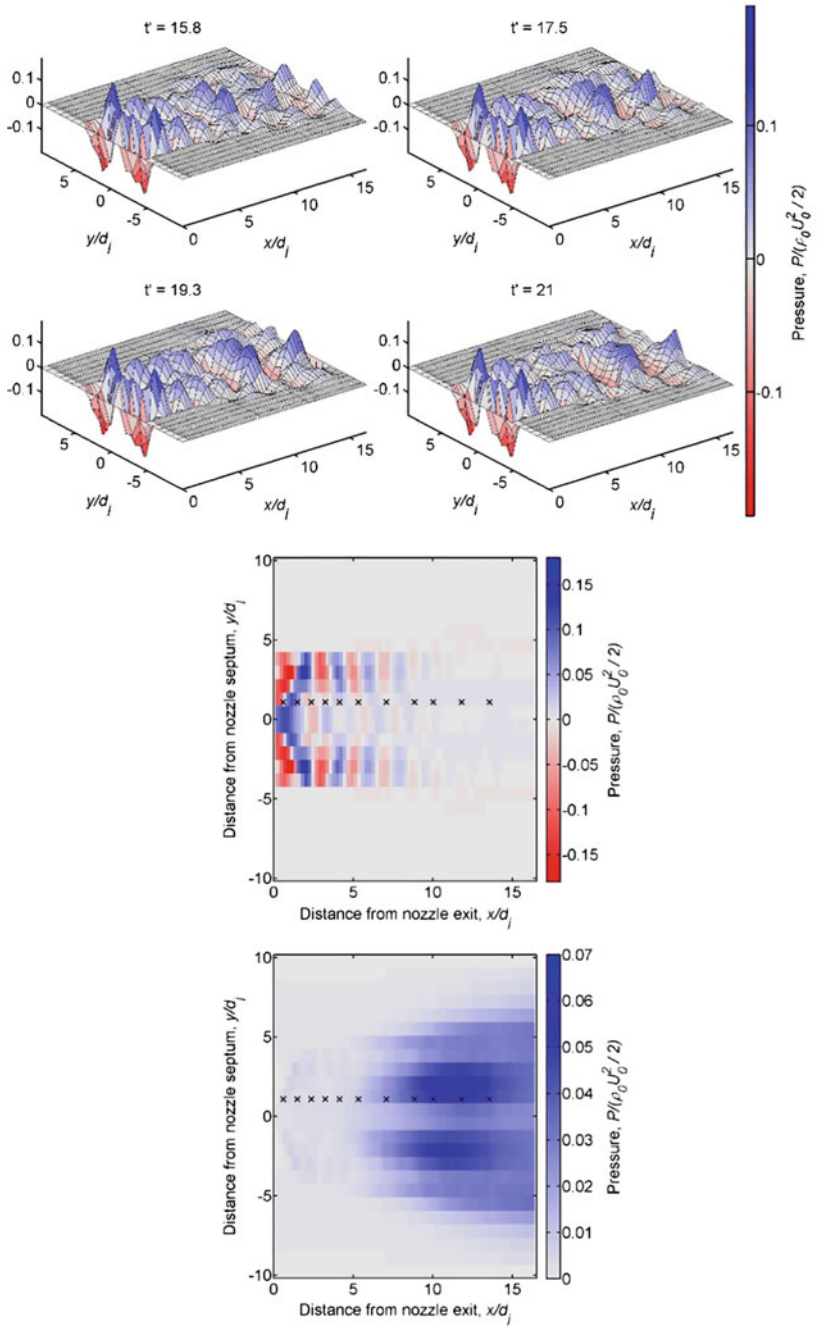

Fig. 3 Top: 'snapshots' of wall pressure at on-design conditions; middle: normalized mean pressure with 'x' markers denoting pressure measurement locations; bottom: normalized RMS values of fluctuating pressures. Pressure is normalized by dynamic head, t' is tU/d_j where d_j is nozzle height, and x and y are normalized by nozzle height

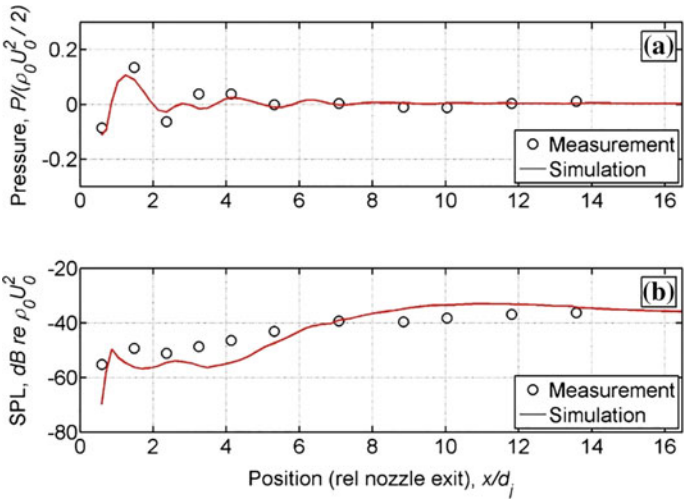

Fig. 4 Comparison of normalized **a** mean and **b** RMS CFD and measured pressures at on-design conditions, with distance scaled by nozzle height and pressures scaled by dynamic pressure

Figure 4 compares measured and simulated mean (static) and RMS (dynamic) total pressures for on-design nozzle conditions along a streamwise array of measurement points halfway between a nozzle end wall and the center septum. The simulated and measured pressures agree reasonably well, but the simulations are slightly low near the nozzle. The lower than expected RMS pressures may be due to neglecting the TBL wall pressure component, along with the fluctuating components in the initial regions of the shear layers in the simulations (recall both the TBL flow and the near-nozzle shear layers are modeled with RANS instead of LES). However, the plot also shows that the downstream fluctuating pressures due to the shear layer turbulence are much stronger and dominate the structural loading and subsequent structural vibration response, so that the discrepancies near the nozzle are less important. Figure 5 compares measured and simulated wall pressure spectra at two locations: one near the nozzle and the other further downstream. As with the RMS comparisons, the spectra match best further downstream where the shear layer turbulence is dominant. The CFD results, while not in perfect agreement with the measurements, are sufficiently representative to be used in structural vibration simulations to assess the relative importance of the convecting and nonconvecting structural loading.

The CFD simulations may be processed using correlation methods similar to Winkler's to estimate the propagation velocities of the peak wall pressures. The dominant propagation velocities are computed from the time delays in the peak correlation between pressures at two points and the separation distances. The distribution of peak convective velocities, normalized by ambient sound speed, is shown in Fig. 6 for subsonic, on-design, and underexpanded conditions. As β increases (corresponding to NPR increase), more backward-traveling surface pressures are evident near the nozzle discharge.

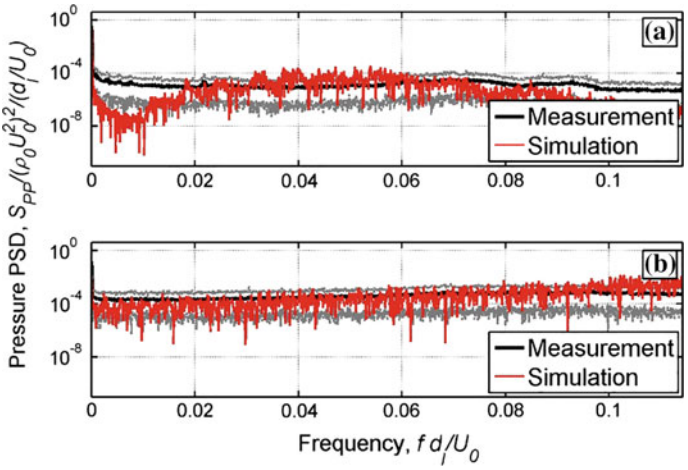

Fig. 5 Comparison of simulated and measured pressure power spectral densities for on-design conditions at two locations along the line denoted in Fig. 3; **a** 2.4 nozzle heights downstream and **b** 11.8 nozzle heights downstream. The dotted gray curves denote ±90% variability spread in the measured data. Frequency is scaled to Strouhal number with respect to nozzle height and bulk velocity and spectra are scaled by dynamic head

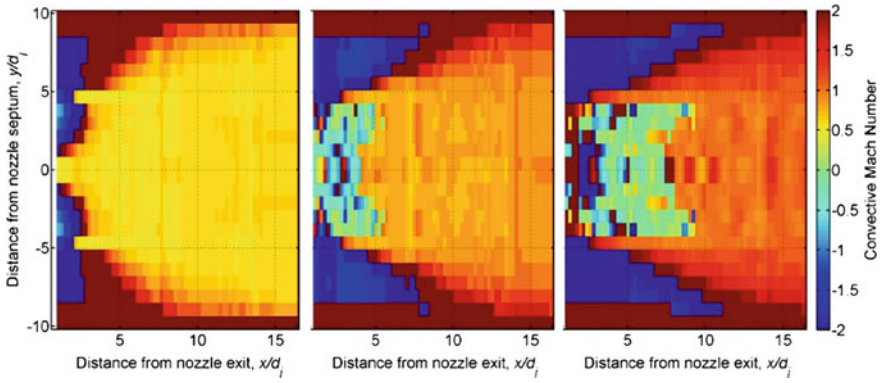

Fig. 6 Distribution of effective 'convective' Mach number over plate surface based on correlation analysis. Top—subsonic ($\beta = -0.55$), middle—on-design ($\beta = 0$), bottom—underexpanded ($\beta = 0.53$). Dark blue (negative) and dark red (positive) regions outside the jet plume are irrelevant

2.3.2 Finite Element Structural Modeling and Modes

A finite element model was constructed of the structure using Nastran thick plate elements, as shown in Fig. 7. The nodal spacing is coincident with the grid used in the CFD simulations so that wall pressure time histories could be applied directly to the FE model without spatial interpolation. Simulations and measurements are compared at two locations: Location 1 is at the center of the jet from the upper

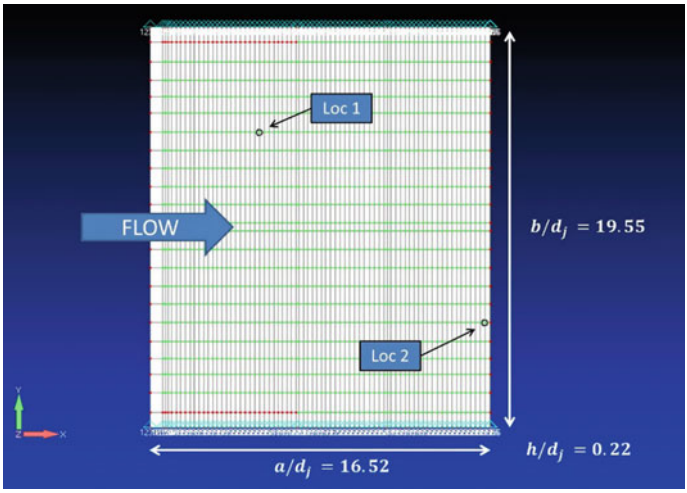

Fig. 7 Finite element model of the structural plate. a, b, and h are the length, width, and thickness, respectively. Flow travels from left to right. Measurements and simulations are compared at the two locations denoted in the model

section of the nozzle and close to the nozzle discharge ($x/d_j = 5.3$, $y/d_j = 4.6$), and location 2 is at the center of the jet from the lower nozzle section at the panel trailing edge ($x/d_j = 16.2$, $y/d_j = -4.6$). The leading and trailing edges of the plate are free, and the streamwise edges are clamped. Using the commercial FE solver NX Nastran, the mass-normalized displacement mode shapes and resonance frequencies of the plate were calculated. The first four mode shapes are shown in Fig. 8: the (0, 1), (1, 1), (2, 1), and (0, 2) modes, where the modes are numbered with the ordered pairs (m, n), where m and n represent the number of half wavelengths in the streamwise and cross-stream directions, respectively.

The resonance frequencies calculated for the FE model assume no fluid loading and ideal boundary conditions. In situ resonance frequencies were measured for the plate without flow using Experimental Modal Analysis (EMA) by UTRC with a force hammer and accelerometers. The EMA resonance frequencies are consistently lower than the idealized FE model simulations, due to imperfect boundary condition modeling. To compensate, the edge boundary conditions were softened using rotational springs at each node along the clamped boundaries, with the rotational stiffness adjusted to tune the resonance frequency of the (1, 1) mode to the measured frequency. All other FE frequencies are shifted downward as well.

Damping loss factors applied to FE models may be estimated based on plate construction and material properties. Predicting damping for structural joints such as the edge boundary conditions, however, is challenging and is the subject of future research. EMA techniques extract modal damping factors along with resonance frequencies, which may be input to the FE modes for forced response calculations.

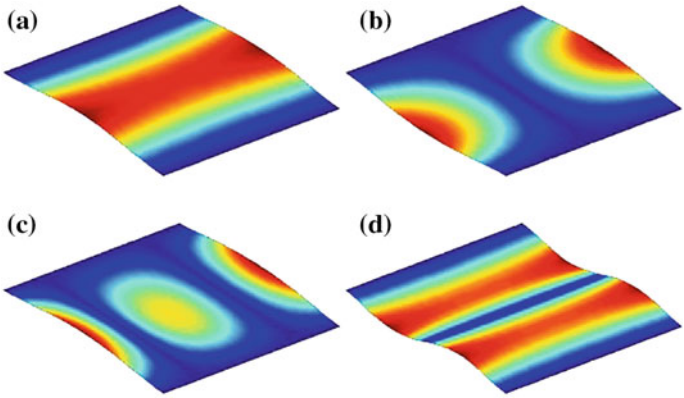

Fig. 8 First four displacement mode shapes for the structural plate computed using NX Nastran: **a** (0, 1) mode, **b** (1, 1) mode, **c** (2, 1) mode, and **d** (0, 2) mode. The jet flows from bottom left to top right

However, resonance frequencies and loss factors change further when the plate is driven with the jet flow, due to aerodynamic loading and/or static preloading of the edge boundaries (thereby affecting frictional stiffnesses and damping). Therefore, operational modal analyses (OMAs) using the software Artemis were also performed by UTRC using measured accelerometer data for each jet flow condition, and flow-dependent resonance frequencies and modal damping factors were extracted.

Figure 9 compares the measured and simulated panel resonance frequencies and the measured damping at quiescent (EMA) and on-design flow (OMA) conditions. The FE resonance frequency estimates (tuned to the edge boundary condition springs) are generally within $\pm 10\%$ of those measured. The measured resonance frequencies are lower when at on-design flow conditions, due to aerodynamic effects, as well as static preloading on the boundaries (the plate is pulled upward and pushed downward at different locations due to the static pressure distribution along the surface). The damping is generally between 1 and 4% of critical, except for the lowest order modes, which have much higher levels.

Since the main focus of this work is simulating flow-excited structural response and determining the components of the supersonic jet flow most responsible for structural vibration (and not on simulating edge effects on resonances and damping), the FE modal parameters are adjusted to those extracted using the OMA results. Since we apply a modal summation approach, this adjustment is straightforward, as the resonance frequencies and loss factors are simply specified as inputs to the calculation. The mass-normalized mode shapes are not adjusted, however. Any differences between measured and simulated vibrations, therefore, are due mostly to inaccuracies in the CFD forcing function simulations.

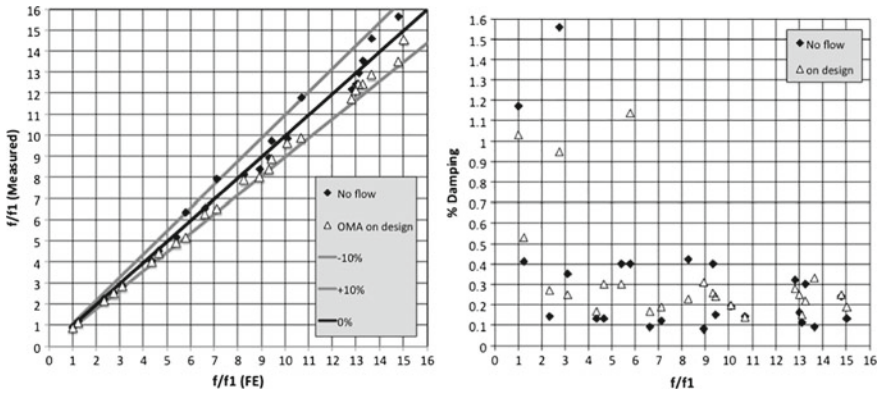

Fig. 9 Left—Measured versus FE modal frequencies; right—modal loss factors at quiescent (no flow, via EMA) and on-design flow (via OMA) conditions. Frequencies are normalized by the fundamental frequency of (0, 1) mode

3 Results

3.1 Vibration Time Histories and Frequency Spectra

A few displaced shapes extracted from the computed vibration time history for on-design nozzle conditions are shown in Fig. 10. Animations of the plate vibration at all three conditions are in Appendix G of [9]. The shapes include both static and dynamic displacements (the downstream edge, for example, has a strong downward static displacement). The dynamic response is dominated by the low-order modes shown in Fig. 8. The displacements are normalized by flow and panel parameters:

$$\left[(ab)^2/D\right]\left(\rho U^2\right)$$

where D is the flexural rigidity, ρ is fluid density, and U is the bulk flow velocity. This normalization accounts for the flow excitation as well as the panel stiffness and surface area.

The computed and measured RMS displacements are compared in Table 1 for the two locations shown in Fig. 7. The displacements for subsonic flow are about twice as high as the measured values. The displacements for supersonic flow at on-design and underexpanded conditions agree reasonably well. Since the FE panel parameters were adjusted to match those in the measurements, the discrepancies between the simulations and measurements are due mostly to errors in the CFD modeling. In particular, the downstream wall pressure fluctuations in the CFD simulations for subsonic flow are markedly higher than those measured, as shown in Fig. 11. Low et al. [7] suggest several improvements which may be pursued in the future to more

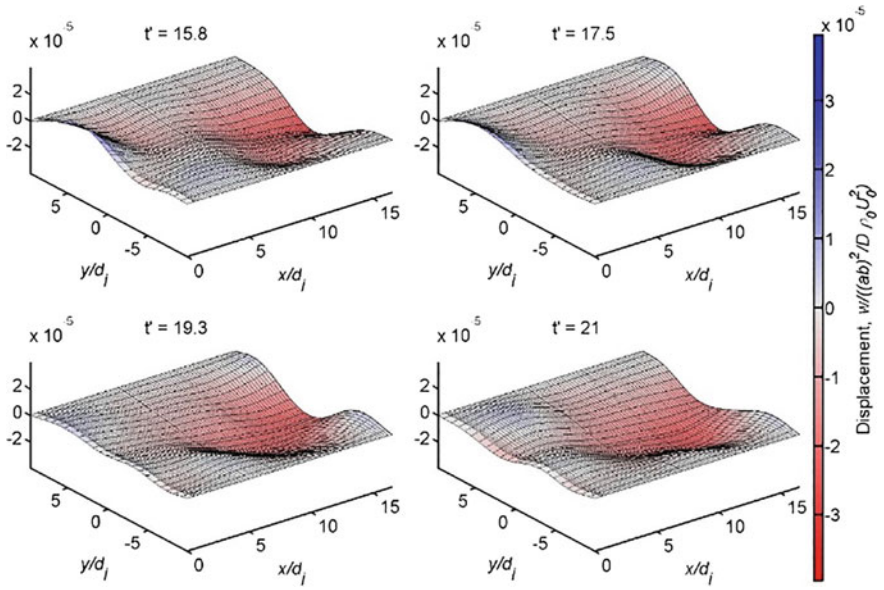

Fig. 10 Snapshots of normalized plate transverse displacement for on-design nozzle conditions. Left is at the nozzle discharge; right is downstream

Table 1 Measured and simulated RMS micro-displacements (normalized by mean static pressure and panel parameters) at two accelerometer locations

Case	$x/d_j = 5.3$, $y/d_j = 4.6$		$x/d_j = 16.2$, $y/d_j = -4.6$	
	Simulated	Measured	Simulated	Measured
Subsonic	13.2	6.53	22.7	12.8
On-design	4.55	3.13	7.92	5.83
Underexpanded	2.65	2.65	4.73	4.90

accurately capture near-nozzle shear layer effects, TBL wall pressures, and turbulence/shock cell interaction.

Simulated and measured normalized displacement spectra are compared in Fig. 12 for on-design and underexpanded conditions at location 1. The spectra agree reasonably well, with several strong resonance peaks evident in the plots. Most peaks are captured properly, with a few exceptions. The exceptions are due to mismatched modes of vibration in the FE model and measured data (recall the modal frequencies and loss factors were set to those inferred from the measured data). Since the number of accelerometers on the panel was limited, positive identification of higher order modes from the measured data is impossible, so that some modes were not properly set to their actual resonance frequencies and loss factors. Note also that the measured data were averaged over much longer time records, reducing the random

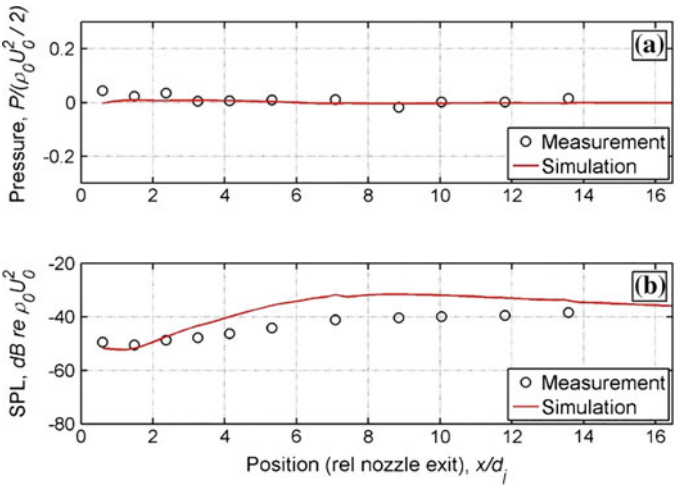

Fig. 11 Comparison of normalized **a** mean and **b** RMS CFD and measured pressures at subsonic ($\beta = -0.55$) conditions, with distance scaled by nozzle height and pressures scaled by dynamic pressure

error in the spectra. The simulated spectra were computed over a much shorter time history, increasing the random error in the plots.

The frequencies and spectra are normalized by flow and panel parameters. Frequency is plotted as Strouhal number (St) based on bulk flow velocity U_o and nozzle height d_j. Displacement spectra as a function of St are normalized by:

$$\left(\frac{(ab)\rho_o U_o^2}{\omega h^2\sqrt{E\rho_s}}\right)^2 (d_j/U_o)$$

where E and ρ_s are the Young's modulus and mass density of the plate.

3.2 *Wavenumber Transform Analysis of Dominant Forcing Terms*

The CFD and structural response simulations agree well enough with the measurements so that wavenumber transform studies of the simulated wall pressures were conducted to determine the relative importance of the forward and backward-traveling pressure loads. Positive wavenumber content in the loading corresponds mostly to shear layer turbulence convecting in the flow direction (recall there is no TBL wall pressure loading in the CFD simulations). Negative wavenumber content is associated mostly with the backward-traveling pressure, acoustic, and entropic waves associated with scattering of the shear layer turbulence from the shock cells.

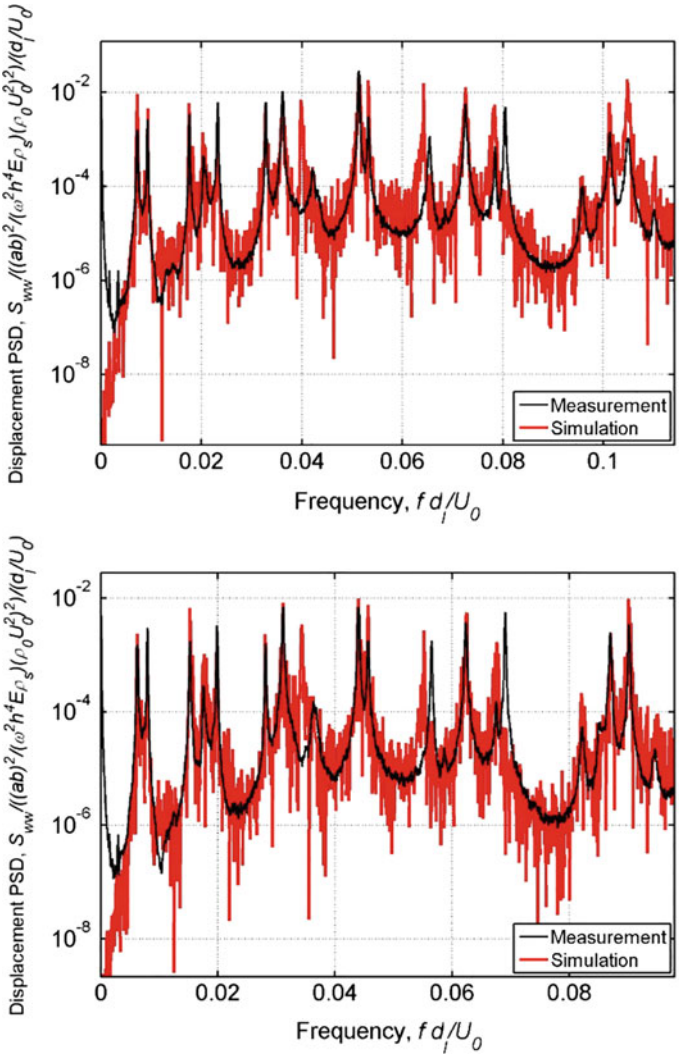

Fig. 12 Simulated and measured normalized displacement spectra for on-design nozzle conditions (top) and for underexpanded nozzle conditions (bottom) at location 1. The Strouhal number axis for the underexpanded calculation has been contracted to align the resonance frequencies with those on the on-design plot

A wavenumber decomposition of the pressure distribution is computed using:

$$S(k_x, k_y, f) = \iint F(x, y, f) e^{jk_x x} e^{jk_y y} dx dy$$

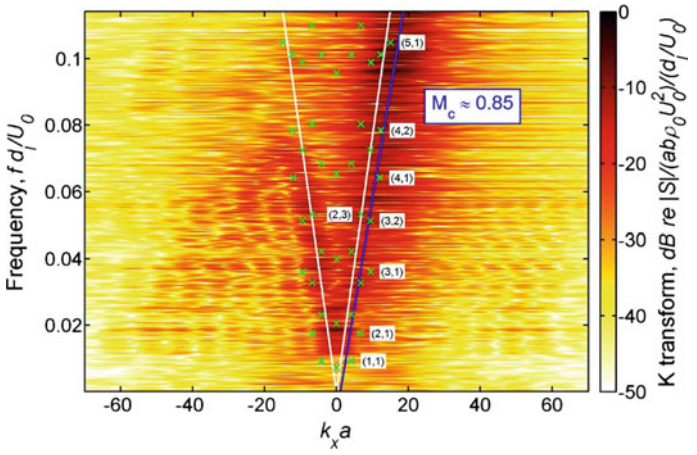

Fig. 13 Normalized streamwise wavenumber transform amplitude of on-design CFD surface pressures for ky = 0 versus nondimensionalized wavenumber $k_x a$ and Strouhal number. The blue line corresponds to the mean convective wavenumber, and the two white lines correspond to acoustic wavenumber. The modal wavenumbers are indicated with green 'x' symbols, with modes aligned with the convective wavenumbers annotated with mode order

where k_x and k_y are the wavenumbers in the x and y dimensions, respectively, $F(x, y, f)$ is the spatial variation of a function at frequency f, and $e^{-j\omega t}$ time dependence is assumed. Note that F and S are complex. $S(k_x, k_y, f)$ is called the wavenumber-frequency spectrum and is integrated separately for each frequency. Even though the integral is computed over all space, for the panel the spatial domain is truncated. This means that the wavenumber-frequency spectrum shows the average over the integrated region. For strongly inhomogeneous wall pressure distributions, the wavenumber transforms show peak regions that are spread over frequency and wavenumber. Computationally, the integral is most efficiently calculated using a fast Fourier transform (FFT), but this requires a uniform grid spacing in each dimension. The computational fluid dynamics (CFD) grid and, therefore, the plate finite element have nonuniform spacing, so the integral was performed manually.

Figure 13 shows a contour of the wavenumber transform of the streamwise-simulated wall pressures for $k_y = 0$ (where k_y is the cross-flow wavenumber) for on-design conditions. Along with the pressure contours, the white lines represent the acoustic wavenumber (ω/c_o), and the blue line represents a mean convective wavenumber (ω/U_c), where U_c is based on the overall bulk velocity (which is generally subsonic). The green symbols denote the modal wavenumbers of several mode shapes (ω/c_{mn}). The annotated wavenumber plots show many important features of the flow excitation, as well as the structural response.

- A strong 'convective ridge' is evident for positive wavenumber, which brackets the blue convective wavenumber line. The wide wavenumber spread indicates the effects of random turbulence, as well as performing the transform over the entire

plate, where the flow-induced wall excitation is inhomogeneous. Specifically, flow velocity decreases from the nozzle inlet to the downstream edge, smearing the convective ridge over wavenumber.

- A modest negative wavenumber 'ridge' tracks the negative acoustic wavenumber line, indicating backscattered sound waves, likely from the shear layer turbulence interacting with the shock cells. This ridge cuts off at fd/U_o of 0.075. Additional subsonic scattering occurs at higher negative wavenumbers (corresponding to lower speeds) below this cutoff frequency. There are likely also forward-scattered acoustic waves in the positive wavenumber transform, but they are masked by the stronger convective terms.
- The mode orders with wavenumbers that are similar to those of the mean convective wavenumber are annotated with their mode orders (m, n) at their resonance frequencies. These modes are strongly excited and have high spectral peaks.

The wavenumber-frequency transforms may be filtered, back-transformed to physical space, and applied to the structural finite element model. Two filters are applied: the first where all negative propagating terms are zeroed, and the second where all forward (convective) propagating terms are zeroed. This exercise will show the relative importance of the forward and backward-traveling pressure loads.

The top of Fig. 14 shows a cumulative integration of the subsonic panel displacement spectrum normalized by the total integration. The far right of the cumulative integration corresponds to the overall RMS displacement (the total integration of the spectrum). Cumulative integrations of the spectra computed using only positive and negative wavenumber contributions to the wall pressures are also shown. As expected, for subsonic flow, the positive convective pressure loading dominates the panel excitation and resulting displacement response. At low frequencies, however, there are some small contributions from negative wavenumber components, which is common for random convecting turbulence.

The middle and bottom of Fig. 14 show cumulative integrations of displacement spectra for on-design and underexpanded nozzle conditions. For on-design conditions, the negative wavenumber wall pressure is comparable to that of the convective terms at frequencies below $St = 0.07$ (consistent with the wavenumber transform contour shown in Fig. 13) and is responsible for about 12% of the structural RMS response. For underexpanded conditions, the negative wavenumber terms become even more important as the shock cell reflections become stronger, contributing to about 25% of the RMS response. Above the cutoff frequencies, however, the loading is dominated by the convecting shear layer turbulence (notice how the negative wavenumber contributions disappear above St ~ 0.6). These results show that backward-traveling acoustic loading is important to the low-frequency excitation of panels loaded by supersonic wall-bounded jet flow. Figure 6 (effective propagation velocities of the wall pressures) implies that the backward-traveling pressure waves are confined to the forward region of the plate just downstream of the nozzle discharge, with convecting pressures dominating the loading on the downstream portion of the plate.

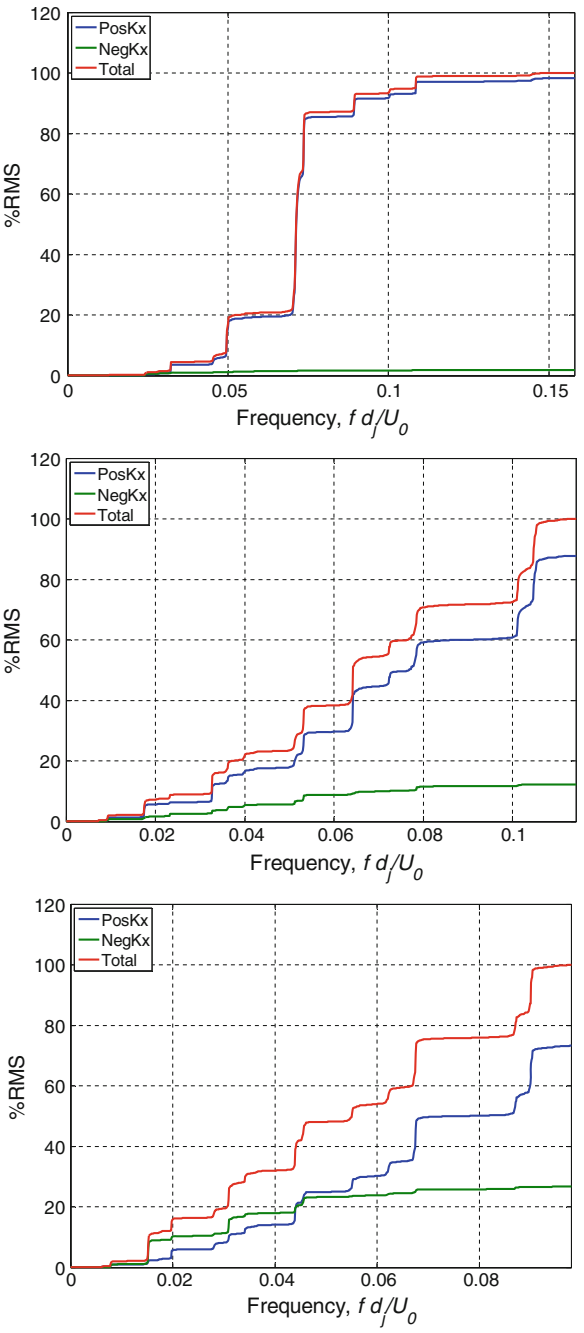

Fig. 14 Cumulative summations of panel displacement spectra at location 1 for: top—subsonic nozzle conditions ($\beta = -0.55$), middle—on-design nozzle conditions ($\beta = -0.55$), bottom—underexpanded nozzle conditions ($\beta = 0.53$); total wall pressure loading, positive wavenumber loading, and negative wavenumber loading

4 Summary and Conclusions

The panel vibrations induced by wall-bounded jet flow from an upstream high aspect ratio rectangular nozzle have been simulated using CFD Hybrid RANS/LES wall pressures applied to a structural FE model using a transfer function time-domain approach. The wall pressures are similar to those measured in a test facility at UTRC. Simulated structural response agrees well with measurements at on-design and underexpanded NPRs.

Correlation analysis and wavenumber-based assessments of the wall pressure loading show that strong negative backward-traveling components within and between shock cells for on-design and underexpanded operating conditions are important exciters of structural vibration (and therefore alternating stress). The negative traveling pressure waves are concentrated near the nozzle discharge and are caused by interaction between the turbulent shear layer and the shock cells, with forward- and backward-scattered sonic, and perhaps aerodynamic waves loading the surface. These loads, however, are limited to lower frequencies, where a cutoff frequency is apparent in the wavenumber transforms of the surface pressure fields. Also, the downstream portions of panels are excited most strongly by the downstream pressures induced by turbulence within the diffusing, expanding shear layer.

The wall pressure loading was filtered to remove backward-propagating (negative wavenumber) loading to assess its relative importance to structural vibration response. For the conditions studied here, the negative wavenumber excitation is responsible for about 12% of the RMS structural displacement at on-design conditions and for about 25% of the RMS displacement at underexpanded conditions.

Future studies will examine how specific structural modes accept energy from supersonic inhomogeneous surface pressure fields downstream of nozzles. Also, alternating structural normal and shear stress time histories and spectra will be analyzed to demonstrate the utility of the methods for assessing structural fatigue life. Finally, less computationally intensive semiempirical methods of the wall pressure excitation (amplitudes and spatial correlations) may be derived in the future. More experimental and computational validation studies are required, however, before such empirical models could be used reliably.

Acknowledgements We are grateful to Rick Labelle at Pratt and Whitney for sponsoring this work. We also acknowledge the data provided by Kenji Homma and Robert Schlinker at UTRC, and the helpful comments and CFD simulations provided by Kerwin Low, Brandon Rapp, and John Liu at Pratt and Whitney.

References

1. Bonness, W.K., Capone, D.E., Hambric, S.A.: Low-wavenumber turbulent boundary layer wall-pressure measurements from vibration data on a cylinder in pipe flow. J. Sound Vib. **329**, 4166–4180 (2010)
2. Bridges, J.E.: Noise from aft deck exhaust nozzles—differences in experimental embodiments. NASA Technical Memorandum 218123 (2014)
3. Hambric, S.A., Hwang, Y.F., Bonness, W.K.: Vibrations of plates with clamped and free edges excited by low-speed turbulent boundary layer flow. J. Fluids Struct. **19**, 93–110 (2004)
4. Hambric, S.A., Jonson, M.L., Fahnline, J.B., Campbell, R.L.: Simulating the vibro-acoustic power of fluid-loaded structures excited by randomly distributed fluctuating forces. In: Proceedings of NOVEM 2005, St. Raphael, France, 18–21 Apr 2005
5. Hambric, S.A., Boger, D.A., Fahnline, J.B., Campbell, R.L.: Structure- and fluid-borne acoustic power sources induced by turbulent flow in 90 degree piping elbows. J. Fluids Struct. **26**, 121–147 (2010)
6. Homma, K., Branwart, P.R., Schlinker, R.H., Rapp, B.M.: Unsteady loading and dynamic response of a structure excited by a high-speed wall-bounded jet, part ii: structural response. In: 22nd AIAA/CEAS Aeroacoustics Conference, Lyon France, May 2016
7. Low, K.R., Bush, R.H., Winkler, J.: Simulating sources of unsteadiness in a high-speed wall-bounded jet. In: 46th AIAA Fluid Dynamics Conference, AIAA Aviation, Washington, DC, June 2016
8. Lurie, M.B.: The prediction of unsteady aerodynamic loading in high aspect ratio wall bounded jets. Ph. D. Dissertation, Penn State University (2015)
9. Shaw, M.D.: Predicting vibratory stresses from aero-acoustic loads. Ph.D. Dissertation, Penn State University (2015)
10. Winkler, J., Schlinker, R.H., Simonich, J.C., Low, K.R.: Unsteady loading and dynamic response of a structure excited by a high-speed wall-bounded jet, part i: aerodynamic excitation. In: 22nd AIAA/CEAS Aeroacoustics Conference, Lyon France, May 2016

Determination of the Acoustic and Hydrodynamic Contributions to the Vibrational Response of an Air-Conveying Rectangular Duct

Florian Hugues, Emmanuel Perrey-Debain, Nicolas Dauchez and Nicolas Papaxanthos

Abstract This paper focuses on the vibratory response of a rectangular duct of finite length excited by an internal turbulent flow. The wall pressure distribution is decomposed into a hydrodynamic and acoustic contribution. Two configurations are investigated: (i) a straight duct with no singularity, in which duct acoustic modes are excited by the TBL and (ii) a straight duct with a diaphragm inserted upstream generating a localized acoustic source. The acoustic contribution is either measured via cross-spectra-based methods or calculated using Computational Fluid Dynamics and aeroacoustic analogies. Semi-analytical predictions are compared with experimental results. It is concluded that in both scenarios, the acoustic contribution is largely dominant.

Keywords Internal turbulent flow · Vibroacoustic response · Numerical methods

1 Introduction and Problem Statement

Gas transport ductwork in industrial plants or air conditioning networks can be subject to vibrations induced by the internal flow. Although most of the fluid-conveying ducts are cylindrical, specific applications require the use of rectangular ducts. This is the case of ventilation and air conditioning systems in buildings for space saving, or in industrial applications requiring large duct sections for gas transportation. For instance, gas treatment centers used in the aluminum industry require such

F. Hugues (✉) · E. Perrey-Debain · N. Dauchez · N. Papaxanthos
Sorbonne Université, Université de Technologie de Compiègne Laboratoire Roberval UMR 7337 BP 20529, 60205 Compiègne Cedex, France
e-mail: florian.hugues@utc.fr

E. Perrey-Debain
e-mail: emmanuel.perrey-debain@utc.fr

N. Dauchez
e-mail: nicolas.dauchez@utc.fr

N. Papaxanthos
e-mail: nicolas.papaxanthos@utc.fr

E. Ciappi et al. (eds.), *Flinovia—Flow Induced Noise and Vibration Issues and Aspects-II*,
https://doi.org/10.1007/978-3-319-76780-2_14

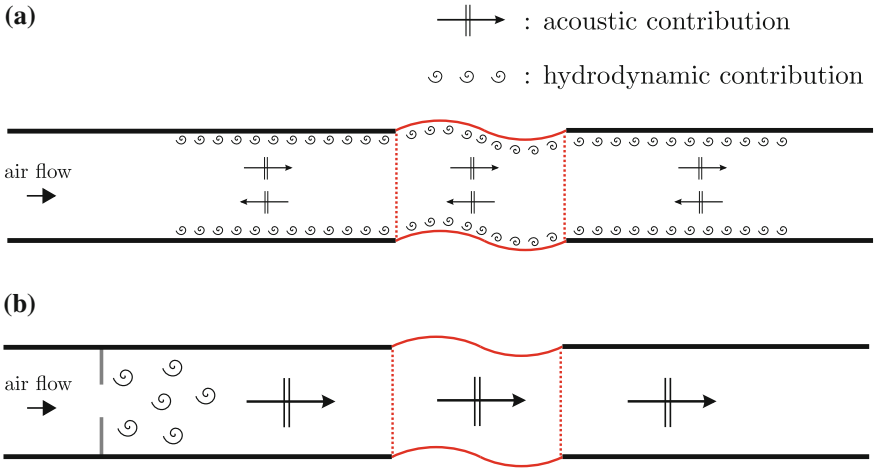

Fig. 1 Problem statement: two scenarios are investigated. **a** There is no singularity and the vibrating structure is subject to both TBL excitation and acoustic waves. **b** There is a flow constriction which generates flow disturbances in the vicinity of the singularity as well as acoustic waves radiating from the obstacle

rectangular ducts due to manufacturing constraint. These ducts which convey gases at low-speed flow condition can be the subject to high levels of vibration induced by the flow acting on the internal faces of the duct. The prediction of such flow-induced vibrations is, therefore, essential in order to optimize the geometry and characteristics of the duct according to the vibration levels and mechanical fatigue objectives. While many studies have been published on the vibrations of cylindrical pipes excited by fluid flow, much less is known about rectangularly shaped ducts.

The problem statement is showed in Fig. 1. In a fully developed turbulent straight pipe flow with no discontinuity or pipe fittings, the vibration of the pipe wall is due to random fluctuating pressures along the inside wall of the pipe. In general, the hydrodynamic turbulent boundary layer (TBL) excitation is considered as responsible for the vibrations of the structure [1]. As a random stochastic source, the wall pressure fluctuation is generally defined via its cross-spectral density (CSD). Various semi-empirical models have been developed since the 60s, and we can cite the well-known Corcos model [2] which is probably the most popular. However, the acoustical contribution produced by the turbulent flow is less understood and little data is available in the literature. Boundary layer pressure fluctuations are distributed over the entire surface of the duct, and acoustic waves within the TBL flow excite acoustic duct modes, which in turn excite the duct walls [3]. In the present work, it is shown that the acoustic field is well described in terms of duct modes that correspond to the primary excitation source of the structure.

The situation is quite different with an internal flow disturbance in the duct due to a singularity such as a bend, a junction, or a flow constriction as shown Fig. 1b. The flow/obstacle interaction generates internal sound waves which propagate through

the piping system. The origin of the sound is relatively well identified and localized. In many instances, the broadband nature of the source generation corresponds to a dipole source due to the drag force fluctuations on the obstacle [4]. The additional propagating sound waves are then superimposed on the hydrodynamic TBL fluctuations. Furthermore, these sound sources are likely to dominate above a certain distance from the discontinuity. Reference [5] offers an overview of the effects of flow disturbances on pipeline noise.

The purpose of this paper is to quantify the TBL and acoustic contributions to rectangular duct vibrations. The TBL excitation comprises an aerodynamic part based on the semi-empirical model of Corcos and an acoustical contribution described in terms of duct acoustic modes. The quantities of interest are the point auto-spectrum of the TBL and the amplitudes of acoustic waves. They are either measured or computed using aeroacoustics simulations.

The paper is organized as follows: The theoretical ingredients, including the vibration model for the structure as well as the hydrodynamic and acoustic excitations, are briefly presented in Sect. 2. The measurement and the numerical computation of both components of the pressure are presented in Sects. 3 and 4. In Sect. 5, experimental results are compared with numerical predictions.

2 Modeling the Vibrational Response of a Rectangular Duct Due to Turbulent and Acoustic Excitation

The vibrational response is given for a $0.2 \times 0.1 \times 0.5\,\mathrm{m}^3$ duct made of 3-mm steel plates excited by 20 m/s or 30 m/s flows as shown in Fig. 2. To facilitate the geometrical coordinate system, curvilinear abscissa s is used and the coordinate system becomes $\mathbf{s} = (s, z)$. The general bending solution w^i for each plate $i = 1 \ldots 4$ can be expressed as a sum of shape functions ϕ^i_{mn} as

$$\phi^i_{mn}(s,z) = \underbrace{\left[A^i_m \sin(\alpha_2 s) + B^i_m \cos(\alpha_2 s) + C^i_m \sinh(\alpha_1 s) + D^i_m \cosh(\alpha_1 s)\right]}_{\varphi^i_m(s)} \sin\left(\frac{n\pi z}{L_z}\right), \tag{1}$$

with $\alpha_1 = \sqrt{\beta^2 + (n\pi/L_z)^2}$, $\alpha_2 = \sqrt{\beta^2 - (n\pi/L_z)^2}$, and $\beta^4 = \omega^2 \rho h / D$. $D = Eh^3/12(1-\nu^2)$ is the bending stiffness of the plate, h the thickness and ω the angular frequency. The shape of the plate i along the s direction is defined as $\varphi^i_m(s)$. For each mode n, the value of coefficients A_m, B_m, C_m and D_m is determined by writing the zero displacement conditions along the coupled edges and the continuity of the rotation and bending momentum. The reader is referred to [6] for more details.

Figure 3 shows global mode shapes computed analytically: The first index stands for the type of section mode, and the second index corresponds to the number of half-periods along the z-axis.

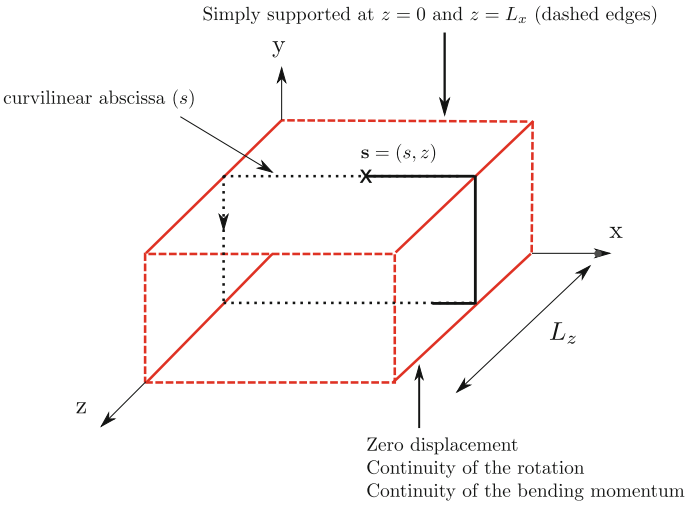

Fig. 2 Duct model

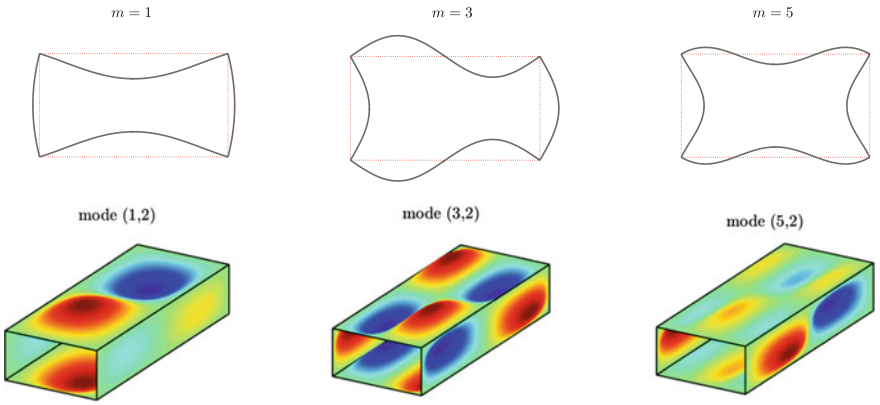

Fig. 3 Section mode shapes φ_m ($n = 1$) and 3D illustration of some global modes of the duct ϕ_{mn}

The frequency response function (FRF) H defining the steady state harmonic response of the duct at point $\mathbf{r}_1$ excited by a point force located at $\mathbf{s}_1$ writes

$$H(\mathbf{r}_1, \mathbf{s}_1, \omega) = \sum_{m,n} \frac{\phi_{mn}(\mathbf{r_1})\phi_{mn}(\mathbf{s_1})}{M_{mn} Z_{mn}}, \tag{2}$$

where $S = 2L_z(L_x + L_y)$ is the duct surface and for a given mode mn, $M_{mn} = \int_S \rho h \phi_{mn}^2 \mathrm{d}\mathbf{s}$ is the generalized mass. The dynamic mechanical impedance is given by

$$Z_{mn}(\omega) = \omega_{mn}^2 - \omega^2 + 2\mathrm{i}\xi_{mn}\omega_{mn}\omega, \tag{3}$$

with ω_{mn} and ξ_{mn} the natural frequency and modal damping of mode (m, n). In this study, FRF are computed analytically (model in vacuum). The natural frequency and modal damping are reassessed from experimental data. The calculation of the vibrational response of the structure is based on random analysis techniques that take into account the stochastic turbulent wall pressure distribution. The quantity of interest is the cross-power spectral density of the resulting vibration between points $\mathbf{r}_1$ and $\mathbf{r}_2$ located on the duct defined as

$$S_{ww}(\mathbf{r}_1, \mathbf{r}_2, \omega) = \int_S \int_S H^*(\mathbf{r}_1, \mathbf{s}_1, \omega) S_{pp}(\mathbf{s}_1, \mathbf{s}_2, \omega) H(\mathbf{r}_2, \mathbf{s}_2, \omega)\, \mathrm{d}\mathbf{s}_1\, \mathrm{d}\mathbf{s}_2, \tag{4}$$

where H corresponds to the frequency response function (FRF) of the structure defined in Eq. (2) and S_{pp} the cross-spectral density (CSD) of the stochastic distributed excitation. This formula can be simplified by considering the modal decomposition response of the plate and by neglecting cross terms. The auto-spectrum is expressed when $\mathbf{r} = \mathbf{r}_1 = \mathbf{r}_2$ as

$$S_{ww}(\mathbf{r}, \omega) = \sum_{mn} \left(\frac{\phi_{mn}(\mathbf{r})}{M_{mn}|Z_{mn}|} \right)^2 \times \overbrace{\int_S \int_S \phi_{mn}(\mathbf{s}_1) S_{pp}(\mathbf{s}_1, \mathbf{s}_2, \omega) \phi_{mn}(\mathbf{s}_2)\, \mathrm{d}\mathbf{s}_1\, \mathrm{d}\mathbf{s}_2}^{I_{mn}(\omega)}. \tag{5}$$

Finally, the quadratic acceleration of the duct:

$$\overline{S_{uu}}(\omega) = \frac{\omega^4}{S} \int_S S_{ww}(\mathbf{r}, \omega)\, \mathrm{d}\mathbf{r}, \tag{6}$$

allows us to quantify the global response of the structure.

The CSD of the wall pressure distribution can be decomposed into a hydrodynamic and acoustic contribution as follows

$$S_{pp}(\mathbf{s}_1, \mathbf{s}_2, \omega) = S_{pp}^h(\mathbf{s}_1, \mathbf{s}_2, \omega) + S_{pp}^{ac}(\mathbf{s}_1, \mathbf{s}_2, \omega). \tag{7}$$

The hydrodynamic contribution can be represented by the Corcos model. Because the Corcos model is known to overestimate the levels in the subconvective domain, a modified Corcos model proposed in [7] (see also [8]), which better estimates low-wavenumber excitation, is also considered in this work, so we take

$$S_{pp}^h(\mathbf{s}_1, \mathbf{s}_2, \omega) = \Phi_{pp}(\omega)(1 + \alpha\gamma_z\omega|\xi_z|/U_c) e^{-\gamma_s\omega|\xi_s|/U_c} e^{-\gamma_z\omega|\xi_z|/U_c} e^{-\mathrm{i}\omega\xi_z/U_c}. \tag{8}$$

If $\alpha = 0$, it corresponds to the original Corcos model and if $\alpha = 1$ to the modified Corcos. The coefficient U_c defines the TBL velocity and is expressed as a fraction

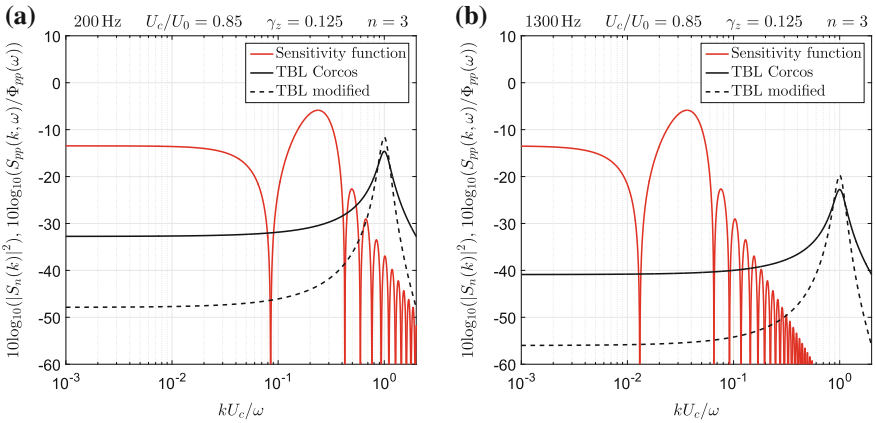

Fig. 4 Coupling of TBL wall pressure cross-spectrum models and the wavenumber transform of a flexural plate mode (wavenumber sensitivity function) **a** at 200 Hz **b** 1300 Hz

of the flow speed at the center of the duct U_0 and this is set to $U_c/U_0 = 0.85$. Corcos parameters γ_z and γ_s are related to the axial and lateral correlation lengths. The Corcos model or the modified one may be easily transformed into wavenumber space and is compared to the wavenumber transform of a plate bending mode for the simply supported case (at modal wavenumber $k_n = n\pi/L_z$, where n is the number of half-periods along the z-axis and L_z the plate dimension). This is shown in Fig. 4 following a similar analysis presented in [9]. In the present study, the frequency of interest ranges from 200 to 1300 Hz and the flow speed is relatively low (30 m/s max) so the convective wavenumber remains always much higher than structural wavenumbers (note that this is not necessarily true for acoustic wavenumbers).

The acoustic contribution is described as a series of propagating duct acoustic mode. The contribution of the pq^{th} acoustic mode on the cross-power spectral density is obtained in the manner of [10] as

$$S_{pp}^{ac}(\mathbf{s}_1, \mathbf{s}_2, \omega) = \sum_{pq} \underbrace{\left|C_{pq}^{\pm}\right|^2 \psi_{pq}(s_1)\psi_{pq}(s_2) \exp\left(\mathrm{i}k_{pq}^{\pm}(z_1 - z_2)\right)}_{S_{pq}^{ac\pm}(\mathbf{s}_1,\mathbf{s}_2,\omega)}, \tag{9}$$

where $C_{pq}^{\pm}$ stands for the amplitude of the downstream (+) and upstream (-) propagating mode. Here acoustic modes are deliberately not normalized so the quantity $|C_{pq}^{\pm}|^2$ can be regarded as the auto-power spectrum for the acoustic pressure on the duct wall. To simplify the analysis, the flow is assumed uniform and we neglect damping. The axial wavenumbers $k_{pq}^{\pm}$ have the well-known expression (here $k = \omega/c$):

$$k_{pq}^{\pm} = \frac{kM \pm \sqrt{k^2 - \left(1 - M^2\right)\left(\left(\frac{p\pi}{L_x}\right)^2 + \left(\frac{q\pi}{L_y}\right)^2\right)}}{1 - M^2}, \tag{10}$$

where M is the Mach number. The condition for an acoustic mode to propagate is that the wavenumber $k_{pq}^{\pm}$ must be real. Otherwise, the wave will decay exponentially and is known as an evanescent wave. The frequency at which a mode (p, q) begins to propagate is known as the cutoff frequency of the mode. Note that the evanescent waves are neglected in our model. In all cases, the integration of Eq. (4) is carried out analytically.

3 Experimental Determination of Hydrodynamic and Acoustic Components

In this section, we present the experimental methods to determine the wall pressure distribution $\Phi_{pp}(\omega)$ and the acoustic modal amplitudes $C_{pq}^{\pm}$.

The experiments have been performed on a test bench, as shown in Fig. 5a, designed for the multimodal characterization of the acoustic properties of obstacles in the presence of a low Mach number flow. The duct facility is a rigid rectangular duct of 0.2 m x 0.1 m section with an anechoic termination at both ends. It is equipped with a radial fan able to generate an air flow up to 30 m/s. The tested part of the duct is made of four 0.5-m-long welded steel plates of 3 mm thickness and is inserted in the test section. The test bench is instrumented with 8 sets of 12 microphones mounted on the wall of the duct. Each set named $\mathbf{a_4}$, $\mathbf{a_3}$, $\mathbf{a_2}$, $\mathbf{a_1}$ located upstream and $\mathbf{b_1}$, $\mathbf{b_2}$, $\mathbf{b_3}$, $\mathbf{b_6}$ located downstream the test section (as indicated in Fig. 5b) corresponds to a given position (in z) along the duct axis. The duct response is measured using two accelerometers: one of them being used as a reference, the other one being successively positioned on the measurement grid in order to get the average quadratic acceleration of the duct. The measurement grid is defined on the duct with a regular interval of 2.5 cm along the cross-flow direction and 5 cm along the flow direction. The point pressure auto-spectrum $\Phi_{pp}(\omega)$ is determined experimentally using upstream as well as downstream microphones sections $\mathbf{a_3}$, $\mathbf{a_2}$, $\mathbf{a_1}$ and $\mathbf{b_1}$, $\mathbf{b_2}$, $\mathbf{b_3}$, respectively.

Two methods are used for determining the acoustic modal amplitude $\left|C_{pq}^{\pm}\right|$ and are presented below.

3.1 Cross-Spectra-Based Method: Case with No Singularity

The duct is straight with no singularity, so that propagating acoustic modes are generated by the TBL itself all along the duct. The estimation of the acoustic component

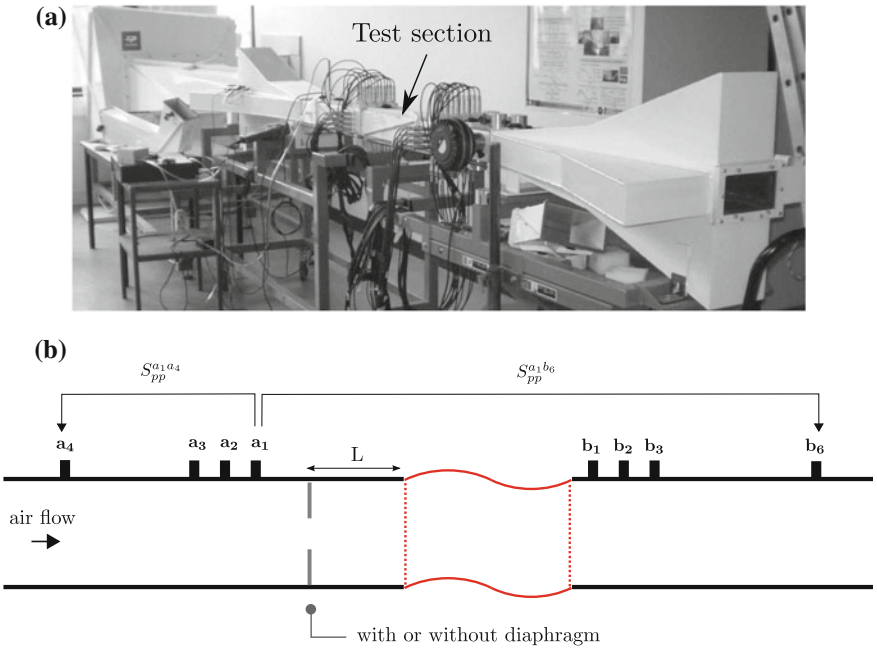

Fig. 5 Overview of the experimental setup

is performed by minimizing an overdetermined system (Eq. (11)). The input data is a set of cross-spectra between microphones at the four sections $\mathbf{a_1}$, $\mathbf{b_3}$, $\mathbf{a_4}$, $\mathbf{b_6}$ as illustrated in Fig. 5b. Distances between microphones are much larger than the correlation lengths of the hydrodynamic wall pressure fluctuations so that only the acoustic part of the pressure is measured and estimated as follows

$$S_{pp}^{\Delta z}(s_i, s_j, \omega) = \left|C_{00}^{+}\right|^2 \psi_{00}(s_i)\psi_{00}(s_j) \exp\left[\mathrm{i}k_{00}^{+}\Delta z\right] + \left|C_{10}^{+}\right|^2 \psi_{10}(s_i)\psi_{10}(s_j) \exp\left[\mathrm{i}k_{10}^{+}\Delta z\right] + \ldots \quad (11)$$

Results using 600 averages are shown in Fig. 6a. The acoustic contribution is found to be 10 dB up to 20 dB lower than the turbulent wall pressure fluctuations. Note that upstream and downstream propagating modes are not distinguished as they have similar amplitudes.

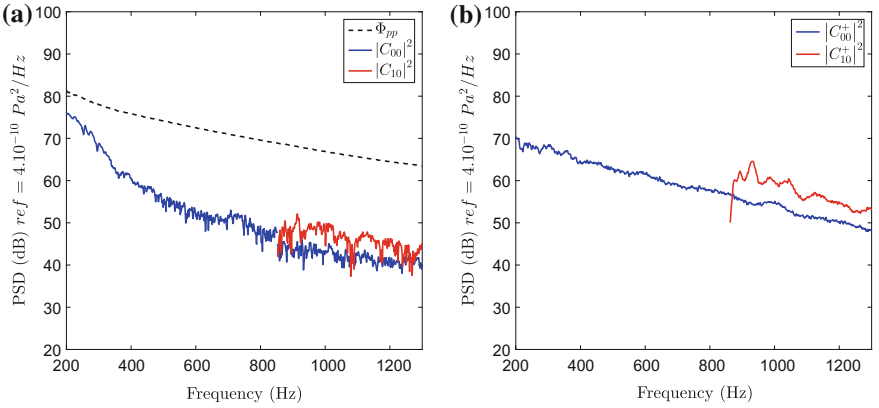

Fig. 6 Estimation of the propagating duct acoustic modes. **a** In the case of a straight duct with no singularity, the flow speed is 30 m/s. **b** With a flow constriction, the flow speed is 6.5 m/s (measured upstream the constriction)

3.2 2N-port Method: Case with a Flow Constriction

In the vicinity of a pipeline singularity such as a flow constriction, acoustic waves are generated due to the drag force fluctuations. In this context, acoustic measurements can be performed on the basis of the so-called Multiport method [11, 12]. The acoustic scattering matrix of the obstructed duct and the impedance of the surrounding environment are first identified by measuring the acoustic response to given external excitations. Then, the aeroacoustic noise produced by the interaction of the obstacle and the flow is extracted. The multiport formulation can be written in a compact form

$$\mathbf{p}^{out} = \mathbf{S}\mathbf{p}^{in} + \mathbf{p}^{s}, \tag{12}$$

where $\mathbf{S}$ is the scattering matrix, vector $\mathbf{p}^{out}$ stands for the acoustic waves radiating away, and $\mathbf{p}^{s}$ is the source vector containing the modal coefficients.

The quantity of interest is the source cross-spectrum matrix defined as

$$\mathbf{G^s} = E[\mathbf{p}^{s}(\mathbf{p}^{s})^{c}], \tag{13}$$

where the superscript c denotes transpose and complex conjugate. We obtain a $[2N \times 2N]$ matrix, where N is the number of acoustic duct modes considered, and the diagonal terms $\langle |C_{00}^-|^2 \ldots |C_{NN}^-|^2, |C_{00}^+|^2 \ldots |C_{NN}^+|^2 \rangle$ represent the modal auto-spectra, respectively, at the section $\mathbf{a_1}(-)$ and $\mathbf{b_1}(+)$. Results are shown in Fig. 6b. We notice the emergence of the first transverse acoustic mode above the cutoff frequency at 853 Hz (below that frequency, only the plane mode propagates).

4 Numerical Determination of the Hydrodynamic and Acoustic Components

In this section, we present a method to determine the two components, on the basis of a Computational Fluid Dynamics approach coupled with an aeroacoustic analogy.

At low Mach number and for sufficiently high Reynolds numbers, the Large Eddy Simulation (LES) of an unsteady incompressible flow coupled with an acoustic analogy is classically used as it should deliver reasonably accurate predictions for both the hydrodynamic and acoustic pressure [13]. Let us recall that the hydrodynamic pressure p_h which is provided by the incompressible-flow simulation (Star-CCM+ is used here) must be solution to the Poisson's equation:

$$\Delta p_h = q, \tag{14}$$

where q is the source term containing mean and fluctuating velocity terms (all physical quantities are interpreted in the frequency domain). Now, in order to take into account compressibility effects, Lighthill's aeroacoustic analogy leads to a somewhat similar equation of the form

$$(\Delta + k^2)p = q, \tag{15}$$

where k is the acoustic wavenumber and p can now be regarded as the true pressure. By combining Eqs. (14) and (15), the acoustic pressure defined as the difference $p_a = p - p_h$ can be shown to be the solution to the following boundary integral equation [13]

$$p_a = \int_{\partial V} \left(p_h \frac{\partial\,(G - G_0)}{\partial n} + p_a \frac{\partial G}{\partial n} \right) \mathrm{d}S + \int_{S_\pm} \left(G_0 \frac{\partial p_h}{\partial n} - GT(p_h) \right) \mathrm{d}S, \tag{16}$$

where the volume integral over the CFD domain, call it V, has been neglected [13]. G_0 is the static Green's function, G is the classical free-field Green's function, and $T(p_h)$ is the operator associated with the anechoic condition at both ends of the duct (the sign $-$ and $+$ corresponds to left and right end, respectively). The resolution of Eq. (16) requires the storage of the incompressible-flow pressure p_h on the surface of the domain and its derivative $\partial_n p_h$ on the inlet and outlet. The mesh used for the CFD comprises 9 million cells. The mesh is built using 4 resolution levels ranging from 0.5 mm to 4 mm. The smallest cells are located in the vicinity of the diaphragm edges in order to capture correctly the physics of the shear layers. A RANS k-ϵ simulation is first performed to give an initial condition for the incompressible Large Eddy Simulation. Inlet boundary conditions, velocity components and turbulent kinetic energy, are prescribed using realistic data provided by PIV measurement. The measured mass flow rate is 565 kg/h which corresponds to an average velocity over the duct section of 6.5 m/s. The LES is carried out with a simulated physical time of 0.32 s and a time step $\delta t = 10^{-5}s$. Due to the difference in size of acoustic and turbulent wavelengths,

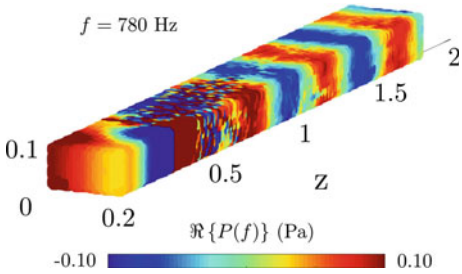

Fig. 7 Computed pressure distribution in the duct

the requirement in terms of grid resolution is less severe for the acoustic computation than for the CFD. The integral equation Eq. (16) is solved by collocation on a coarse mesh which is composed of around 8500 triangular surface cells of maximum dimension 2 cm, which corresponds to $\lambda/8$ at 2125 Hz. The temporal boundary data p_h and $\partial_n p_h$ are summed on the coarse mesh centroids using a conservative mapping from Star-CCM+. The Fourier analysis and the resolution of Eq. (16) are carried out on MATLAB. The physical time of 0.32 s is divided into eight segments of 0.05 s each with 1/4 overlapping. A window function is applied on each segment. A typical result is shown in Fig. 7 where small-scale wall hydrodynamic pressure fluctuations and long wavelength acoustic waves can be identified.

In order to compute the structural loads, two quantities of interest are considered: (i) the CSD of the wall pressure distribution, either of hydrodynamic or acoustic nature

$$S_{pp}^{h,\mathrm{CFD}}(\mathbf{s}_1, \mathbf{s}_2, \omega) = E\left[p_h p_h^*\right] \quad \text{and} \quad S_{pp}^{ac,\mathrm{CFD}}(\mathbf{s}_1, \mathbf{s}_2, \omega) = E\left[p_a p_a^*\right]. \tag{17}$$

and (ii) the duct acoustic modes radiating away from the obstacle, defined as

$$C_{pq}^{+} = \int_{S_+} p_a \psi_{pq} \mathrm{d}S. \tag{18}$$

Figure 8 shows reasonably good agreement between measured data using the $2N$-port method and numerical predictions.

5 Results and Discussion

5.1 Straight Duct with No Obstacle

The global response of the duct, including both the aerodynamic and acoustic contributions, can now be estimated via

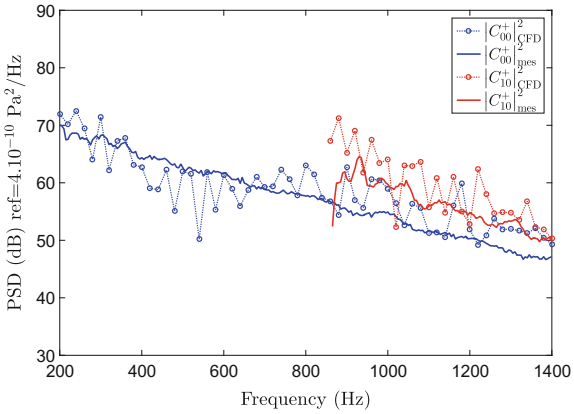

Fig. 8 Computed versus measured duct acoustic mode amplitudes radiating away from the obstacle

$$\overline{S_{uu}} = \overline{S^h_{uu}} + \overline{S^{ac}_{uu}}, \tag{19}$$

where the hydrodynamic component is calculated via Corcos model. Here, Corcos coefficients are set to $\gamma_s = 1$ and $\gamma_z = 1/8$. Figure 9 shows the quadratic acceleration due to each contribution, by using up to 20 structural modes. Note that as opposed to the modified Corcos model, the original Corcos model is known to overestimate low-wavenumber TBL loading showing 10–15 dB differences. Similar results can be found in [14]. In both cases, however, the hydrodynamic contribution remains marginal and the acoustic excitation clearly dominates.

Note that plane wave mode can only be coupled to the structural modes with section mode $m = 1$ or $m = 5$, whereas the first transverse acoustic mode can only be coupled to the section mode $m = 3$. Finally, reasonably good agreements with experimental results are found once all contributions are summed up.

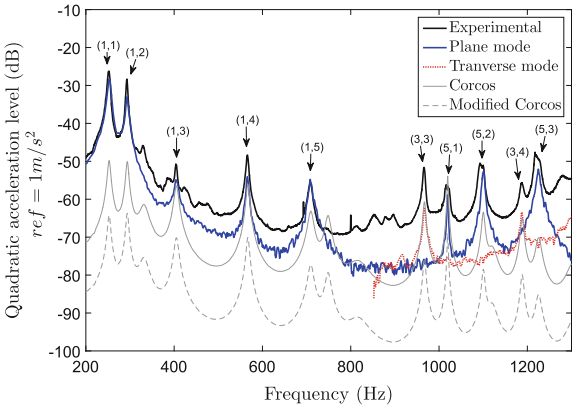

Fig. 9 Quadratic acceleration for each response contribution at 30 m/s

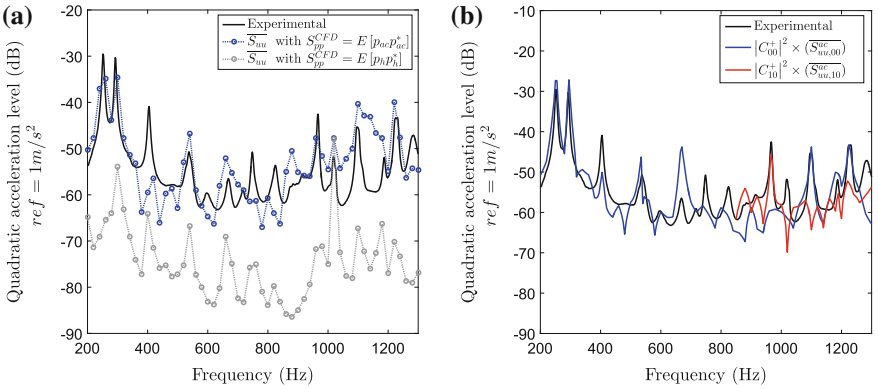

Fig. 10 Quadratic acceleration using **a** the direct approach and **b** the modal approach

5.2 Straight Duct with a Flow Constriction

5.2.1 Direct Approach

The vibrating structure is situated at $L = 40$ cm downstream from the discontinuity. The vibrational response is estimated using a direct approach based on a regular discretization of the duct surface with triangular cells of average dimension of 2 cm. The computation of the quantity $I_{mn}(\omega)$ defined in Eq. (5) is estimated as follows

$$I_{mn}(\omega) \approx \sum_{i}^{N_p} \sum_{j}^{N_p} \phi_{mn}(\mathbf{s}_i) S_{pp}^{h/ac,\mathrm{CFD}}(\mathbf{s}_i, \mathbf{s}_j, \omega) \phi_{mn}(\mathbf{s}_j)\, \Delta_i\, \Delta_j, \tag{20}$$

where N_p is the number of cells and Δ_i is the elementary surface of the triangular cells. Predicted quadratic acceleration is compared to measured data in Fig. 10a. The CSD matrix $S_{pp}^{h/ac,\mathrm{CFD}}$ is computed using either the hydrodynamic pressure p_h provided by LES or the acoustic pressure p_a computed with the acoustic analogy. Once again the acoustic contribution clearly dominates and the overall energy is respected between predicted and measured vibrations using the acoustic loads alone. Note that calculations were performed using a frequency step $\Delta f = 20$ Hz corresponding to about 0.3 s of CFD simulated physical time.

5.2.2 Modal Approach

Since the acoustic part is dominant, it is fair to assume that only acoustic modes propagating downstream are considered as the primary source of excitation. In this case, we have simply

$$I_{mn}(\omega) = \left|C_{pq}^+\right|_{\mathrm{CFD}}^2 \, j_{mnpq}^{2\pm}(\omega), \tag{21}$$

where $j^{2\pm}_{mnpq}(\omega)$ is the joint acceptance function describing the coupling between a structural mode (m, n) and a duct acoustic mode (p, q). Note that it is computed analytically. The modal approach permits to save computation time as the storage of the CSD matrix requires high memory capacity. Figure 10b shows the quadratic acceleration due to each contribution and good agreements can be observed. Here, a linear interpolation (in frequency) is applied to $\left|C^{+}_{00}\right|^2_{\text{CFD}}$ and $\left|C^{+}_{10}\right|^2_{\text{CFD}}$ coefficients. This allows to refine the frequency analysis so as peaks at the resonance frequencies of the structure are better predicted.

6 Conclusion

The vibrational response of a rectangular duct of finite length excited by an internal turbulent flow was investigated both numerically and experimentally. The pressure loading on the structure expressed in terms of CSD accounts for both hydrodynamic and acoustic contributions. A CFD analysis coupled with an acoustic analogy is used to compute these two contributions and assess their relative influence on the vibrational response. Amplitudes of acoustic waves are measured using either a cross-spectra-based method or the $2N$-port method. The vibrational levels have been investigated for two scenarios (i) a straight duct with no obstacle and (ii) with a flow constriction (i.e., a diaphragm) inserted upstream. In both cases, the acoustic pressure field has been shown to have a great impact on the vibrational response. Measured vibrational levels are found to be in good agreement with our numerical simulations.

References

1. Durant, C., Robert, G., Filippi, P., Mattei, P.O.: Vibroacoustic response of a thin cylindrical shell excited by a turbulent internal flow: comparison between numerical prediction and experimentation. J Sound Vib. **229**(5), 1115–1155 (2000)
2. Corcos, G.M.: Resolution of pressure in turbulence. J. Acoust. Soc. Am. **35**(2), 192 (1963)
3. Hwang, S., Moon, Y.: On the computation of low-subsonic turbulent pipe flow noise with a hybrid LES/LPCE method. Int. J. Aeronaut Space Sci. **18**(1), (2017)
4. Nelson, P., Morfey, C.: Aerodynamic sound production in low speed flow ducts. J. Sound Vib. **79**(2), 263–289 (1981)
5. Norton, M.P, Karczub, D.G.: Fundamentals of Noise and Vibration Analysis for Engineers. Cambridge University Press (2003)
6. David, A., Hugues, F., Dauchez, N., Perrey-Debain, E.: Vibrational response of a rectangular duct of finite length excited by a turbulent internal flow. J. Sound Vib. (2017). https://www.sciencedirect.com/science/article/pii/S0022460X17308325
7. Hwang, Y.F., Bonness, W.K., Hambric, S.A.: On modeling structural excitations by low speed turbulent boundary layer flows. Technical Report, ARL/Penn State Technical Report 03-008 (2003)
8. Caiazzo, A., DAmico R, Desmet W.: A Generalized Corcos model for modelling turbulent boundary layer wall pressure fluctuations. J Sound Vib. **372**, 192–210 (2016)

9. Hambric, S.A., Hwang, Y.F., Bonness, W.K.: Vibrations of plates with clamped and free edges excited by low-speed turbulent boundary layer flow. J. Fluids Struct. **19**(1), 93–110 (2004)
10. Norton, M.P.: The effects of internal flow disturbances on the vibration response of and the acoustic radiation from pipes. PhD Thesis, University of Adelaide (1979)
11. Lavrentjev, J., Åbom, M., Bodén, H.: A measurement method for determining the source data of acoustic two-port sources. J Sound Vib. **183**(3), 517–531 (1995)
12. Bennouna, S., Naji, S., Cheriaux, O., Moreau, S., Ouedraogo, B., Ville, J.M.: Aeroacoustic Prediction Methods of Automotive HVAC Noise. In: SAE Technical Paper, SAE International (2015)
13. Papaxanthos, N., Perrey-Debain, E., Bennouna, S., Ouedraogo, B., Moreau, S., Ville, J.M.: Pressure-based integral formulations of LighthillCurle's analogy for internal aeroacoustics at low mach numbers. J. Sound Vib. **393**, 176–186 (2017)
14. Hambric, S., Hwang, Y.F., States, U., America, O.: Vibrations of flat plates excited by low mach number turbulent boundary layers. In: 29th International Congress and Exposition on Noise Control Engineering, 27–30 Aug 2000, Nice, Fr., pp. 1–6 (2000)

Review of Efficient Methods for the Computation of Transmission Loss of Plates with Inhomogeneous Material Properties and Curvature Under Turbulent Boundary Layer Excitation

Alexander Peiffer and Uwe Christian Mueller

Abstract The excitation of structures by turbulent boundary layer requires the consideration of the cross-spectral density for all degrees of freedom excited by the pressure fluctuations. This leads to large and computationally expensive matrices for the calculation of the structural response or even radiation into the fluid. This paper deals with the comparison of different methods to reduce the size of the problem. One option is the decomposition of the cross-spectral matrix into major principal components in order to represent the random matrix by few deterministic load cases. The second option is the conversion of the random equations of motion into modal space. A detailed investigation of the matrix coefficients under diffuse acoustic field and turbulent boundary layer excitation shows in which case the off-diagonal coefficients may be neglected. The paper concludes with an evaluation of the precision and a discussion about the computational expense of all applied methods as far as the advantages and disadvantages of each method.

Keywords Hybrid method · Random response · Turbulent boundary layer Diffuse acoustic field · Transmission

1 Introduction

Modern turbofan aircraft with high bypass ratio engines provide an excellent noise performance during cruise. Due to this, the impact of engine noise is less and less important and the turbulent boundary layer remains as a major source of interior noise, especially in the cockpit and the front sections of the aircraft. The turbulent boundary layer (TBL) is a random excitation that is described by cross-spectral functions or matrices over frequency. As a consequence, the consideration of random

A. Peiffer (✉) · U. C. Mueller
Airbus, 81663 Munich, Germany
e-mail: autor@alexanderpeiffer.de

E. Ciappi et al. (eds.), *Flinovia—Flow Induced Noise and Vibration Issues and Aspects-II*,
https://doi.org/10.1007/978-3-319-76780-2_15

load excitation is computationally very expensive and reduction methods are required to make the computation of realistic structures feasible.

This paper evaluates two different methods regarding precision and reduction in computational expense. The following methods will be investigated:

1. **Singular Value Decomposition** The cross-spectral matrix of the load can be separated into a reduced set of orthogonal deterministic load cases. Here, the degrees of freedom of the load itself are reduced. There are specific criteria that allow to estimate the number of components to get a representative description of the load. The advantage of this method is that every finite element model that provides direct frequency responses can be applied to solve random excitation problems.
2. **Modal Joint Acceptance** Modal condensation can be applied in the random load context. The diagonal form of the structural equation of motion in modal coordinates cannot be sustained. Thus, this paper deals with the modal method using full and diagonal matrices in order to evaluate computation time and precision in both cases.

In the literature, there are many further options to reduce the size of the numerical problem as shown, for example, in [1] some of them are even more efficient. We focus here on the singular value decomposition because this provides some further insight into the characteristics of the load and the main goal is to understand the effect of the diagonal form.

The investigated structures are (i): a cylindrically curved aluminium shell and (ii): realistic aircraft fuselage panel structure. Both are modelled by the finite element method (FEM). Analytical or statistical energy analysis (SEA) methods are not considered here even though they are very efficient but they are of limited use for realistic structures. A mesh-based approach is required to catch all the details of structural dynamics of complex structures.

2 Theory

The transmission problem for random excitation can be interpreted as a hybrid FEM/SEA model as described by Shorter and Langley in [2]. The hybrid method leads to an equivalent approach as shown by Graham [3] and as explained by Peiffer et al. in [4].

2.1 Hybrid FEM/SEA Theory

In the context of hybrid theory, the structure is supposed to be deterministic and modelled by finite elements. This leads to a discrete equation of motion given by the dynamic stiffness matrix such as:

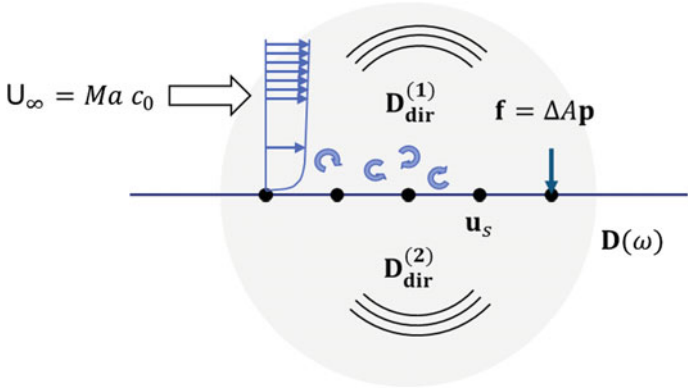

Fig. 1 Configuration of turbulent flow, structure and acoustic radiation

$$\mathbf{D}\,\mathbf{u} = [\mathbf{K} - \omega^2\mathbf{M}]\mathbf{u} = \mathbf{f} \tag{1}$$

The surrounding fluid is considered by introducing a stiffness matrix that accounts for the reacting forces of the free sound field on the vibrating structure, the so-called radiation stiffness. The radiation stiffness of both sides is added to the stiffness matrix of the structure in vacuo as depicted in Fig. 1.

$$\mathbf{D}_{tot} = \mathbf{D} + \mathbf{D}_{dir}^{(1)} + \mathbf{D}_{dir}^{(2)} \tag{2}$$

In free-field configuration, this expression is exact. In the context of hybrid theory, the free-field assumption is based on the fact that the impact of random systems (here the cavity of the aircraft) is given by the free-field radiation stiffness because in an ensemble of random systems, the reflections of the boundaries are not coherent and the mean value of the reflected waves is zero.

The radiation stiffness matrix can be derived by boundary element methods or by numerical integration of the Rayleigh integral as shown, for example, in [5]. In the latter case, the curvature is neglected and both fluid regimes are considered as infinite half spaces.

The external forces are separated into deterministic and random forces the latter representing the turbulent boundary layer.

$$\mathbf{D}_{tot}\mathbf{u}_s = \mathbf{f} + \mathbf{f}_{rnd} \tag{3}$$

In the following, we exclusively deal with random forces and assume $\mathbf{f} = 0$. Random forces are defined by the cross-correlation spectrum of the applied nodal forces given by the expected values of the force spectral vectors:

$$\mathbf{S}_{ff} = \mathrm{E}\left[\mathbf{f}_{rnd}\mathbf{f}_{rnd}^{H}\right] \tag{4}$$

Consequently, the response of the structural system is also given as cross-correlation derived by inversion of (3)

$$\mathbf{S}_{uu} = \mathrm{E}\left[\mathbf{u}\mathbf{u}^H\right] = \mathbf{D}_{tot}^{-1}\mathbf{S}_{ff}\mathbf{D}_{tot}^{-H} \tag{5}$$

This equation theoretically solves the random load problem. However, this requires triple symmetric matrix multiplication being computationally very expensive. So, reduction is needed to make the response calculation of structural subsystems with more than 10^4 degrees of freedom feasible.

2.2 Modal Coordinates

In structural dynamics, the structural equations of motion can be reduced by converting the displacement coordinated into modal space. The mode shapes are the eigenvector solutions of the following equation.

$$[\mathbf{K} - \omega_n^2\mathbf{M}]\boldsymbol{\Phi}_n = \mathbf{0} \tag{6}$$

When these shapes are arranged in transformation matrices $\boldsymbol{\Phi} = [\boldsymbol{\Phi}_\mathbf{1}\boldsymbol{\Phi}_\mathbf{2}\cdots\boldsymbol{\Phi}_\mathbf{N}]$ with the so called mass normalisation

$$\boldsymbol{\Phi}^T\mathbf{M}\boldsymbol{\Phi} = \mathbf{1} \quad \boldsymbol{\Phi}^T\mathbf{K}\boldsymbol{\Phi} = diag(\boldsymbol{\omega}_\boldsymbol{n}^\mathbf{2}) \tag{7}$$

Equation (2) reads in modal coordinates as:

$$\begin{aligned}\mathbf{D}'_{tot} &= \boldsymbol{\Phi}^H\mathbf{D}_{tot}\boldsymbol{\Phi} \\ &= diag(\omega_n^2(1+j\eta) - \omega^2) + \boldsymbol{\Phi}^H\mathbf{D}_{dir}^{(1)}\boldsymbol{\Phi} + \boldsymbol{\Phi}^H\mathbf{D}_{dir}^{(2)}\boldsymbol{\Phi} \\ &= diag(\omega_n^2(1+j\eta) - \omega^2) + \mathbf{D}_{dir}^{'(1)} + \mathbf{D}_{dir}^{'(2)}\end{aligned} \tag{8}$$

In the following matrices and coordinates in modal base are denoted by a prime ($'$). The radiation stiffness destroys the diagonal form of the total stiffness matrix. They are symmetrical but fully populated. With the modal force vector $\mathbf{f}'$ given by

$$\mathbf{f}' = \boldsymbol{\Phi}^H\mathbf{f} \tag{9}$$

and modal coordinates

$$\mathbf{u} = \boldsymbol{\Phi}\mathbf{u}' \tag{10}$$

Equation (5) can also be converted into modal coordinates reading as:

$$\mathbf{S}'_{uu} = \mathbf{\Phi}^H \mathbf{S}_{uu} \mathbf{\Phi} = \mathbf{D}'^{-1}_{tot} \left\{ \mathbf{\Phi}^H \mathbf{S}_{ff} \mathbf{\Phi} \right\} \mathbf{D}'^{-H}_{tot} \tag{11}$$

The term in braces is called the modal joint acceptance due to random excitation. When the structure dynamics can be described by few modes, this will be a reasonable reduction in computation time once the modal transformation is performed. Typically, the structural mode shapes are calculated by commercial tools as, for example, Nastran or Ansys and the maximal mode index N is selected due to frequency criteria. For practical reasons, the shapes are mapped on regular meshes as described, for example, in [4] because excitation, radiation and structure dynamics required different mesh sizes.

2.3 Radiated Power

The radiated power is determined by the work done by the vibrating structure due to the reaction force of the fluid times the surface normal velocity. These reaction forces are given by the radiation stiffness $\mathbf{D}_{dir}$. Summing up all local forces gives the total radiated power [2].

$$\Pi^{(m)}_{dir} = \frac{\omega}{2} \sum_{i,k} \mathrm{Im}\, \mathbf{D}^{(m)}_{dir,ik} \mathbf{S}_{uu,ik} \tag{12}$$

The above expression is valid for displacement- and modal coordinates. The indexes i, k denote row and column in the matrix.

Equation (12) in combination with (11) corresponds exactly to the radiated power in Graham's paper [3] except two differences: (1) Graham considers only the diagonal terms and (2) modal transformation and free-field radiation are performed in wave number space.

2.4 Transmission Loss

For the perfect diffuse acoustic field, the irradiated power at the surface A is related to the root mean square pressure[1] by

$$\Pi_{in} = A \frac{p^2_{rms}}{2\rho_0 c_0} \tag{13}$$

[1] Usualy, expression (13) is given for the mean square pressure in the diffuse field and not at the surface. The surface mean square pressure is doubled compared to the room or diffuse field pressure.

the transmission coefficient τ is given by the power ratio of irradiated and transmitted acoustic power. The transmission loss (TL) is the decibel expression of the reciprocal value of the transmission coefficient.

$$\tau = \frac{\Pi_{rad}}{\Pi_{in}} \qquad TL = 10 \log_{10} \frac{1}{\tau} \tag{14}$$

The wording irradiated power does not make sense for random excitation as, for example, in case of turbulent boundary layer, because the random pressure fluctuation does not correspond to sound irradiation. But in order to define a metric similar to the transmission loss, the hypothetical irradiated power is assumed to be similar to the power of the diffuse acoustic field.

2.5 Singular Value Decomposition of Random Loads

The quadratic cross-spectral matrix can be written as a product of principal component and singular value matrices [6].

$$\mathbf{S}_{ff} = \mathbf{U}\mathbf{\Sigma}\mathbf{U}^H \tag{15}$$

The columns of $\mathbf{U}$ are each orthonormal

$$\mathbf{U}^H\mathbf{U} = \delta_{mn} \tag{16}$$

and $\mathbf{\Sigma}$ is a diagonal matrix that contains the singular values w_n providing information about the *contribution* of each component $\mathbf{U}_n$.

$$\mathbf{\Sigma} = diag(w_n) \tag{17}$$

Typical implementations of the SVD sort the singular values in descending order. Using only a reduced set of N singular values the cross-correlation matrix can be approximated by a set of N components:

$$\begin{aligned} \mathbf{S}_{ff} &= \mathbf{U}\mathbf{\Sigma}\mathbf{U}^H \\ &\approx \left[\mathbf{U}_1\mathbf{U}_2 \cdots \mathbf{U}_N\right] diag(w_1, w_2, \ldots, w_N) \left[\mathbf{U}_1\mathbf{U}_2 \cdots \mathbf{U}_N\right]^H \end{aligned} \tag{18}$$

The number of components that is required to get a precise approximation is determined by the values of w_i . The ratio between the first (highest) and N-th (lowest) singular value provide information about the precision of using only N components.

Taking all components until reaching one 100th of the first value leads to a matrix approximation with a precision in the same order of magnitude.

Entering (18) into (5) reads as

$$\mathbf{S}_{uu} = \mathrm{E}\left[\mathbf{u}\mathbf{u}^H\right] = \mathbf{D}_{tot}^{-1}\mathbf{U}\boldsymbol{\Sigma}\mathbf{U}^H\mathbf{D}_{tot}^{-H} = (\mathbf{D}_{tot}^{-1}\mathbf{U})\boldsymbol{\Sigma}(\mathbf{D}_{tot}^{-1}\mathbf{U})^{-H} \tag{19}$$

When using the approximation (18), the full matrix multiplication can be replaced by N deterministic load cases

$$\mathbf{D}_{tot}\mathbf{u}_n = \sqrt{w_n}\mathbf{U}_n \tag{20}$$

that are typically solved by finite element solvers. The response cross-correlation is finally reconstructed by:

$$\mathbf{S}_{uu} = \left[\mathbf{u}_1, \mathbf{u}_2, \ldots, \mathbf{u}_N\right]\left[\mathbf{u}_1, \mathbf{u}_2, \ldots, \mathbf{u}_N\right]^H \tag{21}$$

The importance of each result does not only correspond to the magnitude of the singular value because the structure acts as a filter to the excitation. This may be critical especially when coincidence occurs. In order to overcome this issue, the wave number representation of the principal components can be compared to the structural wave numbers and the related components can be added to the reduced set. However, this means additional computational effort that will reduce the performance of the SVD method.

2.6 Turbulent Boundary Layer Excitation

In the literature, many different empirical models for the description of turbulent boundary layer excitation are shown. A comprising overview of some models is, for example, given in [7]. For the performance studies in this paper one of the most prominent model from Corcos [8] is chosen. Within the Corcos model, the cross-correlation matrix is defined via two correlation coefficients c_x and c_y in flow (x) and cross-flow (y) direction. The Corcos model is a homogeneous model that means it depends only on the distance vector (Δx, Δy).

$$S_{pp}(\Delta x, \Delta y, \omega) = p_{rms}^2 \exp(-k_c(c_x|\Delta x| + c_y|\Delta y|))\cos(k_c\Delta x) \tag{22}$$

With k_c being the convective wave number $k_c = \frac{U_c}{\omega}$ and the convective flow speed U_c that is often estimated by $U_c = 0.75U_\infty$ from the free-flow speed U_∞. From the authors experience, the Corcos model is not valid for all relevant flight states because this model was developed for subsonic flow, see for example [9]. For the numerical study in this paper, it suits perfectly because there are several reference solutions available, and there is an analytical expression for both wave number and space formulation. The pressure functions are translated into force functions by

considering an element or nodal area ΔA. In addition, a diffuse sound field excitation is considered as with the cross-correlation as given in [10].

$$\mathbf{S}_{pp} = p_{rms}^2 \frac{\sin(k\Delta r)}{k\Delta r} \text{ with } \Delta r = |\sqrt{\Delta x^2 + \Delta y^2}| \tag{23}$$

The foundations of the hybrid theory of Langley and Shorter [2] are based on the diffuse field reciprocity that relates the cross-correlation function to the energy in the diffuse field

$$\mathbf{S}_{ff} = \frac{4E_m}{\pi\omega n_m(\omega)} \operatorname{Im} \mathbf{D}_{dir}^{(m)} \tag{24}$$

Thus, in the actual power balance of Eq. (14) the above equation is used so that only the radiation stiffness is required in case of diffuse field excitation.

3 Test Cases

As test case, a typical cruise condition in civil flight is taken: $Ma = 0.8$ and flight level $FL = 330$ corresponding to a height of $h = 33{,}000\,\text{ft} = 10{,}058\,\text{m}$. With the standard atmosphere, this leads to the following fluid properties $c_0 = 299.2\,\text{m/s}$ and $\rho_0 = 0.409727\,\text{kg/m}^3$. As interior pressure, the current interior height of 8000 ft corresponding to 2400 m leads to the following air properties: $c_0 = 330.8$, $\rho_0 = 0.96287\,\text{kg/m}^3$. The following Corcos coefficients were selected $c_x = 0.116$ and $c_y = 0.7$.

3.1 Singular Value Decomposition

With the above data, a singular value decomposition is performed. In Fig. 2, the first 50 singular values are shown. It can be seen that the random nature of the TBL leads to about 50 required singular values to reach two orders of magnitude at $f = 100\,\text{Hz}$. However, at 1000 Hz the decay of the first 50 singular values is less than ten. Thus, even 50 values are not enough to get a reliable approximation of the TBL load above 400 Hz where the singular value distance is at least one order of magnitude. To conclude, the SVD is an option to reduce the computational expense. The calculation of the SVD is independent from the number of considered components and it took 30 min for 91 frequency steps, thus the gain in computation time cannot be high. The output of the load cases into the text-based NASTRAN input was the most time-consuming process, whereas the NASTRAN computation of the FEM response takes 1 h for the curved plate making computations of realistic structure feasible. However,

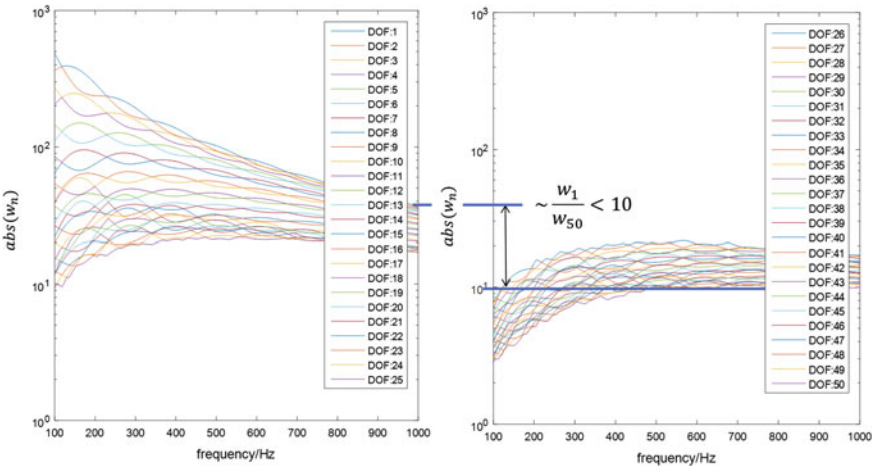

Fig. 2 Singular values of selected Corcos model

in an integrated FEM simulation environment the SVD may be an option, especially when real mode condensation is not possible.

3.2 Test Structures

For the evaluation of each achievable precision and influence of inhomogeneous mass distribution, two test cases are introduced: (i) a curved aluminium shell representing

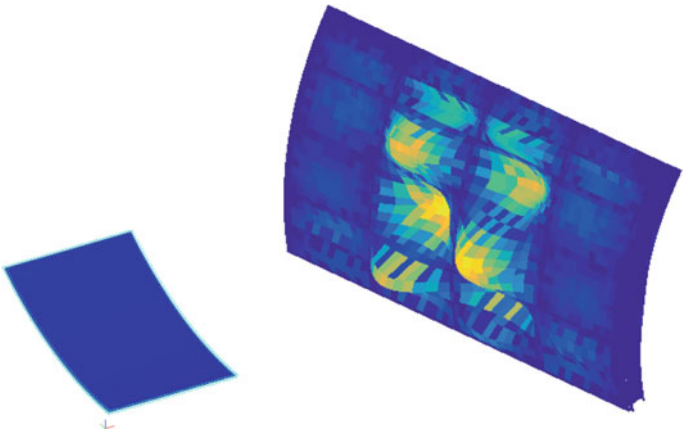

Fig. 3 Test structures, LHS curved, homogeneous aluminium plate, RHS fuselage structure

the homogeneous case and (ii) a typical aircraft panel with frames, stringers and windows as realistic and consequently inhomogeneous test case. The aluminium shell is of size $L_x = 0.8\,\text{m}$ in flow direction and $L_y = 1.2\,\text{m}$ in circumferential direction. The thickness is $t = 4\,\text{mm}$. The aircraft panel is a typical stringer frame stiffened aircraft structure of a regional aircraft with windows not specified in detail with dimensions $L_x = 1.8\,\text{m}$ and $L_y = 1.1\,\text{m}$ (Fig. 3).

4 Simulation Results

In the following, the test structures are excited by TBL represented by the Corcos model and the diffuse sound field. From the experience of the authors, the Graham assumption using only the diagonal terms is appropriate for two cases: (1) TBL excitation for both type of structures and (2) for homogeneous structures and both excitations, TBL and diffuse field. The consideration of only diagonal terms leads to much shorter computation times so it worth investigating the conditions for the validity of this assumption in more detail. In the coming sections, the content of the modal matrices will therefore be presented to evaluate the relevance of each coefficient.

4.1 Transmission Loss

In Fig. 4, the result for the homogeneous panel due to diffuse field excitation is shown. In order to verify the validity of the implementation in MATLAB, the diagonal and the full matrix solution are compared to the commercial result of the software *VAOne* of ESI-Group. One can see that all results agree quite well. There is a slight overestimation of the diagonal results in the high-frequency regime and below the first plate resonance. The TBL results agree also quite well as shown in Fig. 5 except some deviations at anti-resonances (high transmission loss) in the mid-frequency. When cumulating the 50 principal components, the SVD results are also reliable up to 400 Hz as discussed above due to sufficient dynamics in the singular values. But for higher frequencies, the method requires more components. With only 50 components, the TL is overestimated by several decibels at high frequencies.

The situation is different for the fuselage panel. In Fig. 6, there is a large difference between the diagonal and the full result for a diffuse field excitation. The Graham solution overestimates the transmission loss. The Hy-TL solution is according to [4] which is a full Graham implementation in wave number space.

However, in Fig. 7 were the TBL excitation is considered both results coincide well, so one may conclude that the diagonal form is sufficient for both; homogeneous and fuselage panel, leading to a high-speed calculation even for complex structure with a high number of modes. In the following, we will investigate the related matrices in detail to argue on why the diagonal components must be considered or not.

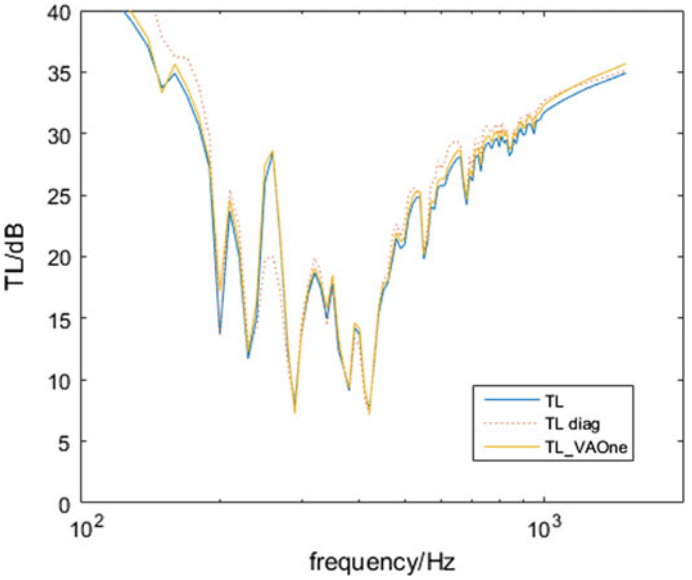

Fig. 4 Diffuse field transmission loss of the homogeneous panel

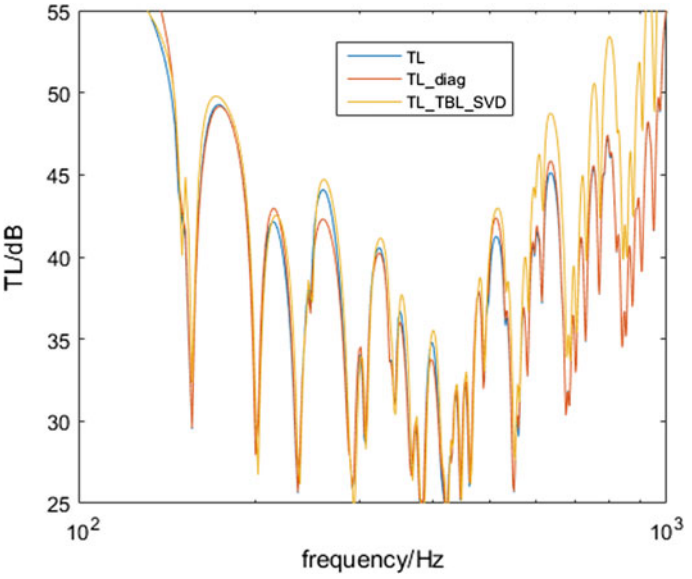

Fig. 5 TBL transmission loss of the homogeneous panel

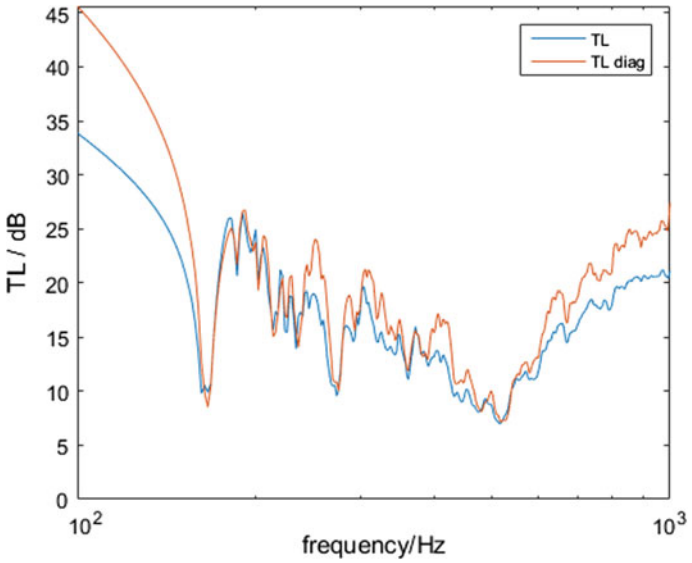

Fig. 6 Diffuse field transmission loss of the fuselage panel

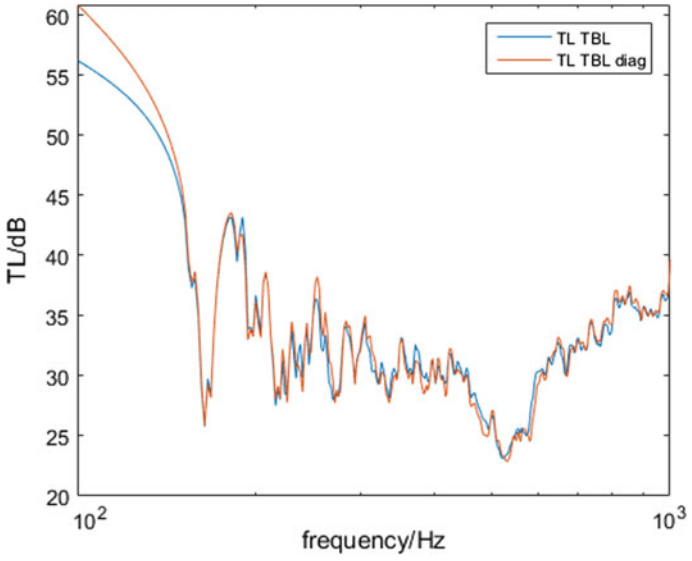

Fig. 7 TBL transmission loss of the fuselage panel

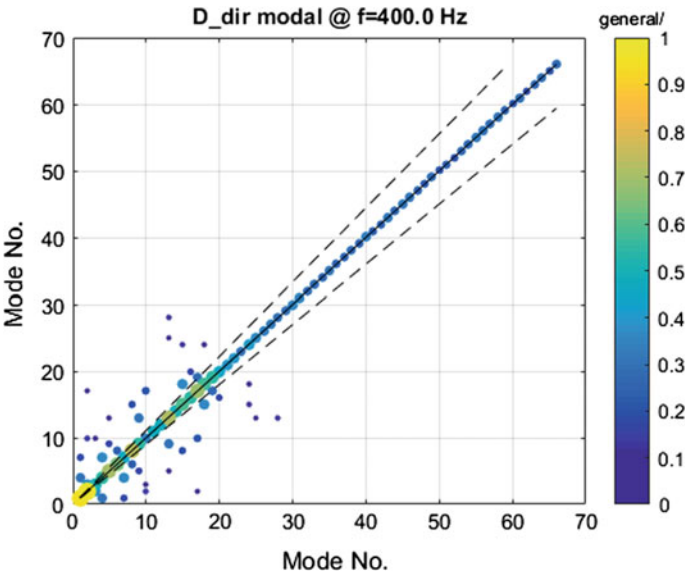

Fig. 8 Modal radiation stiffness of the homogeneous panel at 400 Hz

4.2 Modal Radiation Stiffness

In the power balance of the diffuse field transmission, the radiation stiffness in combination with modal frequencies are relevant. Thus, this quantity will be investigated first for both cases. In the following figures, the absolute value of the matrices is normalised to one for the highest matrix coefficient. All coefficients with absolute values higher than 10% of the maximum are presented by coloured circles. Size and colour of the circle show the value of each coefficient as denoted by the colour bar.

In Fig. 8, the modal radiation stiffness coefficients for the homogeneous plate at 400 Hz are shown. There are few relevant off-diagonal coefficients and less than in Fig. 9. The same effect can be seen for all frequencies. Thus, from the direct radiation stiffness it is obvious that the transmission loss of realistic structures cannot be calculated with the Graham assumption of diagonal modal matrices. The remaining question is why this method works for TBL excitation even with significant off-diagonal components of the matrix.

4.3 Modal Joint Acceptance

The power input into the structure that must not be confused with the power irradiated onto the surface is determined by the modal joint acceptance (Fig. 10).

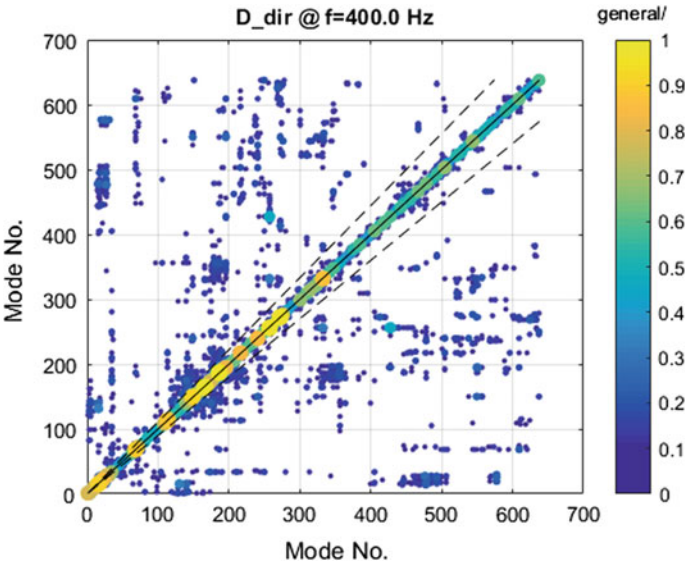

Fig. 9 Model radiation stiffness of the fuselage panel at 400 Hz

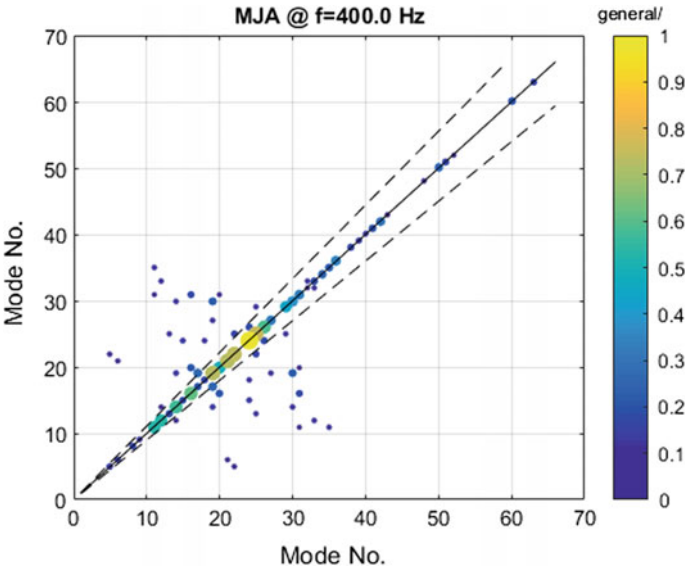

Fig. 10 Modal joint acceptance of homogeneous panel at 400 Hz

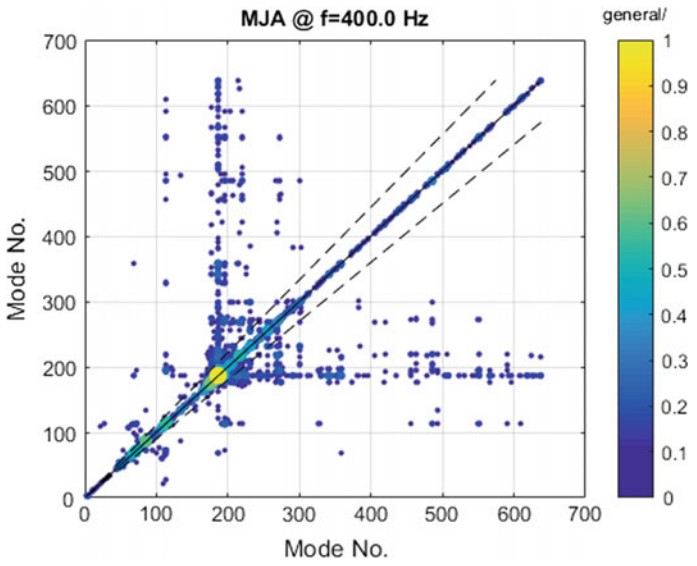

Fig. 11 Modal joint acceptance of the fuselage panel at 400 Hz

When inspecting the coefficients of the modal joint acceptance matrix of both structures, there is no evidence for the off-diagonal components to be irrelevant. In Fig. 11, the fuselage panel has high off-diagonal components. Consequently, the modal joint acceptance cannot be used for an explanation of good transmission results under TBL excitation. For the determination of the modal joint acceptance, the off-diagonal terms must be considered to get reliable results, even more than for the radiation stiffness.

4.4 Modal Response Matrix

The next step is to deal with the full structural response as given by (5). This involves the modal joint acceptance multiplied from left and right with the total stiffness. From the radiation stiffness, it is obvious that the diagonal approximation works for the homogeneous panel. The following studies will therefore focus on the fuselage panel for both excitations as shown in Figs. 12 and 13.

The results show that there is only few major modal components plus some off-diagonal terms for both. The dynamics in the figures is increased from [0.11] to [0.011] to show that for the TBL excitation there are less off-diagonal components. Thus, the structural response cross-spectrum allows the diagonal approach for TBL when the required precision is not too high.

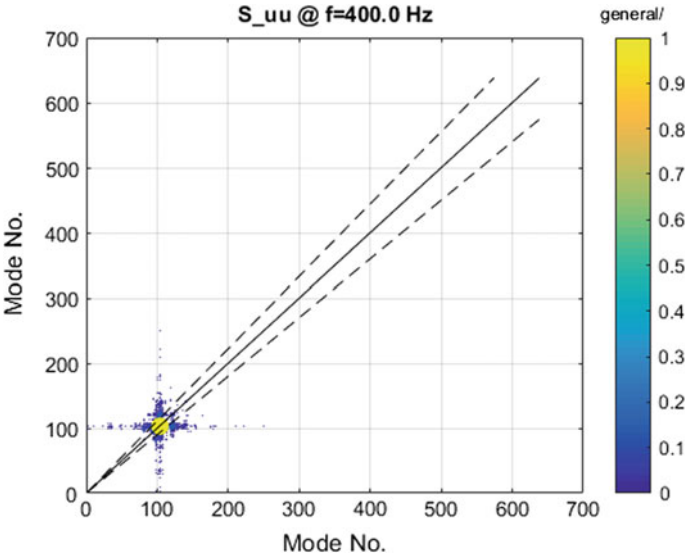

Fig. 12 Displacement cross-correlation matrix of the fuselage panel at 400 Hz for DAF excitation

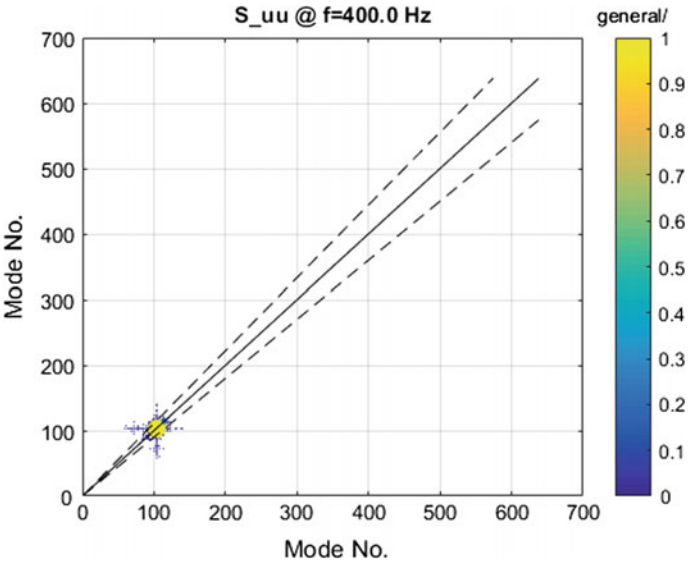

Fig. 13 Displacement cross-correlation matrix of the fuselage panel at 400 Hz for TBL excitation

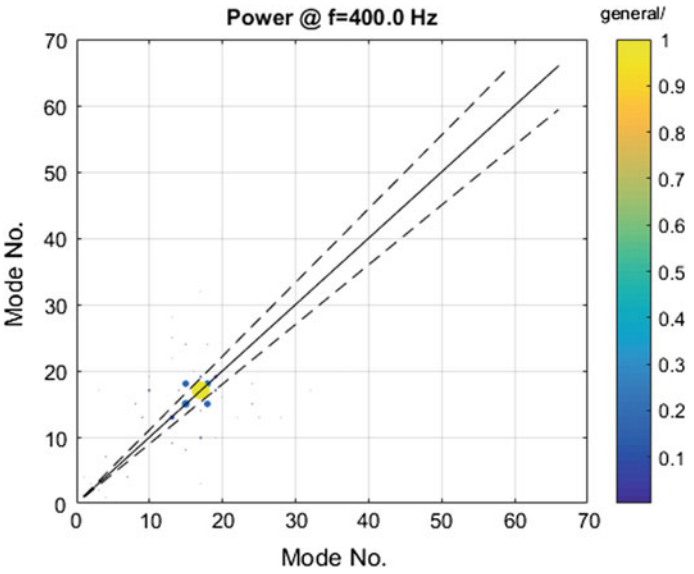

Fig. 14 Radiated power of homogeneous panel due to diffuse field excitation

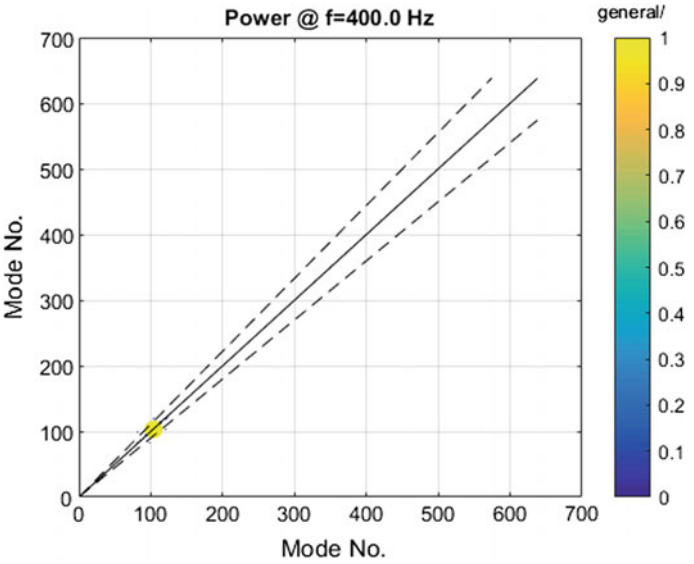

Fig. 15 Radiated power of fuselage panel due to TBL excitation

4.5 Radiated Power

The last remaining step in the flow of acoustic power is the acoustic radiation into the surrounding fluids given by Eq. (12). In Figs. 14 and 15, the coefficients of the sum of (12) are shown.

From Figs. 15 and 14, it becomes clear that even less diagonal components contribute to the radiated power in case of TBL. Thus, the off-diagonal terms may be neglected for the TBL transmission loss. One physical interpretation of this might be the wave number mismatch between the acoustic field (radiation) and the TBL excitation.

5 Conclusions

The modal implementation of the hybrid method is an excellent approach for the evaluation of panel radiation and vibration due to diffuse acoustic field and turbulent boundary layer excitations. For realistic panels with inhomogeneous mass distribution, this requires the consideration of the full modal matrices. For transmission loss and structural response calculations under TBL excitation, the diagonal form of Graham can be used for realistic structures, but with less precision for the vibration response. For more complex structures as, for example, double walls with isolation materials and cabin lining, the modal approach is not applicable. Here, the singular value decomposition is an option to reduce the size of the problem by considering a reasonable but still high number of principal components of the cross-correlation matrix of the turbulent boundary layer.

References

1. Maxit, L., et al.: Discussion about different methods for introducing the turbulent boundary layer excitation in vibroacoustic models. In: Ciappi, E., De Rosa, S., Franco, F., Guyader, J.-L., Hambric, S.A. (eds.) Flinovia—Flow Induced Noise and Vibration Issues and Aspects, p. 249278. Springer International Publishing, Cham (2015)
2. Shorter, P.J., Langley, R.S.: Vibro-acoustic analysis of complex systems. J. Sound Vib. **288**(3), 669–699 (2005)
3. Graham, W.R.: Boundary layer induced noise in aircraft, part i: the flat plate model. J. Sound Vib. **192**(1), 101–120 (1996)
4. Peiffer, A., et al.: Comparison of hybrid modeling tools for interior noise prediction. In: Proceeding Internoise 2009, Ottawa
5. Langley, R.S.: Numerical evaluation of the acoustic radiation from planar structures with general baffle conditions using wavelets. J. Acoust. Soc. Am. **121**(2), 766–777 (2007)
6. Press, W.H., et al.: Numerical Recipes in C, The Art of Scientific Computing, 2nd edn. Cambridge University Press (2002)
7. Graham, W.R.: A comparison of models for the wavenumber-frequency spectrum of turbulent boundary layer pressures. J. Sound Vib. **206**(4), 541–565 (1997)

8. Corcos, G.M.: Resolution of pressure in turbulence. J. Acoust. Soc. Am. **35**(2) (1963)
9. Klabes, A., et al.: Fuselage excitation during cruise flight conditions: from flight test to numerical prediction. In: Ciappi, E., De Rosa, S., Franco, F., Guyader, J.-L., Hambric, S.A. (eds.) Flinovia II—Flow Induced Noise and Vibration Issues and Aspects. Springer International Publishing, Cham (2017)
10. Pierce, A.D.: Acoustics—an introduction to its physical principles and applications. English. 1989th ed. Woodbury, New York 11797,U.S.A. Acoustical Society of America (ASA) (1991). ISBN: 0-88318-612-8
11. Langley, R.S.: On the diffuse field reciprocity relationship and vibrational energy variance in a random subsystem at high frequencies. J. Acoust. Soc. Am. **121**(2), 913–921 (2007)

Numerical Study of Nonlinear Fluid–Structure Interaction of an Excited Panel in Viscous Flow

Harris K. H. Fan, Garret C. Y. Lam and Randolph C. K. Leung

Abstract Vibration of flexible panel induced by flow and acoustic processes in a duct can be used for silencer design, but it may conversely generate noise if structural instability is induced. Therefore, a complete understanding of fluid–structure interaction is important for effective noise reduction. A new time-domain numerical methodology has been developed for the calculation of the nonlinear fluid–structure interaction of an excited panel in internal viscous flow. This paper reports its validation with two experiments. The first aims to validate that the methodology is able to capture flow-induced structural instability and its acoustic radiation. The second one is to show that the methodology captures the aeroacoustic–structural interaction in a low-frequency silencer and its response correctly. The importance of inclusion of viscous effect in both cases is also discussed.

Keywords Fluid–structure interaction · Flow-induced structural instability Aeroacoustic–structural interaction · Viscous effect

Nomenclature

C	Structural damping coefficient
D	Bending stiffness
E	Total energy
E_p	Modulus of elasticity
$\hat{H}$	Duct width and cavity height
K_p	Stiffness of foundation

H. K. H. Fan (✉) · G. C. Y. Lam · R. C. K. Leung
Department of Mechanical Engineering, The Hong Kong Polytechnic University, Hung Hom Kowloon, Hong Kong
e-mail: mr.harrisfan@connect.polyu.hk

G. C. Y. Lam
e-mail: garret.lam.hk@connect.polyu.hk

R. C. K. Leung
e-mail: mmrleung@polyu.edu.hk

E. Ciappi et al. (eds.), *Flinovia—Flow Induced Noise and Vibration Issues and Aspects-II*,
https://doi.org/10.1007/978-3-319-76780-2_16

L_p	Panel length
M	Mach number
N_x	Internal tensile stress of panel
Pr	Prandtl number
$\hat{R}$	The specific gas constant
Re	Reynolds number
S	Duct cross-sectional area
T	Temperature
T_x	External tensile stress of panel
TL	Transmission loss
$\hat{U}$	Inlet mean flow speed
W	Acoustic power
a	Characteristic dimension of a duct cross section
c_0	Speed of sound
dx	Grid size in x-direction
dy	Grid size in y-direction
f	Frequency
h_p	Panel thickness
k	Wave number
l	Size of the fluid volume in normal direction with panel deflection
l''	End correction
l_i	Dimensions of duct in three directions, $i = 1$, 2, and 3
n_i	Mode numbers along three directions, $i = 1$, 2, and 3
p	Pressure
p_A	Amplitude of incident wave
p_{ex}	Net pressure exerted on panel
q_x	Heat flux in x-direction
q_y	Heat flux in y-direction
t	Time
t_1	Time of one period
u	Fluid velocity in x-direction
$\hat{u}_0$	The reference velocity
v	Fluid velocity in y-direction
v_η	Fluid velocity in η-direction
v_ξ	Fluid velocity in ξ-direction
w	Panel displacement
$\dot{w}$	Panel velocity
$\ddot{w}$	Panel acceleration
γ	The specific heat ratio
δ	Size of the fluid volume in normal direction without panel deflection
η	Normal direction of the undeflected panel
θ	Phase
μ	Viscosity

ξ	Tangential direction of the undeflected panel
ρ	Density of fluid
ρ_p	Density of panel

Subscripts

$lface$	Lower fluid–panel interface
$lower$	Fluid element beneath panel
$uface$	Upper fluid–panel interface
$upper$	Fluid element above panel

Superscript

$\hat{}$	Dimensional quantities

1 Introduction

A good understanding of the fluid–structure interaction is important in the design of effective flow duct noise control in many aeronautic, automotive, and building service engineering systems. When the flow unsteadiness and/or the duct geometry are changed, acoustic waves are generated which may propagate back to the source region and modify the flow process generating it. Such aeroacoustic processes always appear in the flow duct. Since the duct wall is constructed by thin panels, it may be excited to vibrate by the aeroacoustic processes and in turn modify the source aeroacoustic processes. There is a nonlinear coupling between the aeroacoustics of the fluid and the structural dynamics of the panel. If the design of flow duct noise control is developed with only one media (fluid or panel) in the consideration, it may be completely counteracted by the dynamics occurring in another media through the nonlinear coupling. A complete understanding of the nonlinear fluid–structure interaction and its acoustics is necessary for devising an effective design.

To control the noise generation and its propagation in air flow ducts, a thick layer of acoustic liner is commonly used that covers the duct to absorb noise and prevent the noise in the duct breaks through the duct walls and annoy the people in the surrounding. However, this kind of noise control method is not effective in low frequency range. A drum-like silencer concept was introduced by Huang [1] in which the nonlinear fluid–structure interaction of flexible panels was used to control low-frequency noise. Huang reported that this design is effective in low frequency range and claimed it gives low-pressure loss when flow is present. However, the effect of mean flow is not considered in his theoretical study [1]. Later, Fan et al. [2,

3] attempted to study numerically the aeroacoustic–structural response of the panel in this design in an inviscid flow framework. The presence of inviscid mean flow produces a completely different response from the case without flow. The fluid–structure interaction was found to play a very important role in the noise reduction. The silencer performance was found strongly reduced in the presence of flow. In real application, viscous flow effect may be another important factor that affects the silencing performance. The viscous flow may excite the flexible panel to vibrate and cause structural instability. An experimental study by Liu [4] on the similar design showed that the instability of the panel can be induced. Probably additional noise will be generated by the vibration which reduces the effectiveness of the silencer. Therefore, it is necessary to investigate the nonlinear fluid–structure interaction in viscous flow.

A numerical methodology that facilitates better understanding of fluid–structure interaction in viscous compressible duct flow for advancing design of silencer with flexible panel has recently been developed. In order to minimize the error generated by the numerical coupling procedure that connects the fluid and structure domains, a treatment that combines all governing equations of different physical domains and solved by a single solver is introduced. The new methodology has to be proven able to resolve the nonlinear fluid–structure interaction and its acoustic problems important to achieving a better design of the drum-like silencer concept for practical use. This paper reports the results of such validation with calculations of two pertinent experiments.

2 A Brief of the Numerical Methodology

The aeroacoustic–structural interaction problem involves the interplay between the flow dynamics, acoustics, and structural dynamics. The effects of all three parts play equally important roles. Since acoustic motion is a kind of unsteady flow motions that a fluid medium supports [5], both the acoustic field and its source unsteady flow must be calculated and accurately resolved simultaneously by the numerical model for fluid medium. In addition, the inherent nonlinear interaction between the acoustics and the unsteady flow must be accurately accounted for solving the problem. The generated acoustic waves inside a duct experience multiple reflection and scattering which may then propagate back and alter the unsteady flow dynamics and the panel structural vibration. These nonlinear interactions cannot be ignored. Thus, direct aeroacoustic simulation (DAS) approach [6, 7] is adopted in modeling the aeroacoustics in fluid medium. At the fluid–structure interface, both flow and panel structural responses are simultaneously involved so proper governing equations that describe these responses are needed. They are however usually not available. Therefore, the responses at the interface are resolved by iterating the aeroacoustic and panel dynamic models by Newton's method. Here only the key components in the formulation of the numerical methodology are described. The details of their numerical implementation are referred to Fan [8].

2.1 Aeroacoustic Model

In DAS, the aeroacoustics of the fluid medium is modeled by solving the two-dimensional compressible Navier–Stokes equations together with ideal gas law for calorically perfect gas. The normalized Navier–Stokes equations without source can be written in the strong conservation form as,

$$\frac{\partial \boldsymbol{U}}{\partial t} + \frac{\partial (\boldsymbol{F} - \boldsymbol{F}_v)}{\partial x} + \frac{\partial (\boldsymbol{G} - \boldsymbol{G}_v)}{\partial y} = 0, \tag{1}$$

where $\boldsymbol{U} = [\rho \quad \rho u \quad \rho v \quad \rho E]$, $\boldsymbol{F} = [\rho u \quad \rho u^2 + p \quad \rho uv \quad (\rho E + p)u]$, $\boldsymbol{G} = [\rho v \quad \rho uv \quad \rho v^2 + p \quad (\rho E + p)v]$, $\boldsymbol{F}_v = (1/Re)[0 \quad \tau_{xx} \quad \tau_{xy} \quad \tau_{xx}u + \tau_{xy}v - q_x]$, $\boldsymbol{G}_v = (1/Re)[0 \quad \tau_{xy} \quad \tau_{yy} \quad \tau_{xy}u + \tau_{yy}v - q_y]$, ρ is the density of fluid, u and v are the velocities in x and y-directions, respectively, t is the time, normal and shear stresses $\tau_{xx} = (2/3)\mu\,(2\partial u/\partial x - \partial v/\partial y)$, $\tau_{xy} = \mu\,(2\partial u/\partial y - \partial v/\partial x)$, $\tau_{yy} = (2/3)\mu$ $(2\partial v/\partial y - \partial u/\partial x)$, μ is the viscosity, total energy $E = p/\rho(\gamma - 1) + (u^2 + v^2)/2$, pressure $p = \rho T/\gamma M^2$, T is temperature, heat flux $q_x = \left[\mu/(\gamma - 1)PrM^2\right]$ $(\partial T/\partial x)$, $q_y = \left[\mu/(\gamma - 1)PrM^2\right](\partial T/\partial y)$, the specific heat ratio $\gamma = 1.4$, the reference Mach number $M = \hat{u}_0/\hat{c}_0$ where $\hat{u}_0$ is the reference velocity, $\hat{c}_0 = (\gamma \hat{R}\hat{T}_0)^{1/2}$, the specific gas constant for air $\hat{R} = 287.058\,\mathrm{J/(kgK)}$, the reference Reynolds number $Re = \hat{\rho}_0\hat{c}_0\hat{L}_0/\hat{\mu}_0$, and Prandtl number $Pr = \hat{c}_{p,0}\hat{\mu}_0/\hat{k}_0 = 0.71$. All the dimensional quantities are indicated with caret.

The conservation element and solution element (CE/SE) method [9] is adopted to solve the DAS governing equations. It has been proven that the inherently low dissipation of CE/SE method allows accurate calculation of the acoustic and flow fluctuations which usually exhibit large disparity in their energy and length scales [7]. Its numerical framework relies solely on strict conservation of physical laws and emphasis on the unified treatment of fluxes in both space and time. Lam [7] showed that CE/SE method is capable of resolving the low Mach number interactions between the unsteady flow and acoustic field accurately by calculating the benchmark aeroacoustic problems with increasing complexity. The formulation of the CE/SE method is not given in this paper. The details can be referred to in the works of Lam [7].

2.2 Structural Dynamic Model

The one-dimensional dynamic response of the flexible panel can be modeled by the simplified nonlinear Von Karman's theory on Kelvin foundation [10, 11]. The panel is assumed to be of uniform small thickness $h_p = \hat{h}_p/\hat{L}_p$ and initially flat. Using the same set of reference parameters adopted in the aeroacoustic model, the normalized governing equation for panel displacement $w(x) = \hat{w}/\hat{L}_0$ can be written as,

$$D\frac{\partial^4 w}{\partial x^4} - (T_x + N_x)\frac{\partial^2 w}{\partial x^2} + \rho_p h_p \frac{\partial^2 w}{\partial t^2} + C\frac{\partial w}{\partial t} + K_p w = p_{ex}, \tag{2}$$

where $N_x = (E_p h_p / 2L_p) \int_0^{L_p} (\partial w/\partial x)^2 \, dx$, $D = \hat{D}/(\hat{\rho}_0 \hat{c}_0^2 \hat{L}_0^3)$ is the bending stiffness, $T_x = \hat{T}_x/(\hat{\rho}_0 \hat{c}_0^2 \hat{L}_0)$ is the external tensile stress resultant per unit length in the tangential direction, N_x is the internal tensile stress in the tangential direction induced by stretching, $E_p = \hat{E}_p \hat{c}_0^2/(\hat{\rho}_0 \hat{L}_0^4)$ is the modulus of elasticity, $L_p = \hat{L}_p/\hat{L}_0$ is the length of panel, $\rho_p = \hat{\rho}_p/\hat{\rho}_0$ is the density of panel, $C = \hat{C}/(\hat{\rho}_0 \hat{c}_0)$ is the structural damping coefficient, $K_p = \hat{K}_p \hat{L}_0/(\hat{\rho}_0 \hat{c}_0)$ is the stiffness of foundation, and $p_{ex} = \hat{p_{ex}}/(\hat{\rho}_0 \hat{c}_0^2)$ is the net pressure exerted on the panel surface.

To satisfy the tangency condition, four equivalent relationships between the fluid at the interface and the panel can be derived [12]. They are equivalents of stress, acceleration, velocity, and displacement. When the fluid element size and the normal velocity are small ($M < 0.3$) [13], the local viscous effect and compressibility of fluid can be ignored. Therefore, the normal pressure difference can be simply given by Newton's second law as $\partial p/\partial \eta = -\rho(\partial v_\eta/\partial t) = -\rho \ddot{w}$ (Fig. 1). Then, the panel acceleration is found as $\ddot{w} = -(\partial p/\partial \eta)/\rho$. The panel velocity and displacement can also be obtained by integrating $\ddot{w}$ and $\dot{w}$ over time, i.e., $\dot{w} = \int \ddot{w} dt$ and $w = \int \dot{w} dt$.

2.3 Boundary Conditions

All solid surfaces obey the tangency condition and the normal pressure gradient condition. At no-slip boundary surface, zero tangential velocity $v_\xi = 0$ is applied.

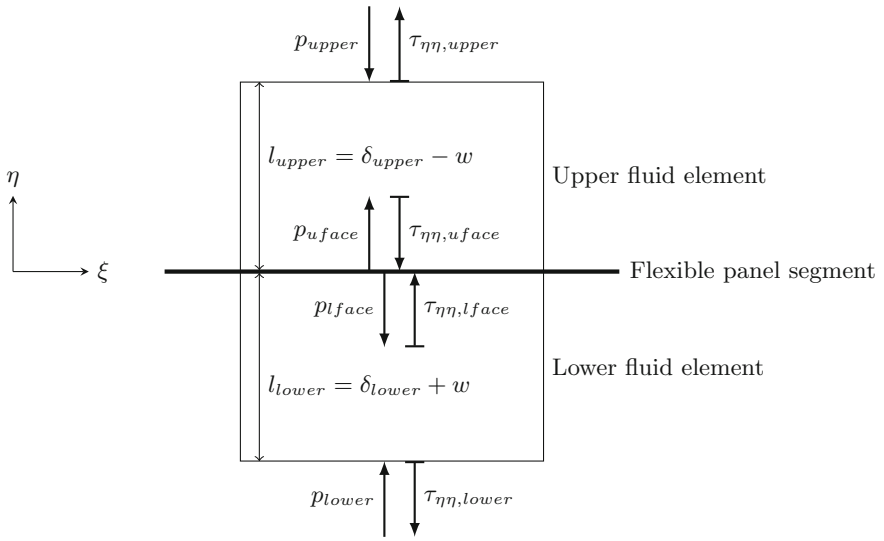

Fig. 1 Small fluid volumes on two sides of the flexible panel

Isothermal condition $T = T_0$ is applied to all solid surfaces, and zero normal velocity $v_\eta = 0$ is applied to all rigid surfaces. At the fluid–panel interface, the normal velocities are set as $\dot{w}$. Pinned conditions are prescribed at both edges for the flexible panel where the displacement and bending moment are set zero, i.e., $w = \partial^2 w/\partial x^2 = 0$.

2.4 Fluid–Panel Coupling

During the time-marching of the numerical solution, aeroacoustics and structural responses occur at the fluid–panel interface. Consider two adjacent infinitely small control volumes of fluid on both sides of flexible panel and their total stress on the normal direction as shown in Fig. 1 in which ξ and η are the tangential and normal directions of the undeflected panel surface, respectively. δ and l are defined as the size of the fluid volume in normal direction without and with panel deflection, respectively. p is the pressure acting from the surrounding on the surface of the fluid volume. The viscosity-induced normal force may be expressed as $\tau_{\eta\eta} = (2/3)\mu\left(2\partial v_\eta/\partial\eta - \partial v_\xi/\partial\xi\right)$, where v_ξ and v_η are the fluid velocities in tangential and normal directions [14]. On the no-slip panel surface, $\partial v_\xi/\partial\xi = 0$ and $\tau_{\eta\eta} = (4/3)\,\mu\left(\partial v_\eta/\partial\eta\right)$. When the fluid is driven by the panel, the additional forces applied within the fluid volume are the difference in stresses over the control volume given by $(p_{uface} - \tau_{\eta\eta,uface}) - (p_{upper} - \tau_{\eta\eta,upper})$ and $(p_{lface} - \tau_{\eta\eta,lface}) - (p_{lower} - \tau_{\eta\eta,lower})$. Meanwhile, the net external force applied to the panel is $p_{ex} = (p_{lface} - \tau_{\eta\eta,lface}) - (p_{uface} - \tau_{\eta\eta,uface})$.

Since variation of viscous stress with fluid volume is very small compared to the pressure, it can be assumed that $\tau_{\eta\eta,uface} - \tau_{\eta\eta,upper} = \tau_{\eta\eta,lface} - \tau_{\eta\eta,lower} = 0$. The additional force per unit volume can thus be written as $(p_{uface} - p_{upper})/l_{upper}$ and $(p_{lface} - p_{lower})/l_{lower}$, and the corresponding mechanical power is $v_{\eta,upper}$ $(p_{uface} - p_{upper})/l_{upper}$ and $v_{\eta,lower}(p_{lface} - p_{lower})/l_{lower}$, respectively. These forces arising from the vibrating fluid–panel interface are responsible for driving the aeroacoustics solution in the neighborhood of the panel. Therefore, it is better to resolve their effects by expressing them as a source term $\boldsymbol{Q}$ in the homogeneous Eq. 1 originally for fixed domain boundary. Thus, the DAS governing equation can now be written as,

$$\frac{\partial \boldsymbol{U}}{\partial t} + \frac{\partial\left(\boldsymbol{F} - \boldsymbol{F}_v\right)}{\partial x} + \frac{\partial\left(\boldsymbol{G} - \boldsymbol{G}_v\right)}{\partial y} = \boldsymbol{Q}, \tag{3}$$

where $\boldsymbol{Q} = [-\sin\theta\, Q' \quad \cos\theta\, Q' \quad v_\eta Q' \quad 0]$, $Q'_{upper} = (p_{uface} - p_{upper})/l_{upper}$ and $Q'_{lower} = (p_{lower} - p_{lface})/l_{lower}$. This modified equation is solved together with the dynamic equation (Eq. 2) by means of an iterative method to resolve the nonlinear fluid–panel coupling. This new approach appears to give a faster convergence than before. The details of the implementation of the numerical treatment of resolving fluid–panel coupling are referred to Fan [8].

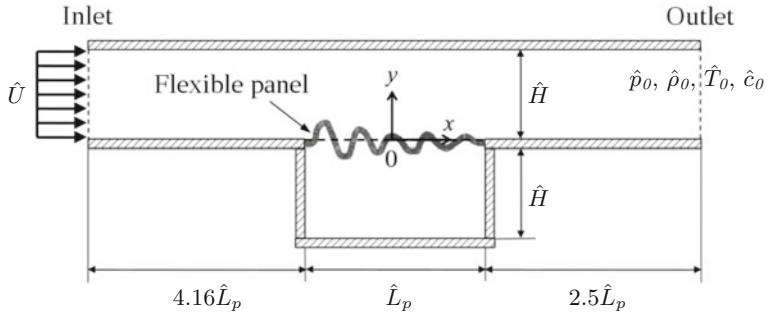

Fig. 2 Schematic configuration of the experiment setting of Liu [4] (not-to-scale)

3 Flow-Induced Structural Instability

In order to validate the capability of the numerical methodology of solving fluid–panel interaction, the experimental study carried out by Liu [4] on the instability of flexible panel installed on the wall of a duct carrying a low-speed uniform $\hat{U} = 35$ m/s is selected as the benchmark for the validation. In the experiment, a 0.025-mm-thick steel sheet was flush-mounted in a section of rigid flow duct and backed by a rigid cavity as shown in Fig. 2. The entire test section was installed in a closed-loop acoustic wind tunnel. When the flow was turned on, the vibrating velocity of the sheet was measured. The same set of physical parameters are taken for the present calculation: the panel and cavity length $\hat{L}_p = 300$ mm, the duct width and cavity height $\hat{H} = 100$ mm, the upstream and downstream length are 1250 mm and 750 mm, respectively, the panel density $\hat{\rho}_p = 7800\,\text{kg/m}^3$, the panel thickness $\hat{h}_p = 0.025$ mm, Young's modulus $\hat{E}_p = 193$ GPa, the panel tension $\hat{T}_x = 40$ N, and the mean flow speed $\hat{U} = 35$ m/s. Since the background noise level within the entire wind tunnel was highly suppressed in its design, the panel vibration was found solely induced by the unsteady viscous effects on its surface flow. All variables are normalized by $\hat{L}_0 =$ panel length $\hat{L}_p$, ambient acoustic velocity $\hat{c}_0 = 340$ m/s, time $\hat{t}_0 = \hat{L}_0/\hat{c}_0$, ambient density $\hat{\rho}_0 = 1.225\,\text{kg/m}^3$, pressure $\hat{\rho}_0\hat{c}_0^2$, and ambient temperature $\hat{T}_0$. Uniform mesh is used with grid sizes $dx = 0.02$ and $dy = 0.0067$ for both x and y directions.

Before carrying out the calculation of panel instability, it is important to realize how accurate the aeroacoustic model can capture the background mean velocity profile of the duct flow. It is because under the action of fluid viscosity a wrong velocity profile on duct wall would induce a wrong wall shear stress which might in turn drive a wrong panel instability mode. Liu [4] reported in his work a structural instability experiment at $\hat{U} = 35$ m/s but only provided a mean velocity profile measurement at $\hat{U} = 30$ m/s. So an additional case with $\hat{U} = 30$ m/s has to be calculated for appropriate comparison with the experimental data in Fig. 3. The figure shows the numerical velocity profile agrees favorably well with experimental data.

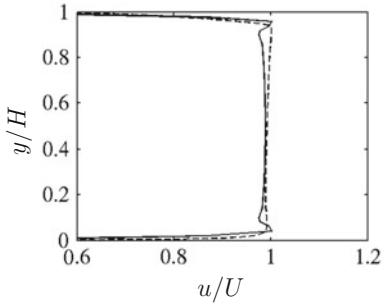

Fig. 3 Mean velocity profile at the inlet. ——, numerical result; – – –, experimental data

The normalized velocity boundary thickness from calculation is 0.039 which agrees very well with that of 0.037 obtained from the experiment. In the very close proximity to duct wall, i.e., $y/H \leq 0.02$, the two profiles overlap fully. It provides further support that the aeroacoustic model is able to generate correct mean velocity profile for initiating the flow-induced panel structural instability observed in experiment.

Liu [4] reported the emergence of dynamic instability, known as flutter, of the panel in his experiment with duct flow velocity $\hat{U} = 35$ m/s. In essence when the panel deflection gets large enough, the panel will exhibit a post-flutter oscillation known as limit cycle oscillation. Such phenomenon arises when the effective panel stiffness is so strengthened by panel deformation up to a level that is strong enough to balance the external force exciting the panel oscillation. The time traces of vibrating velocity at two locations, at $x = -0.17$ and 0, obtained from numerical calculation are shown in Fig. 4. After the onset of instability, the amplitudes of panel vibration grow and become saturated after $t \approx 200$. Eventually they enter into time stationary states after $t \approx 800$, and the limit cycle oscillations occur. Axial mode analysis established in Fan et al. [2] is conducted to derive the spatial responses of panel vibration during limit cycle oscillation (Fig. 5). Evidently, the panel response is dominated by the second in vacuo bending mode with $k = 1$. Its first and second harmonics are also resolved.

Figure 6 shows a comparison of the arithmetic average of the calculated vibration spectra distributed along the panel with the corresponding one reported in experiment. The numerical result shows a favorable agreement with the experimental data. The first numerical peak emerges at frequency $f_0 = 0.07$ which shows a -13.5% frequency shift compared to the experiment result. The difference may be attributed to the limitation of one-dimensional assumption in the calculation of panel dynamics (Eq. 2). The lack of vibration freedom along spanwise direction tends to promote panel resonant vibrations at low frequencies as easily seen from existing analytical solutions [15]. The overall vibration amplitude at dominant frequency appears to be much stronger than that observed in experiment. This might be due to the fact that in experiment the distribution of vibration amplitude over the two-dimensional panel was not uniform so certain canceling effects prevailed in the averaging of spectra.

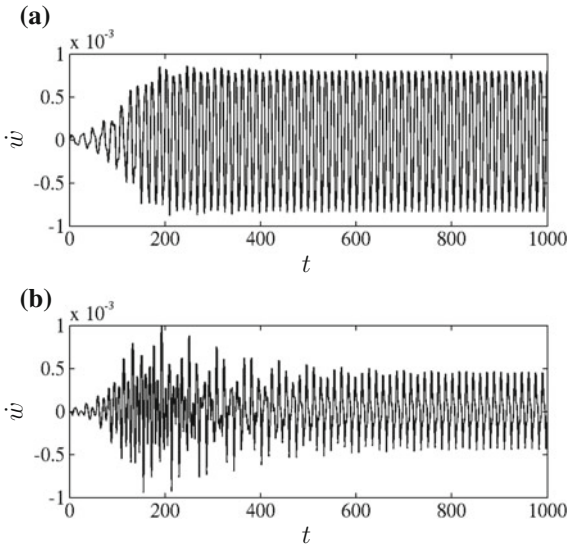

Fig. 4 Time traces of vibrating velocity. **a** At $x = -0.17$. **b** At $x = 0$

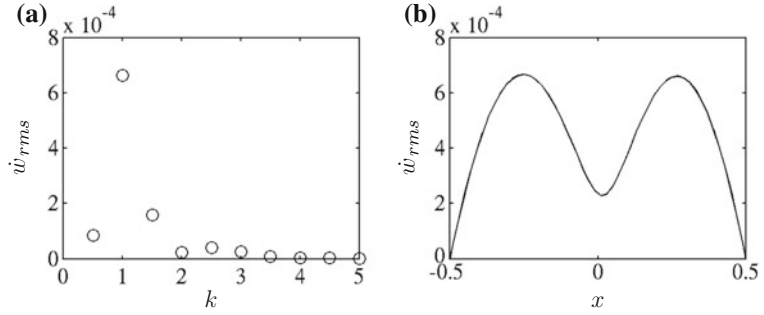

Fig. 5 Panel spatial response. **a** The modal spectrum of panel velocity. **b** The distributions of panel velocity amplitude

Furthermore, it is easy to observe in Fig. 6 that there are two peaks showing up in the experimental spectrum but not in the calculation. After careful investigation, their emergence is found that related to the excitation of wind tunnel duct acoustic modes during the execution of experiment.

The frequency of acoustic resonance within an open-ended duct with rectangular cross section can be estimated from the equation [16, 17] as $f_{n_1,n_2,n_3} = (c_0/2)[{n_1}^2/(l_1 + 2l'')^2 + {n_2}^2/{l_2}^2 + {n_3}^2/{l_3}^2]^{1/2}$, where c_0 is the speed of sound, l_1, l_2, and l_3 are the length, height, and width of the duct, respectively, n_1, n_2, and n_3 are the mode numbers along respective directions, and l'' is the end correction. When resonance occurs, the fluid medium at each open end oscillates and the pressure

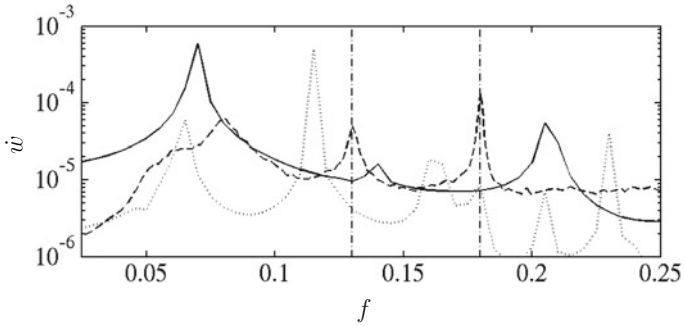

Fig. 6 Frequency spectrum of the vibration velocity on the whole panel. —, numerical result with viscous flow; · · · · · ·, numerical result with inviscid flow; – – –, experimental data; — · — · —, duct mode frequencies

there is not constant. Thus, the effective length for resonant oscillation inside the duct will be a bit longer than its physical length [16, 17] and an end correction is required. For $ka < 0.5$, the end correction can be approximately determined as $l'' = 0.613a$ [17], where $a = (S/\pi)^{1/2}$ is the characteristic dimension of the duct cross section with area S, and $k = 2\pi/\lambda$. The normalized length of the wind tunnel duct section from the nozzle to the diffuser is 7.67 which gives the frequency of the second mode $f_{2,0,0} = 0.13$. This value matches exactly the second peak in the experimental spectrum in Fig. 6. Besides, Liu [4] opened two openings, each with dimension 50 mm × 50 mm, upstream and downstream of the test section in his experiment so as to simulate a mean pressure drop along test section similar to those commonly observed in practical ventilating systems. However, that way might introduce extra possibility of open-ended duct resonance between these two new openings. According to Liu [4], the normalized separation between two openings was approximately 5.56. It is not difficult to determine the frequency of second resonant duct mode as $f_{2,0,0} = 0.18$. Coincidently, this value matches exactly the third peak observed in the experimental spectrum in Fig. 6. Therefore, it is not surprised to see the two identified resonant duct modes, rather than flow-induced instability, might effectively excite the panel to give the two peaks in the spectrum. In our numerical calculation, both the duct inlet and outlet are modeled with truly anechoic boundary conditions so resonance along duct length is impossible. On the other hand, the mean pressure drop in time stationary solution is similar to that in realistic systems so no additional opening is required. These explain why no similar extra peak is observed in the numerical spectrum.

Using inviscid flow assumption, the same problem is also calculated to highlight the importance of fluid viscosity in the onset of flow-induced structural instability. In essence, $\boldsymbol{F}_v = \boldsymbol{G}_v = 0$ are set in Eq. 1 and impose sliding condition on all duct walls and panel surface in the calculation. Evident in Fig. 6, the inviscid solution gives the worst agreement with the experiment. Its first peak occurs at a frequency $f = 0.065$ which is 19.8% lower than that observed in the experiment, a much

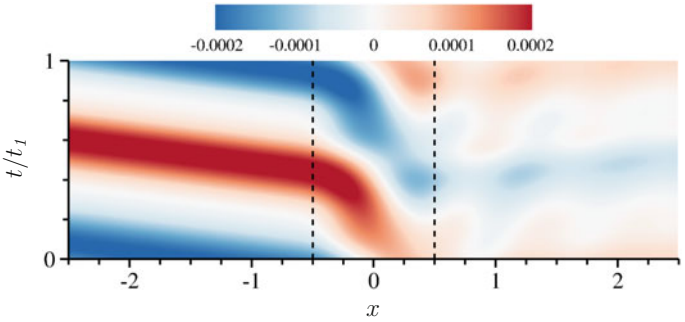

Fig. 7 Pressure fluctuation along the duct centerline within one period of the dominant vibrating frequency, $t_1 = 1/f_0$

larger difference with viscous solution. Furthermore, several more peaks show up in the inviscid spectrum but none of them agrees with experimental data. It is also interesting to see it is the inviscid second peak, rather than the first one, which dominates the spectrum. All these observed discrepancies may be attributed to the fact that duct wall boundary layer does not develop due to the lack of fluid viscosity and the pressure along the duct maintains more or less constant. This also leads to stronger net normal force acting on the panel than in viscous calculation. All these changes altogether contribute to a different exciting force, so a different structural instability result prevails.

The flow-induced vibrating panel radiates acoustic waves to upstream and downstream. The acoustic pressure fluctuation along the duct centerline within one period of the dominant frequency, $t_1 = 1/f_0 = 14.3$, is shown in Fig. 7. The upstream radiation is in the form of simple plane wave and is much stronger than the downstream radiation. The acoustic power W radiated by the panel can be determined by integrating the acoustic intensity passing through duct cross section enclosing the panel [18], as $W = \int_0^H (\bar{\rho}u' + p'\bar{u}/c^2)(p'/\bar{\rho} + \bar{u}u' + \bar{v}v')dy$, where $\bar{\rho}, \bar{u}, \bar{v}$ are the mean values of density and velocities in x- and y-directions, respectively, and p', u', v' are their fluctuations. The average acoustic powers over t_1 in upstream and downstream are -1.5×10^{-9} (through $x = -2.5$) and 3.6×10^{-8} (through $x = 2.5$), respectively. The acoustic power radiated to upstream is 5.9 db larger.

In addition to acoustic radiation, the excited panel also produces flow fluctuations at the same frequency which convect downstream. When the fluid impinges the lower wall, it is forced to turn its direction from negative to positive y; for example, at $x \approx 1.3$ in Fig. 8a, an high-pressure zone is created as shown in the same location (Fig. 8b). On the contrary, a low-pressure zone is created on the wall following fluid motion toward the wall, for example at $x \approx 1$. Together with the acoustic wave, the convecting flow fluctuations create a staggered pressure distribution downstream of the panel.

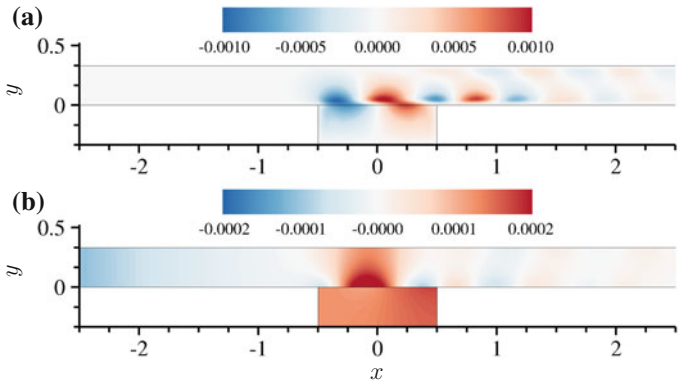

Fig. 8 Snapshot at $t/t_I = 0.2$. **a** Velocity fluctuation in y-direction. **b** Pressure fluctuation

4 Aeroacoustic–Structural Interaction in Practical Silencer Design

An experimental study of the transmission loss of a drum-like silencer installed in a low-speed duct [19] is selected as the benchmark case for the evaluation of the accuracy of the numerical methodology in solving aeroacoustic–structural interaction in realistic situation. According to Fan et al. [2], aeroacoustic–structural interaction refers to a nonlinear problem to which the unsteady flow, acoustics, and structural dynamics contribute equally in a fully coupled manner. The acoustical performance of the drum-like silencer in the selected experimental study fits this context of aeroacoustic–structural interaction very well. The noise reduction of the silencer cannot be deduced accurately by resolving the flow–structure interaction first.

Figure 9 shows a two-dimensional computational domain that replicates key features of the silencer design in the experiment. The silencer is constructed as two opposing side branch cavities each of which is covered by a flexible panel. An acoustic wave propagates along the duct from left to right along with the flow. Each panel responds to the excitation of the convected acoustic wave and vibrates. The induced vibration reflects the incident acoustic wave and modifies the dynamics of flow in its vicinity. As seen from a previous study assuming inviscid duct flow [2], such aeroacoustic–structural interaction plays a critical role in determining the effectiveness of acoustic reflection by the panels and consequently the overall silencer transmission loss performance. However, viscous flow prevails in all practical situation and the effect of viscosity is not understood. The same set of experiment parameters are taken for the calculation: the panel and cavity length $\hat{L}_p = 500$ mm, the duct width and cavity height $\hat{H} = 100$ mm, the upstream and downstream length are 1000 and 870 mm, respectively, and the panel mass per unit area $\hat{\rho}_p \hat{h}_p = 0.17\,\mathrm{kg/m^2}$. The range of frequency of interest goes from 20 to 1000 Hz. The normalization used in the

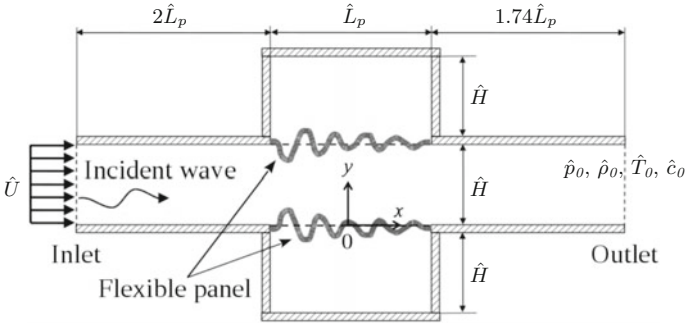

Fig. 9 Schematic configuration of the drum-like silencer (not-to-scale)

calculation is same as that in Sect. 3. The ambient density, pressure, and temperature are fixed at the outlet. No-slip condition is applied for all rigid duct walls and flexible panel surfaces. A broadband incident acoustic plane wave covering frequency range f from 0.0294 to 1.4706 with a resolution $\Delta f = 0.0147$ is introduced into the duct domain. Its excitation function is expressed as $p'_{inc} = p_A \sum_{n=1}^{99} \sin(2\pi t f_n + \theta_n)$, where $p_A = 4.5 \times 10^{-4}$ ($\sim$110 dB) is constant to all f_n, and θ_n is uniformly distributed random phase generated by random number generation function in MATLAB. A uniform flow profile is applied at the inlet to let the duct boundary layer develop freely. A full rigid duct case is first calculated to develop the proper mean flow profile in the whole flow field. The steady solution is then used as the initial condition for the calculation with flexible panel. The initial pressure in the cavity is set as same as the mean pressure in the duct over the panel to avoid large deflection of the panel by the static pressure that affects the panel response. In the mesh, uniform grid distribution is used for both x and y directions with $dx = 0.02$ and $dy = 0.0033$.

The instantaneous distribution of vibrating velocities of a tensioned panel with $T_x = 0.108$ (8213.38 N) excited by an acoustic wave convecting with a flow $M = 0.026$ ($\hat{U} = 9$ m/s) was measured in the experiment [19]. Figure 10 shows a comparison between the calculated transmission loss TL with excitation frequencies $f = 0.294$ (200 Hz) and 0.618 (420 Hz) and the experimental data. The numerical results have good agreement with the experimental data at both frequencies. The maximum difference is 5.2 and 10.8% in the results of $f = 0.294$ and 0.618, respectively.

A comparison of the calculated transmission loss TL with $T_x = 0.116$ (8821.78N) and $M = 0.045$ ($\hat{u}_0 = 15$ m/s) and the experimental data is illustrated in Fig. 11. An excellent agreement between the numerical result with viscous flow and the experimental data is found except the peak at $f = 0.36$. It is underpredicted by approximately 5 db. The difference at this frequency can be explained by an investigation of possible wind tunnel duct modes. In the experiment, the test section outlet is connected to a diffuser. The sudden change in area there may cause acoustic reflection. On the other hand, as confirmed in our previous study (Fan et al. [2]), the panel leading edge is responsible for the reflection of incident wave to upstream due to the sharp

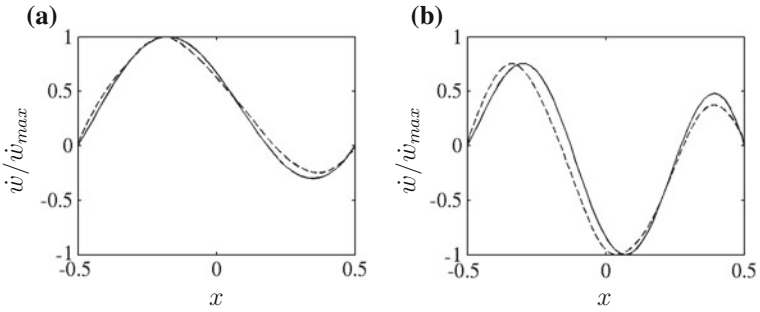

Fig. 10 Comparison of instantaneous distribution of vibrating velocities with $T_x = 0.108$ and $M = 0.026$. **a** $f = 0.294$ (200Hz). **b** $f = 0.618$ (420Hz). —, numerical result; – – –, experimental data

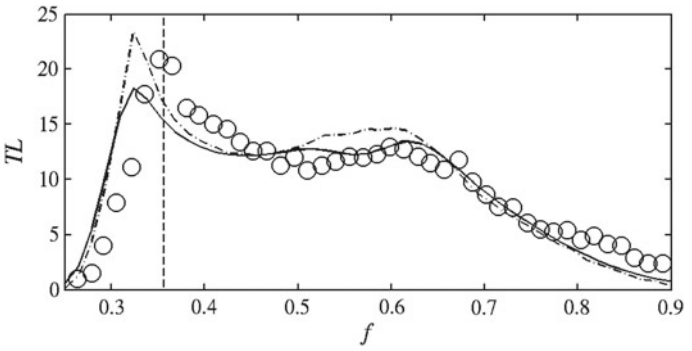

Fig. 11 Comparison of the TL spectra of numerical results to experimental data. —, numerical result with viscous flow; – · – · –, numerical result with inviscid flow; ◯, experimental data; – – –, duct mode frequency $f_{2,0,0}$

area change created by the vibrating panel. Reflection of upstream going acoustic wave to downstream is also possible. If the duct section between these two locations is taken as an open-ended duct, it is not difficult to see that its length equal to 2.74 gives a frequency of the second mode $f_{2,0,0} = 0.36$, which matches the observed peak in the experiment well. In the presence of his mode inside the wind tunnel, the nodal point was just 15mm away from the microphone in the experiment. The microphone then received a very weak acoustic signal that an over-estimated transmission loss was deduced. However, the numerical calculation does not suffer such duct mode problem. All these observations show clearly that the experimental TL at $f = 0.36$ in Fig. 11 is erroneous and not reliable. However, the data at other frequencies is still trustworthy because neither matches any other possible open-ended wind tunnel duct modes. If the data at $f = 0.36$ is ignored, the maximum difference between numerical and experimental TL is only 0.5 db. Such excellent agreement firmly establishes the strong capability of the present numerical methodology in capturing the nonlinear aeroacoustic–structural interaction in the problem correctly.

The other difference in the TL levels might be attributed to two reasons. One is due to the fact that the present two-dimensional calculation does not replicate fully the three dimensionality of the experiment. Some three-dimensional panel vibration and duct acoustic modal behaviors are not properly included. Another is the mesh is not fine enough to capture small-scale flow instability. Any acoustic reactive response caused by the panel vibration in response to such instability in the experiment cannot be captured fully.

The importance of the inclusion of viscous effect is also highlighted in Fig. 11 in which a comparison of TL derived from viscous and inviscid solutions is also shown. They show similar overall trends, but the inviscid solution shows obvious overprediction at around $f = 0.5$–0.6 and at the peak at $f = 0.32$. The difference between inviscid solution and experimental data at the peak is as large as 5.7 db.

5 Concluding Remarks

A numerical methodology has been introduced to study the nonlinear fluid–structure interaction and its acoustics in internal viscous flow. It is solving the coupled governing equations that include both fluid and structural dynamics at the fluid–structure interface. Two experimental studies are selected as the benchmark cases for validation of the methodology.

The first case is to study the flow-induced structural instability of a thin flexible panel flush-mounted in a duct and backed by cavity. Under a subsonic flow, the vibration of the panel is induced and becomes the limit cycle oscillation. The numerical result has a favorable agreement with the experimental data that validated the capability of the numerical methodology for capturing the fluid–structural interaction. An interesting acoustic response is found that the upstream radiation by the panel vibration is 5.9 db larger than the downstream in terms of acoustic power. The result also shows the viscous effect strongly affects the structural response and inviscid assumption can lead to incorrect result.

Another case is a study on a practical silencer design that makes use of a flexible duct segment constructed by elastic panels. Both acoustic and structural responses are validated with excellent agreement with the experiment. On the other hand, the viscous solution also gives a more accurate prediction than the inviscid solution on the aeroacoustic–structural responses.

Acknowledgements The authors gratefully acknowledge the support given by the Research Grants Council of Hong Kong SAR Government under Grant Nos. A-PolyU503/15 and AoE/P-02/12.

References

1. Huang, L.: A theoretical study of duct noise control by flexible panels. J. Acoust. Soc. Am. **106**(4), 1801–1809 (1999)
2. Fan, H.K.H., Leung, R.C.K., Lam, G.C.Y.: Numerical analysis of aeroacoustic-structural interaction of a flexible panel in uniform duct flow. J. Acoust. Soc. Am. **137**(6), 3115–3126 (2015)
3. Leung, R.C.K., Fan, H.K.H., Lam, G.C.Y.: A numerical methodology for resolving aeroacoustic-structural response of flexible panel. In: Ciappi, E., Rosa, S.D., Guyader, F.F.J.l., Hambric, S.A. (eds.) Flinovia—Flow Induced Noise and Vibration Issues and Aspects: A Focus on Measurement, Modeling, Simulation and Reproduction of the Flow Excitation and Flow Induced Response, pp. 321–342. Springer, Cham, Heidelberg, New York, Dordrecht, London (2015)
4. Liu, Y.: Flow induced vibraion and noise control with flow. Ph.D. Thesis, The Hong Kong Polytechnic University (2011)
5. Crighton, D.G.: Acoustics as a branch of fluid mechanics. J. Fluid Mech. **106**, 261–298 (1981)
6. Lam, G.C.Y., Leung, R.C.K., Tang, S.K.: Aeroacoustics of T-junction merging flow. J. Acoust. Soc. Am. **133**(2), 697–708 (2013)
7. Lam, G.C.Y., Leung, R.C.K., Seid, K.H., Tang, S.K.: Validation of CE/SE scheme for low mach number direct aeroacoustic simulation. Int. J. Nonlinear Sci. Numer. Simul. **15**(2), 157–169 (2014)
8. Fan, H.K.H.: Computational aeroacoustic-structural interaction in internal flow with CE/SE method. Ph.D. Thesis, The Hong Kong Polytechnic University (2018)
9. Chang, S.C.: The method of space-time conservation element and solution element-a new approach for solving the Navier-Stokes and Euler equations. J. Comput. Phys. **119**, 295–324 (1995)
10. Dowell, E.H.: Aeroelasticity of Plates and Shells. Noordhoff International Publishing, Leyden (1975)
11. Rao, J.S.: Dynamics of Plates. Narosa Publishing House, New Delhi (1999)
12. Rugonyi, S., Bathe, K.J.: On finite element analysis of fluid flows fully coupled with structural interactions. Comput. Model. Eng. Sci. **2**(2), 195–212 (2001)
13. White, F.M.: Fluid Mechanics, 4th edn. McGraw-Hill (1998)
14. Anderson, J.D.: Fundamentals of Aerodynamics, 5th edn. McGraw-Hill, New York (2011)
15. Blevins, R.D.: Formulas for Natural Frequency and Mode Shape. Van Nostrand Reinhold Company, New York, Cincinnati, Atlanta, Dallas, San Francisco, London, Toronto, Melbourne (1979)
16. Dowling, A.P., Ffowcs Williams, J.E.: Sound and Sources of Sound. Ellis Horwood Limited, Chichester (1983)
17. Beranek, L.L.: Acoustics. Acoustical Society of America, New York (1993)
18. Rienstra, S.W., Hirchberg, A.: An Introduction to Acoustics (2015)
19. Choy, Y.S., Huang, L.: Effect of flow on the drumlike silencer. J. Acoust. Soc. Am. **118**(5), 3077–3085 (2005)

Part VI
Vibroacoustic Response–Innovative Applications

Exact Geometric Similitude Laws for Flat Plate Vibrations Induced by a Turbulent Boundary Layer

Olivier Robin, Francesco Franco, Elena Ciappi, Sergio De Rosa and Alain Berry

Abstract Similitude laws for the vibration response of simply supported plates under random excitations are derived and tested numerically and experimentally for the case of a turbulent boundary layer. Analytical calculations show that under the assumption of proportional sides, perfect similitude in terms of vibration response scaling can be achieved between plates of variable thicknesses. It is also highlighted that even if the similitude conditions are not all satisfied (i.e., a complete scaling of all the involved parameters, from panel dimensions to flow speed), an approximation can be made in the mid-high-frequency domain that leads to satisfactorily scaled results. Based on the analytical study, a series of tests is performed in an anechoic wind tunnel on three-scaled simply supported panels at different flow velocities. Applying the proposed procedure to this set of vibration measurements leads to satisfactory scaling of results between each other.

Keywords Plate vibration · Similitude · Turbulent boundary layer

O. Robin (✉) · A. Berry
Groupe d'Acoustique de l'Université de Sherbrooke (GAUS),
Département de Génie Mécanique, Université de Sherbrooke,
Sherbrooke, QC J1K 2R1, Canada
e-mail: olivier.robin@usherbrooke.ca

A. Berry
e-mail: alain.berry@usherbrooke.ca

F. Franco · S. De Rosa
Pasta-Lab, Department of Industrial Engineering, Aerospace Section,
Universitá degli Studi di Napoli "Federico II", Via Claudio 21,
80125 Napoli, Italy
e-mail: francesco.franco@unina.it

S. De Rosa
e-mail: sergio.derosa@unina.it

E. Ciappi
CNR-INSEAN, Italian National Maritime Research Centre,
Via di Vallerano, 139, 00128 Roma, Italy
e-mail: elena.ciappi@cnr.it

E. Ciappi et al. (eds.), *Flinovia—Flow Induced Noise and Vibration Issues and Aspects-II*,
https://doi.org/10.1007/978-3-319-76780-2_17

1 Introduction

Wall pressure fluctuations (WPFs) beneath a turbulent boundary layer (TBL) have been studied for decades for the impact they have on the on-board comfort and on the correct operation of sensors in naval, aerospace, and automotive engineering. The numerical resolution of this flow-induced vibration problem is computationally demanding even for flat panels at model scale size and ideal flow conditions. In this case, scaling and similitude laws exist and analytical models can be used for the representation of the single-point spectrum and the cross-spectral density of WPF. For complex geometries and/or complex flow conditions, direct numerical simulations (DNSs) of the Navier–Stokes equations should be used to calculate the WPF field, but the actual capabilities of DNS for external wall-bounded flow are generally limited to problems in which the local Reynolds number is in the order of 6600 (based on the momentum thickness). Some attempts to reduce the computational time using LES have been recently made obtaining satisfactory results at least in the low-frequency domain (i.e., large wavelengths). Concerning the numerical solving of the structural equations, the number of degrees of freedom needed to obtain accurate results increases very quickly when the structural wavelengths are small compared to the typical dimension of the problem (i.e., for high frequencies). In this frequency domain, energy methods such as the statistical energy analysis can be used, but the definition of the input power can be very complicated and time-consuming for a model of the pressure cross-spectral density that does not rely on a spatial separation of variables. Some issues about the development of a robust numerical solution are discussed in [1].

Several research groups have addressed the problem of reducing the computational time proposing efficient numerical algorithms, suitable approximations for WPF load representation as well as the identification of scaling laws for the structural response, so as to determine a unique representation independent of flow conditions or structural properties. In [2], a dimensional analysis was used to recover the dimensionless parameters for the definition of the scaling laws for the excitation frequency and the power spectral density of the structural response. An alternative approach can consist in measuring the structural response of plates under a TBL excitation in a wind-tunnel facility. These measurements are mandatory if the structures are complex and cannot be easily modeled using available numerical tools. Unfortunately, these experimental works need the proper wind-tunnel facility (i.e., highly controlled aerodynamic conditions: flow speed, boundary layer thickness) and representative specimen in terms of dimensions and structural details. Such optimal experimental conditions are only occasionally guaranteed. In the same time, the concept of structural similitude provides a powerful tool for engineers and scientists to predict the behavior of a structure using an appropriately scaled model. In particular, this approach is addressed in [3] but it is based on a homothetic transformation of the plate domain and it does not discuss the role of the flow speed and the reduced frequency in this flow-induced vibration problem. The present paper follows a different analytical and conceptual development, and it is based on the previous achievements

detailed in [2, 4, 5]. Hence, this work is a first attempt to address numerical and experimental structural response calculations on scaled domains, dealing with the necessary scaling of the flow speed so as to respect the key similitude parameters. The first sections report the analytical development of the exact similitude laws using the case of a thin, flat, and homogeneous plate with simply supported edges and a Corcos model for describing the TBL load. The capabilities of this analytical framework are fully described through the presented results. The present analyses are only based on analytical solutions, in order to avoid any problem or approximation related to the formulation of the same flow-induced vibration solution in discrete coordinates [1]. In the successive sections, experimental data, that aim at validating the analytical similitude laws, are discussed and the main challenges to be undertaken in order to apply the similitude framework in the context of a TBL excitation are finally summarized.

2 Details of the Analytical Models

2.1 Analytical Solution Using the Corcos Model

In this section, the Corcos model [6] is used to derive an analytical expression for the response of a thin, flat, and isotropic panel to a TBL excitation. This model, on the basis of the experimental evidence of some properties of the fluctuating pressure field, expresses the cross-spectral density of the WPF as a product of the single-point spectral density $S_p(\omega)$ and of functions depending separately on the stream-wise and cross-stream space variables. The Corcos model is given by:

$$X_{pp}(\xi_x, \xi_y, \omega) = S_p(\omega)\Gamma(\xi_x, \xi_y, \omega)e^{-\frac{i\omega\xi_x}{U_c}}, \tag{1}$$

with

$$\Gamma(\xi_x, \xi_y, \omega) = e^{-\alpha_x\left|\frac{\omega\xi_x}{U_c}\right|}e^{-\alpha_y\left|\frac{\omega\xi_y}{U_c}\right|}, \tag{2}$$

where α_x and α_y are the stream-wise and cross-stream correlation coefficients, ξ_x and ξ_y are the stream-wise and cross-stream separation distances, respectively, U_c is the convective flow speed and $i = \sqrt{-1}$. The Corcos model is among the simplest representations of the wall pressure distribution due to a turbulent boundary layer because: (i) the space variables are separated (finally allowing closed-form expression for the response of simply supported plates), (ii) the phase variation is only accounted for along the stream-wise direction, (iii) all functions have the same exponential form, and (iv) it is independent of any couple of points and depends only on their relative separation (comprehensive reviews of TBL models can be found, e.g.,in [7, 8]). As the frequency increases, this TBL model does not usually provide a good fit with experimental data and a main limitation lies in its convective character as a matter of fact (it provides good predictions especially in the convective domain,

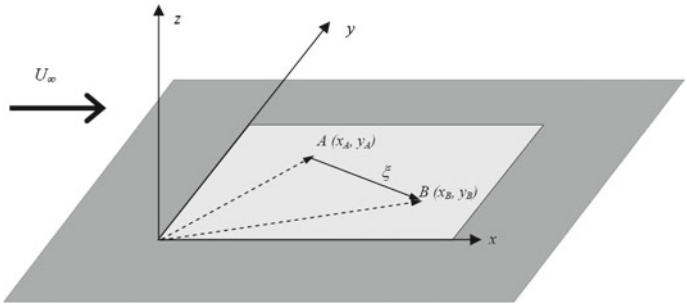

Fig. 1 Elastic plate in an infinite rigid baffle

but results obtained with this model in the sub-convective and acoustic domains are debated) [12, 13]. The above considerations–hypotheses about the Corcos model could be important in the comparison among analytical results and experimental data. To develop an analytical solution, the plate is considered thin, flat, rectangular, and isotropic with no prestress (absence of both pressurization and edge loadings). This plate is simply supported on all four edges and is mounted in an infinite rigid plane baffle as shown in Fig. 1, with a flow developing along the x-axis. The plate lies in a $x - y$ plane and the flexural out-of-plane displacements, $w(x, y, t)$, are along the z-axis. The length and width of the panel are a and b, respectively.

The displacement cross-spectral density between any arbitrary couple of points belonging to the plate, $A(x_A, y_A)$ and $B(x_B, y_B)$, due to an assigned stochastic distributed excitation, can be found with the following modal expansion [10, 11]:

$$X_w(x_A, y_A, x_B, y_B; \omega) = \sum_{j=1}^{\infty}\sum_{n=1}^{\infty}\Big[\frac{\Psi_j(x_A, y_A)\Psi_n(x_B, y_B)}{Z_j^*(\omega)Z_n(\omega)}\Big]\Big[\frac{S_p(\omega)(ab)^2}{\gamma_j\gamma_n}\Big]A_{Q_jQ_n}(\omega), \tag{3}$$

with

$$A_{Q_jQ_n}(\omega) = \int_0^a\int_0^a\int_0^b\int_0^b\Big[\frac{X_{pp}(x, y, x', y'; \omega)}{S_p(\omega)(ab)^2}\Psi_j(x, y)\Psi_n(x', y')\Big]dy'\,dy\,dx'\,dx, \tag{4}$$

$$\gamma_j = \int_0^a\int_0^b\Psi_j^2(x, y)\,dy\,dx, \tag{5}$$

$$Z_j(\omega) = \rho h\big[\omega_j^2 - \omega^2 + i\eta\omega_j^2\big]. \tag{6}$$

where for the plate jth mode, Ψ_j is the analytical mode shape, γ_j is the generalized mass coefficient, ρ is the mass density, h the panel thickness, and Z_j is the plate dynamic impedance. The integrals in Eq. (4) defined by the symbol $A_{Q_j Q_n}(\omega)$ are usually known as the acceptances: joint acceptance for $j = n$, or cross acceptance for $j \neq n$. Further, the formulation contained in Eqs. (3–6) can be applied to any structural operator once its modal basis is known. In the above equations, a hysteretic model for the structural damping is assumed. The auto-spectral density of the displacement X_w at a selected point A is given by

$$X_w(x_A, y_A; \omega) = \sum_{j=1}^{\infty} \sum_{n=1}^{\infty} \left[\frac{\Psi_j(x_A, y_A)\Psi_n(x_A, y_A)}{Z_j^*(\omega) Z_n(\omega)} \right] \left[\frac{S_p(\omega)(ab)^2}{\gamma_j \gamma_n} \right] A_{Q_j Q_n}(\omega), \quad (7)$$

This last quantity is strictly real. It is possible to evaluate the plate mean displacement response over the panel area using a simple space integration

$$\overline{S}_w(\omega) = \frac{1}{ab} \int_{area} S_w(x, y; \omega) dx dy \quad (8)$$

The proper number of the total modal components (NM) has to be selected in the above modal expansions in order to achieve the convergence of the results for the assigned excitation frequency.

For a thin, simply supported and isotropic panel, the mode shape Ψ_j and eigenfrequency ω_j, solutions of the free vibration equation take simple closed-form expressions:

$$\Psi_j(x, y) = \sin\left(\frac{j_m \pi}{a} x\right) \sin\left(\frac{j_n \pi}{b} y\right), \quad (9)$$

and

$$\omega_j = \left(\frac{D}{\rho h}\right)^{1/2} \left[\left(\frac{j_m \pi}{L_x}\right)^2 + \left(\frac{j_n \pi}{L_y}\right)^2 \right], \quad (10)$$

where D is the bending stiffness and j_m, j_n are nonzero strictly positive integers.

Assuming a simply supported plate and a Corcos model for the WPF, closed-form analytical solutions for the integrals in Eqs. (4) and (5) exist. Hence, in this work, all results named as analytical are carried out according to Eqs. (7) and (8).

2.2 Derivation of the Similitude Laws

In this section, the derivation of the similitude laws is based on Refs. [4, 5]. The symbol (ˆ) denotes a parameter in similitude. Let us define a set of scaling parameters, r, as the ratios of the similitude parameter to the original one; for example:

$$r_x = \frac{\hat{a}}{a}; r_y = \frac{\hat{b}}{b}; r_\eta = \frac{\hat{\eta}}{\eta}; r_\omega = \frac{\hat{\omega_i}}{\omega}; r_U = \frac{\hat{U}_c}{U_c}; r_p = \frac{\hat{S}_p}{S_p} \dots \tag{11}$$

In all successive developments, the material remains unchanged and consequently the hysteretic damping is supposed constant; i.e., $r_\eta = \frac{\hat{\eta}}{\eta} = 1$. For sake of simplicity, other damping sources (or mechanisms) are considered "included" in the term η.

The spatial dependences of the analytical mode shapes, in Eq. (9), can be formulated in terms of the dimensionless coordinates of source and response point; thus, they do not need to be posed in similitude. Nevertheless, the derivation of the similitude acceptances $\hat{A}_{Q_j Q_n}(\omega)$ deserves more attention. Assuming the following relationship between the reduced frequencies

$$\frac{r_\omega r_x}{r_U} = \frac{r_\omega r_y}{r_U} = 1, \tag{12}$$

in other words, assuming that the reduced frequency remains unchanged and according to the analytical formulation in [10], it can be demonstrated that

$$\hat{A}_{Q_j Q_n}(\omega) = \frac{A_{Q_j Q_n}(\omega)}{r_x r_y} \tag{13}$$

The above relationships rule the successive steps and, in particular, the design of the experimental phase. In particular, Eq. (12) can be used to scale the flow speed but theoretically limits the complete similitude to plates with proportionally scaled sides (i.e., $r_x = r_y$).

Following the approach defined in [4, 5], the following relationships can be derived

$$\hat{Z}_j = r_h r_\omega Z_j(\frac{\omega}{r_\omega}) \tag{14}$$

$$\hat{\gamma}_j = r_x r_y \gamma_j \tag{15}$$

Finally, the relationship for the cross-spectral densities of the displacement (Eq. (3)) can be expressed as

$$\frac{\hat{X}_\omega}{\hat{S}_p} = \frac{X_\omega}{S_p} \cdot \frac{1}{r_x r_y} \cdot \frac{1}{r_h^2 r_\omega^2} \cdot \tag{16}$$

In particular, for a simply supported plate [4, 5], $r_\omega^2 = \frac{r_h^2}{(r_x r_y)^2}$, and therefore,

$$\frac{\hat{X}_\omega}{\hat{S}_p} = \frac{X_\omega}{S_p} \cdot \frac{r_x r_y}{r_h^4} \tag{17}$$

$$\frac{X_\omega}{S_p} = \left(\frac{\hat{h}}{h}\right)^4 . \left(\frac{ab}{\hat{a}\hat{b}}\right) . \frac{\hat{X}_\omega}{\hat{S}_p} \tag{18}$$

Analogous relationships can be derived for Eqs. (7) and (8). It is finally precised that using a Corcos model and assuming a TBL load with frozen characteristics (i.e., ratios $\frac{\omega \xi_x}{U_c}$ and $\frac{\omega \xi_y}{U_c}$ that are kept identical), the condition expressed in Eq. (13) guarantees that the correlation area is scaled as $r_x \times r_y$ (with the same scaling factor of the structural domain area).

2.3 Design of Experiments

The previous sections already outlined the scaling procedure, and its main steps are listed below for sake of clarity. Once defined the original plate, or reference plate, the conditions of similitude for the numerical solutions or experimental measurements can be developed as follows:

1. The first condition to satisfy is $r_x \equiv r_y$. In other words, a proportional side plate must be designed. On the contrary, the ratio has no specific constraint but this condition introduces avatar domains [4, 5], which are out of the scope of the present analyses.
2. Once defined the scaled plate, the knowledge of $\hat{\omega}_i$ allows the derivation of r_ω.
3. The necessary condition is defined in Eq. (12). A completely correct similitude should be obtained, and since the reduced frequency must remain unchanged, the flow speed in similitude is easily derived.
4. The numerical solutions and the experimental measurements assume that the Corcos coefficients ($\alpha_x, \alpha_y, \beta_c$) remain unchanged.
5. Finally, the relationships defining the similitude among the structural responses are provided in Eqs. (17–18). Unfortunately, the need to define a different flow speed (see item #3 in this list) introduces a difference in the dynamic pressure (i.e., Eqs. (17–18) are not strictly followed because they are derived under the hypothesis $r_p = 1$). Therefore, the solutions must be remodulated with reference to the different dynamic pressures.

In the following sections, all results are derived according to the above procedure.

3 Analytical Results

3.1 List of Specimen

The choice of the plates, herein analyzed, represents an attempt to develop a complete and satisfactory analytical database and are listed in Table 1. The length and width

Table 1 Characteristics of the plates chosen for analytical analysis

Plate	Length (a, [mm])	Width (b, [mm])	Thickness (h, [mm])	'Role'
P0	480	420	3.2	*Original* plate, taken as reference
P1	240	210	1.6	*Replica* plate
P2	600	525	3.2	*Proportional sides* plate, unchanged thickness
P3	600	525	1.6	*Proportional sides* plate, modified thickness
P4	320	280	2.5	*Proportional sides* plate, modified thickness

Table 2 Scaling ratios between reference plate P0 and the other plates

Plate	r_x ($= r_y$)	r_h	r_ω	r_U
P1	0.5	0.5	2	1
P2	1.25	1	0.64	0.8
P3	1.25	0.5	0.32	0.4
P4	0.67	0.78	1.76	1.17

of the panels correspond to stream-wise and cross-wise flow directions, respectively (see Fig. 1). The corresponding scaling ratios between plates P1–P4 and plate P0 are summarized in Table 2. The P1 is a replica plate: the in-plane dimensions and the thickness are scaled by the same factor. As expected, for the plate P1, the flow speed does not need to be scaled. The plate P2 has proportional sides, but its thickness is equal to the reference plate one. On the contrary, the plate P3 introduces a different thickness ratio r_h compared with the plate P2. Finally, the plate P4 is scaled down and is chosen to highlight the possibility of dealing with a smaller plate (in plane) than the reference one. The material properties are those of a typical aluminum alloy, with a Young's modulus value $E = 70$ GPa, a mass density $\rho = 2700\ \mathrm{kg\,m^{-3}}$, a Poisson coefficient $\nu = 0.3$, and a structural damping $\eta = 0.02$ (considered constant as a function of frequency).

3.2 Analytical Results

The chosen values for the stream-wise and cross-wise coefficients of the Corcos model are $\alpha_x = 0.116$ and $\alpha_y = 0.7$, respectively. These values are close to those commonly used by several authors for the case of smooth surfaces (values found in the literature for these parameters typically range from 0.10 to 0.12 and 0.7 to 1.2, respectively [9]). As outlined in Sect. 2.3, the coefficients values remain unchanged

in each analytical solution. Finally, the free flow U_∞ and convective flow U_c speeds are related by a convective constant $\beta_c = 0.8$ ($U_c = 0.8\ U_\infty$).

In each figure of this section, the results are plotted in terms of mean value of the auto-spectral density of the plate acceleration per unitary auto-spectral density of the wall pressure distribution due to the turbulent boundary layer (i.e., S_w/S_p) versus frequency. The mean value is computed according to Eq. (8). The asymptotic free-flow speed value for the reference plate is set at 100 m/s, and the considered frequency range is [0–5000] Hz. For this flow speed, the convective coincidence frequency value is approximately 200 Hz for plate P0 (i.e., when the convective wavenumber k_c and flexural bending wavenumber k_b values are equal [1]). Below this frequency, the convective excitation couples well with the panel and structural resonances but is then strongly filtered out above this frequency. Next section provides few considerations about obtained results as frequency increases. All results are analytical ones, and the solution algorithm is well verified in [1, 8]; analogously the convergence criteria, to properly set the number of total components for the structural response (NM), are verified too (39×16 modal components along x and y directions). Each analytical solution, before introducing the r_ω factor to modulate the structural responses, uses a similar frequency resolution of 1 Hz. The figures report on the top the unscaled results and on the bottom the remodulated ones. The values on the y-axis are computed according to Eqs. (17–18). The values on the x-axis are computed using the ratio r_ω. In the figure legend, the scaled asymptotic speed, according to Table 2, is highlighted.

Figure 2 shows the results for the plate P1. This is a replica plate and, as shown in Table 2, it does not need any scaling of the flow speed. The comparison of scaled results obtained for panels P0 and P1 shows perfect agreement.

Figure 3 shows the results for the plate P2. It is the proportional sides plate with scaling parameter $r_h = 1$. Nevertheless, it requires a scaled flow speed. The agreement of the results is also perfect for this case.

No further evidence is introduced by Figs. 4 and 5 (plates P3 and P4, respectively). For each domain in similitude, once applied the proper scaled flow speed, the results are well remodulated following derived similitude laws. It can only be highlighted that, for the plate P4, the solution, up to 5000 Hz, is not able to reconstruct completely the solution of the plate P0 above 2800 Hz. In fact, this test-article has a frequency similitude scaling parameter $r_\omega > 1$ and, therefore, the solution for the plate P4 should be carried out over a larger frequency range (i.e., up to a frequency $5000 \times r_\omega = 8800$ Hz (see Table 2).

3.3 High-Frequency Approximation

The TBL load becomes a spatially uncorrelated pressure field as frequency increases (with corresponding exponentially decreasing correlation lengths). Therefore, in the high-frequency range the solution should be less affected by the role of the

[1] Defined by $k_c = \omega/U_c$ and $k_b = \left(\frac{\rho \times h \times \omega^2}{D}\right)^{\frac{1}{4}}$, respectively.

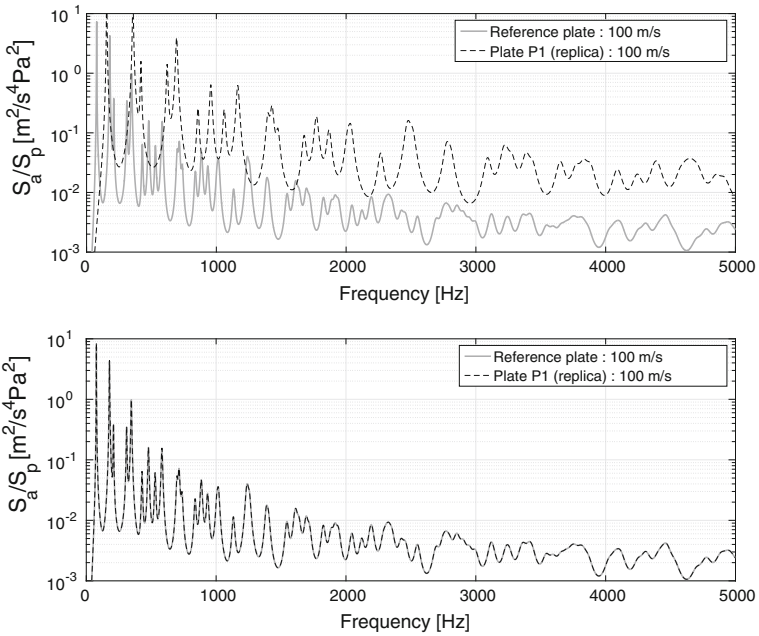

Fig. 2 Plate P1 versus P0—top: unscaled results—bottom: scaled results (original and scaled flow velocity are indicated in legend)

acceptance integrals (Eq. (4)). It must be underlined that the condition expressed by Eq. (12) guarantees a full similitude in the whole frequency range. On the contrary, if the frequency range of interest is limited to the high frequency one, the condition of Eq. (12) becomes a constraint that can be nevertheless disregarded. Upper part of Fig. 6 shows the results for the plate P2 and P3 obtained without scaling the flow speed: in the plot, the three curves are obtained setting the flow speed at 100 m/s for all plates and using the relationships in Eqs. (18) to re-modulate the values. Above 1000 Hz, the solution of P2 converges to the plate P0 one. It must be underlined that the plates P0 and P2 have the same convective coincidence frequency because they have the same thickness. In addition, for the plate P2, $r_U = 0.8$. On the contrary, for the plate P3 the convective coincidence frequency is doubled (thickness is divided by a factor of 2) and $r_U = 0.4$. Figure 6 shows that the solution of plate P3 converge asymptotically to the plate P0 solution as frequency increases. This result can be useful when dealing with problems especially having low convective coincidence frequencies, and most of the measured or computed frequency range could be analyzed under the high-frequency approximation.

To give an estimation of the frequency at which the curves merge and thus generalize this result, a dimensionless expression derived from an energetic formulation for the response of flat thin panels excited by a TBL [2] can be used. This law depends on material properties, convection velocity, and plate thickness (thus ignoring plate

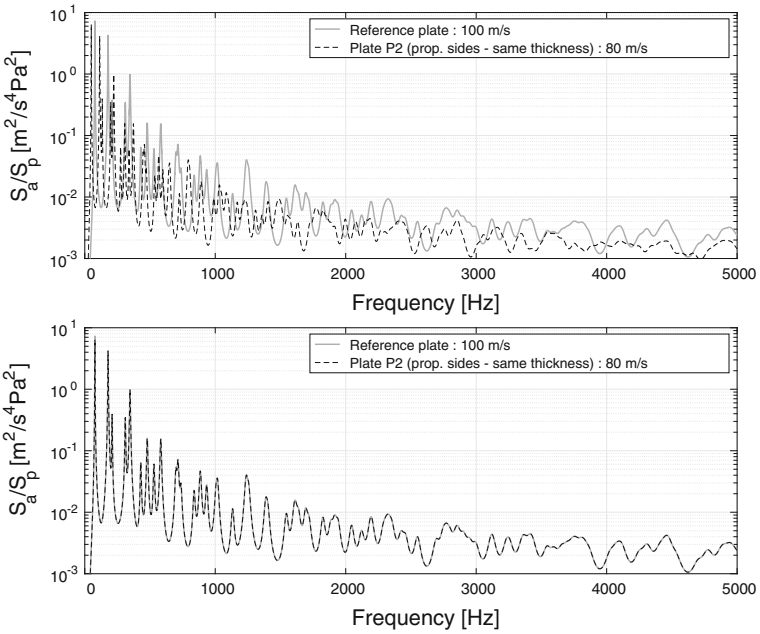

Fig. 3 Plate P2 versus P0—top: unscaled results—bottom: scaled results (original and scaled flow velocity are indicated in legend)

dimensions and boundary conditions) and is supposed to become more and more accurate when frequency increases. In particular, it provides a satisfactory fit with experimental data when the dimensionless frequency $\frac{\omega h}{U_c} > 0.35$. If this condition is directly applied to plates $P0$ and $P2$ that have similar thicknesses (and material properties and flow speed), it provides an overlapping frequency of 1400 Hz (rounded to the nearest hundred) which is in good agreement with the result shown in the upper part of Fig. 6. Defining a simple and precise dimensionless frequency for panels having different thicknesses is not as trivial as in this previous case and is to be studied in future developments.

4 Experimental Activities and Results

The experimental activities are based on the previous analytical results, and their aim is to demonstrate the suitability of the proposed framework for putting this flow-induced vibration problem in similitude in realistic conditions. Three plates denoted A1, A2, and A3 are considered, strictly similar to plates P0, P2, and P3 in terms of dimensions and material properties, at the only exception of the thickness of the third considered panel (i.e., the only difference is that the thickness is 2.4 mm for

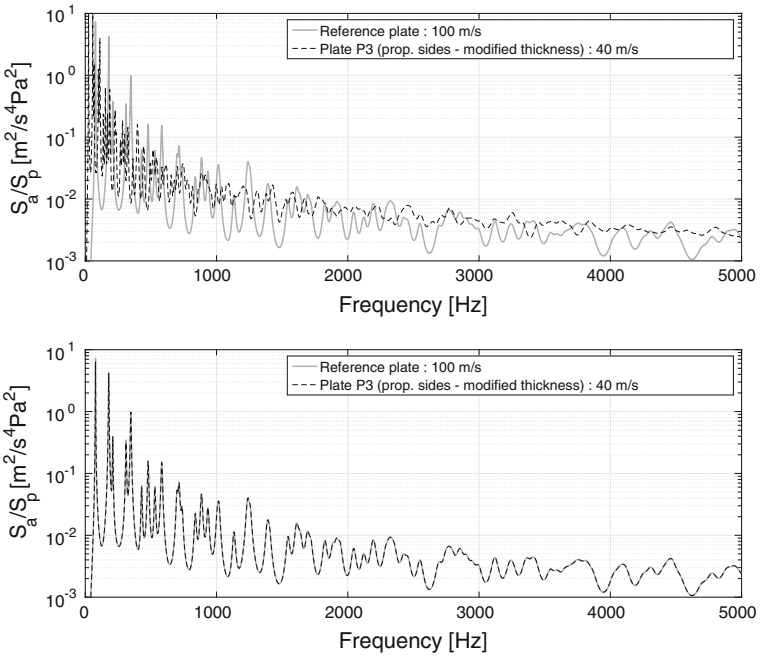

Fig. 4 Plate P3 versus P0—top: unscaled results—bottom: scaled results (original and scaled flow velocity are indicated in legend)

panel A3 instead of 1.6 mm for panel P3 in the analytical section). The A1, A2, and A3 panels respective dimensions are $480 \times 420 \times 3.2$ mm^3, $600 \times 525 \times 3.2$ mm^3, and $600 \times 525 \times 2.4$ mm^3. According to the procedure described in Sect. 2.3, the relative flow speeds can be defined. The experimental measurements were carried at scaled flow speeds, which for the results presented in this section are 35, 28, and 21 m/s, respectively. These flow speeds are selected in agreement with the available wind-tunnel facility that can reach free-stream velocities of 40 m/s.

The panels were all assembled and constructed following the method described in [15], which has proven to be efficient for reproducing simply supported boundary conditions. All measurements were held in the anechoic flow facility at Université de Sherbrooke (Fig. 7). Each plate was flush mounted in a 8 in. $\times$ 4 in. $\times 1/2$ in. wood baffle placed at the convergent nozzle exit, and mechanical decoupling was ensured and verified (the panel was individually supported by its own stand). Three low-weight accelerometers were glued on the panel (added mass $\approx$10 g) in order to estimate the vibration autospectrum under TBL excitation. In order to obtain the autospectrum of the forcing pressure field to apply the scaling procedure, wall pressure statistics were estimated using a single surface microphone ($B\&K$ 4949 surface microphone) but a microphone array was also used to collect data with which the correlation lengths can be also further extracted and will be included in coming works (large 2D rotative 60 microphone array [16]). Nevertheless, some

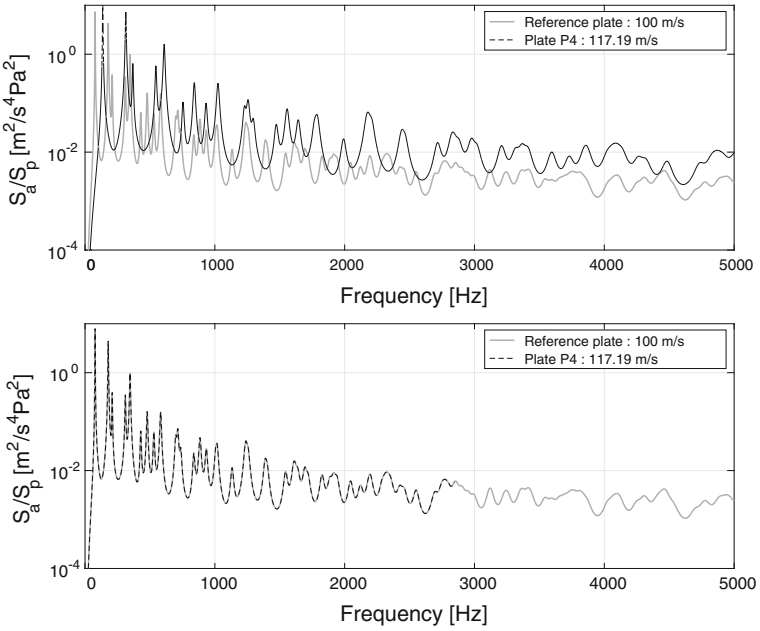

Fig. 5 Plate P4 versus P0—top: unscaled results—bottom: scaled results (original and scaled flow velocity are indicated in legend)

measurement issues at low frequency were encountered so that the ratio r_p was finally numerically estimated using Goody's model [14].

In Fig. 8 are presented unscaled and scaled experimental results. The presented vibration velocity autospectrum are averaged over six measurement points (i.e., two acquisition runs each using three accelerometers, with the center of the panel being a common measurement point between the two runs). For the case of unscaled results between the three considered panels, the vibration magnitude can differ by a factor of 10^4 and modal densities distributions are dissimilar (especially between panel A1 and panels A2–A3—a zoomed sub-figure between 300 and 500 Hz is included to highlight these differences). In other words, they represent completely different 'problems'. When the similitude laws are applied to measurement results, they are satisfactorily scaled between each other up to a frequency of 1500 Hz. Up to this frequency, the agreement among the structural responses is clear and confirm the robustness of the proposed approach. To modulate the response function, the frequency scale has to be multiplied for the similitude ratio r_ω evaluated from the experimental data that are in excellent agreement with the analytical estimation.

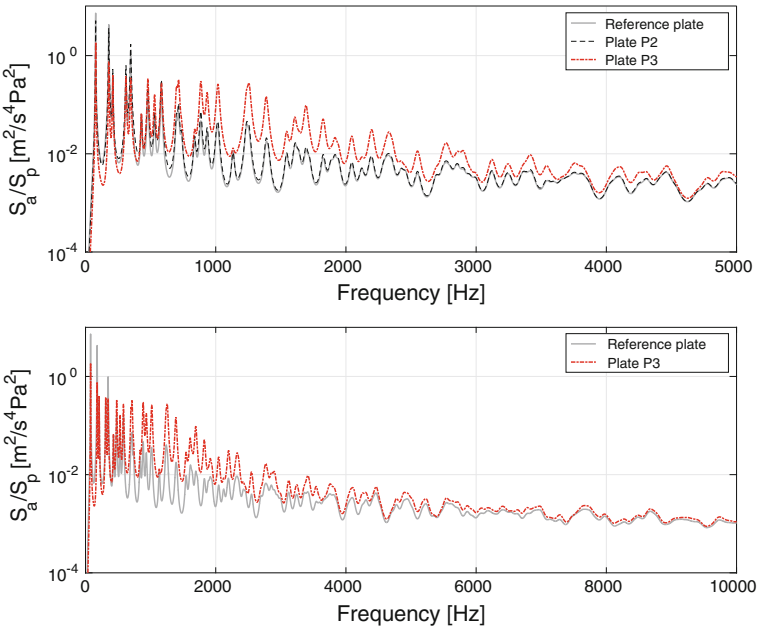

Fig. 6 Top: Unscaled flow results for reference P0, P2, and P3 plates for the [0–5] kHz frequency range—Bottom: Unscaled flow results for reference P0 and P3 plates for the [0–10] kHz frequency range. A flow speed of 100 m/s is considered

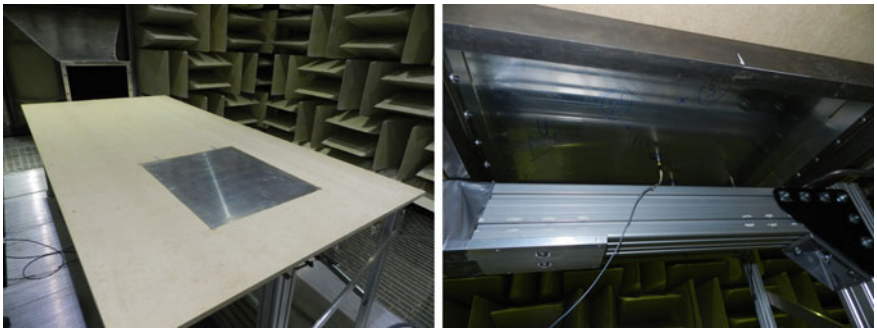

Fig. 7 Left: view from above of the installed baffled panel in the flow facility—Right: view from below of the installed panel with accelerometers installed

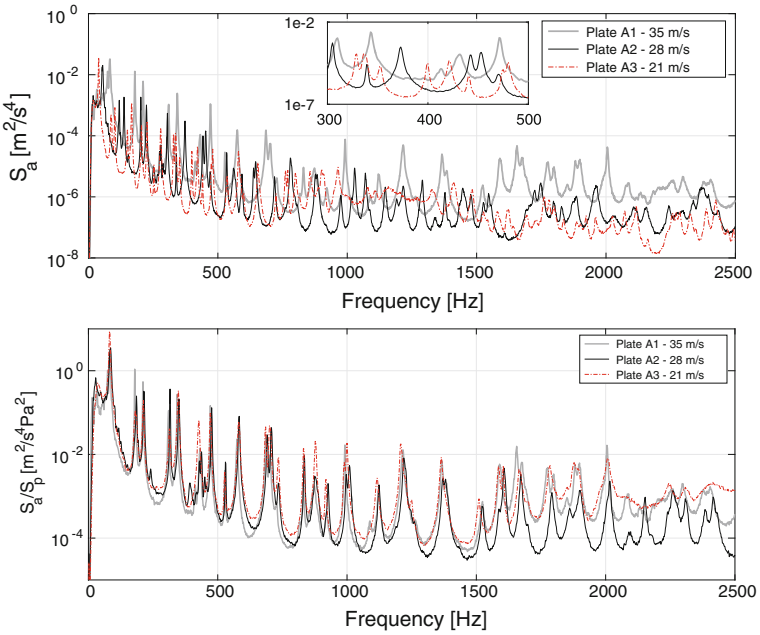

Fig. 8 Top: Unscaled experimental results for plates A1, A2, and A3—Bottom: Scaled experimental results

5 Conclusion/Discussion

This paper presented numerical and experimental results concerning the scaling of the vibration response of panels excited by a turbulent boundary layer forcing field. The general aim is to achieve the same results through different structural domains and flow speeds by using some similitude expressions. It was evidenced that if proportional side panels are used, applying the suggested similitude laws provide perfect scaling for the numerical section of the study, and satisfactory scaling for experimental results up to a frequency of 1500 Hz. After this first simplified work, next steps mainly involve:

1. Expanding the measurement database using other panel dimensions (including some avatar) and panels made of different isotropic materials—cross-validating the method under two random excitations (turbulent boundary layer and diffuse acoustic field) and expanding the methodology to the calculations of radiated pressure field under such excitations.
2. Verifying the observed trends and defining generalized scaling laws so that the definition of a "reference" plate becomes meaningless. Ideally, being able to provide practical methodologies or key-points (given the real dimensions of a panel of interest, should an enlarged or reduced panel, in terms of dimensions, be tested to comply with experimental means and the desired confidence?).

3. Following an engineer-oriented approach, that focus more on the global representativeness of results (obtained by scaling compared with results directly obtained, without scaling) than their absolute precision and estimate the relative confidence of scaled results.

References

1. Franco, F., De Rosa, S., Ciappi, E.: Numerical approximations on the predictive responses of plates under stochastic and convective loads. J. Fluids Struct. **42**, 296–312 (2013)
2. Ciappi, E., Magionesi, F., De Rosa, S., Franco, F.: Analysis of the scaling laws for the turbulence panel responses. J. Fluids Struct. **32**, 90–103 (2012)
3. Xiaojian, Z., Bangcheng, A., Ziqiang, L., Dun, L.: A scaling procedure for panel vibro-acoustic response induced by turbulent boundary layer. J. Sound Vib. **380**, 165–179 (2016)
4. De Rosa, S., Franco, F., Meruane, V.: Similitudes for the structural response of flexural plates. Proc. IMechE Part C: J. Mech. Eng. Sci. **230**(2), 174–188 (2016)
5. Meruane, V., De Rosa, S., Franco, F.: Numerical and experimental results for the frequency response of plates in similitude. Proc. IMechE Part C: J. Mech. Eng. Sci. **230**(18), 3212–3221 (2016)
6. Corcos, G.M.: Resolution of pressure in turbulence. J. Acoust. Soc. Am. **35**, 192–199 (1963)
7. Bull, M.K.: Wall-pressure fluctuations beneath turbulent boundary layers: some reflections on forty years of research. J. Sound Vib. **190**(3), 299–315 (1996)
8. Miller, T.S., Gallman, J.M., Moeller, M.J.: Review of turbulent boundary layer models for acoustic analysis. In: Proceedings of the 49th AIAA Aerospace Sciences Meeting, 4–7 Jan 2011, Orlando, Florida—AIAA paper 2011-1083 (2011)
9. Hwang, Y.F., Bonness, W.K., Hambric, S.A.: Comparison of semi-empirical models for turbulent boundary layer wall pressure spectra. J. Sound Vib. **319**(1), 199–217 (2009)
10. Elishakoff, I.: Probabilistic Methods in the Theory of Structures. Wiley, New York (1983)
11. De Rosa, S., Franco, F.: Exact and numerical responses of a plate under a turbulent boundary layer excitation. J. Fluids Struct. **24**, 212–230 (2008)
12. Blake, W.K.: Mechanics of Flow Induced Sound and Vibration. Academic Press, Orlando (1986)
13. Farabee, T.M., Casarella, M.J.: Spectral features of wall pressure fluctuations beneath turbulent boundary layers. Phys. Fluids A **3**, 2410–2420 (1991)
14. Goody, M.: An experimental investigation of pressure fluctuations in three-dimensional turbulent boundary layers. Ph.D. Thesis, Department of Aerospace and Ocean Engineering, Virginia Tech, USA (1999)
15. Robin, O., Chazot, J.D., Boulandet, R., Michau, M., Berry, A., Atalla, N.: A plane and thin panel with accurate simply supported boundary conditions for laboratory vibroacoustic tests. Acta Acust. United Acust. **102**(1), 170–182 (2016)
16. Robin, O., Moreau, S., Padois, T., Berry, A.: Measurement of the wavenumber-frequency spectrum of wall pressure fluctuations: spiral-shaped rotative arrays with pinhole-mounted quarter inch microphones. In: Proceedings of the 19th AIAA/CEAS Aeroacoustics Conference, Aeroacoustics Conferences, pp. 1–18 (2013)

Flow Noise Estimation with the Vibroelastic Analogy: Effect of Material Properties

Ian MacGillivray, Alex Skvortsov and Paul Dylejko

Abstract Quantifying flow noise reduction caused by different surface coatings is a ubiquitous topic in aero- and hydroacoustics and is still an area of active research. Methods for doing so commonly involve huge costs in computational power (coupled CFD and FE simulations) and infrastructure (experimental studies). These high costs often make assessment, prototyping or rigorous sensitivity analysis a challenging undertaking. A self-consistent analytical framework is proposed for rapid estimation of relative flow noise intensity for a significantly subsonic turbulent flow over an elastic boundary (such as a turbulent boundary layer). The method utilises the well-known analogy between motion of viscous flow and wave propagation in soft elastic media (materials with low shear moduli). Together with the turbulent flow represented by an ensemble of viscous (shear or vortex) waves, the problem is transformed into that of elastic wave propagation within a multi-layered medium. The resulting noise within the fluid layer is determined by quantifying the transformation of shear waves into longitudinal waves at the flow boundary. This framework extends on previous work that examined the half-space idealisation by including the complex wave propagation within multi-layered coatings and by including the effect of the stream-wise convective velocity. The technique is demonstrated by assessing the influence of different homogenous and voided materials on flow noise from turbulent flow. Last, it is shown how these effects could be quantified by measuring the noise in the interior space of a body in flow.

Keywords Flow noise · Turbulent boundary layer · Vibroelastic materials

I. MacGillivray (✉) · A. Skvortsov · P. Dylejko
Defence Science and Technology, Fishermans Bend, VIC 3207, Australia
e-mail: Ian.MacGillivray@dst.defence.gov.au

A. Skvortsov
e-mail: Alex.Skvortsov@dst.defence.gov.au

P. Dylejko
e-mail: Paul.Dylejko@dst.defence.gov.au

E. Ciappi et al. (eds.), *Flinovia—Flow Induced Noise and Vibration Issues and Aspects-II*,
https://doi.org/10.1007/978-3-319-76780-2_18

Nomenclature

$\lvert\cdot\rvert$	Magnitude of a complex quantity
$\lVert\cdot\rVert$	Magnitude of a vector quantity
$\mathcal{A}$	Vector velocity potential
a	Cylinder radius
c; c_{li}, c_{le}	Sound speed in a fluid; internal, external
c_l	Longitudinal wave speed of a viscoelastic solid
c_s	Shear (transverse) wave speed of a viscoelastic solid
f	Coupling function describing void interaction
E	Energy
h	Cylinder spacing, centre to centre
J	Power flow
K; K_{e}	Plane wave longitudinal modulus; effective void layer K
k	General wavenumber
$\mathbf{k_s}$	Shear wave vector, with magnitude $k_s = \omega/c_s$
l_{e}	Effective void layer thickness
M	Mach number U/c
p	Average (root-mean-square) acoustic pressure
R	Range to field point
S	Surface area
U	Fluid flow velocity
V	Amplitude reflection coefficient
$\mathbf{v} = \mathbf{v}_{\parallel} + \mathbf{v}_{\perp}$	Velocity vector field
$\mathcal{V}$	Interior volume
Z	Specific acoustic impedance ρc of a fluid
α	Energy absorption coefficient for outward sound waves (Sect. 3.3)
α, α_{e}, α'	Void volume concentration parameters (Sect. 3.1, Eqs. 18–23)
β	Energy transmission coefficient for outward sound waves
γ	Volume absorption coefficient (Eq. 28)
ϵ	Energy densities of shear (ϵ_{se}) or longitudinal (ϵ_{ir}, ϵ_{id}) waves
η_s	Incident shear wave vector component normal to the surface
η_l	Reflected longitudinal normal wave vector component
θ	Angle of incidence of a shear wave
κ	Energy coefficient for shear–longitudinal reflection
Λ	Aggregated body-in-flow noise parameter (Sect. 3.3, Eq. 35)
$\lambda = \lambda_r + i\lambda_i$	First Lamé elastic parameter
$\mu = \mu_r + i\mu_i$	Second Lamé elastic parameter, equal to the shear modulus
ν	Kinematic viscosity of the fluid
ξ	Wave vector component parallel to the surface
ρ	Mass density
τ	Energy coefficient for shear–longitudinal transmission
φ	Scalar velocity potential
χ_{v}	Sound wave attenuation coefficient in nepers per metre

χ_{d}	Sound wave attenuation coefficient in decibels per metre
Ω_0	Natural resonance frequency of the voided layer
ω	Angular frequency

1 Introduction

Generation of acoustic waves by turbulent flow near elastic boundaries has been a traditional topic of aero- and hydroacoustics [1, 2], environmental acoustics [3, 4] and geophysics [5]. There is a vast amount of the literature devoted to this subject [3–5]. Although the main models for flow noise are nowadays discussed in textbooks, it is still a challenging task and an area of active scientific research and engineering effort. The numerical framework for flow noise estimation involves advanced models of a turbulent flow coupled with the equations of an elastic boundary and the model of noise generation (the so-called acoustic analogy [2, 3]). These problems are usually intractable analytically and require intensive computer simulations. There are many software tools available that capture this phenomenology with different levels of fidelity. Unfortunately, the application of these tools very often requires an expert-level knowledge of Computational Fluid Dynamics (CFD) and Finite Element (FE) modelling and advanced computing facilities in order to produce even very basic estimates. This was the motivation for the development of a simplified analytical framework which is easier to implement, in comparison with the full-scale CFD and FE simulations, while still capturing the complex phenomenology of the underlying process and producing relative quantitative results of acceptable accuracy.

Our analysis is restricted to that of a slightly compressible fluid, i.e. flows for which Mach number $M = U/c$ is much less than unity, where c is the speed of sound and U is the velocity of unperturbed flow (far from the underlying surface).

The proposed framework is used to provide quantitative evaluation of the difference between different surface materials and cannot be used for absolute estimates of flow noise. We also demonstrate its application for the case of flow noise generated by a body moving in a fluid with an elastic coating.

2 Theoretical Framework

It is well known that the velocity field of arbitrary motion of any slightly compressible medium can be represented through Helmholtz decomposition as a sum of two components, $\mathbf{v} = \mathbf{v}_{\parallel} + \mathbf{v}_{\perp}$, where $\mathbf{v}_{\parallel}$ is an irrotational (curl-free) component with $\mathbf{v}_{\parallel} = \nabla\varphi$ (φ is a scalar potential, and ∇ is the gradient operator) and $\mathbf{v}_{\perp}$ is a rotational (divergence-free) component with $\mathbf{v}_{\perp} = \nabla \times \mathcal{A}$ ($\mathcal{A}$ is a vector potential, and $\nabla\times$ is the curl operator). For the case of elastic isotropic materials, $\mathbf{v}_{\parallel}$ and $\mathbf{v}_{\perp}$ (and

potentials φ and $\mathcal{A}$) satisfy the standard wave equations for the longitudinal and shear (transverse) waves

$$\frac{1}{c_l^2}\frac{\partial^2}{\partial t^2}\varphi + \nabla^2\varphi = 0, \tag{1}$$

$$\frac{1}{c_s^2}\frac{\partial^2}{\partial t^2}\mathcal{A} + \nabla^2\mathcal{A} = 0, \tag{2}$$

where

$$c_l = \sqrt{(\lambda + 2\mu)/\rho} \tag{3}$$

and

$$c_s = \sqrt{\mu/\rho} \tag{4}$$

are the speeds of longitudinal and shear waves, respectively. The attenuation of these waves can be taken into account by assuming complex Lamé elastic moduli $\lambda = \lambda_r + i\lambda_i$ and $\mu = \mu_r + i\mu_i$. These equations can be applied to a fluid where $|c_l| \gg |c_s|$ ($|\lambda| \gg |\mu|$) and the attenuation of shear waves is high. (The modulus operation $|\cdot|$ here refers to the magnitude of the complex quantity.) Note that the longitudinal waves are those for which the motion of the medium is parallel to the wave direction, and shear waves are those for which the motion is transverse (at right angles) to the wave direction.

Our aim is to model turbulent flow as a system of random shear (vortex) waves in an elastic material governed by Eq. (2). It will be shown that the material is equivalent to a damped 'soft' (rubber-like) material. The properties of this 'soft' material can be mapped to the parameters of turbulent flow in the boundary layer. Conventional methods of the elastic wave transformation can then be used to study the process of flow noise generation near the elastic boundary by considering the transformation of vorticity perturbations (shear waves) into sound waves (longitudinal waves) at the boundary (as shown in Fig. 1). In some respects, this mapping procedure is similar to the fluid-elastic analogy well known in the mechanics of composites [6].

The first step is to find effective parameters of an elastic medium in Eqs. (1) and (2) that correspond to turbulent flow in a slightly compressible fluid medium. According to the results of Chu and Kovasznay [7] (see also [8]) for mode decomposition of compressible flows, in a slightly compressible fluid the dynamics of vorticity perturbations and sound waves can be decoupled. The vorticity perturbations are described by the equation

$$\frac{\partial}{\partial t}\Omega + (\mathbf{v}_\perp\nabla)\Omega = \nu\nabla^2\Omega, \tag{5}$$

while for sound waves the wave equation (1) applies. In the above equation, $\Omega = \nabla \times \mathbf{v}_\perp = \nabla^2\mathcal{A}$ is the vorticity field and ν is the kinematic viscosity of the fluid. For a flow with constant velocity $\mathbf{U}$, the linear approximation leads to $(\mathbf{v}_\perp\nabla)\Omega \approx (\mathbf{U}\nabla)\Omega$.

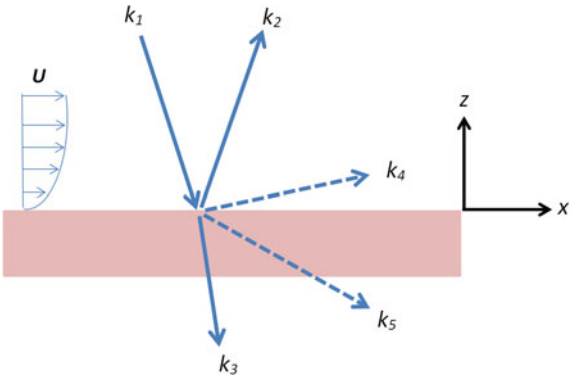

Fig. 1 Transformation of vorticity perturbations (shear waves) into sound waves (longitudinal waves) at the elastic boundary: k_1, k_2 and k_3 are the wave vectors of the incident, reflected and transmitted shear waves, respectively; k_4 and k_5 are the wave vectors of generated sound waves in reflection and transmission, respectively

Assuming the vortex perturbations move only in one direction, determined by $U = \|\mathbf{U}\|$ (which corresponds to boundary layer flow), and by substituting a harmonic component of vorticity $\Omega \propto \exp[i(\mathbf{k_s} \cdot \mathbf{x} - \omega t)]$ into Eq. (5), a dispersion relation for the vorticity perturbations is obtained. For an effective transverse velocity $c_s = \omega/k_s$, where wavenumber k_s is the magnitude of the wave vector $\|\mathbf{k_s}\|$, the matching of the dispersion relations leads to the following equivalence [9, 10]

$$c_s = U - i\nu k_s, \tag{6}$$

which is to be equated with c_s from Eq. (4)

$$c_s = \sqrt{(\mu_r + i\mu_i)/\rho}. \tag{7}$$

Matching of the real and imaginary parts of these equations leads to the effective shear modulus for the fluid in the presence of the flow. When $|c_s| \ll |c_l|$ and $U \ll c$ (slightly compressible limit, $M \ll 1$), the components are $\mu_r \approx \rho U^2$ and $\mu_i \approx -2\rho\omega\nu$, providing $\nu k_s \ll U$ and $\nu\omega \ll 1$. The effective longitudinal wave speed of the fluid in the presence of the flow is simply

$$c_l \approx c, \tag{8}$$

with

$$k_l = \omega/c_l. \tag{9}$$

The velocity U in Eq. (6) is actually the convective velocity which is comparable in magnitude to the velocity of the unperturbed flow. However, it will be shown later that the numerical results are relatively insensitive to the value of U.

The 'correspondence' conditions given by Eqs. (6) and (8) can be employed in the modelling framework to estimate the relative effect of different surface coatings on the noise generated by a turbulent boundary layer [10] adjacent to those surfaces. Transformation of elastic waves in layered structures has been well studied [11–14].

The coefficients of reflection, transmission and absorption are derived by requiring continuity of pressure, stress and displacement across the interfaces between the layers. The processes are modelled numerically by implementing known theory for plane wave reflection [11–13]. Results for arbitrary waves can be modelled as linear combinations of plane waves, but the important conclusions do not require this to be done. The boundary layer turbulence is modelled as an ensemble of transverse waves of arbitrary frequency distribution and propagation direction, with vector potential of one wave component

$$\mathcal{A} = \mathcal{A}_0 \exp(-i\omega t + i\xi x - i\eta_s z), \tag{10}$$

incident on the boundary adjacent to the flow from the half-space $z > 0$, and a reflected longitudinal component with scalar potential

$$\varphi = \varphi_0 \exp(-i\omega t + i\xi x + i\eta_l z). \tag{11}$$

The direction z is normal to the layers and into the fluid, and x is parallel to the layers, as shown in Fig. 1. The wave vector components ξ, η_s and η_l are related by

$$\eta_s^2 = k_s^2 - \xi^2, \tag{12}$$

$$\eta_l^2 = k_l^2 - \xi^2, \tag{13}$$

with equivalent expressions for the lower layers. The incidence angle θ is related to the horizontal wave vector component through

$$\xi = k_s \sin(\theta). \tag{14}$$

The transformation coefficients can be estimated as angle-averaged values assuming uniform angle distribution. In the cases to be considered here, where $|c_l| \gg |c_s|$, there is a critical angle past where no conversion into reflected travelling wave components occurs. As this angle is very small, only those components with wave nearly normal to the surface reflect as sound.

As a demonstration, this method is used to estimate the generation of acoustic waves for a single vortex wave ('harmonic') of frequency ω of Eq. (10). See also the results of Danilov and Mironov [15] on the same subject. Assume the ratio of the scalar potential of the reflected longitudinal wave to the magnitude of the vector potential of the incident transverse wave is V. Then, V represents the efficiency of conversion of transverse waves into longitudinal waves at a plane surface. For a given input medium, the reflected energy is proportional to $|V|^2$. For a simple interface between a fluid and a fluid-like medium (such as a rubber), Ref. [15] gives the approximation

$$\frac{V}{V_*} = -\frac{1 - \rho^{(1)}/\rho - 2(\eta_l^{(1)}/k_s)(-1 + \sqrt{\rho\mu^{(1)}/\rho^{(1)}\mu})}{(\rho^{(1)}/\rho + \eta_l^{(1)}/\eta_l)(1 + \sqrt{\rho\mu/\rho^{(1)}\mu^{(1)}})}, \tag{15}$$

where $\rho^{(1)}$ and $\mu^{(1)}$ are the density and shear modulus in the reflecting fluid-like half-space and ρ is the density of the fluid medium. Wave vector components η_l, $\eta_l^{(1)}$ and k_s are connected to the incidence angle, complex moduli and wave speeds through Eqs. (3), (4), (12), (13) and (14). V has been normalised here by V_*, which is the transformation coefficient at a rigid boundary (obtained by setting $\rho^{(1)} = \infty$ in the expression for V).

Equation (15) provides insightful criteria for material selection for flow noise reduction that would be very difficult to deduce by other means. When $|c_s^{(1)}| \gg |c_s|$, as with a water–rubber boundary, Eq. (15) at angles close to normal incidence can be simplified to

$$V/V_* \simeq \rho^{(1)}/\rho - 1\,, \tag{16}$$

implying that the intensity of turbulent boundary layer noise can be significantly decreased, provided the material underlying the turbulent boundary layer has fluid-like properties (such as with rubber) and its density is close to the density of the fluid. Note that Eq. (16) is a complex amplitude ratio and can be negative. This is strikingly different from an intuitive assumption of impedance match, $\rho^{(1)}c_s \simeq \rho c$. The equation is, however, only valid for an infinite half-space boundary. More complex multi-layer material calculations, which avoid this assumption, can be made using the theory of Lévesque and Piché [11]. Some numerical results are shown in the next section.

More realistic predictions for noise intensity from turbulent flow over an elastic interface can be derived by summation of relative contributions from all vorticity harmonics v_ω from a spectrum of a wall-bounded turbulent flow, $E_\omega \propto |v_\omega|^2$ (i.e. by evaluation of convolution integral of Eq. (15) and E_ω). For a particular flow, the spectrum E_ω can be calculated numerically or deduced from some analytical models (see [16, 17] and references therein).

3 Case Studies

In this section, the formalism proposed above is applied to three test cases to estimate the effect of elastic materials at the flow boundary on turbulent boundary layer noise. The technique is demonstrated by assessing the influence of different homogeneous and voided materials on flow noise from turbulent flow. Last, it is shown how these effects can be quantified by measuring the noise in the interior space of a body in flow.

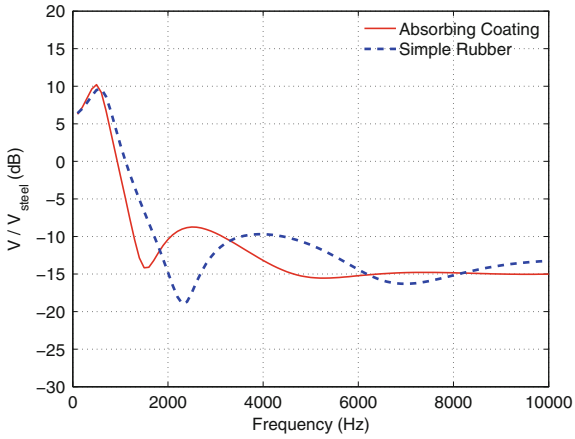

Fig. 2 Relative efficiency of two rubber coating layers as a function of flow noise frequency

Table 1 Water properties

Parameter	Value	Units
ρ	1000	kg/m^3
c_l	1500	m/s
ν	1×10^{-6}	m^2/s
U	3	m/s

3.1 Noise from Turbulent Flow over an Elastic Interface

The first modelling case is for flow noise generated by a turbulent boundary layer over an elastic interface moving at 3 m/s relative to water. The relative efficiencies of two rubber-like materials that can be used as a coating for flow noise reduction are presented in Fig. 2. The rubbers, of centimetre-scale thickness, cover steel of 20 mm thickness which is backed by air. The water parameters are given in Table 1, and the rubber-like materials have full complex frequency dependence (not specified here).

The figure shows the field-averaged reflection of longitudinal waves V, with random incidence, relative to the reflection from the steel alone, V_{steel}. The calculation again uses the theory of [11]. The dashed curve is for an actual rubber material, with known frequency-dependent elastic moduli, and the solid curve is for a nominal rubber material designed as a good absorber of longitudinal pressure waves. Note that there is very little difference between the absorbing coating and a simple uniform layer of rubber. This comparison demonstrates the predictive capability of the proposed method.

3.2 Effect of Voided Coating

This section presents the effect on flow noise of a more complex vibroelastic coating containing cylindrical voids, as shown in Fig. 3. Such a material has some interesting resonance properties which could be beneficial for flow noise mitigation. The theory used for the effective properties of the vibroelastic coating is the 'homogenised' model presented in Refs. [18, 19], consisting of a rubber-like polymer material containing a periodic array of cylindrical voids of radius a and spacing h. The polymer has density ρ and plane wave modulus $K = \lambda + 2\mu$ (which is close to but not the same as the bulk modulus). The void layer within the full polymer layer is modelled as a homogeneous layer with effective thickness l_e, density ρ_e and plane wave modulus $K_\mathrm{e} = \lambda_\mathrm{e} + 2\mu_\mathrm{e}$ given by:

$$l_\mathrm{e} = \frac{2h}{\pi} \ln \sec\left(\frac{\pi a}{h}\right), \tag{17}$$

$$\rho_\mathrm{e} = \rho(1 - \alpha'), \tag{18}$$

$$K_\mathrm{e} = \frac{K(1-\alpha)}{(\alpha'(1+Q) + (1-\alpha)}, \tag{19}$$

where

$$Q = \frac{\lambda/\mu + 2}{1 - (\omega/\Omega_0)^2}, \tag{20}$$

$$\alpha_\mathrm{e} = l_\mathrm{e}/h, \tag{21}$$

$$\alpha' = \alpha/\alpha_\mathrm{e}. \tag{22}$$

Parameter α is the 'global' filling fraction $\pi a^2/h^2$ of cylindrical voids, and $\Omega_0 = f c_s/a$ is the natural resonance frequency of the coating voided layer in the polymer with shear modulus c_s. Here, $f \equiv f(a/h)$ is a coupling function (describing effect of void interaction) calculated in [18, 19]. The remaining thicknesses of the voided material are treated as the pure polymer. In this work, for random incidence modelling the effective shear modulus of all layers must be known. The homogenised shear modulus of the voided layer is therefore approximated as

$$\mu_e = \mu(1 - \alpha_\mathrm{e}) \tag{23}$$

and is assumed isotropic for the purposes of the shear wave reflection modelling.

Figure 3 shows the arrangement of the cylindrical voids, of diameter $2a = 1$ cm, placed centrally in a 10 cm thickness layer of polymer on 2 cm thickness steel, backed by air. The cylinders are spaced with period $h = 5$ cm. The polymer properties, nominally polydimethylsiloxane (PDMS), are given in Table 2.

Figure 4 shows the relative efficiency of conversion of shear motion into flow noise for the voided coating, compared to the plain steel–air interface, obtained in the

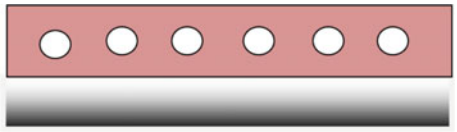

Fig. 3 Cylindrically voided coating with steel backing

Table 2 Polymer properties (PDMS) for the voided layer of Sect. 3.2

Parameter	Value	Units
ρ	1000	kg/m^3
$K = \lambda + 2\mu$	$1000 \times (1 - 0.01i)$	MPa
μ	$0.6 \times (1 - 0.3i)$	MPa

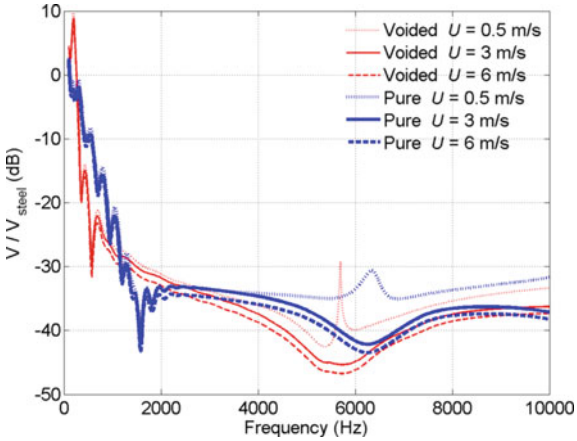

Fig. 4 Relative efficiency of two 10 cm polymer coating layers as a function of flow noise frequency and flow velocity U. With cylinder voids (thin lines) and without voids (thick lines), with flow velocities $U = 0.5$ m/s (dotted), $U = 3$ m/s (solid) and $U = 6$ m/s (dashed)

same manner as Sect. 3.1, for three flow velocities. Also shown is the coating with the cylinders removed. There is little difference between the two coatings, even though the void resonance at about 1600 Hz causes dramatic changes in the conversion of sound waves (not shown). The dramatic decrease in conversion of both coatings, less than about -30 dB above 2 kHz, is due to the density of the PDMS matching that of water, as discussed in Sect. 2. Improved performance at the lowest frequencies, when compared with Fig. 2, is attributed to the increased layer thickness. Note also that the efficiencies are relatively insensitive to the flow velocity magnitude, especially at the lower frequencies. For example, the results obtained with a flow velocity of 6 m/s agree with 3 m/s to within 1–2 dB.

The absolute efficiencies V above are amplitudes with power proportional to $|V|^2$. Although not shown, the modelling using the above method shows that $|V|^2$ is proportional to the flow velocity U. Since U is much less than the sound speed in water, the critical angle is small and therefore proportional to U. The total solid angle contributing energy is then proportional to U^2. Since the intensity of shear waves in the boundary layer is known to be proportional to U^3 [4, 8], the total scattered

Fig. 5 Examples of buoyancy-driven models. Large-scale model, NSWC, Lake Pend Oreille [20] (at left); light composite model, DST Group (middle); extendable modular model, DST Group (right)

acoustic power is then proportional to $U \cdot U^2 \cdot U^3 = U^6$, in agreement with the expected M^6 scaling for boundary turbulent flow [4, 8].

3.3 Noise from a Body in Flow

The last modelling case considered here is the acoustic noise generated by a turbulent flow around a body in water. This setting is typical for experimental investigation of flow noise, when a model is propelled through the water driven by buoyancy [20–22] (see Fig. 5). It is assumed that the body has an internal fluid-filled reverberant volume $\mathcal{V}$ and surface area S, with a shell which may be externally coated with elastomeric (rubber) materials. Our primary interest is to quantify the effect of an elastic coating on flow noise and to infer the relationship between acoustic noise intensity measured inside the body and in the far field.

This problem has been numerically treated with the framework of transformation of elastic waves in layered structures described above [10]. The transformation of waves of each type (shear and sound) at the boundary, travelling in both directions through the body surface (inward and outward from the volume $\mathcal{V}$), is modelled. In order to properly account for conditions of low reverberation and the effect of internal volume losses, both direct and reverberant components of the internal acoustic field need to be considered [23]. In what follows, a relation between the outward acoustic intensity and the acoustic intensity inside the body can be found from the balance of energy flow of the form

$$\frac{dE}{dt} = J_{\text{in}} - J_{\text{out}} - L_{\text{v}}\,, \tag{24}$$

where J_{in} is the inward rate of flow of acoustic energy from turbulence boundary layer excitation, J_{out} is the outward flow of acoustic energy through the shell of the body, and L_{v} is the rate of energy loss from the volume (due to air absorption, for example). In the steady state, the net energy flow is zero so $dE/dt = 0$.

Both the total acoustic power radiated from the body and the internal pressure can be derived in terms of vortex wave input, with an energy density (energy per unit volume) near the exterior of the surface ϵ_{se}. The internal longitudinal wave energy

density ϵ_{i} is divided into its reverberant ϵ_{ir} and direct ϵ_{id} components for correct modelling of the energy flow, which allows the internal volume to be less than highly reverberant. The inward and outward energy flows due to vortex excitation are then given by

$$J_{\mathrm{in}} = \tau \epsilon_{\mathrm{se}} c_{\mathrm{se}} S, \tag{25}$$

$$J_{\mathrm{out}} = \beta \epsilon_{\mathrm{ir}} c_{\mathrm{li}} S/4 + \beta \epsilon_{\mathrm{id}} c_{\mathrm{li}} S/2, \tag{26}$$

where c_{se} is the effective vortex (shear) velocity of the exterior, moving fluid, c_{li} is the sound velocity of the interior fluid, τ is the energy coefficient of transformation of vortex waves (turbulence) into inward sound waves, and β is the coefficient of transmission of outward sound waves (noise) at the internal surface. Direct reflection into the exterior space of the vortex wave input at the exterior surface is

$$J_{\mathrm{ref}} = \kappa \epsilon_{\mathrm{se}} c_{\mathrm{se}} S, \tag{27}$$

where κ is the coefficient of reflection of vortex waves into outward sound waves at the external surface of the body. For the surface type varying over the body, equations (25)–(27) would be replaced by surface integrals. Note that the average reflectance of the outward waves at the internal surface is equal to $1 - \alpha$, where α is the coefficient of absorption of outward acoustic waves through the surface of the body, and $\beta \leq \alpha$. If there is no loss mechanism in the wall surface, then $\alpha = \beta$. These parameters are schematically shown in Fig. 6. The energy parameters α, β, κ and τ must be appropriately spherically averaged (the equivalent of field-incidence) values.

The volume energy loss is given by $L_{\mathrm{v}} = \gamma E = \gamma \epsilon \mathcal{V}$, where γ is total rate of energy loss within the volume and ϵ is the relevant direct or reverberant energy density. Parameter γ is related to the conventional attenuation loss for propagating plane waves χ_{v} in Np/m (nepers per metre) or χ_{d} in dB/m, through

$$\gamma = 2 c_{\mathrm{li}} \chi_{\mathrm{v}}, \tag{28}$$

$$\chi_{\mathrm{v}} = \chi_{\mathrm{d}} \ln(10)/20. \tag{29}$$

The balancing of the energy flow equation (24) for both the direct and reverberant components of the internal pressure then leads to the following expressions for the components [23]:

$$\epsilon_{\mathrm{ir}} = \frac{(1-\alpha)}{\gamma \mathcal{V} + \alpha c_{\mathrm{li}} S/4} J_{\mathrm{in}}, \tag{30}$$

$$\epsilon_{\mathrm{id}} = \frac{1}{\gamma \mathcal{V} + c_{\mathrm{li}} S/2} J_{\mathrm{in}}. \tag{31}$$

As the input source is distributed over the body surface, the average internal pressure p_{i} will be

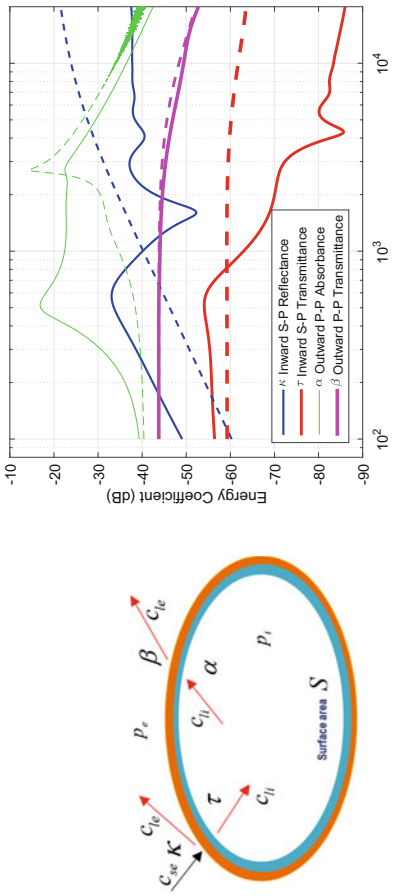

Fig. 6 Conceptual diagram of the transmittance and reflectance parameters of the proposed formalism (top) and those parameters plotted (bottom) for a steel layer (dashed lines) and for steel with rubber coating (solid lines) as a function of flow noise frequency. Parameters α, β, κ and τ appear in Eq. (35)

Table 3 Rubber properties for Sect. 3.3

Parameter	Value	Units
ρ	1200	kg/m^3
$K = \lambda + 2\mu$	$3000 \times (1 - 0.01i)$	MPa
μ	$70 \times (1 - 0.8i)$	MPa

$$p_{\mathrm{i}}^2 = \epsilon_{\mathrm{i}} \rho_{\mathrm{i}} c_{\mathrm{li}}^2, \tag{32}$$

where the total internal energy density of sound waves is

$$\epsilon_{\mathrm{i}} = \epsilon_{\mathrm{ir}} + \epsilon_{\mathrm{id}}. \tag{33}$$

The external pressure p_{e} on average, at range R from the body, assuming omnidirectional spherical spreading, is obtained from the sum of direct vortex reflection and the outwardly transmitted internal field components as

$$p_{\mathrm{e}}^2 = \frac{\rho_{\mathrm{e}} c_{\mathrm{le}}}{4\pi R^2} (J_{\mathrm{ref}} + J_{\mathrm{out}}). \tag{34}$$

These equations fully define the average internal and external pressure relative to the external shear energy density ϵ_{se} outside and close to the surface, and can be used to derive an expression for the ratio of the external to internal pressure that does not depend on ϵ_{se}.

The resulting equation for this ratio can be considerably simplified on the assumption that the volume losses inside the body can be ignored and that the interior is highly reverberant, giving

$$\frac{p_{\mathrm{e}}}{p_{\mathrm{i}}} = \frac{1}{4} \left(\frac{\Lambda}{\pi} \frac{Z_{\mathrm{e}}}{Z_{\mathrm{i}}} \frac{S}{R^2} \right)^{1/2}, \quad \Lambda = \beta + \frac{\kappa \alpha}{\tau}. \tag{35}$$

Here, $Z_{\mathrm{e}} = \rho_{\mathrm{e}} c_{\mathrm{le}}$ and $Z_{\mathrm{i}} = \rho_{\mathrm{i}} c_{\mathrm{li}}$ are the acoustic impedance of the external and internal fluids, respectively, and Λ is an aggregated parameter involving averaged energy transmission and reflection parameters of the wall of the body.

This theory is applied to the case of acoustic noise generated by turbulent flow around a body in water with properties given by Table 1. We assume that the body has an internal air-filled volume $\mathcal{V} = 1\,\mathrm{m}^3$ and surface area $S = 7\,\mathrm{m}^2$, has a steel shell of 6 mm thickness, and may be externally coated with a 40 mm layer of elastomeric (rubber) material as defined by the properties in Table 3 and Eqs. (3) and (4). It is assumed that the body moves in the water with velocity 3 m/s, with parameters as defined in Table 1.

Plots of parameters α, β, κ and τ as a function of frequency are presented in Fig. 6 for the wall of the body with and without the rubber coating, computed using the theory of [11]. These parameters allow estimation of the ratio given by Eq. (35)

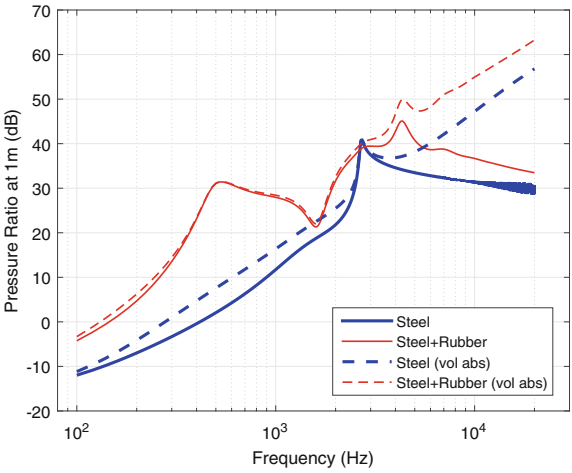

Fig. 7 Ratio of external radiated pressure (normalised to 1 m) to internal pressure for the body with and without a rubber coating, ignoring internal volume absorption, using Eq. (35) (solid curves), and also by accounting for volume absorption (dashed curves)

for any frequency with a targeted flow noise experiment design. This equation could be used to estimate radiated pressure from internal measurements. For instance, from Eq. (35) it is clear that in order to minimise the ratio p_e/p_i one needs either to minimise 'material' parameter Λ (i.e. either β or ratio $\kappa\alpha/\tau$) and this can be translated to a selection of coating material and its thickness. Note that the more comprehensive form of Eq. (35) using the full Eqs. (24)–(34) includes the effect of bulk losses and includes a volume $\mathcal{V}$ dependence. More analysis of Eq. (35) and associated insights into targeted design of flow noise experiments will be presented elsewhere.

Figure 7 shows the ratio of external pressure to internal pressure of Eq. (35) for the body with both a bare and a rubber-coated shell wall. More complex calculations accounting for volume absorption in the internal air space (at 25 °C and 50% relative humidity) are also shown as the dashed curves. Note that as the figure shows external pressure relative to internal pressure it should not be assumed from this plot that the case of steel coated with rubber radiates more than the case of pure steel.

The analysis that leads to Eq. (35) can also be used to evaluate the relative effect of a coating on the interior sound. For example, the relative effect of sonar window coating type on sonar self-noise can be estimated using this method.

4 Concluding Remarks

We propose an analytical framework that explores the intrinsic analogy between sound generation by wall-bounded turbulent flows and transformation of elastic waves in layered elastic media. Several points must be made about the assumptions behind the analytical framework used in this paper. First, the flow must be significantly subsonic. Second, the compliance of the surface should have little effect on

the vorticity sources that are the starting point for this analysis (i.e. they are the same as for rigid surface). For situations where there is strong fluid-structure coupling, this would not be the case. Third, plane wave reflection coefficients have been used for flow sources that are clearly not planar. However, arbitrary sources of vorticity in a turbulent boundary flow can often be decomposed into linear combinations of plane waves so if a consistent trend in reduced reflection is observed this is not likely to be an issue.

We believe that the proposed approach will be useful for rapid evaluation of numerous 'what-if' scenarios in flow noise mitigation including the effects of flow speed, body size, fluid density and viscosity and elastic properties of coating material.

Acknowledgements The authors thank Dr. Chris Norwood for useful discussions and support of this work.

References

1. Urick, R.: Principles of Underwater Sound, 3rd edn. McGraw-Hill, US (1983)
2. Goldstein, M.: Aeroacoustics. McGraw-Hill, US (1976)
3. Howe, M.: Acoustics of Fluid-Structure Interactions. Cambridge University Press, UK (1998)
4. Crocker, M. (ed.): Handbook of Noise and Vibration Control. Wiley, Hoboken, NJ (2007)
5. Ardhuin, F., Herbers, T.: Noise generation in the solid earth, oceans and atmosphere, from nonlinear interacting surface gravity waves infinite depth. J. Fluid Mech. **716**, 316–348 (2013)
6. Christensen, R.: Mechanics of Composite Materials. Dover Publications, New York (2005)
7. Chu, B.T., Kovasznay, L.: Nonlinear interaction in a viscous heat-conducting compressible gas. J. Fluid Mech. **3**, 494–502 (1958)
8. Monin, A., Yaglom, A.: Statistical Fluid Mechanics. Dover Publications, New York (2007)
9. Naugolnykh, K., Rybak, S.: Sound radiation from a turbulent boundary layer. Sov. Phys.—Acoust. **26**(6), 502–504 (1980)
10. MacGillivray, I., Skvortsov, A.: Estimation of pressure pluctuations in a turbulent boundary layer based on vibro-elastic models. In: Proceedings of 43rd International Congress on Noise Control Engineering (INTERNOISE2014), Nov 2014
11. Lévesque, D., Piché, L.: A robust transfer matrix formulation for the ultrasonic response of multilayered absorbing media. J. Acoust. Soc. Am. **92**(1), 452–467 (1992)
12. Brekhovskikh, L.: Waves in Layered Media. Academic Press, New York (1960)
13. Cervenka, P., Challande, P.: A new efficient algorithm to compute the exact reflection and transmission factors for plane waves in layered absorbing media (liquids and solids). J. Acoust. Soc. Am. **89**(4), 1579–1589 (1991)
14. Ainslee, M.: Plane-wave reflection and transmission coefficients for a three-layered elastic medium. J. Acoust. Soc. Am. **97**(2), 954–961 (1995)
15. Danilov, S., Mironov, M.: Conversion of transverse into longitudinal waves at an interface and the problem of sound generation by wall turbulence. Sov. Phys.—Acoust. **31**(4), 314–315 (1985)
16. Glegg, S., Devenport, W.: Aeroacoustics of Low Mach Number Flows. Academic Press, Oxford (2017)
17. Lysak, P.D., Brungart, T.A.: Velocity spectrum model for turbulence ingestion noise from computational-fluid-dynamics calculations. AIAA J. **41**(9), 1827–1829 (2003)
18. Sharma, G.S., Skvortsov, A., MacGillivray, I., Kessissoglou, N.: Sound transmission through a periodically voided soft elastic medium submerged in water. Wave Motion 101–112 (2017)

19. Sharma, G.S., Skvortsov, A., MacGillivray, I., Kessissoglou, N.: Acoustic performance of gratings of cylindrical voids in a soft elastic medium with a steel backing. J. Acoust. Soc. Am. **141**(6), 4694–4704 (2017)
20. Fox, D.: Small subs provide big payoff for submarine stealth. http://www.public.navy.mil/subfor/underseawarfaremagazine/Issues/Archives/issue_11/submarine_stealth.html (2003)
21. Galib, T., Katz, R., Ko, S., Sandman, B.: Measurements of turbulent pressure fluctuations using a buoyant vehicle coated with a thin elastomer layer. J. Acoust. Soc. Am. **96**(6), 3800–3803 (1994)
22. Skvortsov, A., MacGillivray, I., Dylejko, P.: Scaling law for flow noise: effect of material properties. In: Proceedings of the 23rd International Congress on Sound and Vibration (2016)
23. Dylejko, P., MacGillivray, I., Moore, S., Skvortsov, A.: The influence of internal resonances from machinery mounts on radiated noise from ships. IEEE J. Ocean. Eng. (2016). https://doi.org/10.1109/JOE.2016.2593648

Part VII
Vibroacoustic Response–Experiments

Fuselage Excitation During Cruise Flight Conditions: From Flight Test to Numerical Prediction

Alexander Klabes, Sören Callsen, Michaela Herr and Christina Appel

Abstract In the context of aircraft cabin interior noise, the fuselage structural excitation by turbulent boundary layer (TBL) flows is an important noise source for aircraft manufacturers to deal with. During cruise flight, it is the dominant source of cabin noise for state-of-the-art aircraft. Aircraft at cruise conditions is flying at high Mach numbers, typically between Ma = 0.78…0.85, dependent on the type and mission of the aircraft. The vortices within the TBL cause pressure fluctuations on the fuselage and therefore, its structure receives energy and starts to vibrate. In this paper, methods to estimate the aerodynamic TBL sources by numerical and semi-empirical tools are presented. Besides, also the induced vibration of real aircraft structures is calculated with existing industrial tools. Furthermore, measured flight test data used for validation are presented and finally measurements and predictions are compared.

Keywords Aircraft · Flight test · Measurements · CFD · CAA · SEA · TBL Structural vibration

1 Introduction

Many sources of noise contribute to the sound pressure level (SPL) inside an aircraft cabin (cf. Fig. 1). Passengers have high comfort expectancy and therefore expect cabin noise as low as possible. The turbulent boundary layer (TBL) around an aircrafts fuselage is one of the main sources for cabin noise. It causes pressure fluctuations, which excite structural vibrations and noise. Via complex transfer paths energy is transmitted through the fuselage structure and is radiated into the cabin.

Aircraft manufacturers, like Airbus, are interested in an exact estimation of cabin SPL at any position inside the cabin. Therefore, detailed knowledge of the structural excitation by the TBL is essential, which is addressed in this paper. This knowledge

A. Klabes (✉) · M. Herr · C. Appel
German Aerospace Center (DLR), Lilienthalplatz 7, 38108 Braunschweig, Germany
e-mail: alexander.klabes@airbus.com

A. Klabes · S. Callsen
Airbus Operations GmbH, 21129 Hamburg, Germany

E. Ciappi et al. (eds.), *Flinovia—Flow Induced Noise and Vibration Issues and Aspects-II*,
https://doi.org/10.1007/978-3-319-76780-2_19

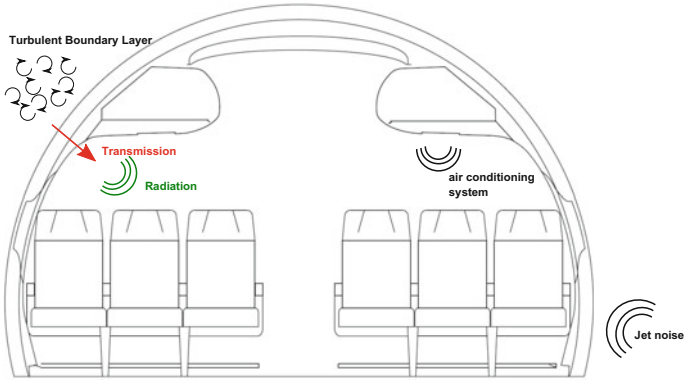

Fig. 1 Examples of noise sources driving cabin SPL (from [1])

enables engineers to implement shape optimisations of the aircraft structure or to improve the insulation concept of today's existing and of future aircraft designs. Finally, this is required to reach the lowest cabin SPL and the highest passenger comfort in the market.

The present work addresses the development of a full tool chain to estimate aircraft fuselage vibration at cruise flight conditions. This work includes two streams, a numerical and a semi-empirical one, to calculate the TBL excitation. The research strategy behind this double tracked approach is to generate the capability of a fast and simple semi-empirical prediction tool for auto-spectra, which is fully validated by flight test data. Besides, the full numerical approach is necessary to calculate the spatio-temporal development of turbulence in terms of wavenumber–frequency spectra. The development of a fast and simple wavenumber–frequency model, like it is done for the auto-spectra, is not possible because of lacking validation data. Flight test data were only measured in three areas on the aircraft. Therefore, a new computational fluid dynamics (CFD)-based auto-spectrum model for aircraft in cruise flight conditions with and without moderate local pressure gradients is developed. Besides, in the second stream, computational aeroacoustics (CAA) tools are employed to calculate the same quantities but focussing more on the wavenumber–frequency spectra. This new model and the purely numerical results are validated with flight test data. Furthermore, the vibration of a real aircraft structure is calculated by using existing statistical energy analysis (SEA) models. Finally, the SEA estimation of structural vibration is validated with measured structural vibrations from the mentioned flight test campaigns.

The working tasks to achieve these goals are the following:

- Postprocessing and analysis of the mentioned flight test data in terms of auto-spectra, to prepare a reliable validation database.
- Extensive study of existing semi-empirical models for auto-spectra prediction and comparison with the measurement database.

- Conduct CFD calculations corresponding to the flight test configurations, to gain detailed knowledge of the aerodynamics all-around the aircraft.
- Development of an enhanced auto-spectra prediction model, based on CFD input data and validation with flight test data.
- Performing CAA computations of auto-spectra and wavenumber–frequency spectra as an input for SEA.
- Coupling TBL excitation with a simply supported flat plate for parameter studies to analyse the influence of different auto-spectra and wavenumber–frequency models and their robustness against parameter variation.
- Coupling TBL excitation from semi-empirical and numerical models to real aircraft structures by making use of existing aircraft SEA models at Airbus without doing any optimisation on these models or the formulation of the structure.
- Validate the SEA estimations of structural vibration with in-flight measured vibrations.

Most of the mentioned tasks are recapitulatory described in the following. In its entirety, the whole work is described in [1].

2 Experimental Validation Database

Experiments were conducted with an Airbus A320, the Advanced Technology Research Aircraft (ATRA) of DLR. The range of flight conditions was between Ma = 0.68…0.82 and FL = 250…410, compare [2] for further information. Flight tests were conducted during three campaigns, each focussing on a different area of the aircraft. Here, blue depicts the front, red the mid and green the aft area, respectively. On the outside of the aircraft two different sensor types, to measure the TBL-induced surface pressures were installed. Kulite pressure transducers of type XCL-093 [3] were installed during all three test campaigns and thus in all areas of the aircraft (front, mid, aft). For each configuration, a total of 30 transducers were installed in three dummy windows, which replaced the standard passenger windows, coloured windows in Fig. 2. The Kulite installation set-up was developed by the DLR team of Spehr and is described in [3]. Besides the Kulite pressure transducers, which are limited to be installed in the passenger window plane, flush-mounted microphones were installed. These flush-mounted Brüel & Kjaer 4948-W-003 (special type of 4948-A) sensors were only installed during two flight test campaigns and only in two regions (front and aft). The sensor installation and data recording were performed by Airbus during the campaigns. The sensor itself was especially developed for aircraft applications. A big advantage of these sensors is the flexibility of the positioning because they can be glued everywhere on the surface of an aircraft. The flush-mounted microphones were installed in groups of three or five sensors as well as stand-alone microphones. Besides the pressure fluctuation measurements on the outer surface, vibrational measurements on the primary structure were performed as well. Therefore, accelerometers with an approximate weight of 2.8 g were installed.

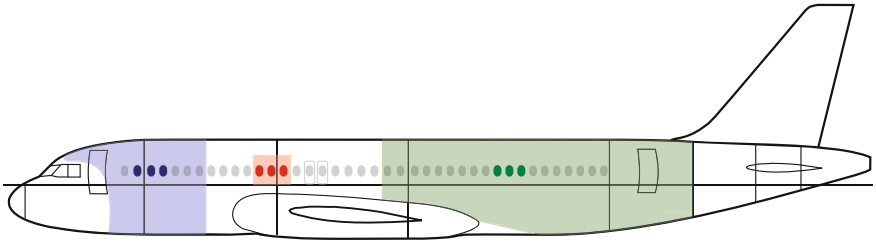

Fig. 2 Sketch of ATRA with Kulite positions (wing profile changed; from [1])

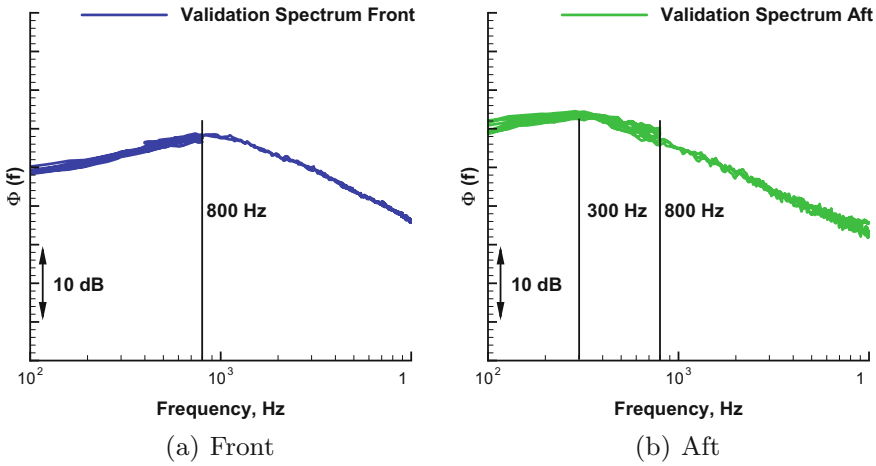

Fig. 3 Validation auto-spectra, similar to [2]

According to the Kulite window positions, the accelerometers are mainly installed in the respective three frame bay areas from floor to roof.

With frequency-dependent limitations of different sensor types and different sensor installation situations, highlighted in [1], validation auto-spectra can be combined for the whole frequency range of interest (f = 100…10000 Hz). This is possible for the front and aft aircraft region, where all different sensor types are installed side by side. For the front area, the validation auto-spectrum is given in Fig. 3a, with a maximum at f = 800 Hz. Kulite data from the front region are plotted from f = 100…800 Hz and data from B&K microphones from f = 400…10000 Hz. Therefore, a data overlap of 400 Hz is ensured. Figure 3b shows the respective validation auto-spectrum for the aft region, with a maximum at f = 300 Hz, for orientation, the 800 Hz line from the front spectrum is plotted as well. Kulite data from the aft region are shown from f = 100…800 Hz and data from B&K microphones from f = 400…10000 Hz. The presented validation auto-spectra are valid for Ma = 0.78 and FL350 and idle engine thrust conditions.

3 Fundamentals of Fuselage Excitation by Turbulent Boundary Layer

For the estimation of structural vibration of an aircraft's fuselage, excited by TBL flow, two types of TBL models are necessary. On the one hand, the auto-spectrum, that sorts the energy at a single point into frequencies, is required. On the other hand, a normalised wavenumber–frequency spectrum, that sorts the energy distribution into wavenumbers and gives information about the spatio-temporal development of turbulence, is needed.

An overview of the multiple developments of semi-empirical models to calculate the TBL wall pressure frequency spectrum is given in [2]. Models most often found in the literature of the past 50 years are provided in a summarised form. Furthermore, in [1] this overview is further extended to the wavenumber–frequency models. Besides the excitation modelling, a description of the structural coupling is indispensable. The idea of Graham [4] and its application in this paper is shortly summarised in [1].

The characterisation of the wall pressure spectra that have been formed over the years is summarised and complemented in the following. Figure 4 presents the characteristic shape of a TBL wall pressure spectrum (auto-spectrum), which is based on a determination of which scaling variables work best in particular frequency regions. The spectrum is divided into four characteristic regions, with its frequency intervals formulated by dimensionless frequencies. For a more detailed analysis compare [1]. The wall pressure spectrum in the low- and mid-frequency regions are composed of pressure fluctuations impressed on the wall by a physical process that occurs largely in the outer layer, away from the wall, while the higher spectral frequencies reflect physical behaviour occurring close to the wall. This duality contributes to the non-homogeneous nature of the wall pressure [8]. In the following, plots with all semi-empirical TBL models introduced in [2] are presented for FL350 and Ma = 0.78 at front and aft Kulite positions. Figure 5a, b present the predictions for front and aft region with their respective validation auto-spectra from flight test measurements. All models are fed with the local flow parameters from CFD calculation.

Models can be divided into two major groups, and they are detailed described in [1]. A rough description of the models is given in [2] as follows: "On the one hand, the green and blue lines describing the Robertson [35]/Cockburn & Robertson [36], respectively, the Efimtsov 1, 2 [31, 37]/Rackl & Weston [38] models. These models are based on flight test and wind tunnel data at high Mach number and Reynolds number. Distinctive for these models is a large plateau in the low-frequency range with a roll-off at higher frequencies.

On the other hand, the Goody [5], Chase-Howe [39] and Smol'yakov [6] models represent the second group. This group obviously provides spectra with different shapes, especially in the low-frequency range. The absolute values of these predictions increase with increasing frequency until a maximum in the mid-frequency range is reached, and then it is followed by a decreasing behaviour with increasing frequency.

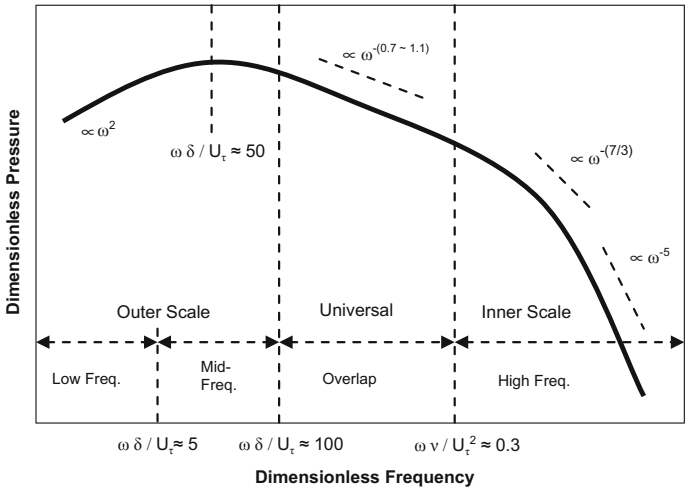

Fig. 4 General spectral characteristics of a TBL wall pressure spectrum at various frequency regions, according to [7]

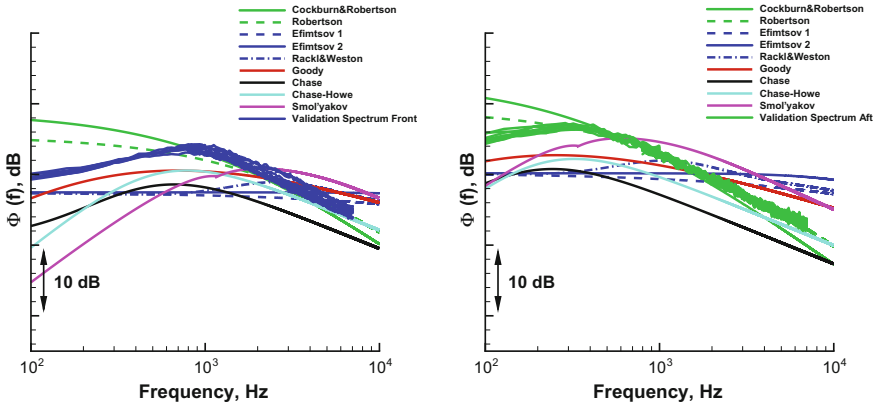

(a) Front (b) Aft

Fig. 5 Comparison of predictions from all auto-spectra models with validation auto-spectra; Ma = 0.78, FL350, front and aft area [9]

The Chase [7] model is with regard to the shape, something in between these two mentioned groups. In the low-frequency range, a large plateau is characteristic, as it is for the Robertson [35]/Cockburn & Robertson [36] and the Efimtsov 1, 2 [31, 37]/Rackl & Weston [38] models. For higher frequencies the predicted spectrum peaks and afterwards it is characterised by a roll-off similar to the Goody, Chase-Howe and Smol'yakov models." It is remarkable that each model has its own shape and slightly different characteristics. None of the models fits perfectly to the validation auto-spectra measured by DLR and Airbus. For model development, it is

decided to go further with the Goody model because it is based on different measurement databases. Besides, the model family beginning with Chase's model and being further developed to the Goody model is closest to the measurement data and to the theoretical shape of an auto-spectrum, presented in Fig. 4.

Besides, the second mentioned group of models are the wavenumber–frequency models. A schematical sketch with all characteristic regions is given in Fig. 6 at constant frequency. Here, k_x is the wavenumber, corresponding to the flow direction, and k_y is the wavenumber corresponding to the cross-flow direction. This description can, e.g., be found in [10–12]. Bull states in [11] that the general shape of the spectrum underneath TBL is driven by pressure-field components with phase velocities $\omega/k_\omega = U_c$. This area is called the convective ridge of the wavenumber spectrum (centred around $k_\omega = \frac{\omega}{U_c}$), where most of the TBL turbulence energy is located. Furthermore, acoustic radiation is associated with components with phase velocities which are equal or greater than the speed of sound in the fluid. Therefore, detailed knowledge of the whole wavenumber–frequency spectrum is necessary. The spectrum depicted in Fig. 6 is subdivided in: (1) supersonic region (not marked), $k < \omega/c \ (= k_0)$; (2) sonic or acoustic region, $k \simeq \omega/c$; (3) subconvective region, $\omega/c < k < \omega/U_c$; (4) convective region, centred around $k = \omega/U_c$; (5) viscous region, $k \gg \omega/U_c$ [11].

Besides, Graham [13] supposed that the subconvective region, which is important for underwater applications, is not dominant to aircraft applications. It is the convective region, where most of the energy of the TBL is positioned and which is the major driver of exciting structures on aircraft. Finally, the viscous region is that region, where small-scale turbulence occurs [12].

4 CFD Calculations and Analysis

For the prediction of the introduced auto-spectra and wavenumber–frequency spectra models, aerodynamic input is necessary. Usually, this input is calculated by theoretical formulae, whose validity is limited by drastic simplifications, when applied to an aircraft. Furthermore, measurement data are not always available to feed the models. Therefore, it is decided to establish a new approach by using data from CFD calculations, to have a clear picture of the aerodynamics on the fuselage. CFD calculations were performed with DLR's in-house RANS solver TAU [15, 16], applying a Reynolds stress turbulence model (RSMg) [17]. In [2], an overview of the CFD calculations performed and the analysis methods conducted is provided, to achieve the required aerodynamic parameters as an input for the models. Besides, CFD data needed as an input for CAA calculations that are performed as well and presented in [1].

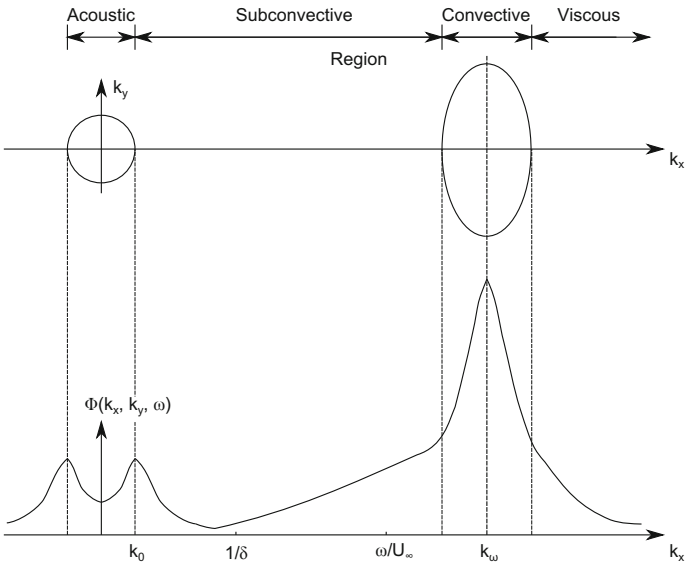

Fig. 6 Characteristic regions of wavenumber spectrum, according to Howe [14]

5 Prediction Models

This section recaps all modelling activities on auto-spectra and wavenumber–frequency prediction models. It is divided into two major parts. Firstly, in a part this presents the enhancement of the semi-empirical Goody model for auto-spectra predictions. Secondly, a part showing the full numerical approach for the prediction of auto-spectra as well as wavenumber spectra is presented.

5.1 CFD-Based Semi-empirical Auto-spectra Prediction Model

A new model for CFD-based auto-spectra prediction was developed, whose final version is in detail described in [1]. A rough overview of a forerunner of this new model can also be found in [9, 18]. After comparison of the available measurement data with published auto-spectra models in Fig. 5a, b it was decided to use Goody's [5] model as a starting point for further development. Besides, the Goody model is part of the Chase and Chase-Howe model family and is the most validated model with zero pressure gradient TBL measurement data sets. Remarkable is the history of these models because they were developed for low-speed applications. Nevertheless, the applicability seems to be better, when compared with the original high-speed models, like the one of Efimtsov. This decision is also backed with the findings

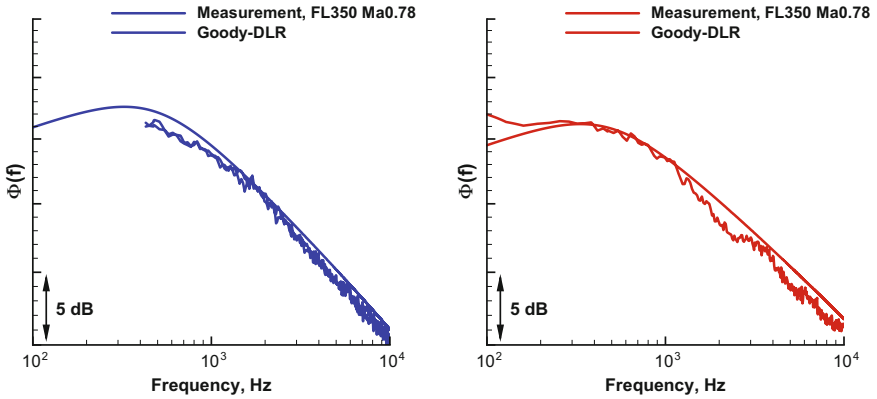

(a) Overwing position far above the trailing edge

(b) Wing wake position behind the Belly fairing

Fig. 7 Measurements compared with adapted Goody-DLR auto-spectrum model, also compare [9]

of Gloerfelt [19] and Alaoui [20] that Mach number and compressibility effects for flows, ranging from Ma = 0.5…0.9 have very low effect on the structure of turbulence.

Few results of this model are presented in Fig. 7, in comparison with measurement data. A full set of results for all aircraft areas is published in [1].

5.2 CFD/CAA Based Prediction

Containing the full numerical prediction approach, this section constitutes, besides the semi-empirical modelling approach in the previous section, the second part of the prediction model activities within this paper.

For the numerical prediction of wall pressure fluctuations, the method of Hu [21, 22] is applied. To this end, a turbulent boundary layer flow on an aircraft is simulated, using synthetic turbulence, generated by the Fast Random Particle-Mesh Method (FRPM) of Ewert [23, 24]. The stochastic realisation is based on time-averaged turbulence statistics calculated from full aircraft RANS computations as described before. According to Hu [22], for incompressible quasi-parallel flow, the fluctuating pressure at the fuselage surface is determined by solving a Poisson equation. The detailed process beginning with the preparation of the CFD data, the calculation with FRPM and the analysis of the numerical results is in detail described in [1]. Results for numerically calculated auto-spectra are given in Fig. 8 for the front and aft aircraft regions. Numerically calculated auto-spectra are plotted in pink and red for the front and aft region, respectively. A bunch of virtual microphones located in each calculation patch is analysed and plotted as thin lines; the mean value is shown as

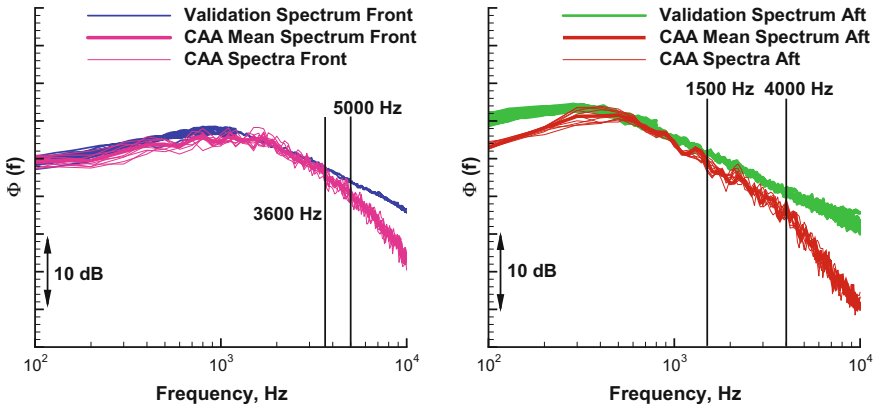

Fig. 8 Validation auto-spectra: CAA versus Measurements (from [1])

a thick line. The presented numerical predictions reproduce the measurements quite well. Absolute levels fit over a large frequency band, and the position of the maximum is well represented. Especially in the low- and high-frequency range, measurement and prediction diverge. Explanations for this behaviour are manifold and in detail discussed in [1].

6 Results and Discussion

Finally, the application of the new auto-spectrum model as well as semi-empirical and numerical wavenumber–frequency spectra to real aircraft structures is presented in this section. According to the Kulite window measurement regions (cf. Fig. 9), SEA models are developed for the respective regions, mainly by Callsen[1] and supported by the work of Teschner [25] and Klabes [26] and the commercial software VA One was employed for the computations. The SEA models always stretch across four frame bays and are sketched in Fig. 9 together with the Kulite windows and their global position on the aircraft. Furthermore, the different naming of the SEA subsystem regions is presented. During the collaboration with Airbus, detailed analysis was performed for all aircraft models. In this paper, only results for the front model from floor to floor are presented in the following.

The influence of different wavenumber–frequency models is analysed on the structural vibration of the *Roof* subsystem. A detailed description of the used models is given in [1] and not in this paper; only the characteristical shape of a wavenumber–frequency spectrum was discussed beforehand in Sect. 3. This analysis is presented in Figs. 10a–12b. In all plots, 0 dB is the median value of the measured acceleration,

[1] Airbus Acoustic Engineer

while all other data are plotted in Δ dB to this value. The grey line gives the scatter band of the flight test data. Furthermore, all wavenumber–frequency models are calculated with the actual aerodynamic parameters from CFD and the auto-spectrum input is calculated with the Klabes model [9], which has been calibrated against ATRA flight test data. Therefore, errors due to the auto-spectrum model are negligible. The procedure for the comparison of the wavenumber–frequency models is that the rhombic models [29–31] are tested first. Secondly, the best performing rhombic model is retained and compared with the results from elliptical models [32–34]. Thirdly, the best models of both families are compared with wavenumber–frequency results from the full numerical FRPM approach and with an adapted Efimtsov model [28], here the model is adapted to measured coherence length from flight tests.

Figure 10a shows the results for the applied Jolly, Corcos and Efimtsov original wavenumber–frequency models. Results are plotted for the $\frac{1}{3}$-octave bands from $f = 100...5000$ Hz. From $f = 100...400$ Hz, the Efimtsov model shows the lowest deviation from flight test data, whereas the Jolly and Corcos models show huge differences to the measurements. In the mid-frequency range from $f = 500...1600$ Hz, this effect is inverted and the Efimtsov model gives results outside the measured scatter band. The Corcos model shows slightly higher levels than the Jolly model, which is according to expectation. Finally, in the high-frequency range $f = 2000...5000$ Hz all three models deliver similar results. A further comparison with the Jolly, Smol'yakov, Chase 1 and Smol'yakov & Tkachenko wavenumber–frequency models is presented in Fig. 10b for the *Roof* subsystem as well. The Smol'yakov and Chase 1 models produce equal results in the mid- to high-frequency ranges, $f = 500...5000$ Hz. While they differ in the low-frequency range, the Smol'yakov & Tkachenko model results are plotted and give satisfying results, by generating the lowest offset from the measurements for the whole mid- to high-frequency ranges. Only in the low-frequency range below $f < 400$ Hz the Smol'yakov & Tkachenko model results are outside the measured scatter band. Finally, the Jolly as well as the Smol'yakov & Tkachenko models create best results as representatives of the rhombic and elliptical models, respectively. Therefore, further comparisons are only performed with these two models.

Furthermore, a wavenumber–frequency spectrum, fully numerically calculated with FRPM is applied to the SEA model as well and presented in Fig. 11a. The results calculated with the FRPM model give satisfying results within their validity range, which was estimated to be up to $f < 3000$ Hz [1]. This assumption can be confirmed by the predicted vibration results with FRPM wavenumber–frequency input, because the vibration levels increase above $f > 2500$ Hz abnormally. Besides, an adapted Efimtsov wavenumber–frequency model is also applied to the SEA model. This model is modified according to the work of Haxter [28], who fitted the model parameters ($a_1...a_7$) in a way that the model coherence length collapse with the measured coherence length from flight test data. A comparison of the structural vibrations shows a good reproduction of the measured vibrations from $f = 400...5000$ Hz in Fig. 11b with some exceptions at $f = 500$ and 800 Hz. In the frequency range below, estimated vibration data deviate from the measurements, like

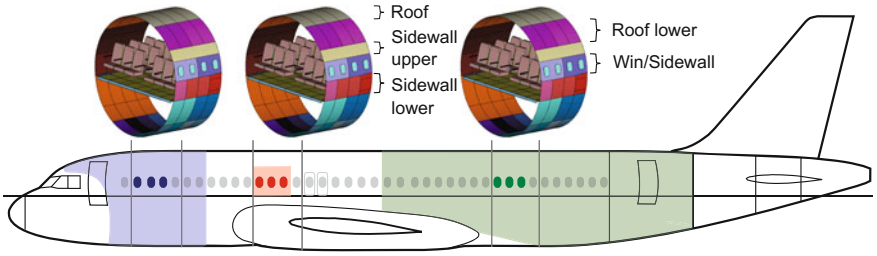

Fig. 9 Sketch of ATRA with SEA model and Kulite positions (from [1])

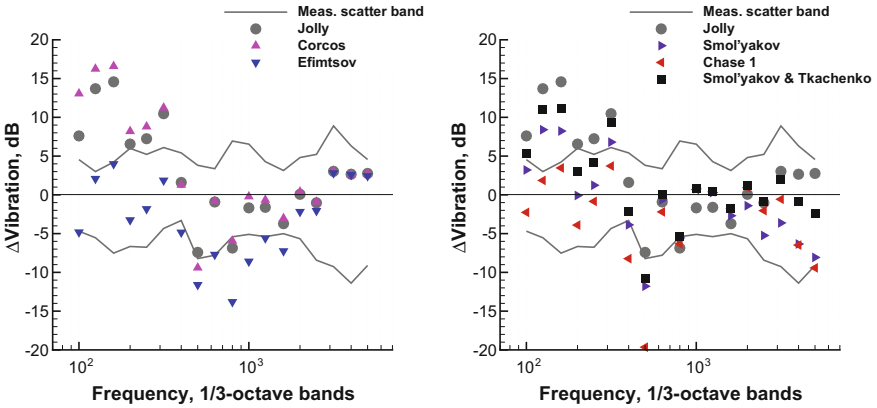

(a) Jolly vs. Corcos vs. Efimtsov

(b) Jolly vs. Smol'yakov vs. Chase 1 vs. Smol'yakov & Tkachenko

Fig. 10 Comparison of structural vibration due to different wavenumber–frequency models—Roof (from [1])

the results from all other semi-empirical wavenumber–frequency models do, except the original Efimtsov model in Fig. 10a. Comparing both models, the FRPM and the adapted Efimtsov, in Fig. 12a, both models give a good estimate within different frequency ranges. The FRPM model is satisfactory between $f = 100...2500$ Hz and the adapted Efimtsov between $f = 400...5000$ Hz. Also, the plotted results from the Smol'yakov & Tkachenko model are satisfactory between $f = 200...5000$ Hz, when predictions lie inside the measurement scatter band. Haxter showed in [28] that the coherence length of the Smol'yakov & Tkachenko model collapse with the measured coherence length. Including as well the Jolly model in this group in Fig. 12b, the model behaviour is comparable with the other models (except FRPM) between $f = 400...5000$ Hz. Again, the predicted levels are too high below $f < 400$ Hz, while this phenomenon cannot be observed with the FRPM model. This leads to the assumption that especially the rhombic wavenumber–frequency models (Corcos, Jolly, Efimtsov) have drawbacks in the low-frequency range ($f = 100...400$ Hz).

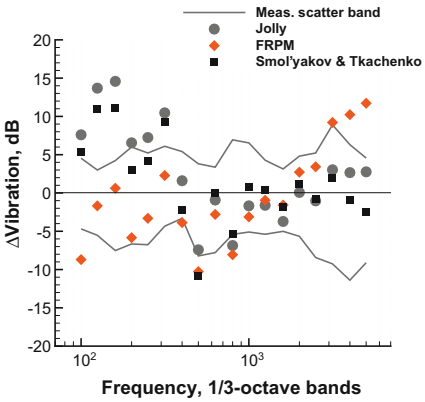

(a) Jolly vs. Smol'yakov & Tkachenko vs. FRPM

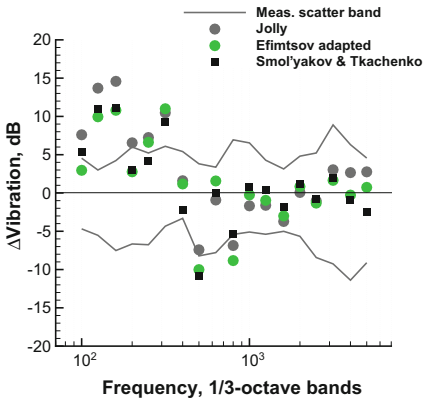

(b) Jolly vs. Smol'yakov & Tkachenko vs. Efimtsov adapted

Fig. 11 Comparison of structural vibration due to different wavenumber–frequency models—Roof (from [1])

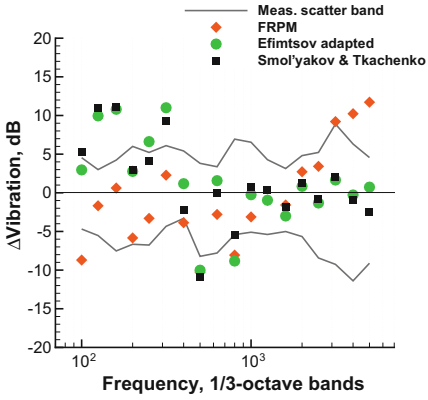

(a) Efimtsov adapted vs. Smol'yakov & Tkachenko vs. FRPM

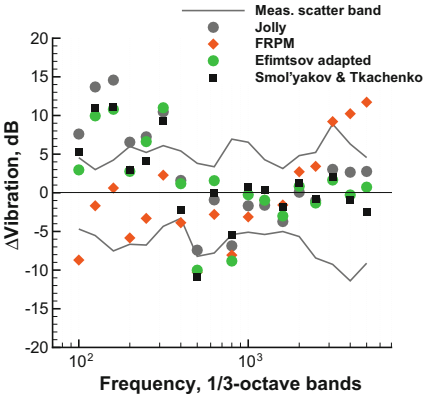

(b) Jolly vs. Smol'yakov & Tkachenko vs. Efimtsov adapted vs. FRPM

Fig. 12 Comparison of structural vibration due to different wavenumber–frequency models—Roof (from [1])

7 Conclusion

This work was performed in the context of aircraft cabin interior noise and in detail focussing on the fuselage structural excitation by turbulent boundary layer (TBL) flows at typical cruise flight conditions. For the prediction knowledge about the strength of the TBL and the development over space and time is necessary, which is described by the auto-spectrum and the wavenumber–frequency spectrum, respectively. TBL estimations in areas on the aircraft subjected to disturbed flows by integration effects like the junction of wing and fuselage or changing fuselage diameter were not possible with today's semi-empirical methods.

The objective of this work was to close this gap. For this purpose, an existing semi-empirical model was further developed to tackle these challenges after reviewing available models in the literature. The main technological innovation of the new auto-spectrum model consists in taking aerodynamic parameters of the flow from computational fluid dynamics (CFD) calculations. This new model is validated with measured auto-spectra from flight tests and therefore, it is valid in a rather large parameter space, covering the operational range of a short- to medium-haul aircraft. In parallel, a full numerical approach to estimate the auto-spectrum as well as the wavenumber–frequency spectrum was executed by making use of the Fast Random Particle-Mesh Method (FRPM) of DLR. This approach is based on the synthetic reconstruction of turbulence over space and time, using CFD data input. The FRPM approach showed being able to estimate auto-spectra as well as wavenumber–frequency spectra in selected areas of high quality. Currently, the only drawback is a frequency limitation to high frequencies, especially visible in the wavenumber spectra over $f > 2500$ Hz.

Finally, the developed auto-spectrum model as well as the different reviewed wavenumber spectrum models, also the FRPM wavenumber spectrum and a model fitted to analysed flight test data were applied to the real aircraft, by using SEA. For the SEA computations, the commercial software VA One was employed with Airbus A320 SEA models used for research and development at Airbus. Fuselage vibration data estimated with these models were finally compared with measured structural vibrations from flight tests in different areas of the aircraft. Estimated structural vibrations gave a good collapse with the measured accelerations, but also showed challenges for different wavenumber–frequency models in distinct frequency ranges. Especially in the low-frequency range, semi-empirical models tend to deviate from measurements. In the mid- and high-frequency ranges, reliable models could be identified. However, SEA modelling of fuselage components also has its limits and the confidence in the structural modelling has to be independently analysed. For a more detailed description of the whole work, it is suggested to read [1].

Acknowledgements The authors would like to thank Airbus Operations GmbH (Dept. Interior Noise) for the financial support of this project. Furthermore, the authors thank for the excellent and close teamwork between the Airbus Interior Noise Department and the DLR Acoustics Department during the last years.

References

1. Klabes, A.: Aircraft fuselage vibration excitation by turbulent boundary layer flow in cruise. Ph.D. thesis. German Aerospace Center, DLR-Forschungsbericht FB 2017-49 (2017)
2. Klabes, A., Appel, C., Herr, M.: Fuselage excitation during cruise flight conditions: measurement and prediction of pressure point spectra. AIAA paper 2015-3115, June 2015
3. Spehr, C., Hennings, H., Buchholz, H., Bouhaj, M., Haxter, S., Hebler, A.. In-flight sound measurements: a first overview. In: AIAA paper 2012-2208, 18th AIAA/CEAS Aeroacoustics Conference, Colorado Springs, CO, USA, 04–06 June 2012
4. Graham, W.R.: Boundary layer induced noise in aircraft, Part I: The flat plate model. J. Sound Vib. (1996)
5. Goody, M.: Empirical spectral model of surface pressure fluctuations. AIAA J. **42** (2004)
6. Smolyakov, A.V.: Calculation of the spectra of pseudosound wall-pressure fluctuations in turbulent boundary layers. Acoust. Phys. **46** (2000)
7. Hwang, Y.F.: Comparison of semi-empirical models for turbulent boundary layer wall pressure spectra. J. Sound Vib. (2009)
8. Palumbo, D.: Measurement of the correlation and coherence lengths in boundary layer flight data. NASA Langley Research Center, TM-2011-217060, Feb 2011
9. Klabes, A., Appel, C., Herr, M., Callsen, S.: Fuselage excitation during cruise flight conditions: a new CFD based pressure point spectra model. Inter-Noise (Paper 140) (2016)
10. Blake, W.K.: Mechanics of Flow-Induced Sound and Vibration, Volume II, Complex Flow-Structure Interactions (1986)
11. Bull, M.K.: Wall-pressure fluctuations beneath turbulent boundary layers: some reflections on forty years of research. J. Sound Vib. (1996)
12. Miller, T.S.: Turbulent boundary layer models for acoustic analysis. Doctoral thesis. Department of Aerospace Engineering and the faculty of Graduate School of Wichita State University (2011)
13. Graham, W.R.: A comparison of models for the wavenumber frequency spectrum of turbulent boundary layer pressures. J. Sound Vib. (1997)
14. Howe, M.S.: Acoustics of Fluid-Structure Interactions. Cambridge University Press (2008)
15. Gerhold, T., Friedrich, O., Evans, J., Galle, M.: Calculation of complex threedimensional configurations employing DLR-TAU-Code. In: 35th Aerospace Sciences Meeting and Exhibit, Jan 1997
16. Schwamborn, D., Gerhold, T., Heinrich, R.: The DLR TAU-Code: recent applications in research and industry. In: ECCOMAS CFD 2006 Conference, Aug 2006
17. Togiti, V., Eisfeld, B.: Assessment of g-equation formulation for a second-moment reynolds stress turbulence model. AIAA paper 2015-2925, June 2015
18. Klabes, A., Appel, C., Herr, M., Callsen, S.: Fuselage excitation during cruise flight conditions: CFD based prediction of pressure point spectra; Aeroacoustics research in Europe: The CEAS-ASC report on 2015 highlights. J. Sound Vib. **381**, (2016)
19. Gloerfelt, X., Margnat, F.: Effect of Mach number on boundary layer noise. AIAA paper 2014-3291 (2014)
20. Alaoui, M., Gloerfelt, X., Collery, O., Etchessahar, M.: Effect of pressure gradients on turbulent boundary layer vortical structures and wall-pressure fluctuations. AIAA paper 2015-3116, June 2015
21. Hu, N., Appel, C., Herr, M., Reiche, N., Ewert, R.: Numerical study of wall pressure fluctuations for zero and non-zero pressure gradient turbulent boundary layers. AIAA paper 2016-2911 (2016)
22. Hu, N., Reiche, N., Ewert, R.: Simulation of turbulent boundary layer wall pressure fluctuations via Poisson equation and synthetic turbulence. J. Fluid Mech. (2016)
23. Ewert, R.: Broadband slat noise prediction based on CAA and stochastic sound sources from a fast random particle-mesh (RPM) method. Comput. Fluids **37** (2008)
24. Ewert, R., Dierke, J., Neifeld, A., Appel, C., Siefert, M., Kornow, O.: CAA broadband noise prediction for aeroacoustic design. J. Sound Vib. **330** (2011)

25. Teschner, M.: Validierung eines vibroakustischen Berechnungsmodells für einen Flugzeugrumpf in unterschiedlichen Flugzuständen. Airbus Operations GmbH & Hamburg University of Applied Sciences (2013)
26. Klabes, A.: Validation of a simulation model for the "Statistic EnergyAnalysis" (SEA) of the Airbus A320 for different flight parameters. Airbus Operations GmbH & German Aerospace Center (DLR) (2012)
27. Medeiros, A.A., Alimonti, L., Gardner, B., Callsen, S., Klabes, A.: An SEA modeling of general surface pressure excitation based on their wavenumber-frequency spectrum. Inter-Noise (Paper 1013) (2016)
28. Haxter, S., Spehr, C.: Comparison of model predictions for coherence length to in-flight measurements at cruise conditions. J. Sound Vib. **390** (2016)
29. Corcos, G.M.: The structure of the turbulent pressure field in boundary-layer flows. J. Fluid Mech. (1964)
30. Cockburn, J.A., Jolly, A.C.: Structural-acoustic response, noise transmission losses and interior noise levels of an aircraft fuselage excited by random pressure fields. Air Force Flight Dynamics Laboratory, Air Force Systems Command, AFFDL-TR; 68-2. WR (1968)
31. Efimtsov, B.M.: Characteristics of the field of turbulent wall pressure fluctuations at large Reynolds numbers. Sov. Phys.—Acoust. (1982)
32. Smol'yakov, A.V.: A new model for the cross spectrum and wavenumber frequency spectrum of turbulent pressure fluctuations in a boundary layer. Acoust. Phys. **52**(6) (2006)
33. Chase, D.M.: Modeling the wavevector-frequency spectrum of turbulent boundary layer wall pressure. J. Sound Vib. **70**(1) (1980)
34. Smol'yakov, A.V., Tkachenko, V.M.: Model of a field of pseudosonic turbulent wall pressures and experimental data. Akusticheski Zhurnal **37** (1991)
35. Robertson, J.E.: Prediction of in-flight fluctuating pressure environments including protuberance induced flow. NASA, CR-119947, Mar 1971
36. Cockburn, J.A., Robertson J.E.: Vibration response of spacecraft shrouds to in-flight fluctuating pressures. J. Sound Vib. (1974)
37. Efimtsov, B.M.: Similarity criteria for the spectra of wall pressure fluctuations in a turbulent boundary layer. Sov. Phys.-Acoust. (1984)
38. Rackl, R., Weston, A.: Modeling of turbulent boundary layer surface pressure fluctuation auto and cross spectra-verification and adjustments based on TU-144LL Data. NASA/CR-2005-213938, The Boeing Company (2005)
39. Miller, T.S., Gallman, J.M., Moeller, M.J.: Review of turbulent boundary layer models for acoustic analysis. AIAA paper 2011-1083, Jan 2011

Turbulent Flow Noise Generation Under Sea Conditions

Jan Abshagen, Dennis Küter and Volkmar Nejedl

Abstract Flow-induced noise contributes to the self-noise level of a hydroacoustic antenna that is either attached to or towed behind a moving platform at sea. It is induced in the interior of the antenna by hull vibrations excited by an outer turbulent boundary layer. Two different hull configurations were studied in a research cruise with an underwater towed body measurement system in Sognefjord, Norway. While the hydrophones were embedded into the hull structure in one of the flat plate configurations, they were separated from the hull by a water layer in the other. Material properties and hydrophone positions with respect to the flow were very similar in both configurations. By means of wavenumber–frequency analysis, the (flow-induced) spectral noise level is determined for towing speeds ranging from 4 to 12 kn. The noise level at the embedded hydrophones is systematically higher for all speeds than that at the separated hydrophones.

Keywords Flow-induced noise · Turbulent boundary layer · Underwater experiment · Towed body

1 Introduction

Noise induced in the interior of a (moving) mechanical structure or vehicle by an outer turbulent boundary layer [1, 2] is of importance in many applications [3], with cabin noise of cars and aircrafts being prominent examples (see, e.g., [4, 5]). In underwater acoustics, the significance of flow-induced interior noise arises from its role as an interference source of a hydroacoustic antenna. In case the antenna is in motion, either towed behind or attached to a moving platform, a turbulent boundary layer forms at the outside of the hull and induces hydroacoustic noise in the interior of the antenna [6–10]. This contributes to the so-called *sonar self-noise* and can significantly limit the performance of a sonar system [11].

J. Abshagen (✉) · D. Küter · V. Nejedl
Bundeswehr Technical Center for Ships and Naval Weapons, Maritime Technology and Research (WTD 71), 24340 Eckernförde, Germany
e-mail: JanAbshagen@bundeswehr.org

E. Ciappi et al. (eds.), *Flinovia—Flow Induced Noise and Vibration Issues and Aspects-II*,
https://doi.org/10.1007/978-3-319-76780-2_20

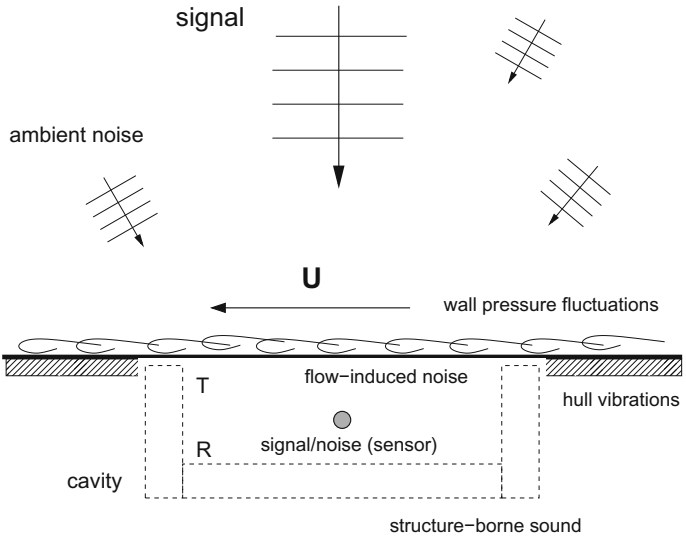

Fig. 1 Generic setup of a hydroacoustic sensor inside a (moving) cavity: Hull structure (with transmission coefficient T) and cavity (with reflection coefficient R) are designed to enhance signal detection, but also to shield the sensor from flow-induced noise and structure-borne sound, respectively

A generic setup of a hydroacoustic antenna integrated into a platform for underwater applications (moving with speed U) is depicted in Fig. 1. Here, the hydroacoustic sensor is embedded in a cavity that shields, on the one hand, the sensor from structure-borne sound in the interior of the platform. On the other hand, the elastic wall structure of the hull, that forms the outer boundary of the cavity, is excited by wall pressure fluctuations beneath an outer boundary layer flow (or in principle interacts with the boundary layer). The excited hull vibrations induce hydroacoustic (near-field) noise in the quiescent fluid on the reverse side of the hull, i.e., in the interior of the cavity.

Since hydroacoustic antennas aim to detect signals in the sea, the role of flow-induced noise components in sonar self-noise is in general evaluated from the perspective of signal processing, in particular with respect to the signal-to-noise ratio, instead of the noise level alone. Therefore, the use of hull materials with preferable hydroacoustical properties is a constraint to any method that aim to reduce (flow-induced) self-noise. Ambient noise has also some influence on the signal-to-noise ratio, but it is not considered as a part of sonar self-noise, because its level is not related to the antenna design [12].

Though challenging due to the very high Reynolds numbers involved in realistic underwater applications, basic mechanisms of flow noise generation are in principle amenable to numerical simulations as well as to laboratory and channel experiments [3, 6, 13–16]. For underwater applications, however, it is also necessary to understand

and evaluate the relevance of the basic mechanisms of turbulent flow noise generation under the particular acoustical and environmental conditions present at sea.

Turbulent flow noise generation has been studied previously for two different flat plate configurations with a towed body in underwater experiments. In the first configuration, the hydrophones were embedded into the mechanical hull structure [17], while in the second they were separated by a thin layer of water from the (sandwich) plate in another configuration [10]. In this work, a comparison of the vibroacoustic response of these two configurations to turbulent boundary layer excitation with respect to flow-induced interior noise is performed.

2 Underwater Experiment

The underwater experiment reported in this work has been conducted with a towed body measurement system during a research cruise with RV Elisabeth Mann Borgese (IOW, Germany) in Sognefjord, Norway, in 2014 (see Refs. [10, 17] for more details).

2.1 Towed Body Measurement System

The towed body measurement system has been developed by ATLAS Elektronik (Bremen, Germany) in collaboration with FWG (Bundeswehr Research Institute for Underwater Acoustics and Marine Geophysics, integrated into WTD 71 in 2009) for the investigation of turbulent flow noise generation under sea conditions. Two pictures of the so-called Flow Noise Analysis and Measurement Equipment (FLAME) towed body with flat plate configurations laterally attached to each side are depicted in Fig. 2. Length, width, and height of the towed body are 5.26 m, 1.353 m (0.935 m without fins), and 1.715 m, respectively. The weight in air is about 2800 kg, the total mass in water about 3500 kg, and the net buoyancy about 3000 N.

On the starboard side of the towed body depicted in Fig. 2a, a sandwich plate configuration is mounted laterally. The plate (brown rectangle) has a size of 2000 mm $\times$ 770 mm in length and width, respectively, and is in principle replaceable by other plates. The measurement of flow-induced noise is performed in the rear area of the plate (inner white rectangle) in order to ensure a sufficiently long entrance length for the boundary layer flow. On the port side of the towed body shown in Fig. 2b, a flat plate configuration (gray rectangle) is laterally mounted where the hydrophones are embedded into the mechanical structure of the hull.

Fig. 2 Flow Noise Analysis and Measurement Equipment (FLAME) towed body with two different flat plate configurations: sandwich plate (brown rectangle) with measurement area (inner white rectangle) on starboard side (**a**) and flat plate area (gray rectangle) with embedded hydrophone array on port side (**b**) of the towed body

2.2 Measurement Setup

The setup for (flow-induced) noise measurements beneath the sandwich plate is depicted in Fig. 3a. Outside of the measurement area, the plate configuration consists of steel plate of 3 mm thickness supported by a 10 mm layer of damping material attached to the inside. The steel plate is covered by a 2 mm layer made of fiber-reinforced plastic over the entire plate area. This layer covers in particular also a rectangular recess of 575 mm $\times$ 300 mm in length and width, respectively, within the steel plate, which forms the measurement area. The thin FRP layer is surfaced with a 13 mm layer of (hard) foam at the outside and of polyurethane (PU) at the inside of the measurement area. The polyurethane layer appears as a white rectangle inside of the brown foam layer and marks the measurement area in Fig. 2a.

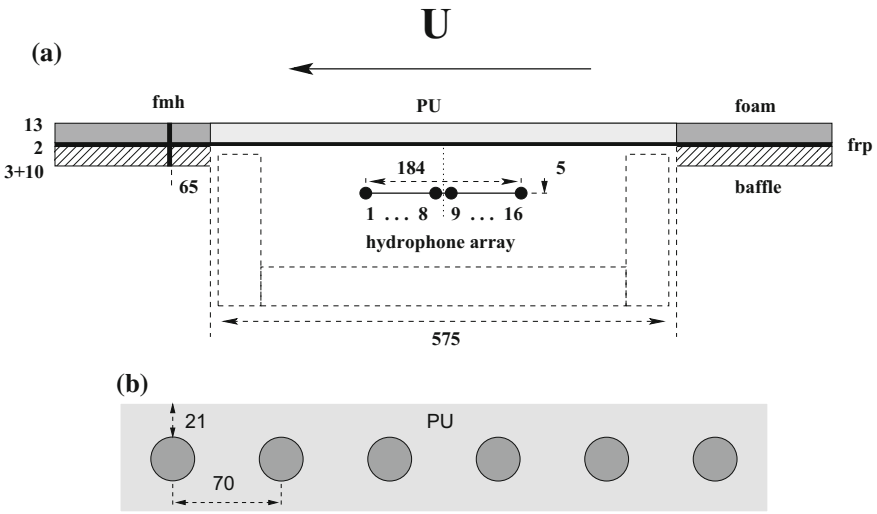

Fig. 3 Measurement setup of sandwich plate configuration (**a**) and principle setup of (part of) embedded hydrophone configuration (**b**)

Wall pressure fluctuations are measured with a flush-mounted hydrophone of type Reson TC4050 located 65 mm downstream of the measurement area on the centerline of the plate. Flow-induced noise is measured with a line array of 16 Reson TC4013 hydrophones having an equidistant spacing of $d_s = 11.5$ mm. The array is aligned along the centerline and mounted inside of a cavity at a distance of 5 mm beneath the plate. The cavity shields the hydrophones from (interior) structure-borne sound and ambient noise. The total distance between flow and hydrophones is 20 mm.

In Fig. 3b, a part of the second measurement configuration showing six hydrophones embedded into a flat plate made of polyurethane is depicted. The line array consists altogether of 30 hydrophones that are equally spaced in streamwise direction with a spacing of $d_e = 70$ mm. The array has a total acoustic length of 2100 mm. The hydrophones are located 21 mm beneath the flow and therefore at a very similar distance from the flow as beneath the sandwich plate.

2.3 Towing Experiments

During a measurement run, the towed body went on a straight track without any machinery active and flow-induced interior noise (as well as wall pressure fluctuations on starboard side) was measured simultaneously for both configurations. The sampling frequency was $f_s = 31{,}250$ Hz, and the measurement time for each run was T ≈ 300 s. Power spectral densities are calculated from an average of 300 non-overlapping short-time spectra (with $T_s = 1.0485$ s) with a bandwidth of $\Delta f = 1/T =$

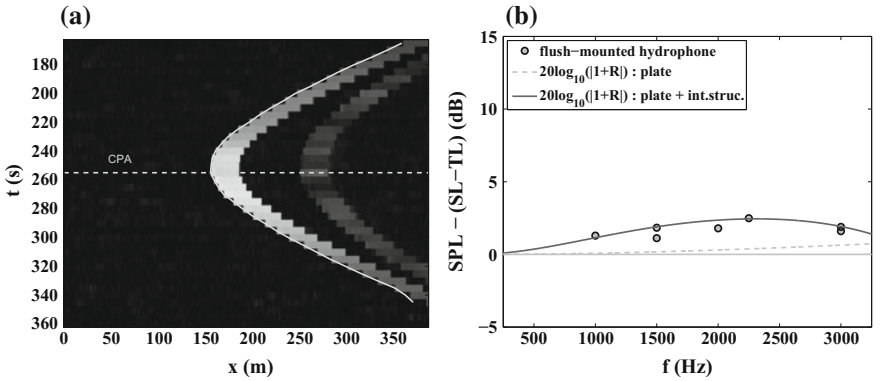

Fig. 4 Space-time diagram showing (the amplitude of) continuous-wave pulses that are repeatedly emitted from a freely drifting projector buoy (at $x = 0$ m) while the towed body is passing the buoy on a straight track (**a**). Difference of sound pressure level (SPL) measured with the flush-mounted hydrophone and the projector source level (SL) at the position of the hydrophone, i.e., corrected by the transmission loss (TL). The departure from zero is due to reflections at internal mechanical structures of the towed body (**b**)

0.9537 Hz. The effective noise bandwidth amounts $\Delta f_e = 1.36\ \Delta f$ because of Hamming windowing that is applied to the each (short) time series. The towing depth during each measurement run was in the range of 90 to 150 m depth. This towing corridor was well below the local thermocline in Sognefjord during the period of the research cruise. The length of the towing cable varied between 400 and 600 m in order to ensure a sufficient towing depth and a sufficiently large distance from the towing vessel in order to minimize interfering noise. Measurements were conducted for the towing speeds U = 4.7, 6.1, 8.1, 9.9, and 12.0 kn. These speeds correspond to outer flow velocities $U_\infty = 2.6$, 3.4, 4.6, 5.6, and 6.8 ms^{-1} of the boundary layer flows (see Ref. [10] for calculation method).

In addition to noise measurements, a sensor calibration has been performed at sea. During a calibration run, a freely drifting buoy system with a projector located at 90 m depth emitted repeatably every 5 s a continuous-wave pulse of 20 ms length. The projector source level was 180 dB$_{re1\mu Pa,1m}$. The towed body passed the buoy on a straight track at the same depth as the projector and a distance of about 150 m at the closest point of approach (CPA). The CPA denotes the point on the track line where the horizontal distance between towed body and projector has a minimum value. In a space-time plot shown in Fig. 4a, the distance between projector and towed body is depicted for each GPS-triggered pulse. Here, the position $x = 0$ m corresponds to the position of the projector. For reasons of clarity only the amplitude of the 3 kHz pulses is depicted in Fig. 4a, which is calculated from Hilbert transform. A second (weaker) pulse traveling a larger distance between projector and towed body than the direct pulse can also be seen in the figure. These pulses originate from a reflection at the sea surface.

The difference between the sound pressure level (SPL) measured at the flush-mounted hydrophone and the projector source level (SL) at the position of the hydrophone, i.e., corrected by the transmission loss (TL), is depicted in Fig. 4b in the frequency range from 1 to 3 kHz. The departure from zero is not only due to the reflection behavior R of the plate where the hydrophone is mounted to, but also due to the internal mechanical structure of the towed body. Calibration of the other sensors can be done in a similar manner.

2.4 Low-Frequency Noise

External underwater noise that originates, e.g., from the towing vessel can interfere with a measurement of flow-induced noise. The spatial coherence along the embedded hydrophone array is represented in Fig. 5a for a measurement run at $U_\infty = 5.6$ ms^{-1}. The coherence is calculated with respect to the most rearmost hydrophone at $x = 0$ m. Several peaks with large spatial coherence length occur up to a frequency of 180 Hz. These peaks are related to external sound sources that originate (most likely) from the towing vessel. In this frequency regime, the spatial coherence length of underwater noise is large compared to the size of the array. The coherence of the turbulent boundary layer flow has, compared with this, already disappeared almost entirely at the hydrophone after the next, i.e., at $x = 140$ mm. Note that a sufficient distance to other ships was ensured during each measurement run by visible inspection and AIS monitoring of the measurement area.

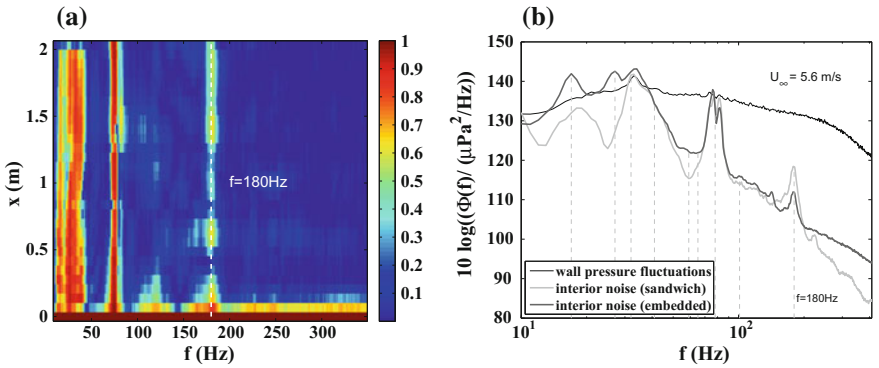

Fig. 5 Spatial coherence along the (embedded) hydrophone array with respect to the rearmost hydrophone at $x = 0$ m (**a**) and power spectral densities of flow-induced interior noise at the embedded array as well as beneath the sandwich configuration. The power spectral density of wall pressure fluctuations (on starboard side) is plotted for comparison. The vertical (dashed) lines correspond to frequency peaks from external sound sources. The towing speed was $U = 9.9$ kn and the outer flow velocity $U_\infty = 5.6$ ms^{-1}

The power spectral densities of interior noise averaged over each array as well as the (Corcos corrected) power spectral density of wall pressure fluctuations [10, 18, 19] measured on the starboard side of the towed body are plotted in Fig. 5b. It can be seen that below 200 Hz the spectra of interior noise are contaminated with frequency peaks (marked by vertical dashed lines). These peaks have been identified as external underwater noise, among others, by coherence analysis. Furthermore, the peak level in the interior is, e.g., at about 30 Hz equal to that of wall pressure fluctuations due to the (almost complete) acoustic transparency of the sandwich plate to low-frequency sound.

Wall pressure was not measured on port side, but because of the (approximate) symmetry of the towed body, a very similar turbulent boundary layer forcing can be assumed on both sides. The vibroacoustic response of the two flat plate configurations to turbulent boundary layer excitations is investigated in the following for frequencies above 200 Hz.

3 Wavenumber–Frequency Analysis

An analysis of a wavenumber–frequency spectrum allows in principle to identify physical processes that underly the (averaged) power spectral densities and in particular to separate individual spectral contributions. Every point in a spectrum at an angular frequency ω and wavenumber k represents the power of a plane wave that travels with wave speed $c = \omega/k$ (or $c = f/\tilde{k}$ with $k = 2\pi\tilde{k}$ and $\omega = 2\pi f$) along the array.[1] Dispersion relations of wave or wave-like processes can therefore be identified by characteristic signatures in a wavenumber–frequency spectrum. Sound waves, e.g., are non-dispersive in sea water, and their dispersion relation is $\omega(k) = c_w \cdot k$ with sound speed c_w. In a wavenumber–frequency spectrum calculated from the array data (with wavenumber k given in m^{-1} and frequency f given in Hz), the dispersion relation manifests in two straight lines for sound waves traveling either upstream or downstream according to the relation $k_w(f) = \pm f/c_w$.

3.1 Sandwich Configuration

In Fig. 6, a wavenumber–frequency spectrum of noise beneath the sandwich plate for an outer flow velocity of 5.6 ms^{-1} together with the relation $k_w(f)$ for sound waves with a sound speed c = 1484 ms^{-1} is shown. The lines for positive and negative wavenumbers correspond to sound wave traveling along the array in upstream and downstream directions, respectively. Sound waves with oblique incidence appear in

[1] In hydroacoustics, the notation k is often used for both a wavenumber given in ($2\pi m^{-1}$) and in (m^{-1}). Since the former is used in relation to the angular frequency ω while the latter in relation to the frequency f, we will adopt the common notation and also write k instead of $\tilde{k}$ in the following.

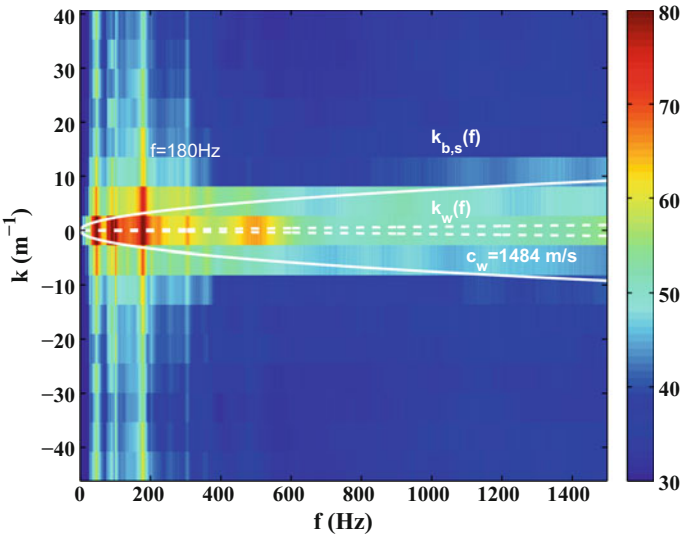

Fig. 6 Wavenumber–frequency spectrum of noise beneath the sandwich plate for an outer flow velocity of U = 5.6 ms^{-1}. The relation $k_w(f)$ of underwater sound with speed $c_w = 1484$ ms^{-1} and that of bending waves $k_{b,s}(f)$ is depicted. The spectrum is high-pass filtered for reasons of visibility

the spectrum with a projected wave speed, that is larger than the speed of sound. Spectral contributions from sound waves are therefore confined at each frequency to wavenumbers lower in magnitude than that given by the dispersion relation. Spectral contributions to wavenumbers larger in magnitude can be attributed to physical processes different from underwater sound.

The relation $k_{b,s}(f)$ for bending waves of a plate is also depicted in Fig. 6 in addition to that of underwater sound. As for sound wave, this relation results from the dispersion relation and corresponds to bending waves traveling upstream or downstream along the array. Bending waves traveling in oblique directions contribute to wavenumbers lower in magnitude, and spectral contributions to wavenumbers larger in magnitude are, as for sound waves, not related to bending waves. The dispersion relation for bending waves of a plate reads

$$\omega(k) = (D/m_s)^{1/2} \cdot k^2 \tag{1}$$

with flexural rigidity D and mass (per unit area) $m_s = \rho h$. Here, ρ and h denote plate density and thickness, respectively. The dispersion relation yields wavenumbers for bending waves traveling in upstream or downstream direction according to the relation

$$k_{b,s}(f) = \pm \frac{\sqrt{2\pi f_{water}}}{2\pi (D/m_s)^{1/4}}. \tag{2}$$

Generic values of D and ρ are chosen to fit both the experimentally observed relation $k_{b,s}(f)$ as well as typical material parameters. Exact values are not available for both configurations. In Fig. 6, this relation is plotted with generic values $m_s = 20$ kg/m^2 and $D_s = 10^3$ Nm for the sandwich plate. The decrease in oscillation frequency for each wavenumber due to fluid loading is taken into account by a generic factor of $f/f_{water} = 2.5$ (see, e.g., [20]), because numerical values for each wavenumber were not available for both configurations. The speed of the bending wave $c_{b,s}$ traveling in upstream or downstream direction can be derived from this relation for each frequency.

3.2 Embedded Hydrophone Configuration

In Fig. 7, the corresponding wavenumber–frequency spectrum of noise measured with the embedded hydrophones is depicted. Generic values chosen to fit the experimentally observed relation $k_{b,e}(f)$ of bending waves for the embedded hydrophone configuration are $m_e = 90$ kg/m^2 and $D_e = 75 \times 10^3$ Nm. The speed of the bending waves $c_{b,e}$ is significantly larger than that of the corresponding sandwich plate $c_{b,s}$ for each frequency. It should be stressed that the two arrays have different wavenumber resolution and Nyquist wavenumbers. Additionally, a weak signature of the convective ridge originating from turbulent wall pressure fluctuations can be seen in the low-frequency regime of the spectrum. For reasons of visibility, both wavenumber–frequency spectra are high-pass filtered with a slope of 35 dB/decade asymptotically below 2 kHz.

4 Flow-Induced Noise

From the wavenumber–frequency spectra depicted in Figs. 6 and 7, it becomes apparent that above 200 Hz noise induced from excited plate vibrations is dominant in the wavenumber regime $|k_w| < |k| \leq |k_{e,s}|$. In the acoustic regime $|k| \leq |k_w|$, on the other hand, different spectral contributions, e.g., from ambient noise or from flow-induced noise, cannot clearly be separated from each other in the wavenumber–frequency spectrum.

4.1 Power Spectral Density of Excited Plate Modes

In order to estimate the power spectral densities $\Phi_{pl,(e,s)}(f)$, which represent the noise components that originate from excited plate vibrations, the averages $\langle \Phi_{pl,(e,s)}(f,k) \rangle_{K_f}$ over the wavenumber regime $K_f = \{k : |k_w(f)| < |k| \leq |k_{e,s}(f)|\}$ are calculated for each frequency from the wavenumber–frequency spectra.

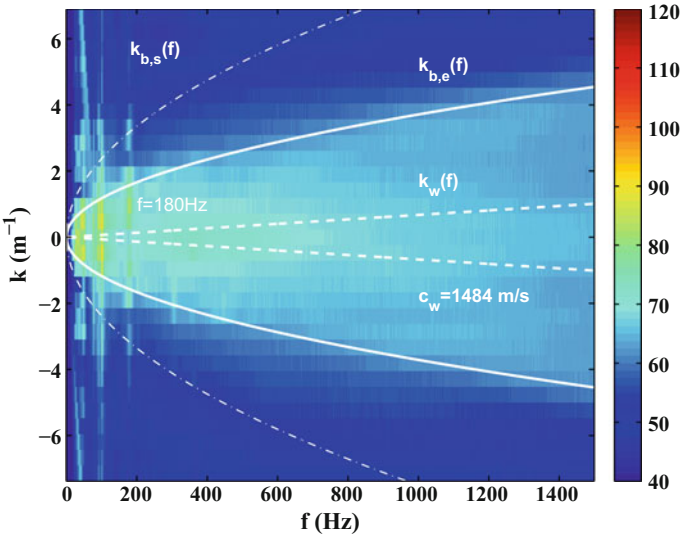

Fig. 7 Wavenumber–frequency spectrum of noise at the embedded hydrophones for the same outer flow velocity than in Fig. 6. For comparison, the relation $k_w(f)$ of underwater sound with speed $c_w = 1484\ \mathrm{ms}^{-1}$ and that of bending waves $k_{b,s}(f)$ and $k_{b,e}(f)$ is depicted. Note the difference in color scale in comparison to Fig. 6

It is assumed that these averages provide reasonable estimates for the flow-induced noise levels also inside the acoustic regime of each configuration. These are not amenable to measurements. Under this assumption, the power spectral densities $\Phi_{pl,(e,s)}(f)$ are calculated from

$$\Phi_{pl,(e,s)}(f) = 2 \cdot |k_{e,s}(f)| \cdot \langle \Phi_{pl,(e,s)}(f,k) \rangle_{K_f}. \tag{3}$$

These spectral densities of the embedded hydrophone configuration (a) as well as of the sandwich configuration (b) are depicted in Fig. 8 for five different towing speeds. A spectral decay according to an f^{-4} law is plotted for comparison. A qualitatively similar behavior can be seen for both configurations with respect to their spectral decay toward higher frequencies and with respect to the increases of spectral power with towing speed for each frequency.

The level of flow-induced noise approaches the noise floor of the measurement system that is used for the sandwich configuration (dashed line in Fig. 8b) at low towing speeds and high frequencies. Spectral levels below a threshold of 60 dB are not considered in the following, because the departure from an unperturbed spectral decay (for a theoretical f^{-4} decay law) exceeds 0.5 dB due to the noise floor.

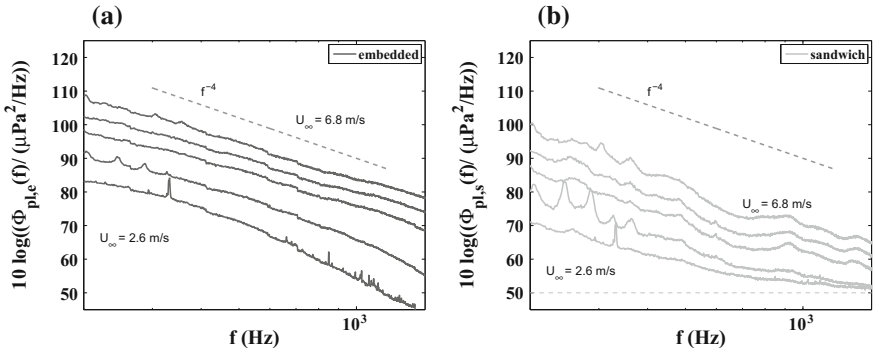

Fig. 8 Estimated power spectral density $\Phi_{pl,(e,s)}(f)$ of interior noise that originates from excited plate modes at the embedded hydrophones (**a**) and beneath the sandwich plate (**b**) for different towing speeds. The electronic noise floor of the sensor system of the sandwich plate configuration is indicated (dashed horizontal line) in (**b**)

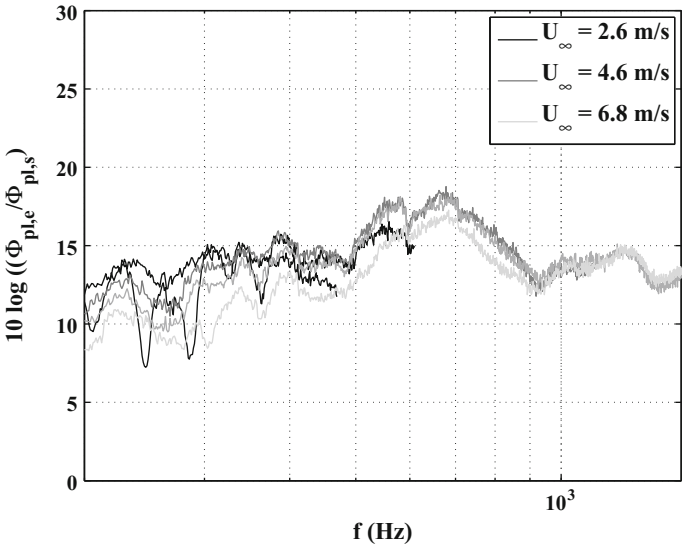

Fig. 9 Differences in spectral level at the embedded hydrophones and beneath the sandwich configuration for different towing speeds

4.2 Comparison of Flow-Induced Spectral Level

The difference in spectral level of flow-induced noise at the embedded hydrophones and that at the hydrophones beneath the sandwich plate is plotted for each towing speed in Fig. 9. It can be seen that the interior noise level induced by excited plate vibrations is substantially higher at the embedded hydrophones than beneath

the sandwich plate. The difference amounts from about 10 dB to more than 15 dB. Moreover this difference is (almost) independent from the towing speed in the frequency regime depicted in Fig. 9.

5 Conclusion

Results from an underwater experiment on interior noise coming from plate vibrations that are excited by an outer turbulent boundary layer are presented. Measurements of flow-induced noise under sea conditions were performed with a towed body measurement system in Sognefjord, Norway. Two different plate configurations were considered: one with the hydrophones embedded into a plate, while in the other configuration the hydrophones were positioned beneath the plate. By means of wavenumber–frequency analysis, the spectral contribution from excited plate vibrations has been identified and separated from interference sound sources. It is found that the flow-induced noise level at hydrophones being embedded into the mechanical hull structure of a plate can exceed the noise level at a hydrophone separated by an additional layer of water systematically by more than 10 dB. This result is (almost) independent from the towing speed. Since the excitation from the turbulent boundary layer flow can be considered as very similar due to the symmetry of the towed body, this difference in vibroacoustic response can be attributed to the mechanical properties of the plate configurations.

Acknowledgements The excellent support from the engineering branch of WTD 71, from ATLAS Elektronik, and from Captain and Crew of RV Elisabeth Mann Borgese (IOW, Germany) is gratefully acknowledged.

References

1. Schlichting, H.: Grenzschicht-Theorie (Engl.: Boundary Layer Theory). G. Braun, Karlsruhe (1965)
2. Farabee, T.M., Casarella, M.J.: Spectral features of wall pressure fluctuations beneath turbulent boundary layers. Phys. Fluids A **10**, 2410–2420 (1991)
3. Ciappi, E., De Rosa, S., Franco, F., Guyader, J.L., Hambric, S.A. (eds.): Flinovia—Flow Induced Noise and Vibration Issues and Aspects. Springer, Cham (2015)
4. Müller, S., Becker, S., Gabriel, Ch., Lerch, R., Ulrich, F.: Flow-induced input of sound to the interior of a simplified car model depending on various setup parameters. In: 19th AIAA/CEAS Conference (2013). https://doi.org/10.2514/6.2013-2019
5. Hu, N., Buchholz, H., Herr, M., Spehr, C., Haxter, S.: Contribution of different aeroacoustic sources to aircraft cabin noise. In: 19th AIAA/CEAS Conference (2013). https://doi.org/10.2514/6.2013-2030
6. Blake, W.K.: Mechanics of Flow-Induced Sound and Vibration, vols. 1, 2. Academic Press, New York (1986)
7. Dowling, A.P.: Underwater flow noise. Theoret. Comput. Fluid Dyn. **10**, 135–153 (1998)

8. Keith, W.L., Cipolla, K.M., Furey, D.: Turbulent wall pressure fluctuation measurements on a towed model at high Reynolds numbers. Exp. Fluids **46**, 181–189 (2009)
9. Elboth, T., Reif, B.A., Andreassen, Ø., Martell, M.B.: Flow noise reduction from superhydrophobic surfaces. Geophysics **77**, P1–P10 (2012)
10. Abshagen, J., Küter, D., Nejedl, V.: Flow-induced interior noise from a turbulent boundary layer of a towed body. Adv. Aircr. Spacecr. Sci. **3**(3), 259–269 (2016)
11. Urick, R.: Principles of Underwater Sound, 2nd edn. McGraw-Hill, New York (1975)
12. Carey, W.M., Evans, R.B.: Ocean Ambient Noise: Measurement and Theory. Springer, New York (2011)
13. Hambric, S.A., Hwang, Y.F., Bonness, W.K.: Vibration of plates with clamped and free edges excited by low-speed turbulent boundary layer. J. Fluids Struct. **19**, 93–110 (2004)
14. De Rosa, S., Franco, F.: Exact and numerical response of a plate under turbulent boundary layer excitation. J. Fluids Struct. **24**, 212–230 (2008)
15. Ciappi, E., Magionesi, F., De Rosa, S., Franco, F.: Analysis of the scaling laws for the turbulence driven panel responses. J. Fluids Struct. **32**, 90–103 (2013)
16. Abshagen, J., Schäfer, I., Will, Ch., Pfister, G.: Coherent flow noise beneath a flat plate in a water tunnel experiment. J. Sound Vib. **340**, 211–220 (2015)
17. Abshagen, J., Nejedl, V.: Towed body measurements of flow noise from a turbulent boundary layer under sea conditions. J. Acoust. Soc. Am. **135**(2), 637–645 (2014)
18. Corcos, G.M.: Resolution of pressure in turbulence. J. Acoust. Soc. Am. **35**, 192–199 (1963)
19. Lueptow, R.M.: Transducer resolution and the turbulent wall pressure spectrum. J. Acoust. Soc. Am. **97**, 370–378 (1995)
20. Kerboua, Y., Lakis, A.A., Thomas, M., Marcouiller, L.: Vibration analysis of rectangular plates coupled with fluids. Appl. Math. Modell. **32**, 2570–2586 (2008)

Measurement Techniques of the Sensitivity Functions to Characterize the Vibration Response of Panels Under Turbulent Boundary Layer Excitation

Christophe Marchetto, Laurent Maxit, Olivier Robin and Alain Berry

Abstract This study aims at developing an experimental method for characterizing the vibro-acoustic behavior of panels excited by random pressure fields. Although the method would be theoretically applicable to any stationary in time and spatially homogeneous random process, and for points belonging to the acoustic medium or to the panel, the turbulent boundary layer excitation is considered in this study while considering the vibration response exclusively. The interest of industrials toward this excitation has grown over the years. The main reasons being that the associated test means (i.e., wind tunnel or *in situ* measurements) are hard to control and very expensive. They are also subjected to large variabilities between laboratories, which makes it hard to attest the validity of the measuring technique. The proposed method allows to experimentally characterize a panel under such an excitation by separating the contribution of the excitation from the vibration behavior of the panel.

Keywords Panel vibration · Turbulent boundary layer · Sensitivity functions Reciprocity principles

C. Marchetto (✉) · L. Maxit
Laboratoire Vibrations Acoustique, INSA-Lyon, University of Lyon,
69621 Villeurbanne, France
e-mail: christophe.marchetto@usherbrooke.ca

L. Maxit ·
e-mail: laurent.maxit@insa-lyon.fr

C. Marchetto · O. Robin · A. Berry
Groupe d'Acoustique de l'Université de Sherbrooke, Université de Sherbrooke,
Sherbrooke J1K 2R1, Canada

O. Robin
e-mail: olivier.robin@usherbrooke.ca

A. Berry
e-mail: alain.berry@usherbrooke.ca

E. Ciappi et al. (eds.), *Flinovia—Flow Induced Noise and Vibration Issues and Aspects-II*,
https://doi.org/10.1007/978-3-319-76780-2_21

1 Introduction

The experimental vibration characterization of panels under a turbulent boundary layer (TBL) excitation is of great interest for the transport industry. The usual associated test means (wind tunnel or *in situ* measurements) are hard to control, very costly, and subjected to variabilities between laboratories and/or measuring techniques. A considerable work has been conducted to experimentally characterize the vibration behavior of panels under TBL excitations without the use of those usual test means. Most of the recently developed methods consist in synthesizing the pressure field induced by a TBL using an array of acoustic sources [1–6]. The common issues of those methods are: the number of sources required to reproduce small correlation lengths, which becomes prohibitive at high frequency, and/or the inability to accurately reproduce the induced pressure field outside the acoustic wavenumber domain, which is the predominant domain for subsonic TBL.

In this context, the aim of this study is to investigate an alternative and robust approach to experimentally characterize the response of panels to a TBL excitation by separating the contributions of the forcing excitation and those of the dynamic behavior of the panel. Indeed, the mathematical formulation of a panel vibration response when submitted to random excitations in the wavenumber domain allows estimating the system response at any point on the structure from wall-pressure cross-spectral density (CSD) functions (characterizing the excitation) and from so-called sensitivity functions. The latter are defined as the panel response to wall-pressure acoustic plane waves and characterize the panel vibration behavior. The estimation of the panel response to a TBL excitation therefore only requires the experimental measurement of sensitivity functions in the acoustic wavenumber domain and an estimation of the wall-pressure CSD functions of the considered excitation.

A method is proposed for estimating the sensitivity functions experimentally. Whereas the direct interpretation of the sensitivity functions would require exciting the panel by sets of wall plane waves, which is not easy from an experimental point of view, an alternative method based on the reciprocity principle is proposed. The reciprocity principle states that the sensitivity functions at any point on the structure are equivalent to the panel velocity response expressed in the wavenumber domain when the system is excited by a normal force at the same point. The proposed experimental process consists in exciting the panel with a normal force at the point where the panel response is to be determined. The spatial vibratory response of the panel is then measured with a scanning laser vibrometer. In a subsequent post-processing phase, a discrete 2-D wavenumber transform of the measured vibratory field is performed to deduce the sensitivity functions. Finally, using measured wall-pressure fluctuations and the previously estimated sensitivity functions, the response of the panel when excited by a TBL can be deduced at the point of interest.

The paper is organized as follows: The mathematical formulation of the vibro-acoustic problem is presented in Sect. 2.1 where the sensitivity functions involved in the problem are defined. An alternative interpretation of these functions based on the reciprocity principle is proposed in Sect. 2.2. This interpretation suggests a simple

implementation for measuring the sensitivity functions. The proposed methodology for characterizing the panel response under a turbulent boundary layer is summarized in Sect. 3. An experimental validation of the determination of the sensitivity functions is provided in Sect. 4. Finally, a comparison with measurements performed in an anechoic wind tunnel is shown in Sect. 5 along with an experimental characterization of the wall-pressure fluctuations induced by the reproduced TBL.

2 Vibration Behavior of Panels Under Turbulent Boundary Layer

Let us consider a baffled panel of surface Σ_p with arbitrary boundary conditions separating two semi-infinite acoustic domains. As shown in Fig. 1, one supposes that a fully developed TBL is exciting the panel on one side. The TBL is characterized by its flow velocity U_∞ outside the boundary layer and is considered stationary in time and spatially homogeneous. We also define two points on the panel surface ($z = 0$), $\mathbf{x} = (x, y)$ the observation point and $\tilde{\mathbf{x}} = (\tilde{x}, \tilde{y})$ the excitation point. Both points are defined in the Cartesian coordinate system (x, y, z) with the origin at the center of the panel shown in Fig. 1.

To experimentally characterize the vibration response of this panel, the one-sided normal velocity frequency response v at a given point on the panel is considered. As the excitation is random, the velocity response is derived from the auto spectral density (ASD) function of the normal velocity $G_{vv}(\mathbf{x}, f)$. An approach for evaluating this quantity based on deterministic transfer functions and using a reciprocity principle is presented in Sects. 2.1 and 2.2.

2.1 *Mathematical Formulation of the Vibration Response*

Let us consider the blocked wall-pressure field $p_b(\tilde{\mathbf{x}}, t)$ exerted on the panel by a TBL excitation at point $\tilde{\mathbf{x}}$ as a function of time. The vibration response of the panel

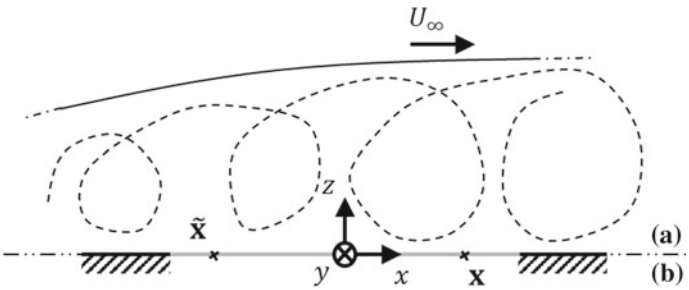

Fig. 1 Panel (gray line) and coordinate system. **a** Source side: TBL excitation. **b** Receiving side: semi-infinite domain

at point $\mathbf{x}$ when the panel is excited by $p_b(\tilde{\mathbf{x}}, t)$ is denoted $v(\mathbf{x}, t)$. This response can be expressed by the convolution product [7]

$$v(\mathbf{x}, t) = \iint_{\Sigma_p} \int_{-\infty}^{\infty} h_{v/F_n}(\mathbf{x}, \tilde{\mathbf{x}}, t - \tau)\, p_b(\tilde{\mathbf{x}}, \tau)\, d\tau d\tilde{\mathbf{x}}, \tag{1}$$

where $h_{v/F_n}(\mathbf{x}, \tilde{\mathbf{x}}, t)$ is the structural velocity impulse response at point $\mathbf{x}$ for a normal unit force applied at point $\tilde{\mathbf{x}}$. Assuming that the random process is ergodic, the cross-correlation function $R_{vv}(\mathbf{x}, t)$ is defined by

$$R_{vv}(\mathbf{x}, t) = \int_{-\infty}^{\infty} v(\mathbf{x}, \tau)\, v(\mathbf{x}, t + \tau)\, d\tau. \tag{2}$$

Introducing Eq. (1) in Eq. (2) and performing a time Fourier transform of the resulting expression of the cross-correlation function give the space-frequency spectrum $G_{vv}(\mathbf{x}, f)$, which after some manipulations (see [7] for details) can be written as

$$G_{vv}(\mathbf{x}, f) = \iint_{\Sigma_p} \iint_{\Sigma_p} H_{v/F_n}(\mathbf{x}, \tilde{\mathbf{x}}, f)\, H^*_{v/F_n}\left(\mathbf{x}, \tilde{\tilde{\mathbf{x}}}, f\right) G_{p_b p_b}\left(\tilde{\mathbf{x}}, \tilde{\tilde{\mathbf{x}}}, f\right) d\tilde{\mathbf{x}} d\tilde{\tilde{\mathbf{x}}}, \tag{3}$$

where $H_{v/F_n}(\mathbf{x}, \tilde{\mathbf{x}}, f)$ is the time Fourier transform of $h_{v/F_n}(\mathbf{x}, \tilde{\mathbf{x}}, t)$ and corresponds to the panel velocity frequency response function at point $\mathbf{x}$ when it is excited by a normal force F_n applied at point $\tilde{\mathbf{x}}$, and $G_{p_b p_b}(\tilde{\mathbf{x}}, \tilde{\tilde{\mathbf{x}}}, f)$ is the time Fourier transform of the cross-correlation function of the blocked wall-pressure. Defining the wavenumber-frequency spectrum of the wall-pressure $G_{p_b p_b}(\boldsymbol{k}, f)$ as the Fourier transform of the space-frequency spectrum $G_{p_b p_b}(\tilde{\mathbf{x}}, \tilde{\tilde{\mathbf{x}}}, f)$, the inverse of this transform can be written

$$G_{p_b p_b}\left(\tilde{\mathbf{x}}, \tilde{\tilde{\mathbf{x}}}, f\right) = \frac{1}{4\pi^2} \iint_{-\infty}^{\infty} G_{p_b p_b}(\boldsymbol{k}, f)\, e^{j\boldsymbol{k}\left(\tilde{\tilde{\mathbf{x}}} - \tilde{\mathbf{x}}\right)} d\boldsymbol{k}. \tag{4}$$

where $\boldsymbol{k} = (k_x, k_y)$ is the wavevector defined in the plane (x, y) and $d\boldsymbol{k}$ is the two-dimensional wavenumber element. By introducing Eq. (4) in Eq. (3) and rearranging the terms, we get

$$G_{vv}(\mathbf{x}, f) = \frac{1}{4\pi^2} \iint_{-\infty}^{\infty} |H_v(\mathbf{x}, \boldsymbol{k}, f)|^2 G_{p_b p_b}(\boldsymbol{k}, f)\, d\boldsymbol{k}. \tag{5}$$

In practice, this integral is approximated considering a set of wavevectors in an appropriately defined wavenumber domain $\Omega_{\boldsymbol{k}}$ and using the rectangular integration rule. Equation (5) shows that the panel has a filtering effect on the excitation [7], which somehow limits the wavenumber domain $\Omega_{\boldsymbol{k}}$ while ensuring a correct estimation of the integral (see Sect. 4.1). The one-sided frequency ASD function of the velocity at point $\mathbf{x}$ is thereby estimated with

$$G_{vv}(\mathbf{x}, f) \approx \frac{1}{4\pi^2} \sum_{\boldsymbol{k} \in \Omega_{\boldsymbol{k}}} |H_v(\mathbf{x}, \boldsymbol{k}, f)|^2 G_{p_b p_b}(\boldsymbol{k}, f)\, \delta \boldsymbol{k}, \tag{6}$$

where $\delta \boldsymbol{k}$ represents the wavenumber resolution and $G_{p_b p_b}(\boldsymbol{k}, f)$ is the one-sided frequency CSD function of the blocked wall-pressure.

The $H_v(\mathbf{x}, \boldsymbol{k}, f)$ functions are called the sensitivity functions [8] and characterize the vibration behavior of the panel. They are defined by

$$H_v(\mathbf{x}, \boldsymbol{k}, f) = \iint_{\Sigma_p} H_{v/F_n}(\mathbf{x}, \tilde{\mathbf{x}}, f)\, e^{-j\boldsymbol{k}\tilde{\mathbf{x}}}\, d\tilde{\mathbf{x}}, \tag{7}$$

where $H_{v/F_n}(\mathbf{x}, \tilde{\mathbf{x}}, f)$ is the time Fourier transform of $h_{v/F_n}(\mathbf{x}, \tilde{\mathbf{x}}, t)$ and, therefore, corresponds to the transfer function between the panel velocity and the applied force in the frequency domain. The sensitivity functions can be interpreted directly from Eq. (7) as the velocity frequency response at point $\mathbf{x}$ when the panel is excited by a wall-pressure plane wave of wavevector $-\boldsymbol{k}$ (i.e., due to the pressure field $e^{-j\boldsymbol{k}\tilde{\mathbf{x}}}$). This direct interpretation is depicted in Fig. 2a.

The sensitivity functions must, therefore, be estimated only at the point of interest $\mathbf{x}$ and for the set of wavevectors in $\Omega_{\boldsymbol{k}}$. From an experimental point of view, wall-pressure plane waves cannot be easily reproduced, especially at high wavenumbers. To circumvent these issues, another interpretation of these sensitivity functions based on the reciprocity principle is given in Sect. 2.2.

2.2 Sensitivity Functions Based on the Reciprocity Principle

In order to propose another interpretation of the sensitivity functions, let us consider the standard reciprocity principle which states that the response of a system is invariant with respect to the exchange of points of excitation and observed response [9]. For the particular case of a normal force applied at point $\tilde{\mathbf{x}}$ and normal velocity observed at point $\mathbf{x}$, the reciprocity relationship can be translated following the previous notation into

$$H_{v/F_n}(\mathbf{x}, \tilde{\mathbf{x}}, f) = H_{v/F_n}(\tilde{\mathbf{x}}, \mathbf{x}, f), \tag{8}$$

Introducing Eq. (8) in Eq. (7), one obtains

$$H_v(\mathbf{x}, \boldsymbol{k}, f) = \iint_{\Sigma_p} H_{v/F_n}(\tilde{\mathbf{x}}, \mathbf{x}, f) e^{-j\boldsymbol{k}\tilde{\mathbf{x}}}\, d\tilde{\mathbf{x}}. \tag{9}$$

The right hand side of Eq. (9) can be interpreted as the space-wavenumber transform of $H_{v/F_n}(\tilde{\mathbf{x}}, \mathbf{x}, f)$ with respect to the spatial variable $\tilde{\mathbf{x}}$. The points $\tilde{\mathbf{x}}$ become

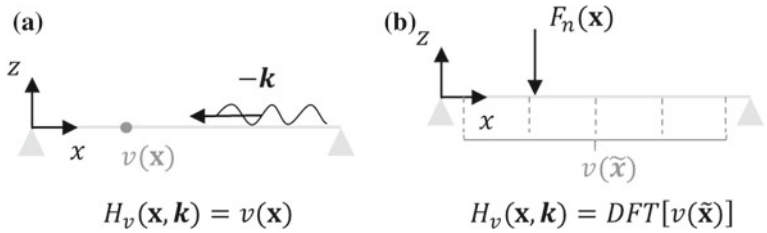

Fig. 2 Sensitivity functions H_v: **a** direct interpretation and **b** reciprocal interpretation

observation points on the panel surface Σ_p, which means that the space-wavenumber transform is performed over the vibration velocity field of the panel.

To sum up, the sensitivity function $H_v(\mathbf{x}, \boldsymbol{k}, f)$ may be obtained by exciting the panel with a normal effort F_n of unit amplitude at point $\mathbf{x}$ and by calculating the space-wavenumber transform of the panel velocity frequency response (as illustrated in Fig. 2b).

In practice, the vibratory field has to be measured on a regular grid of points denoted $\Gamma_{\tilde{\mathbf{x}}}$, using a scanning laser vibrometer, for example. The space-wavenumber transform is therefore approximated by a discrete Fourier transform (DFT). In order to avoid aliasing effects, the spatial resolution $\delta\tilde{\mathbf{x}}$ over $\Gamma_{\tilde{\mathbf{x}}}$ should be determined so that the spatial variations of the vibratory field can be correctly represented by the grid of points. For a homogeneous isotropic thin panel, $\delta\tilde{\mathbf{x}}$ should be less than or equal to a quarter of the natural flexural wavelength of the panel λ_f at the highest frequency of interest. For a more complex panel, a preliminary study should be carried out to define this parameter (for instance, by using a numerical model of the panel or by using a trial and error procedure).

3 Description of the Proposed Methodology

A methodology for experimentally estimating the vibration response of a panel excited by a TBL is now presented. This methodology for evaluating the velocity ASD function G_{vv} at a given point $\mathbf{x}$ of the panel ($z = 0$) is based on Eq. (6) and the second interpretation of the sensitivity functions, as described in Sect. 2.2. It can be summarized as follows:

- Excite the panel with a normal mechanical force at point $\mathbf{x}$ (for instance by using a shaker) and measure the normal velocity response of the panel at points $\tilde{\mathbf{x}} \in \Gamma_{\tilde{\mathbf{x}}}$ to determine $H_{v/F_n}(\tilde{\mathbf{x}}, \mathbf{x}, f)$,
- Perform a DFT of the panel velocity response $H_{v/F_n}(\tilde{\mathbf{x}}, \mathbf{x}, f)$ (with respect to $\tilde{\mathbf{x}}$) to obtain the sensitivity functions $H_v(\mathbf{x}, \boldsymbol{k}, f)$ at point $\mathbf{x}$ for $\boldsymbol{k} \in \Omega_{\boldsymbol{k}}$,

- Use Eq. (6) and a model or measurement of the wall-pressure CSD function of the TBL excitation to estimate the velocity ASD function G_{vv} at point $\mathbf{x}$ (in the present paper, measured wall-pressure CSD functions are used to estimate the vibration response, and they are presented in Sect. 5.1).

4 Experimental Validation of the Proposed Approach

4.1 Test Case Description

For numerical and experimental validation purposes, a test case is considered, which consists in a rectangular thin aluminum plate, simply supported on its four edges and submitted to a TBL excitation on one side. The plate geometrical and mechanical properties are detailed in Table 1. A mean value of the structural loss factor $\eta = 0.005$ has been measured using the -3 dB bandwidth method and taken into account in the numerical simulations. Simply supported boundary conditions have been chosen because they lead to a simple analytical solution of the plate equation of motion. In addition, the experimental setup proposed by Robin et al. [10] for reproducing these boundary conditions has already been validated.

The considered excitation is a TBL-like excitation reproduced in a low-speed anechoic wind tunnel (Mach ≤ 0.12) at a flow velocity $U_\infty = 40\ \mathrm{m\,s^{-1}}$. The frequency range of interest is [170, 2000 Hz] with a frequency resolution of 0.625 Hz. This frequency range is well above the aerodynamic coincidence frequency f_c, given by

$$f_c = \frac{U_c^2}{2\pi}\sqrt{\frac{\rho h}{D}}, \tag{10}$$

where $D = \frac{Eh^3}{12(1-\nu^2)}$ is the flexural stiffness and $U_c = 0.75 \times U_\infty$ is the convection speed, assumed constant with the frequency. For the considered case, $f_c \approx 30$ Hz. It has been shown, through Eq. (5), that the plate filters out the TBL excitation above f_c. To explain this effect, the theoretical sensitivity functions have been plotted in Fig. 3a at point $\mathbf{x}_M$, for wavenumbers along k_x ($k_y = 0$) and as a function of the frequency.

Table 1 Properties of the simply supported aluminum plate

Parameter (symbol), unit	Value
Youngs modulus (E), GPa	68.9
Poisson's ratio (ν)	0.3
Mass density (ρ), kg/m^3	2740
Length (L_x), mm	480
Width (L_y), mm	420
Thickness (h), mm	3.17

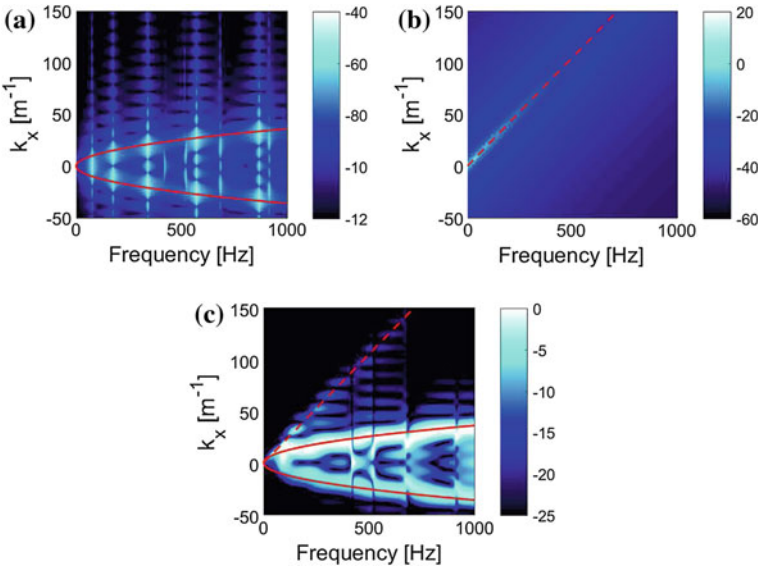

Fig. 3 Illustration of the filtering effect of the plate. **a** Theoretical sensitivity functions $H_v(\mathbf{x}_M, k_x, 0, f)$ (dB). **b** Corcos model $G_{p_b p_b}(k_x, 0, f)$ (dB), $U_\infty = 40$ m.s^{-1}. **c** Product $|H_v(\mathbf{x}_M, k_x, 0, f)|^2 \times G_{p_b p_b}(k_x, 0, f)$ (dB) normalized by the maximum at each frequency. Continuous red line: k_f. Dashed red line: k_c

The strongly decreasing magnitude of $H_v(\mathbf{x}_M, k_x, f)$ above the flexural wavenumber can be noticed. Similarly, the Corcos model for $G_{p_b p_b}$ in the wavenumber domain [11] (which seems to correctly represent the wall-pressure fluctuations measured in the wind tunnel, see Sect. 5.1) is plotted in Fig. 3b. Strong contributions around the convective wavenumber $k_c = \omega / U_c$ can be noticed. Figure 3c shows the product of the squared sensitivity functions and the wall-pressure CSD functions (which is involved in the calculation of the vibration response of the plate), normalized by the maximum value at each frequency. For this particular case, the excitation is not completely filtered out as significant contributions from the TBL (along k_c) can be noticed in Fig. 3c. It should be noted that in this paper, the excitation is a low-speed subsonic TBL. The higher the flow velocity, the lower the slope of the curve $k_c(f)$ and therefore the less the plate filtering effect is effective. It can be directly related to the fact that for a given plate with fixed parameters, f_c increases with the flow velocity.

For the considered test case and reproduced TBL, a preliminary study (not shown here) indicated that the convective peak was almost entirely filtered out on the whole considered frequency range, which means that the vibration response to the reproduced TBL is mainly driven by the region inside the circle of radius k_f. Although defining the limit of the wavenumber domain by the flexural wavenumber (at 2000 Hz, $k_f \approx 51$ m^{-1}) would probably lead to satisfying results, we have

voluntarily retained the worst case scenario and fixed the wavenumber domain $\Omega_{\boldsymbol{k}}$ over which the sensitivity functions should be determined as follows:

$$\begin{aligned} k_x^+ &\simeq 113 \text{ m}^{-1} \; ; \; k_x^- \simeq -66 \text{ m}^{-1} \\ k_y^+ &\simeq 66 \text{ m}^{-1} \; ; \; k_y^- \simeq -66 \text{ m}^{-1}. \end{aligned} \tag{11}$$

4.2 Determination of the Sensitivity Functions

In this section, we focus on the sensitivity functions H_v at point $\mathbf{x}_M$ of coordinates ($x = 0.18$ m, $y = 0.09$ m) on the plate. To apply the methodology described in Sect. 3, the panel velocity field has to be measured or calculated on a grid of points $\Gamma_{\tilde{\mathbf{x}}}$. In the following, a uniform mesh of 37×27 points is considered in directions x and y, respectively, and a gap of 10 mm along the edges is left for practical reasons. This leads to a spatial separation of $\delta_x \approx 12.8$ mm and $\delta_y = 15.4$ mm and ensures at least four points per flexural wavelength for all frequencies of interest. The highest wavenumbers k_x^{max} and k_y^{max} that can be resolved in directions x and y, respectively, are given by

$$k_x^{max} = \frac{\pi}{\delta_x} \simeq 246 \text{ m}^{-1} \; ; \; k_y^{max} = \frac{\pi}{\delta_y} \simeq 204 \text{ m}^{-1}. \tag{12}$$

These wavenumbers are well above twice the maximum wavenumbers k_x^+ and k_y^+. As a consequence, the considered grid of points provides correct estimation of the sensitivity functions in the considered wavenumber domain $\Omega_{\boldsymbol{k}}$. The wavenumber resolutions δk_x and δk_y in directions x and y, respectively, are given by

$$\delta k_x = \frac{2\pi}{L_x} \simeq 13 \text{ m}^{-1} \; ; \; \delta k_y = \frac{2\pi}{L_y} \simeq 15 \text{ m}^{-1}. \tag{13}$$

These wavenumber resolutions are relatively large because of the small dimensions of the panel. In order to improve the wavenumber resolution, zero-padding is used to obtain a uniform wavenumber resolution of 1 m^{-1} along k_x and k_y.

In order to assess the accuracy of the reciprocity approach for evaluating the panel sensitivity functions, experimental results obtained with this approach are compared with numerical results obtained by considering the direct interpretation of these functions (as described at the end of Sect. 2.1). This comparison allows validating the uniform mesh of 37×27 points used for the spatial DFT of the panel velocity field. The numerical model used for this study is described in Ref. [12].

Figure 4 shows the experimental setup used to measure the sensitivity functions. The plate was glued on thin blades and fixed on a frame as described in [10] to

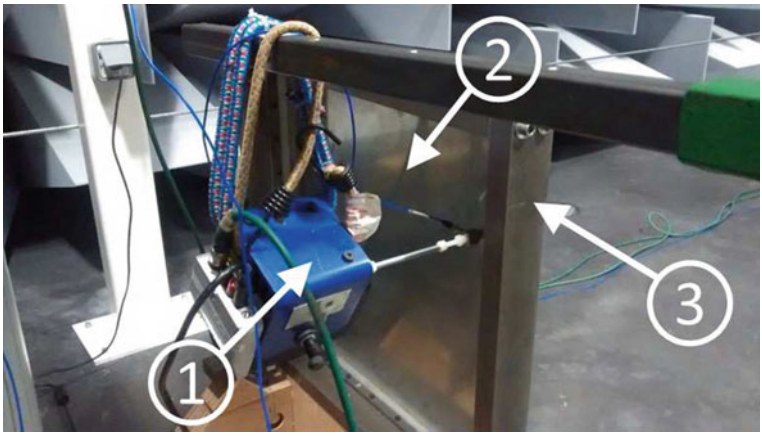

Fig. 4 Experimental setup, plate excited by a shaker to determine H_v. 1—Shaker with impedance head. 2—Plate. 3—Frame

reproduce simply supported boundary conditions. To determine the velocity sensitivity functions H_v, the plate was excited by a normal force at point $\mathbf{x}_M$ of coordinates ($x = 0.18$ m, $y = 0.09$ m). This force was applied using a TMS SmartShaker K2007E01 with integrated amplifier, which was fed with a swept sine over the considered frequency range, and the force was measured using an impedance head PCB288D01. An adapter was used between the impedance head and the plate reducing the area of mechanical coupling to approximately a 5 mm diameter circle. The vibratory response of the panel was measured on the grid of 37×27 points with a single point laser vibrometer (PSV-300 Polytec), and a time Fourier transform was directly performed in the post-processing software with ten linear averages.

Figure 5 shows the velocity sensitivity functions H_v obtained with the direct numerical calculation and the reciprocal approach using experimental data. They are provided for three different frequencies, the lowest corresponding to the (2, 1) vibration mode frequency (Fig. 5a) and the two others being off-resonance cases (Fig. 5b and c). The circle of radius $k_f = (\omega^2 \rho h / D)^{1/4}$, corresponding to the natural flexural wavenumber, is also indicated in Fig. 5. The numerical and experimental results are generally in good agreement. One can observe that the experimental sensitivity functions are slightly overestimated at the (2, 1) vibration mode frequency compared to the numerical results. This can be explained by the fact that the modal damping loss factor has been estimated from the response of the plate to a shaker excitation. The added mass from the impedance head and adapter possibly had an influence on the evaluation of the damping of the (2, 1) mode.

A good agreement is particularly noticed within the flexural wavenumber circle (delineated by a continuous line). Again, mainly the values in the flexural wavenumber circle contribute to the plate's vibration response to a TBL. However, the experimental sensitivity functions are also correctly estimated for wavenumbers higher than the flexural wavenumber.

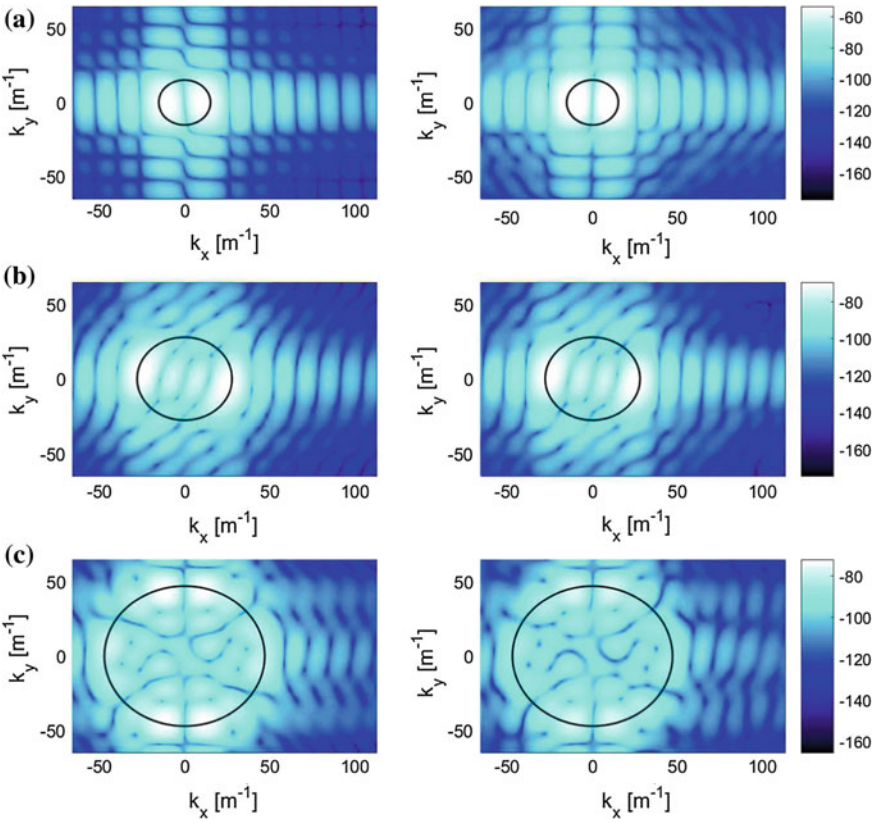

Fig. 5 Velocity sensitivity functions at point $\mathbf{x}_M$, $|H_v|^2$ (dB, ref. 1 m^2 s^{-2}): direct calculation (left), experimental reciprocity approach (right). **a** $f = 178$ Hz. **b** $f = 600$ Hz. **c** $f = 1710$ Hz—circle of radius k_f

5 Comparison with Measurements in an Anechoic Wind Tunnel

Finally, the proposed methodology is fully conducted as described in Sect. 3 to estimate the response of the plate G_{vv} and compare it with direct measurements in an anechoic wind tunnel. The proposed methodology requires data in the form of CSD functions expressed in the wavenumber domain to describe the TBL excitation. The considered data describing the wall-pressure fluctuations are first presented in Sect. 5.1, and then, the response of the plate predicted with the proposed approach is compared to wind tunnel measurements in Sect. 5.2.

5.1 *Measurement of the Wall-Pressure Fluctuations in an Anechoic Wind Tunnel*

Several analytical and semi-empirical models of a TBL excitation can be found in the literature such as Corcos and Chase models [13, 14], but currently no model accurately predicts the wall-pressure fluctuations induced by a TBL excitation. For the sake of validating the proposed methodology by comparison with actual measurements in an anechoic wind tunnel, the CSD functions were estimated from measurements of wall-pressure fluctuations of the TBL reproduced in the wind tunnel. The wall-pressure fluctuations have been measured using the spiral-shaped rotating antenna introduced by Robin et al. [15] at a flow velocity of $U_\infty = 40$ m.s^{-1} (see Fig. 6b). To help the TBL develop, a sandpaper strip was glued at the end of the convergent.

The pattern over which the 61 microphones are positioned (see Fig. 6a) has been designed to keep the microphone density reasonable so that each microphone has a different radial position r_m ($m = 1 : M$, with $M = 61$) with a radial resolution $\Delta r = 2$ mm. Measurements made following N consecutive rotations θ_n ($n = 1 : N$) allowed reaching an angular resolution $\Delta\theta = 360/N°$ and thereby reconstructing a high-density microphone array (as illustrated in Fig. 6a) at a post-processing step. This implies that the excitation is stationary in time and spatially homogeneous. The wavenumber–frequency CSD functions are estimated as follows [16]:

$$\bar{G}_{p_b p_b}(\boldsymbol{k}, f) = \sum_{m=1}^{M} \sum_{n=1}^{N} \bar{G}_{p_b p_b}(r_m, \theta_n, f)\, e^{-j\left(k_x r_m \cos\theta_n + k_y r_m \sin\theta_n\right)} r_m \Delta r \Delta\theta, \quad (14)$$

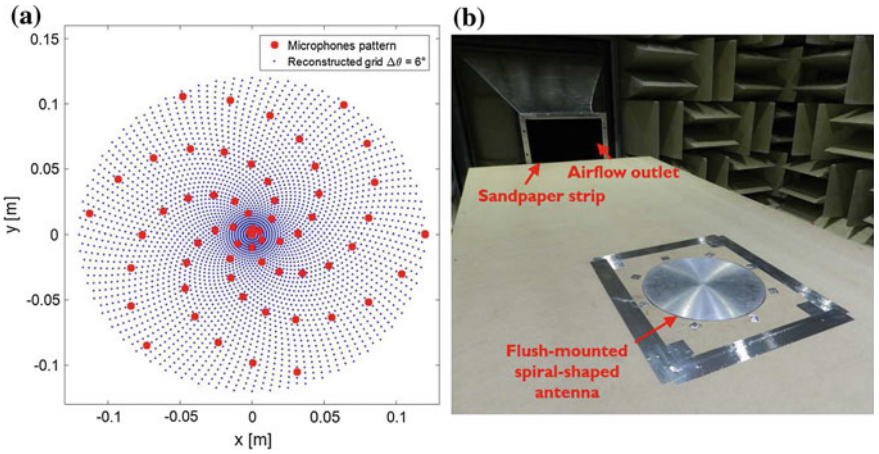

Fig. 6 Measurement of the wall-pressure fluctuations. **a** Antenna pattern and illustration of the reconstructed grid when rotating the antenna with $\Delta\theta = 6°$ increments. **b** Spiral-shaped array flush-mounted in the wind tunnel

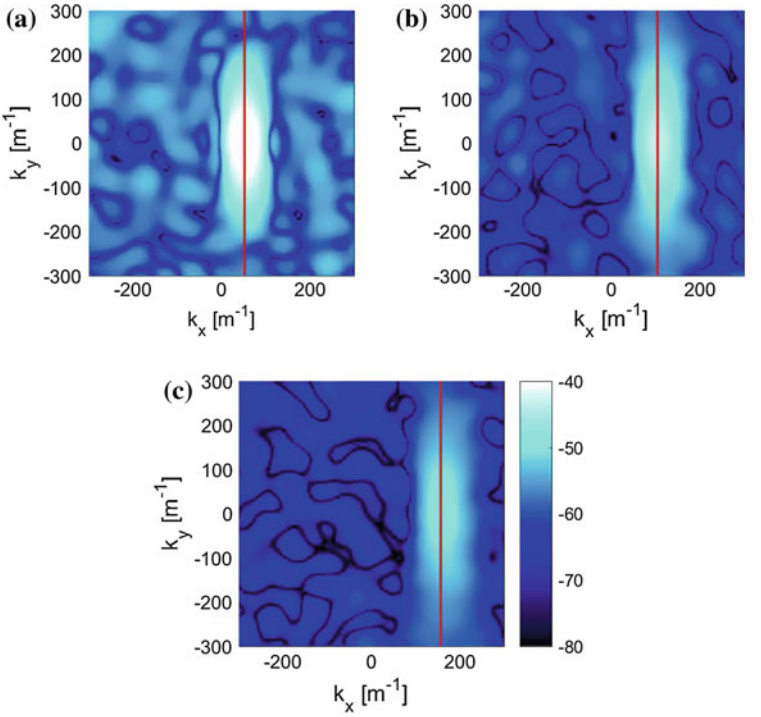

Fig. 7 Wall-pressure CSD functions $\bar{G}_{p_b p_b}(\boldsymbol{k}, f)$ (dB, ref. 1 Pa^2) estimated from measurements. **a** $f = 250$ Hz. **b** $f = 500$ Hz. **c** $f = 750$ Hz. Vertical red line, $k_x = k_c$

where $\bar{G}_{p_b p_b}(r_m, \theta_n, f)$ is the one-sided spatial CSD function of the wall-pressure. The spatial CSD functions have been estimated from the measured wall-pressure in the time domain $\bar{p}_b(r_m, \theta_n, t)$ at each position (r_m, θ_n) using "cpsd" MATLAB command. The spiral-shaped array was flush-mounted 1.8 m away from the convergent and 30 seconds acquisitions were performed for each of the $N = 180$ rotations. The reconstructed grid theoretically allows reaching a maximum wavenumber of 1570 m^{-1}, which is well above the limits of the previously defined wavenumber domain $\Omega_{\boldsymbol{k}}$. Applying Eq. (14) leads to an estimation of the wavenumber-frequency CSD functions at the center of the array ($x = 0$, $y = 0$). The obtained estimation of the wall-pressure CSD function is presented for 3 frequencies in Fig. 7.

5.2 Vibration Response

The vibration response of the plate estimated from the proposed approach is finally compared to direct measurement in the wind tunnel. On one hand, measurements in the wind tunnel were performed with a plate similar to the one used in the previous

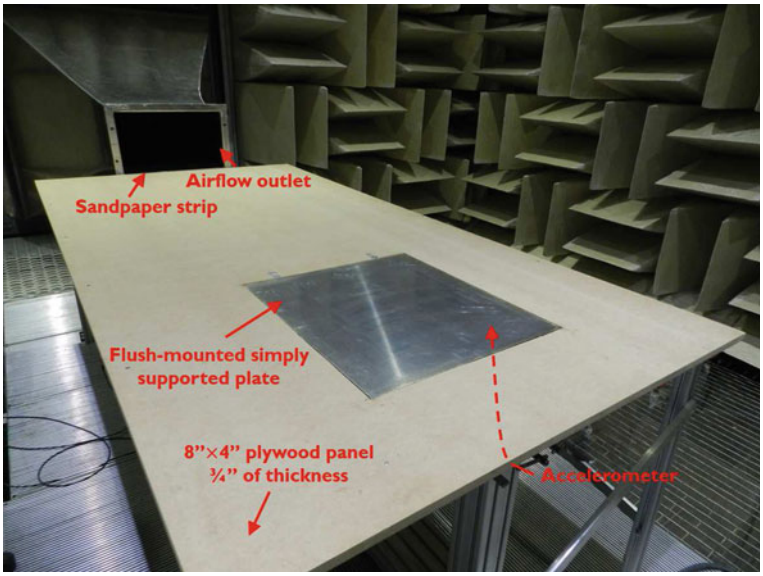

Fig. 8 Experimental setup used to measure the vibration response of the plate to the TBL reproduced in the wind tunnel

section (similar dimensions, material and boundary conditions). The plate was flush-mounted at the location of the previously mounted spiral-shaped array (as shown in Fig. 8) and excited at a flow velocity of $U_\infty = 40$ m.s^{-1} (aside from replacing the spiral-shaped array with the plate, the setup remained unchanged).

The vibration velocity of the plate was measured at point $\mathbf{x}_M$ using an accelerometer, and time signals were extracted from the post-processing software. The velocity ASD function G_{vv} was estimated using the "cpsd" MATLAB command.

On the other hand, the velocity ASD function was estimated by applying the proposed methodology using Eq. (6) and the measured wall-pressure CSD function $\bar{G}_{p_b p_b}(\boldsymbol{k}, f)$.

The plate velocity ASD function measured in the anechoic wind tunnel room at point $\mathbf{x}_M$ is compared to the result obtained with the proposed method in Fig. 9. The two curves are in very good agreement, which shows that for the considered test case, the velocity response of the plate can be fairly well estimated experimentally by simply applying a normal effort at the point of interest. Slight shifts of the resonance peaks in the high-frequency range are noticed. They can be explained by the fact that the sensitivity functions were measured on a plate which is slightly different to the one mounted in the wind tunnel to directly measure the response. Differences in terms of peak values of the velocity ASD functions can also be noticed. The structural damping is implicitly taken into account through the measurement of the

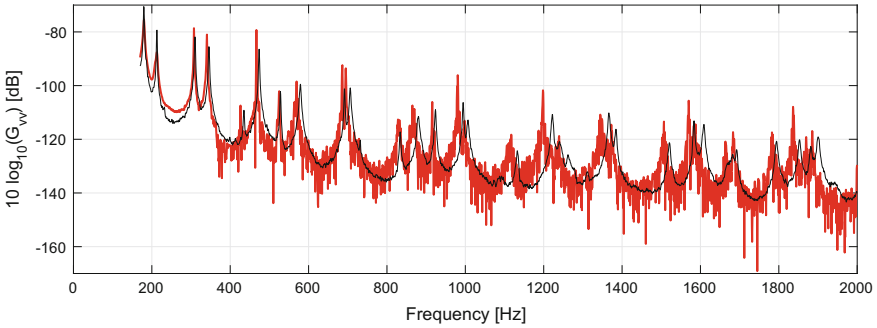

Fig. 9 Velocity ASD functions G_{vv} (dB, ref. 1 $m^2\,s^{-2}\,Hz^{-1}$): experimental reciprocity approach (bold red line) versus wind tunnel measurements (light black line)

sensitivity functions for the reciprocal approach and through the direct measurement of the vibration response in the wind tunnel. These differences in peak values are therefore again linked to the fact that two separate plates have been used with different structural damping.

6 Conclusion

In this paper, a methodology for characterizing the response of flat panels to a turbulent boundary layer excitation without using common measuring techniques (i.e., wind tunnel, *in situ* measurements) was proposed. This approach is based on the mathematical formulation of the random excitation problem in the wavenumber domain. This formulation indicates that the panel response at point **x** on the panel to a random field depends on two quantities in the wavenumber domain: the wall-pressure cross-spectral density function of the excitation and so-called sensitivity functions at point **x** which characterize the panel. Using the reciprocity principle, it has been shown that these functions can be determined from the panel velocity field in the wavenumber domain when it is excited by a normal force of unit amplitude at the point of interest **x**. The sensitivity functions can be estimated easily by experiment based on this reciprocal interpretation.

The proposed approach avoids using very costly facilities or measurement techniques such as wind tunnels or *in situ* measurements and is fairly simple to apply. It should, however, be underlined that the main limitations of the proposed approach rely on the assumptions of the mathematical formulation of the problem: The system should be linear (i.e., elastic material, small deformations) and time invariant. Also, a good estimation of the considered excitation is required. Models provided in the literature can be used but may lead to unsatisfactory results when it comes to comparing the proposed approach with other measuring techniques involving an actual reproduction of a turbulent boundary layer. This is the main reason why the

wall-pressure fluctuations have been measured in this paper, but it is not mandatory to apply the method.

From a practical point of view, an accurate experimental reproduction of the reciprocal source is required (i.e., normal force). A vibration measuring device is also needed to determine the vibratory response over the entire panel. A scanning laser vibrometer was used in this study, but with the recently developed full-field vibration measuring techniques (such as digital image correlation or deflectometry [17]), time of experiment could be significantly reduced in the future.

The method has been validated numerically and experimentally for the considered test case. Comparisons of numerical and experimental results have shown that the sensitivity functions are well estimated both inside and outside the natural flexural circle in the wavenumber domain. The proposed approach has finally been confronted to direct measurements in an anechoic wind tunnel. Results have shown that a fairly good estimate of the vibration response can be obtained by applying the proposed methodology. This methodology has been extended to the prediction of acoustic quantities [12] such as the radiated power. In the near future, it will be applied to determine the acoustic response of a panel to a turbulent boundary layer.

References

1. Aucejo, M., Maxit, L., Guyader J.-L.: Experimental simulation of turbulent boundary layer induced vibrations by using a synthetic array. J. Sound Vib. **331**(16), 3824–3843 (2012). https://doi.org/10.1016/j.jsv.2012.04.010
2. Berry, A., Dia, R., Robin, O.: A wave field synthesis approach to reproduction of spatially correlated sound fields. J. Acoust. Soc. Am. **131**(2), 1226–1239 (2012). https://doi.org/10.1121/1.3675942
3. Robin, O., Berry, A., Moreau, S.: Reproduction of random pressure fields based on planar nearfield acoustic holography, J. Acoust. Soc. Am. **133**(6), 3885–3899 (2013). https://doi.org/10.1121/1.4802898
4. Bravo, T., Maury, C.,: The experimental synthesis of random pressure fields: methodology. J. Acoust. Soc. Am. **120**(5), 2702–2711 (2006). https://doi.org/10.1121/1.2354008
5. Bravo, T., Maury, C.: A synthesis approach for reproducing the response of aircraft panels to a turbulent boundary layer excitation. J. Acoust. Soc. Am. **129**(1), 143–153 (2011). https://doi.org/10.1121/1.3514530
6. Maury, C., Bravo, T.: Focussed synthesis of a turbulent boundary layer excitation. In: 22nd AIAA/CEAS Aeroacoustics Conference, pp. 1–12 (2013). https://doi.org/10.2514/6.2016-2763
7. Maury, C., Gardonio, P., Elliott, S.J.: A wavenumber approach to modelling the response of a randomly excited panel, part 1: General theory. J. Sound Vib. **252**(1), 83–113 (2002). https://doi.org/10.1006/jsvi.2001.4028
8. Lin, Y.K.: Probabilistic theory of structural dynamics, p. 207. McGraw-Hill, New York (1967)
9. Fahy, F.J.: Some applications of the reciprocity principle in experimental vibroacoustics. Acoust. Phys. **49**(2), 217–229 (2003). https://doi.org/10.1134/1.1560385
10. Robin, O., Chazot, J.-D., Boulandet, R., Michau, M., Berry, A., Atalla, N.: A plane and thin panel with representative simply supported boundary conditions for laboratory vibroacoustic test. Acta Acust. United Ac. **102**(1), 170–182 (2016). https://doi.org/10.3813/AAA.918934
11. Corcos, G.M.: Resolution of pressure in turbulence. J. Acoust. Soc. Am. **35**(2), 192–199 (1963). https://doi.org/10.1121/1.1918431

12. Marchetto, C., Maxit, L., Berry, A., Robin, O.: Vibroacoustic response of panels under diffuse acoustic field excitation from sensitivity functions and reciprocity principles. J. Acoust. Soc. Am. **141**(6), 4508–4521 (2017). https://doi.org/10.1121/1.4985126
13. Miller, T.S., Gallman, J.M., Moeller, M.J.: Review of turbulent boundary layer models for acoustic analysis. In: 49th AIAA Aerospace Sciences Meeting, pp. 1–20 (2011). https://doi.org/10.2514/1.C031405
14. Caiazzo, A., D'Amico, R., Desmet, W.: A Generalized Corcos model for modelling turbulent boundary layer wall pressure fluctuations. J. Sound Vib. **372**, 192–210 (2016). https://doi.org/10.1016/j.jsv.2016.02.036
15. Robin, O., Moreau, S., Padois, T., Berry, A.: Measurement of the wavenumber-frequency spectrum of wall pressure fluctuations: spiral-shaped rotative arrays with pinhole-mounted quarter inch microphones. In: 19th AIAA/CEAS Aeroacoustics Conference, pp. 1–18 (2013). https://doi.org/10.2514/6.2013-2058
16. Arguillat, B., Ricot, D., Bailly, C., Robert, G.: Measured wavenumber: frequency spectrum associated with acoustic and aerodynamic wall pressure fluctuations. J. Acoust. Soc. Am. **128**(4), 1647–1655 (2010). https://doi.org/10.1121/1.3478780
17. Grédiac, M., Hild, F.: Full-Field Measurements and Identification in Solid Mechanics, Chap. 3 and 6. ISTE Ltd. and Wiley, London (2013)

Inference of Random Excitations from Contactless Vibration Measurements on a Panel or Membrane Using the Virtual Fields Method

Patrick O'Donoughue, Olivier Robin and Alain Berry

Abstract This paper aims at identifying random excitations acting on thin, plane structures from their measured vibration response. For random pressure fields such as the diffuse acoustic field (DAF) and turbulent boundary layer (TBL), two quantities of interest are to be determined, namely the wall pressure auto-spectral and cross-spectral density functions. These quantities are reconstructed using the virtual fields method, an identification technique based on the principle of virtual work. Numerical identification results for the auto-spectral and cross-spectral density functions are presented for both a plate and a membrane submitted to DAF and TBL excitations. Experimental identification results are then presented for the pressure auto-spectrum applied to an aluminum panel under DAF excitation from vibration response measurements that were obtained using deflectometry, a full-field optical measurement technique.

Keywords Virtual fields method · Identification · Random excitations

1 Introduction

In several engineering domains (aeronautical, naval, civil, etc.), dynamic forces acting on structures (fuselage, hull, partition, etc.) need to be identified. Special interest is given to practical cases when a direct measurement of the force is hardly feasible. The effective loading must therefore be inferred from the measured dynamic response of the studied structure. Such force identification is commonly referred to

P. O'Donoughue (✉) · O. Robin · A. Berry
Groupe d'Acoustique de l'Université de Sherbrooke, Faculté de Génie,
2500, Boulevard de l'Université, Sherbrooke, Québec, Canada
e-mail: patrick.odonoughue2@usherbrooke.ca

O. Robin
e-mail: olivier.robin@usherbrooke.ca

A. Berry
e-mail: alain.berry@usherbrooke.ca

E. Ciappi et al. (eds.), *Flinovia—Flow Induced Noise and Vibration Issues and Aspects-II*,
https://doi.org/10.1007/978-3-319-76780-2_22

as an inverse problem (comprehensive reviews of these problems can be found in [1, 2]).

Several approaches were developed to address the inverse problem. Notably, a stream of work by a group of authors concerned the force analysis technique (FAT) [3] and later the corrected force analysis technique (CFAT) [4], applied to simple and thin structures (beams, plates, and shells). This method involves injecting a measured displacement field into the local equilibrium equation of the structure discretized by a finite difference scheme. The technique can be applied locally on a structure but nevertheless requires fourth-order spatial derivatives of measured displacements, which calls for regularization approaches to avoid instability in the reconstruction process. The technique was successfully applied to vibration source identification and localization [3, 4] and to the identification of the acoustic component within a turbulent boundary layer [5, 6] (both on plates). The FAT was also once applied to the time-resolved identification of a diffuse acoustic field loading on a plate [7].

In parallel to the development of the FAT and CFAT approaches, the principle of virtual work was applied to identify mechanical constitutive parameters of materials and led to the establishment of the virtual fields method (VFM) [8]. In [9], the VFM was used to identify a mechanical point load excitation from an electrodynamic shaker and a distributed acoustic excitation from a monopole source, both applied to a bending panel. The VFM was also applied to the identification of spatially correlated excitations on plates [10]. In these two last works, vibration measurements were performed using scanning laser Doppler vibrometry (LDV), which provides the vibration response from a combination of measurements at discrete points taken at different times. This limits the application of the VFM to stationary excitations in both space and frequency, and a high spatial density calls for a long acquisition time.

Recently, the VFM was coupled with spatially and temporally resolved full-field optical measurements obtained with the deflectometry technique using a high-speed camera [11]. This technique directly provides local slope fields so that no scan operation is required. As a result, the acquisition time is independent of the number of measurement points, allowing for dense spatial measurements to be performed in a fraction of the time required for an LDV measurement. For example, [11] shows a tenfold increase in the number of data points for a 1 s deflectometry measurement compared to a 15 min LDV measurement. Moreover, the integral nature of the virtual work principle is well adapted to process such spatially dense data since the integrals can be adequately approximated by discrete sums.

All the previously cited works rely on "bending plate" test cases, whereas other structures like membranes have been seldom used even if they provided convincing results [12]. This paper will detail the implementation of the VFM for the identification of random excitations on plates and the theory will also be extended to membranes. In this formulation, the unknown pressure field is determined by its associated auto-spectral density (ASD) and cross-spectral density (CSD) functions. Numerical simulations will be presented for the identification of these two parameters in the case of diffuse acoustic field (DAF) and turbulent boundary layer (TBL) excitations on both a plate and a membrane. Next, a brief review of the deflectometry technique will be provided and experimental identification results from full-field measurement data will finally be presented for a panel under DAF excitation, where

the need of a membrane to obtain sufficient signal-to-noise ratio in experiments will be highlighted.

2 Virtual Fields Method for Random Excitations

2.1 Principle of Virtual Work: Bending Plate

Consider a thin, flat plate S in pure bending submitted to a transverse loading $q(\mathbf{x}, t)$ [Pa], where $\mathbf{x} = (x, y)$ are the cartesian coordinates of an arbitrary point on S. The local equilibrium of the plate is given by the Love–Kirchhoff equation:

$$\rho h a(\mathbf{x}, t) - \frac{h^3}{12}\{1\ 1\ 2\}\begin{pmatrix} \frac{\partial^2}{\partial x^2} & 0 & 0 \\ 0 & \frac{\partial^2}{\partial y^2} & 0 \\ 0 & 0 & \frac{\partial^2}{\partial x \partial y} \end{pmatrix} \mathbf{C}(\mathbf{x})\mathbf{k}(\mathbf{x}, t) = q(\mathbf{x}, t) \tag{1}$$

with ρ the mass density of the plate material, h the plate thickness, and $\mathbf{C}(\mathbf{x})$ the 3×3 plane stress stiffness matrix. In Eq. 1, the vibration response of the plate is defined by the acceleration field $a(\mathbf{x}, t)$ [m/s^2] and curvature field $\mathbf{k}(\mathbf{x}, t)$ [m^{-1}]. Under the assumption of pure bending where the out-of-plane contribution is at least one order of magnitude greater than the in-plane contribution, the acceleration is reduced to its transverse component $a(\mathbf{x}, t) = \frac{\partial^2 w}{\partial t^2}(\mathbf{x}, t)$ and the curvature is related to the transverse displacement by $\mathbf{k}(\mathbf{x}, t) = -\left\{\frac{\partial^2}{\partial x^2}\ \frac{\partial^2}{\partial y^2}\ 2\frac{\partial^2}{\partial x \partial y}\right\}^\top w(\mathbf{x}, t)$, where $\top$ denotes the vector transpose.

In theory, the local equilibrium equation can be used directly to extract the unknown loading $q(\mathbf{x}, t)$, provided bending displacements $w(\mathbf{x}, t)$ and curvatures $\mathbf{k}(\mathbf{x}, t)$ are measured and assuming that the mechanical properties of the plate are perfectly known. However, due to possible amplification of measurement noise from the fourth-order spatial differentiation of measured displacements on the left-hand side of Eq. 1, this approach generally requires strong regularization [3, 4, 6].

An alternative is to start from the principle of virtual work for the plate [9]:

$$-\omega^2 h \int_S \rho w^v(\mathbf{x}) \tilde{w}(\mathbf{x}, \omega)\, \mathrm{d}\mathbf{x} + \frac{h^3}{12}\int_S \mathbf{k}^{v\top}(\mathbf{x}) \tilde{\mathbf{C}}(\mathbf{x}, \omega) \tilde{\mathbf{k}}(\mathbf{x}, \omega)\, \mathrm{d}\mathbf{x} = \int_S w^v(\mathbf{x}) \tilde{q}(\mathbf{x}, \omega)\, \mathrm{d}\mathbf{x} \tag{2}$$

This equation is written in the frequency domain where ω is the angular frequency and $\sim$ denotes a complex phasor (e.g., $q(\mathbf{x}, t) = \tilde{q}(\mathbf{x}, \omega)\exp(j\omega t)$, $j = \sqrt{-1}$). The acceleration has been written in terms of the displacement as $\tilde{a}(\mathbf{x}, \omega) = -\omega^2 \tilde{w}(\mathbf{x}, \omega)$ and damping is introduced by means of a complex elastic matrix $\tilde{\mathbf{C}}(\mathbf{x}, \omega) = \mathbf{C}(\mathbf{x}, \omega)(1 + j\eta)$, where η is the structural loss factor. It should be noted that the virtual displacement has also been reduced to its out-of-plane component $w^v(\mathbf{x})$. Since only out-of-plane external loads $\tilde{q}(\mathbf{x}, \omega)$ contribute to the plate bending, the virtual work along the other directions is negligible.

The main advantage of using the VFM for identification purposes is avoiding computing the aforementioned fourth-order derivatives. The differentiation order on the measured displacements in Eq. 2 has been reduced to 2, which amounts to a single derivative on the slope fields provided by optical deflectometry. However, the method introduces a virtual displacement $w^v(\mathbf{x})$ and associated virtual curvatures $\mathbf{k}^v(\mathbf{x})$ (again, for pure bending, curvature is directly related to the transverse displacement). These quantities are called "virtual fields" and must be carefully defined, as detailed in Sect. 2.3.

In order to describe the random pressure distribution, the principle of virtual work is rewritten in terms of the loading power spectral density $S_{qq}(\mathbf{x}, \mathbf{x}', \omega) = E[q^*(\mathbf{x}, \omega)q(\mathbf{x}', \omega)]$, where $*$ denotes the complex conjugate and $E[\,]$ is the mathematical expectation. This is achieved by multiplying Eq. 2 with it's complex conjugate and taking the mathematical expectation of both sides [10]:

$$\begin{aligned}
\omega^4 h^2 \int_S \int_S \rho^2 w^v(\mathbf{x}) S_{ww}(\mathbf{x}, \mathbf{x}', \omega) w^v(\mathbf{x}')\, \mathrm{d}\mathbf{x}\mathrm{d}\mathbf{x}' \\
- \omega^2 \frac{h^4}{12} \int_S \int_S \rho w^v(\mathbf{x}) S_{w\mathbf{k}}(\mathbf{x}, \mathbf{x}', \omega) \tilde{\mathbf{C}}^\top(\mathbf{x}', \omega) \mathbf{k}^v(\mathbf{x}')\, \mathrm{d}\mathbf{x}\mathrm{d}\mathbf{x}' \\
- \omega^2 \frac{h^4}{12} \int_S \int_S \rho \mathbf{k}^{v\top}(\mathbf{x}) \tilde{\mathbf{C}}^*(\mathbf{x}, \omega) S_{\mathbf{k}w}(\mathbf{x}, \mathbf{x}', \omega) w^v(\mathbf{x}')\, \mathrm{d}\mathbf{x}\mathrm{d}\mathbf{x}' \\
+ \frac{h^6}{144} \int_S \int_S \mathbf{k}^{v\top}(\mathbf{x}) \tilde{\mathbf{C}}^*(\mathbf{x}, \omega) S_{\mathbf{kk}}(\mathbf{x}, \mathbf{x}', \omega) \tilde{\mathbf{C}}^\top(\mathbf{x}', \omega) \mathbf{k}^v(\mathbf{x}')\, \mathrm{d}\mathbf{x}\mathrm{d}\mathbf{x}' \\
= \int_S \int_S w^v(\mathbf{x}) S_{qq}(\mathbf{x}, \mathbf{x}', \omega) w^v(\mathbf{x}')\, \mathrm{d}\mathbf{x}\mathrm{d}\mathbf{x}'
\end{aligned} \tag{3}$$

Assuming that the spectral properties S_{ww}, $S_{w\mathbf{k}}$, $S_{\mathbf{k}w}$, and $S_{\mathbf{kk}}$ of the plate response are available from continuous measurements, Eq. 3 can be used to identify the loading ASD and CSD functions from the spectral properties S_{qq} [Pa^2] of the unknown excitation.

2.2 Principle of Virtual Work: Stretched Membrane

Consider a thin membrane stretched over a flat domain S with a uniform tensile force per unit length T [N/m]. The local equilibrium equation is:

$$\sigma a(\mathbf{x}, t) + T\left(\frac{\partial^2 w}{\partial x^2}(\mathbf{x}, t) + \frac{\partial^2 w}{\partial y^2}(\mathbf{x}, t)\right) = q(\mathbf{x}, t) \tag{4}$$

where σ is the area density of the membrane. Multiplying Eq. 4 by an arbitrary virtual displacement $w^v(\mathbf{x})$ and integrating over the surface lead to the principle of virtual

work. After simplifying using integration by parts, the equation in the frequency domain is:

$$-\omega^2 \int_S \sigma w^v(\mathbf{x}) \tilde{w}(\mathbf{x}, \omega)\, \mathrm{d}\mathbf{x} + \int_S \tilde{T} \boldsymbol{\alpha}^{v\top}(\mathbf{x}) \tilde{\boldsymbol{\alpha}}(\mathbf{x}, \omega)\, \mathrm{d}\mathbf{x} = \int_S w^v(\mathbf{x}) \tilde{q}(\mathbf{x}, \omega)\, \mathrm{d}\mathbf{x} \quad (5)$$

The spatial derivatives of the virtual and measured displacements (slopes) are denoted, respectively, $\boldsymbol{\alpha}^v(\mathbf{x}) = \left\{ \frac{\partial}{\partial x} \; \frac{\partial}{\partial y} \right\}^\top w^v(\mathbf{x})$ and $\tilde{\boldsymbol{\alpha}}(\mathbf{x}, \omega) = \left\{ \frac{\partial}{\partial x} \; \frac{\partial}{\partial y} \right\}^\top \tilde{w}(\mathbf{x}, \omega)$. Damping is now introduced by means of a complex tensile force $\tilde{T} = T(1 + j\eta)$. It is also interesting to note from Eq. 5 that loading identification on membranes requires only a single spatial integration and no differentiation of the measured slope fields from deflectometry, eliminating previous concerns about the noise amplification associated with derivatives.

Finally, the virtual work principle expressed in terms of the power spectral density functions for a membrane is:

$$\begin{aligned}
&\omega^4 \int_S \int_S \sigma^2 w^v(\mathbf{x}) S_{ww}(\mathbf{x}, \mathbf{x}', \omega) w^v(\mathbf{x}')\, \mathrm{d}\mathbf{x}\mathrm{d}\mathbf{x}' \\
&\qquad -\omega^2 \int_S \int_S \sigma \tilde{T} w^v(\mathbf{x}) S_{w\boldsymbol{\alpha}}(\mathbf{x}, \mathbf{x}', \omega) \boldsymbol{\alpha}^v(\mathbf{x}')\, \mathrm{d}\mathbf{x}\mathrm{d}\mathbf{x}' \\
&\qquad -\omega^2 \int_S \int_S \sigma \tilde{T} \boldsymbol{\alpha}^{v\top}(\mathbf{x}) S_{\boldsymbol{\alpha}w}(\mathbf{x}, \mathbf{x}', \omega) w^v(\mathbf{x}')\, \mathrm{d}\mathbf{x}\mathrm{d}\mathbf{x}' \\
&\qquad + \int_S \int_S \tilde{T}^2 \boldsymbol{\alpha}^{v\top}(\mathbf{x}) S_{\boldsymbol{\alpha}\boldsymbol{\alpha}}(\mathbf{x}, \mathbf{x}', \omega) \boldsymbol{\alpha}^v(\mathbf{x}')\, \mathrm{d}\mathbf{x}\mathrm{d}\mathbf{x}' \\
&\qquad\qquad = \int_S \int_S w^v(\mathbf{x}) S_{qq}(\mathbf{x}, \mathbf{x}', \omega) w^v(\mathbf{x}')\, \mathrm{d}\mathbf{x}\mathrm{d}\mathbf{x}'
\end{aligned} \quad (6)$$

2.3 Virtual Fields

In this work, the virtual fields are defined as piecewise functions over a limited region comprised within S. The virtual displacement takes on nonzero values only over a small rectangular window $S_\mathbf{x} = [a_x \; b_x] \times [a_y \; b_y]$. The support $S_\mathbf{x}$ of such a virtual field will be referred to hereafter as the "virtual window." Since Eqs. 3 and 6 involve double surface integrals, two independent virtual windows at positions $S_\mathbf{x}$ and $S_{\mathbf{x}'}$ are needed to extract the unknown loading spectral density $S_{qq}(\mathbf{x}, \mathbf{x}', \omega)$ (see Fig. 1).

The virtual displacement $w^v(\mathbf{x})$ is any C^1 continuous function. Although there are an infinite number of possible virtual fields that obey this requirement, another important practical requirement is that it must be "kinematically admissible." In other words, the virtual fields must not introduce unwanted shear forces and bending

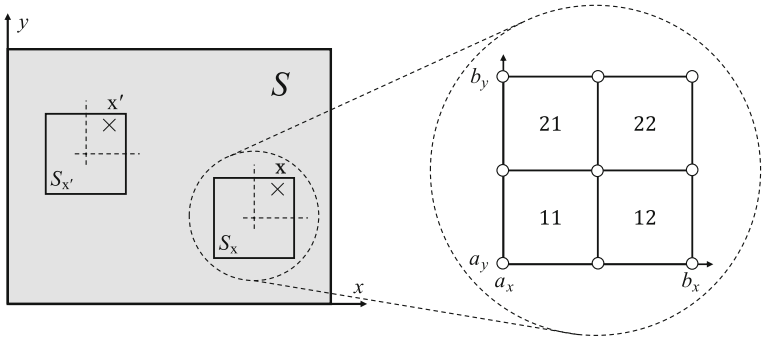

Fig. 1 Virtual windows $S_{\mathbf{x}}$ and $S_{\mathbf{x}'}$ comprised within S

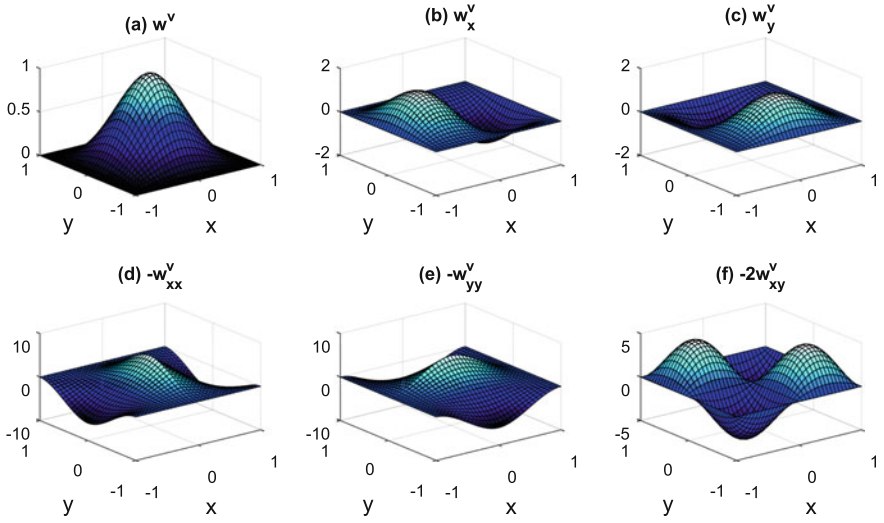

Fig. 2 The Hermite 16 virtual fields. **a** Virtual displacement $w^v(\mathbf{x})$, associated virtual slopes, **b** $\alpha_x = \partial w^v(\mathbf{x})/\partial x$, **c** $\alpha_y = \partial w^v(\mathbf{x})/\partial y$, and curvatures, **d** $k_1 = -\partial^2 w^v(\mathbf{x})/\partial x^2$, **e** $k_2 = -\partial^2 w^v(\mathbf{x})/\partial y^2$, **f** $k_6 = -2\partial^2 w^v(\mathbf{x})/\partial x \partial y$

moments at the edge of the virtual window. Moreover, this renders the method independent of the boundary conditions so that it can be applied locally on any simple plate or membrane structure. The chosen virtual displacement is based on the Hermite 16 interpolation functions used in the finite element method [8]. These shape functions have displacements and slopes that vanish at the borders of $S_{\mathbf{x}}$ to provide kinematic admissibility. The equations for the chosen virtual fields are detailed in previous work by the authors [9]. The displacement is normalized such that the value at the center node is 1, and the virtual slope and curvature functions are directly obtained from the displacement by analytical differentiation. Graphs of the chosen virtual fields are presented in Fig. 2.

Since the virtual fields are null outside the virtual window, the terms in Eqs. 3 and 6 can be rewritten as integrals over $S_{\mathbf{x}}$ and $S_{\mathbf{x}'}$. However, solving for the unknown integrand $S_{qq}(\mathbf{x}, \mathbf{x}', \omega)$ requires an approximation. Supposing that $S_{qq}(\mathbf{x}, \mathbf{x}', \omega)$ varies slowly over the virtual windows, it can be assumed constant in the integration. Therefore, the right-hand side of Eqs. 3 and 6 becomes:

$$\int_{S_{\mathbf{x}'}} \int_{S_{\mathbf{x}}} w^v(\mathbf{x}) S_{qq}(\mathbf{x}, \mathbf{x}', \omega) w^v(\mathbf{x}') \, \mathrm{d}\mathbf{x}\mathrm{d}\mathbf{x}'$$

$$\approx S_{qq}(\mathbf{x_c}, \mathbf{x}'_{\mathbf{c}}, \omega) \int_{S_{\mathbf{x}}} w^v(\mathbf{x}) \, \mathrm{d}\mathbf{x} \int_{S_{\mathbf{x}'}} w^v(\mathbf{x}') \, \mathrm{d}\mathbf{x}' = S_{qq}(\mathbf{x_c}, \mathbf{x}'_{\mathbf{c}}, \omega) \frac{A_{\mathbf{x}} A_{\mathbf{x}'}}{16} \tag{7}$$

where $A_{\mathbf{x}}$, $A_{\mathbf{x}'}$ are the respective areas of $S_{\mathbf{x}}$ and $S_{\mathbf{x}'}$, and $\mathbf{x_c}$, $\mathbf{x}'_{\mathbf{c}}$ are the center points of each virtual window. For this approximation to be feasible, the spatial resolution of the vibration response measurements must be high enough to accommodate virtual windows that are small compared to the spatial variations of $S_{qq}(\mathbf{x}, \mathbf{x_0}, \omega)$. In this regard, optical measurement techniques such as deflectometry are convenient for achieving high spatial density measurements in a short acquisition time.

To calculate the loading CSD, the virtual window $S_{\mathbf{x}'}$ is fixed at an arbitrary position and the point $\mathbf{x}'_{\mathbf{c}}$ is considered as the reference for the cross-spectrum. Depending on the structure, Eq. 3 or 6 is then applied iteratively by scanning the surface S with overlapping virtual windows $S_{\mathbf{x}}$ to obtain the loading CSD at each successive point $\mathbf{x_c}$. Alternatively, the loading ASD can be calculated by setting $\mathbf{x} = \mathbf{x}'$ so that both virtual windows coincide and scan the surface. However, it must be noted that in both cases the loading cannot be identified at the boundary of S since it is only determined at the center of each virtual window. The next section will present numerical simulation results for the identification of DAF and TBL excitations using the VFM.

3 Numerical Simulations

The following loading reconstruction results are based on simulations of the structure's response spectral density functions. These functions are calculated using the matrix equations developed in [10] and considering mode orders up to 20 in x and y. The chosen material parameters for the plate are typical values for a 1/8" (3.19 mm) aluminum panel, whereas the membrane was given arbitrary but realistic values (based on preliminary investigations). The properties of the plate and membrane used in the simulations are listed in Table 1.

Both diffuse acoustic field and turbulent boundary layer excitations are considered. The cross-spectral density of a DAF is given by [13]:

$$S_{qq}(\mathbf{x}, \mathbf{x}', \omega) = S_{qq}(\mathbf{x}, \mathbf{x}, \omega) \frac{\sin(k_0 |\mathbf{x} - \mathbf{x}'|)}{k_0 |\mathbf{x} - \mathbf{x}'|} \tag{8}$$

Table 1 Material parameters of the simulated plate and membrane

Plate		Membrane	
Parameter	Value	Parameter	Value
Dimensions	48 cm × 42 cm	Dimensions	48 cm × 42 cm
Thickness (h)	3.19 mm	Area density (σ)	0.1 kg/m^2
Mass density (ρ)	2700 kg/m^3	Linear tensile force (T)	500 N/m
Young's modulus (E)	70 GPa	Structural loss factor (η)	10^{-3}
Poisson's ratio (ν)	0.3		
Structural loss factor (η)	4×10^{-3}		

where $S_{qq}(\mathbf{x}, \mathbf{x}, \omega)$ is the pressure auto-spectrum, $k_0 = \omega/c_0$ the acoustic wave number, and c_0 the speed of sound. The TBL excitation is defined using the empirical Corcos model [14]. For a flow in the positive x direction, the wall pressure CSD is:

$$S_{qq}(\mathbf{x}, \mathbf{x}', \omega) = S_{qq}(\mathbf{x}, \mathbf{x}, \omega) \exp\left(-\frac{\omega|x - x'|}{\alpha U_c}\right) \exp\left(-\frac{\omega|y - y'|}{\beta U_c}\right) \exp\left(j\frac{\omega|x - x'|}{U_c}\right) \tag{9}$$

where $S_{qq}(\mathbf{x}, \mathbf{x}, \omega)$ is again the auto-spectral density, α and β are the spatial correlation decay constants in the x and y directions, respectively, and U_c is the convection velocity. The chosen parameters are $\alpha = 1.2$, $\beta = 0.8$, and $U_c = 0.7U_\infty$, where U_∞ is the freestream velocity.

The reference point $\mathbf{x}'$ for the cross-spectra is taken to be at the center of S, and the excitations are normalized assuming a unitary auto-spectrum: $S_{qq}(\mathbf{x}, \mathbf{x}, \omega) = 1$ Pa^2. The cross-spectral density reconstructions using the VFM are performed on a regular mesh of 49 × 43 equally spaced points (1 cm spatial resolution), while the auto-spectral density reconstructions are done on a coarser mesh of 33 × 29 points (1.5 cm spatial resolution) to keep the execution time below one hour on a regular laptop computer running MATLAB®. However, there is room for future optimization using parallel processing since the calculations of $S_{qq}(\mathbf{x_c}, \mathbf{x'_c}, \omega)$ on successive virtual windows are independent.

In order to uphold the approximation in Eq. 7, small virtual windows containing 3 × 3 mesh points are used. Evidently, there is a trade-off between keeping the window size small compared to the spatial scale of the loading and ensuring that a sufficient number of points are used to accurately perform the surface integrations in Eqs. 3 and 6. Nevertheless, the estimation of these integrals is improved by spatial oversampling and cubic interpolation of the vibration response spectral density functions prior to integration.

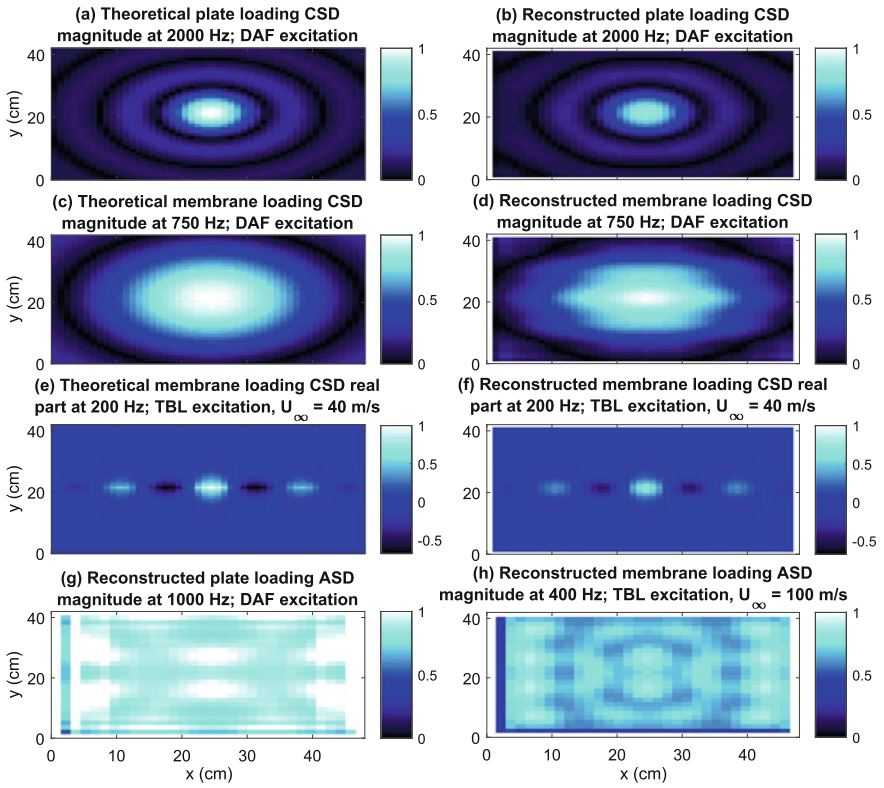

Fig. 3 **a–f** Comparisons of the theoretical and reconstructed loading CSD. **g–h** Reconstructed loading ASD on the plate and membrane (the theoretical auto-spectrum is unitary)

Figure 3 presents some examples of reconstruction results for different combinations of the structures and excitations. Comparing Fig. 3a–d, it is seen that the peak magnitude of 1 Pa^2 in the DAF cross-spectrum is better predicted in Fig. 3d than in Fig. 3b, whose peak values are 0.99 Pa^2 and 0.84 Pa^2, respectively. This is due to the lower spatial variation of the CSD at 750 Hz which more closely approximates a constant square pressure over the 3×3 point virtual windows, upholding the assumption in Eq. 7. However, there are noticeable errors on the reconstructed shape of the loading CSD in Fig. 3d. This is attributed to a slight spatial undersampling of the membrane's spectral response functions S_{ww}, $S_{w\alpha}$, $S_{\alpha w}$ and $S_{\alpha\alpha}$. In fact, the evaluation frequency of 750 Hz is close to the membrane's 63rd resonance, or the $(m, n) = (10, 2)$ mode, where m is the mode number in x and n is the mode number in y. Therefore, the current spatial resolution is insufficient for the response peaks along the x direction to be properly resolved. Conversely, the pattern in Fig. 3b is well reproduced since the plate's response at 2000 Hz is only near its 35th resonance or (7, 3) mode. The higher modal density of the membrane is a general result as it

increases linearly with frequency, while a plate's modal density remains constant. The equations for the modal densities of both structures are as follows [15]:

$$D_{\text{plate}} = \frac{A_p}{h}\sqrt{\frac{3\rho(1-\nu^2)}{E}} \tag{10}$$

$$D_{\text{memb}}(f) = \frac{2\pi\sigma A_m}{T} f \tag{11}$$

where A_p and A_m are the respective surface areas of the plate and membrane, E the Young's modulus, and ν the Poisson ratio. Otherwise, Fig. 3e, f shows a decent reconstruction of the real part of the CSD at 200 Hz for a TBL with $U_\infty = 40$ m/s applied to the membrane, but the amplitudes are again underestimated due to the short spatial correlation scale compared to the size of the virtual window: The peak value reconstructed at the center is 0.63 Pa^2, while the theoretical value is 1 Pa^2. Finally, Fig. 3g, h is the reconstructed auto-spectral density for DAF and TBL excitations, respectively. The result in Fig. 3g shows a slight underestimation of the DAF auto-spectrum on the plate with a mean value of 0.90 Pa^2. This is due to the spatial averaging involved in Eq. 7, as well as the approximate numerical integrations over the virtual window. For similar reasons, the reconstructed pressure ASD on the membrane in Fig. 3h has a mean value of 0.67 Pa^2. However, the more pronounced underestimation in this case is again attributed to the undersampling of the membrane's spectral response functions. In general, using a higher spatial resolution will lead to more accurate results since these functions will be well-resolved and more mesh points can be included in the virtual window to improve the numerical integrations. Despite the membrane's higher modal density, one of its important practical advantages is that no spatial differentiation is required for the VFM calculation, potentially leading to more accurate identification results from experimental measurements.

4 Optical Deflectometry

Deflectometry is an optical technique that directly provides a full-field measurement of local slopes estimated from an image that is observed by specular reflection over the target structure, which must have a mirror-like finish. This technique is sensitive to small out-of-plane surface deformations and is therefore well-suited for measuring the dynamic bending of thin and plane structures. The observed image is a regular two-dimensional grid, and the measurement configuration is illustrated in Fig. 4.

Any transverse loads applied to the structure will distort the grid image seen by the camera. These distortions can then be directly related to the local slopes on the surface using simple geometrical considerations. For example, suppose that the pixel on the camera sensor observing point M in Fig. 4 sees the reflected image of point P on the grid. If an out-of-plane deformation induces a local slope $d\alpha$ at point M,

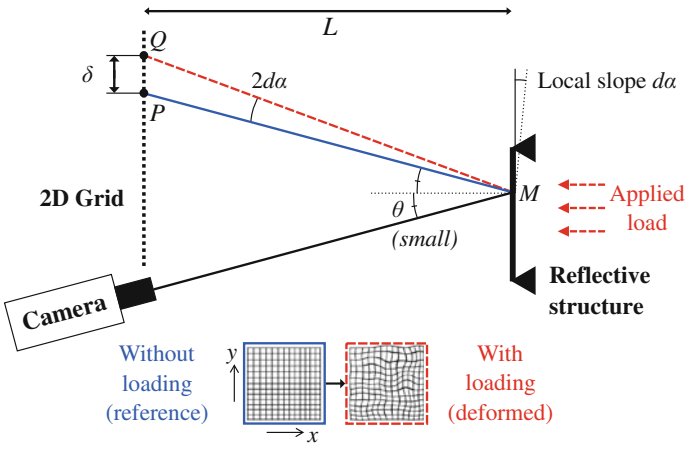

Fig. 4 Deflectometry measurement on a plane structure with and without transverse loading

the imaged point will shift from P to Q. In the small angle approximation for θ and $d\alpha$, the length of segment $\overline{PQ}$ is given by:

$$\delta = 2Ld\alpha \tag{12}$$

where L is the grid-target distance. A complete geometrical derivation can be found in [16].

Next, a second expression for δ can be established in terms of the local phase variations $\Delta\phi$ in the grid images. These phase values are obtained by performing spatial phase shifting on the images using a windowed discrete Fourier transform (WDFT) algorithm [17]. Since the phase values returned by the WDFT are between $[-\pi, \pi]$ radians, a two-dimensional phase unwrapping algorithm must also be implemented to ensure a continuous phase map [18]. For practical purposes, the phase is defined relative to the equilibrium position to account for any small initial curvature of the surface. Therefore, a reference image is taken without external loads applied to the structure. The phase variations under load are then given by $\Delta\phi = \phi_d - \phi_r$, where ϕ_d and ϕ_r are the calculated phase maps from the deformed and reference images, respectively.

Using the observed phase variation at point M in Fig. 4, the length of segment $\overline{PQ}$ can be written as:

$$\delta = \left(\frac{p}{2\pi}\right)\Delta\phi \tag{13}$$

where p is the grid pitch (spatial grid period). Combining Eqs. 12 and 13 yields:

$$2Ld\alpha = \left(\frac{p}{2\pi}\right)\Delta\phi \tag{14}$$

This analysis is performed in both the x and y axes of the structure to obtain simple geometrical relations between the phase maps $\Delta\phi_{x,y}$ and corresponding slope fields $d\alpha_{x,y}$ on the surface:

$$\begin{cases} d\alpha_x(x, y) = \dfrac{p}{4\pi L}\Delta\phi_x(x, y) \\ d\alpha_y(x, y) = \dfrac{p}{4\pi L}\Delta\phi_y(x, y) \end{cases} \tag{15}$$

An interesting property of this measurement technique is that increasing the grid-target distance L effectively increases the slope resolution without changing the spatial resolution. The physical limit of this increase is determined by the magnification and quality of the camera lens used [19].

5 Experiment: Plate Under DAF Excitation

5.1 Experimental Methods

The experimental setup used to perform deflectometry measurements on a panel submitted to a DAF excitation is depicted in Fig. 5. Since the images are recorded using a Photron SA-X2 RV high-speed camera on a very short exposure, an independent light source (LED spotlight) is required to illuminate the grid.

A rectangular panel of dimensions 0.48 m $\times$ 0.42 m, thickness $h = 3.19$ mm, and made of standard aluminum (mass density $\rho = 2700$ kg/m^3, Young's modulus $E = 70$ GPa, Poisson ratio $\nu = 0.3$) was used in this experiment. Simply supported conditions are achieved along all the plate boundaries using a dedicated method [20]. There are several approaches for producing a mirror-like finish on a surface in order to perform deflectometry measurements. However, since a metal panel was used, it was simply buffed and polished using car body polishing techniques, providing a convenient and inexpensive way to obtain a highly reflective finish.

The panel was installed in a transmission loss facility and a diffuse acoustic field was generated in the reverberant room using a loudspeaker fed with a white noise signal. A 9×9 microphone array was placed in front of the panel on the reverberant side (see Fig. 5b) to serve as a reference measurement for comparison with the reconstructed pressure auto-spectral density. Images were then recorded on the high-speed camera at 5,000 frames per second for a little over 2 seconds, producing 10,918 images with a resolution of 1024×1024 pixels. After performing the phase extraction and scaling using Eqs. 15, each image yields the x and y slope fields with 145×145 measurement points and a spatial resolution of 2.1 mm. The resulting vibration response data is resolved in both space and time and contains nearly 230 million data points. The displacements and curvatures needed to compute the response spectral density functions S_{ww}, $S_{w\mathbf{k}}$, $S_{\mathbf{k}w}$, and $S_{\mathbf{kk}}$ in Eq. 3 are obtained by numerical integration and differentiation of the measured slope fields, respectively. Moreover, the high spatial density of these full-field measurements allows for

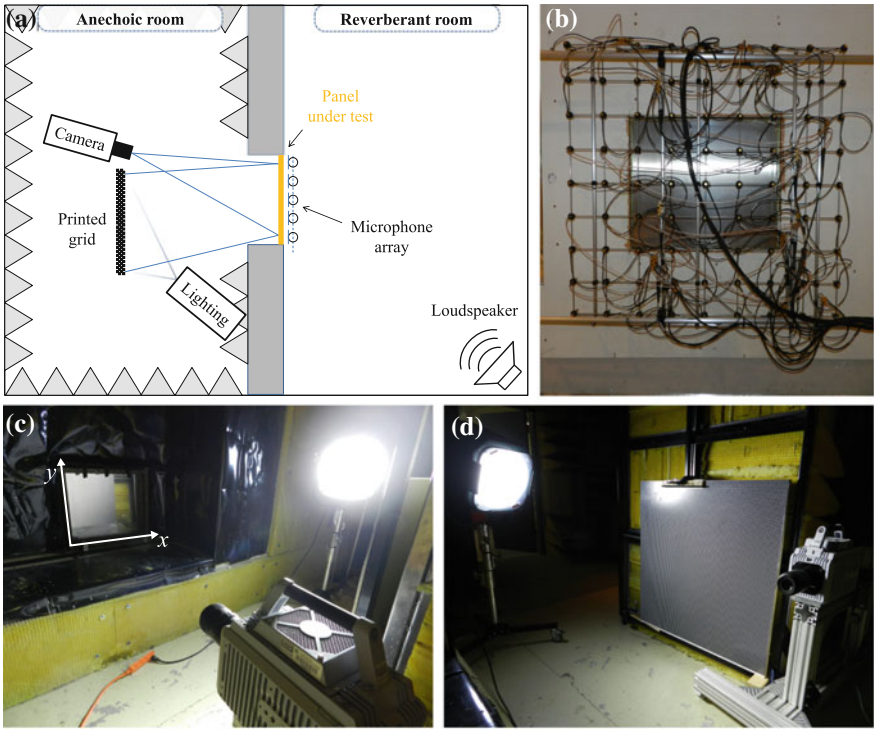

Fig. 5 **a** Illustration of the deflectometry measurement on the panel installed in a transmission loss facility. **b** Picture of the 9 × 9 microphone array. **c–d** Pictures showing the placement of the camera, panel, and grid

curvatures to be calculated using a simple numerical gradient without the need for regularization. Finally, the VFM was applied using 25 × 25 point virtual windows, which avoids the need for spatial oversampling when performing the numerical integrations as it is computationally intensive.

5.2 Results

The auto-spectral density of the wall pressure applied to the panel was identified using the virtual fields method from full-field deflectometry measurements. In order to compare the results with the 9 × 9 microphone array, Fig. 6a presents a graph of the measured and reconstructed spatially averaged loading auto-spectrum. The black line was obtained by applying the VFM in 1 Hz increments between 100 and 1000 Hz and taking the mean value of the ASD at each frequency. Below 500 Hz, the curves show a good overall agreement, except at structural resonance frequencies at which

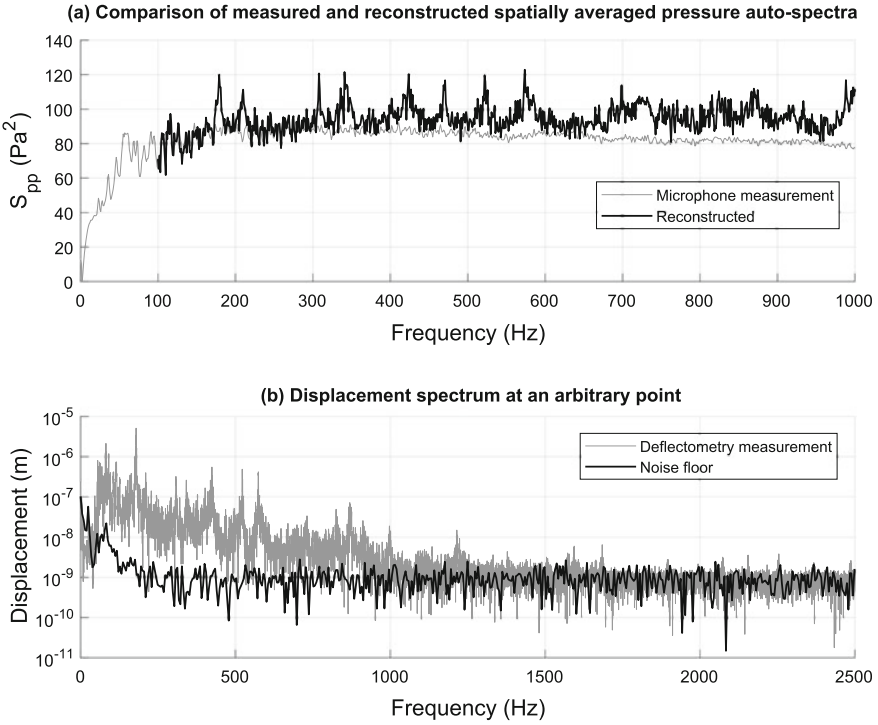

Fig. 6 **a** Reconstructed pressure ASD under DAF excitation compared with the measured ASD using a microphone array. **b** Spectrum of the measured displacement with and without the excitation

the reconstructed wall pressure is considerably overestimated. In practice, it is difficult to accurately identify the loading magnitude at a structural resonance frequency in the case of a lightly damped structure. The problem is ill-conditioned because the virtual work terms of the inertial and elastic forces on the left-hand side of Eqs. (2) and (5) become large. As a result, small errors in the material properties or numerical derivatives can lead to a substantial bias in the reconstructed magnitude. The problem of estimating applied force distributions from the response of one dominant structural mode using the VFM was also mentioned in [10]. On the other hand, there is a significant discrepancy between the measured and reconstructed auto-spectra above 500 Hz. This is due to an inadequate signal-to-noise ratio in the deflectometry measurement. In other words, the 1/8" aluminum panel did not respond with a sufficient amplitude at higher frequencies. Fig. 6b demonstrates this by comparing the Fourier transform of the measured displacement at an arbitrary point on the panel to the Fourier transform of the displacement noise floor. The noise floor was obtained by performing the deflectometry analysis on a series of 1000 reference grid images taken with the panel at rest. Above 500 Hz, the amplitude of the measured displacements reaches the noise floor, leading to the observed bias in the reconstructed ASD.

However, these results also show that the displacement sensitivity of the deflectometry measurement is on the order of a nanometer, which is very reasonable for a vibration measurement technique. Increasing the sound intensity of the DAF excitation could potentially lead to measurable deformations, but it would require several loudspeakers and a sound pressure level that is undesirably high (the overall sound pressure level on the considered frequency range already reached a value of 113 dB). In any case, the measurement of nanometer-scale vibrations using deflectometry is not ideal in an industrial setting. Therefore, the use of a membrane as the receiving structure will be considered for future experiments in order to improve the signal-to-noise ratio and hence the viability of the proposed identification approach.

6 Conclusion

This paper reported identification results of random excitations acting on plate and membrane structures from their measured vibration response. It was shown by numerical simulations that the auto-spectral and cross-spectral density functions could both be reconstructed with suitable accuracy using the virtual fields method. Since spatial measurements are needed to apply this method and can hardly be achieved using contact measurements (e.g., heavy and complex arrays of accelerometers), laser Doppler velocimetry measurements were previously used and the optical deflectometry technique is introduced here. Experimental reconstruction results for the auto-spectrum of a diffuse acoustic field are finally presented and were obtained using the virtual fields method coupled with full-field optical measurements on an aluminum plate. At the exception of structural resonances, the auto-spectrum magnitude is well identified, but the reconstruction accuracy is limited to an upper frequency determined to be caused by a poor signal-to-noise ratio. As a consequence, a circular membrane (for which the tensile force can be easily adjusted compared with a rectangular one) is being developed for measurements under both diffuse acoustic field and turbulent boundary layer excitations since a membrane is expected to produce larger displacements and thus a better signal-to-noise ratio while avoiding the possible amplification of measurement noise as no spatial differentiation is required.

References

1. Stevens, K.K.: Force identification problems—an overview. In: Proceedings of the 1987 SEM Spring Conference on Experimental Mechanics, pp. 838–844. Houston, TX, USA (1987)
2. Sanchez, J., Benaroya, H.: Review of force reconstruction techniques. J. Sound Vib. **333**, 2999–3018 (2014)
3. Pézerat, C., Guyader, J.-L.: Force analysis technique: reconstruction of force distribution on plates. Acta Acust. United Acust. **86**, 322–332 (2000)
4. Leclère, Q., Ablitzer, F., Pézerat, C.: Practical implementation of the corrected force analysis technique to identify the structural parameter and load distributions. J. Sound Vib. **351**, 106–118 (2015)

5. Totaro, N., Pézerat, C., Leclère, Q., Lecoq, D., Chevillotte, F.: Identification of boundary pressure field exciting a plate under turbulent flow. In: Ciappi, E., De Rosa, S., Franco, F., Guyader, J.-L., Hambric, S.A. (eds.) Flinovia—Flow Induced Noise and Vibration Issues and Aspects, pp. 187–208. Springer (2014)
6. Lecoq, D., Pézerat, C., Chevillotte, F., Bessis, R.: Measurement of the low-wavenumber component within a turbulent wall pressure by an inverse problem of vibration. J. Acoust. Soc. Am. **140**, 1974–1980 (2016)
7. Leclère, Q., Pézerat, C.: Time domain identification of loads on plate-like structures using an array of acoustic velocity sensors. In: Proceedings of Acoustic'08 Congress, pp. 1–5. Paris, France (2008)
8. Pierron, F., Grédiac, M.: The Virtual Fields Method: Extracting Constitutive Mechanical Parameters from Full-field Deformation Measurements. Springer, New-York (2012)
9. Berry, A., Robin, O., Pierron, F.: Identification of dynamic loading on a bending plate using the Virtual Fields Method. J. Sound Vib. **333**, 7151–7164 (2014)
10. Berry, A., Robin, O.: Identification of spatially correlated excitations on a bending plate using the Virtual Fields Method. J. Sound Vib. **375**, 76–91 (2016)
11. O'Donoughue, P., Robin, O., Berry, A.: Measuring the vibration response of plane panels under stationary and transient mechanical excitations using deflectometry. In: Proceedings of Inter-Noise 2016 Congress, Hamburg, Germany (2016)
12. Martin, N.C., Leehey, P.: Low wavenumber wall pressure measurements using a rectangular membrane as a spatial filter. J. Sound Vib. **52**, 95–120 (1977)
13. Rafaely, B.Z.: Spatial-temporal correlation of a diffuse sound field. J. Acoust. Soc. Am. **107**, 3254–3258 (2000)
14. Corcos, G.M.: The structure of the turbulent pressure field in boundary-layer flows. J. Fluid Mech. **18**, 353–378 (1964)
15. Chaigne, A., Kergomard, J.: Acoustics of Musical Instruments. Springer, New-York (2016)
16. Devivier, C.: Damage identification in layered composite plates using kinematic full-field measurements. Ph.D. thesis, Université de Technologie de Troyes, Troyes, France (2012)
17. Surrel, Y.: Design of phase-detection algorithms insensitive to bias modulation. Appl. Opt. **36**, 805–807(1997)
18. Herráez, M.A., Burton, D.R., Lalor, M.J., Gdeisat, M.A.: Fast two-dimensional phase-unwrapping algorithm based on sorting reliability following a noncontinuous path. Appl. Opt. **41**, 7437–7444 (2002)
19. Devivier, C., Pierron, F., Glynne-Jones, P., Hill, M.: Time-resolved full-field imaging of ultrasonic Lamb waves using deflectometry. Exp. Mech. **56**, 345–357 (2015)
20. Robin, O., Chazot, J.-D., Boulandet, R., Michau, M., Berry, A., Atalla, N.: A plane and thin panel with representative simply supported boundary conditions for laboratory vibroacoustic tests. Acta Acust. United Acust. **102**, 170–182 (2016)